(4)

Stress- and Velocity-Field Evolution in Viscoelastic Planar Contraction Flow

by

Lars Herbert Genieser

B.S.E., Chemical Engineering, Princeton University (1989)
M.S.Ch.E.P., Massachusetts Institute of Technology (1994)

Submitted to the Department of Chemical Engineering in
partial fulfillment of the requirements for the degree of

DOCTOR OF PHILOSOPHY IN CHEMICAL ENGINEERING

at the

MASSACHUSETTS INSTITUTE OF TECHNOLOGY

SEPTEMBER 1997

Author .....
Chemical Engineering
July 16, 1997

Certified by .....
Robert C. Armstrong
Professor of Chemical Engineering
Thesis Supervisor

Certified by .....
Robert A. Brown
Professor of Chemical Engineering
Thesis Supervisor

Accepted by .....
Robert E. Cohen
Professor of Chemical Engineering
Chairman, Committee for Graduate Students

Stress- and Velocity-Field Evolution in Viscoelastic Planar Contraction Flow

by

Lars Herbert Genieser

Submitted to the Department of Chemical Engineering
on July 16, 1997, in Partial Fulfillment of the
Requirements for the Degree of Doctor of Philosophy in
Chemical Engineering

Abstract

Planar contraction flow was used as a model system to investigate two topics in viscoelastic fluid mechanics: 1) the origin and structure of transitions in viscoelastic flow and 2) the transient elongational response of a polymer solution to shearfree flow. The flow cell was adjustable to contraction ratios of 2, 8, or 32. A semidilute polymer solution composed of high molecular weight (MW) polyisobutylene in medium MW polybutene was used as the test fluid. This "Boger" fluid was characterized by a long relaxation time and nearly constant viscosity; inertia had negligible influence on the flow.

Laser Doppler velocimetry (LDV) and light sheet visualization were used to characterize the spatiotemporal structure of, and onset conditions for transition from two-dimensional to three-dimensional, steady flow. The three-dimensional flow had the form of "viscoelastic Görtler" vortices previously observed in other flow geometries. Characteristic length scales of the three-dimensional flow indicated an influential role of curved streamlines around the outer corner. The critical Weissenberg number at onset of instability was determined as a function of contraction ratio; a "viscoelastic Görtler" scaling proved valid. The scaling and structure indicated that the flow transition was driven by interaction of streamwise "elastic" stress with streamline curvature. Onset of a second transition to time-dependent flow at elevated Weissenberg number and/or contraction ratio was detected. LDV measurements and consideration of upstream-channel aspect ratio indicated that the temporal transition was induced by nonideal, three-dimensional boundary conditions.

Flow induced birefringence, in conjunction with LDV, was used to determine the transient elongational viscosity profile along the shearfree centerline. Constitutive models were evaluated with this data; however, it was found that the centerline flow could only excite a linear viscoelastic response, despite the attainment of moderate Hencky strains of 3.5 and high Weissenberg numbers of 2.9. The nonhomogeneous centerline strain-rate profile was much less "efficient" in stretching the polymer molecule than a homogeneous profile. Increase of the flow rate or contraction ratio or tapering the entry region did not improve the "efficiency" of the centerline flow.

Thesis Supervisors: Robert C. Armstrong
Professor
Chemical Engineering

Robert A. Brown
Professor
Chemical Engineering

Acknowledgements

I wish to thank professors Robert Armstrong and Robert Brown for their guidance and counsel throughout the course of this research. Their extensive knowledge of polymer fluid mechanics, in theoretical and experimental contexts, has shaped this thesis; our many constructive discussions have played an essential role in my professional development. I am also grateful to the other members of my thesis committee, professors Robert Cohen and Gareth McKinley, for the valuable perspective and advice which they provided. I would like to acknowledge the National Science Foundation and the E.I. Dupont de Nemours company for providing financial support for this research.

I am fortunate to have had the fellowship of the other members of the Bob^2 research group. You have been a source of stimulating conversation and moral support which lightened my experience in the labs and 66-246. Susan Dusenbery who worked with me as a UROP student deserves a special thanks for her assistance. Over the years I have formed a number of lasting friendships in the Chemical Engineering Department which have enriched my experience - I won't cite names, you know who you are. I am thankful for the support and goodwill of the members of the administrative staff, in particular Arline Benford, throughout my stay at MIT.

Mom and Dad, you have walked this path together with me. You experienced both the exhilarating and wearing moments of my doctoral work, yet could only provide advice from afar; this must have been most frustrating. I am grateful for your support throughout the years. I wish my sister the best in her pursuit of her professional and life goals; Anya, I am thankful for your advice and encouragement.

This thesis is dedicated to

my father,

who first kindled my fascination with science and technology,

and my mother,

who awakened my enthusiasm for art and literature.

Table of Contents

List of Figures

List of Tables

Chapter 1

Introduction

1.1 Motivation

Extrusion and injection molding are only two examples of processes which transform the tens of millions of tonnes of thermoplastics produced in the United States each year into useful, high value-added products. Understanding of the fluid mechanics of viscoelastic polymer melts and solutions is necessary to optimize the economics of these polymer processing operations. The ultimate goal of polymer fluid mechanics research is the development of accurate constitutive equations, derivable from consideration of the molecular structure of the material, in conjunction with efficient numerical solution algorithms. Such a thorough understanding of the structure, process, and property interrelation would allow the prediction of product properties in their end-use applications. Of potentially greater importance is solution of the inverse problem; i.e., given required properties of a given product in an application, an "expert system" would identify specific polymer materials and associated processing operations and parameters as solutions.

At the present time, much work is required to advance the state of the field to the point where development of such an "expert system" could be realistically considered. The development of efficient numerical algorithms which will ultimately allow solution of the set of three-dimensional and time-dependent partial differential equations comprised of the equations of motion and energy and the constitutive equation has advanced considerably; however, further progress is required before the governing equation set can be solved at an acceptable computational cost. Accurate constitutive equations, which relate the stress of a fluid element at a given point in time and space to the strain history, are required. Determination of continuum constitutive equations from details of molecular structure of a polymeric material is an active area of research (Öttinger, 1996). Regardless of whether a constitutive model is derivable from molecular considerations or is purely empirical, its accuracy must be verified by comparison of model predictions with experimental measurements.

Measurement of the response of a viscoelastic fluid to a shear flow can be readily carried out in commercial devices; however, the measurement of the nonlinear elongational response remains a challenge. The utility of information obtained in previous investigations has often been limited by inadequate characterization of the strain history of the test flow (Walters, 1992). Other investigations have carefully characterized the strain history, but the small imposed Hencky strain resulted in only the linear viscoelastic response of the fluid being probed (Quinzani *et al.*, 1995). Accurate experimental characterization of the elongational response remains an important problem since the effects of the elongational response in certain polymer processing operations cannot be ignored. For example, in fiber spinning of high tensile-strength polyethylene, high draw ratios and tensile stresses are attained which act to align the polymer molecules; the alignment results in the fiber having extremely high tensile strength. Conversely, in injection molding operations, the molecular orientation which may be found in the wake of obstacles can result in the formation of weak "weld lines" (Baird and Collias, 1995). Accurate modeling of such operations requires that a constitutive equation correctly represent the elongational response of a fluid.

Onset of instabilities in a polymer process can severely compromise the economics of the operation. Specifically, throughput can be limited by the requirement to run a machine below a critical volumetric flow rate. Alternately, the onset of flow transitions can result in a product having unacceptable properties. An example, shown in Fig. 1.1b, is the "sharkskin" instability which results in a material having low gloss; at sufficiently high flow rates, unstable flow results in complete breakup of the extrudate (cf. Fig. 1.1d) (Piau *et al.*, 1990). Understanding of the mechanisms driving unstable flow could allow more accurate prediction of the economics of a planned process, and possibly reveal ways to achieve high throughput while avoiding flow transitions. Computational resources currently limit numerical simulation of three-dimensional and/or time-dependent viscoelastic instabilities in complex flows. However, better understanding of the physics which underpin instability onset may allow the development of heuristics which allow flow transitions to be predicted and averted.

Common spatio-temporal features of viscoelastic flow instabilities have been noted in work which has been published in the literature; these investigations are reviewed in

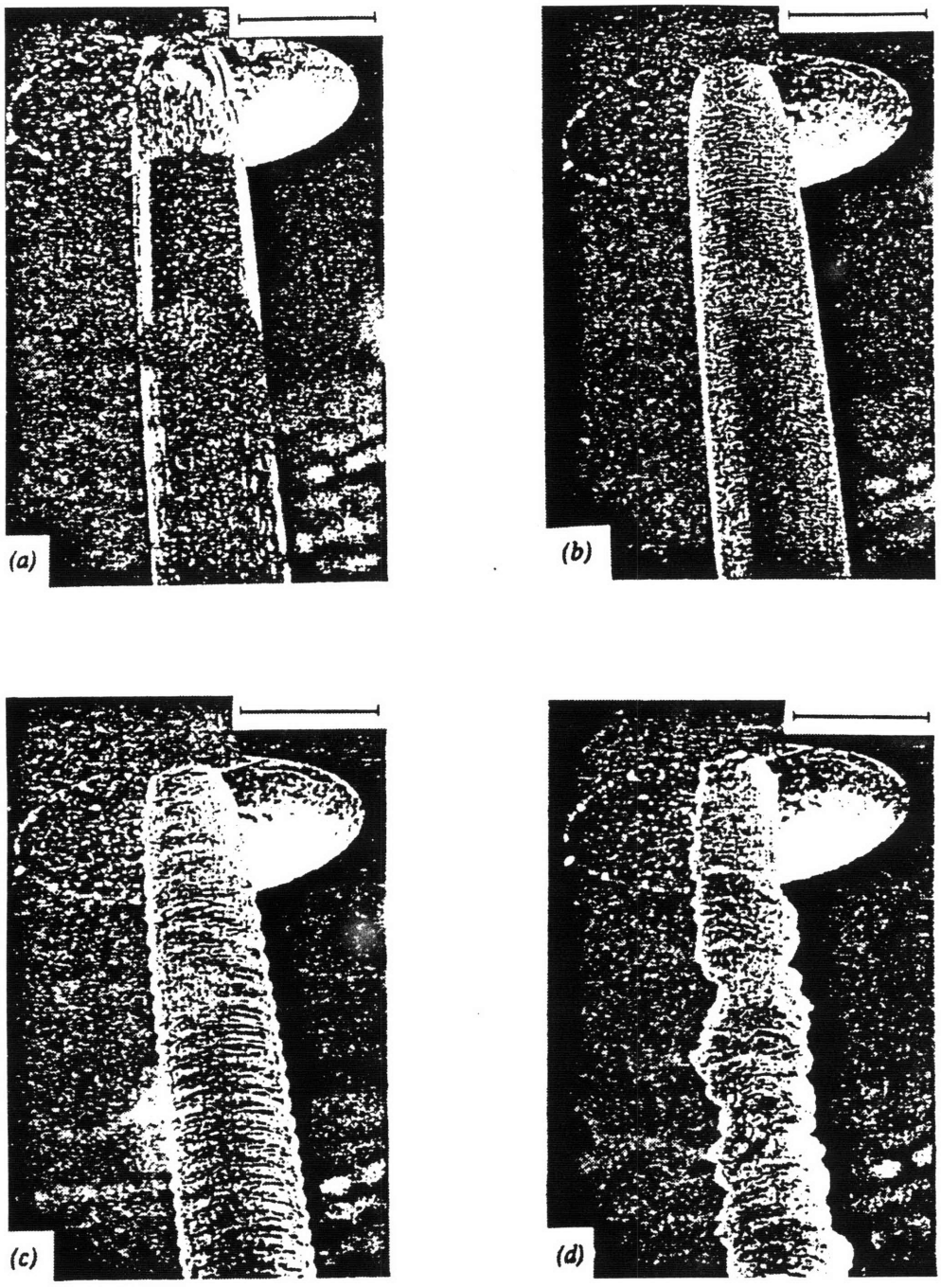

Figure 1.1 Onset of flow instabilities in the extrusion of a silicone gum through an orifice die: (a) ΔP = 50 [kPa], Wi = 0.14; (b) ΔP = 600 [kPa], Wi = 0.30; (c) ΔP = 675 [kPa], Wi = 0.31; (d) 1000 [kPa], Wi = 0.35. (*reproduced from* (Piau *et al.*, 1990)).

Chapter 2. Linear stability and energy analyses of systems with a simple base flow have led to development of the concept that many of these flow instabilities have a common underlying mechanism related to interaction between streamline curvature and streamwise stress (Joo and Shaqfeh, 1992; Joo and Shaqfeh, 1994). This concept has led to development of a scaling which may be applied to complex base flows (McKinley *et al.*, 1996). This scaling has been successfully applied to experimental data from several test flows; however, the body of quantitative data, especially for complex flows, is limited. One should also note that a range of quantitative data for various flows will be required to verify the accuracy of predictions of three-dimensional and/or time-dependent flows, once these become feasible.

The investigations comprising this thesis are also of interest from a fundamental, scientific point of view. Assessment of the accuracy of constitutive equations derived from molecular considerations may provide insight into polymer kinetic theory. Evaluation of the predicted elongational response is of particular interest. A polymer molecule in an elongational flow can achieve an extended and aligned conformation which is fundamentally different from the moderately stretched and tumbling configuration which occurs in a shear flow (Larson, 1988). Identification and characterization of viscoelastic flow instabilities provides insight into the interaction of a polymer molecule with a surrounding flow field (Joo and Shaqfeh, 1992; Joo and Shaqfeh, 1994). Viscoelastic instabilities are also interesting from a mathematical perspective in that they are physical manifestations of phenomena anticipated by nonlinear dynamical theory, a field which has seen an explosion of activity over the last two decades (Strogatz, 1995; Guckenheimer and Holmes, 1983).

1.2 Experimental Approach

A typical industrial polymer processing flow is highly complex, as illustrated by the representation of a pipe extrusion operation in Fig. 1.2. To render the problem tractable, such an operation is generally decomposed into individual subproblems of which the flow geometry may be further idealized. For example, the flow from the barrel of the extruder into the annular slit around the mandrel can be represented as an entry flow. Since the gap width of the annular slit, d, is often much smaller than its radial distance from the center of

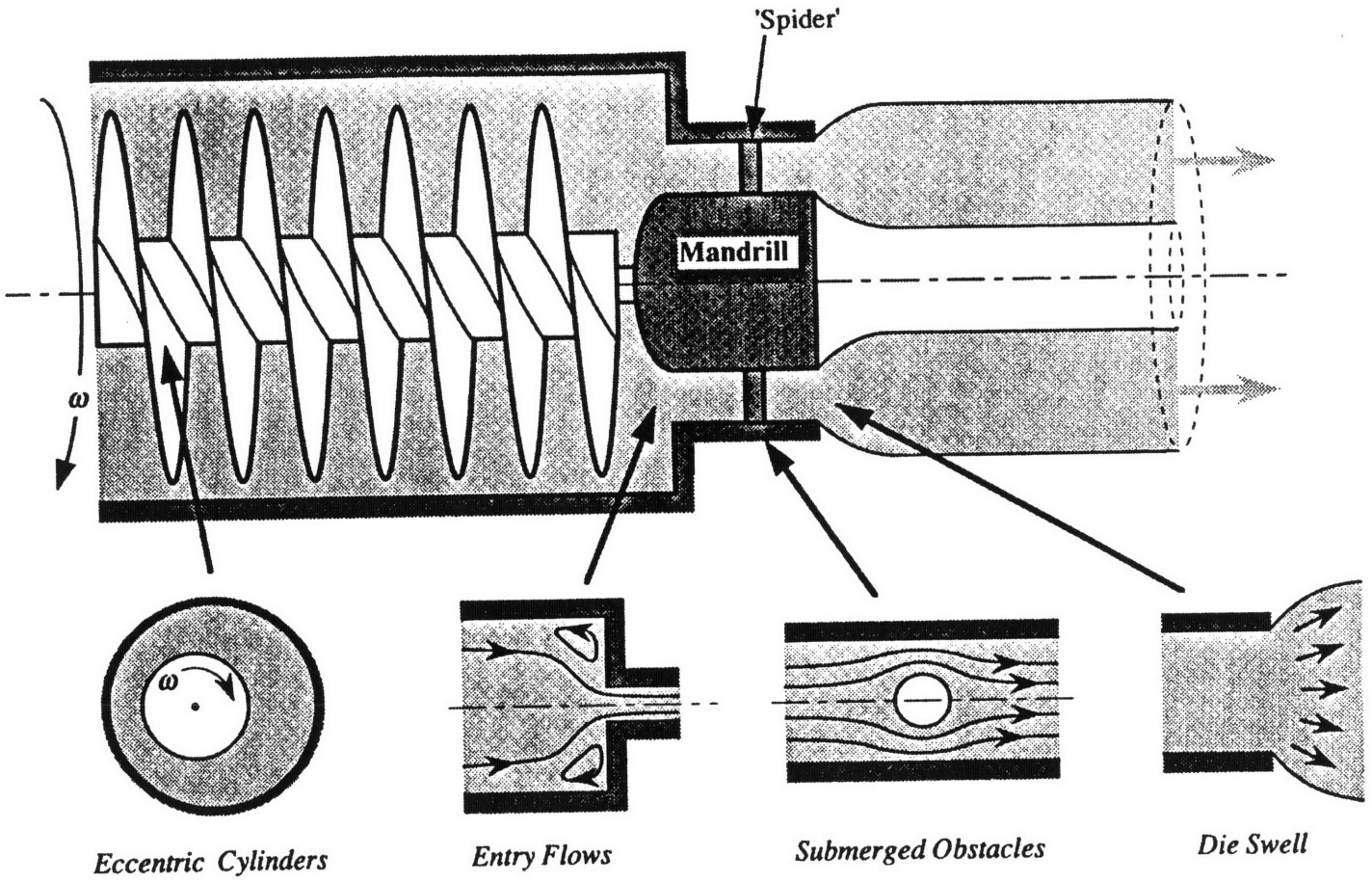

Figure 1.2 Schematic diagram of a polymer pipe extrusion process and its decomposition into a number of simpler subproblems. (*reproduced from* (McKinley, 1991)).

the mandrel, R, the curvature, d/R, is small, and the entry flow can be approximated by flow through an abrupt planar contraction. Examples of other subproblems are shown in Fig. 1.2. One should be aware that the utility of the problem decomposition approach is primarily in the advancement of fundamental understanding of polymer fluid mechanics and the development of analytical and numerical tools. Because a viscoelastic fluid has "memory" of its deformation history, the flow field at a given point in a processing operation will affect the flow field at all points farther downstream in the operation. Consequently, accurate modeling of a polymer processing operation could not be conducted by solving individual subproblems and "combining" them to reconstruct the entire process.

A good set of quantitative experimental data exists for viscoelastic flow through the axisymmetric contraction. In contrast, most of the previous investigations of instabilities in planar contraction flow have been qualitative. Furthermore, several of these prior studies did not fully characterize the shear-flow rheology of the test fluid. Inertia was not negligible, and it was difficult to distinguish the influence of inertia on the velocity field from that of memory of nonlinear elastic effects. Hence, quantitative characterization of the onset and spatio-temporal structure of instabilities in the planar contraction is needed to complement the available data. The flow in the planar contraction (cf. Fig. 1.3) is also well suited for the characterization of the elongational response of a viscoelastic fluid. Specifically, throughout most of the flow, the rate-of-strain tensor is complex; i.e., has both elongational and shear contributions. However, because of symmetry, the flow on the centerplane is shearfree and exclusively elongational. As discussed in Chapters 4 and 6, direct interpretation of a flow induced birefringence (FIB) measurement in terms of the stress field requires a flow which is two-dimensional and planar. Since the flow on the centerplane of the planar contraction is two-dimensional, planar, and shearfree, it is well suited for the measurement of the transient elongational response of a viscoelastic fluid. In consequence, the abrupt planar contraction is used as the test geometry throughout this thesis.

Several non-invasive, optical measurement techniques, described in detail in Chapter 3, are applied in the investigations presented in Chapters 5 and 6 to obtain velocity- and stress-field information. Light sheet visualization is useful in observing the form of the streamlines within a given two-dimensional plane ("streaklines") and thereby obtaining

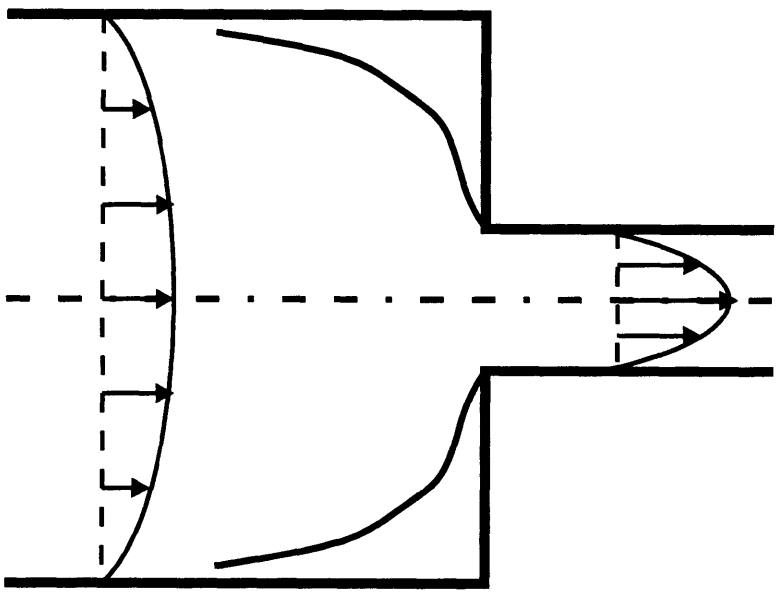

Figure 1.3 Flow through the planar contraction; the flow on the centerline is shearfree.

qualitative velocity field information. By taking successive "slices" in space, a qualitative, three-dimensional representation of the velocity field is reconstructed. Such qualitative, full-field velocity information is complemented by the quantitative laser Doppler velocimetry (LDV) technique. The LDV system used for the experiments of this thesis can acquire highly accurate velocity information at a given point in space. A scan can also be performed across a given line to characterize quantitatively variation of the velocity field in space. Alternately, time-series velocity data can be acquired at a given point. Application of the light sheet visualization and LDV techniques allows for extensive and accurate characterization of the spatio-temporal structure of and onset conditions for viscoelastic flow instabilities. The flow induced birefringence (FIB) technique, in conjunction with the linear stress-optical rule, is used to obtain quantitative, pointwise stress-field information for two-dimensional, planar flows. Such stress-field information, in conjunction with velocity-field information obtained via LDV, is used to characterize the viscoelastic response of the fluid to the elongational flow along the shearfree centerline.

Viscoelastic fluids differ in several fundamental ways from the Newtonian fluids which are familiar from everyday experience. The characteristics of viscoelastic fluids and the constitutive models used to describe them are presented in detail in Chapter 4, a brief description of some essential characteristics is given here. The stress tensor of a Newtonian fluid element responds instantaneously and exclusively to the local rate-of-strain tensor. In contrast, the stress tensor of a viscoelastic fluid element is affected not only by the current rate-of-strain tensor, but also the entire prior strain history of the element. Strains experienced more recently have a greater effect on the current stress than strains experienced farther in the past; viscoelastic fluids are described as having a "fading memory". The importance of memory effects in the determination of the stress and velocity field for a given flow is parameterized by the Deborah number

$$De \equiv \frac{\lambda}{t_{flow}} \tag{1.1}$$

where λ represents a relaxation time characteristic of the viscoelastic material and t_{flow} represents a characteristic timescale of the process.[1] In the limit $De(\dot{\gamma}) = 0$, obtained for an

inelastic fluid or a viscoelastic fluid in a very slow flow, a fluid element in the flow has essentially no memory of its previous history and behaves inelastically. On the other hand, a perfectly elastic solid, which does not forget its past history, is characterized by $De(\dot{\gamma}) \rightarrow \infty$. Viscoelastic flows are characterized by intermediate values, $De(\dot{\gamma}) \sim O(1)$.

Viscoelastic materials also exhibit nonlinear behavior which distinguishes them from Newtonian fluids. For example, viscoelastic fluids exhibit normal stresses in simple shear flow. Viscoelastic fluids can also exhibit elongational thickening; i.e., the elongational viscosity of a viscoelastic fluid can rise to a value 1000 times or greater than the viscosity. In contrast, the ratio of the elongational viscosity, $\bar{\eta}$, to the viscosity of a Newtonian fluid, μ, is constant and depends only on the class of elongational flow; e.g. for planar elongational flow $\bar{\eta}_1/\mu = 4$. The importance of nonlinear effects arising from the elastic nature of a flow is parameterized by the Weissenberg number

$$Wi \equiv \lambda \dot{\Gamma} \tag{1.2}$$

where $\dot{\Gamma}$ represents a characteristic strain rate of the flow. For a flow characterized by Wi << 1, the fluid will respond in a Newtonian manner; e.g., effects such as shear thinning, elongational thickening, and shear-induced normal stresses will be negligible (Bird *et al.*, 1987a). Note that Wi and De are often used interchangeably in the literature; however, the definitions given in this and the preceding paragraph are used consistently throughout this thesis.

Polymer melts are of greater industrial and economic importance than polymer solutions. However, polymer solutions have several characteristics which have favored their use in the experiments presented in this thesis. Polymer solutions are fluid at room temperature, so that the pressures required for conducting experiments are order one atmosphere. The maximum pressure differential used for the experiments of this thesis was 700 [kPa]. The use of moderate temperatures and pressures simplifies the design of experiments which use polymer solutions instead of polymer melts. Polymer solutions have the same essential characteristics of viscoelastic fluids as polymer melts; experiments conducted

1. M. Reiner coined the term "Deborah number"; his illustrative and amusing monologue on the origin and utility of this dimensionless parameter may be found in (Reiner, 1964).

with polymer solutions in complex flows are generally suitable for the evaluation of the accuracy of isothermal numerical flow simulations. Although polymer melts are generally of greater technological interest, polymer solutions are used in some industrial processes; e.g., the fiber spinning of cellulose triacetate (Rodriguez, 1989).

The polymer solutions used for the experiments of this thesis fall into the class of Boger fluids. These materials are characterized by a viscosity which is nearly independent of shear rate; this characteristic is obtained by dissolving a low concentration of a high molecular weight (MW) polymer in a highly viscous solvent such that the viscosity of the solvent dominates over the contribution of the high MW polymer. However, one should note that the Boger fluids used in this thesis *do* exhibit shear thinning of the first normal stress coefficient. The characteristic of constant viscosity potentially simplifies modeling the rheology of the Boger fluid and numerical simulation of flow. The property of high and constant viscosity, in conjunction with long relaxation times, also results in inertia being negligible for most test flows; this simplifies interpretation of experimental results and corresponding numerical flow simulations.

1.3 Thesis Goals

The discussion in §1.1 provided motivation for the characterization of viscoelastic flow instabilities and measurement of the elongational response of viscoelastic fluids. Section 1.2 gave a brief outline of the reasoning which has led to the selection of a planar contraction and Boger fluid as the test system. Experimental techniques used to acquire stress- and velocity-field information were introduced.

Literature reviews of previous investigations of viscoelastic flow instabilities are presented in the first part of Chapter 2. Investigations which highlight the importance and the difficulty of obtaining well-characterized elongational material function data for polymer solutions are discussed in the second part of Chapter 2. The best characterized measurements to date of the elongational response of polymer solutions are then described. Chapter 3 presents the fluid handling system and test geometry used throughout the thesis and discusses characteristics and limitations of the optical measurement techniques of light sheet visualization, laser Doppler velocimetry, and flow induced birefringence. In the first

part of Chapter 4, material functions which characterize the response of viscoelastic fluids to shear and shearfree flows and experimental techniques used in the determination of these functions are presented. Characteristics of the constitutive models used throughout this thesis to model the rheological response of the test fluid are described. The second part of Chapter 4 presents in detail the experimentally determined shear-flow rheology of the test fluid and the parameter fits of constitutive models.

In Chapter 5, the spatiotemporal structure and conditions for onset of a viscoelastic instability in planar contraction flow are described; the study was conducted with specific objectives required to advance the field.

- The spatio-temporal structure of the velocity field of the instability is qualitatively characterized via light sheet visualization. The effects of inertia are negligible; this facilitates comparison of the structure of the instability in the planar contraction with the structure of instabilities observed in other geometries (e.g. the axisymmetric contraction).
- The velocity field is quantitatively characterized in select regions of the unstable flow via LDV. This information provides a "benchmark" set of data for the evaluation of three-dimensional and/or time-dependent numerical simulations in the future. The quantitative velocity-field information also serves to identify regions of flow and flow conditions (i.e. volumetric flow rate) for which FIB measurements are directly interpretable in terms of stress.
- The velocity-field data obtained via flow visualization and LDV are used to determine whether the interaction of streamline curvature with streamwise stress drives the instability. Specifically, the region in the flow where the instability is localized and the scaling of the spatial extent of the instability with geometrical parameters are identified. The scaling of the critical Weissenberg number for instability onset with geometrical parameters is determined; a scaling criterion for onset of viscoelastic flow instabilities (McKinley *et al.*, 1996) is evaluated with this information.

In Chapter 6, the experimental determination of the transient elongational response of the test fluid to the nonhomogeneous planar elongational flow on the centerline of the contraction geometry is discussed; the investigation enables the achievement of specific goals.

- Experimental measurements are conducted in test geometries of different contraction ratios to allow the attainment of different total Hencky strains; the volumetric flow rate is varied to adjust the magnitude of the centerline strain-rate profile. Both the elongational strain rate and the stress tensor are measured in a quantitative manner along the centerline; from this information, a well-characterized transient elongational viscosity profile is determined. The data are used to evaluate the accuracy of the predictions of nonlinear constitutive equations.
- The experimental results are also compared with the predictions of linear constitutive equations under different flow conditions. This comparison allows evaluation of the efficacy of the transient elongational flow on the centerline of the planar contraction in stimulating a quasilinear or nonlinear viscoelastic response.
- Limitations of the FIB technique in obtaining quantitative stress-field information in planar contraction flow are assessed. Specifically, the effect of stress-field inhomogeneities within the cross-sectional area sampled by the probe beam and inhomogeneities along the beam path on the measured birefringence and calculated "apparent" stress tensor are evaluated.

Essential findings and conclusions of this thesis are summarized in Chapter 7; suggestions for future research are given.

Chapter 2

Literature Review

Two aspects of viscoelastic flow through the planar contraction were considered for this thesis. Transition from the two-dimensional, steady base flow to three-dimensional and time-dependent flow is linked to interaction between streamline curvature and streamwise stress in Chapter 5. A more restricted region of the flow is used in Chapter 6; the viscoelastic response to the transient shearfree flow on the centerline of the planar contraction is considered. This Chapter reviews work previously reported in the literature which serves to motivate and is drawn on in the interpretation of investigations presented in Chapters 5 and 6.

2.1 "Elasticity-Driven" Flow Transitions

Previous investigations of viscoelastic flow through diverse geometries have noted transitions in the structure of the flow field associated with the "elastic" nature of the flow; time-dependent and nonlinear rheological character of the fluids in the flow. The investigation presented in Chapter 5 of this thesis has focused on the classification of *global* flow transitions in the planar contraction; i.e., those which occur over the longest characteristic length scale of the geometry, the upstream half-height. In accordance with this emphasis, global flow transitions observed in previous investigations are discussed in this Section.

Transitions associated with two-dimensional rearrangement of the flow field in different geometries with complex flow (having both shear and elongational components of the rate-of-strain tensor) are addressed in §2.1.1. These rearrangements precede transition to three-dimensional and/or time-dependent behavior in complex flow, which is discussed in §2.1.2. Transition to three-dimensional and/or time-dependent flow has also been noted in simple, viscometric flows, in which they have been attributed to the interaction of streamwise stress with streamline curvature. A scaling concept which *can* be used to understand critical conditions associated with such stress/curvature interaction in complex flows is

presented in §2.1.3. This scaling is applied to the transition observed in the planar contraction in Chapter 5.

The review provided in this Section is intended to motivate the study of flow transitions in the planar contraction, presented in Chapter 5, and provide background information useful for interpreting the results presented in this thesis. The review given here is not intended to be comprehensive and is restricted in several respects. Transitions in the flow field localized to the reentrant corner in abrupt contraction flows have been observed. These are not discussed here; rather, the global flow transitions akin to those which were the focus of the study presented in Chapter 5 are discussed. Studies in which the inertia was negligible, i.e. flow transitions were solely a consequence of the viscoelastic nature of the fluid are emphasized here. Investigations in which inertia was significant are presented only where there are an insufficient number of investigations for which the flows were inertialess for a given test geometry. A polymer solution was used as the viscoelastic test fluid for the experiments comprising this thesis; consequently, the literature reviewed is restricted to studies conducted with polymer solutions. Since polymer solutions were used, all the flows discussed here may be considered isothermal. Note that at the end of §2.1.2 only a brief comparison of transition behavior among the different geometries is given. A more thorough discussion is deferred to §5.4, so that the transition behavior observed for viscoelastic flow through the planar contraction in this study may be included. Throughout this Section, all of the flows considered have a two-dimensional and steady base state.

2.1.1 Two-Dimensional Velocity-Field Rearrangement

Two-dimensional rearrangement associated with the elastic nature of the flow has been noted in diverse geometries of complex flow. In this Section, rearrangement phenomena occurring in the driven-cavity and in the cylinder-in-channel geometries are presented first. Rearrangement in contraction geometries is then discussed; the axisymmetric and planar contraction flows exhibit similar behavior, onset of a "diverging streamline" pattern is observed. A qualitative interpretation of the mechanism driving the transition to diverg-

ing streamlines, particularly for the case of contraction flows, is given at the end of this Section.

Cylinder in Channel

Viscoelastic flow around a cylinder in a channel is a nominally two-dimensional and planar geometry which has been studied by Byars (1996) and McKinley (1991). The formulation of the polyisobutylene based Boger fluid used was similar to the fluid used in the investigation for this thesis; the rheology was similar in nature, although the viscosity and the relaxation time were lower than that of the test fluid described in Chapter 4. Inertia was negligible in the test runs. At non-zero Weissenberg number, $0 < \mathrm{Wi} \lesssim 1$, a two-dimensional rearrangement of the flow field was noted; specifically, downstream of the cylinder there was a shift of the streamlines in the downstream direction.

Driven Cavity

The driven-cavity geometry is schematically illustrated in Fig. 2.1. The base flow in the driven cavity is nominally two-dimensional and planar, i.e., invariant in the "neutral" x-direction. The rate-of-strain tensor has both shear and elongational components (complex flow). The evolution of the velocity field for increasing values of the Weissenberg number, Wi, for a viscoelastic fluid was studied by Pakdel and McKinley (1996).[1] The formulation and rheology of the polyisobutylene based Boger test fluid were similar to the test fluid used for the investigations of this thesis and described in Chapter 4; inertia was negligible in the test runs. A two-dimensional flow rearrangement was observed at non-zero Wi (Pakdel *et al.*, 1997). Specifically, the elliptic point of the flow recirculation, initially located at the midpoint of the z-dimension (at $z = L/2$), shifted in the upstream direction (to $z < L/2$).

Axisymmetric Contraction

Onset of two-dimensional flow rearrangement in the form of streamlines which diverge from the centerline has been observed in the axisymmetric abrupt contraction. In

1. Wi quantifies the importance of nonlinear effects, associated with the "elastic" nature of a flow, in determining the stress and velocity fields for the flow (cf. §1.1).

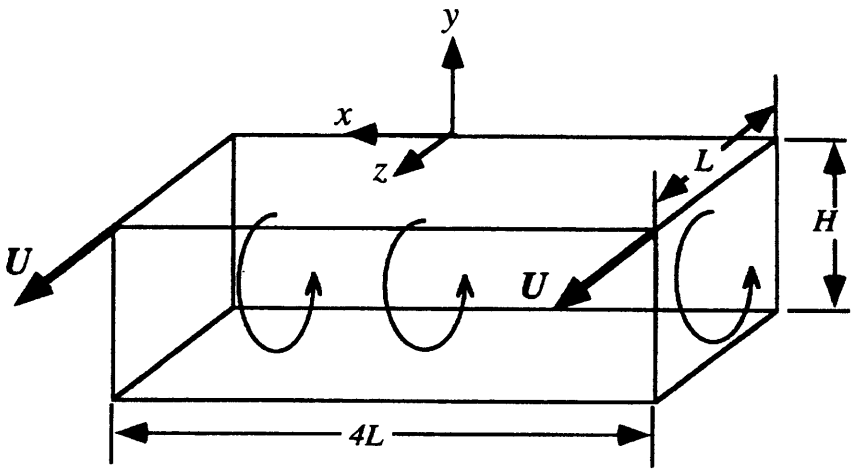

Figure 2.1 Schematic diagram of two-dimensional base flow in the driven cavity. No-slip conditions hold for all of the bounding surfaces. All the boundaries are fixed, except the top "lid" which moves at a constant velocity, U. (*Modified from* (Pakdel and McKinley, 1996)).

the McKinley et al. (1991) study of axisymmetric contraction flow; diverging flow in the rz-plane was noted for contraction ratios of R_{Up}/R_{Dn} = 3, 4, and 5; a streakline image is reproduced in Fig. 2.2. An increase in maximum dimensionless centerline strain rate with Wi associated with the transition to diverging flow was also found. The ratio of the mean upstream velocity to the minimum dimensionless velocity was greatest for the case of low contraction ratios; i.e. the diverging flow was most pronounced. McKinley et al. did not observe diverging flow in geometries for which $R_{Up}/R_{Dn} \geq 6$. The distance of the point of minimum centerline velocity upstream from the contraction plane increased monotonically, although not linearly proportionally, with upstream tube radius, R_{Up}.

Binding and Walters (1988) investigated viscoelastic flow through an axisymmetric contraction geometry of ratio R_{Up}/R_{Dn} = 14. A polyacrylamide-based Boger fluid, of constant viscosity, was used; inertia was negligible in the experiments. No diverging flow was noted in the flow through the axisymmetric contraction. Although Binding and Walters did not investigate flow through geometries of lower contraction ratio, the absence of diverging flow in a large ratio axisymmetric contraction is consistent with the study of McKinley et al. in which diverging flow was not noted for $R_{Up}/R_{Dn} \geq 6$.

Planar Contraction

Only a limited number of studies of the viscoelastic flow of polymer solutions through planar contraction geometries have been conducted. Evans and Walters (Evans and Walters, 1989) noted a two-dimensional rearrangement of the velocity field at high flow rates in a planar contraction of upstream to downstream half-height ratio H/h = 4. Specifically, for $Wi_{Dn} \geq 3.8$, a pattern of diverging streamlines upstream of the contraction plane was noted.[2] A polyacrylamide solution which exhibited shear thinning of the viscosity was used in the experiments. In consequence, inertia was a significant factor; $Re_{Dn} \geq 130$ at the flow rate for which diverging flow was observed.[3] The interaction of inertial with elastic phenomena can give rise to essentially different behavior from that observed under inertialess conditions (Joseph, 1990); as a result, it is difficult to unambiguously interpret

2. The shear-rate-dependent Weissenberg number based on downstream flow parameters, Wi_{Dn}, is defined in §5.1.

3. The shear-rate-dependent Reynolds number based on downstream flow parameters, Re_{Dn}, is defined in §4.5.2.

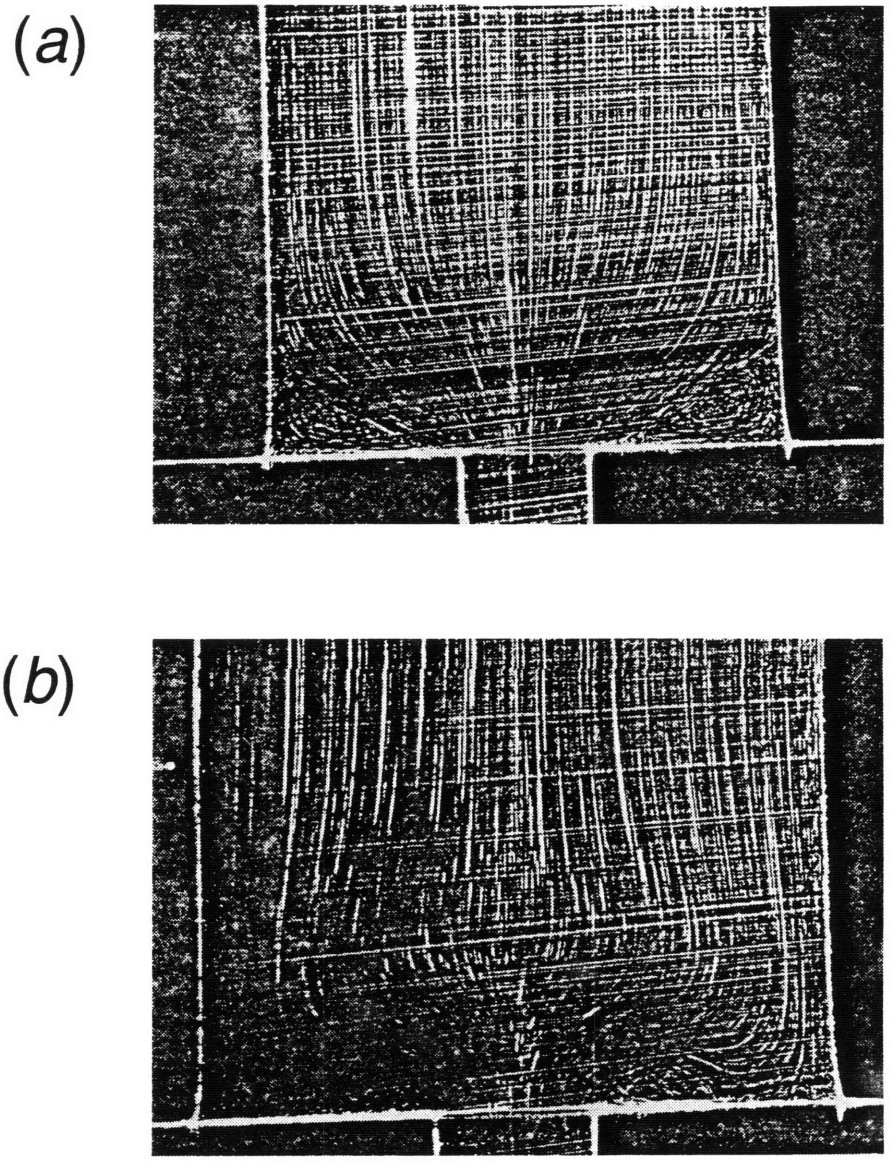

Figure 2.2 Streakline images of viscoelastic flow through a 4:1 axisymmetric contraction: (a) low flow rate (Wi = 0.90), continuously converging streamlines; (b) elevated flow rate (Wi = 3.40), diverging streamlines. (*Reproduced from* (McKinley, 1991)).

the rearrangement to diverging streamlines as arising solely from the "elastic" nature of the flow.

The studies of Chiba et al. (Chiba *et al.*, 1990; Chiba *et al.*, 1992) used shear-thinning, aqueous polyacrylamide (PAC) solutions with solute concentrations of 0.1% and 0.5% flowing through planar contractions. In H/h = 3.3 and 5 planar contraction geometries, Chiba et al. observed diverging flow. In the case of the 5:1 contraction, the critical flow rate corresponded to $Re_{Dn} = 26$; Wi_{Dn} was not known since the first normal stress coefficient of the test fluid was not measured. For the 3.3:1 contraction, the critical flow rate was not reported. Onset of a diverging flow field was not found for the 10:1 contraction. As in the Evans and Walters study, inertia was a significant factor, complicating interpretation of the results.

In contrast to the studies of Chiba et al. and Evans and Walters, inertia was not a significant factor in the investigation conducted by Binding and Walters (1988) of flow through a planar contraction of ratio H/h = 14.4. Binding and Walters used a polyacrylamide-based Boger fluid, which was identical to that used in their study described in the Section above. Diverging flow was noted in the planar contraction at a flow rate corresponding to $Wi_{Dn} = 0.6$ and $Re_{Dn} = 0.01$.

The investigations discussed above have revealed a similar evolution with Weissenberg number for viscoelastic flows through both planar and axisymmetric geometries; i.e., two-dimensional flow rearrangement to a pattern of "diverging streamlines". This common behavior was noted for Boger and shear-thinning fluids, solutions composed with organic and with aqueous solvents. Specifically, as the Wi is increased above a critical value, diverging streamlines are noted; associated with this flow field is an increase in the maximum dimensionless centerline strain rate. The diverging flow behavior is most pronounced for geometries of low contraction ratio. In fact, two of the studies (Binding and Walters, 1988; McKinley *et al.*, 1991) indicated that diverging flow did not occur for axisymmetric geometries of large contraction ratio.

The precise mechanism driving the diverging flow has not been elucidated; however, it is probable that both shear and elongational components of the strain-rate field upstream of the contraction plane play a role. A mechanism suggested by McKinley et al. (1991) is

discussed here. The fluid near the walls upstream of the contraction plane experiences a much higher shear component of the rate-of-strain tensor than the fluid near the centerline. This elevated shear rate induces shear-thinning of the fluid elasticity. In contrast, near the centerline, the shear contribution is low but the elongational contribution to the rate-of-strain tensor is high. The elongational strain rate generally has an elasticity-thickening effect on unstructured polymer solutions (although the elongation stress-growth response is only slightly higher than predicted by linear viscoelasticity for the flow along the centerline of abrupt contractions - see Chapter 6). Because of the elasticity thinning near the upstream wall and possible thickening near the centerline, the fluid flow redistributes from the center of the flow to the region adjacent to the upstream walls, resulting in streamlines which diverge from the centerline.

This reasoning is consistent with the observation that lower contraction ratio geometries in both the planar and axisymmetric contractions have more pronounced diverging flow behavior (lower centerline velocity minimum relative to mean upstream velocity, $v_z/\langle v_z\rangle_{Up}$) than higher contraction ratio configurations. For example, it was discussed above that in the investigation of McKinley et al. (1991) of viscoelastic flow through the axisymmetric contraction, diverging flow was noted for $R_{Up}/R_{Dn} \leq 5$ but not for $R_{Up}/R_{Dn} \geq 6$. Specifically, the region of high elongational strain rate is primarily governed by the flow near the downstream slit entrance; the influence of the contraction ratio on elongational thickening is therefore minimal (cf. Chapter 6). In contrast, the shear rate of the flow adjacent to the upstream wall decreases with increasing contraction ratio. Hence, a less substantial, or even nonexistent diverging flow is observed for geometries of high contraction ratio. The argument also is consistent with the differences in diverging flow behavior observed for the axisymmetric and planar contraction geometries. The upstream-wall shear rate for fully-developed flow will decrease as $(H/h)^{-2}$ for the planar contraction but as $(R_{Up}/R_{Dn})^{-3}$ for the axisymmetric contraction. This is consistent with the observation that the maximum contraction ratio for which diverging flow can be observed is typically greater for planar contraction flow than axisymmetric contraction flow. For example, in the study of Binding and Walters (1988) flow of a specific test fluid through the planar and axisymmetric contractions was investigated. The contraction ratio for the geometries was nearly identical, $H/h \approx R_{Up}/R_{Dn} \approx 14$; however, diverging flow was observed in the pla-

nar contraction but not in the axisymmetric contraction. The effect of contraction ratio on diverging-flow behavior is revisited during the discussion of the study presented in Chapter 5.

More detailed understanding of the mechanism driving transition to diverging flow will require numerical simulations which accurately incorporate both the shear and elongational rheological response of the test fluids. Such simulations may also prove useful in identifying common bases of two-dimensional velocity-field rearrangement phenomena shared by different flow geometries; e.g., the abrupt contraction and driven-cavity flows. Note that observation of the diverging flow behavior underscores the importance of the experimental investigation of complex viscoelastic flows. Diverging of the streamlines in flow through abrupt contractions at elevated Weissenberg number has not been not noted in numerical simulations (Coates, 1992). The absence of this flow rearrangement may indicate that the constitutive equation used in the simulation did not fully capture the rheological character of the fluid; in particular, the response of the fluid to a rate-of-strain field with a strong elongational component may not have been accurately represented.

2.1.2 Transitions to Three-Dimensional and/or Time-Dependent Flow Driven by Interaction of Streamline Curvature with Streamwise Stress

Previous investigations have indicated that the interaction of streamwise elastic stresses with streamline curvature may induce flow transitions in diverse flow fields, which have rate-of-strain tensors which have exclusively shear contributions or have both shear and elongational contributions (complex flow). Studies of simple viscometric flows, in which only shear contributes to the velocity gradient field, are discussed first; these flow ate amenable to treatment with analytical mathematical techniques. Observations of transitions in complex flows, which more closely resemble aspects of industrial processes, are then presented. Discussion of a scaling approach to consideration of stress/curvature interaction in complex flows is deferred to §2.1.3.

Viscometric Flows

Couette Cell

The spatial and temporal structure of flow after an elastically-driven transition in Couette cell flow in the annular gap between two concentric cylinders was described in the paper by Larson et al. (1990). The geometry was designed to approximate the small gap limit,

$$\delta = (R_2 - R_1)/R_1 \rightarrow 0 \tag{2.1}$$

where R_2 is the radius at the wall of the outer cylinder, R_1, the radius of the inner cylinder, and (R_2 - R_1) denotes the gap width. Larson et al. used a constant viscosity Boger fluid so that inertia was negligible, Re << 1. When a critical shear rate was exceeded, the flow underwent a transition from axisymmetric to three-dimensional flow. Specifically, flow visualization revealed toroidal vortex structures which were evenly spaced along the axis of the cylinders. Throughout the remainder of this discussion these structures will be termed "Görtler-like vortices"; the rationale for this terminology is made clear below. The structure of the flow resembled that of the Taylor-Couette flow after onset of instability; however, since inertia was insignificant, the transition was exclusively an elastic phenomenon.

Baumert and Muller (Baumert and Muller, 1995) characterized the flow evolution from start-up of flow for runs of successively increasing Weissenberg number (Wi). They used light sheet visualization in conjunction with digital image processing to determine the onset Wi and observe the transient evolution of the flow field. For low Wi < 1.50 the flow remained in the two-dimensional, steady base state for the entire duration of observation. At intermediate Weissenberg number, 1.50 ≤ Wi ≤ 3.00, a direct transition from the base flow state to a three-dimensional and steady state of "Görtler-like" vortices evenly spaced along the cylinder axis was observed. The elapsed time from start-up to onset of the instability was long, ranging from 39.0×10^3 [s] for the lower shear rate (Wi = 1.50) to 5.1×10^3 [s] for the higher shear rate (Wi = 3.00). Baumert and Muller did not make the quantitative amplitude measurements required to definitively classify the bifurcation at onset of instability; however, indications of hysteretic behavior were observed and they

believed the bifurcation to be subcritical. This is consistent with the nonlinear analysis of Sureshkumar et al. which predicted a subcritical bifurcation from the base state for the case of narrow-gap viscoelastic Couette flow (Sureshkumar *et al.*, 1994). Baumert and Muller noted a different time evolution sequence when the Wi was increased to a high value, $Wi \geq 3.75$. Specifically, for the case of $Wi = 3.75$ they found that after a brief induction time of 0.18×10^3 [s] axisymmetric Görtler-like vortices formed which moved along the axial length of the cylinder, irregularly oscillating about a mean axial position. After a total of 3.1×10^3 [s] the spatio-temporal structure became regular; pairs of vortices were formed at fixed, evenly spaced axial positions and moved away from each other in the axial direction until two vortices met at a "cell boundary" and were annihilated. After a total induction time of 4.1×10^3 [s], the time-dependent behavior ceased; steady, axisymmetric, evenly-spaced vortices persisted. A three-dimensional schematic diagram and an rz-planform of the spatial structure of this persistent state, inferred from flow visualization, is shown in Fig. 2.3. A similar transition sequence was observed for flows of higher Wi, although the duration of each stage in the transient evolution sequence was of shorter time.

Larson et al. (Larson *et al.*, 1990) investigated the elastically-driven flow transition in the Couette cell via linear analysis. Using the Oldroyd-B constitutive equation they correctly predicted that the critical Weissenberg number, Wi_{Crit}, for the onset of instability was related to the dimensionless gap width, δ (defined in eq. (2.1)), and a constant parameter, M_{crit}, as

$$Wi_{crit} = \delta^{-1/2} M_{crit} \tag{2.2}$$

Northey et al. (1992) numerically computed the solution for the nonlinear equation set describing flow of an upper convected Maxwell fluid in the Couette cell with dimensionless gap widths in the range $0.01 \leq \delta \leq 0.1$. The computation was time-dependent and performed over a domain in the rz-plane. The computed solution had the form of pairs of counter-rotating vortices which were nested in the radial (r-) direction. These vortices were "born" at the bounding wall of the inner cylinder, moved outward (in the positive r-direction), and "died" at the bounding wall of the outer cylinder. A supercritical Hopf

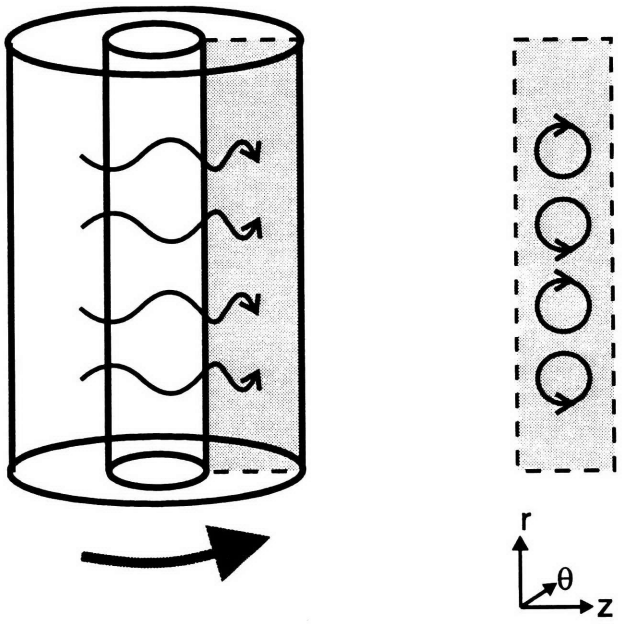

Figure 2.3 Three-dimensional view and rz-planform of the spatial structure of the flow after transition to three-dimensional, steady flow inferred from light sheet visualization of flow in the Couette cell conducted by Baumert and Muller (1995).

bifurcation was associated with the transition from the two-dimensional, steady base flow to the time-dependent, three-dimensional state. A limitation of the work of Northey et al. (1992) was that since the computational domain was two-dimensional only axisymmetric solutions could be computed; nonaxisymmetric modes, e.g. "barber-pole" structures, could not be computed. This limitation is highlighted by the linear analysis conducted by Joo and Shaqfeh (1994, 1992), which indicated that of two possible modes of flow to which transition could occur, axisymmetric and non-axisymmetric, the non-axisymmetric mode was the more dangerous. Joo and Shaqfeh also applied an energy analysis to obtain insight into the mechanism driving the flow transition. A numerical nonlinear analysis conducted by Sureshkumar et al. (1994) indicated that the solution branch corresponding to the non-axisymmetric mode was itself unstable. Although the computations of Sureshkumar et al. (1994) were not pursued beyond the point of identifying the stability of this branch, it is possible that the stable solution to which the system ultimately evolves after bifurcation from the base flow is a nonlinear axisymmetric state. This would be consistent with the experimental observations of Baumert and Muller (1995). These experimental observations and theoretical investigations of viscoelastic Couette flow revealed that the flow transition was induced by interaction between the curvature of the streamlines and the normal "elastic" stresses along the streamlines associated with the high molecular weight polymer component.

Recently, work has been conducted regarding the onset of Taylor-like instabilities in a narrow-gap Couette cell for which both inertial (parameterized with the Reynolds number, Re) and time-dependent elastic effects (parameterized via the Deborah number, De) were significant. Renardy et al. (1996) found that a bifurcation of codimension-2 occurred when either two Hopf modes, or a Hopf and a steady mode were simultaneously at criticality. They also determined via a nonlinear analysis, that unless the ratio De/Re was very small, a finite transition associated with a subcritical bifurcation occurred at the limit of stability of the base Couette flow, in agreement with the prior results of Sureshkumar et al. (1994).

Cone and Plate

Onset and structure of an elastically-driven flow transition in the viscometric cone-and-plate flow, which bore resemblance to that observed in the Taylor-Couette flow, was

experimentally and theoretically investigated by McKinley et al. (1995). The vortices which comprised the flow after transition had the form of non-axisymmetric, self-similar Bernoulli spirals which slowly translated toward positions of smaller radius. The local structure within the spiral resembled "Görtler-like" vortices. The base flow underwent a subcritical Hopf bifurcation to this three-dimensional, time-dependent state; hysteretic behavior was observed. Inertia was negligible in the test runs; the formulation and rheology of the polyisobutylene based Boger fluid used was similar to the test fluid used for the investigations of this thesis and described in Chapter 4. A linear analysis using the Chilcott-Rallison model for the constitutive equation qualitatively predicted the dependence of the critical Wi on the cone angle. Özetkin and Brown (1994) used a more sophisticated multi-mode Giesekus model in their linear analysis and were able to quantitatively predict the critical Wi for onset of the instability.

Complex Flows

Cylinder in Channel

The flow of a Boger fluid around a cylinder centered in a channel was experimentally investigated by Byars (Byars, 1996; Özetkin *et al.*, 1997) who built on the work of McKinley (1991). LDV was used to measure quantitatively the velocity field for several geometries with different ratios of channel half-height to cylinder radius (H_{chan}/R_{cyl}). At a flow rate above that required to observe the downstream shift of the streamlines described in §2.1.1, a supercritical bifurcation from two-dimensional and steady to three-dimensional and steady flow occurred. For the geometry with a channel half-height (H_{chan}) twice the cylinder radius (R_{cyl}) the critical parameter was Wi = 1.3. The spatial structure of the flow after transition was a series of Görtler-type counter-rotating vortex pairs noted for other complex flows described in this Section. The experiments of Byars and of McKinley indicated that both the length scales of cylinder radius, R_{cyl}, and gap between the cylinder and the wall, $H_{chan} - R_{cyl}$, played roles in setting the wavelength between pairs of vortices. When the flow rate is increased further, a transition to three-dimensional, time-dependent flow occurs at Wi = 1.9 for the case of the $H_{chan}/R_{cyl} = 2$ geometry. After the temporal transition, vortex pairs were continually "born" at the midpoint of the x-dimension

(dimension along the cylinder axis) and moved in opposite directions toward the walls bounding the x-dimension. The class of bifurcation was not determined and time series measurements were only performed at the midpoint of the cylinder, therefore it was not known whether the waves associated with the temporal transition were superimposed on the waves associated with the spatial transition (supercritical bifurcation) or if the waves associated with the spatial transition suddenly started to move as a unit (subcritical bifurcation). Moreover, it was not determined whether the amplitude of the oscillations associated with the temporal transition was constant over the entire width (x-dimension) or if the amplitude was greater at the bounding walls or at the midpoint of the cylinder axis. Nevertheless, the walls bounding the x-dimension seemed to act as an imperfection to the two-dimensional base flow and set the direction of vortex movement.

The observed spatial extent of the oscillations in the x-direction associated with flow transition supported the concept that the transition was induced by interaction of streamwise stresses with curved streamlines, rather than phenomena associated with the elongational flow near the downstream stagnation point. Specifically, the region over which spatial oscillations associated with the flow transition were observed extended from the downstream stagnation point of the cylinder ($\theta = 0$) to an azimuthal position of at least $\theta = \pi/4$ [rad] upstream of this point. The flow in this region is complex, with both shear and elongational contributions to the rate-of-strain tensor; the streamlines are curved. Özetkin et al. (Özetkin *et al.*, 1997) performed a linear analysis of viscoelastic flow around a cylinder in an unbounded medium using the Oldroyd-B and Giesekus constitutive equations; the correct dependence of wavelength and critical Wi for onset of the instability on the H_{chan}/R_{cyl} ratio was predicted, although the model was too simple to be quantitatively accurate.

Driven Cavity

Pakdel and McKinley (1996) have observed the onset of an elastically-driven instability in driven-cavity flow of a Boger fluid; inertia was negligible in the flow. At Wi greater than that required for the two-dimensional flow rearrangement described in §2.1.1, a three-dimensional and time-dependent flow structure was observed near the corner where the moving top plate emerged (Pakdel and McKinley, 1996). Qualitative visual observa-

tion indicated that the spatio-temporal structure of the flow was of the form of "Görtler-type" vortices. The wavelength in the "neutral" x-direction of the flow structure associated with transition scaled with the height (the y-dimension, cf. Fig. 2.1) of the stationary wall adjacent to the corner (the depth (z-dimension) and width (x-dimension) of the box were held constant).

Axisymmetric Abrupt Contraction

Binding and Walters (1988), investigated flow through a 14:1 axisymmetric contraction. They observed a transition to an asymmetric velocity field at elevated flow rates. Specifically, a light sheet in the rz-plane passing through the centerline indicated that the outer corner vortex in one half of the image was larger than the vortex located on the opposite half (π [rad] in the θ-direction) of the image. The temporal structure of the flow after transition was not described.

Muller (Muller, 1986) and Raiford (Raiford, 1989) conducted studies of velocity field transitions observed in the flow of polyisobutylene-based, "elastic", constant viscosity (Boger) fluids through the axisymmetric contraction. Laser Doppler velocimetry (LDV) was used to obtain quantitative information and determine the class of bifurcation associated with a given flow transition. McKinley et al. (1991) built on this work by characterizing flow for a range of geometries with different contraction ratios (ratio of upstream to downstream tube radius, R_{Up}/R_{Dn}). This information was used to construct a transition map (cf. Fig. 2.4) of flow states in axisymmetric contraction flow. This map has proven useful in unifying the observations obtained for several investigations (Boger *et al.*, 1986). At elevated flow rates, a transition from steady to time-dependent flow was observed. For lower contraction ratios, $R_{Up}/R_{Dn} \leq 4$, the vortex remained axisymmetric but grew and decayed with a characteristic frequency (pulsating mode). In contrast, for $R_{Up}/R_{Dn} \geq 5$ the vortex after onset of the instability was non-axisymmetric; as noted by Binding and Walters (Binding and Walters, 1988), in the rz-plane the outer corner vortex on one half of the plane was larger than in the other half. The structure precessed around the perimeter of the cylinder with a characteristic frequency (rotating mode). Note that in the lower contraction ratio geometries, $R_{Up}/R_{Dn} \leq 5$, the transition to diverging flow, discussed in §2.1.1, occurred at Wi below that for transition to time-dependent flow.

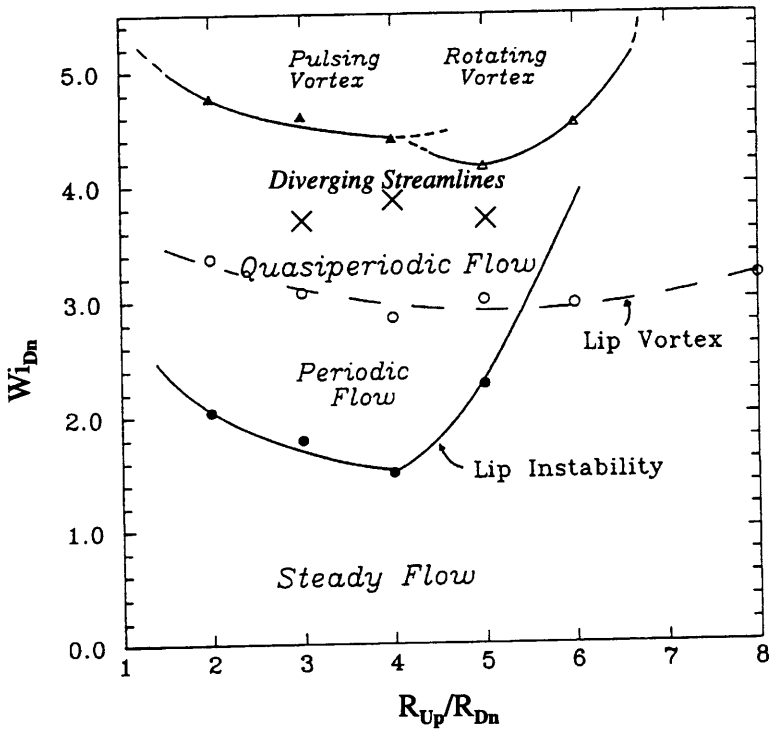

Figure 2.4 Flow transitions in the axisymmetric abrupt contraction as functions of the contraction ratio for $2 \leq R_{Up}/R_{Dn} \leq 8$. (●), critical Wi_{Dn} for Hopf bifurcation to time-dependent flow near the lip; (○) critical Wi_{Dn} for formation of a vortex near the lip; (▲), first observation of pulsing mode (axisymmetric) of global time-dependent flow; (△), first observation of rotating mode (nonaxisymmetric) of global time-dependent flow; (×), first observation of diverging streamlines reported in text. (*Modified from* (McKinley, 1991)).

Boger et al. (1986, 1987) used qualitative streakline visualization to study velocity field transitions in axisymmetric abrupt contractions with contraction ratios in the range $2 \leq R_{Up}/R_{Dn} \leq 16$. Two different Boger fluids were used, one an organic solution based on polyisobutylene (PIB), the other an aqueous solution based on polyacrylamide (PAC). The fluids were composed so as to have similar shear flow material functions. However, distinct differences in the evolution of the velocity field with Wi for a given contraction ratio was noted. For example, in the 4:1 contraction, the PAC solution exhibited a continuous *increase* in the reattachment length of the outer corner vortex with Wi. In contrast, for the PIB solution, the reattachment length of the outer corner vortex initially *decreased* with Wi. At sufficiently high Wi, an independent vortex (the lip vortex) formed near the reentrant corner of the contraction. This lip vortex grew in size with Wi, eventually annihilating the outer corner vortex. The single remaining vortex continued to grow with Wi until the reattachment length once again exceeded the value observed at low Wi. This difference in velocity field evolution between the PAC- and PIB-based Boger fluids was ascribed to an (unmeasured) variation in the elongational flow material functions of the fluids.

Planar Abrupt Contraction

Binding and Walters (Binding and Walters, 1988) investigated the flow of a polyacrylamide Boger fluid through a planar contraction geometry with a contraction ratio of H/h = 14. The qualitative streakline visualization technique used revealed asymmetry in the velocity field at elevated flow rates which has also been noted for viscoelastic flow through the axisymmetric contraction. This transition occurred at a Wi greater than that associated with the transition to diverging flow described in §2.1.1. Streakline images were only taken in the plane normal to the "neutral" direction; nevertheless, the spatial structure of the flow after transition appeared consistent with the form of "Görtler-like" vortices.

Chiba et al. (Chiba *et al.*, 1990; Chiba *et al.*, 1992) used shear-thinning polyacrylamide solutions in their qualitative studies of flow through planar contraction geometries with contraction ratios in the range $3.3 \leq H/h \leq 10$. A transition from two- to three-dimensional flow was noted at flow rates above that required for the onset of diverging flow

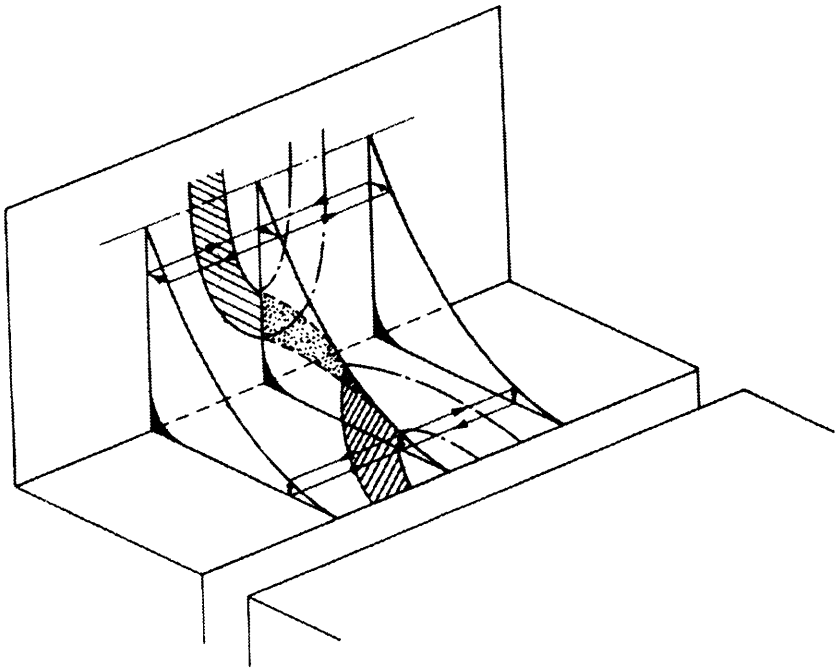

Figure 2.5 Schematic diagram of "Görtler-like" vortex in flow through the planar contraction. (*Reproduced from* (Chiba *et al.*, 1992)).

described in §2.1.1. With streakline photography, Chiba et al. showed that the spatial structure of the flow consisted of interlaced pairs of counter-rotating vortices on each side of the centerplane. A representation of flow of a "ribbon" of fluid is shown in Fig. 2.5. These counter-rotating vortex pairs resemble the Görtler vortices for Newtonian fluids found in flows at high Reynolds number (Re) with streamline curvature (Saric, 1994). In the studies of Chiba et al., the dimensionless wavelength in the "neutral" x-direction of the spatial oscillation associated with the flow transition was found to depend on contraction ratio, increasing from $\lambda_x/H = 1.3$ for the 3.3:1 contraction to $\lambda_x/H = 1.9$ for the 10:1 contraction for the 0.1wt% polyacrylamide (PAC) in water solution. The wavelength was considerably greater for the 0.5 wt% PAC solution flowing through the 10:1 contraction, $\lambda_x/H = 3.8$. At yet higher flow rates, Chiba et al. noted a transition from the three-dimensional and steady flow to three-dimensional and time-dependent flow; the temporal structure of the flow after transition was qualitatively characterized. Chiba et al. found that the vortex pairs oscillated in the "neutral" direction about a fixed point rather than continuously moving from the walls bounding the x-dimension toward the center. A limitation of the Chiba et al. study was that at flow rates for which elasticity had a substantial effect on the flow field, $Wi \gtrsim 1$, the shear thinning behavior resulted in $Re \gtrsim 1$; therefore, inertia was not negligible in the flows investigated. Since both inertial and elastic effects were significant, it was difficult to identify unambiguously the mechanism driving the flow transition. As mentioned above, the interaction of inertial with elastic phenomena can give rise to essentially different behavior from that observed under inertialess conditions (Joseph, 1990).

The velocity-field transition sequences for the diverse complex flows described here share a number of features in common. In all cases for which a two-dimensional flow rearrangement occurred, the critical Wi was lower than the onset Wi for transition to three-dimensional and/or time-dependent flow. The interaction between streamline curvature and streamwise stress appeared to be the mechanism driving the flow transition. In all cases, the spatial structure of the flow after transition had the form of "Görtler-type" vortices. However, substantial work remains to be done before a unified picture of transitions in complex viscoelastic flows is obtained. For example, some of the transitions described above are directly from a two-dimensional and steady flow to a three-dimensional and

time-dependent flow; other transition first undergo a spatial transition to three-dimensional flow and then a temporal transition to time-dependent flow. No criterion which can predict the transition route for a particular flow geometry currently exists.

2.1.3 Scaling of Elastically-Driven Transitions in Flows with Curved Streamlines

The experimental and theoretical investigation described in §2.1.2 have indicated that the interaction of streamwise stresses with streamline curvature can induce transition from two- to three-dimensional flow. The stress-curvature interaction can be quantitatively and mathematically described for viscometric flows such as that in the Couette cell. However, non-viscometric flows are generally not amenable to analytical solution. Moreover, the streamline curvature varies in a complicated manner throughout the flow, making analytical treatment difficult. McKinley et al. (1996) developed a dimensionless scaling which relates a characteristic shear rate, streamwise stress, fluid residence time, and streamline curvature in a flow to a "viscoelastic Görtler number", which sets the critical conditions for onset of instability. The principles underlying the scaling and examples of its application are briefly given below; see McKinley et al. (1996) for more detail.

The "viscoelastic Görtler number", M_{VG}, is defined as

$$M_{VG} \equiv \left(\frac{\lambda_{1p} U}{R_c} \cdot \frac{\tau_{11p}}{\eta \dot{\gamma}} \right)^{1/2} \tag{2.3}$$

The first term within the bracket on the right side of eq. (2.3) represents a ratio of a characteristic length over which perturbations to the viscoelastic stress relax over a characteristic radius of curvature in the flow, R_c. The "relaxation length" in the numerator is composed of a characteristic velocity, U, and the characteristic relaxation time of the polymer, $\lambda_{1p} = \Psi_1/2(\eta - \eta_s)$, where Ψ_1 represents the first normal stress coefficient, η is the solution viscosity, and η_s denotes the solvent viscosity. The second term within the bracket on the right side of eq. (2.3) represents the magnitude of the coupling of perturbative elastic stresses to the stresses in the base flow. τ_{11p} is the polymeric contribution to the streamwise stress and $\dot{\gamma}$, a characteristic shear rate. A more rigorous justification of eq. (2.3) based on the linearized governing equations is given in McKinley et al. (1996)

and is not reproduced here. Applications of the scaling to a viscometric flow and comparison with the predictions of linear analysis are discussed first; application to complex flows is then considered.

In the Couette cell the characteristic geometric ratio is $\delta = (R_2 - R_1)/R_1$. For the case of the narrow gap limit, $\delta \rightarrow 0$; the shear rate is uniform throughout the gap. When the Oldroyd-B constitutive equation is used together with eq. (2.3), the criterion for flow transition is obtained,

$$Wi_{crit} = \frac{M_{VG,\,crit}}{\delta^{1/2}\sqrt{2(1-\eta_s/\eta_0)}} \tag{2.4}$$

Which has the same form as the criterion for onset of instability obtained in the linear analysis of Larson et al. (1990), cf. eq. (2.2). Comparison of eq. (2.4) with the analysis of Larson et al. (1990) indicates that for a fluid with $\eta_s/\eta_0 = 0.5$ the "critical viscoelastic Görtler number" is $M_{VG,\,crit} = 5.9$.

A similar result is obtained for the case of small angle cone-and-plate flow; the geometrical parameter, δ, in eq. (2.4) is replaced by the angle between the cone and the plate, θ. Subsequent comparison with the linear analysis of Olagunju (1997) indicates that for a fluid with $\eta_s/\eta_0 = 0.5$ the "viscoelastic Görtler number" is $M_{VE,\,crit} = 4.6$. McKinley et al. (1996) also extended the utility of the scaling approach by using a multimode Giesekus constitutive equation which could represent shear thinning of the material functions $\Psi_1(\dot{\gamma})$ and $\eta(\dot{\gamma})$. With this more sophisticated model, McKinley et al. (1996) found that the neutral stability loci on the θ_{crit} versus Wi transition map predicted by the scaling closely matched the linear stability calculations of Özetkin and Brown (1994), and were in reasonable agreement with experiments conducted with the cone-and-plate geometry.

McKinley et al. (1996) also explored the ability of the scaling defined by eq. (2.4) to fit experimental data for transitions in two different complex flows: driven-cavity flow and cylinder-in-channel flow. In each case, the term δ in eq. (2.4) was replaced by an estimate of the streamline curvature, $1/R_c$, based on characteristic geometric parameters of the system. A good fit with experimental data acquired for the driven cavity was obtained for geometric ratios in the range $0.25 \leq H/L \leq 4$; the fit yielded $M_{VG,\,crit} = 4.8$. Application

of eq. (2.4) to the experimental data for the cylinder-in-channel geometry for geometric ratios in the range $1.25 \leq H_{chan}/R_{cyl} \leq 20$ also demonstrated a good fit to the data; the fit yielded $M_{VG,\,crit} = 5$.

Thus, eq. (2.4) is able to match the experimentally or numerically determined dependence of Wi_{crit} on characteristic ratios of geometric parameters for several viscometric and complex flows. Note that the $M_{VG,\,crit}$ which were determined for these flows were of similar magnitude, indicating the general applicability of eq. (2.4) to transitions in viscoelastic flows with curved streamlines. However, for the case of complex flows, parameters which relate the characteristic streamline curvature, $1/R_c$, to geometric parameters must be fit or assumed. These parameters cannot presently be estimated *a priori* for an arbitrary geometry and fluid system.

2.2 Elongational Viscosity of Polymer Solutions

As discussed in Chapter 1, the measurement of the elongational response is important from both practical and theoretical points of view. In many polymer processing operations the rate-of-strain tensor contains a substantial elongational component; e.g., in fiber drawing, the flow is almost exclusively elongational. To understand the influence of the elongational response on the stress and velocity fields of a flow, and ultimately on product properties, it is essential to have accurate experimental data on the elongational material properties of a viscoelastic fluid. Such information could be immediately applied to help guide the design and optimization of polymer processing operations.

On a more fundamental level, experimental information on the elongational response of a viscoelastic fluid is useful in evaluating the accuracy of constitutive models. Often the parameters of a constitutive model are obtained via an empirical fit to readily obtainable shear-flow rheological information. The predictive capability of such a constitutive model can then be assessed by comparing the predicted elongational response with experimental data. Before a constitutive model can be reliably applied in a numerical simulation of a complex flow (for which the rate-of-strain tensor has both shear and elongational components) the accuracy of the predicted elongational response must be evaluated. If necessary, the parameters must be refitted to optimize the accuracy of both predicted shear and elon-

gational responses. Note that although the predictive accuracy of a constitutive model for exclusively elongational and exclusively shear flows does not *guarantee* accuracy in a complex flow, predictive accuracy for these limiting cases is certainly necessary.

Polymer kinetic theory has the goal of ultimately being able to predict a constitutive equation solely from consideration of the molecular structure of the polymer such that no parameters would have to be empirically fitted. In this case, comparison of the predicted with the experimentally observed shear rheological response would serve as a check on the validity of the theory. However, evaluation of the shear-flow rheological response would provide only a partial test of validity. In particular, for the shear rates typically attainable in commercial rheometers which provide information on both shear and normal stresses (e.g. RMS-800, Rheometrics), the configurational state of the polymer does not approach the fully extended state. Moreover, the orientational state of a given molecule in a "weak" shear flow is different from that in a "strong" elongational flow. Specifically, an elongational flow has no vorticity, and at a given point in the flow the molecules will be oriented in a single direction for all time. In contrast, vorticity is present in a shear flow, and at a given point in space, the molecules, while exhibiting an average preferred orientation over time, will at any given instant be executing a tumbling motion. Consequently, measurement of the elongational viscosity can be used to assess the accuracy of polymer kinetic theory for a class of flow distinct from shear flow.

In this Section, previously published results of experimental measurement of the elongational response of polymer solutions is discussed. In §2.2.1 a review of results obtained for a common polymer-solution test fluid in different experimental configurations is presented. This serves to illustrate the difficulty of obtaining well characterized elongational data suitable for the evaluation of constitutive models. A detailed discussion of the various experimental configurations is deferred to Chapter 4. Section 2.2.2 presents a review of recent implementations of the filament stretching technique; these investigations have arguably obtained the best-characterized elongational response data for polymer solutions to date.

The approach of the studies of §2.2.2 is to determine the elongational response of a polymer solution by closely approximating a *homogeneous* shearfree flow. An alternative is to use a *nonhomogeneous* shearfree flow, but measure the velocity and stress fields in

pointwise manners within the flow. A given constitutive equation can then be integrated with the velocity field to predict the stress field. The predicted and measured stress fields could then be compared to assess the accuracy of the model for the test fluid in the elongational flow. In Chapter 3, the design of a planar contraction geometry, within which the flow on the centerline is nonhomogeneous and shearfree, is discussed. This shearfree flow is used in the presentation of Chapter 6 to determine the transient elongational response of a viscous polymer solution. An assessment of the efficaciousness of the flow in extending the polymer molecules and exciting a nonlinear elongational response is given in Sections 6.4 and 6.5. Note that detailed discussion of the response of a polymer molecule to an elongational flow, from a microscopic viewpoint, is deferred to §6.1; the characteristics of specific constitutive models are also addressed. It is felt that such detailed discussion is most appropriately located before the interpretation of the experimental results obtained for this thesis.

2.2.1 Experimental Indications of the Importance of Well-Defined Strain-Rate History in Measurement of Elongational Viscosity

The majority of previous investigations have focused on the determination of the steady-state elongational viscosity of a polymer solution as a function of strain rate, much as the steady-state value of the viscosity as a function of shear rate is a standard and commonly used rheological function. However, the exponential (as opposed to linear) separation with increasing time of fluid elements makes development of a homogeneous flow of sufficient extent for the fluid to reach steady state much more challenging for the measurement of the elongational viscosity than for the measurement of the viscosity.

The difficulty of achieving and measuring a true steady-state elongational response has not been fully appreciated in most previous investigations. Often, what was reported as the steady-state elongational viscosity was in actuality a transient quantity. In principle, a transient response measured in a well-characterized flow can also provide information useful for the evaluation of constitutive equations. However, since the strain history of the streamlines in the test flows used by these previous investigations was not fully characterized and reported, comparison of results obtained in different apparatus or use of these results in the fitting and evaluation of constitutive models was difficult or impossible.

The limited utility of transient elongational measurements obtained in devices for which the test flow was incompletely characterized was highlighted by the "M1 Project" (Proc. of Int'l Conf. on Extensional Flow, 1990). Comparison of results obtained in different experimental configurations was facilitated by the use of a single, standard test fluid of which the shear rheology was thoroughly characterized. The reported "extensional viscosity" which was determined for this standard test fluid via a variety of experimental configurations ranged over as much as three decades at a given strain rate; a summary figure by Walters is reproduced in Fig. 2.6. James and Walters (1992) emphasized that the data obtained in these experiments were accurate and reproducible and the variation was a consequence of the transient nature of the tests and the differing strain histories.

In §2.2.2 recent experiments in which careful attention has been paid to the development and measurement of a steady-state elongational response in homogeneous flows (which have a spatially uniform rate-of-strain tensor) are discussed. Nonidealities in these experiments and their effect on the apparent elongational viscosity are discussed in detail. The results of these experiments, which arguably represent the best-characterized elongational material function information to date, are presented.

2.2.2 Elongational Viscosity Measurements in Filament-Pulling Apparatus

Experimental tensile-pulling configurations for imposing uniaxial strain on a test sample have been used by numerous groups for the characterization of the elongational response of polymer melts (Cogswell, 1968; Münstedt, 1975; Münstedt, 1979; Laun and Münstedt, 1976; Vinogradov *et al.*, 1970; Vinogradov *et al.*, 1972; Franck and Meissner, 1984). However, use of this configuration with polymer solutions, which typically have much lower viscosities, is more difficult. Under the influence of surface tension and gravitational body forces, an extended filament will tend to deform in a nonhomogeneous and undesirable manner, potentially resulting in erroneous measurement.

Sridhar et al. (1991) reported measurements conducted with a filament stretching device on a sample of polymer solution. The test fluid had essentially constant viscosity (acted as a Boger fluid) and had a zero-shear-rate viscosity of $\eta_0 = 36.0$ [Pa s]. A drop of fluid was placed between two disks. One disk was connected to a normal force transducer,

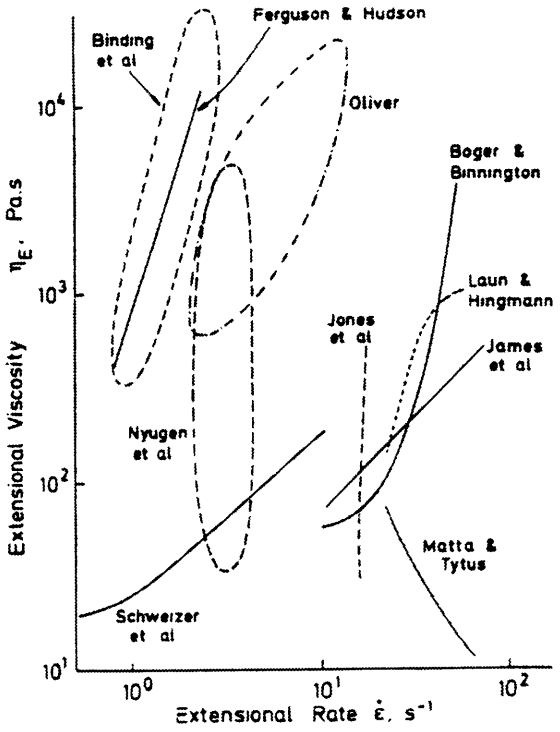

Figure 2.6 Extensional viscosities as a function of extensional rate reported for the M1 fluid. The lines and envelopes represent data by the various M1 Project investigators as published in (Proc. of Int'l Conf. on Extensional Flow, 1990). (*Reproduced from* (Walters, 1992)).

the other disk was connected to a drive system configured such that the distance between the disks increased exponentially with time. In the ideal case, a filament of uniform diameter between the disks would undergo a homogeneous uniaxial elongational flow with constant elongational strain rate over time.

Sridhar et al. (1991) used a photographic technique and a light-beam measuring device to characterize the diameter of the filament at the midpoint between the disks at a given time. By measuring the diameter at evenly spaced time intervals the instantaneous strain rate experienced by a fluid element at the midpoint was determined. These measurements indicated that shortly after inception of straining, the actual strain rate at the midpoint was approximately twice that expected from the "apparent" strain rate imposed by the moving endplates. After this time, the strain rate rapidly decreased to nearly the same value as the "apparent" quantity. Consequently, the flow within the filament was non-homogeneous for at least some time following inception of flow.

Despite the nonideality of the flow, Sridhar et al. (1991) found that the transient elongational viscosity which they determined for the test fluid exhibited essential features expected from predictions of constitutive models. They defined the elongational viscosity as

$$\eta_E^+ = \frac{(F_0/A - F_g - F_\gamma)}{\dot{\varepsilon}} \tag{2.5}$$

where F_0 is the measured force exerted on the end disk, F_g is the gravitational body force, and F_γ is the surface tension force. $\dot{\varepsilon}$ represents the "applied" strain rate imposed by movement of the disks and A is the average cross-sectional area of the filament calculated from conservation of mass. Sridhar et al. use the Trouton ratio, defined as

$$\frac{\eta_E^+(\dot{\varepsilon})}{\eta(\dot{\gamma})} \tag{2.6}$$

to represent their data. Note that the shear-thinning viscosity term in the denominator of eq. (2.6), $\eta(\dot{\gamma})$, is evaluated at a shear rate equal to the second invariant of the nominal rate-of-strain tensor experienced by the fluid, such that $\dot{\gamma} = \dot{\varepsilon}\sqrt{3}$. The viscosity is nearly

constant for a test fluid which acts as a Boger fluid, $\eta(\dot{\gamma}) \approx \eta_0$. For the test fluid used in the study, Sridhar et al. (1991) observed an initial approach to the Newtonian Trouton ratio, $\eta_E^+(\dot{\varepsilon})/\eta(\dot{\gamma}) = 3$, at early times. At a critical accumulated Hencky strain, $1 < \varepsilon < 2$, an increase in the elongational viscosity above the Trouton value was observed. The dependence of this increase on accumulated strain, rather than time, is characteristic of onset of the nonlinear viscoelastic response. The Trouton ratio was then observed to increase with strain up to values of the order $\eta_E^+(\dot{\varepsilon})/\eta(\dot{\gamma}) \sim 1000$; however, "leveling out", characteristic of approach to the steady value, was not observed in the experiments.

In a later publication, Tirtaatmadja and Sridhar (1995) reported the results of measurement of the elongational response of three different polymer solutions in the filament stretching device. Two different polyisobutylene-based Boger fluids were used, the M1 fluid mentioned in §2.2.1 and the fluid which had been characterized by Quinzani et al. (1990), identified as fluid "A". A third, shear thinning fluid (fluid "A1") was also used. The results for fluid A for an applied strain rate of $\dot{\varepsilon} = 2.7$ [s^{-1}] are shown in Fig. 2.7. Onset of the nonlinear response is observed at a strain of $\varepsilon = 1.4$. The Trouton ratio[4] increases until the apparent attainment of a steady-state value of $\eta_E^+(\dot{\varepsilon})/\eta_0 \sim 1000$ at a time corresponding to an accumulated strain of $\varepsilon = 4.7$. Figure 2.7 also shows the predictions of several four-mode nonlinear constitutive models; the parameters of the models had been fitted to steady and dynamic shear rheology data. Three of the models, Oldroyd-B, Giesekus, and FENE-P, show quantitative agreement with the data up to an accumulated Hencky strain of $\varepsilon = 3.8$. At greater strains the model predictions deviate from the data; this is expected for the Oldroyd-B model which predicts an unbounded elongational viscosity. The Giesekus and FENE-P models predict the correct trend, an approach of the elongational viscosity to a steady state value. The M1 and A1 fluids exhibited similar behavior, although the steady state value of the Trouton ratio was not attained; values as high as $\eta_E^+(\dot{\varepsilon})/\eta_0 \sim 8000$ were observed for the M1 fluid and $\eta_E^+(\dot{\varepsilon})/\eta_0 \sim 1000$ for the A1 fluid.

---

4. Note that in the paper of Tirtaatmadja and Sridhar (1995) the usual definition of the Trouton ratio, $\eta_E^+(\dot{\varepsilon})/\eta_0$, was used. $\eta_E^+(\dot{\varepsilon})$ is defined as in eq. (2.5); η_0 is the zero-shear-rate limit of the viscosity.

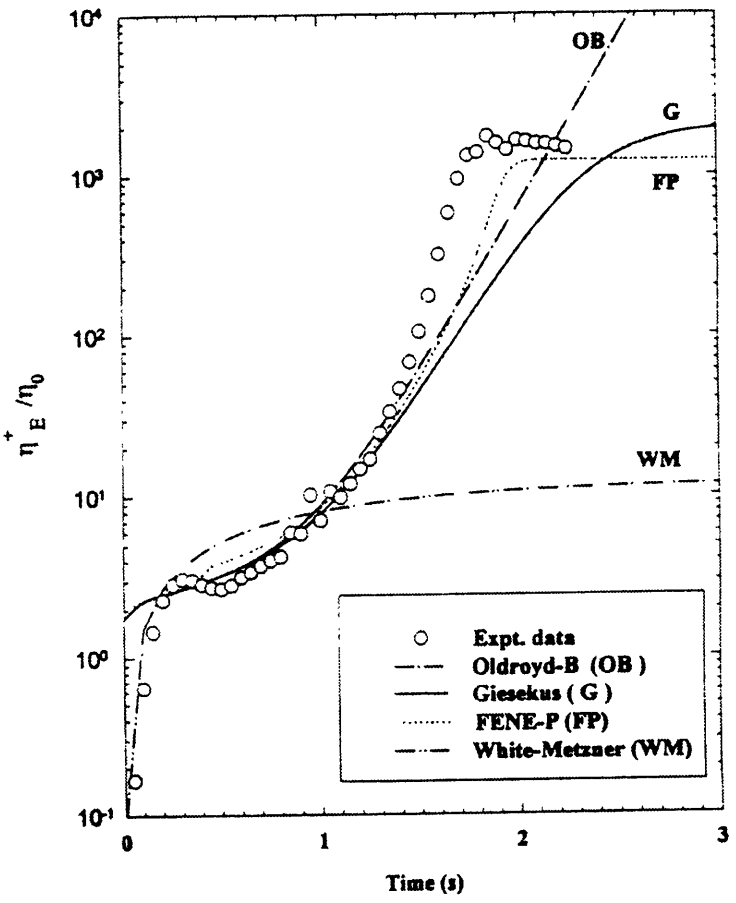

Figure 2.7 Trouton ratio, η_E^+/η_0, for fluid A as a function of time for an applied strain rate of $\dot{\varepsilon} = 2.7\ [s^{-1}]$. Experimental data and predictions of multimode nonlinear constitutive models are shown. (*Reproduced from* (Tirtaatmadja and Sridhar, 1995)).

Spiegelberg et al. (1996) characterized the elongational response of viscoelastic fluids in a filament stretching device similar to that of Sridhar et al. (1991). The major contribution of Spiegelberg et al. was a careful analysis of the effect of nonideal boundary conditions on the rate-of-strain field throughout the filament. This was achieved by capturing video images of the filament, and digitizing them to determine their profiles of radius as a function of axial position, $r = r(z)$, at successive instants in time. To evaluate the accuracy of the device, initial test runs were performed with a Newtonian fluid, for which the elongational response is simple and known. Spiegelberg et al. (1996) found that the no-slip condition at the endplates, termed the "pinning condition", modified the rate-of-strain field throughout the filament from an exclusively homogeneous, shearfree state, and rendered it nonhomogeneous and introduced shear components. This was readily apparent by the "hourglass" shape of the filament profile at times soon after inception of straining imposed by the endplates. The fact that the filament has a fixed diameter in the immediate vicinity of the endplate results in a depletion of the volume of fluid near the midpoint of the filament relative to the case of ideal boundary conditions at the endplate. It follows from continuity that the actual strain rate at the midpoint of the filament is greater than the "ideal" strain rate imposed by the motion of the endplates. Consequently, for a Newtonian fluid, at times shortly after inception of plate motion, the strain rate at the midpoint will be substantially greater than the ideal value; at later times, the strain rate will decrease and approach the ideal value. Knowledge of the effect of the pinning conditions was used by Spiegelberg et al. to modify the velocity versus time profile of the endplates such that the strain rate experienced by a fluid element near the midpoint of the filament, $\dot{\varepsilon}_0$, was constant in time. However, the rate-of-strain field in the vicinity of the endplates was still nonhomogeneous; moreover, the rate-of-strain tensor experienced by fluid elements in the vicinity of the endplates was not constant in time.

The "pinning condition" also results in the rate-of-strain tensor of the fluid near the endplates having a substantial shearing component. The associated shear stress results in an initial overshoot of the apparent Trouton ratio soon after inception of straining; at later times a decrease to the Newtonian value of $\eta_E^+(\dot{\varepsilon}_0)/\eta_0 = 3$ is observed. The magnitude of the overshoot is dependent on the initial aspect ratio of the fluid volume, L_0/R_0, and is greatest for low aspect ratios. Typically, Hencky strains in the range $1.5 < \varepsilon < 2$ must be

achieved before the "pinning condition" has a negligible effect on the apparent Trouton ratio of a Newtonian fluid.

The "pinning condition" affects the rate-of-strain field and measured Trouton ratio over the straining operation of a viscoelastic fluid somewhat differently than those of a Newtonian fluid. The fluids exhibit similar behavior at times soon after inception of straining; specifically, the "pinning condition" leads to an "hourglass" shape of the profile (cf. Figs. 2.8a - 2.8c) and an increase in the strain rate at the midpoint of the filament above the ideal value. However, at later times, elongational thickening results in the filament's having a nearly constant radius throughout most of its length, except in the vicinity of the endplates (cf. Figs. 2.8d - 2.8e). The volume of fluid near the endplates acts as a "reservoir" which feeds the constant radius section of the filament. In consequence, the actual strain rate near the midpoint of the filament drops *below* the ideal value at later times. Eventually, the "reservoir" of fluid near the endplates becomes exhausted. The fluid has at this point achieved a sufficient degree of elongational thickening for the acting normal stress to cause the filament to partially detach from the endplate, preventing continuation of the test to longer times and higher Hencky strains.

At times soon after the inception of straining the plot of Trouton ratio as a function of time for a viscoelastic fluid is similar to that observed for a Newtonian fluid. Specifically, the shear stresses induced by the "pinning condition" result in an overshoot of the measured Trouton ratio immediately after inception of straining which decays at later times. However, the elongational thickening nature of the fluid subsequently results in a rise in the Trouton ratio which continues monotonically until the end of the test. The pronounced inhomogeneity of the velocity field at times immediately after inception of straining have distinctly different effects on the elongational response of Newtonian and viscoelastic fluids at later times. The stress tensor of a Newtonian fluid element is linearly proportional to the local rate-of-strain tensor at a given instant; Newtonian fluids have no "memory" of their previous strain history. In contrast, viscoelastic fluids do have "memory" of their prior deformation history. In consequence, adjustment of the aspect ratio of the initial fluid volume of a Newtonian fluid affects the apparent Trouton ratio at short, but not at long times. For viscoelastic fluids, adjustment of the aspect ratio not only affects the apparent Trouton ratio at short times, but also for *all* times. In consequence, the utility of modifying

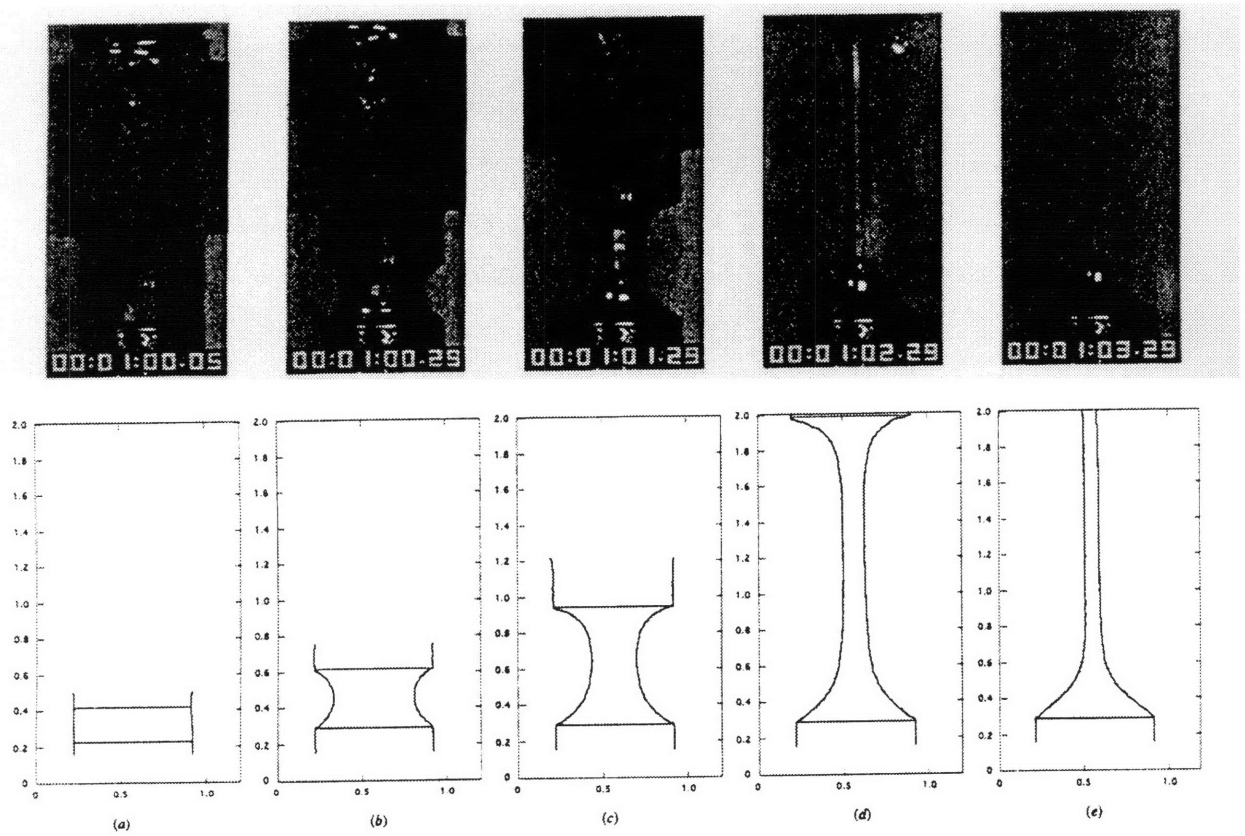

Figure 2.8 Video images and digitized profiles of the stretched filament of fluid BG-1 at a strain rate of $\dot{\varepsilon}_0 = 1.22\ [s^{-1}]$. Frames are spaced 1 [s] apart. Corresponding Hencky strains are: (a) $\varepsilon = 0$; (b) $\varepsilon = 0.74$; (c) $\varepsilon = 1.73$; (d) $\varepsilon = 3.46$; (e) $\varepsilon = 4.41$. Indicated dimensions are in units of [cm]. *(Reproduced from* (Spiegelberg *et al.*, 1996)*).*

the motion of the endplates to achieve a constant strain rate at the midpoint of the filament is limited.

Despite the nonideal "pinning condition" imposed by the endplates, the measured Trouton ratio for two viscoelastic fluids was in qualitative agreement with the predictions of constitutive models which had been fit to shear-flow rheological data (Spiegelberg *et al.*, 1996). Two viscoelastic fluids were used. The first (BG-1) was the same fluid characterized in Quinzani et al. (1990) and designated "fluid A" in the paper by Tirtaatmadja and Sridhar (1995). The second fluid (BG-2) used the same high molecular weight polymer solute at the same concentration, but a Newtonian solvent of higher viscosity was used. Consequently the relaxation time of fluid BG-2 was greater than that of fluid BG-1. For the test, the strain rates for each of the fluids was selected so that the Weissenberg number, $\mathrm{Wi} = \dot{\varepsilon}_0 \lambda_1$, was identical. A plot of the Trouton ratio as a function of Hencky strain for the two fluids is shown in Fig. 2.9. The experimental data for the two fluids are in agreement within the measurement error, as is be expected since they only differed in the solvent viscosity. The data agree with the prediction of the Oldroyd-B model up to a Hencky strain of $\varepsilon \approx 4$. At greater strains, the data are in closer agreement with the predictions of the CR model than the prediction of the Oldroyd-B model. The deviation of the prediction of the Oldroyd-B model from the predictions of the CR model and the experimental data at high strains is a consequence of the Oldroyd-B model's predicting a physically unrealistic unbounded steady-state elongational viscosity. In contrast, the Chilcott-Rallison model always predicts a bounded steady-state elongational viscosity which is dependent on the extensibility parameter, $Q = L_c / \sqrt{\langle r^2 \rangle_0}$; L_c represents the maximum extensible length of the polymer molecule, and $\sqrt{\langle r^2 \rangle_0}$, its root-mean-square radius of gyration at equilibrium. At high Hencky strains the data were in closer accordance with a CR model with Q = 40 than one with Q = 55. However, sufficiently high values of strain to observe the steady-state Trouton value were not achieved in the experiment, precluding definitive identification of Q. The data do indicate a lower bound on the parameter, $Q \geq 40$. Consideration of the molecular weight of the polymer and its conformation in the solvent led to an extensibility parameter value of Q = 55, consistent with this lower bound.

Spiegelberg et al. (1996) concluded that while the semiquantitative data obtained in the filament stretching rheometer was reasonable, further refinements would be necessary

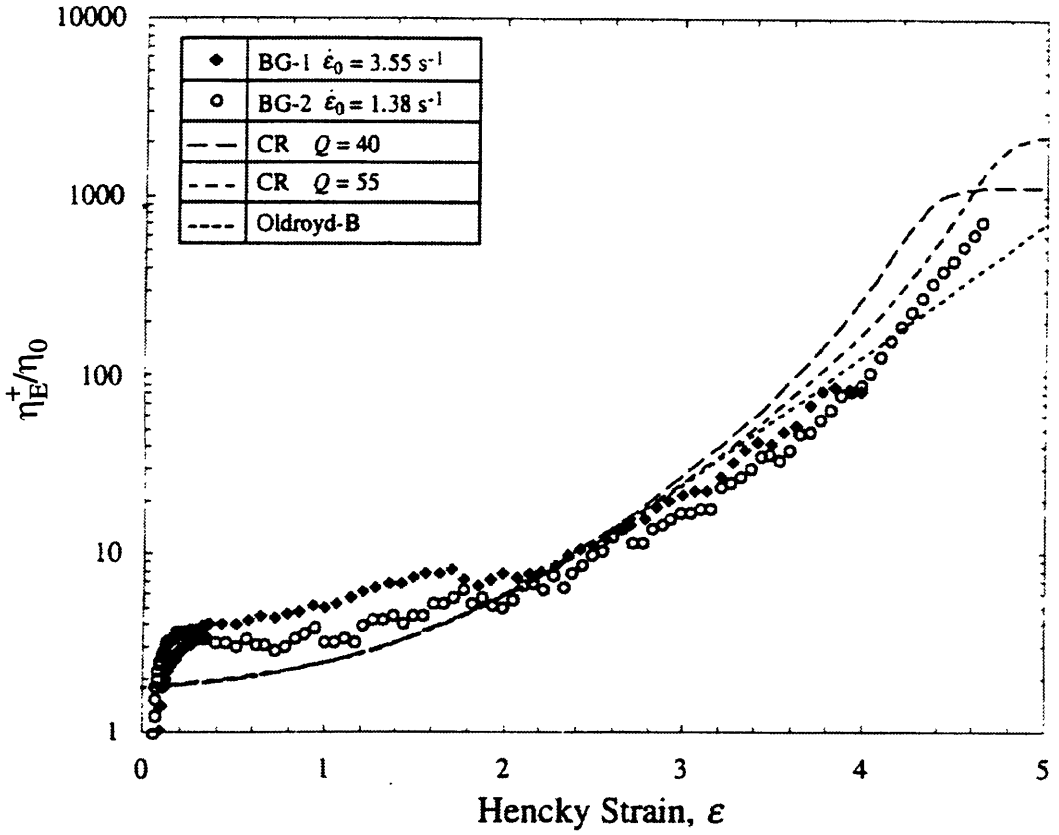

Figure 2.9 Transient elongational response, represented as Trouton ratio, η_E^+/η_0, for two different polyisobutylene-based viscoelastic fluids (BG-1 and BG-2) at Wi = 3.7 as a function of Hencky strain. Prediction of constitutive models are also shown: Chilcott-Rallison (CR), Q = 40 and Q = 55; Oldroyd-B. *(Reproduced from* (Spiegelberg *et al.*, 1996)*)*.

to allow accurate quantitative data, suitable for evaluation and fitting of constitutive models, to be obtained. Specifically, to avoid the "pinning condition" and achieve a homogeneous strain rate throughout the filament, endplates whose radius would decrease during the stretching of the filament would have to be used. Such variable radius endplates have been successfully used in the investigation of Berg et al. (1994). Note that only low Hencky strains $\varepsilon < 1.4$ were attained in the experiments of Berg et al. (1994). Consequently, although the work was of interest from an experimental design viewpoint, the strains were too low to be of use for rheological measurement. It is interesting to note that in spite of the simplicity of the principles underlying the filament stretching rheometer, the determination of accurate and well characterized data requires consideration of a number of physical principles. Furthermore, maximal constraints on the size of the apparatus and minimal constraints of the dimensions of the test sample at the start of the test (L_0 and R_0) continue to make measurement of the steady state elongational viscosity difficult.

Chapter 3

Experimental Method

This chapter describes the experimental system used for the investigations presented in this thesis. The test geometry and fluid handling system are described in §3.1. The flow visualization technique used to obtain full field streakline images of the flow is discussed in §3.2 and the laser Doppler velocimetry (LDV) technique used to acquire pointwise quantitative velocity field information is described in §3.3. In §3.4 the flow induced birefringence (FIB) technique which enables pointwise determination of the stress field in a flow is introduced. Section 3.5 describes the FIB system used for the investigation presented in Chapter 6; §3.6 gives a brief description of the Couette cell apparatus used for obtaining stress-optical coefficients.

3.1 Test Geometry and Fluid Handling System

A schematic diagram of the fluid handling system is given in Fig. 3.1. The fluid was driven by nitrogen pressure from a supply tank (*a*) through the test cell (*b*) and into a receiving tank (*c*) maintained at atmospheric pressure. The fluid flow rate was adjusted by controlling the gas pressure with a self-relieving regulator (*d*). A batch mode of operation was used; after the supply tank was emptied it was necessary to stop the test and drive the fluid from the receiving tank back to the supply tank through a bypass (*e*). A continuous flow system would have required the use of a mechanical pump; this was avoided since high localized shear rates in the pump might have induced fluid degradation. A mechanical pump would also have produced mechanical vibrations and oscillations not present with pressure driven flow.

A schematic of the abrupt planar contraction test geometry is shown in Fig. 3.2. The exterior of the geometry was constructed of aluminum which was anodized to minimize reflection of the laser beams. Fluid flowed in the z-direction from an upstream duct of half-height H into a smaller, downstream duct of half-height h. The width, W, is fixed throughout the geometry. A downstream insert constructed of anodized aluminum and

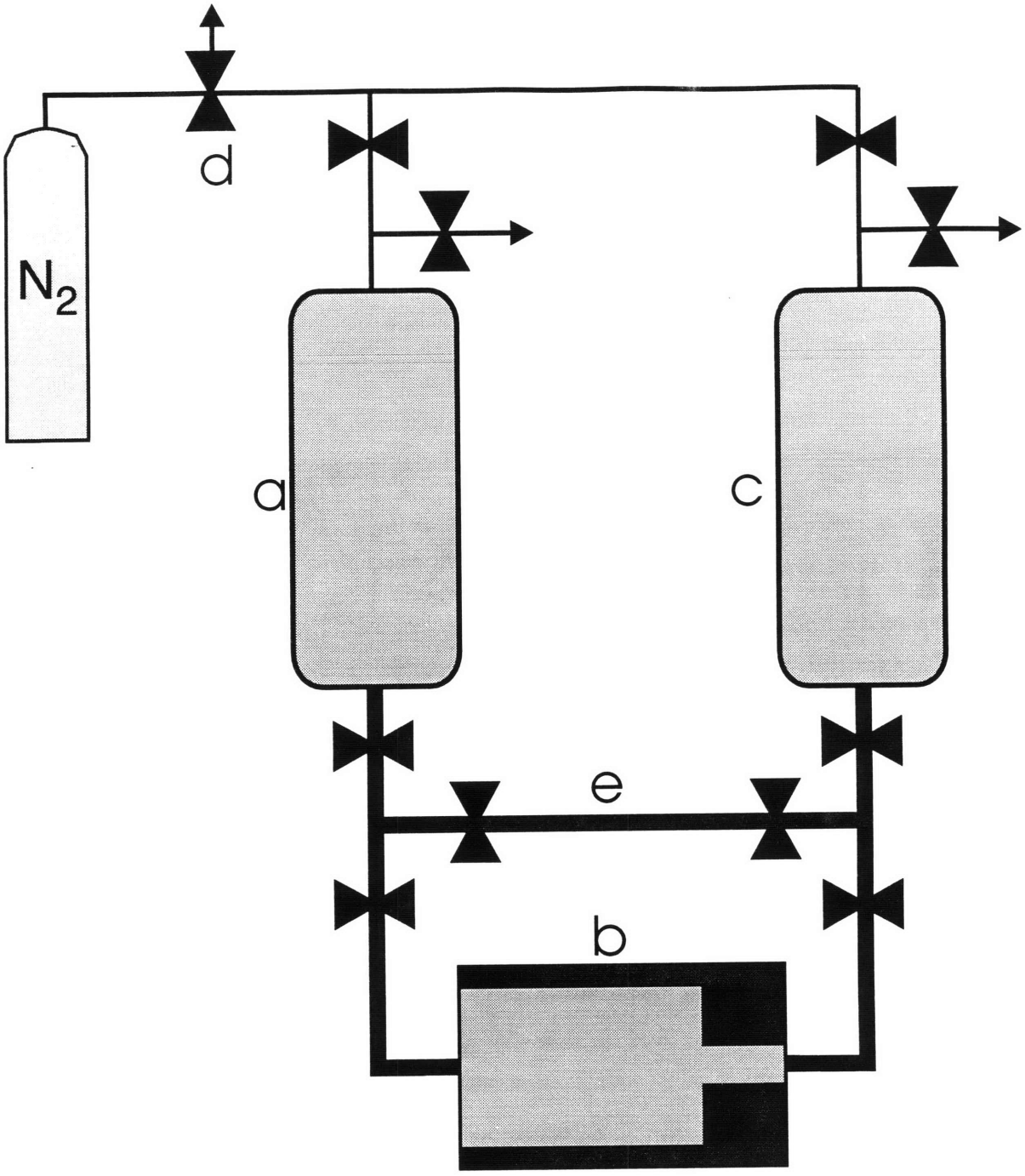

Figure 3.1 Fluid handling system. Shown are the source tank for nitrogen (N_2) pressure, (*a*) fluid supply tank, (*b*) test geometry, (*c*) fluid receiving tank, (*d*) self-relieving regulator, (*e*) bypass line. Gas lines are shown as thin lines, fluid lines as thick lines, valves are indicated as (⧗).

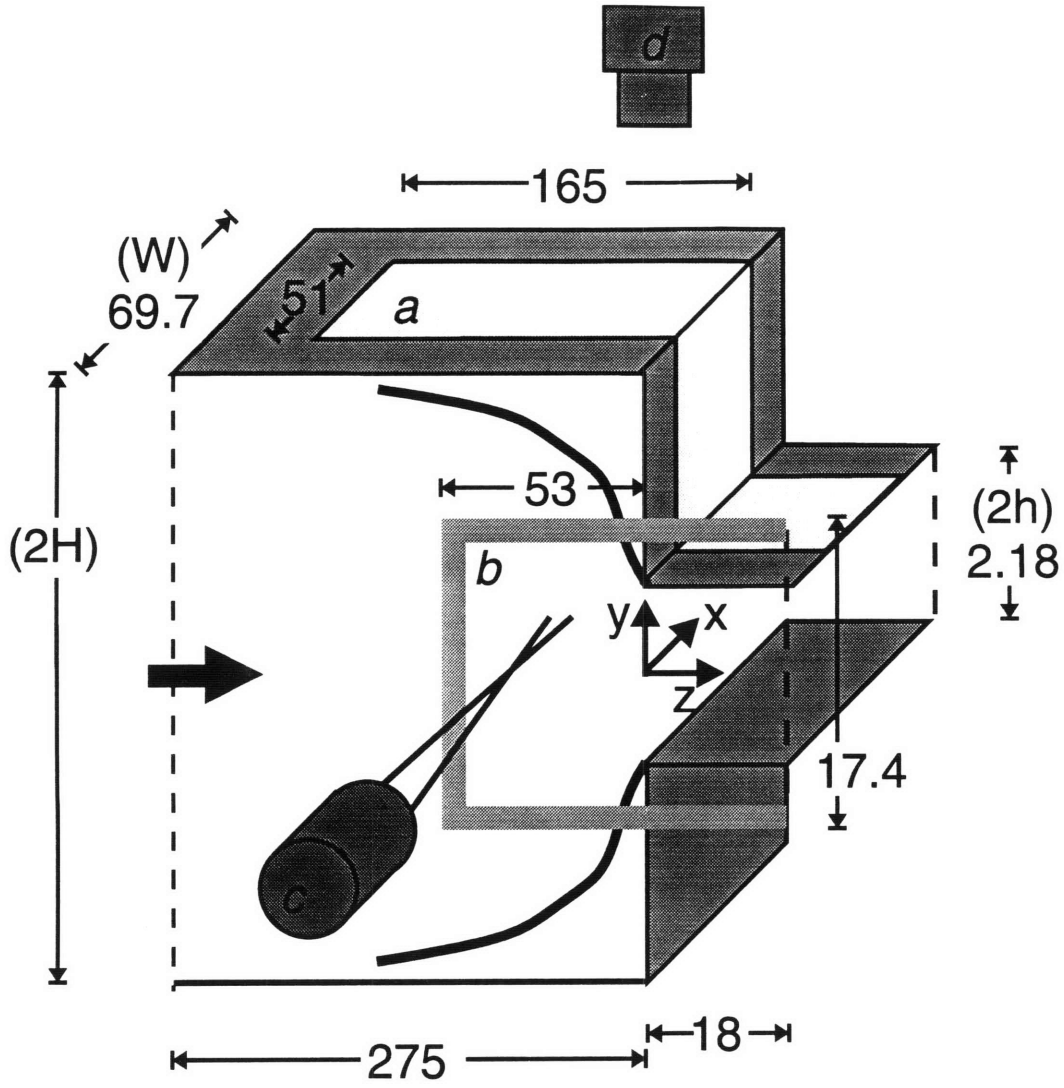

Figure 3.2 Planar contraction test geometry. Fixed dimensions of the geometry, W and 2h, and dimensions of the windows are shown; note that the upstream channel height, 2H, is variable. Specific components of the geometry are indicated: (*a*) top window, constructed of PMMA and BK-10 glass, used for flow visualization in the xz-plane; (*b*) side window, constructed of SF-57 glass, used for flow visualization in the yz-plane and LDV and FIB measurements; (*c*) final focusing optics of the LDV system; (*d*) videocamera for recording light sheet visualization images in the xz-plane. All dimensions are in millimeters.

borosilicate glass (BK-10, Schott Glass Technologies) was used to set the half-height of the downstream slit, h = 1.09 [mm]; careful machining ensured that variation in h did not exceed ±0.05 [mm]. The contraction ratio, H/h, was varied by changing the upstream insert which set the upstream half-height, H; contraction ratios ranging from H/h = 2 to 32 could be used. The upstream insert was constructed of anodized aluminum and polymethylmethacrylate (PMMA). Qualitative, full-field streakline observations of the kinematic structure of the flow in the xz-plane were made through windows placed in the top of the geometry, *a*. Quantitative LDV measurements of the v_y or v_z velocity component and full-field streakline observations of flow in the yz-plane were made through a window placed in the side of the contraction geometry, *b*. The FIB measurements also were conducted through the window, *b*. To minimize the influence of parasitic birefringence on the FIB measurement, the window was constructed of SF-57 glass (Schott Glass Technologies); this material has a low stress optical coefficient of $C = 0.02 \times 10^{-12}$ [Pa^{-1}] at 589 [nm]. The faces of the glass were polished and coated to minimize reflections. The test geometry was designed to withstand static pressures of at least 600 [kPa]; this construction allowed flow rates to be used which corresponded to a downstream shear-rate dependent Weissenberg number of order $Wi_{Dn} \sim 3$ (cf. eq. 6.2 for definition of Wi_{Dn}).

The coordinate system used throughout this paper is indicated in Fig. 3.2. The origin is located in the center of the downstream duct, at the contraction plane (z = 0, where the upstream and downstream ducts join). The dimensional coordinates (x, y, z) are given in millimeters; dimensionless coordinates are based on the downstream half-height: $\chi = x/h$, $\upsilon = y/h$, $\zeta = z/h$. The term "centerplane" refers to the plane defined by (χ, $\upsilon = 0$, ζ); "centerline" refers to any line in this plane with a constant value of χ. Because the geometry is nominally two-dimensional, x is referred to as the "neutral" direction.

3.2 Flow Visualization

The light sheet visualization technique was used to record a streakline image of the velocity field in a selected two-dimensional plane. The technique enables the experimenter to rapidly acquire a qualitative impression of the global spatial and temporal structure of the flow field. A laser beam is passed through a cylindrical lens to form a light

sheet with thickness of approximately 100 [μm] throughout the illuminated region of the flow field. As the particles in the fluid travel through the sheet they scatter light which is recorded by a video camera; the axis of the video camera is normal to the light sheet. Two configurations were used in the experiments: in the first the light sheet was formed in the xz-plane to acquire a top view (camera (*d*) shown in Fig. 3.2, light sheet not shown); in the second the light sheet was formed in the yz-plane to acquire a side view (not illustrated). The video camera signal was stored on videotape for later analysis.

The characteristic length scale of the instability discussed in Chapter 5 was of the order of the upstream half-height H, for which the smallest value was 2.18 [mm] for the geometries used. The coarsest resolution of an image stored on videotape was approximately 6 [pixels mm^{-1}], sufficient to resolve essential spatial features of the instability. The time scale of the instability was greater than 10 [s]; images were stored at a rate of 30 [frames s^{-1}], adequate for resolving the temporal structure of the instability.

Images were digitized using a frame grabber board (model LG-3, Scion Corp.) equipped with 16 Mb of memory on a Macintosh Quadra platform. Frames in a time series were superimposed and averaged using image processing software (NIH Image v. 1.55). By averaging together several frames separated by equal intervals of time streakline images were produced. The length and direction of a given streak corresponded to the local velocity vector in the plane of the light sheet; this qualitative information was used to acquire an overview of the structure of the velocity field. One can note that a more sophisticated version of this technique has been developed, digital particle imaging velocimetry (DPIV), which extracts a quantitative, two-dimensional velocity vector field from images of flows illuminated with light sheets (Pakdel and McKinley, 1997). However, qualitative streakline images in conjunction with quantitative laser Doppler velocimetry were suitable for elucidating the structure of the instability in this investigation.

To develop understanding of the three-dimensional spatial structure of the instability, images were acquired for a given flow with light sheets in the xz-plane at several y-positions and in the yz-plane at various x-positions. These sets of two-dimensional images were used to construct a three-dimensional schematic picture of the flow field. Automated tomographic image processing was not required; examination and interpretation of the

images by the experimenter was sufficient to produce an accurate qualitative representation of the velocity field.

3.3 Laser Doppler Velocimetry (LDV)

A brief description of the physical principles of the laser Doppler velocimetry technique is given below. More extensive discussions can be found in the books by Drain (Drain, 1980) and Durst (Durst *et al.*, 1981); good summaries of the application of LDV to viscoelastic flows are found in the theses of McKinley (McKinley, 1991) and Byars (Byars, 1996). The specific configuration of the LDV system used in the experiments presented in this thesis also is discussed.

Laser Doppler velocimetry is a non-invasive optical technique used to acquire quantitative information on components of the velocity vector at a single point in a fluid flow. Various implementations of the technique have been used to characterize a wide range of gas and liquid flows; velocities ranging from 1 [$\mu m\ s^{-1}$] to 1000 [$m\ s^{-1}$] have been measured (TSI,).

When a beam of light is scattered from a particle moving relative to an observer, the light beam undergoes a frequency, or Doppler, shift. The magnitude of the shift is directly proportional to the velocity of the particle. However, for subsonic particle velocities the magnitude of the shift is small compared with the frequency of the incident light beam and cannot be directly measured. Several optical techniques exist which involve the combining of two beams to generate an observable oscillation of the scattered light intensity which has frequency equal to that of the Doppler shift, f_s. One class of these techniques involves recombining, or heterodyning, the scattered light with a reference light beam. The frequency shift, f_s, of the scattered light then manifests itself as an optical "beating" or oscillation of intensity of the combined light (Drain, 1980).

The most commonly applied class of LDV techniques, used in the current investigation, is termed the "differential Doppler" technique. A schematic drawing of this technique in the backscatter mode of operation is shown in Fig. 3.3. Two coherent, monochromatic light beams are focused on a region in space. An interference pattern is

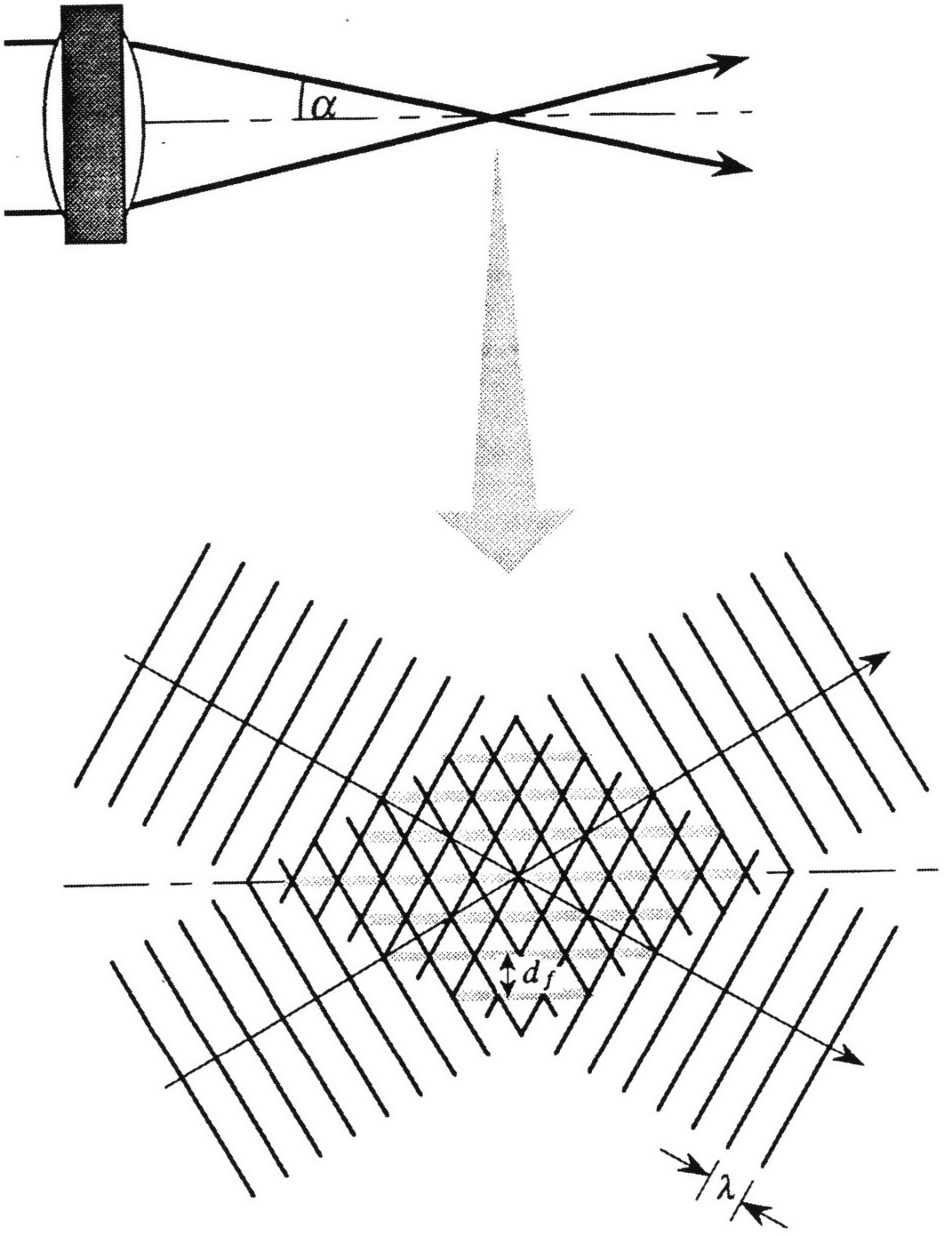

Figure 3.3 Geometric arrangement for a "dual-beam" laser Doppler velocimeter (*a*) and its interpretation in terms of the "fringe model" (*b*). Note that the included half-angle of the beams, α, and the wavelength of the light, λ, set the fringe spacing, d_f. (*reproduced from* (McKinley, 1991)).

established in the "measuring volume" where the beams cross. The fringe spacing, d_f, is dependent on the wavelength of the light, λ, and angle between the beams, 2α,

$$d_f = \frac{\lambda}{2\sin\alpha} \tag{3.1}$$

When a "seed" particle passes through the measuring volume, light is scattered from the "bright" fringes of constructive interference. For a seed particle smaller than the fringe spacing, a pulse train of scattered light (termed a "Doppler burst") is detected by a photo-multiplier tube. The frequency, f_s, of this train (i.e. inverse of time interval between "bright" fringe crossings) can be measured. Because the fringe spacing is known, the velocity component of the particle which is perpendicular to the plane of the fringes is calculated as (McKinley, 1991; Byars, 1996)

$$v_z = \frac{d_f}{(f_s)^{-1}} = \frac{\lambda f_s}{2\sin\alpha} \tag{3.2}$$

One should note that the "optical beating" and "fringe model" interpretations of the LDV technique are approximations which are valid in different limits. The "fringe model" is usually the more appropriate interpretation for the differential Doppler technique; the model is strictly valid only when a single particle of size smaller than the fringe spacing, d_f, resides in the measuring volume at a given time. However, the relation of the measured shift frequency, f_s, to the particle velocity, v_z, is the same for both models. Consequently, it is useful to use the "fringe model" for calculation purposes even though in a real system scattering events may occur with more than one particle in the measuring volume at a given time (Drain, 1980).

The specific configuration of the LDV system (TSI, Model 9100-12) used has been described in (Byars, 1996) and is only briefly discussed here. As illustrated in Fig. 3.4, the output of a 4 [W] multiline argon-ion laser is passed through a series of optical elements and a final focusing lens of focal length F_L = 250 [mm] to form two pairs of intersecting beams orthogonal to each other and capable of measuring the v_y (blue beam pair) and v_z (green beam pair) velocity components. The half-angle included by each beam pair is

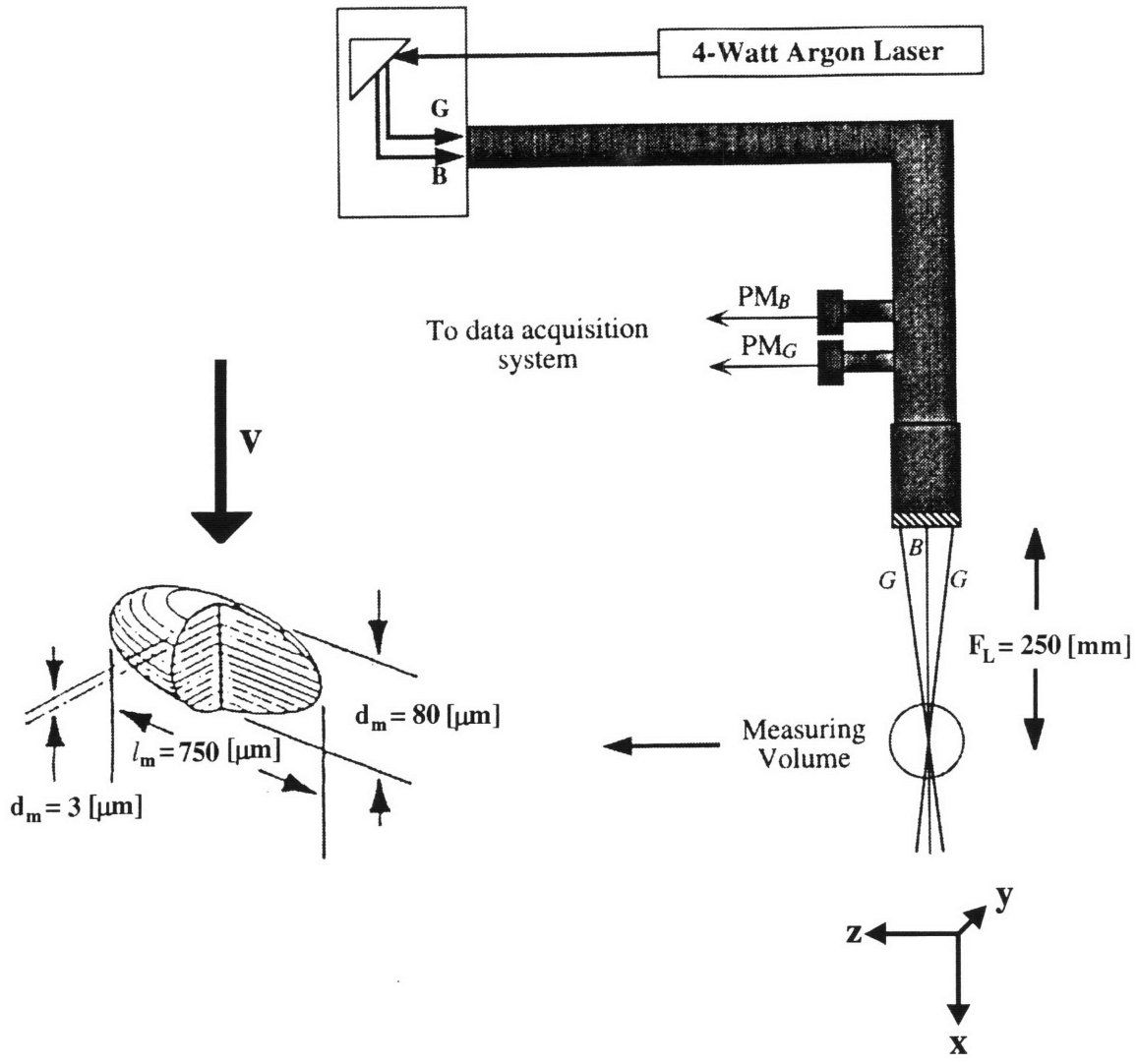

Figure 3.4 Schematic diagram of the two-component LDV system used in this study and the measuring volume. (*modified from* (Byars, 1996)).

0.083 [rad]; the half-angle in conjunction with the wavelength sets the fringe spacing of d_f = 3.1 [μm]. The superimposed measuring volumes from the two beam pairs are ellipsoids of which the dimensions were experimentally determined to be approximately 80 × 80 × 500 [μm] in air, the long axis positioned along the x-direction (in the 0.30 wt% PIB in PB test fluid, which has a relative refractive index of 1.50, the dimensions of the measuring volume are approximately 80 x 80 x 750 [μm]). The LDV optics are mounted on a three-axis translating table (TSI, Model 9500) capable of positioning the measuring volume to within ±4 [μm]. Figure 3.1 illustrates how a pair of beams leaving the final focusing lens travel through the glass bounding the geometry in the x-direction to form the measuring volume in the fluid; the beam pair which measures the v_z velocity component is shown.

Under steady flow conditions, velocity data is collected by operating the system in the "spectrum analysis mode". The Doppler burst signals detected by the photomultiplier (PM) tube are passed through an FFT spectrum analyzer (Nicolet, Model 660B) which calculates the power spectrum (PS). The velocity of the particles passing through the measuring volume is then determined from the characteristic frequency of the peak in the PS. The PS of a number of successive bursts is averaged together to enable accurate measurement of low velocities. The nominal dynamic range of the instrument when operated in "spectrum analysis mode" is 0.4 to 4000 [mm s^{-1}] with an accuracy of ±1%.

For time-dependent flows, it is necessary to use a frequency tracker (DISA, Model 55N20/21) to follow the Doppler frequency. The tracker requires a high Doppler burst rate, approximately 100 [bursts s^{-1}], if the rate is too low, the phase-locked-loop circuit will "drop out", resulting in noisy data. To ensure an adequate data rate, the fluid was seeded with 2 [μm] silicon carbide scattering particles (TSI 10081); a seeding density of 0.036 [g l^{-1}] was used. The seeding ameliorated the problem of tracker "drop out". However, since a given data point corresponds to only a single Doppler burst, velocity data obtained with the tracker is inevitably "noisier" than data obtained with the spectrum analysis technique which uses the information from several Doppler bursts.

3.4 Flow Induced Birefringence (FIB)

The physical principles underlying the FIB technique are discussed along with inherent limitations of the technique in §3.4.1. In §3.4.2 brief descriptions of several implementations of the FIB technique are given.

3.4.1 Physical Principles Underlying Flow Induced Birefringence

The derivation of the "stress-optical rule" from considerations of polymer dynamic and limits on its validity are discussed below. Inherent limitations to spatial resolution attainable with the FIB technique are also described.

Derivation of Stress-Optical Rule from Molecular Theory

The "stress-optical rule", was initially proposed by Lodge (Lodge, 1955) for polymer melts and concentrated polymer solutions. The "rule" postulates a linear relation between the refractive index and stress tensors

$$\mathbf{n} = C\boldsymbol{\tau} \tag{3.3}$$

where $\mathbf{n}$ is the refractive index tensor, $\boldsymbol{\tau}$ the stress tensor, and C the stress-optical coefficient. Lodge postulated the stress-optical rule based on network theory; specifically, he showed the common dependence of the stress and refractive index tensors on the strain history. The affect of a medium on a beam of light travelling along a given coordinate axis is fully described by the submatrix of the refractive index tensor comprised of terms associated with the coordinates which lie in the plane normal to the direction of propagation of the light beam. The difference of the eigenvalues of this submatrix is referred to as the *birefringence*, $\Delta n = n_e - n_o = \sqrt{4n_{21}^2 + (n_{11} - n_{22})^2}$. The eigenvector is termed the *optic axis*, which can be represented in terms of the extinction angle, $\chi = \frac{1}{2}\tan^{-1}\left(\frac{2\tau_{21}}{\tau_{11} - \tau_{22}}\right)$, formed with respect to the first coordinate axis. The extraordinary refractive index, n_e, is related to the velocity with which light polarized parallel to the optic axis travels, $v_{||} = c/n_e$; c is the speed of light in vacuum. The ordinary refractive index, n_o, is related

to the velocity with which light polarized perpendicularly to the optic axis travels $v_{\perp} = c/n_o$.

Later experimental and theoretical work indicated that the stress-optical rule also can be applied to flows of dilute and semidilute polymer solutions. The birefringence of oriented polymer molecules has its molecular origin in the difference between the parallel and perpendicular polarizabilities of a polymer chain segment, $\alpha_{\parallel} - \alpha_{\perp}$ (Doi and Edwards, 1986; Dupuis *et al.*, 1986). Specifically, the local state of the electron cloud causes light to propagate at different velocities when polarized with different orientations to the chain backbone, giving rise to different values of the ordinary and extraordinary refractive indices, n_o and n_e. To determine the net effect of the entire polymer molecule on the polarization state of the transmitted light, one calculates a contour integral which considers the local relative orientation of the polarized light to the chain backbone along the contour length of the chain. In the case of a polymer molecule at equilibrium, there is no preferred direction of orientation of the chain segments comprising the backbone and hence no resultant birefringence. When the polymer molecule is deformed, e.g. by the surrounding flow field, the molecule elongates, resulting in a preferred direction of orientation of the segments. When this preferred direction of orientation is projected onto the plane which is normal to the direction of propagation of the light beam, the angle which the projected vector forms with the first coordinate axis is equal to the extinction angle, χ, described in the preceding paragraph. In the linear Hookean limit, for which the end-to-end length of the polymer molecule is less than approximately 40% of the total contour length, the contour integral which relates the stress to the chain configuration has the same form as the expression which relates the chain configuration to the birefringence. This similarity of the relation to the chain configuration is manifested macroscopically as the linear stress-optical rule.

The stress-optical rule breaks down when the molecule becomes highly extended, with the end-to-end distance approaching the contour length (Wales, 1976; Janeschitz-Kriegl, 1969; Kobe and Wiest, ; Wiest,). This extremely high degree of orientation was not approached in the investigations described in Chapter 6, and the stress-optical rule is expected to hold. Nevertheless, one should be aware of an additional caveat. In principle, a polymer molecule could adopt an "accordion" or "kinked" configuration in which the

end-to-end distance would approach the contour length, but the chain segments would have no mean preferred orientation. Thus, although the molecule would be highly stressed and stretched, the net birefringence would be small or zero. Brownian molecular dynamics simulations have indicated that such a configurational state may occur (Shaqfeh, 1996). However, such a configuration is not expected in the set of experiments presented in Chapter 6, for which the molecules are in the "perturbed coil" configuration and not highly extended.

The test fluid used for the investigations presented in this thesis (described in Chapter 4) consists of a high molecular weight (MW) polyisobutylene (PIB) polymer dissolved in a medium MW polybutene (PB) polymer which acts as a Newtonian solvent. Since both polymer components contribute substantially to the stresses in the flow, it is necessary to extend the stress-optical rule, eq. (3.3), to polymer blends. The net birefringence is simply the linear superposition of the stress contributed by each of the components weighted by the respective stress-optical coefficients (Fuller, 1995). For the case of the test fluid used in these experiments one obtains the equation

$$\mathbf{n} = C_{PIB}\boldsymbol{\tau}_{PIB} + C_{PB}\boldsymbol{\tau}_{PB} \tag{3.4}$$

Knowledge of the refractive index tensor and the stress-optical coefficients is insufficient to determine individual contributions to the stress of the polymer components, $\boldsymbol{\tau}_{PB}$ and $\boldsymbol{\tau}_{PIB}$. Since the PB component acts as a Newtonian solvent, information as to the value of the rate-of-strain field and the viscosity of the PB allows determination of the stress field, $\boldsymbol{\tau}_{PB} = \eta_{PB}\dot{\boldsymbol{\gamma}}$. Subsequently, the contribution of the PIB to the stress is calculated as $\boldsymbol{\tau}_{PIB} = (\mathbf{n} - C_{PB}\boldsymbol{\tau}_{PB})/C_{PIB}$. This approach is used for determining the stress of the components and the total stress, $\boldsymbol{\tau} = \boldsymbol{\tau}_{PIB} + \boldsymbol{\tau}_{PB}$, in the investigation presented in Chapter 6.

Limits to Resolution of FIB Measurements

As described in Sections 3.4.2 and 3.5 for specific implementations of the technique, the flow induced birefringence is measured by sending a laser beam with a characteristic polarization state through a sample. The polarization state of the transmitted light is then

measured and the birefringence and extinction angle determined. The probe beam is affected by the sample along the entire beam path length. Specifically, one can write

$$\frac{d}{dx}\mathbf{S}(x) = \mathbf{m}(x) \cdot \mathbf{S}(x) \tag{3.5}$$

where $\mathbf{S}(x)$ is the Stokes vector describing the polarization state of the light. The differential propagation matrix, $\mathbf{m}(x)$, describes the effect of a "slab" of the sample of infinitesimal thickness dx on the polarization state of the beam traveling in the x-direction (Galante, 1991)(Azzam, 1978)(Azzam and Bashara, 1987). Given the initial polarization state of the beam, $\mathbf{S}(x_0)$, eq. (3.5) is integrated along the beam path, $x_0 \leq x \leq x_1$, using the known $\mathbf{m}(x)$, to give the Stokes vector, $\mathbf{S}(x_1)$, for the exiting beam. However, an FIB measurement requires solution of the inverse problem: given a measured $\mathbf{S}(x_0)$ and $\mathbf{S}(x_1)$, determine the $\mathbf{m}(x)$ along the path length. Since $\mathbf{S}(x_1)$ is an integral quantity, information about $\mathbf{m}(x)$ at each point x along the beam path is lost. However, if $\mathbf{m}(x)$ does not vary throughout the sample (i.e. $\mathbf{m}(x) = \mathbf{m}$) the problem becomes tractable. Specifically, one obtains

$$\mathbf{S}(x_1) = \mathbf{M} \cdot \mathbf{S}(x_0) \tag{3.6}$$

where $\mathbf{M} = \Xi \cdot e^{\Lambda(x_1 - x_0)} \cdot \Xi^{-1}$ is the Mueller matrix containing the birefringence and extinction angle information; note that Ξ represents the matrix of eigenvectors and Λ the matrix of eigenvalues of the constant differential propagation matrix, $\mathbf{m}$. To ensure that $\mathbf{m}$ is constant along the beam path the flow under investigation must be a two-dimensional, planar flow which does not vary along the "neutral" x-direction. Clearly all real flows must have a wall bounding the x-direction which will introduce some three-dimensionality into the flow. Throughout the results presented in Chapter 6 the effect of such non-idealities on the measurement will be considered. One may note that analyses have been undertaken to extend the application of FIB to flows which are three-dimensional or non-planar (Andrienko *et al.*, 1992b; Andrienko *et al.*, 1992a; Funatsu and Kajiwara, 1988). However, the challenge of implementing a tomographic-type measurement and subsequent deconvolution of the information is daunting when one considers that an integral tensorial equation must be solved. A tomographic approach is most likely to prove successful when

the flow has a high degree of symmetry (e.g. axisymmetric); Funatsu et al. obtained promising results in their measurement of the stress field in viscoelastic flow around a sphere (Funatsu *et al.*, 1988). However, quantitative FIB measurement in a general three-dimensional flow field is still an unsolved problem.

A second limitation of the FIB technique also concerns an averaging effect, but within the plane (yz) perpendicular to the beam propagation direction (x) (Galante, 1991). Specifically, a real probe beam has a finite diameter. If the actual Mueller matrix of the sample has different values throughout this beam area, the Mueller matrix which is back-calculated from the measured Stokes vectors $\mathbf{S}(x_0)$ and $\mathbf{S}(x_1)$ will represent a mean value. More precisely, one integrates the local Mueller matrix $\mathbf{M}(y, z)$, weighted by the beam intensity at a given point $I(y, z)$, over the beam area to obtain the observed Mueller matrix $\langle\mathbf{M}\rangle$,

$$\langle \mathbf{M} \rangle = \frac{\iint \mathbf{M}(y, z) I(y, z) dy dz}{\iint I(y, z) dy dz} \tag{3.7}$$

Since the relations between the components of the Mueller matrix and the refractive index tensor are generally not linear, knowledge of this "mean" Mueller matrix does not allow determination of the "mean" stress field over the area.

One apparent solution to the problem is to reduce the size of the beam so that variations in the stress field over the beam area are negligible. Although feasible in certain cases, divergence of a Gaussian laser beam in conjunction with the requirement of approximating a two-dimensional planar flow places severe constraints on this approach. The radius of a Gaussian beam over a particular length of the beam path can be derived from the Maxwell equations and represented by the formula

$$\frac{r(z)}{r_0} = \sqrt{1 + \left(\frac{z\lambda}{\pi r_0^2}\right)^2} \tag{3.8}$$

where r_0 is the radius of the beam at the waist, r(z) is the radius of the beam at a distance z from the waist, and λ is the wavelength of the light. For the case of the planar contraction, when the beam waist is located in the middle of the x-dimension, the maximum beam radius, $r_{W/2} = r(W/2)$, is at the walls of the geometry. The width of the geometry, W, also is related to the aspect ratio in the upstream duct, $\Lambda = W/2H$, and the half-height of the upstream duct, H, is related to that of the downstream duct, h, by the contraction ratio H/h. Substituting these relations into eq. (3.8) gives

$$r_0 = \frac{(h/r_0)}{\sqrt{(r_{W/2}/r_0)^2 - 1}}\left(\frac{\Lambda(H/h)\lambda}{\pi}\right) \tag{3.9}$$

where the ratio of the beam waist radius to the downstream half-height, r_0/h, is a measure of the resolution of the system. A geometry with a contraction ratio as great as H/h = 32 was used in the investigations presented in Chapter 6. The effect of the aspect ratio on the two-dimensionality of the flow field is considered in more detail in Chapter 6; a minimum required upstream aspect ratio of $\Lambda = 1$ is assumed here. When the beam is collimated to within 5% over the width of the geometry, $r_{W/2}/r_0 = 1.05$, and the resolution of the system is $r_0/h = 0.125$, solution of eq. (3.9) yields a beam waist radius of $r_0 = 0.13$ [mm] and a downstream half-height of h = 1.05 [mm]. Using the downstream half-height as a measure of the size of the geometry (upstream half-height and width will scale proportionally) gives the inverse square dependence on the resolution

$$h \propto (r_0/h)^{-2} \tag{3.10}$$

Consequently, a large increase in the size of the geometry is required to improve the resolution. As the width of the geometry increases, thermally induced beam divergence effects become significant. This, in conjunction with the experimental difficulty and expense of working with a large geometry, restricts the attainable resolution. The interrelated constraints imposed by Gaussian beam divergence and geometrical parameters guided the design of the geometry described in §3.1.

An alternate approach which has been tried to improve the resolution of FIB measurements consists of masking all but a small center section of the beam which has been transmitted through the sample immediately in front of the photodetector. However, it has been shown (Galante, 1991)(Durnin *et al.*, 1987) that this method does not reduce the effective area probed by the beam. Specifically, the Maxwell equations for propagation of electromagnetic radiation were used to show that conventional geometrical optics is not appropriate for analyzing the propagation of energy (and consequently information) within a Gaussian beam. A Gaussian beam exhibits very little divergence; i.e., the intensity distribution remains nearly constant over successive axial positions. However, the energy at a given point in the beam generally does not travel in a straight line coaxial to the beam path; rather, the energy diffracts within the beam. Potential "in-plane" beam averaging effects and their influence on FIB measurements are addressed in Chapter 6; approaches for obtaining useful stress field information despite such averaging effects are discussed in Chapter 7.

3.4.2 Examples of Flow Induced Birefringence Measurement Techniques

As described above, the Mueller matrix of the sample, **M**, is calculated from the observed difference in polarization state of the incident $\mathbf{S}(x_0)$ and transmitted $\mathbf{S}(x_1)$ beams. The birefringence and extinction angle are in turn calculated from the Mueller matrix. Subsequently, the stress-optical rule is invoked to determine the stress field.

Several different FIB measurement techniques exist which differ in the optical elements which comprise the polarization state generator (PSG), located before the sample, and the polarization state analyzer (PSA), located after the sample. A simple polarimeter is discussed first. The two-color technique is then discussed and compared with the polarization modulated flow birefringence technique.

Simple Polarimeter

In the simple polarimeter shown in Fig. 3.5a, a beam of monochromatic light of wavelength λ_G is passed through the PSG, a linear polarizer, $P(\theta)$, oriented at an angle θ with respect to the observer's reference frame. The polarizer transmits only a component of the

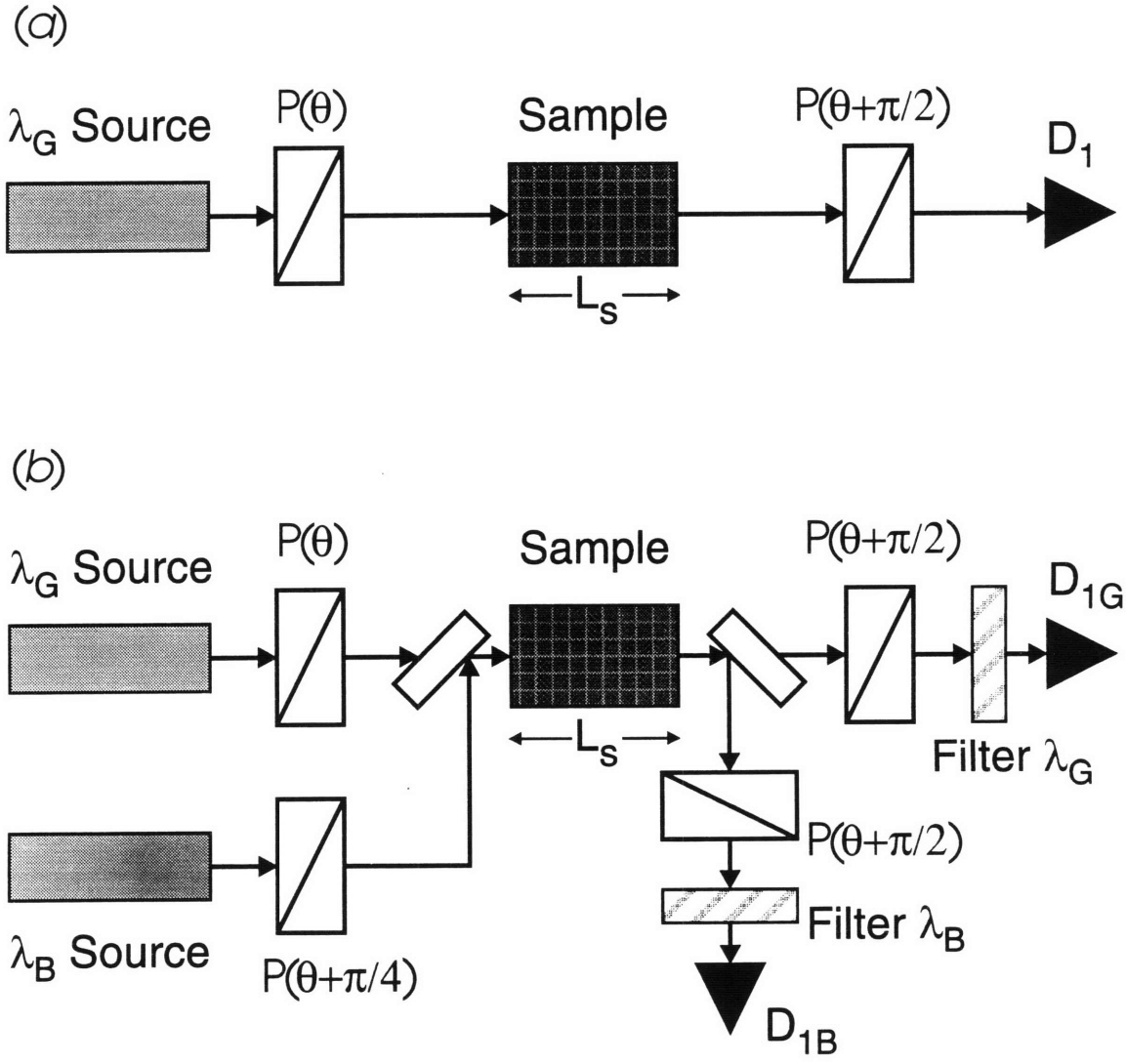

Figure 3.5 Flow induced birefringence measurement systems: (*a*) simple polarimeter arrangement; (*b*) two-color flow induced birefringence system.

light wave which has the electric vector in a specific direction. The beam then passes through a distance, L_S, of the sample being studied. The light emerging from the sample passes through the PSA, a linear polarizer, $P(\theta + \pi/2)$, oriented $\pi/2$ [rad] relative to the PSG. Finally, the light impinges on a photodetector, D_1, which measures the intensity. If the light beam were unaffected by the sample, the PSA would not transmit any of the light. However, as described in §3.4.1, the preferred direction of orientation of the polymer segments in conjunction with the difference in polarizability of the chain to light travelling parallel and perpendicular to the backbone causes a stressed polymeric material to have a net birefringence. Consequently, the electric vector will, in general, no longer be perpendicular to the direction which can be transmitted through the polarizer; light will reach the photodetector. It can be shown (Azzam and Bashara, 1987)(Quinzani, 1991) that the extinction angle, χ, and the birefringence, Δn, are related to the ratio of the light beam intensity entering the flow cell, I_0, and the light beam intensity measured at the detector, I, by

$$\frac{I}{I_0} = \sin^2\left(\frac{\delta'}{2}\right)\sin^2(2(\chi - \theta))$$
$$\delta' = 2\pi\frac{\Delta n}{\lambda}d \tag{3.11}$$

where λ is the wavelength of the light and $(\chi - \theta)$ the orientation of the incident linearly polarized light with respect to the extinction angle. One should note that eq. (3.11) assumes that aside from the dichroic attenuation in the linear polarizers, no light is scattered or absorbed in the system.

Several different configurations of this simple polarimeter exist. Full field devices have been constructed which usually provide qualitative information. From eq. (3.11), when $\delta' = 2\pi N$ (with N an integer) no light will be transmitted; the dark regions associated with these values of the retardance, δ', are termed the isochromatic fringes. When the stress-optical rule is valid, the isochromatic fringes indicate constant magnitude of the first principal stress, $\Delta\tau$. By counting the number of isochromatic fringes from a point of known stress in the flow, one can estimate the stress in a specific region of the flow. Equation (3.11) indicates that when $(\chi - \theta) = N\pi/2$ no light will be transmitted; the dark regions

associated with these extinction angles are termed the isoclinic lines. The isoclinic lines indicate regions of common orientation, χ, of the molecules in the flow and in conjunction with the known $\Delta\tau$ allow calculation of the components of the stress tensor in the observer's frame of reference. By varying θ by simultaneously rotating the orientation of the PSG ($P(\theta)$) and the PSA ($P(\theta + \pi/2)$, in principle, estimates are made of Δn and χ at each point in the flow. However, if χ is determined at each point by varying θ until the isoclinic is superimposed on the point, the method is laborious (Gortemaker *et al.*, 1976).

To minimize the number of measurements required, Osaki et al. (Osaki *et al.*, 1979) noted that if the intensity of the transmitted light was quantitatively measured, Δn and χ could be determined at a given point in the flow with only two measurements, with the polarizers positioned at $\theta = 0$ and $\theta = \pi/4$ [rad]. Although the method allows for much faster data acquisition than the isochromatic counting and isoclinic identification technique described in the preceding paragraph, manual intervention on the part of the operator is still required. Moreover, if a transient flow changes on a time scale of the order of or faster than the time required to perform the two measurements, the method cannot be applied.

Two-Color Technique

The two-color flow birefringence (TCFIB) technique developed by Chow and Fuller (Chow and Fuller, 1984; Chow and Fuller, 1985) is an extension of the method used by Osaki et al. (Osaki *et al.*, 1979). The TCFIB technique is illustrated in Fig. 3.5b. Two monochromatic light beams of different wavelengths, λ_G and λ_B, are passed through the system. The PSG and PSA for a beam of a given wavelength are rotated $\pi/4$ [rad] with respect to the PSG and PSA of the other beam. A combination of beam splitters and wavelength filters are used to direct the two beams of differing wavelength along the same path within the sample and subsequently separate the light into distinct beams of different wavelength. Because eq. (3.11) holds independently for each beam, a system of two equations is solved to obtain Δn and χ. Consequently, the method is fully automated, no operator intervention is required. In principle, Δn and χ data can be acquired instantaneously, measurements of flows with very short time scales can be made.

Polarization Modulated Technique

The polarization modulated flow birefringence (PMFIB) technique generally uses only one laser beam for which the polarization state of the PSG is modulated with time. One implementation of the PMFIB technique uses a quartz photoelastic modulator; several groups have obtained favorable results with this implementation (Frattini and Fuller, 1984; Fuller, 1990; Galante, 1991). PMFIB techniques are limited to observation of phenomena with time scales substantially longer than the inverse of the modulation frequency, $O > 10/\omega_{mod}$, whereas the TCFIB technique is in principle instantaneous. Nevertheless, a PMFIB system typically requires the alignment of only one beam, and is usually more compact than a TCFIB system.

3.5 Two-Color Flow Induced Birefringence Experimental System

A two-color flow induced birefringence (TCFIB) system was used in the investigations presented in this thesis to measure simultaneously the extinction angle and the birefringence at a point in the flow. The TCFIB apparatus used in this set of experiments was originally constructed by Quinzani (Quinzani, 1991) and was based on the experimental design of Chow and Fuller (Chow and Fuller, 1984; Chow and Fuller, 1985). A comprehensive discussion of the configuration of the system used has been presented in Quinzani (Quinzani *et al.*, 1994); therefore, the description here will be brief and focus primarily on modifications made to the original system.

A schematic diagram of the system is shown in Fig. 3.6. The original system used a laser-line interference filter to combine simultaneously (or split) and filter the blue and green beams. It was found that the multiple layers comprising the filter in conjunction with inherent stresses in the element introduced an unacceptable level of parasitic birefringence in the transmitted beam. To overcome this problem, the beam splitting and filtering functions were separated into two optical elements. Specifically, the laser line filter was placed before the initial polarizer (or after the analyzer polarizer) to avoid the introduction of parasitic birefringence. A beamsplitter, composed of a single piece of glass and coated to provide 50% transmission at an incident beam angle of $\alpha = 0$ [rad], was used to combine or split the beams. A different collimator, C, and pair of focusing lenses, LB and LG,

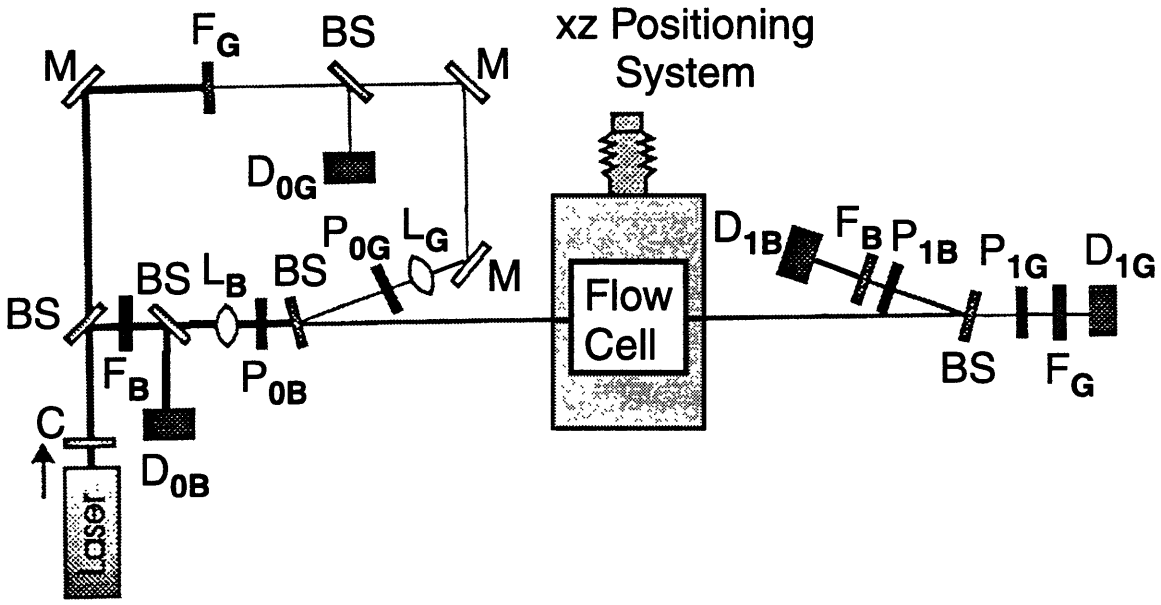

Figure 3.6 Schematic Diagram of the TCFIB system used in this study. Specific optical elements are shown: C, collimator; BS, beamsplitter, M, mirror; F, filter; L, lens; P, linear polarizer; D, photodetector. A "B" subscript indicates that blue light is transmitted, polarized, or the intensity measured by the specific optical element; a "G" indicates similar action performed by an element on green light. A "0" subscript indicates that an optical element acts on the light before it has passed through the flow cell; a "1" subscript indicates that the light which has already passed through the cell (*modified from* (Quinzani, 1991)).

than used in the original configuration of Quinzani were used so as to improve the resolution of the system. Details on the resolution of the current system are provided below.

As described in Quinzani (Quinzani *et al.*, 1994), four photodetectors are used in the system. Each detector is connected to a power meter which is in turn linked to an analog to digital signal board to allow continuous data acquisition on an IBM PC. Two photodetectors, D_{1B} and D_{1G}, measure the intensity of the light transmitted through the sample and the polarizing optics, I_{1B} and I_{1B}. The other two photodetectors, D_{0B} and D_{0G}, provide a reference measurement of the intensity of the light before passage through the sample and polarizing optics, I_{refB} and I_{refG}. A transmitted intensity, I_1, is then normalized with the reference measurement, I_{ref}, to correct for variation in the intensity of light emitted by the laser over time; specifically, one uses

$$i = I_1 / I_{ref} \tag{3.12}$$

The attenuation of the light by scattering and absorption in the sample and the optics must also be accounted for. One sets the polarizers to the parallel position and measures the light transmitted through the sample and the polarizers, $I_{||}$; this value is normalized to obtain $i_{||}$. $i_{||}$ represents the intensity of the initial beam, corrected for attenuation by scattering and absorption and normalized with respect to the reference beam. The equations for the transmitted intensity of the blue beam ($\theta_B = 0$ [rad]) and the green beam ($\theta_G = \pi/4$ [rad]) are then

$$\begin{aligned} \frac{i_B}{i_{B||}} &= \sin^2\left(\frac{\pi \Delta n d}{\lambda_B}\right)\sin^2(2(\chi - \theta_B)) \\ \frac{i_G}{i_{G||}} &= \sin^2\left(\frac{\pi \Delta n d}{\lambda_G}\right)\sin^2(2(\chi - \theta_G)) \end{aligned} \tag{3.13}$$

where $\lambda_B = 488$ [nm] and $\lambda_G = 514.5$ [nm], the wavelengths of the blue and green beams respectively. Equations (3.13) are then solved numerically to determine the birefringence and extinction angle at a specific point in the flow sample.

The constraints imposed by the geometrical parameters and divergence of the Gaussian beam governed selection of the dimensions of the geometry and radius of the beams.

Specifically, beams of radius $r_0 = 0.25$ [mm] at the beam waist were used; the radius of a given beam did not exceed this minimum value by more than 10% over the width of the geometry, W = 70 [mm]. Consequently, the resolution of the system in dimensionless terms was $r_0/h = 0.23$, where h is the downstream half-height of the contraction geometry. As described in Quinzani (Quinzani, 1991), a two-axis translating system (Klinger Scientific Model, MT160.100 and MT160.200) allowed the measuring volume to be positioned to a relative accuracy of ± 2 [μm]. The alignment procedure allowed the origin of the coordinate system to be located to within approximately ± 20 [μm].

The accuracy of the TCFIB system was assessed by using a quarter-wave plate in the place of the flow cell. This optical element induced a nominal $\delta'_R = 90$ [deg] retardation between the phase of a light wave of wavelength 632.8 [nm] with the electric vector parallel to the characteristic orientation of the plate and the electric vector perpendicular to the orientation of the plate. The element was rated to an accuracy of ±2% of the nominal value of the retardation. The measured values of the extinction angle, χ, and the retardation for a wavelength of 632.8 [nm], δ'_R, are shown as a function of the orientation of the quarter wave plate, θ_{QW}, in Fig. 3.7. The average of the measured value of the retardance was $\delta'_R = 92.6 \pm 1.8$ [deg], nearly within the rated accuracy of the element. A good, linear, unit-slope fit to the measured extinction angle was obtained; the standard deviation was ±0.25 [deg]. The lowest value of Δn for which data could be obtained (i.e. the sensitivity of the system) was set by the parasitic birefringence of the glass and other optical elements located before and including the polarizers. The parasitic birefringence was assessed at the beginning of each run by measuring the birefringence with no fluid flowing. This measurement was consistent, with an average value and standard deviation of $\Delta n_{Parasitic} = 4.2 \times 10^{-8} \pm 0.5 \times 10^{-8}$. The accuracy and sensitivity of the system are compared with those used in previous investigations in Table 3.1.

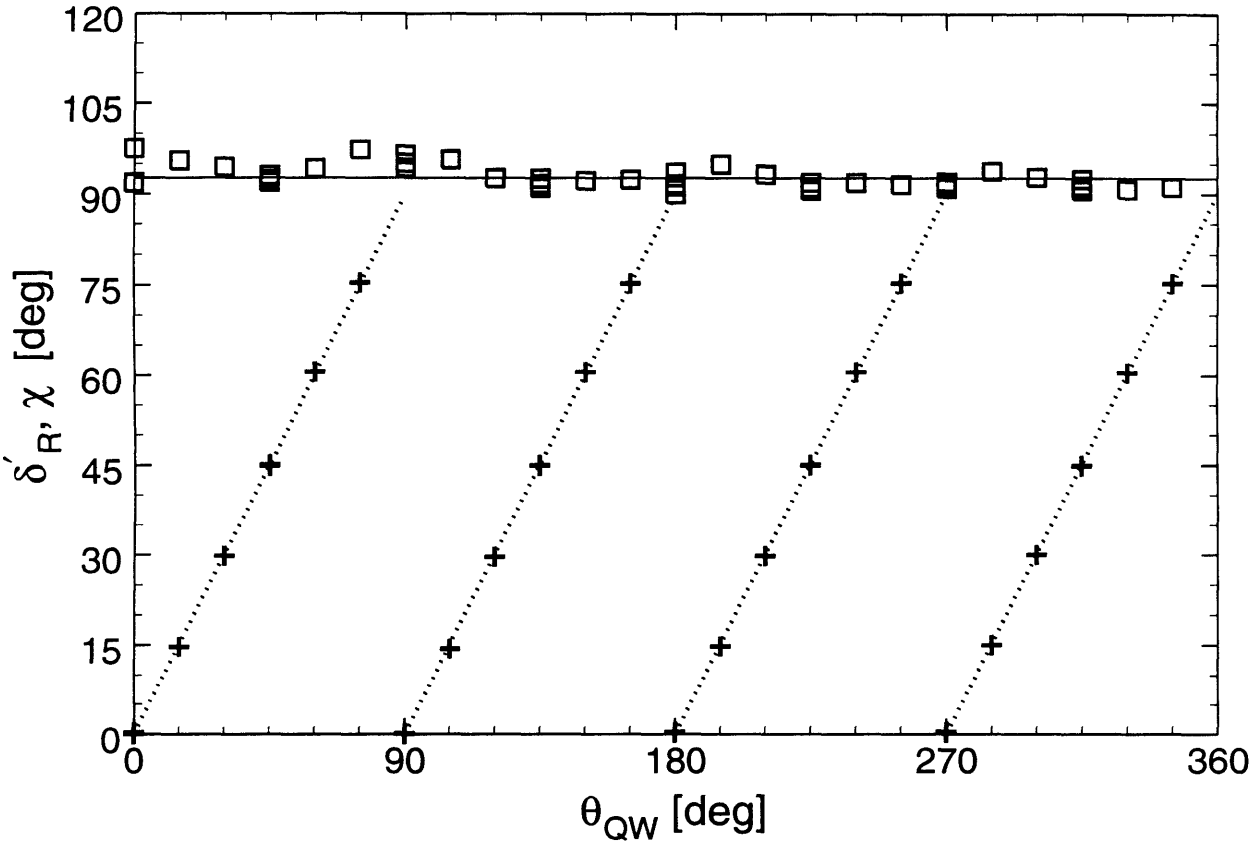

Figure 3.7 Evaluation of the accuracy of the TCFIB system with a quarter wave plate (nominal δ'_R = 90 [deg] at 632.8 [nm]), quantities are measured as a function of wave plate orientation angle, θ_{QW}: (□) measured retardance, δ'_R, in terms of wavelength λ = 632.8 [nm], and average value of retardance over all orientation angles, (——); (+) measured extinction angle, χ, and linear fit (- - - -).

Reference	System	Quarter-Wave Plate (QWP) Assessment			Minimum Detectable Δn
		Accuracy of QWP δ'	Fractional Error in δ'	Deviation in χ [deg]	
Frattini & Fuller, 1984	PMFIB	±1%	2.4% ± 2%	0.25	
Chow, 1984	TCFIB	±2%	2.2% ± 1%	0.15	2×10^{-7}
Quinzani, 1991	TCFIB	±2%	0.4% ± 0.5%	0.2	2.3×10^{-7}
Genieser, 1997	TCFIB	±2%	2.9% ± 2%	0.25	2.1×10^{-7}

Table 3.1 Comparison of the accuracy and sensitivity of several FIB systems using a quarter-wave plate retarder.

The accuracy of the retardation (δ') of the quarter-wave plate used to assess a given system is given in the table. Clearly, the absolute accuracy of the system cannot be assessed more precisely than the accuracy of the quarter-wave plate used to test it. For the fractional error in the measurement of δ', the first value quoted is the percent deviation of the mean of the measurement from the nominal value of 90 [deg]; the second is the standard deviation about the mean of the measured values. The fractional errors reported by Frattini & Fuller and Chow and in this study are all of the same order; the fractional error reported by Quinzani is somewhat smaller. The deviation of the extinction angle (χ) measurement conducted with the quarter-wave plate is of the same order for all of the experiments. In the right-most column, the minimum detectable birefringence for the systems is given. The value of Chow is given as reported. For the investigation of Quinzani and this study, the given value is based on the parasitic birefringence. Specifically, $\Delta n_{Parasitic}/\Delta n_{Min} = 0.2$; i.e., this Δn_{Min} is the smallest birefringence which can be measured such that the error does not exceed 20%.

3.6 Couette Cell: Used to Determine Stress-Optical Coefficient

As indicated by eq. 3.4, in order to interpret the birefringence measurements taken for the planar contraction flow in terms of the stress, it was necessary to first obtain the stress-optical coefficients of the polyisobutylene solute (C_{PIB}) and the polybutene solvent (C_{PB}).

To determine the coefficients, it was necessary to measure the refractive index tensor (equivalently, the birefringence and extinction angle) in a test flow for which the stress tensor was known. The specific details and the results of the measurement are described in §6.4.1; the test geometry is described here.

A simple geometry which allows the measurement to be conducted is narrow gap Couette flow. The same device was used as in the investigation of Quinzani (Quinzani, 1991); a schematic showing essential features is shown in Fig. 3.8. The apparatus consists of an inner, cylindrical spindle of radius R_1 = 80 [mm] contained within a hollow cylindrical housing of which the inner radius was R_2 = 81.5 [mm]. Both the spindle and the housing were constructed of aluminum which was anodized in order to minimize reflections of the laser beam. The region between these spindle and the inner surface of the housing is an annular gap of constant width $R_2 - R_1$ = 1.5 [mm]. The geometry provides a good approximation to the narrow gap limit, specifically one obtains the dimensionless gap width of $(R_2 - R_1)/R_1 = \delta = 0.019$. One may note that in the limit of $\delta \rightarrow 0$, the shear rate is uniform throughout the gap with $\dot{\gamma}_0 = -\Omega/\delta$, where Ω is the angular rotation rate of the inner spindle. For a viscosity non-shear-thinning fluid, the fractional deviation from the limiting shear-rate value, at any position within the gap, $R_1 \leq r \leq R_2$, does not exceed $(\dot{\gamma}(r) - \dot{\gamma}_0)/\dot{\gamma}_0 = \pm\delta/2$ (Leal, 1992). In the case of the Couette cell used to obtain the stress-optical coefficients, this value is $\delta/2$ = .0094. Consequently, the stress field may be assumed to be homogeneous over the gap width.

To generate the shear flow, the inner spindle is rotated by a variable speed DC electric motor. To precisely determine the speed of rotation, a four-bladed chopper wheel was placed on the shaft extending from the spindle. A light beam was shown through the chopper wheel and onto a photodetector. The output of the photodetector was sent to an analog-to-digital board and subsequently a personal computer, which determined the rotation rate of the spindle, Ω, by timing the interval between successive light pulses.

As shown in Fig. 3.8, the laser beams of the TCFIB system travel through the annular gap, parallel to the axis of rotation of the spindle. The beam travelled through a distance L_S = 80 [mm] of sheared sample, the high aspect ratio of the shear region, $L_S/(R_2 - R_1)$ = 53, ensured that the influence of end effects on the birefringence measurement was negligible. The windows through which the laser beam passed were constructed of silica glass.

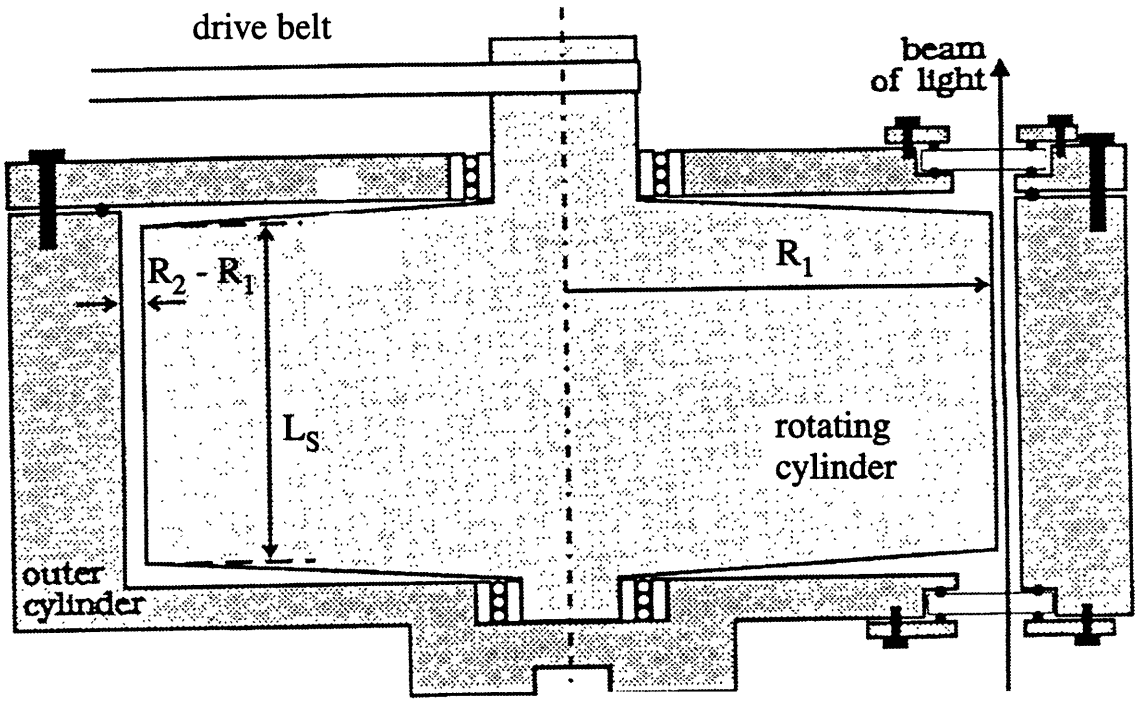

Figure 3.8 Couette cell used to measure stress-optical coefficients. (*modified from* (Quinzani, 1991)).

Parasitic birefringence induced by stresses within the glass was experimentally determined to be negligible. Additional detail on the design of the Couette cell is found in the thesis of Quinzani (Quinzani, 1991).

Chapter 4

Test Fluid Rheology

This Chapter describes the composition and rheological characterization of the test fluid developed for the experiments described in this thesis. To allow the experiments to be conducted at room temperature and moderate pressures a polymer solution rather than a melt was used. In order to maximize the utility of the experimental results of this thesis for comparison with future numerical simulations, the same fluid was used for both the investigation of elastically driven instabilities in Chapter 5 and the elongational response in Chapter 6. Since viscoelastic fluids which have been used in previous studies could not satisfy all the requirements for both of these studies a new test fluid had to be developed.

High Weissenberg numbers had to be attained in order to observe elastically driven instabilities in the study of Chapter 5. At the same time, the test fluid had to be essentially non-shear-thinning in viscosity over the range of shear rates characteristic of the flow in order to avoid the attainment of high Reynolds number, Re. Hi Re could result in onset of inertially-driven instabilities or the modification of elastic instabilities, which would complicate interpretation of the results. These considerations motivated use of a Boger fluid which had long relaxation time and high and constant viscosity.

The studies conducted in Chapter 6 on the measurement of the elongational viscosity of the fluid also required use of a fluid with long relaxation time, so that the critical strain rate required to elongate the molecule was within the range attainable by the fluid handling system. For the study of Chapter 6, the shearfree centerline of the planar contraction flow was used as a "tool" to characterize the elongational response of the test fluid. Modification of the flow field via an inertial mechanism was not, in and of itself, of consequence. However, measurement of the transient elongational viscosity profile required a flow which was steady in an Eulerian sense. Moreover, as discussed in Chapter 3, direct interpretation of birefringence measurement in terms of the stress field necessitated that the flow field be two-dimensional. Both of these requirements would not be met if use of a viscosity shear-thinning fluid resulted in attainment of high Re and consequent onset of an inertially driven instability. These considerations indicated the use of a Boger fluid as the

test fluid. However, previous investigations found that use of a ternary polyisobutylene (PIB) in polybutene (PB) and tetradecane (C14) polymer solution resulted in divergence of a beam passing through the solution, probably associated with structural changes in composition (shear-induced phase separation or concentration fluctuation enhancement). One of the achievements of this thesis was the development of a new test fluid which possessed the properties required for the investigations of Chapters 5 and 6, i.e., a binary Boger fluid with long relaxation time and constant viscosity which did not induce beam divergence when sheared.

The composition of the test fluid and its molecular character are discussed in §4.1. A description of standard material functions used to characterize the rheology of viscoelastic fluids is given in §4.2. Experimental techniques used to obtain rheological information are described. §4.3 presents the origins, applications, and limitations of constitutive models used to model viscoelastic fluid flow in this thesis. In §4.4 the background information presented in Sections 4.1 through 4.3 is used in conjunction with experimental data to describe the rheology of the test fluid in shear flow and fit parameters of constitutive models. §4.5 defines the shear-rate-dependent Weissenberg number, and presents the Weissenberg number of the test fluid as a function of shear rate.

4.1 Fluid Composition and Molecular Character

In §4.1.1, common characteristics of the composition of Boger fluids are discussed; general methods for producing these fluids are described. In §4.1.2 the rheological properties of solutions in the dilute limit are compared with those in the concentrated regime. Scaling arguments which assess whether a solution is in the dilute or concentrated limit are discussed; Boger fluids, including the test fluid used in this thesis, are found generally to be in an intermediate, semidilute regime. Consideration of the dimensions of the high MW PIB solute in the limiting coiled and fully stretched configurations provides additional information on the fluid microstructure. In §4.1.3 previous experimental and theoretical investigation of the phenomenon of "shear-induced phase separation" or "shear-induced concentration fluctuation enhancement" are discussed. Specific reference to the shear-induced beam divergence observed for a ternary PIB in PB and C14 Boger fluid is

made, this phenomenon prevented FIB measurements from being taken in a previous investigation (McKinley *et al.*, 1991; Byars, 1996). A new, two-component Boger fluid was developed for the investigations of this thesis; the test fluid does not exhibit shear-induced beam divergence. Specific detail on the composition of the 0.30 wt% PIB in PB binary Boger fluid used for experiments in this thesis is given in §4.1.4.

4.1.1 Composition of Boger Fluids

Previous investigations of viscoelastic fluid flow have used test fluids with the character of Boger fluids, which are nearly non-shear-thinning in viscosity (although they may exhibit shear thinning of the first normal stress coefficient) (Boger, 1977/1978; McKinley *et al.*, 1991; Byars, 1996). Since the viscosity does not shear thin, flow effects induced by the elastic nature of the fluid can be studied (i.e. high Weissenberg number can be attained) while neglecting inertia. To compose a Boger fluid, a low concentration of high molecular weight (MW) polymer is dissolved in a medium MW polymeric solvent. The high MW component gives the fluid its elastic nature (non-zero first normal stress coefficient and memory) while only making a small or moderate contribution to the viscosity. The medium MW polymer exhibits Newtonian behavior over the shear rates investigated, but is highly viscous. The viscosity of the medium MW solvent, η_s, dominates over the moderate viscosity contribution of the high MW solute, η_p; consequently, shear thinning of the solution viscosity, $\eta = \eta_s + \eta_p$, is negligible.

Although they have similar shear rheology, and exhibit some similarity in composition, the chemical character of Boger fluids can differ widely. Boger fluids have been composed of polar, high MW solutes dissolved in aqueous polymeric solvents as well as non-polar, high MW solutes dissolved in organic polymeric solvents. In the case of the non-polar solutes, since the polymer solvent is of medium molecular weight (typically $M_w \sim 10^3$ [g mol^{-1}]) the direct dissolution of the high MW polymer in the solvent is unacceptably slow. To accelerate the mixing, a low MW oligomeric cosolvent is used. This cosol-

vent may either remain as part of a ternary solution, or a volatile cosolvent may be removed to form a binary solution.

4.1.2 Rheological and Molecular Characteristics of Dilute and Concentrated Solutions

In a dilute solution, the polymer molecules are spaced sufficiently far apart that direct interaction between macromolecules is negligible. Material functions such as the elongational viscosity are solely related to interaction of the solvent flow field with the individual macromolecules and associated changes in conformation, e.g. stretching, of these macromolecules. Consequently, the magnitudes of material functions such as η_p and the first normal stress coefficient, Ψ_1, are directly proportional to the polymer concentration.

In contrast, in a concentrated solution, the polymer molecules form an entangled network. Forces can be transmitted directly between macromolecules rather than through an intermediate solvent. In fact, in the limiting case of a single-component polymer melt, no solvent is present. Consequently, in addition to considering changes in conformation of the individual macromolecules, constraints imposed on the motion of a given macromolecule by its neighbors must be considered. Because of these nonlinear interactions, the zero-shear-rate viscoelastic material functions exhibit a nonlinear, power-law dependence on polymer concentration. In addition, the dependence of material functions on polymer molecular weight is much more sensitive than for the case of dilute solutions. The zero-shear rate material functions of solutions in the concentrated regime have been shown

experimentally and for the dilute regime experimentally and theoretically to scale as given in Table 4.2.

Zero-Shear-Rate Material Function	Dilute Solution	Concentrated Solution
Viscosity	$\eta_{p0} \sim \eta_s cM^{1/2}$	$\eta_0 \sim (cM)^{3.4}$
First Normal Stress Coefficient	$\Psi_{10} \sim \eta_s^2 cM^2$	$\Psi_{10} \sim (cM)^{2(3.4)}$
Relaxation Time	$\lambda_{p0} \sim \eta_s M^{3/2}$	$\lambda_0 \sim (cM)^{3.4}$

Table 4.1 Scaling of steady shear material functions with solute concentration, c, and molecular weight, M, for dilute and concentrated polymer solutions.

The relaxation time at zero-shear rate is defined in the Table as $\lambda_0 = \Psi_{10}/2\eta_{p0}$ for dilute solutions and $\lambda_{p0} = \Psi_{10}/2\eta_0$ for concentrated solutions. One should note that the transition between dilute and concentrated behavior is not sharp; a transition region of semidilute behavior exists (Bird *et al.*, 1987a; Bird *et al.*, 1987b).

The critical concentration, c* (mass of high MW polymer solute per mole of solvent), at which the polymer molecules first begin to interact is dependent on the polymer solute molecular weight and on the solvent "power". Higher MW polymer solutes have lower critical concentration. Solvent "power" refers to the ability of a solvent to dissolve a polymeric solute of a particular MW, more specifically, to the change in free energy upon mixing, ΔG_{mix}. In a "good" solvent the solute polymer chains will be extended relative to their conformation in a theta-solvent.[1] Consequently, the "better" the solvent (more negative ΔG_{mix}), the lower the critical concentration (Rosen, 1982).

De Gennes considered a solution of long polymer molecules (e.g. the $M_w = 2 \times 10^6$ [g mol^{-1}] polyisobutylene (PIB) used in these experiments) in a good, athermal solvent of medium MW polymer chains (e.g. the $M_n = 1.3 \times 10^3$ [g mol^{-1}] polybutene (PB)) (de Gennes, 1979). An athermal medium MW solvent such as PB behaves as a theta-solvent when the polymer chains have a contour length, L_L, greater than the square root of the

1. A polymer solution is said to be at the theta-condition when the Gibbs free energy of the system does not change upon mixing of the solute (for which the MW approaches infinity) with the solvent, $\Delta G_{mix} = 0$; i.e., the polymer/solvent system is thermodynamically neutrally stable.

chain length of the high MW solute, L_H. That is, when $L_L > L_H^{1/2}$, the increase in entropy upon mixing is minimal, $\Delta S_{mix} \approx 0$; since the solvent is athermal, $\Delta H_{mix} = 0$, the increase in free energy is also minimal, $\Delta G_{mix} = \Delta H - T\Delta S \approx 0$. In contrast, if the solvent chains are shorter than the critical value, ΔG_{mix} is expected to be sufficiently negative for the medium MW component to function as a moderately good solvent. In the 0.31 wt% PIB in PB and C14 solution, one obtains $L_L \sim L_H^{1/2}$; i.e. the polybutene is in the transition region between a good, athermal and a neutral, theta-solvent.

For the case of a good, athermal solvent, the critical concentration, c^*, scales with the square-root of the molecular weight

$$c^* \propto M^{1/2} \tag{4.1}$$

More specifically, the critical concentration of a solution of $M_w = 2 \times 10^6$ [g mol^{-1}] PIB molecules in a good, athermal solvent is calculated as (de Gennes, 1979; McKinley, 1991)

$$c^* = \frac{3M}{4\pi N_A \langle r^2 \rangle_0^{1/2}} = 8.1 \times 10^4 \text{[g mol}^{-1}\text{]} \tag{4.2}$$

which would correspond to a 0.08 wt% PIB in PB solution. Note that M is the molecular weight for a polymer of monodisperse molecular weight distribution (MWD); N_A is the Avogadro number and $\langle r^2 \rangle_0^{1/2}$ the equilibrium root-mean-square (r.m.s.) end-to-end length of the polymer coil. Since the solvent "power" of the medium MW PB used in this study is in the intermediate range between a good and a theta-solvent, the high MW PIB molecules are expected to be more tightly coiled than they would be in a good solvent. Consequently, the actual critical concentration for the PIB in the PB will be higher than c^* = 0.08 wt%. The test fluid used in this study, with a concentration of 0.30 wt% PIB in PB, greater than but of the same order as the critical concentration, c^*, should be in an intermediate, or semidilute, regime of concentration.

This semidilute regime is less well understood from a theoretical perspective than the limiting dilute or concentrated regimes; accepted empirical scalings, as are available for concentrated solutions, do not exist. Nevertheless, one may note that most Boger fluids

previously used in experimental investigations of viscoelastic fluid flow have been semi-ilute solutions. The requisite property of viscosity non-shear-thinning excludes the use of concentrated solutions for these fluids. Dilute solutions are, in principle, ideal Boger fluids since the high MW polymer makes only an infinitesimal contribution to the solution viscosity. However, the first normal stress coefficient of these solutions is also small. In general, it is too difficult to achieve experimental conditions of high Weissenberg number to allow the use of dilute solutions.

Understanding of the response of the high MW polymer molecule to an imposed flow field is developed by consideration of the limiting dimensions of the molecule in the coiled state at equilibrium and a hypothetical, fully stretched state. A simple estimate can be obtained by treating the chain as a "random-walk" distribution; the bond angles are taken into consideration but the steric and excluded volume effects are neglected. From the known molecular weight ($\overline{M}_w$), mass of the isobutylene repeat unit (m_0), and bond angle (θ) and length ($l_{C\text{-}C}$) of a carbon-carbon bond, the equilibrium r.m.s. end-to-end length of the polymer is determined to be

$$\sqrt{\langle r^2 \rangle_{0f}} = l_{C\text{-}C} \sqrt{\left(\frac{1+\cos\theta}{1-\cos\theta}\right)\left(\frac{2\overline{M}_w}{m_0}\right)}; \tag{4.3}$$

For the case of the high MW PIB polymer, which has the constants $\overline{M}_w = 2 \times 10^6$ [g mol^{-1}], $m_0 = 56$ [g mol^{-1}], $\theta = 109.5$ [deg], and $l_{C\text{-}C} = 1.54 \times 10^{-10}$ [m], one obtains $\sqrt{\langle r^2 \rangle_{0f}} = 6 \times 10^{-8}$ [m] (McKinley, 1991; Flory, 1953). However, the effects of excluded volume and the pendant -CH_3 groups along the backbone will result in the polymer at equilibrium in a theta solvent being expanded relative to this simple "random-walk" estimate. These effects are taken into consideration by experimental determined Mark-Houwink parameters for the polymer in a theta solvent. McKinley (McKinley, 1991) used the parameters K = 107 $\times$ 10^{-3} [cm^3 g^{-1}] and a = 0.50 for PIB in benzene, which acts as a theta solvent at the test temperature of 24 [C] (Brandup and Immergut, 1975); the r.m.s. end-to-end length was then calculated to be $\sqrt{\langle r^2 \rangle_0} = 1.0 \times 10^{-7}$ [m]. The contour length of the fully extended chain can be directly

calculated from the molecular weight of the polymer, molecular weight of the repeat unit, and bond length and angle as

$$L_c = l\left(\frac{2\bar{M}_w}{m_0}\right)\cos\left(\frac{180° - \theta}{2}\right) \tag{4.4}$$

(McKinley, 1991). For the high MW PIB polymer used for the investigations of this thesis $L_c = 8 \times 10^{-6}$ [m]. Hence the ratio of end-to-end lengths which the polymer molecule can, in principle, have is large,

$$\frac{L_c}{\sqrt{\langle r^2\rangle_0}} = 80. \tag{4.5}$$

A fully extended state could only be attained in elongational flow of extremely high strain rate. More detailed consideration of the response of a polymer molecule to an elongational flow is given in Chapter 6.

Polymer solution theory provides a useful guide for understanding the nature of the semidilute polymer solution which was used as the test fluid for the investigations comprising this thesis. However, the theory, which contains a number of assumptions, cannot be applied in a quantitative manner. For example, the scalings of polymer solution theory are based on a monodisperse molecular weight distribution (MWD) of the components of a polymer solution. In actuality, both the high MW solute and the medium MW solvent comprising the test fluid had broad MWDs. Note that the MWD also implies a distribution of polymer end-to-end length in the coiled, $\sqrt{\langle r^2\rangle_0}$, and in the extended, L_c, configurations.

4.1.3 Shear-Induced Turbidity in Polymer Solutions

A Boger fluid which has been extensively characterized is the ternary solution of 0.31 wt% high MW polyisobutylene dissolved in a solvent of 5 wt% tetradecane in polybutene (Quinzani *et al.*, 1990). It was initially attempted to use this fluid in the flow induced birefringence (FIB) investigation discussed in Chapter 6. The stress-optical coefficient was

obtained using a Couette cell filled with the test fluid and by passing a laser beam through the sample in the "neutral" direction. Immediately upon shearing, the beam was observed to diverge (Quinzani *et al.*, 1992). This effect was not attributed to a refractive index gradient associated with viscous heating since it occurred at low shear rates and immediately upon shearing. Similar phenomena have been noted for other ternary and binary polymer solutions (van Egmond and Fuller, 1993; Yanase *et al.*, 1991; Krämer-Lucas *et al.*, 1988a). Elucidation of the origin of "shear-induced turbidity" remains an active area of investigation. The hypotheses initially proposed suggested a thermodynamic mechanism of shear-induced phase separation (Rangel-Nafaile *et al.*, 1984; Krämer-Lucas *et al.*, 1988b). The theoretical basis of this hypothesis was criticized by Helfand and Frederickson (Helfand and Frederickson, 1989) and by Onuki (Onuki, 1989) who sought an explanation in terms of shear-induced growth of concentration fluctuations which could precede the formation of aggregated polymer structures. Both of these interpretations could explain the phenomena of "shear induced turbidity" and an associated decrease in solution viscosity (Schmidt and Wolf, 1979); neither interpretation is in perfect agreement with experiment (Yanase *et al.*, 1991; Onuki, 1989).

Determination of the origin of the "shear-induced turbidity" phenomenon is outside of the scope of this thesis. However, it was crucial to find a polymer solution which did not cause the broadening of the probe beam which prevented an FIB measurement from being taken. In the ternary solution, the low molecular weight tetradecane oligomers will diffuse much more rapidly than the medium or high molecular weight polymers. It was speculated that the presence of rapidly diffusing oligomer would render the solution more susceptible to "shear induced turbidity". Specifically, phase separation could occur (thermodynamic reasoning) or the concentration fluctuations could grow to an observable size on the time scale of the experiment. In contrast, if the tetradecane oligomer were removed, the system might be in a thermodynamically unstable state or have growing concentration fluctuations; however, since the time scale for diffusion of the medium and of the high molecular weight polymers would be long compared with the time scale of the experiment, the phenomenon would not manifest itself macroscopically (Muller, 1992; Byars, 1992).

The procedure for composing the binary high MW polyisobutylene in medium MW polybutene solution is described in §4.1.4. When this solution was used in the Couette

cell, no beam divergence was observed; FIB measurements could be taken. However, one must realize that this observation does not in and of itself validate the speculation of the above paragraph which led to the use of a binary solution. Presently, the absence of beam divergence upon shearing of the binary solution must be taken only as an empirical finding.

4.1.4 Composition of Test Fluid

As discussed in §4.1.2, the "solvent power" of the medium molecular weight (MW) polybutene solvent (PB) with respect to the polyisobutylene solute (PIB) is in the intermediate regime between a good, athermal solvent and a neutral, theta solvent. Consequently, in order to dissolve the high MW polyisobutylene ($M_w = 2 \times 10^6$ [g mol^{-1}], Exxon Chemicals, Vistanex L-120 (McKinley, 1991)) in the medium MW polybutene ($M_n = 1.3 \times 10^3$, Amoco Chemical, Panalane H300E (Amoco Chemical Company, 1992)) within an acceptable period of time, it was necessary to use hexane as a cosolvent. The PIB was initially dissolved to a concentration of 2 wt% in chromatography grade hexane. The solution was stirred for 24 [hr]. Completeness of dissolution was assessed by observing the solution through the glass walls of the flask, any region of non-homogeneous concentration would show up as a "shimmering" caused by variation in refractive index; at the end of the 24 [hr] period no such "shimmering" was apparent. The PIB in hexane solution was then combined with the PB in a 20 [*l*] container. Dissolution was promoted by placing the container on a roll mill for at least 24 [hr]; after "rolling" the visual appearance of the solution was homogeneous. The PIB in hexane and PB ternary solution was then poured into a set of shallow trays to a depth of approximately 1 [cm]. The solution was heated for 24 [hr] under a nitrogen purge at a temperature of approximately 70 [°C] . The solution then underwent heating at 70 [°C] for an additional 48 [hr] under vacuum to complete removal of the hexane. A fluid sample was taken and the viscosity and first normal stress coefficient measured in a rheometer (RMS-800, Rheometrics). The fluid in the trays was then heated under vacuum, at 70 [°C], for an additional 6 [hr]. A second sample from the same tray as the first sample was then taken and its rheological properties also measured. The additional 6 [hr] of heating under vacuum had no effect on the rheological properties,

within experimental error. Hence, it was concluded that heating for 24 [hr] under nitrogen and 48 [hr] under vacuum was sufficient to remove the hexane to a trace level where it no longer had any measurable effect on rheological properties. The net yield of PIB in PB test fluid after evaporation of an initial 13 [*l*] of PIB in PB and hexane solution was approximately 7 [*l*]; note that some material was lost during the transfer of the fluid from the vacuum oven to storage containers. The above procedure was repeated several times to obtain a sufficient quantity of fluid, approximately 33 [*l*], to fill the fluid handling system described in §3.1.

Despite the homogeneous appearance of the solution after the "rolling" procedure, there was evidence that the dissolution of the PB with the PIB in hexane solution was incomplete. Specifically, after evaporation of the hexane, samples taken from different trays exhibited significant variation in rheology. It was concluded that after rolling and then standing for several hours, the fluid in the upper section of the 20 [*l*] container was richer in the PIB/hexane solution than the lower section. However, the average concentration of a batch (all the trays taken together) of the PIB in PB solution after evaporation was 0.30 wt%. Therefore, once a sufficient total volume of the two-component PIB in PB fluid had been made, the fluid was poured into the flow handling system (cf. Fig. 3.1). The fluid was heated to 60 [°C] in order to temporarily lower the viscosity and pumped from the supply to the receiver tank and back again ten times. A set of samples from different points in the tank was then taken and the η and Ψ_1 material functions measured; the rheology of the samples was identical to within the error of the instrument (±5% for η and ±10% for Ψ_1). Therefore, the pumping procedure in the fluid handling system homogenized the composition of the fluid to an 0.30 wt% concentration of PIB in PB throughout, with no detectable hexane.

4.2 Rheological Methods and Definition of Material Functions

A polymer flow in a typical industrial process is highly complex; the rate-of-strain tensor varies throughout the system, may be time-dependent, and has both shear and elongational components. Although the ultimate goal is the ability to accurately simulate numerically such a system; it is first necessary to characterize and understand viscoelastic

fluid behavior in kinematically simple test flows. Information from such standard test flows, in conjunction with a suitable constitutive equation, could then be used to predict phenomena in complex flows more closely resembling industrial processes. The two main categories of standard flow patterns are shear and shearfree flows. A summary of test flows used to determine the material functions of non-Newtonian fluids can be found in Bird, et al. (Bird *et al.*, 1987a); the flows used for the investigations comprising this thesis are described here.

4.2.1 Shear Flows Material Functions

A simple shear flow is defined by the velocity field:

$$\begin{aligned} v_x &= \dot{\gamma}(t)y \\ v_y &= 0 \\ v_z &= 0 \end{aligned} \tag{4.6}$$

where $\dot{\gamma}(t)$ represents the "shear rate".[2] For simple shear flow the shear rate can be a function of time but is independent of position; it is a homogeneous, or uniform, flow. Several shear flow material functions are defined in this Section; specific measurement techniques are then discussed in.

Steady Shear Flow

A subclass of simple shear flow is the time-independent, or steady, flow case with $\dot{\gamma}(t) = \dot{\gamma}_0$; this flow is illustrated in Fig. 4.1a. The viscosity is defined as

$$\eta(\dot{\gamma}) = -\frac{\tau_{yx}}{\dot{\gamma}_0} \tag{4.7}$$

where τ_{yx} denotes the shear stress. In the case of a Newtonian fluid the viscosity is constant and independent of shear rate, $\eta(\dot{\gamma}) = \mu$. In contrast, non-Newtonian fluids may

2. For a general flow, the shear rate is defined as the magnitude of the rate-of-strain tensor, $\dot{\gamma}$, via $\dot{\gamma} = +\sqrt{(1/2)(\dot{\gamma} : \dot{\gamma})}$.

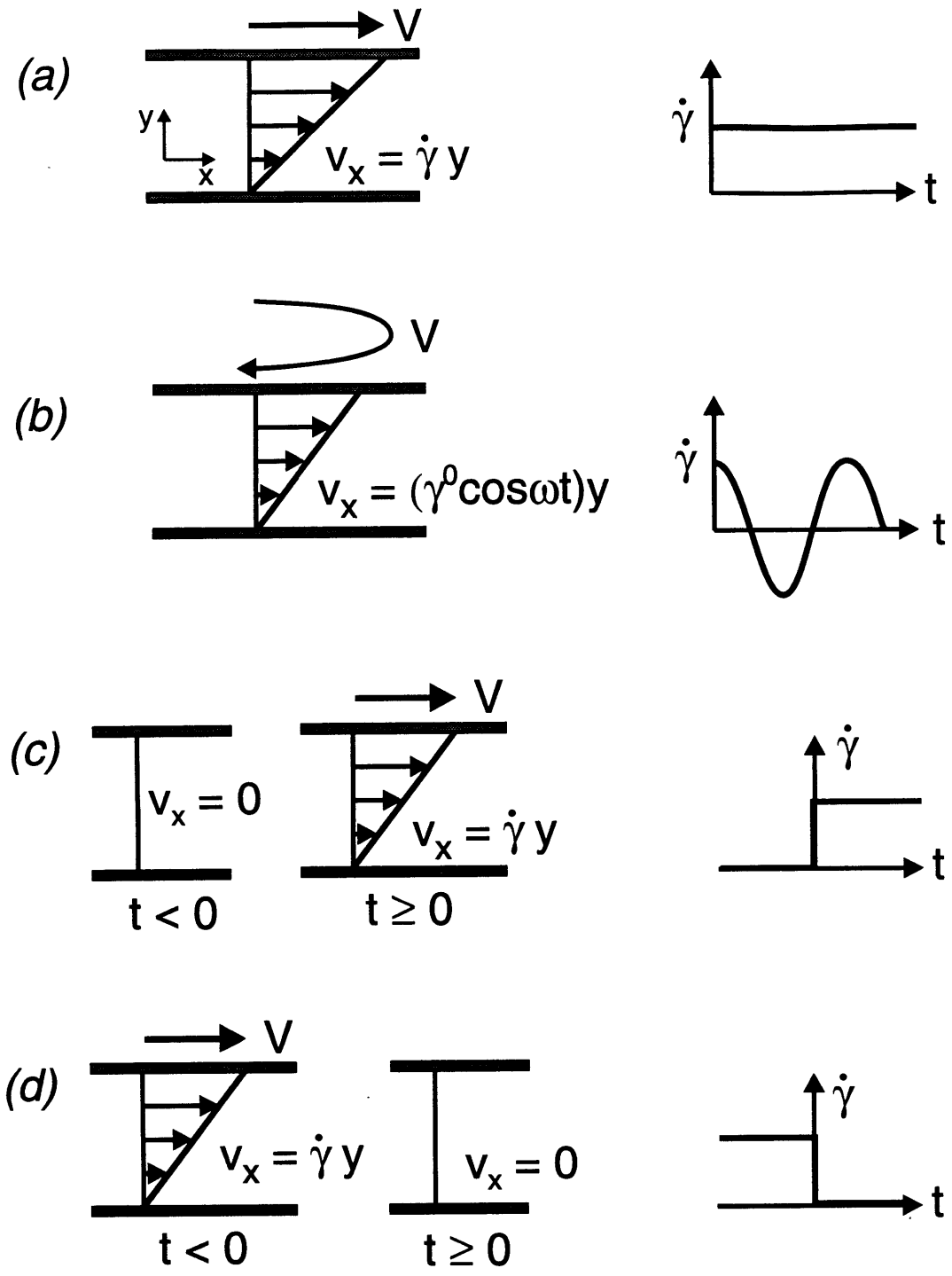

Figure 4.1 Four simple shearing flow experiments used to characterize the rheology of a viscoelastic fluid: (a) steady shear flow; (b) small-amplitude oscillatory shear flow; (c) stress growth after inception of steady shear flow; (d) stress relaxation after cessation of steady shear flow. (*After* (McKinley, 1991; Bird *et al.*, 1987a)).

exhibit shear-thinning (viscosity decrease with shear rate) or shear-thickening (viscosity increase with shear rate) behavior (Bird *et al.*, 1987a).

The first and second normal stress coefficients are defined as

$$\Psi_1(\dot{\gamma}_0) = -\frac{(\tau_{xx} - \tau_{yy})}{\dot{\gamma}_0^2} = -\frac{N_1}{\dot{\gamma}_0^2}$$
$$\Psi_2(\dot{\gamma}_0) = -\frac{(\tau_{yy} - \tau_{zz})}{\dot{\gamma}_0^2} = -\frac{N_2}{\dot{\gamma}_0^2} \tag{4.8}$$

where τ_{xx}, τ_{yy}, and τ_{zz} represent the normal components of the stress tensor, and N_1 and N_2 corresponding normal stress differences. Note that in simple shear flow a Newtonian fluid will have $\Psi_1(\dot{\gamma}_0) = \Psi_2(\dot{\gamma}_0) = 0$; complex fluids may have non-zero normal stress coefficients.

Small-Amplitude Oscillatory Shear Flow

A subclass of the non-Newtonian fluids are the viscoelastic fluids, which have the characteristic of "remembering" a previous state of deformation (Larson, 1988; Bird *et al.*, 1987a). To characterize the "memory" of viscoelastic fluids, a number of time-dependent, or unsteady, test flows exist. Small-amplitude oscillatory shear flow is used to characterize the linear viscoelastic response and determine the linear viscoelastic spectrum of a material as discussed in §4.3. The small-amplitude oscillatory shear flow is defined by the velocity field of eq. (4.6) with $\dot{\gamma}(t) = \dot{\gamma}_0 \cos \omega t$; the flow is illustrated in Fig. 4.1b. Associated material properties, the dynamic viscosity, η', and the dynamic rigidity, η'', are defined by

$$\tau_{yx} = -\eta'(\omega)\dot{\gamma}_0 \cos \omega t - \eta''(\omega)\dot{\gamma}_0 \sin \omega t \tag{4.9}$$

where ω is the frequency of oscillation. These dynamic quantities are related to the storage and loss moduli by

$$\begin{aligned} \text{storage modulus: } G' &= \eta''\omega \\ \text{loss modulus: } G'' &= \eta'\omega \end{aligned} \tag{4.10}$$

Note that η' and G'' are in-phase with the instantaneous shear rate, $\dot{\gamma}(t)$, whereas η'' and G' are out-of-phase. Complex quantities may be defined as

$$\begin{aligned} \text{complex viscosity: } \eta^* &= \eta' - i\eta'' \\ \text{complex modulus: } G^* &= G' + iG'' \end{aligned} \tag{4.11}$$

Note that for a perfectly elastic solid $G' = G$, the constant shear modulus, and $G'' = 0$. Conversely, for a Newtonian fluid $G' = 0$ ($\eta'' = 0$), whereas $G'' = \mu\omega$ ($\eta' = \mu$). In the limit of low shear rate and low frequency the steady-state and small-amplitude oscillatory (dynamic) material functions are related as

$$\begin{aligned} \lim_{\omega \to 0} \eta'(\omega) &= \lim_{\dot{\gamma} \to 0} \eta(\dot{\gamma}) = \eta_0 \\ \lim_{\omega \to 0} \frac{2\eta''(\omega)}{\omega} &= \lim_{\dot{\gamma} \to 0} \Psi_1(\dot{\gamma}) = \Psi_{10} \end{aligned} \tag{4.12}$$

Stress Growth upon Inception of Shear Flow

Other time-dependent, transient flows may be defined. These are generally used to characterize the nonlinear response of a viscoelastic fluid. For measurement of stress growth material functions, the velocity field is as given in eq. (4.6), but with sudden inception of the shear rate

$$\begin{aligned} t < 0: &\qquad \dot{\gamma} = 0 \\ t \geq 0: &\qquad \dot{\gamma} = \dot{\gamma}_0 \end{aligned} \tag{4.13}$$

imposed; the test flow is illustrated in Fig. 4.1c. Subsequently, one defines

$$\eta^+(t, \dot{\gamma}_0) = -\frac{\tau_{yx}^+}{\dot{\gamma}_0}$$
$$\Psi_1^+(t, \dot{\gamma}_0) = -\frac{N_1^+}{\dot{\gamma}_0^2} \tag{4.14}$$
$$\Psi_2^+(t, \dot{\gamma}_0) = -\frac{N_2^+}{\dot{\gamma}_0^2}$$

Stress Relaxation after Cessation of Shear Flow

The velocity field associated with the stress relaxation material functions is defined as in eq. (4.6) but with sudden cessation of the shear rate

$$\begin{aligned} t < 0: &\qquad \dot{\gamma} = \dot{\gamma}_0 \\ t \geq 0: &\qquad \dot{\gamma} = 0 \end{aligned} \tag{4.15}$$

the flow is shown in Fig. 4.1d. One then defines

$$\eta^-(t, \dot{\gamma}_0) = -\frac{\tau_{yx}^-}{\dot{\gamma}_0}$$
$$\Psi_1^-(t, \dot{\gamma}_0) = -\frac{N_1^-}{\dot{\gamma}_0^2} \tag{4.16}$$
$$\Psi_2^-(t, \dot{\gamma}_0) = -\frac{N_2^-}{\dot{\gamma}_0^2}$$

Shear Flow Material Function Measurement Techniques

Steady, small-amplitude oscillatory, and inception or cessation shear flows can all be produced in the cone-and-plate viscometer. Such a device consists of a truncated cone of small angle θ_0 located above a circular flat plate of radius R (cf. Fig. 4.2). The plate can rotate in a single direction at a controlled rate, Ω, for the measurement of steady-state,

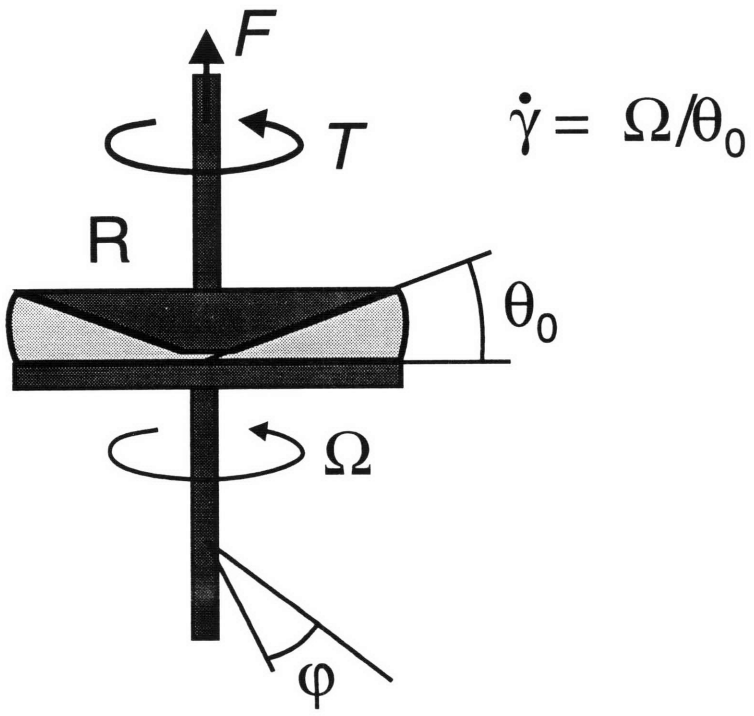

Figure 4.2 Cone-and-plate geometry used for characterization of simple shear material functions.

stress growth, or stress relaxation material functions. The plate can also oscillate azimuthally in φ about a fixed position, allowing dynamic properties to be measured. The cone is connected to force transducers which measure the torque, T, and the upward force normal to the plate, F.

The cone-and-plate geometry has the advantage that a nearly homogeneous flow is developed between the surfaces. Specifically, it has been shown (Bird *et al.*, 1987a) that in the limit of small angle, typically $\theta_0 \leq 0.1$ [rad], the shear rate has a constant value of

$$\dot{\gamma} = \frac{\Omega}{\theta_0} \tag{4.17}$$

throughout the sample, where Ω is the angular rotation rate of the plate. The shear stress may then be calculated as

$$\tau_{\theta\varphi} = -\frac{3T}{2\pi R^3} \tag{4.18}$$

and the first normal stress difference as

$$N_1 = -\frac{2F}{\pi R^2} \tag{4.19}$$

Note that because of the small gap angle and the homogeneity of the flow, one may associate the spherical coordinate system (θ, φ, r) with the Cartesian system (x, y, z) used to define the steady and dynamic material functions above. From the known values of F, T, and $\dot{\gamma}(t)$ the material functions can be calculated.

The apparatus primarily used to determine the shear material functions of the test fluid used in this thesis was the Rheometrics Mechanical Spectrometer (RMS-800). The instrument functions by imposing a rotation on the bottom plate and measuring F and T on the top cone. At low shear rates or oscillation frequencies measurements were limited by the sensitivity of the transducer, accurate readings could be obtained for values as low as $F \approx 0.02$ [N] and $T \approx 2 \times 10^{-4}$ [N m]. Cone fixtures were used of geometry R = 12.5 [mm] with $\theta_0 = 0.1$ [rad] and R = 60 [mm] with $\theta_0 = 0.04$ [rad]. As discussed in §4.4 the material

functions are affected by the sample temperature. For the smaller cone fixture the temperature could be held constant to within ±0.1 [°C]. The temperature could not be set for the larger fixture, but was instead measured to within ±0.1 [°C] and the measured material functions subsequently adjusted by means of time-temperature superposition to a reference temperature, T_0.

Two factors were found to restrict the maximum strain rate for which steady measurements could be taken. The first of these was viscous heating. When a viscous fluid is sheared, mechanical energy is converted to heat. At sufficiently high shear rates, for a given cone geometry (characterized by θ_0 and R), the maximum temperature within the gap will rise to a level where the material functions are affected. To ameliorate this problem, the cone angle may be decreased; however, limitations on the precision of the alignment can result in deleterious effects on accuracy of the measured material functions.

The second limiting factor was the onset of a three-dimensional, time-dependent instability which was related to the interaction of streamwise stresses with streamline curvature. McKinley, et al. have studied this phenomenon in detail via experimental and theoretical means (McKinley *et al.*, 1995); various manifestations of instabilities related to stress-curvature interaction are discussed in Chapter 5 of this thesis. It suffices here to point out that after onset of the instability, the flow no longer has the velocity field character of simple shear flow, preventing the material functions from being determined. Higher shear rates can be attained before instability onset by using a smaller cone angle; however, the cone angle may only be decreased so far before alignment problems affect accuracy.

One should note that other configurations besides the cone and plate may be used to obtain material function data. The parallel-plate geometry is similar to the cone-and-plate configuration with a flat plate replacing the upper cone. The parallel-plate configuration has the advantage that the gap height, which is analogous to the cone angle, can be continuously varied. However, unlike the cone and plate, a homogeneous flow is not approximated: the local shear rate increases linearly as one moves radially from the center to the edge of the plate. The steady material functions $\eta(\dot{\gamma})$, $\Psi_1(\dot{\gamma})$, and $\Psi_2(\dot{\gamma})$ may still be obtained, even for a shear thinning fluid; however, the data reduction procedure is more involved. The interested reader may consult texts such as Bird et al. (Bird *et al.*, 1987a) for details. Factors limiting the minimum and maximum shear rates for which data may be

obtained are essentially the same as described above for the cone-and-plate configuration. The cone-and-plate configuration was primarily used to obtain the shear rheological data presented in §4.4. However, the parallel-plate configuration with small gap height was used in certain instances to avoid instability onset and thereby obtain data at elevated shear rates.

4.2.2 Shearfree Flows

Shearfree flows are defined by the velocity field

$$\begin{aligned} v_x &= -\frac{\dot{\varepsilon}}{2}(1+b)x \\ v_y &= -\frac{\dot{\varepsilon}}{2}(1-b)y \\ v_z &= \dot{\varepsilon}z \end{aligned} \tag{4.20}$$

where $0 \le b \le 1$ and the elongation rate is defined as

$$\dot{\varepsilon} = \frac{\partial v_z}{\partial z}. \tag{4.21}$$

Three different limiting types of elongational flow exist and depend on the values of b and $\dot{\varepsilon}$,

$$\begin{aligned} &\text{uniaxial elongation: } b = 0, \dot{\varepsilon} > 0 \\ &\text{biaxial stretching: } b = 0, \dot{\varepsilon} < 0 \\ &\text{planar elongation: } b = 1 \end{aligned} \tag{4.22}$$

Figure 4.3 illustrates these limiting cases for deformation of a unit cube fluid element. The Hencky strain experienced by a fluid element over a time interval $t_2 - t_1$ is defined as

$$\varepsilon \equiv \int_{t_1}^{t_2} \dot{\varepsilon} dt \tag{4.23}$$

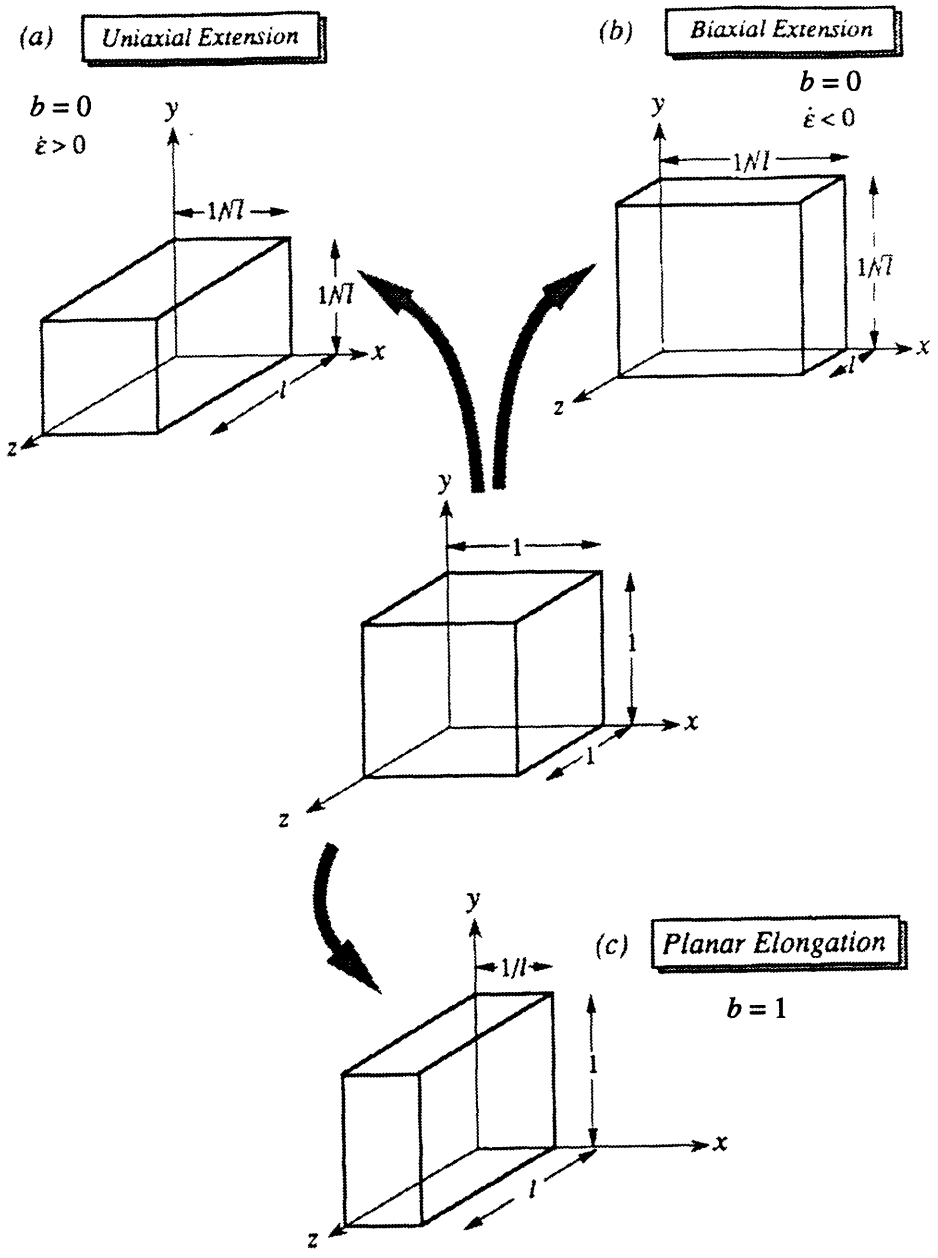

Figure 4.3 Deformation of a unit cell in limiting shearfree flows: (a) uniaxial elongation; (b) biaxial stretching; (c) planar elongation. (*Modified from* (Bird *et al.*, 1987a; McKinley, 1991)).

Shearfree Material Functions

The steady-state shearfree material functions are defined as

$$\begin{aligned} \text{first elongational viscosity: } \bar{\eta}_1 &= -\frac{\tau_{zz} - \tau_{xx}}{\dot{\varepsilon}} \\ \text{second elongational viscosity: } \bar{\eta}_2 &= -\frac{\tau_{yy} - \tau_{xx}}{\dot{\varepsilon}} \end{aligned} \tag{4.24}$$

For the limiting case of b = 0, uniaxial or biaxial flow, one has

$$\begin{aligned} \bar{\eta} &= \bar{\eta}_1 \\ \bar{\eta}_2 &= 0 \end{aligned} \tag{4.25}$$

where $\bar{\eta}$ is referred to simply as the elongational viscosity. In the Newtonian limit the first elongational viscosity for the limiting flows defined above reduces to

$$\begin{aligned} \text{uniaxial elongation or biaxial stretching:} \quad & \bar{\eta} = 3\mu \\ \text{planar elongation:} \quad & \bar{\eta}_1 = 4\mu \end{aligned} \tag{4.26}$$

where the viscosity of the Newtonian fluid is given as μ.

Transient elongational material properties can also be defined. For example, one can measure stress growth on inception of steady shearfree flow

$$\begin{aligned} t < 0, \dot{\varepsilon} &= 0 \\ t \geq 0, \dot{\varepsilon} &= \dot{\varepsilon}_0 \end{aligned} \tag{4.27}$$

and determine the associated material functions:

$$\begin{aligned} \bar{\eta}_1^+ &= -\frac{\tau_{zz} - \tau_{xx}}{\dot{\varepsilon}_0} \\ \bar{\eta}_2^+ &= -\frac{\tau_{yy} - \tau_{xx}}{\dot{\varepsilon}_0} \end{aligned} \tag{4.28}$$

Shearfree Flow Material Function Measurement Techniques

By comparison with the shear flow material functions, the shearfree material functions are difficult to measure experimentally. In contrast with shear flows, where particles in different shearing surfaces diverge approximately linearly in time at steady state, in steady shearfree flows particles diverge exponentially in time. Furthermore, establishment of boundary conditions which result in a homogeneous flow field is much more difficult for shearfree than for shear flows. Consequently, it can be difficult or impossible to observe the steady-state values of the material functions.

In this Section, techniques which produce a nominally homogeneous flow field and subsequently determine the shearfree material functions of the test fluid are discussed. The requirement of a homogeneous flow field can constrain the test fluids which may be used and the attainable Hencky strain and, hence, the range of application of these techniques. Methods which characterize the elongational material behavior of a test fluid in non-homogeneous flows are then described. A broader range of test fluids may be used for several of these techniques. However, most of the methods do not fully characterize the strain history of the streamlines comprising the flow field. Consequently, only an "apparent elongational viscosity" is measured; this quantity may bear little relation to the shearfree material functions defined in above. More significantly, the "apparent elongational viscosity" is difficult to compare with results obtained in other experiments and is usually not suitable for quantitative evaluation of constitutive models. In the last part of this Section, the use of rheo-optical techniques to obtain stress and velocity field information is discussed. The pointwise measurements obtained by rheo-optical techniques allow quantitative and well-defined elongational property data to be obtained in certain non-homogeneous flows.

One may note that summaries of mechanically based elongational material property measurement techniques are given in Bird et al. (Bird *et al.*, 1987a). The thesis of Quinzani (Quinzani, 1991) also provides useful perspective.

Measurement of Shearfree Material Functions in Nominally Homogeneous Flow Fields

In this Section several experimental techniques which use mechanical methods to measure shearfree material functions of a test fluid in a homogeneous flow field are described. Limitations on the types of fluids which can be studied and the Hencky strain which can be achieved with these methods are discussed; such constraints motivate techniques which use non-homogeneous flow fields, discussed below.

Two experimental configurations which generate well characterized, homogeneous flows are the homogeneous stretching method (Cogswell, 1968; Münstedt, 1975; Münstedt, 1979; Laun and Münstedt, 1976) and Meissner's apparatus (Meissner, 1971). In the homogeneous stretching method, shown in Fig. 4.4a, a cylinder of material is placed between two clamps, which are then pulled apart at a constant strain rate, $\dot{\varepsilon}$, to produce a uniaxial elongational flow. The sample length increases as

$$l = l_0 \exp(\dot{\varepsilon}_0(t - t_0)) \tag{4.29}$$

where l_0 is the length at time t_0. At the end of the test, the polymer sample is simultaneously cut into pieces of equal length, which are then weighed to ensure that the strain experienced by a given fluid element was homogeneous throughout the sample. It is apparent that this exponential dependence in conjunction with restrictions on the physical size of the device will limit the Hencky strain, $\varepsilon = \dot{\varepsilon}_0(t - t_0)$, to low values. Nevertheless, the transient elongational viscosity, $\bar{\eta}^+$, associated with start-up of elongational flow, can be determined by measuring the tensile force exerted on the clamps and applying eq. (4.28). Meissner's apparatus, illustrated in Fig. 4.4b, is a similar technique but allows attainment of substantially higher values of ε. In this device the material sample is stretched at a constant strain rate by two counterrotating pairs of clamps, which remain a fixed distance apart. Hencky strains as great as $\varepsilon \sim 7$ have been attained with this device. Meissner observed a maximum in $\bar{\eta}^+$ for a polyethylene melt at $\varepsilon \sim 6$ followed by a decline in $\bar{\eta}^+$; even at $\varepsilon \sim 7$ a steady state was not observed (Meissner, 1985). A related apparatus capable of producing a more general class of elongational flow was also constructed by Meissner (Meissner, 1985). A sheet of polymer is surrounded on the perimeter

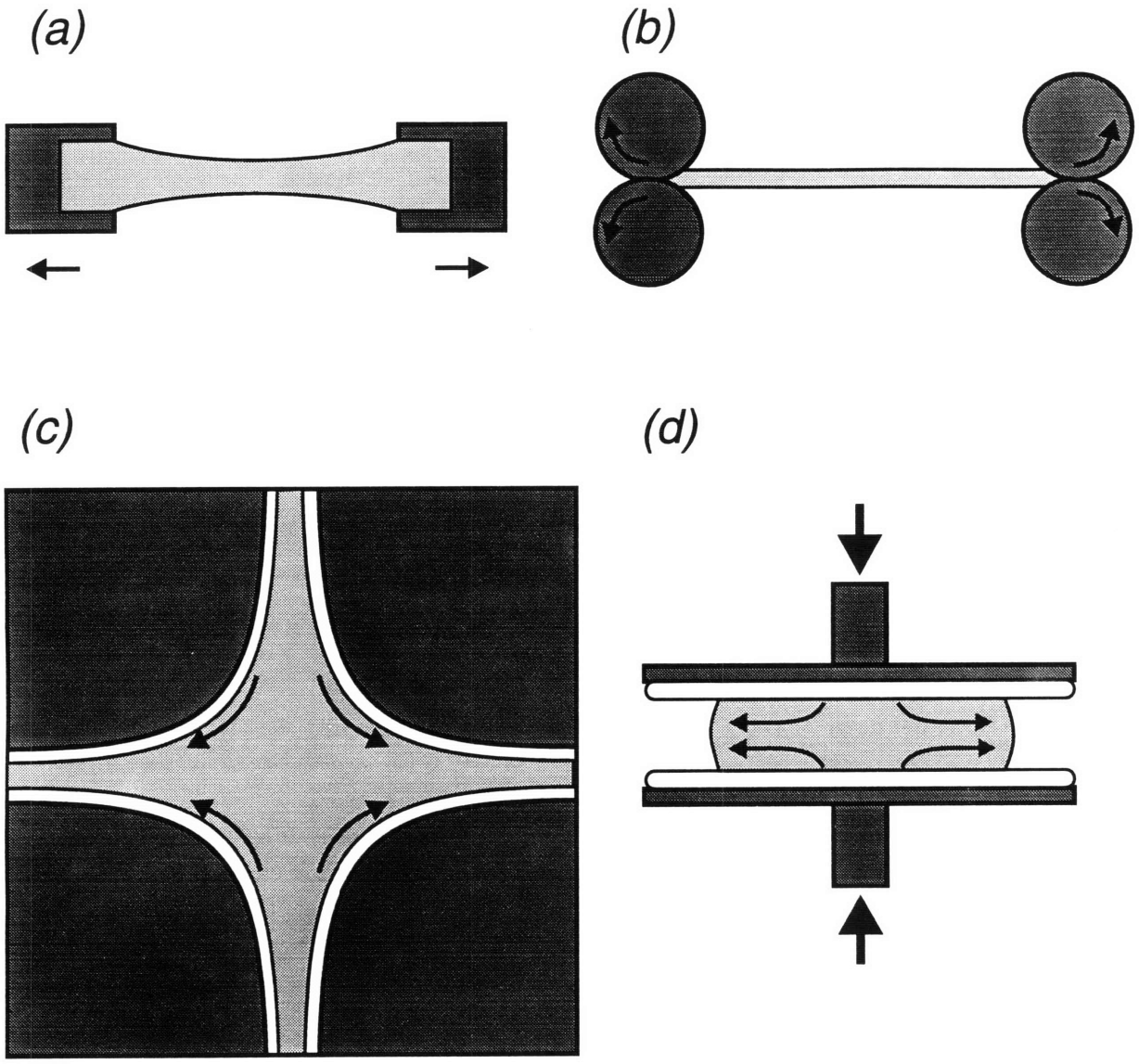

Figure 4.4 Schematic diagrams of arrangements for measuring elongational material functions in nominally homogeneous shearfree flows: (a) "homogeneous stretching"; (b) Meissner's apparatus; (c) lubricated die; (d) lubricated squeezing. (*After* (Quinzani, 1991)).

by rotating clamps. The configuration and relative rotation rate of the clamps can be adjusted to generate, in principle, a shearfree flow field (as described by eq. (4.20)) with any selected value of $0 \leq b \leq 1$. One should note that both the homogeneous stretching method and both versions of Meissner's apparatus are only suitable for high viscosity materials; e.g., polymer melts.

Modifications of the homogeneous stretching technique have been used to obtain elongational viscosity data on polymer solutions with viscosities which are high, but much lower than for melts. In particular, the constant viscosity Boger fluids, described in §1.1, can be used. As for the case of polymer melts, high Hencky strains must be achieved in order to observe the steady-state elongational viscosity of a polymer solution; this requirement complicates the development of devices which also provide well-characterized data. In Chapter 6, the Hencky strain required to attain the steady-state elongational response for the test fluid used for experiments of this thesis is estimated to be at least $\varepsilon \sim 4.4$ and probably considerably greater. In the experiments of Tirtaatmadja & Sridhar (1995) and Sridhar et al. (1991), discussed in Chapter 2, a column of fluid was placed between two plates and the plates separated so that the distance exponentially increased with time, generating an elongational flow with nominally uniform $\dot{\varepsilon}$. The normal force exerted on the plates was measured and an elongational viscosity determined. The experimental results on a polyisobutylene based Boger fluid seemed to indicate that the steady-state elongational viscosity was attained. However, experimental measurements and numerical simulations conducted by Spiegelberg, Ables & McKinley (1996), described in Chapter 2, have indicated nonidealities associated with the experimental configuration used by Tirtaatmadja, Sridhar et al. which may have introduced substantial error into the measurements. An important nonideality concerns "end effects" in the flow region adjacent to the end plates. Spiegelberg & McKinley are currently developing a device in which control over the end plate boundary conditions will result in ideal uniaxial elongational flow being more closely approached. Their device is designed for use in a microgravity environment (aboard the Space Shuttle) which will allow data to be acquired for a broader range of strain rates and fluids of lower viscosity. One should note that the behavior of capillary "bridges" of polymer solutions between separating end plates has also been studied by Berg, Kröger & Rath (1994). An experimental design incorporating end plates for which

the radius contracted during stretching was used, more closely simulating an ideal boundary condition. Several of the experiments were conducted in a free-fall tower which allowed simulation of a local microgravity environment. The primary limitation of the experiment was the low Hencky strains ($\varepsilon = 1.4$) achieved during the duration of free-fall; such low strains are ineffective in stretching the high MW polymer solute molecules and stimulating a nonlinear viscoelastic response.

The methods described above require that the fluid be capable of forming a filament ("spinnable") and retain this form over the time scale of the experiment. Only a part of the surface of the fluid sample had a boundary condition imposed on it (e.g. the end plates in the capillary stretching devices) the remaining surface was "free" (e.g. the fluid/air boundary of the filament). In contrast, other methods impose a boundary condition over nearly the entire surface of the fluid sample. Consequently, the fluid does not have to be "spinnable". For example, in the lubricated converging flow rheometer (shown in Figure 4.4.c), the viscoelastic material is confined to travel between the walls of a hyperbolically shaped die. The approximation to a homogeneous, shearfree rate-of-strain field is dependent on the ability of a low viscosity Newtonian lubricant to create a perfect slip boundary condition between the sample material and the confining walls. The need for a lubricant with viscosity sufficiently low to approximate a slip boundary condition, yet sufficiently high so that it will form a stable intermediate layer between the fluid under investigation and the die walls presents a considerable challenge, especially since this process must be undertaken for each test fluid studied. The requirements for the test fluid and the lubricant to both be stable under the conditions of temperature and stress in the experiment and chemically non-interacting impose additional constraints (Jones *et al.*, 1987). Moreover, the total Hencky strain, ε, is limited by the physical dimensions of the device.

A related method is lubricated squeezing flow (Soskey and Winter, 1985) (Fig. 4.4d). Two opposed plates are lubricated with a low viscosity fluid and the fluid sample placed between them. The plates are then driven together at a constant negative strain rate. As in the case of the lubricated die device, the approximation to biaxial flow is dependent upon the ability of the lubricant to provide a perfect-slip boundary under the operating conditions of the experiment. In practice, the total achievable Hencky strain (ε), where in this

case $\dot{\varepsilon} < 0$, is ultimately limited by the failure of the lubricant to provide the required boundary condition.

Measurement of Shearfree Material Properties in Non-Homogeneous Flows

Certain techniques use non-homogeneous flows to characterize the elongational material properties of a test fluid; several of these methods allow a wider range of test fluids to be used than the homogeneous methods described above. However, most of the techniques determine an "apparent elongational viscosity"

$$\bar{\eta}_{app} = \frac{N_{char}}{\dot{\varepsilon}_{char}} \tag{4.30}$$

N_{char} is a characteristic normal stress which often represents an average over a range of streamlines with different strain history. The characteristic strain rate, $\dot{\varepsilon}_{char}$, is obtained from measurement of global parameters such as volumetric flow rate and mean cross-sectional area; the local $\dot{\varepsilon}$ may vary considerably throughout the flow. Consequently, the $\bar{\eta}_{app}$ is in general not a well-defined quantity: quantitative comparison with results obtained in other experiments and evaluation of constitutive models is not possible.

Suitable for use with fluids of moderate viscosity are the spin-line rheometer and open-siphon techniques (Jones *et al.*, 1987; Laun and Schuch, 1989). In the spin-line rheometer (shown in Fig. 4.5a), a reservoir contains the material sample. The material is then forced by pressure through a die into the form of a filament and subsequently drawn by and collected on a take-up reel, or in a suction device. An "apparent elongational viscosity" is determined from measurement of the force exerted between the die and the reel and a characteristic elongational strain rate of the filament (Oliver, 1994; Gupta *et al.*, 1986; Sridhar *et al.*, 1986). The spin-line rheometer bears some resemblance to the capillary stretching techniques discussed above. However, the boundary conditions at the die exit and at the take-up reel result in variation of the local strain rate, $\dot{\varepsilon}$, along the length of the fiber; i.e. a homogeneous flow is not well approximated. Moreover, the flow in the die and the reservoir is complex, with the rate-of-strain tensor having both shear and elongational components, and is not well characterized. Since the fluid has memory, these upstream

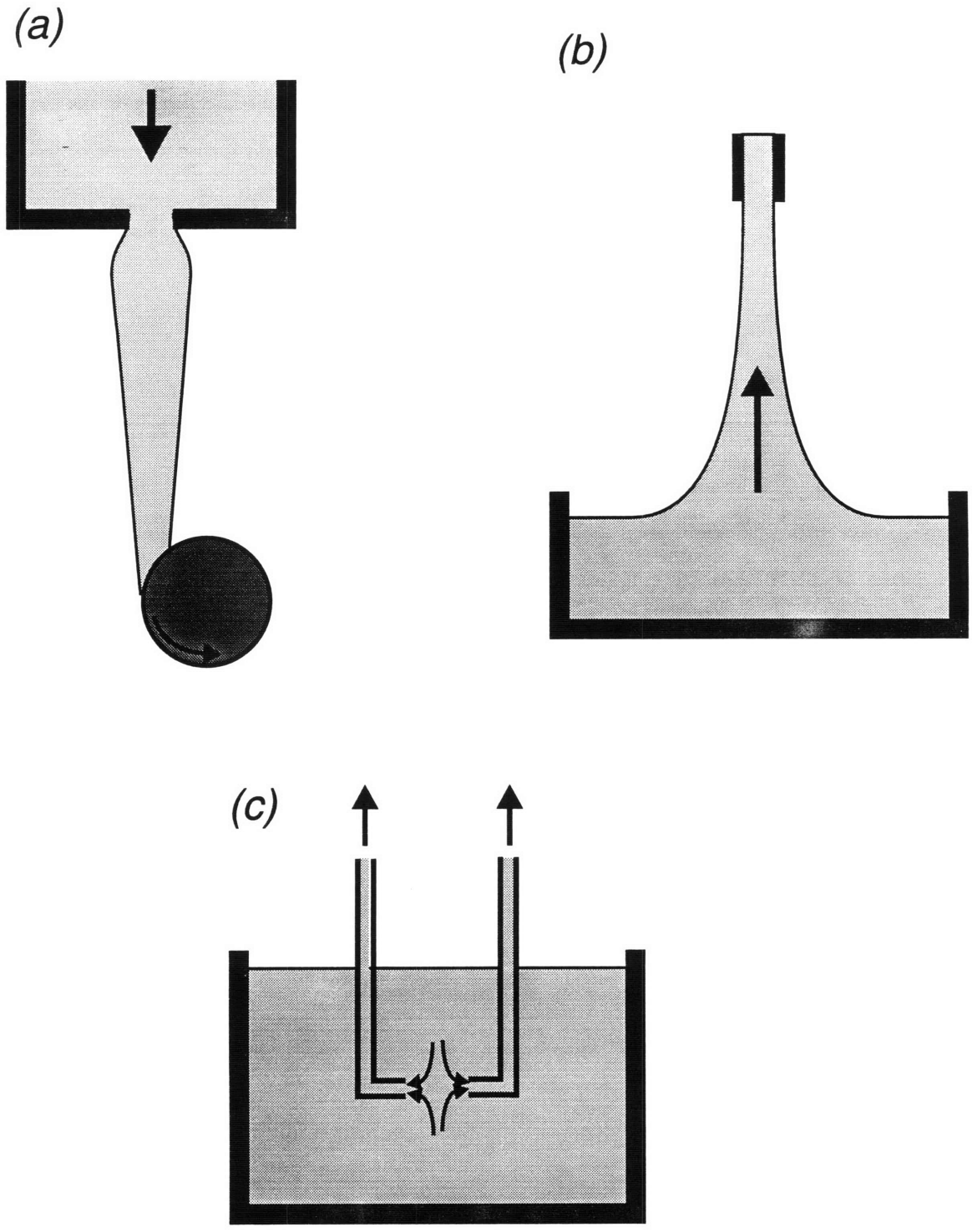

Figure 4.5 Schematic diagrams of arrangements for measuring elongational material properties in non-homogeneous shearfree flows: (a) spin-line rheometer; (b) open-siphon technique; (c) opposed-jet apparatus. (*After* (Quinzani, 1991)).

flow conditions continue to be manifested in the stress field of the filament after it leaves the die (Matthys and Khatami, 1988). A related method is the open-siphon technique (Moan and Mageur, 1988) (cf. Fig. 4.5b). Fluid is pulled by suction from a reservoir in which the fluid is nearly stagnant, through the surrounding air, and into a tube; the tensile force exerted on the tube is measured. The flow is somewhat better characterized than that of the spin-line rheometer, since the fluid in the reservoir is nominally unstressed and at equilibrium. However, the flow is not homogeneous: the strain rate, $\dot{\varepsilon}$, varies along the axis of the fluid column.

The opposed-jet apparatus, shown schematically in Fig. 4.5c approximates a uniaxial elongational flow field by siphoning the test fluid from a reservoir into a pair of opposed tubes or "jets"; conversely, a biaxial flow can be approximated by expelling fluid from the jets (Fuller *et al.*, 1987). This experimental configuration has been realized in a commercial instrument, the RFX device (Rheometrics). Using the assumption that a shearfree flow is well approximated in conjunction with the known volumetric flow rate a characteristic strain rate is calculated; the force required to maintain a constant gap between the jets is measured. The characteristic strain rate and separation force are then used to determine an "apparent elongational viscosity". However, the non-ideal boundary conditions imposed by the nozzles and the surrounding bath of stagnant fluid have non-trivial effects on the measurements; the "apparent elongational viscosity" may differ considerably from the actual steady state value, $\bar{\eta}$. These non-ideal effects have been clarified by an investigation of Newtonian flow in an opposed jet apparatus with the separation between the nozzles approximately equal to the inner diameter of the nozzles, $2r_d$ (Schunk *et al.*, 1990). The extension rate in the axial direction, $\partial v_z/\partial z$, was found to fall with radial distance; at the midplane between the nozzles, $z = 0$, at a distance r_d from the centerline, the strain rate drops to a value as low as 50% of the centerline rate. Since the flow is not bounded by a free surface, but rather surrounded by a bath of stagnant fluid, the isotropic pressure will not necessarily cancel the radial normal deviatoric stress at the midplane, $p + \tau_{rr} \equiv \pi_{rr} \neq 0$, resulting in a non-ideal contribution to the force imposed on the nozzles. In addition, even if the effects of non-uniformity in the elongational strain rate and non-zero total radial normal stress at the midplane could be neglected, the total Hencky strain experienced by a given fluid element would still vary across the streamlines. Near the axis of the flow the

total Hencky strain approaches infinity, near the periphery of the flow which enters the jets the Hencky strain may be only order one or less. As mentioned above, the attainment of the steady-state elongational viscosity typically requires Hencky strains of order $\varepsilon > 4$. Since the separation force is measured across an area of the flow which includes streamlines with a broad distribution of Hencky strains, quantitative comparison of the "apparent elongational viscosity" with predictions of constitutive models is not possible. As discussed in the next Section, quantitative elongational material property information can be obtained in certain non-homogeneous flows, but the flow fields must be well characterized.

Application of Rheo-optical Techniques to Measurement of Shearfree Material Properties in Non-Homogeneous Flows

The experimental techniques described above, use mechanical measurements to obtain information on the normal stress of the fluid, which is subsequently used in the calculation of an elongational viscosity. Since the stress field is a mechanical entity, approaches which measure the normal stress by mechanical means are ostensibly "direct" and straightforward. However, use of mechanical techniques most often employs measurement of a total force over a finite area. In the case of the opposed-jet apparatus, streamlines with different strain histories contribute to this average force. In the case of the spin-line rheometer, the strain rate varies along the filament; consequently, even if the streamlines have similar strain history the detailed nature of this history is unknown. As discussed above, the "apparent elongational viscosity" is of limited utility.

However, if the strain history and the stress are measured in a pointwise manner along the individual streamlines, constitutive models *can* be quantitatively evaluated. The "transient elongational viscosity" profile which is measured will not necessarily have been defined above as a standard material function, but can be of comparable utility in evaluating the accuracy of a constitutive equation. Rheo-optical methods allow the requisite quantitative and pointwise stress and velocity field information to be obtained. Specific details on the flow induced birefringence (FIB) technique, used to obtain stress-field information, and the laser Doppler velocimetry (LDV) technique, used to obtain velocity field information, have been given in Chapter 3 and are not reiterated here. Rather, background

on the application of rheo-optical techniques to several experimental configurations is provided in this Section.

FIB has been used in an opposed jet apparatus, similar to that described above, in order to identify transitions in the configuration of the polymer molecules between the coiled and the stretched state and the nature of entanglements between the macromolecules (Müller, 1988). In the investigation, semi-quantitative data were obtained; consequently, the utility of the data in assessing the accuracy of constitutive models was limited. However, the FIB measurement allowed conclusions to be drawn as to the dependence of the configurational state of polymers in elongational flows of different strain rates; comparable information on the configurational state could not have been obtained via mechanical measurements.

Studies of the configurational state of polymers in an elongational flow were also conducted by using FIB measurement in conjunction with a two- and a four-roll mill apparatus (Ng and Leal, 1993). The device consisted of two or four cylinders immerged in a reservoir of the test fluid, as illustrated in Fig. 4.6a. The relative rotation rate of the rollers could be adjusted to generate a range of flow fields at the center of the device, ranging from shear flows with little or no elongational component to shearfree flows; intermediate, complex flows could also be produced. Since the strain history of individual streamlines in the flow was not characterized, the experimental data could not be used for quantitative assessment of the accuracy of constitutive models. However, useful information on the effect of solute concentration on polymer chain extension in an elongational flow was obtained.

Pointwise stress and velocity field measurements in the flow through the planar contraction have provided quantitative information on elongational material properties of polymer solutions (Fig. 4.6b). The flow on the centerline is shearfree, specifically it is a planar elongational flow. The velocity and stress field are measured at each point on the centerline with the LDV and FIB techniques respectively. The flow is non-homogeneous, and transient from a Lagrangian perspective; however, constitutive models can be quantitatively evaluated. Specifically, the centerline velocity profile can be used in conjunction with a particular constitutive model to predict the stress profile; this predicted stress pro-

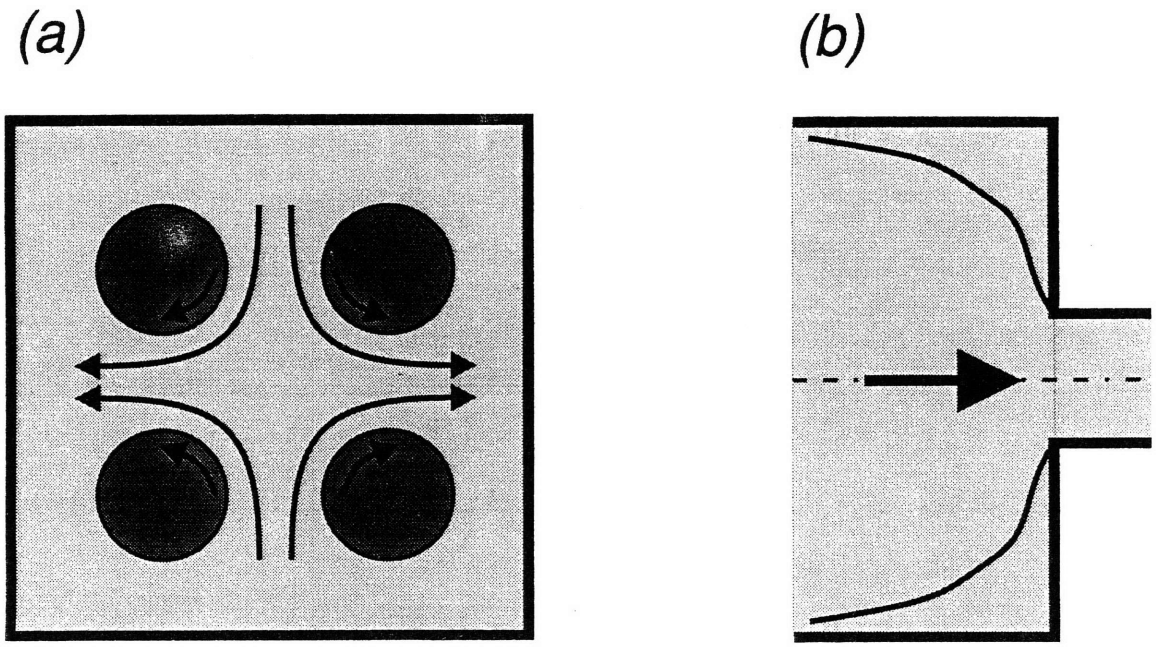

Figure 4.6 Schematic diagrams of arrangements for measuring elongational material properties in nonhomogeneous shearfree flows via application of rheo-optical techniques: (a) four-roll mill; (b) planar contraction.

file can then be compared with the measured stress profile in order to evaluate the accuracy of the model.

Galante and Frattini used polydimethylsiloxane melts in their investigation of flow through a planar contraction with an upstream to downstream half-height contraction ratio of 4 (Galante, 1991; Galante and Frattini, 1993). The experiment was carefully conducted; the effect of non-idealities on the FIB measurement such as those introduced by the walls bounding the "neutral" direction of the flow were assessed. However, the centerline velocity profile was not directly measured, an "engineering approximation" was used. Consequently, it was difficult to compare the measured stress profile with the prediction of a constitutive equation. A centerline Hencky strain of only $\varepsilon = 1.4$ was achieved, and the shear-rate-dependent Weissenberg number defined in terms of the downstream parameters was less than unity. Therefore, the potential of the experiment to probe the nonlinear response of the test fluid was limited. Necessary conditions for observation of a nonlinear viscoelastic response are considered in detail in Chapter 6.

Quinzani et al. (1991, 1994, 1995) investigated the flow of a shear-thinning viscoelastic polymer solution of PIB in tetradecane through a 4:1 planar contraction. A Boger fluid was not used for the study since the available ternary polymer solution of PIB in PB and tetradecane induced light beam divergence when subjected to shearing flow, as described in §4.1.3. Because of the shear-thinning nature of the test fluid used, the highest value of the downstream, shear-rate-dependent Weissenberg number attained was only $Wi_{Dn} = 0.77$. As in the studies of Galante and Frattini, the low Weissenberg number and the low centerline Hencky strain limited the potential of the experiment to stimulate a nonlinear viscoelastic response.

Despite the limitations of previous investigations, rheo-optical measurement of stress and velocity fields on the centerline of planar contraction flow is an experimental technique which allows the determination of a well-defined "transient elongational viscosity" profile. In the study conducted for this thesis, the method was extended to higher center-

line Hencky strains and a test fluid was used which allowed higher Weissenberg numbers to be attained; the investigation is presented in Chapter 6.

4.2.3 Correlation of Material Functions with Temperature

Polymeric materials exhibit dependence of the material functions on temperature. For thermo-rheologically simple fluids, such as the PIB in PB test fluid used for this thesis, a method of reduced variables, time-temperature superposition, allows material function data obtained at a given temperature to be shifted to values observed at a different temperature. In particular, data for a given material function is often obtained over a range of temperatures and then shifted to a single reference temperature, T_0, to create a master curve (Ferry, 1980; Bird *et al.*, 1987a). Specifically, one may note in Table 4.2 how several common steady and dynamic material functions are shifted

$\omega(T_0) = a_T\omega(T)$	$\dot{\gamma}(T_0) = a_T\dot{\gamma}(T)$
$\eta'(T_0) = a_T^{-1}\eta'(T)$	$\eta(T_0) = a_T^{-1}\eta(T)$
$\eta''(T_0) = a_T^{-1}\eta''(T)$	$\Psi_1(T_0) = a_T^{-2}\Psi_1(T)$

Table 4.2 Time-temperature shift relations for frequency (ω), strain rate ($\dot{\gamma}$), and several material functions.

The shift factor is defined as

$$a_T = \frac{\eta_0(T)T_0\rho_0}{\eta_0(T_0)T\rho} \approx \frac{\eta_0(T)}{\eta_0(T_0)} \tag{4.31}$$

η_0 is the zero-shear-rate viscosity at the indicated temperature. T is the absolute test temperature, and T_0 the absolute reference temperature; ρ is the density at T, and ρ_0 is the density at T_0. The simplification in eq. (4.31) is valid for the restricted range of temperatures used in the experiments conducted for this thesis, $288 \leq T \leq 308$ [K].

The time-temperature superposition principle is also valid for quantities other than those listed in Table 1.1; e.g., t (time, used for transient material functions) or $\bar{\eta}$. In gen-

eral, one shifts a rheological quantity, X, which includes the dimension of time, $X = X(t^m)$ as

$$X_0(t^m) = a_T^{-m} X(t^m) \tag{4.32}$$

where the zero subscript denotes the value of the quantity at the reference temperature, T_0.

In certain cases time-temperature superposition can be used to extend the range of shear rates or frequencies over which measurements may be conducted for a given instrument. For example, the RMS-800 rheometer used for the shear flow rheological tests described in §4.4 can perform oscillatory measurements over the frequency range $10^{-3} \leq \omega \leq 100$ [s^{-1}]. A shift factor of $a_T = 10$ would effectively shift this range upward, allowing material function data to be obtained for frequencies as great as 1000 [s^{-1}]. Conversely, a shift factor of $a_T = 0.1$ would shift the range downward. Running the test for a frequency of $\omega = 10^{-2}$ [s^{-1}] at temperature T would yield information on the linear viscoelastic response at temperature T_0 for $\omega = 10^{-3}$ [s^{-1}]. Such a shift is useful since data acquisition at low frequencies is extremely time consuming. For the investigations presented in this thesis, time-temperature superposition was primarily used to shift all experimental data to a single reference temperature, $T_0 = 25$ [°C], in order to facilitate the comparison of data obtained in different test runs. Shifting to the reference temperature was especially useful for the experiments conducted with the flow cell, in which the temperature was stable over the course of the trial, but could not be set by the experimenter.

4.3 Constitutive Models

The material functions described in §4.2 characterize the response of a viscoelastic fluid to a viscometric flow. However, use of this information to predict the behavior of the fluid in a complex flow, for which the rate-of-strain tensor has both shear and elongational components, requires a constitutive model. The constitutive equation relates the stress in a viscoelastic flow at a specific point in time and space to the strain history of the fluid element at that point. Constitutive models are classified as linear or nonlinear; a subset of the nonlinear class are the quasi-linear models in which the stress depends linearly on the his-

tory of a strain tensor. The generalized linear Maxwell model (described in §4.3.1) can be used to determine the linear viscoelastic relaxation spectrum of a fluid. Whereas a linear Maxwell model only applies to flows with infinitesimal strains, the convected Maxwell model (§4.3.2) can be applied to flows with finite strains; however, the convected Maxwell model cannot describe shear thinning of the viscometric functions. The Giesekus model (§4.3.3) can describe this nonlinear shear-thinning behavior. The linear Maxwell and the nonlinear Giesekus models are used in Chapter 6 to characterize the response of the test fluid to a transient elongational flow as linear or nonlinear; the models allow conclusions to be drawn about the nature of the flow required to excite a nonlinear response. To facilitate use of the models in Chapter 6, their physical basis is briefly described here; classes of flows for which the models may be appropriately applied and limitations to their application are presented. The monographs of Bird, Armstrong & Hassager (1987) and Bird et al. (1987b) were the primary reference sources used for §4.3.

4.3.1 Multimode Formulation of Models

In order to represent accurately the relaxation spectrum of the fluid the multimode formulation of the models was used

$$\boldsymbol{\tau}(t) = \sum_{k=1}^{N_{modes}} \boldsymbol{\tau}_k(t) + \boldsymbol{\tau}_s \tag{4.33}$$

where τ represents the stress tensor. The unsubscripted variable represents the total "observable" stress whereas the subscript on a given variable indicates that the quantity is associated with the k^{th} mode of the relaxation spectrum. Note that the total stress is a linear superposition of the individual modes (Bird *et al.*, 1987a).

Since the PB solvent exhibits a Newtonian response on the time scale and for the stress levels attained in these experiments, it is useful to include the contribution of a Newtonian

solvent to the total stress in the models. The constitutive equation for the mode associated with a Newtonian solvent of viscosity η_s is written as

$$\tau_s = -\eta_s \dot{\gamma} \tag{4.34}$$

This solvent mode is then included in the summation over the modes, eq. 4.29, to yield the total stress.

4.3.2 Linear Maxwell Model

A specialization of the general linear viscoelastic fluid is the generalized linear Maxwell model for which the k^{th} mode can be written as

$$\tau_k + \lambda_k \frac{\partial \tau_k}{\partial t} = -\eta_k \dot{\gamma} \tag{4.35}$$

where τ_k represents the stress tensor, $\dot{\gamma}$, the strain-rate tensor, λ_k, the relaxation time, η_k, the viscosity, and t, the time. The Maxwell model can be physically viewed by analogy to a mechanical system with a "spring" and "dashpot" in series. The "spring", with modulus $\lambda_k \eta_k$, represents the elastic response of the fluid; a consequence of the entropic forces which induce polymer chains to return to a coiled configuration. The "dashpot", with viscosity η_k, represents the viscous nature of the fluid; a portion of the kinetic energy of the molecules comprising the fluid is converted to heat. These elastic and viscous characteristics which are simultaneously present result in the fluid having a "fading memory" (Ferry, 1980). Linear viscoelastic models are appropriate for flows in which the fluid experiences infinitesimally small strains. Additionally, linear viscoelastic models may be applied to flows which are sufficiently slow that over a period of a relaxation time only an infinitesi-

mal strain is experienced by a fluid element. These restrictions arise from the fact that linear viscoelastic models are not rheologically invariant (Oldroyd, 1984).[3]

4.3.3 Convected Maxwell: a Quasilinear Model

The convected Maxwell constitutive equation is admissible; i.e. rheologically invariant. Consequently, it can be used to model viscoelastic flows in which the fluid element "remembers" a finite amount of strain. In contrast to the linear Maxwell model described above, the quasilinearity[4] of the convected Maxwell model results in its predicting finite normal stresses in steady shear flow; such normal stresses are observed in viscoelastic shear flows of typical polymer solutions and melts. The convected Maxwell model can be written as

$$\boldsymbol{\tau}_k + \lambda_k \boldsymbol{\tau}_{k(1)} = -\eta_k \dot{\boldsymbol{\gamma}} \tag{4.36}$$

The equation superficially resembles that for the linear Maxwell model; however, the partial time derivative of stress has been replaced by a *convected time derivative* of stress,

$$\boldsymbol{\tau}_{k(1)} = \frac{D}{Dt}\boldsymbol{\tau}_k - \{(\nabla \mathbf{v})^{\dagger} \cdot \boldsymbol{\tau}_k + \boldsymbol{\tau}_k \cdot (\nabla \mathbf{v})\} \tag{4.37}$$

where D/Dt represents the material derivative and $\nabla \mathbf{v}$ the velocity gradient tensor. One should note that although the convected Maxwell model is admissible, and its simplicity favors its application in viscoelastic flow simulations, the model has several limitations which prevent it from realistically modeling certain viscoelastic flow systems. For example, the model cannot predict viscometric material functions, η and Ψ_1, which exhibit shear-thinning behavior. The convected Maxwell model also predicts physically unrealis-

---

3. A constitutive model which is rheologically invariant must be "(a) form invariant under a change of coordinate system, (b) value invariant under a change of translational or rotational motion of the fluid element as it goes through space, and (c) value invariant under a change of rheological history of neighboring fluid elements ((Bird *et al.*, 1987a))." Note that while eq. (4.35) satisfies (a) and (c), it does not satisfy (b).

4. The term "quasilinear" is used since the stress depends *linearly* on the history of a relative strain tensor; this linear dependence is evident when the model is written in integral form. However, note that the relative strain tensor exhibits *nonlinear* dependence on the displacement gradients (Bird *et al.*, 1987a).

tic values for the steady-state shearfree material functions at elevated strain rates. Specifically, for planar elongational flow the first elongational viscosity, $\bar{\eta}_1$, is

$$\bar{\eta}_1 = \frac{4\eta_0}{(1 + 2\lambda_1\dot{\varepsilon}_0)(1 - 2\lambda_1\dot{\varepsilon}_0)} \tag{4.38}$$

where $\dot{\varepsilon}_0$ represents the strain rate; $\bar{\eta}_1$ is undefined in the limit of $\lambda_1\dot{\varepsilon}_0 = \pm 1/2$. One may note that, when a Newtonian solvent contribution to the viscosity is included in the summation over the modes (cf. eq. (4.32)) of the convected Maxwell equation, the resultant model is termed "Convected Jeffreys" or "Oldroyd-B". Note that the Oldroyd-B model is derivable from consideration of a "dumbbell" model. Specifically, one may represent the polymer molecule as two beads, which interact hydrodynamically with the surrounding Newtonian solvent, connected by a spring which obeys a linear or "Hookean" force law. The individual "dumbbells" do not interact with each other: Oldroyd-B is a dilute solution model (Bird *et al.*, 1987a; Bird *et al.*, 1987b). More detailed consideration of the response of dumbbell models to an elongational flow is given in Chapter 6.

4.3.4 Giesekus: a Nonlinear Model

Another admissible nonlinear model is the Giesekus model (Giesekus, 1982b; Giesekus, 1982a; Giesekus, 1983). In contrast with convected Maxwell, shear thinning of the material functions η and Ψ_1 can be predicted; the steady-state elongational viscosity is bounded for all strain rates. The Giesekus model is based on the concept of including anisotropic Brownian motion and hydrodynamic drag in the dumbbell model. Specifically, when external forces are neglected, kinetic theory predicts that the equation of change for the phase-space averaged dyadic product of the dumbbell vector, $\mathbf{Q}$, is

$$\frac{1}{2}\langle \mathbf{QQ} \rangle_{(1)} = kT\langle \boldsymbol{\xi}^{-1} : \left\{ \left(\frac{\partial \boldsymbol{\zeta}^{-1}}{\partial \mathbf{Q}} \right) \mathbf{Q} + \left[\left(\frac{\partial \boldsymbol{\zeta}^{-1}}{\partial \mathbf{Q}} \right) \mathbf{Q} \right]^{\dagger} \right\} \rangle \tag{4.39}$$

$$+ kT\langle \{ \boldsymbol{\zeta}^{-1} \cdot \boldsymbol{\xi}^{-1} \} + \{ \boldsymbol{\xi}^{-1} \cdot \boldsymbol{\zeta}^{-1} \} \rangle - \langle \{ \boldsymbol{\zeta}^{-1} \cdot \mathbf{F}^{(c)} \mathbf{Q} \} + \{ \mathbf{Q} \mathbf{F}^{(c)} \cdot \boldsymbol{\zeta}^{-1} \} \rangle$$

where kT expresses the thermal energy of the system. The Kramers form for the stress tensor is written as

$$\boldsymbol{\tau}_p = n\langle \mathbf{Q}\mathbf{F}^{(c)} \rangle + nkT(2\langle \boldsymbol{\xi}^{-1} \rangle - \boldsymbol{\delta}) \tag{4.40}$$

where $\boldsymbol{\tau}_p$ represents the contribution of the polymer to the deviatoric stress and n the number density of "dumbbells". As for the case of Oldroyd-B, the "connector force" term is that for a Hookean spring, $\mathbf{F}^{(c)} = H\mathbf{Q}$, where H represents the spring constant. The following empiricism is used for the anisotropic friction tensor,

$$\boldsymbol{\zeta}^{-1} = \frac{1}{\zeta}\left(\boldsymbol{\delta} - \frac{\alpha\lambda_1}{\eta_p}\boldsymbol{\tau}_p\right), \tag{4.41}$$

where η_p represents the zero-shear-rate contribution of the polymer to the viscosity, $\zeta = 4H\lambda_1$ the magnitude of the anisotropic friction tensor when the polymer molecule is near its equilibrium configuration, and α the "mobility factor", which has a value in the range $0 \le \alpha \le 0.5$. For the anisotropic Brownian motion tensor, the empiricism is

$$\boldsymbol{\xi}^{-1} = \boldsymbol{\delta} - \left(\frac{\lambda_1}{2\eta_p} - \frac{1}{2nkT}\right)\boldsymbol{\tau}_p. \tag{4.42}$$

The anisotropy of eqs. (4.41) and (4.42) make the Giesekus model suitable for representing concentrated polymer solutions and polymer melts. The representation of the motion of an actual polymer chain by the Giesekus "dumbbell model" can be viewed as follows. The anisotropic Brownian motion tensor reflects the confinement of the motion of a given polymer chain within a "reptation tube" imposed by the neighboring chains. The anisotropic friction tensor reflects the fact that the polymer chain can more easily move a given distance in its mean direction of orientation, $\mathbf{Q}/\|\mathbf{Q}\|$, when the chain is extended (straight "reptation tube") than when the chain is coiled (convoluted "reptation tube"). It must be born in mind that eqs. (4.41) and (4.42) are empiricisms which must be fitted to experimental data; these empiricisms are not derivable from detailed modeling of chain-chain interactions. Equations (4.39) and (4.40), in conjunction with eqs. (4.41) and (4.42) are

then solved to represent the Giesekus model in terms of the stress and rate-of-strain tensors. The model can be extended to a multimode formulation to represent a fluid with a spectrum of relaxation times, although this multimode formulation cannot be described by the "physically intuitive" picture given above. The k^{th} mode of the multimode Giesekus model is written as

$$\tau_k + \lambda_k \tau_{k(1)} - \alpha_k \frac{\lambda_k}{\eta_k} \{\tau_k \cdot \tau_k\} = -\eta_k \dot{\gamma} \tag{4.43}$$

Note that when $\alpha_k = 0$ for all the modes, the Giesekus model reduces to convected Maxwell. The texts of Bird et al. (1977a, 1977b) were drawn on for the above discussion; Bird et al. (1987b) is especially useful in relating the macroscopic constitutive eq. (4.43) to kinetic theory concepts. More detailed consideration of the Giesekus model in the context of elongational flow is given in Chapter 6; e.g., the effect of the "mobility factor", α, on the steady and the transient elongational response is described.

4.4 Test Fluid Shear Flow Rheology

In this Subsection the experimentally determined rheology of the 0.30 wt% PIB in PB test fluid and the polybutene solvent are presented. In §4.4.1 the temperature dependence of the material functions of the test fluid and the solvent is described. Section 4.4.2 presents the rheology of the polybutene solvent, which acts as a Newtonian fluid. Dynamic material functions of the 0.30 wt% PIB in PB test fluid are presented in §4.4.3 and used to fit the coefficients, η_k and λ_k, comprising the linear viscoelastic spectrum. The shear thinning parameters, α_k, of the Giesekus model are fit with the steady shear material functions for the test fluid given in §4.4.4. In §4.4.5 the transient material functions for the test fluid are presented; this information provides a check on the models which were fit to the dynamic and steady data in Sections 4.4.3 and 4.4.4.

4.4.1 Temperature Dependence of Fluid Rheology

The temperature dependence of the material functions for the 0.30 wt% PIB in PB test fluid was determined by measuring the dynamic viscosity of a fluid sample undergoing oscillatory shear in a cone-and-plate configuration and sweeping the temperature over a range from 15 to 35 [°C]. A Carri-Med CSL-500 controlled stress rheometer (TA Instruments) was used because the temperature could be accurately ramped at a constant rate. A semilog plot in Fig. 4.7 shows the measured dependence of the zero-frequency dynamic viscosity, η'_0, on the difference between the inverse of the absolute temperature and the inverse reference temperature, $T^{-1} - T_0^{-1}$. An Arrhenius expression (Bird *et al.*, 1987a)

$$a_T = \exp\left(\frac{\Delta H}{R}\left(\frac{1}{T} - \frac{1}{T_0}\right)\right) \tag{4.44}$$

was accurately fit to the data, where $a_T = \eta'_0(T)/\eta'_0(T_0)$ and R = 8.314 [J mol^{-1} K^{-1}]; the fit is indicated in the Figure by a solid line. The data and corresponding Arrhenius fit for the pure PB solvent are also shown in Fig. 4.7. The "activation energy", ΔH, for the 0.30 wt% PIB in PB test fluid and for the solvent of pure PB is given in Table 4.3.

Fluid	ΔH/R [K]
0.30 wt% PIB in PB	7.56×10^3
pure PB	7.59×10^3

Table 4.3 "Activation energy", ΔH/R, of the 0.30 wt% PIB in PB test fluid and the PB solvent.

The similarity of the activation energy of the 0.30 wt% PIB in PB solution to that of the PB solvent is a consequence of the low concentration of the PIB solute. The 0.30 wt% PIB in PB solution exhibits a sensitive dependence of the material properties on the temperature; a 1 [°C] change in temperature induces an 8% change in the viscosity within the temperature range used in the investigations, $15 \leq T \leq 35$ [°C]. All quantitative experimental

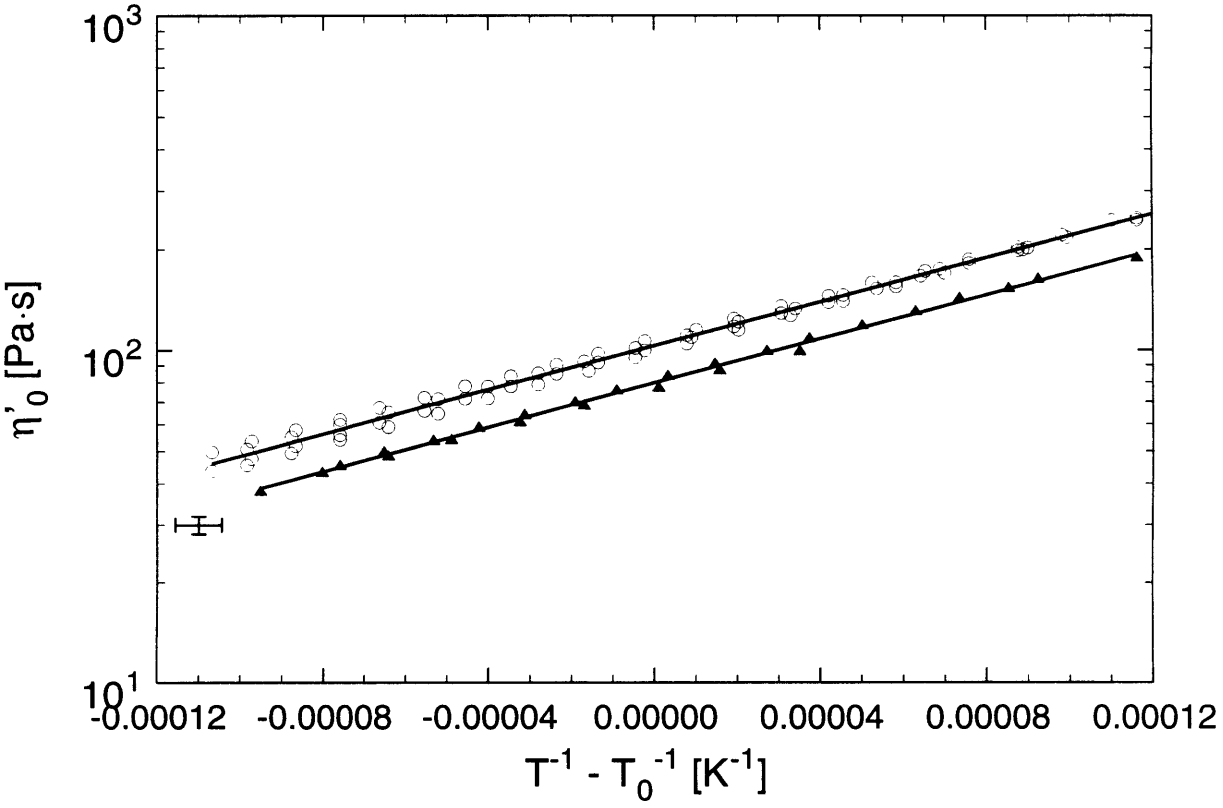

Figure 4.7 Temperature dependence of zero-shear-rate dynamic viscosity, η'_0: (○), 0.30 wt% PIB in PB test fluid; (▲), PB solvent. Lines show the Arrhenius fit to the data.

results presented in this Section have been time-temperature shifted to the reference temperature, T = 25 [°C].

4.4.2 Rheology of the Polybutene Solvent

The rheology of the polybutene solvent was characterized in the RMS-800 mechanical spectrometer. The dynamic viscosity, η', is shown in Fig. 4.8a. No decreasing trend in η' with increasing frequency can be discerned up to $\omega_{max} = 100$ [s^{-1}]. Consequently, either the instrument was insufficiently accurate or insufficiently high frequencies could be attained to detect any elastic character in the fluid. More specifically, an upper bound on the longest relaxation time of the fluid may be identified as

$$\lambda_{Longest} < 1/\omega_{max} = 0.01 \text{ [s]} \tag{4.45}$$

The straight line in Fig. 4.8a at $\eta'_s = \eta_s = 79$ [Pa s] indicates the solvent viscosity obtained by fitting to the dynamic and the steady shear data.

Figure 4.8b shows the viscosity of the polybutene measured in steady-shear flow. The viscosity has a constant value of $\eta_s = 79$ [Pa s] up to a shear rate of 26 [s^{-1}]. At greater shear rates a gradual decrease in the viscosity with shear rate is apparent; this was attributed to viscous heating. Calculations of the effect of viscous heating indicated that for $\dot{\gamma} >$ 40 [s^{-1}] the apparent viscosity would drop by more than 6% when the cone-and-plate fixture was used with radius of R = 12.5 [mm] and angle of $\theta_0 = 0.1$ [rad]. Up to at least $\dot{\gamma} =$ 26 [s^{-1}] the viscosity of the polybutene fluid was shear-rate independent.

4.4.3 Dynamic Properties of the Test Fluid: Fitting of the Linear Viscoelastic Spectrum

The dynamic shear flow material functions, $\eta'(\omega)$ and $(2\eta''(\omega))/\omega$, of the 0.30 wt% polyisobutylene (PIB) in polybutene (PB) test fluid were measured in small-amplitude oscillatory shear flow in a cone-and-plate configuration and are shown in Fig. 4.9. This linear viscoelastic data, in conjunction with the steady data described in §4.4.4, were used to fit a four-mode linear Maxwell model; the parameters η_k and λ_k which define the relaxation spectrum are given in Table 4.4. The fitting of the constants was done manually,

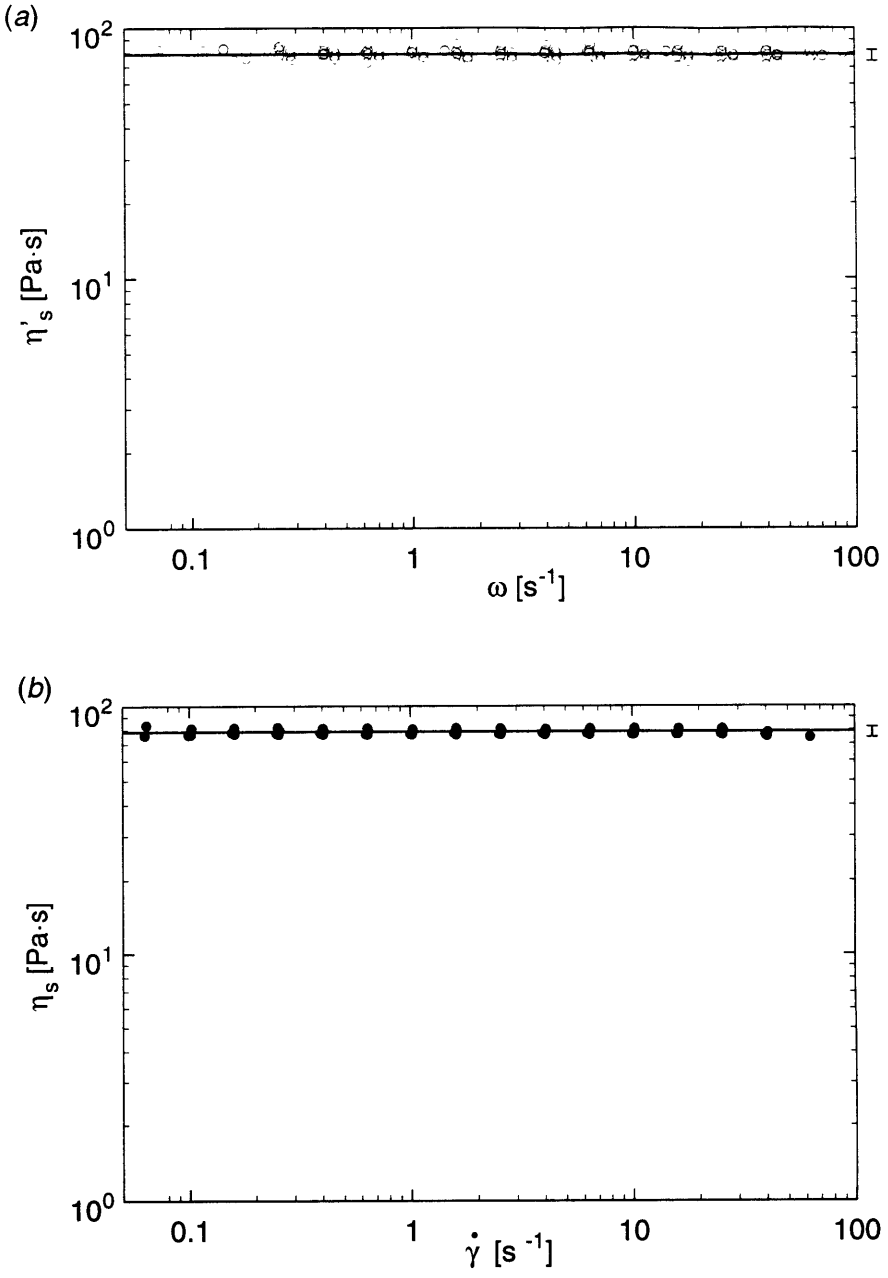

Figure 4.8 (a) Dynamic viscosity (measured in small-amplitude oscillatory shear flow) of the PB solvent. Line shows the fit to the data, $\eta'_s = 79$ [Pa s]. (b) Viscosity (measured in steady shear flow) of the PB solvent. Line shows the fit to the data, $\eta_s = 79$ [Pa s]. Note the bars indicating the ±5% error at the right of the plots.

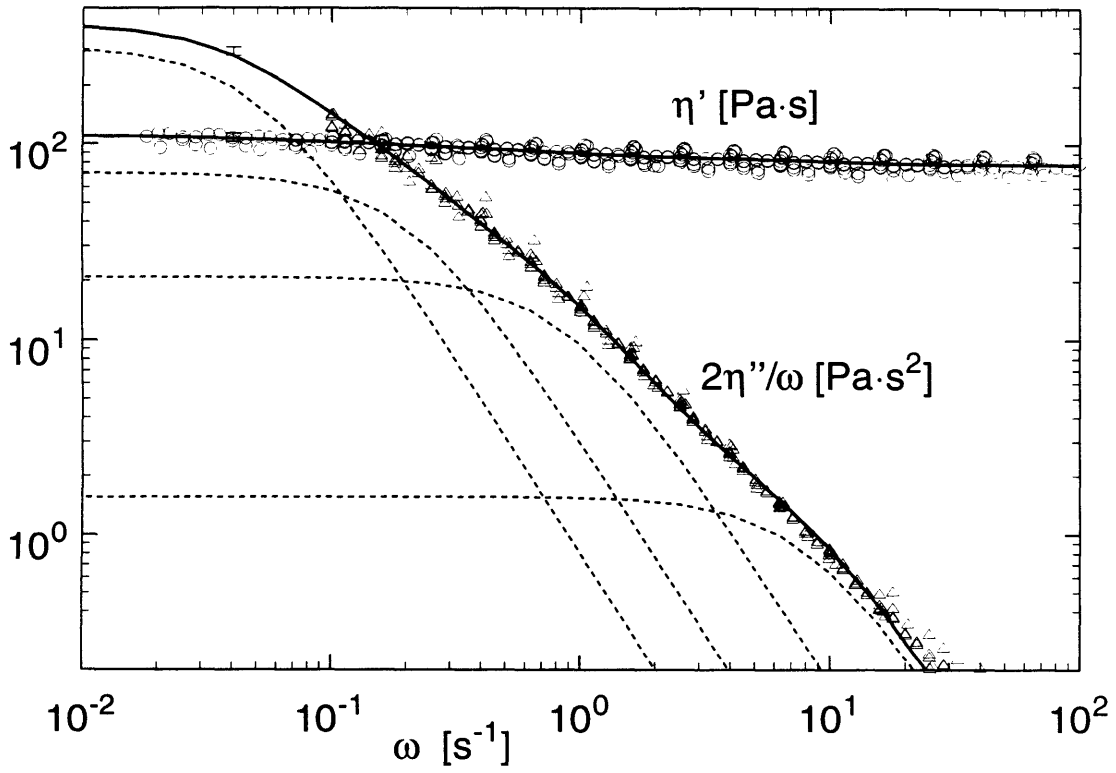

Figure 4.9 Linear viscoelastic properties, $\eta'(\omega)$ and $2\eta''(\omega)/\omega$, of the 0.30 wt% PIB in PB test fluid. (——), fit of the four-mode linear Maxwell model to the data; (- - -), individual spectral contributions, $(2\eta''/\omega)_k$, of the modes. Error bars are given near the upper-left corner of the graph.

by adjusting parameters until the difference between the predicted and experimental curves was minimized.

Mode No.	η_k [Pa s]	λ_k [s]
1	8.0	20
2	7.4	4.8
3	9.5	1.1
4	6.5	0.12
Solvent	79	(< 0.01)

Table 4.4 Linear viscoelastic spectrum of the 0.30 wt% PIB in PB test fluid.

The individual contributions of the modes of the linear Maxwell fit to the total value of $2\eta''/\omega$ are also indicated by the dashed lines in Fig. 4.9. Each mode is dominant in a different region of the spectrum; a given mode starts to shear thin once a critical frequency is exceeded, $\omega_k \sim 1/\lambda_k$. In the case of η', a similar pattern can be observed for the modal contributions, η'_k, originating from the high molecular weight solute; however, these contributions are not shown in Fig. 4.9 since the contribution of the non-frequency-thinning solvent, $\eta_s' = \eta_s$, dominates over the other modes.

It is often found that the zero-frequency plateau of the material functions can be more closely approached in a dynamic shear flow experiment that the zero-shear-rate plateau of the material functions in a steady shear flow experiment. Consequently, dynamic measurements are useful in obtaining information on the longest relaxation time of a fluid. Furthermore, as discussed in §4.2, in the limit of zero frequency, the dynamic material functions, when written as η' and $2\eta''/\omega_0$, are equivalent to the zero-shear-rate steady properties η_0 and Ψ_{10} (viscosity and first-normal-stress coefficient). The fit of the linear Maxwell model to the data indicated that the zero-frequency limit for the dynamic viscosity was $\eta'_0 = 110$ [Pa s]. In the case of the material function $2\eta''/\omega$, a gradual leveling off was observed with decreasing frequency; however, the rheometer was not sufficiently

sensitive for the zero-frequency plateau to be reached. The data *did* allow a lower bound on the zero-frequency limit to be defined, $2\eta''/\omega_0 > 130[\text{Pa s}^2]$.

4.4.4 Steady Shear Rheology of the Test Fluid: Fitting of Nonlinear Giesekus Model

The steady shear flow material functions of the 0.30 wt% PIB in PB solution were measured by using the rheometer in the cone-and-plate and in the parallel-plate configurations. A plot of $\eta(\dot{\gamma})$ and $\Psi_1(\dot{\gamma})$ is shown in Fig. 4.10. The linear Maxwell fit indicated a decrease in viscosity from $\eta_0 = 110$ [Pa s] to $\eta = 90$ [Pa s] at the maximum shear rate, for which data was obtained, of 40 [s^{-1}]. Because of this decrease of only 18% in the viscosity over nearly three decades of shear rate the test fluid closely approximated an elastic, constant viscosity non-shear-thinning Boger fluid (Boger, 1977/1978). The highest shear rate for which material functions were measured was 40 [s^{-1}]; at shear rates exceeding this value viscous heating would act to decrease η by more than 9% and Ψ_1 by more than 18%.

Substantial shear thinning is observed for the first-normal-stress coefficient, Ψ_1. The zero-shear-rate limit for Ψ_1 could not be reached because of the sensitivity limits of the normal force transducer. However, at 0.25 [s^{-1}], the lowest shear rate for which results reproducible to within ±25% could be obtained, the data indicated a lower bound on the zero-shear-rate limit of $\Psi_1 > 200$ [Pa s^2]. Note that the "flat" region of $\Psi_1(\dot{\gamma})$ over the range $0.6 \leq \dot{\gamma} \leq 2.5$ [s^{-1}] is the "knee" which has been noticed for a similar PIB based Boger fluid (Quinzani *et al.*, 1990); this flat region is *not* the zero-shear-rate plateau. The nonlinear viscoelastic four-mode Giesekus model is capable of capturing the shear thinning of the η and Ψ_1 material functions; values of the α_k, which control the shear thinning

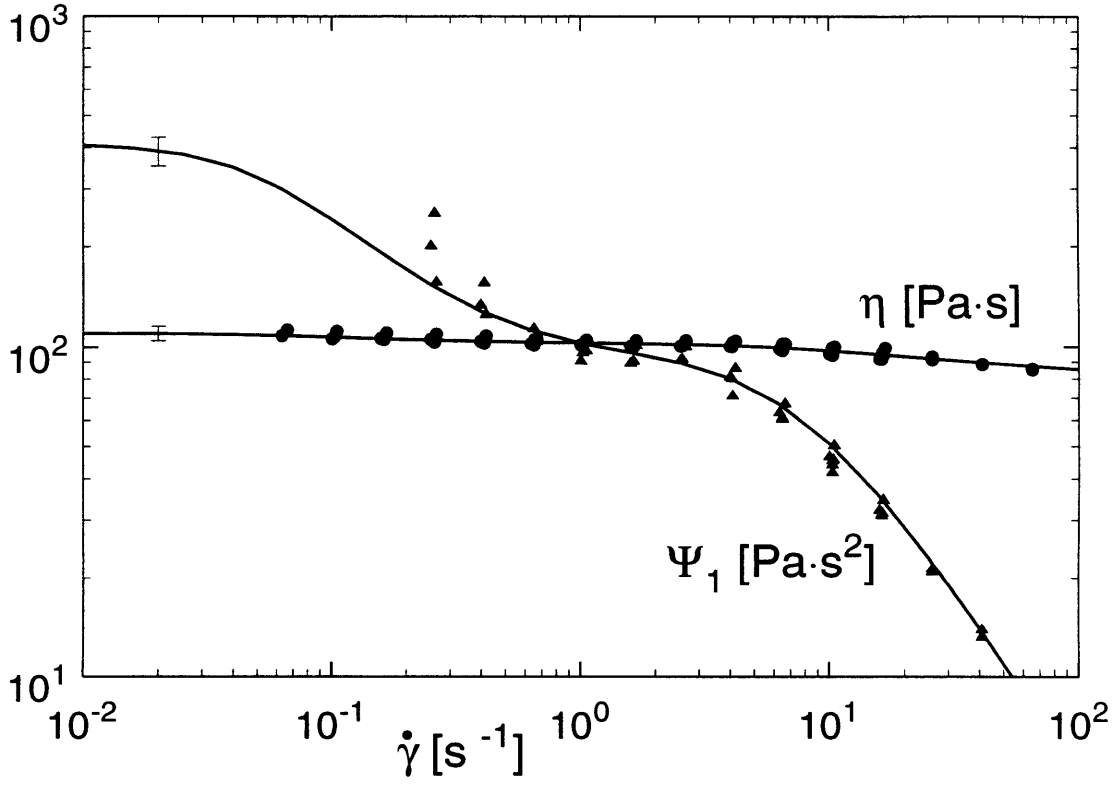

Figure 4.10 Steady shear material functions, $\eta(\dot{\gamma})$ and $\Psi_1(\dot{\gamma})$, of the 0.30 wt% PIB in PB test fluid. (——), fits of the four-mode Giesekus model to the data. Error bars are given at the left of the plots.

behavior of the steady shear material functions, in addition to the coefficients η_k and λ_k discussed in §4.4.3, are given in Table 4.5.

Mode No.	η_k [Pa s]	λ_k [s]	α_k
1	8.0	20	0.1
2	7.4	4.8	1.3×10^{-4}
3	9.5	1.1	1.3×10^{-3}
4	6.5	0.12	3×10^{-3}
Solvent	79	(< 0.01)	—

Table 4.5 Fitted parameters of the four-mode Giesekus model.

The α_k were determined manually, by minimizing the difference between the predicted viscometric functions, especially Ψ_1, and the experimental data.

4.4.5 Transient Shear Rheology of the Test Fluid

The transient shear flow material functions of the 0.30 wt% PIB in PB solution, used as the test fluid in the investigations presented in Chapters 5 and 6, were measured with a cone-and-plate fixture of θ_0 = 0.1 [rad] in the Rheometrics Mechanical Spectrometer (RMS 800). The stress growth and the stress relaxation response of the viscosity and the first normal stress coefficient were measured under shear rate conditions of $\dot{\gamma}_0$ = 2.6 and 10 [s^{-1}]. Data at $\dot{\gamma}_0$ = 0.65 [s^{-1}] and lower shear rates were taken, but there was too much scatter in the data for them to be useful in quantitatively evaluating the model predictions. Above 10 [s^{-1}], onset of a viscoelastic instability for a cone-and-plate configuration of θ_0 = 0.1 [rad] prevented measurement of the transient shear rheology (McKinley *et al.*, 1995). Use of a parallel-plate configuration with small gap could have allowed higher shear rates to be used without onset of the instability. However, determination of the transient material functions requires differentiation of the measured force and torque data; differentiation acts to increase the severity of experimental noise. Decrease of the gap distance in and of itself increases measurement noise, consequently, the quality of the data which would be obtained would be too low to justify use of the parallel-plate configuration. Both the test with $\dot{\gamma}_0$ = 2.6 [s^{-1}] and $\dot{\gamma}_0$ = 10 [s^{-1}] stimulated a nonlinear transient

response. For a material to exhibit a linear response, one must have the shear-rate-dependent Weissenberg number less than one. Note from Fig. 4.14 (discussed in §4.5.1) that $\mathrm{Wi}(\dot{\gamma} = 2.2\ [s^{-1}]) \approx 1$, corresponding to a shear rate lower than those used for the transient tests.

Stress Growth Response

Plots of $\eta^+(\dot{\gamma}_0, t)$, time-temperature shifted to the reference temperature of $T_0 = 25$ [°C], are presented in Fig. 4.11. Experimental data are shown as symbols; predictions of the four-mode Giesekus model are shown by dashed lines. The Giesekus prediction for $\dot{\gamma}_0 = 10\ [s^{-1}]$ shows a good quantitative match to the data. The data and model agree up to t ~ 5 [s], at which time both exhibit an overshoot. However, the quantitative magnitude of the overshoot of the experimental data is greater. Despite this difference, the maximum fractional deviation of the data and the model is only 3%. The model prediction for $\dot{\gamma}_0 = 2.6\ [s^{-1}]$ shows the same time-dependent response as the data; specifically, levelling out is observed around t ~ 10 [s]. No overshoot is noted for the experimental data. The prediction of the model lies approximately 5 [Pa s] below the experimental data for the times shown; this 5% deviation lies within the instrument error. The linear viscoelastic envelope, shown in Fig. 4.11 by a solid line, is the curve to which all viscoelastic fluids conform in the limit $\dot{\gamma}_0 \ll \dot{\gamma}_c$, where $\mathrm{Wi}(\dot{\gamma}_c) = 1$. At finite shear rates; the curve representing the response of a nonlinear viscoelastic fluid will fall below the linear viscoelastic curve (within the envelope). Note that the torque transducer on the RMS-800 mechanical spectrometer can resolve torques as low as 0.05 [mN m] (better than the specified value of 0.2 [mN m]). For the specific cone-and-plate fixture used, this resolution corresponds to a minimum value of the viscosity which may be accurately determined of $\eta^+ = 4.6$ [Pa s] for the lower shear rate of $\dot{\gamma}_0 = 2.6\ [s^{-1}]$, and $\eta^+ = 1.2$ [Pa s] for the higher shear rate of $[s^{-1}]$.

The stress growth response of the first normal stress coefficient, $\Psi_1^+(\dot{\gamma}_0, t)$, is shown in Fig. 4.12. For a shear rate of $\dot{\gamma}_0 = 2.6\ [s^{-1}]$, the multimode Giesekus model quantitatively predicted the response for all times. In the case of the higher shear rate, $\dot{\gamma}_0 = 10\ [s^{-1}]$, a quantitative match between the model prediction and the data was observed up to a time of t ~ 4 [s]. The prediction of the model is then found to lie below the experimental data val-

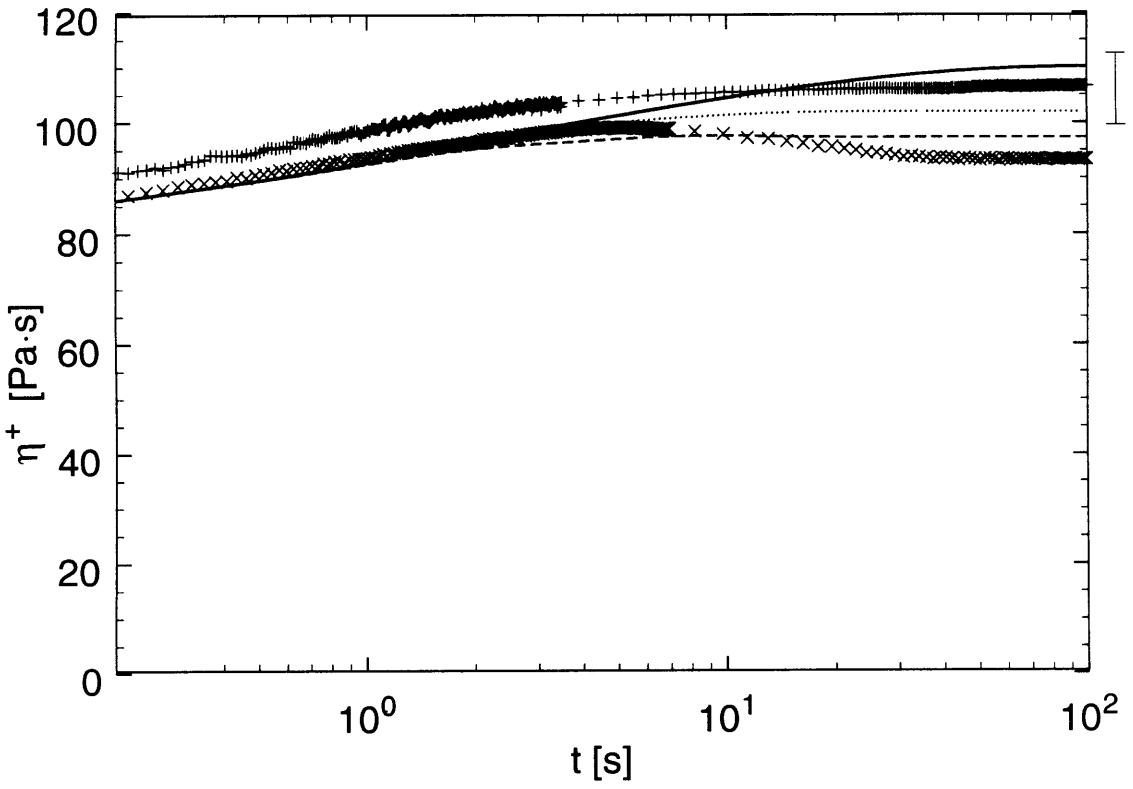

Figure 4.11 Stress growth function $\eta^+(t, \dot{\gamma}_0)$ of the 0.30 wt% PIB in PB test fluid. Experimental data: (+), $\dot{\gamma}_0$ = 2.6 [s^{-1}]; (×), $\dot{\gamma}_0$ = 10 [s^{-1}]. Predictions of four-mode Giesekus model: (·····), $\dot{\gamma}_0$ = 2.6 [s^{-1}]; (— —), $\dot{\gamma}_0$ = 10 [s^{-1}]. (——), prediction of four-mode linear Maxwell model. An error bar is given at the left of the graph.

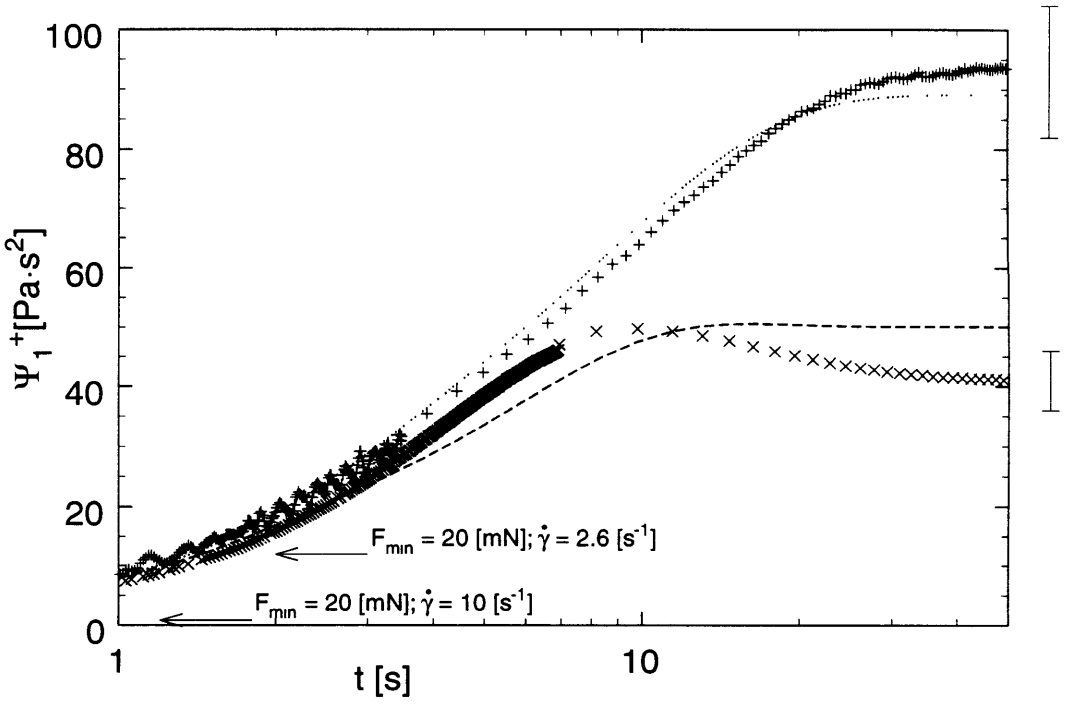

Figure 4.12 Stress growth function $\Psi_1^+(t, \gamma_0)$ of the 0.30 wt% PIB in PB test fluid. Experimental data: (+), $\dot{\gamma}_0$ = 2.6 [s^{-1}]; (×), $\dot{\gamma}_0$ = 10 [s^{-1}]. Predictions of four-mode Giesekus model: (·····), $\dot{\gamma}_0$ = 2.6 [s^{-1}]; (— —), $\dot{\gamma}_0$ = 10 [s^{-1}]. Error bars are given at the right of the plots.

ues. Both the model and the experimental data exhibit an overshoot; as for the case of the η^+ function, the overshoot exhibited by the experimental data is greater than that of the model. The normal force transducer on the RMS-800 can resolve forces as low as 0.02 [N]. For the cone and plate fixture used, this corresponds to the following values of the first normal stress coefficient which can accurately be measured: $\Psi_1 = 12$ [Pa s^2] for the lower shear rate of $\dot{\gamma} = 2.6$ [s^{-1}] and $\Psi_1 = 0.8$ [Pa s^2] for the higher shear rate of $\dot{\gamma} = 10$ [s^{-1}]. These limiting values are indicated on Fig. 4.12.

Stress Relaxation Response

The stress relaxation response of the viscosity is shown in Fig. 4.13. For the case of a shear rate of $\dot{\gamma}_0 = 2.6$ [s^{-1}], a good match between the experimental data and the prediction of the multimode Giesekus model is observed for the range 0.2 [s] < t < 3.5 [s]; the fractional error between the model and the data is of order 20%. For the shear rate $\dot{\gamma}_0 = 10$ [s^{-1}], the model quantitatively predicts the experimentally observed response for all times t > 1 [s]. The minimum values of η^- which can be accurately measured, associated with the limited resolution of the transducer, are indicated in Fig. 4.13. For the case of the test performed at the lower shear rate of $\dot{\gamma} = 2.6$ [s^{-1}], the limited resolution explains the increasing discrepancy with time between predicted and experimentally measured values for t > 3.5 [s].

The dynamic and steady shear measurements of §4.1.4 have been used to fit the parameters of the linear Maxwell and nonlinear Giesekus models. The accuracy of these fits was confirmed by comparing the experimental data with model predictions of the transient response. For the η^+ material function, good agreement within the instrument error of ±5% was observed. For the case of Ψ_1^+, the maximum error was greater, ±25%; this error was larger than expected. For η^-, the error was as great as ±20%, larger than expected. However, the predicted and experimental data exhibit the same exponential-like decay with time. In summary, the dynamic, steady, and transient shear measurements form a set of complimentary techniques for determining the rheological characteristics of the test fluid in shear flow. The experimental measurements and predictions of the Giesekus model for the transient material functions did not quantitatively match (within the expected error of the measurement) in all cases. Nevertheless, the trends were the same

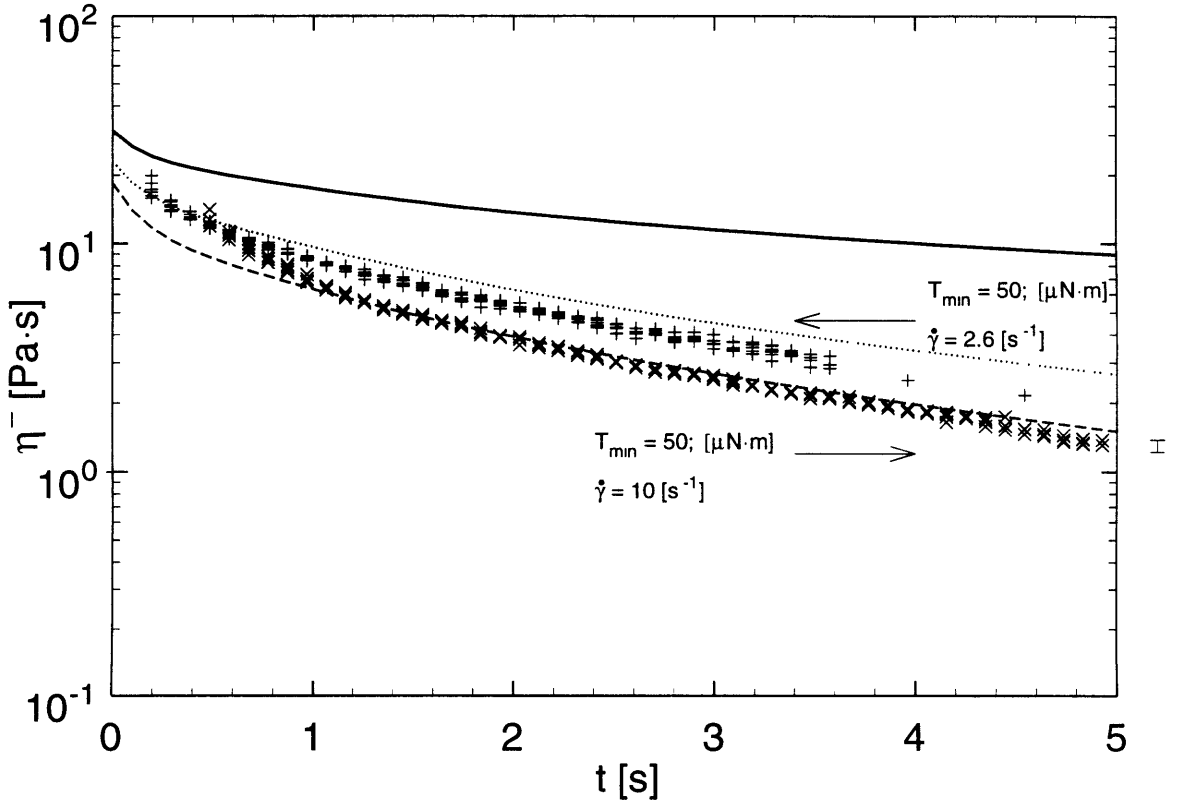

Figure 4.13 Stress relaxation function $\eta^-(t, \dot{\gamma}_0)$ of the 0.30 wt% PIB in PB test fluid. Experimental data: (+), $\dot{\gamma}_0$ = 2.6 [s^{-1}]; (×), $\dot{\gamma}_0$ = 10 [s^{-1}]. Predictions of four-mode Giesekus model: (· · · · · ·), $\dot{\gamma}_0$ = 2.6 [s^{-1}]; (— —), $\dot{\gamma}_0$ = 10 [s^{-1}]. (——), prediction of four-mode linear Maxwell model. An error bar is given at the right of the graph.

and the transient tests corroborated the Giesekus model which was fit to the dynamic and shear rheological data.

4.5 Dimensionless Flow Parameters

The Weissenberg number and the Reynolds number are used throughout this thesis to parameterize the effect of nonlinear viscoelasticity and the inertia, respectively, on the flow field (i.e. the stress and velocity fields). The appropriate characteristic shear rate, velocity, and geometric parameters used in the calculation of these dimensionless parameters depend on the viscoelastic flow phenomenon under consideration; their selection will be discussed in Chapters 5 and 6.

4.5.1 Relaxation Time and the Weissenberg Number

Viscoelastic fluids are distinguished by the fact that a given fluid element has memory of its past deformation history. A characteristic relaxation time, which represents the duration required for a fluid element to "forget" its previous strain history in a flow may be defined. A spectrum of relaxation times (shown in Table 4.5) was fitted to the material functions of the fluid in §4.4. Use of the longest relaxation time, λ_1, is appropriate for flows with low characteristic shear rates, $\dot{\gamma}_{Low}$, such that for the shorter relaxation times associated with the other modes one obtains $(\lambda_{k>1})\dot{\gamma} \ll 1$. However, because of the shear-thinning nature of the fluid, use of the longest relaxation time will over-predict the characteristic relaxation time for elevated flow rates. Consequently, a shear-rate-dependent relaxation time, $\lambda(\dot{\gamma})$, (Bird *et al.*, 1987a) is defined as

$$\lambda(\dot{\gamma}) \equiv \frac{\Psi_1(\dot{\gamma})}{2\eta(\dot{\gamma})} \tag{4.46}$$

The Weissenberg number, introduced in Chapter 1, is used throughout this thesis to parameterize the influence of nonlinear viscoelastic effects on the flow field. However,

because of the shear-thinning nature of the fluid, accurate representation of these nonlinear effects requires the definition of a shear-rate dependent Weissenberg number

$$\mathrm{Wi}(\dot{\gamma}) \equiv \lambda(\dot{\gamma})\langle\dot{\gamma}\rangle \tag{4.47}$$

where $\lambda(\dot{\gamma})$ is defined in eq. (4.46).

A plot of $\mathrm{Wi}(\dot{\gamma})$ for the 0.30 wt% polyisobutylene (PIB) in polybutene (PB) test fluid is given in Fig. 4.14. To maximize the utility of the experimental data reported in this thesis for comparison with future numerical simulations, the predictions of $\Psi_1(\dot{\gamma})$ and $\eta(\dot{\gamma})$ from the fitted Giesekus model, with parameters given in Table 4.5, are used in eq. (4.46); as described above, eq. (4.46) is used in the definition of eq. (4.47). Table 4.5 showed that relaxation modes with time scales as great as 20 [s] were fit to the shear rheology information; reproducible dynamic data were obtained for frequencies as low as 0.1 [s^{-1}]. As stated in §4.4.4, the steady material functions were accurately measured over the range of shear rates from 0.25 to 40 [s^{-1}]. The dynamic measurement shown in Fig. 4.9 indicated that although the slope of the $2\eta''/\omega$ function was found to decrease for decreasing ω, the zero-shear-rate limit, $\lim_{\omega \to 0} 2\eta''/\omega = \Psi_{10}$, was not attained. In consequence, the plot of $\mathrm{Wi}(\dot{\gamma})$ in Fig. 4.14 is corroborated by experimental viscometric material function data for $\dot{\gamma} \geq 0.25$ [s^{-1}]. However, for shear rates $\dot{\gamma} < 0.25$ [s^{-1}] the $\mathrm{Wi}(\dot{\gamma})$ is an extrapolated prediction of the fitted Giesekus model.[5]

4.5.2 Reynolds Number

The Reynolds number, Re, describes the influence of the fluid inertia on the flow field. The use of the Reynolds number in the analysis of fluid mechanical problems is discussed in depth in a number of texts (Lamb, 1945; Bird *et al.*, 1960; Batchelor, 1967); the definition used throughout this thesis is

$$\mathrm{Re} \equiv \frac{2\rho L\langle v\rangle}{\eta} \tag{4.48}$$

5. Note further that for the calculation of Wi < 0.044, which corresponds to a shear rate of $\dot{\gamma} < 0.025$ [s^{-1}], the relaxation time used in eq. (4.47) is held fixed at $\lambda = 1.74$ [s].

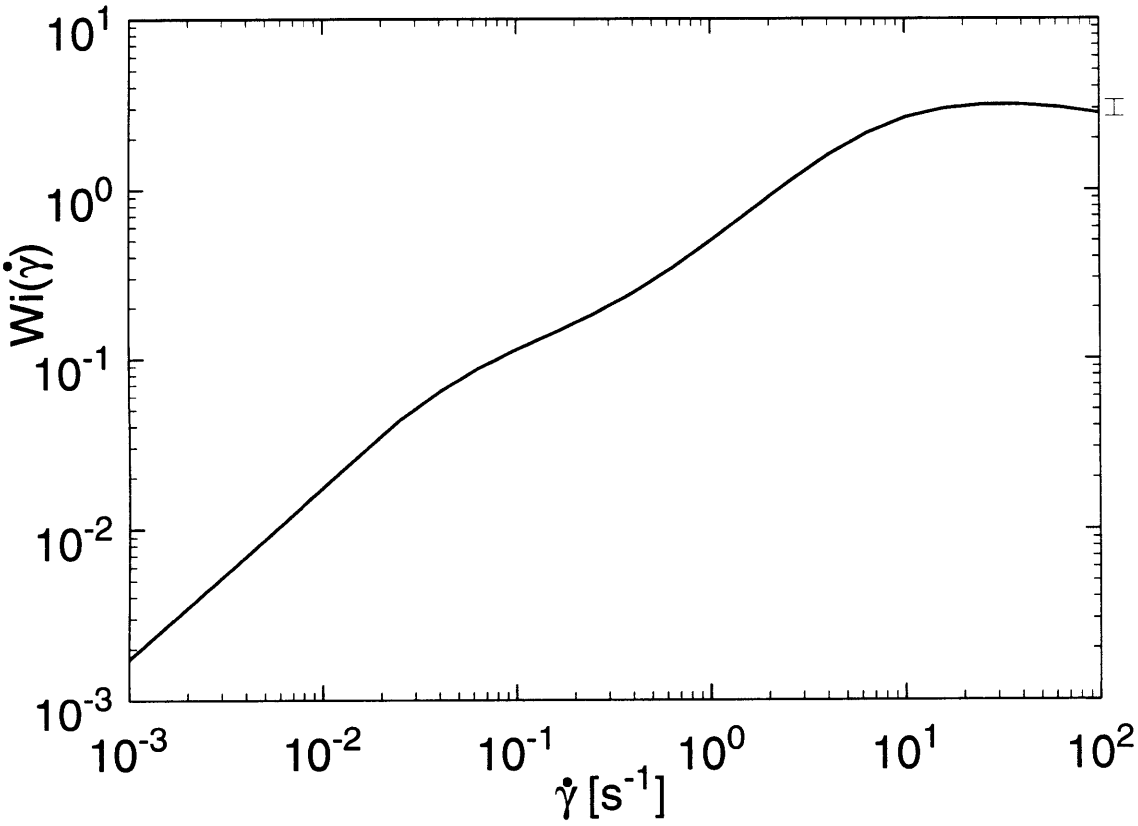

Figure 4.14 Weissenberg number, $\mathrm{Wi}(\dot{\gamma}) = \lambda_1(\dot{\gamma})\dot{\gamma}$, as a function of shear rate for the 0.30 wt% PIB in PB test fluid. An error bar which applies to the part of the curve with $\dot{\gamma} \geq 0.25\ [s^{-1}]$ is given at the right of the graph.

The density of the fluid is represented by ρ, the fluid viscosity is indicated as η, a characteristic velocity is given by $\langle v \rangle$, and a characteristic length is denoted by L.

Although a Boger fluid was used for the investigations presented in this thesis, shear-thinning fluids have been used in previous studies to which comparison is made in Chapter 5. To obtain an upper bound on the importance of inertia in flow of a shear-thinning fluid, the Reynolds number used throughout this thesis was defined in terms of downstream parameters of the contraction. The average velocity in the downstream slit is applied, $\langle v \rangle = \langle v_z \rangle_{Dn}$, the mean shear rate in the downstream slit is used, $\dot{\gamma} = \langle \dot{\gamma} \rangle_{Dn}$, and the downstream slit half-height is employed, $L = h$, to yield the definition

$$Re_{Dn} \equiv \frac{2\rho h \langle v_z \rangle_{Dn}}{\eta(\langle \dot{\gamma} \rangle_{Dn})} \tag{4.49}$$

The maximum value of the Reynolds number for a test run in any investigation performed for this thesis was $Re_{Dn}(\dot{\gamma}) = 7\times10^{-4}$, so that inertial effects were negligible in all of the experiments.

Chapter 5

Viscoelastic Flow Transitions in Abrupt Planar Contractions

Literature pertaining to the experimental characterization of viscoelastic flow transitions observed in viscometric and in complex flows has been discussed in Chapter 2. The unifying concept of streamline curvature and streamwise stress acting as the mechanism driving a class of viscoelastic flow transitions was presented. In particular, a "viscoelastic Görtler" scaling based on this concept was presented; the validity of this scaling has been demonstrated in its application to viscometric and to complex flows. Studies of viscoelastic flow transitions in planar contractions have been conducted; however, these prior investigations were limited in several respects. The shear rheology of the test fluid was often incompletely characterized, inertia was a significant factor in determination of the flow field, and only qualitative velocity-field information was obtained. In consequence, the utility of the studies in evaluating the "viscoelastic Görtler" scaling or serving as "benchmarks" for the assessment of numerical flow simulations was limited. Quantitative information on the structure of viscoelastic flow transitions in planar contraction flow is needed to complement analogous work which has been conducted for axisymmetric contraction flow (McKinley *et al.*, 1991).

In §5.2 of this Chapter, characterization of the spatiotemporal structure of viscoelastic flow transitions occurring in the 2:1, 8:1, and 32:1 planar contraction geometries is presented. Specifically, the light sheet visualization technique is used to develop a model of the velocity field structure. Laser Doppler velocimetry (LDV) is used to quantitatively characterize the critical Weissenberg number associated with onset of the instability; a detailed description of the experimental apparatus and measurement techniques is provided in Chapter 3. Wavelength and time scales associated with the velocity field after onset of the instability are measured with LDV; two-dimensional rearrangement of the velocity field preceding instability onset is identified. The data are interpreted in §5.3. Characteristic dimensions of the velocity field after flow transition are related to geometrical parameters in the flow. The validity of the "viscoelastic Görtler" scaling for the case of

flow transition in the planar contraction is assessed by representing the experimental data in the form of a transition map in §5.3.1. In the summary of §5.4, the set of quantitative information is used to compare and contrast the spatiotemporal structure of the instability observed in planar contraction flow with that of instabilities which have been identified in other geometries. Future research to investigate questions raised by and develop concepts presented in this study is suggested in §5.5.

5.1 Flow Parameters

The Weissenberg number (Wi) is used to characterize the importance of elastic effects in determining stress and velocity fields in a flow; a general definition is given in eq. (1.2) of Chapter 1. To represent accurately the effect of elasticity on the flow field, a relaxation time is used which reflects the shear thinning of Ψ_1 at elevated shear rates. The mean relaxation time at a given shear rate is defined in this Chapter as

$$\lambda(\dot{\gamma}) \equiv \frac{\Psi_1(\dot{\gamma})}{2\eta(\dot{\gamma})} \tag{5.1}$$

The shear rheology of the test fluid has been described in Chapter 4; a plot of Wi as a function of shear rate is given in Fig. 4.15.

One should note that a single parameter, Wi, will not necessarily accurately describe the importance of elasticity in all regions when the velocity gradient tensor varies throughout the flow, as in the case of the planar contraction. In general, a characteristic shear rate is selected so that global transitions in the flow field associated with elastic phenomena correspond with Wi ~ O(1). However, in flow regions with shear rates above the selected characteristic value, local elastically induced flow phenomena may occur at Weissenberg number much less than one.

Throughout this chapter, a Weissenberg number, Wi_{Up}, based on the upstream mean shear rate, $\langle\dot{\gamma}\rangle_{Up} = \langle v_z\rangle/H$, is used. Several considerations motivate this choice. As discussed in Sections 5.2 and 5.3, the experimental results indicate that onset of the instability is associated with flow conditions (shear rate and streamline curvature) upstream of the

contraction plane. Furthermore, the critical Wi_{Up} for instability onset is observed to decrease with increasing contraction ratio; this is consistent with the concept that streamline curvature plays a key role in onset of the instability.

The reader will note that in flows through geometries with large contraction ratios, H/h ≥ 8, very low values of $Wi_{Up\ Crit} << 1$ are observed for instability onset. This supports the concept that the Wi_{Up} parameter alone does not capture the physics controlling onset of instability. A scaling which incorporates the interaction of elastic effects with streamline curvature has been described in Chapter 2 (McKinley *et al.*, 1996) and is applied to the planar contraction flow in §5.3. However, as discussed in Chapter 2, the theory is presently insufficiently developed to *a priori* predict all requisite scaling parameters; these parameters are obtained by fitting to experimental data. By contrast, Wi_{Up} can be determined solely from information on flow conditions for a given test run and known shear rheological data and is therefore used throughout this Chapter.

The highest value of mean upstream shear rate attained in these experiments was $\langle\dot{\gamma}\rangle_{Up} = 4.9\ [s^{-1}]$ with an associated $Wi_{Up} = 1.80$, within the range for which steady shear rheological data could be obtained, in the 2:1 contraction. The lowest value of upstream shear rate for which an experimental result (taken in the 32:1 contraction) is reported was $\langle\dot{\gamma}\rangle_{Up} = 0.0021\ [s^{-1}]$ which corresponds to $Wi_{Up} = 0.004$. The shear rheological data are extrapolated to estimate Wi_{Up} at this low shear rate, as discussed in §4.5.1. As discussed at the end of Chapter 2, the maximum value of the Reynolds number for a test run in this study was $Re_{Dn} = 7 \times 10^{-4}$; inertial effects were negligible for all experiments performed.

5.2 Experimental Results

In this Section a qualitative overview of the spatio-temporal structure of flow states observed in the viscoelastic planar contraction flow is first given. A schematic diagram based on analysis of streaklines in the xz- and yz-planes over a range of flow rates is presented. Next, quantitative velocity field information, obtained via pointwise LDV measurement, for several different regions of the flow, is discussed. Off-centerline scans in space and time-series data acquired at a point are used to identify the Wi_{Up} at onset of instability as well as the characteristic spatial wavenumbers and temporal frequencies

associated with a given global flow state. The transitions of the global flow field are contrasted with transitions associated with the local flow near the walls bounding the x-dimension at $\chi = \pm 32$. Velocity measurements on the centerplane are used to identify a flow rearrangement which may be related to, but has a structure distinct from, off-centerline flow transitions.

5.2.1 Qualitative, Velocity-Field Visualization

Results from light sheet visualization of the flow at different flow rates are presented in detail for the 8:1 contraction. The data are used to reconstruct the spatial and temporal structure of the flow field after onset of the instability. Comparison with observations of flow transitions in the 2:1 and 32:1 contractions is then made.

Flow Transitions in 8:1 Contraction

The evolution of the velocity field with increasing Wi_{Up} will now be discussed. The Newtonian-like base flow for low Wi_{Up} is described first. The first observed non-Newtonian phenomenon is the two-dimensional flow rearrangement to diverging streamlines. At a sufficiently high Wi transition to three-dimensional and steady flow is found; this is followed by the onset of time-dependent flow.

Base Flow at Low Wi_{Up}

At $Wi_{Up} \leq 0.112$ the planar contraction flow of the test fluid resembled Newtonian flow. Specifically, the yz-sheet streakline image (cf. Fig. 5.1a) for $Wi_{Up} = 0.052$ indicates that the streamlines converged smoothly from the upstream channel into the downstream duct and that the flow was steady and symmetric about the centerplane ($\upsilon = 0$). The xz-sheet images gave no indication of flow in the x-direction. The resolution of the streakline images was insufficient to quantitatively determine the reattachment length of the outer vortex (L_v) in the upstream channel. However, the streakline image is consistent with an eddy in the outer corner with reattachment length of $L_V/H = 0.34$, which has been predicted numerically for Stokes flow (Re = 0) of a Newtonian fluid (Coates, 1992); note that

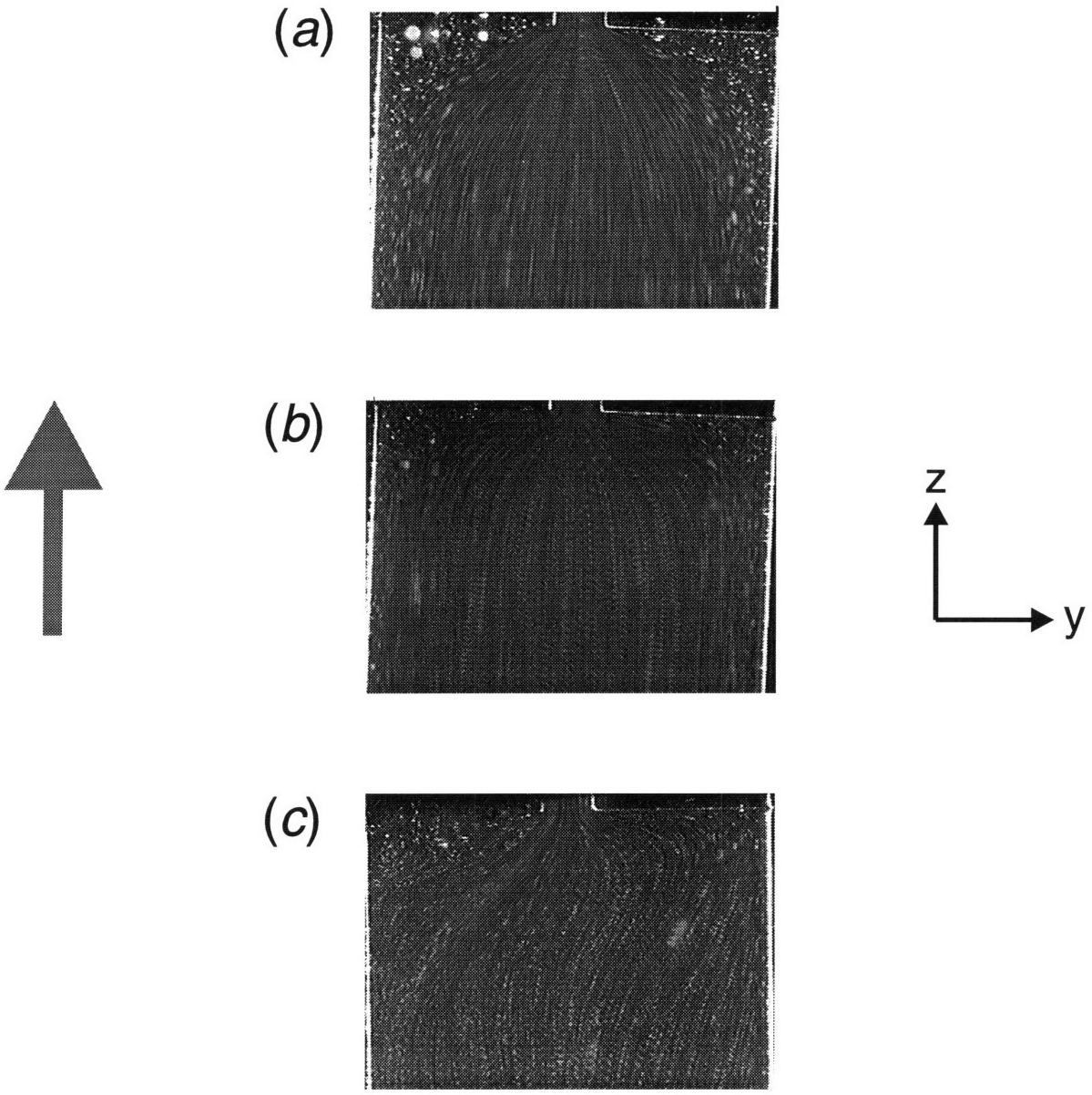

Figure 5.1 Side view of viscoelastic flow through the abrupt 8:1 planar contraction:(a) low flow rate with converging streamlines and Moffat vortex in outer corner, $Wi_{Up} = 0.052$ (number of superimposed frames (N_{frames}) = 15, time interval between frames (Δt_{frames}) = 0.33 [s]); (b) reduction in size of corner vortex and development of diverging streamlines, $Wi_{Up} = 0.138$ ($N_{frames} = 10$, $\Delta t_{frames} = 0.20$ [s]); (c) asymmetric, three-dimensional structure at high flow rates, $Wi_{Up} = 0.229$ ($N_{frames} = 4$, $\Delta t_{frames} = 0.12$ [s]).

analytical treatment of Stokes flow around a corner with a $\pi/2$ [rad] included angle also predicts the existence of eddies (Moffat, 1964).

Transition to Diverging Flow

For $Wi_{Up} \geq 0.138$, an essential change in the spatial structure of the steady-state and two-dimensional velocity field was noted. As shown in the yz-sheet view of Fig. 5.1b, the streamlines appear symmetric about the centerplane; however, instead of uniformly converging to the centerplane as the downstream slit is approached, the streamlines slightly diverge in a region approximately one half-height, H, upstream of the contraction plane ($\zeta = 0$). This corresponds to a deceleration of fluid in the upstream region, $\partial v_z/\partial z < 0$. Furthermore, the distance in the z-direction over which the streamlines exhibited the most rapid continuous convergence from the upstream channel to the downstream slit moved closer to the contraction plane; note in Fig. 5.1b that the streamlines appear "squashed" toward the contraction plane when compared with the image in Fig. 5.1a. Associated with the streamline shift was an apparent *decrease* in the reattachment length of the outer corner vortex.

Transition to Three-Dimensional, Steady Flow

At $Wi_{Up} = 0.124 \pm 0.012$, a transition occurred to steady, three-dimensional flow; the qualitative structure of the velocity field is described here in detail. Above $Wi_{Up} = 0.171 \pm 0.035$, the flow became fully time-dependent as well as three-dimensional; however, the spatial structure of the flow at a given instant in time remained essentially unchanged and resembled the structure described here. This fact allows the use of images of flows with $Wi_{Up} > 0.171$ to illustrate the spatial structure of the flow: at higher Wi_{Up} spatial features of the instability are more readily apparent.

A streakline image in the yz-plane after onset of the spatial instability for $Wi_{Up} = 0.229$ is shown in Fig. 5.1c. The streaklines are asymmetrical about the centerplane. On the right half of the image the streaklines continuously converge from the upstream channel into the downstream slit. A separated vortex in the outer right corner is evident; the reattachment length of the vortex appears to be approximately $L_v/H \approx 0.3$, similar to the Moffat eddy. The in-plane flow speed, $\sqrt{v_z^2 + v_y^2}$, in the region immediately adjacent to

the boundary of the right outer vortex is greater than in any other part of the image; a very high velocity gradient exists in the vicinity of the vortex boundary.

In the upstream region of the flow ($\zeta < -0.2$), the v_z velocity component of the flow is uniform throughout the left half of Fig. 5.1c, in contrast with the right side where the fast flow is located adjacent to the outer vortex. In the left half of the upstream region of Fig. 5.1c, streaklines initially approach the outer left wall; they move in the positive y-direction, away from the centerplane. When they near the outer left corner ($\zeta \gtrsim -0.2$), the streaklines abruptly change direction and travel in the negative y-direction, following along the wall which defines the contraction plane ($\zeta = 0$). No outer corner vortex could be observed on the left side of the image. When the streamlines reach the downstream slit, they again change direction in order to enter the slit. Near the left lip corner of the downstream slit, a small but distinct vortex is observed. This lip vortex is separated from any vortical flow which may be present in the outer left corner. Although the most dramatic effect of the flow transition on the velocity field is observed near the outer walls and near the contraction plane, the transition has a noticeable effect on the entire flow field up to at least a distance O ~ 1.5H before the contraction plane. For example, the streaklines near the centerplane appear snakelike: the mean direction of flow is in the positive z-direction, and the streaklines execute a sinusoidal motion in the y-direction.

Images of slices in the xz-plane located at positions ranging from near the outer wall to near the centerplane are shown in Fig. 5.2. These are discussed in order of increasing υ-position, starting from near the outer wall and following the mean flow of fluid toward the downstream slit. At a position $\upsilon = -8.2$, streaks oriented in the z-direction are visible in Fig. 5.2a. These streaks have a mean separation from each other in the x-direction of O ~ 1.5H; this separation defines the wavelength of the three-dimensional flow. The fluid in the vicinity of the streaks has a much faster v_z-component than fluid in the intermediate regions. Moreover, fluid is observed to flow out of the intermediate regions in the x-direction and feed into the streaks; this accounts for the arced appearance of the streaklines on either side of the fast streaks in Fig. 5.2a. In the slice taken at $\upsilon = -4.4$ (Fig. 5.2b), the fast flow regions continue to be fed by the slow flow regions at distances greater than 0.3H upstream of the contraction plane. Near the contraction plane the flow spreads out to assume a more uniform profile of v_z along the x-direction. Specifically, fluid appears to

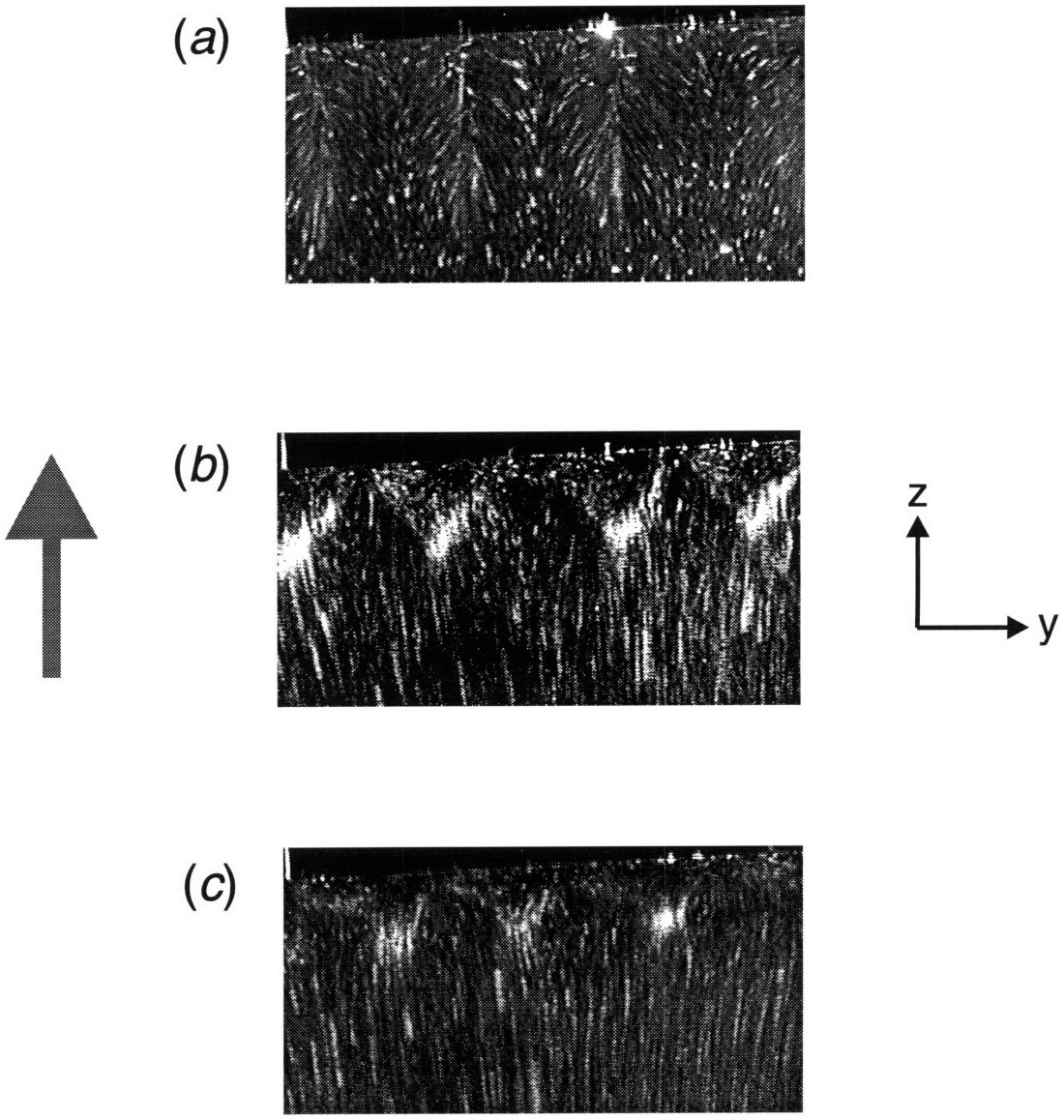

Figure 5.2 Top view of the abrupt 8:1 planar contraction at high flow rate, Wi_{Up} = 0.229 (N_{frames} = 15, Δt_{frames} = 0.1 [s] for all images). Structure is three-dimensional, slices in the xz-plane at different y-elevations are shown: (a) flow near the outer wall (υ = -7.5), fluid flows in the x-direction to "feed" regions of fast flow visible as bright areas; (b) far from the contraction plane fluid "feeds" the fast regions, near the contraction plane fluid "spreads out" to assume a more uniform profile in the x-direction, υ = -4.0; (c) at υ = -2.0, closer to the centerplane, the flow is more uniform in the x-direction, within the triangular structures fluid "wells up" from planes closer to the outer wall.

travel along the bright boundaries which demarcate the triangular structures between the contraction plane and the end of a given streak. In the interior of these triangular structures, the flow is directed primarily in the y- (out of plane) direction. An image of a slice taken at position $\upsilon = -2.2$ is shown in Fig. 5.2c. The triangular structures are now confined to a region nearer to the contraction plane. Although the resolution of the streakline image in Fig. 5.2c is limited, careful study of the source videotape indicated that within the triangular structures there was flow in the x-direction, directed away from the center of the structure. The primary direction of flow within the triangular structures was still in the y-direction, toward the centerplane. Throughout the image (with the exception of the region located immediately before the contraction plane, where the triangular structures are located) the v_z-component of the flow is more uniform along the x-direction than the slices taken closer to the outer wall (Fig. 5.2ab). Hence, close to the centerplane ($\upsilon = 0$), the flow rearranges to adopt a more uniform velocity profile along the x-direction before entering the downstream slit.

A slice taken at $\upsilon = -7.8$ is contrasted with a slice on the opposite side of the centerplane at $\upsilon = +7.8$ in Fig. 5.3. Regions of fast flow, indicated by the streaks in the z-direction, on a given side of the centerplane correspond to regions of slow flow at the same x-position on the other half of the centerplane. This was confirmed by continuously moving the xz light sheet through the entire upstream height over a period of 45 [s], much less than the time scale of the temporal oscillation discussed below. These observations are consistent with the bundles of counter-rotating vortex pairs having an interlaced structure (Chiba *et al.*, 1990; Chiba *et al.*, 1992).

From the light sheet slices in the xz- and yz-planes it was possible to reconstruct a qualitative sketch of the three-dimensional spatial structure of the flow. The history of a fluid element traveling along a streamline which passes through the fast region of flow will now be summarized with reference to Fig. 5.4. Fluid near the wall of the upstream channel travels in the z-direction of mean flow (*a*). When it reaches a distance of the order of the upstream half-height, H, before the contraction plane, the fluid begins to also travel in the x-direction, toward the fast region (*b*). As it more closely approaches the fast region, the fluid begins to travel in the y-direction, away from the outer wall and towards the downstream slit (*c*). When the fluid approaches to within the order of the downstream

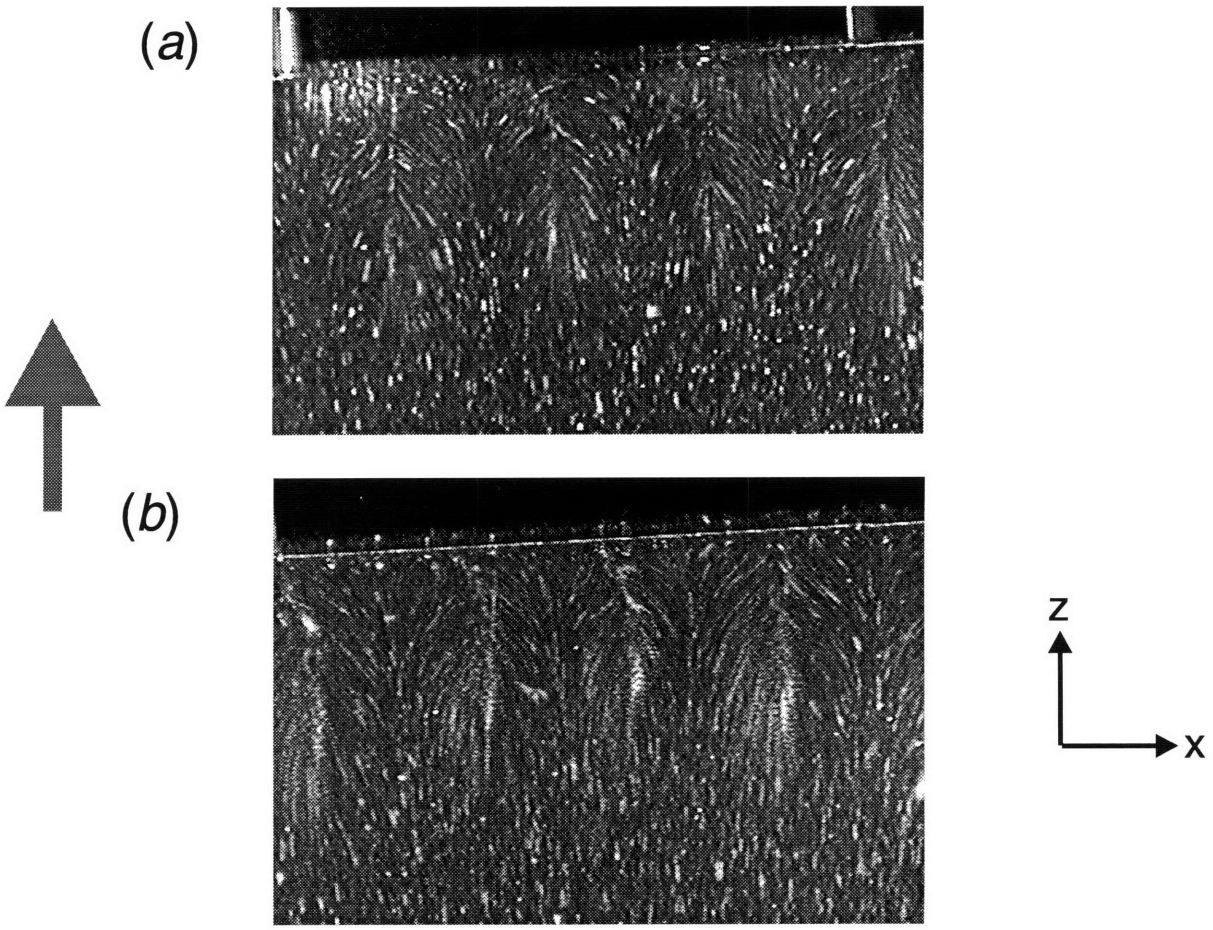

Figure 5.3 Top view of the abrupt 8:1 planar contraction at high flow rate, Wi_{Up} = 0.229 (N_{frames} = 15, Δt_{frames} = 0.1 [s] for both images): (a) flow near the top outer wall (υ = +7.8); (b) flow near the bottom outer wall (υ = -7.8). The pair of images show that the fast regions of flow (brighter areas) are opposed by slow regions of flow (darker areas) on the opposite side of the centerplane.

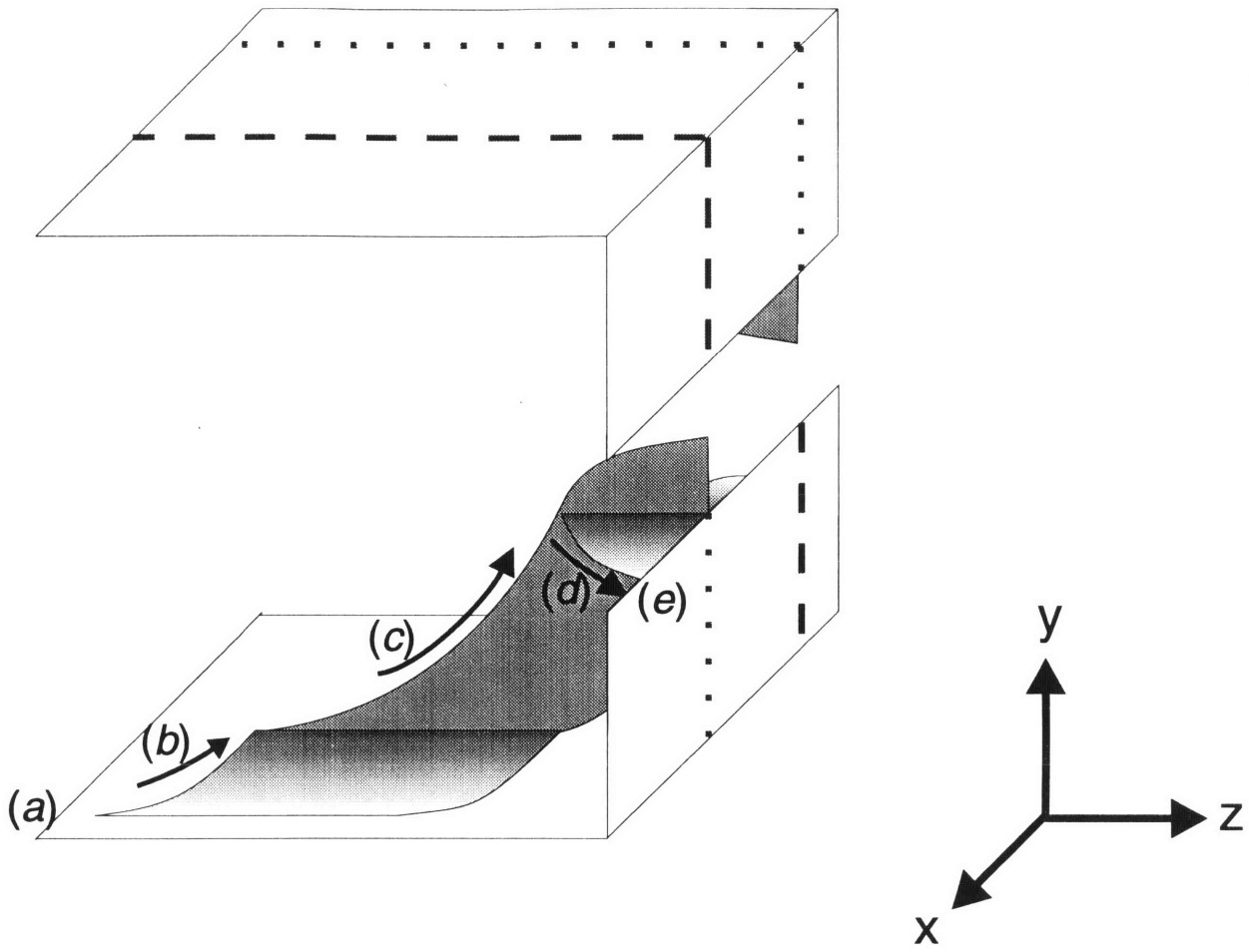

Figure 5.4 Diagram representing the three-dimensional structure of the flow after onset of the instability: (a) far upstream fluid near wall fluid element travels in z-direction; (b) at distance order H before contraction plane element feeds into "fast" region; (c) element in "fast" region flows toward downstream slit; (d) at distance order h before contraction plane fluid "spreads out" to achieve v_z more uniform along x; (e) fluid enters downstream slit.

slit half-height, h, of the contraction plane, it travels back in the positive x-direction, away from the center of the region of fast flow (*d*). When the fluid reaches the contraction plane (*e*), the magnitudes of v_x and v_y are small when compared with that of v_z. The "spreading out" of the flow near the contraction plane makes the v_z-component nearly uniform along the x-direction near the contraction plane, $\zeta = 0$.

Onset of temporal instability at high Wi_{Up}

The temporal structure of the instability is elucidated by sets of yz- and xz-sheet images taken successively in time. A yz-plane of the flow through the 8:1 contraction is shown in Fig. 5.5a and corresponds to $Wi_{Up} = 0.229$ at t = 0 [s]; the streaklines are asymmetric with the region of fast flow on the right half of the image. An xz-plane of the flow taken with the light sheet located near the outer wall, at $\upsilon = -7.8$, is shown in Fig. 5.5b. The yz- and xz-views were taken at different absolute times, but at the same flow conditions. Dashed arrows on a given image (e.g., yz-plane) indicate the position of the corresponding image (e.g., xz-plane). At t = 105 [s], the streaklines in Fig. 5.5c appear nearly symmetrical about the centerplane. The corresponding xz-image (Fig. 5.5d) shows that the vortices have moved toward the center of the flow ($\chi = 0$) by comparison with Fig. 5.5b. Hence, the light sheet in Fig. 5.5c is located half-way between the fast and slow regions on both sides of the centerplane ($\upsilon = 0$). The flow shown in Fig. 5.5e at t = 270 [s] is again asymmetric; however, the region of fast flow is now on the left half of the image. The flow in Fig. 5.5f shows that this reversal of features in Fig. 5.5e with respect to Fig. 5.5a is a result of the vortices having moved farther toward the $\chi = 0$ center of the flow. Specifically, the region of fast flow in Fig. 5.5a has been replaced by a region of slow flow in Fig. 5.5e.

The flow closest to the walls bounding the x-direction at $\chi = \pm 32$ could not be observed with light sheet slices in the yz- or the xz-plane; only positions in the range $-23 \leq \chi \leq 23$ were accessible. However, visual observations in conjunction with the LDV measurements described below indicated that after onset of the temporal instability the vortex structures in the flow are continually born at the walls bounding the x-direction ($\chi = \pm 32$) and move toward the center ($\chi = 0$) of the flow. As a result, the mean spacing between the vortex bundles decreases. Eventually a vortex bundle must be destroyed to maintain an

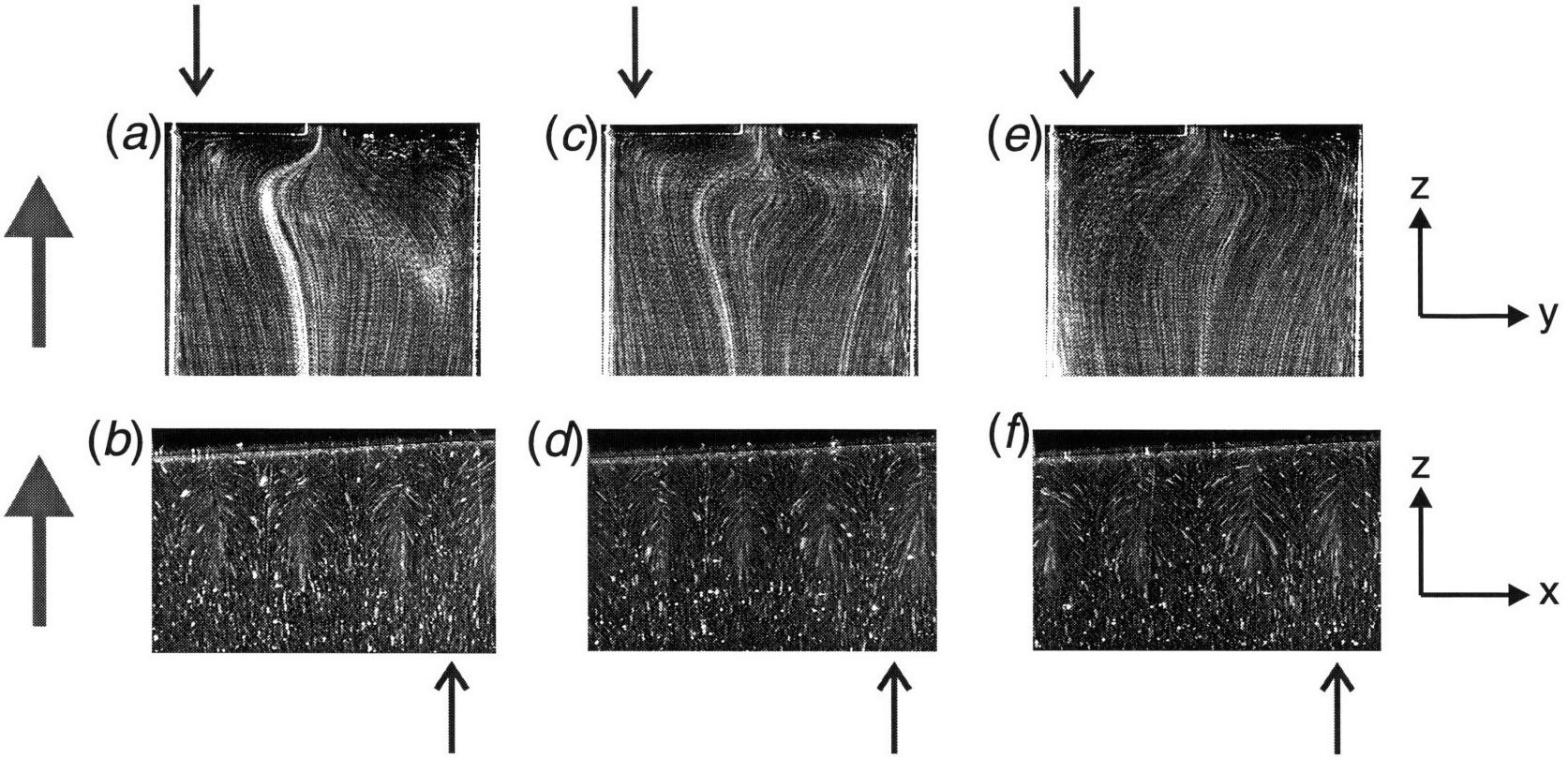

Figure 5.5 Successive images in time, yz- and xz-planes (fixed in space) of the abrupt 8:1 planar contraction at high flow rate, Wi_{Up} = 0.229 (N_{frames} = 15, Δt_{frames} = 0.1 [s] for yz-images, N_{frames} = 40, Δt_{frames} = 0.1 [s] for xz-images): (ab) views at t = 0 [s], asymmetrical streaklines are shown in the yz-image with region of fast flow on the right half of the image; (cd) views at t = 105 [s], xz-image shows that vortex bundles have moved toward the center of the flow (χ = 0), streaklines in the yz-image appear nearly symmetrical; (ef) views at t = 270 [s], the yz-image shows asymmetrical streaklines, now with the fast flow on the left side of the image, xz-image shows that vortex bundles have moved toward the center of the flow, the fast flow region in (b) has been replaced by a slow flow region.

average spacing between the bundles on the order of the upstream half-height. This occurs through one of two mechanisms. Two neighboring streamline bundles near the center of the flow may move closer to each other until eventually they merge into one. Alternately, a vortex bundle near the center of the flow may decrease in size and intensity as neighboring streamline bundles on either side approach. Eventually the streamline bundle in the middle disappears entirely; this process of "absorption" by neighboring bundles, is shown in Fig. 5.6 via successive xz-images in time. A destruction mechanism which has elements of both the "merging" and "absorption" processes, i.e. preferential absorption into one of the neighboring vortex bundles, was also observed.

Flow Transitions in the 2:1 and 32:1 Contractions

The flow transition sequence with increasing Wi_{Up} in the 2:1 contraction was qualitatively similar to that observed in the 8:1 contraction. However, the transitions occurred at higher values of Wi_{Up}. The wavelength and the upstream extent of the spatial instability were both of the order of the upstream half-height, H, as found for the 8:1 contraction. There were visual indications of time-dependent behavior of the vortex bundles at elevated flow rates. However, the movement of the vortices in the xz-plane was not as distinct as in the images acquired with the 8:1 contraction flow.

In the 32:1 contraction, the low aspect ratio, W/2H = 1, of the upstream channel affected the transition sequence and spatio-temporal structure of the flow. Onset of three-dimensional flow, specifically flow in the x-direction, could be detected via light sheet visualization at the periphery of the observable region encompassing $-23 \leq \chi \leq 23$. Additional detail on the spatio-temporal structure of the flow after onset of the instability is given in §5.2.2.

5.2.2 Off-Centerline Velocity Measurements of Global Flow Transitions

Quantitative velocity field information was obtained to characterize the spatial and temporal structure of flows after, and the class of bifurcation at instability onset; the laser Doppler velocimetry (LDV) technique was used. To parallel the qualitative observations

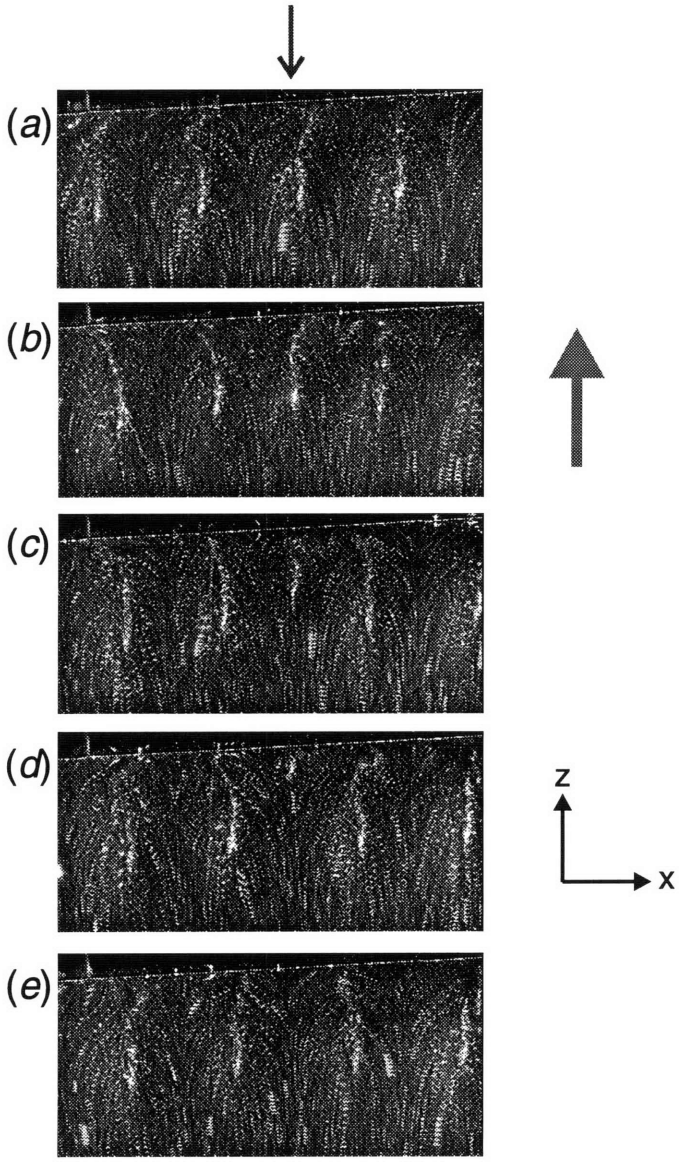

Figure 5.6 Successive streakline images in time, top view, of the abrupt 8:1 planar contraction at high flow rate, $Wi_{Up} = 0.229$ ($N_{frames} = 6$): (a) t = 0 [s], vortex bundles of equal strength are evenly spaced 1.5H apart, note the arrow at top which indicates the location of the "center vortex bundle" on which attention is focused here; (b) view at t = 120 [s], the vortex bundles have moved toward the center of the flow ($\chi = 0$), resulting in closer spacing; (c) at t = 180 [s] vortex bundles have moved yet closer together and the center vortex bundle has weakened relative to the neighboring bundles; (d) at t = 210 [s] the center vortex has weakened further and is barely distinguishable; (e) at t = 240 [s] the center bundle vortex has been completely absorbed into the neighboring bundles.

discussed above, results are given for transitions occurring at increasing Wi_{Up}. Off-center-line LDV data were taken for the 2:1 and 32:1 contractions but not for the 8:1 contraction.

Transition to and Evolution of Three-Dimensional Flow in the 2:1 Contraction

The LDV system was operated with the frequency tracker in order to characterize the wavelength of the three-dimensional flow field in the x-direction after onset of the instability. Specifically, the measuring volume was scanned through the region corresponding to $-26 < \chi < 0$, $\upsilon = -1.75$, $\zeta = -1.80$ at a constant rate of $v_{x\ scan} = 1.43$ [mm/s]. The acquired set of velocity versus time data was then converted to velocity versus spatial position information. Data could not be obtained for $\chi \geq 0$ since the backscattered light had to travel through too much fluid. Specifically, the light was obscured by the seed particles in the fluid, reducing the amount of backscattered light received by the LDV optics to too low a level for effective use of the tracker.

As the volumetric flow rate was increased from an initially low value, the structure of the flow field evolved. The spatial evolution described in this Section consisted of a sequence of transitions: onset of three-dimensional, steady flow; wavenumber doubling; and appearance of multiple harmonics. At the end of this Section, the bifurcation to spatial oscillation is classified.

Spatial Profile of v_z at Intermediate Wi_{Up}

At volumetric flow rates corresponding to $Wi_{Up} \leq 0.37$ the profile of v_z versus x was uniform, indicating that the flow was two-dimensional. When the flow rate was increased such that the Weissenberg number was in the range $0.51 \leq Wi_{Up} \leq 1.37$, the profile of v_z versus x was no longer uniform, a transition to a three-dimensional, steady flow had occurred. The spatial scans typically had a substantial amount of instrument induced noise at a frequency of about 14 [Hz]; this complicated direct interpretation of the v_z-versus-x profile. However, the information on the spatial period of the instability corresponded to a tracker output of between 0.1 and 1.5 [Hz]. Since the frequencies of the flow-structure information and the noise were well separated, a power spectrum (PS) of the data could be used to identify oscillations associated with the viscoelastic instability. The PS of the velocity versus position data was calculated using data in the range of -26.1

$< \chi <$ -1.6, for which the strongest signal was obtained. To obtain a more accurate estimate of the "true" PS, a set of eight velocity versus position scans was made for a given flow rate. The Welch windowing function was applied to each scan before calculation of the PS.[1] The eight PS were then averaged to generate a mean PS with a standard deviation $1/\sqrt{8} = 35\%$ of a single PS.

A plot of the mean power spectral density (PSD) as a function of the wavenumber made dimensionless with the upstream half-height, H, is shown in Fig. 5.7a for a flow with $Wi_{Up} = 0.67$. Wavenumber is used for the abscissa since the PS is calculated for equal wavenumber intervals. The large peak centered about a dimensionless wavenumber of 0.69 corresponds to the characteristic wavelength of the three-dimensional flow. The partially shown peak at the extreme left of the plot is an artifact and not physically significant.[2]

The power associated with the peak representing the spatial oscillation in the PS was estimated by summing the power spectral density (PSD) values of a continuous range of wavenumbers for which the PSDs were greater than 10% of the peak value. The amplitude of a peak in the PS is defined as the square root of this total power under the peak; the spatial oscillation shown in Fig. 5.7a has an amplitude of 0.065 [mm s^{-1}]. Since the peak has a finite breadth, an estimate of the wavenumber of the spatial oscillation should consider the entire peak, not only the wavenumber associated with the maximum power. Therefore, the wavenumbers were weighted with their associated PSD values and summation performed over the range. The sum was then normalized with the total power over the

1. The discrete PS obtained for a finite set of data provides an approximation to the actual, continuous PS of the physical system. If the physical system has a peak in the continuous PS which is not located between two frequency "bins" of the discrete approximation, the power associated with the peak is not only partitioned between these adjacent "bins" but also "leaks" into bins which are farther removed. Application of a windowing function to the data set prior to computation of the PS serves to ameliorate spurious features in the PS which can arise via "leakage" (Press *et al.*, 1988).
2. A decreasing trend in the velocity with increasing χ-position was noted; this slope was manifested as a peak at the lowest non-DC frequency "bin" of the PS. This was found for flows in the two-dimensional base state as well as the three-dimensional flows. In consequence, the trend did not appear to be related to the "elastic" nature of the flow. As the measuring volume is moved to more positive values of c, the backscattered light must travel through more fluid; in consequence the effective Doppler burst rate "seen" by the tracker decreases. The decreased rate may have aggravated tracker "dropout" (cf. Chapter 3) and resulted in a decreased apparent velocity for data obtained at more positive χ-positions (far from the wall). Note that individual "dropout" events would appear as high frequency peaks in the PS far removed from the low frequency peaks associated with the (real, physical) spatial oscillation.

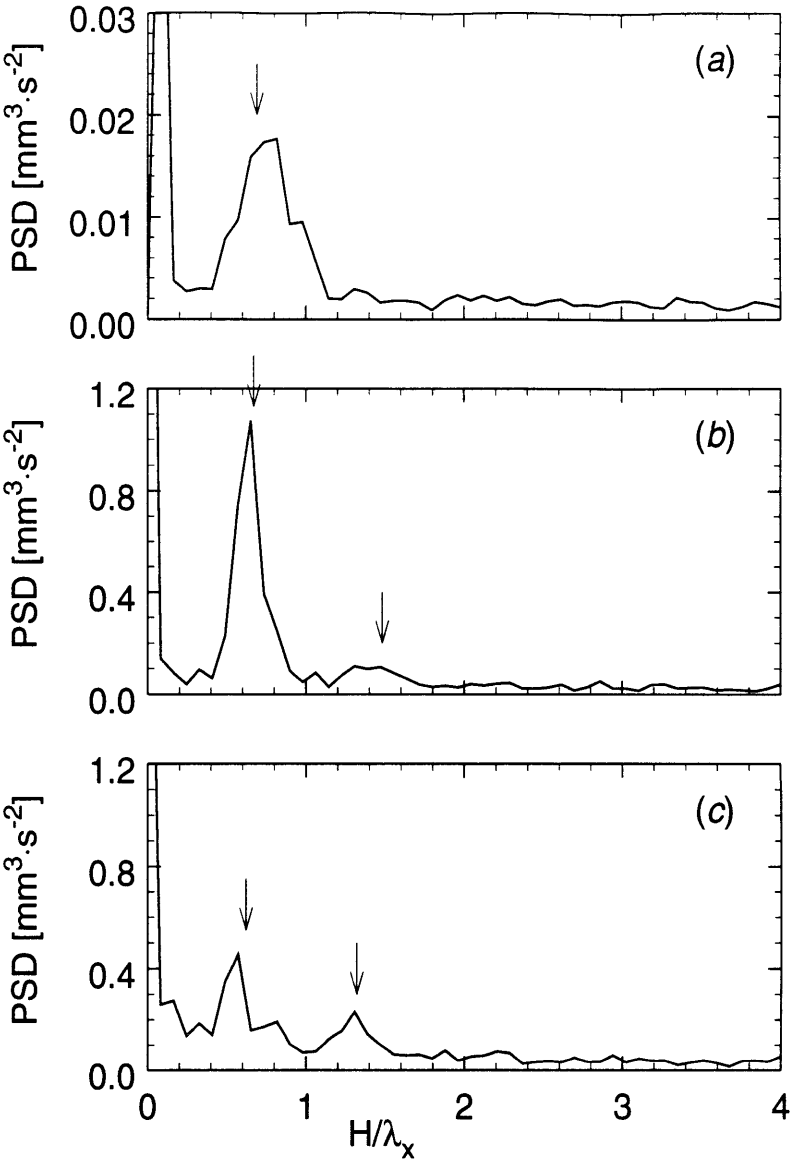

Figure 5.7 (a) Mean power spectrum (PS) of scan in the x-direction (υ = -1.75, ζ = -1.79) for flow through the 2:1 contraction with Wi_{Up} = 0.67. Mean dimensionless wavenumber of primary peak is $\overline{(H/\lambda_x)}_1$ = 0.69; (b) PS of scan in x-direction (υ = -1.75, ζ = -1.79), 2:1 contraction, Wi_{Up} = 1.53. Wavenumber doubling behavior; primary peak wavenumber is $\overline{(H/\lambda_x)}_1$ = 0.67, secondary peak wavenumber is $\overline{(H/\lambda_x)}_2$ = 1.48; (c) PS of scan in x-direction (υ = -1.74, ζ = -1.80), 2:1 contraction, Wi_{Up} = 1.72. Primary peak wavenumber is $\overline{(H/\lambda_x)}_1$ = 0.62, secondary peak wavenumber is $\overline{(H/\lambda_x)}_2$ = 1.32. Higher order harmonics (in addition to the primary and secondary peaks) are present. Note that the mean dimensionless wavenumber of the peaks shown in (a - c) are indicated by arrows.

range to determine a first moment quantity corresponding to the mean wavenumber. The characteristic dimensionless wavenumber of the spatial oscillation shown in Fig. 5.7a was $H/\lambda_x = 0.74$ which corresponds to a wavelength of $\lambda_x = 1.35H$.

Wavenumber-Doubling Behavior of Spatial Oscillation in v_z at High Wi_{Up}

For volumetric flow rates corresponding to $1.14 \leq Wi_{Up} \leq 1.53$, a secondary peak at approximately twice the spatial wavenumber of the primary peak was observed. The PS of the flow corresponding to $Wi_{Up} = 1.53$ is shown in Fig. 5.7b. The primary peak has a mean dimensionless wavenumber of 0.67; a broad secondary peak with a dimensionless wavenumber of 1.48 is now also apparent.

Multiple Harmonics in Spatial Oscillation of v_z at High Wi_{Up}

The PS of a flow with $Wi_{Up} = 1.72$ is shown in Fig. 5.7c. The secondary peak at a dimensionless wavenumber of 1.32 has increased in strength whereas the primary peak at 0.62 has weakened. Additional peaks appear between the primary and secondary peaks and below the primary peak. The PSD values within these additional peaks are above the level of the broadband noise, indicating that they are physical phenomena, i.e. additional harmonics. However, the resolution of the PS (the wavenumber interval) is limited by the finite distance in the x-direction which can be probed, and the limited number of data sets restricts the accuracy of the PSD estimate at a given wavenumber. These considerations prevent specific identification of the higher-order harmonics.

As discussed below, a transition to time-dependent behavior occurs in the range $1.37 \leq Wi_{Up} \leq 1.43$; the frequency associated with this temporal oscillation is of order 0.006 [Hz]. In contrast, the output from the tracker which contains the information on the spatial period of the instability for the scan speed used corresponds to a frequency between 0.1 and 1.5 [Hz]. Therefore, the time-dependent behavior does not have a deleterious effect on the measurement of the spatial form of the instability.

Classification of Bifurcation to Spatial Oscillation

The amplitude of the spatial oscillation is plotted as a function of Wi_{Up} in Fig. 5.8. In order to check for the occurrence of hysteresis, the volumetric rate was first set to a value

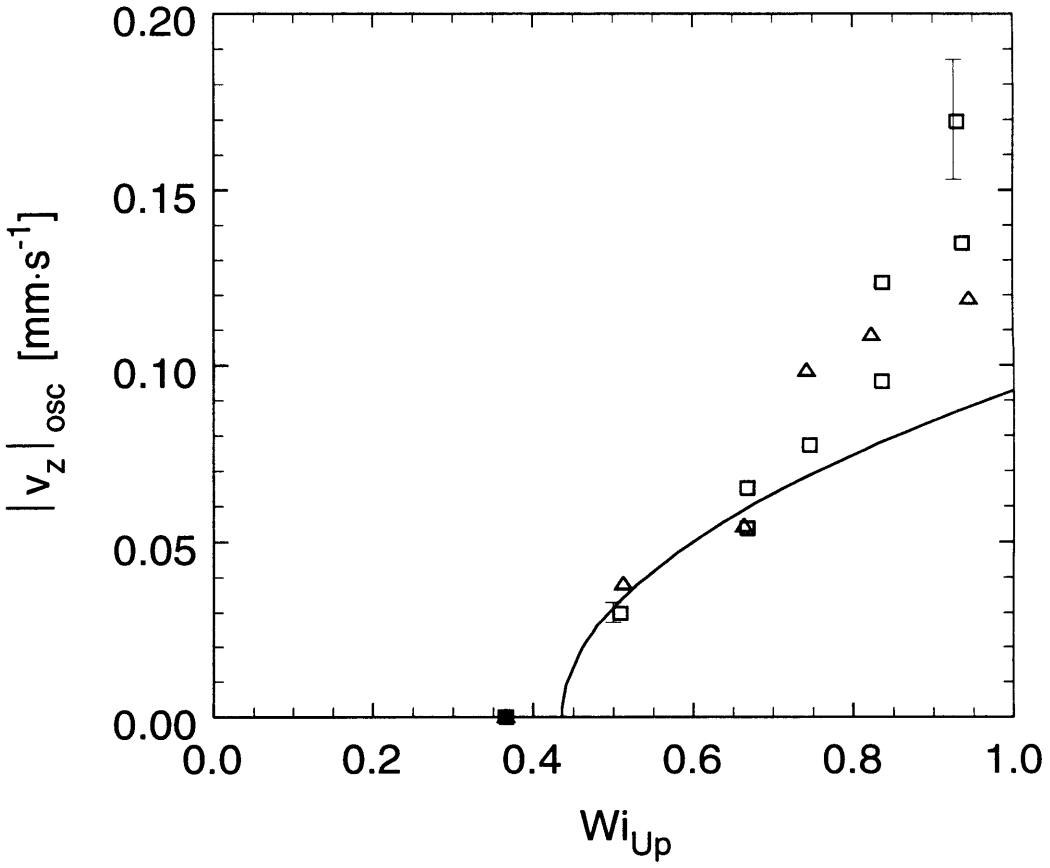

Figure 5.8 Amplitude of spatial oscillation, $|v_z|_{osc}$, from scans of v_z vs. χ (υ = -1.75, ζ = -1.80) as a function of Wi_{Up} in 2:1 contraction flow. Data taken with ($\triangle$) successively increasing flow rates; ($\square$) decreasing flow rates; note the absence of hysteresis. Solid symbols indicate two-dimensional flow; hollow symbols denote three-dimensional flow; (—), fit of eq. (5.2) to data near onset. The order ±10% error associated with the determination of the amplitude of oscillation is indicated by the two representative error bars.

such that the flow was in the two-dimensional base state; specifically $Wi_{Up} \leq 0.37$. Measurements of the velocity profile were then taken at successively increasing flow rates; the amplitude of a peak associated with the spatial oscillation for a given Wi_{Up} is shown in the plot. In a second set of runs, the flow rate was initially set to a value such that the flow was in the three-dimensional and steady state. Velocity profile measurements were then taken at successively decreasing flow rates; the peak amplitudes for these measurements are shown in Fig. 5.8. Since there is no significant difference between the amplitudes of the sequences of measurements conducted for increasing and for decreasing flow rates, no hysteresis is evident; absence of hysteresis is characteristic of a supercritical bifurcation (Strogatz, 1995). The standard deviation of the amplitude of oscillation of the eight power spectra which were averaged together was of order ±10%; error bars of ±10% are indicated in Fig. 5.8.

Asymptotic analysis of a supercritical bifurcation predicts that near onset of instability, the amplitude of oscillation will scale as

$$|v_z|_{osc} = C_{S2}(Wi_{Up} - Wi_{Up,\,S2})^{1/2} \tag{5.2}$$

where C_{S2} is a constant (Strogatz, 1995).[3] In Fig. 5.8 two-dimensional, steady base flow is indicated by filled symbols and three-dimensional flow by hollow symbols. The amplitude of spatial oscillation data near the value of Wi_{Up} for onset of the instability was then fit by eq. (5.2) with $C_{S2} = 0.124$ [mm s^{-1}] and the critical value $Wi_{Up\,S2} = 0.44 \pm 0.07$; the error bounds are derived from data points with Wi_{Up} immediately greater than or less than $Wi_{Up\,S2}$, for which stability of the base flow or spatial oscillation was observed. At elevated $Wi_{Up} \geq 0.74$, a departure from the square root scaling is observed; this behavior is associated with the onset of harmonics of the fundamental wavenumber of the spatial oscillation.

3. The letter in the subscript of parameters in eq. (5.2) indicates the particular flow transition with which the parameter is associated: S indicates transition from two-dimensional, steady to three-dimensional, steady flow; T denotes transition from steady to time-dependent flow. The number indicates the contraction ratio, H/h, for which the parameter applies.

Transition to Time-Dependent Flow in 2:1 Contraction

In order to characterize the temporal structure of the flow after transition to time-dependent behavior, the measurement volume of the LDV system was placed at the point χ =-20.0, υ =-1.75, and ζ =-1.80. This point was chosen since it was expected to provide the clearest signal; specifically, in the spatial scan it was within the region of maximum difference between the crest and trough of the measured v_z. The flow rate was then set to a value corresponding to a specific Wi_{Up}, and the velocity recorded as a function of time. The evolution in the temporal structure of the flow is described here; the classification of the bifurcation to time-dependent behavior is given at the end of this Section.

At low volumetric flow rates, corresponding to $Wi_{Up} \leq 1.37$, no characteristic temporal oscillation was noted in the power spectrum (PS). Once the volumetric flow rate was increased to a value corresponding to $Wi_{Up} \geq 1.43$ oscillation was noted in the time-series data and characterized by calculating the PS in a similar manner as for the space data. Overlapping data sets were extracted from the time series; the Welch windowing function was applied to each set; individual PS were calculated; and the results were averaged to compute a mean PS with a lower standard deviation than the individual PS. The PS of at least three time-series segments were averaged together, each segment consisted of approximately 900 data points representing 1500 [s] of flow. The mean frequency was calculated in an analogous manner as the mean wavelength for the case of the spatial instability. Figure 5.9 shows the PS for a flow with $Wi_{Up} = 1.72$. The primary peak has a mean frequency of 0.0047 [s^{-1}] which corresponds to a period of 214 [s]. The two local maxima within the primary peak are not physically significant, they result from the PS of only three sets of time-series data being averaged together.

As discussed above, the spatial oscillation of the three-dimensional flow undergoes wavenumber doubling. The secondary peak in the temporal PS of Fig. 5.9 at 0.0102 [s^{-1}] may be a manifestation of this wavenumber doubling. At $Wi_{Up} \geq 1.80$ the power of the secondary peak in the temporal PS exceeds that contained in the primary peak; an increase in the amplitude of the secondary peak with Wi_{Up} and a decrease for the primary peak was also noted in the PS of the spatial oscillation discussed above. This observation further

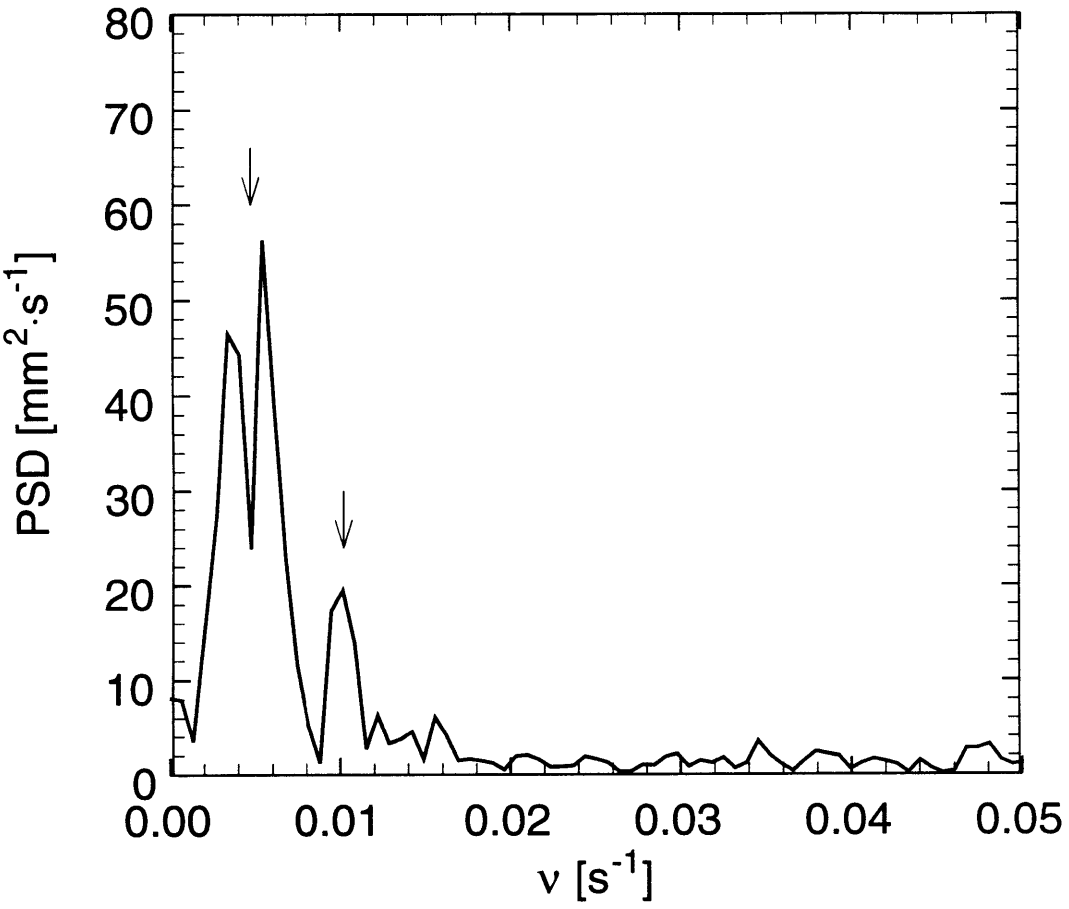

Figure 5.9 Mean power spectrum of time-series data for flow through 2:1 contraction with Wi_{Up} = 1.72, data taken at the point (χ =-20.0, υ =-1.75, ζ =-1.80). Primary peak mean frequency is $\bar{\nu}_1$ = 0.0047 [s^{-1}], secondary peak mean wavenumber is $\bar{\nu}_2$ = 0.0102 [s^{-1}]. Mean frequencies of the peaks are indicated by arrows.

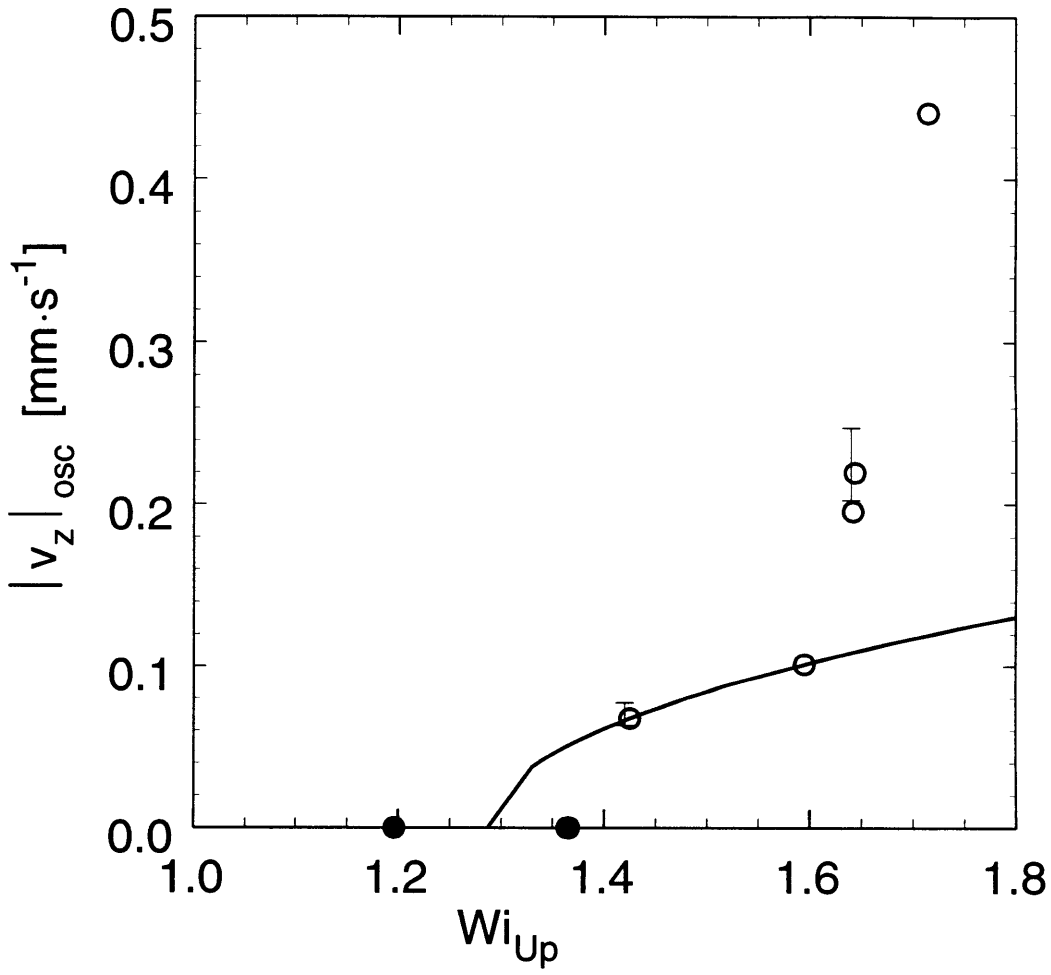

Figure 5.10 Amplitude of oscillation, $|v_z|_{osc}$, for temporal instability at the point χ = -20.0, υ = -1.75, ζ = -1.80 as a function of Wi_{Up} in 2:1 contraction flow. Solid symbols indicate steady flow; hollow symbols denote time-dependent flow; (—), square-root-scaling fit to data near onset. The order ±10% error associated with determination of the amplitude of oscillation is indicated by the two representative error bars.

supports the idea that the secondary peak observed in the temporal PS of Fig. 5.9 is a manifestation of period doubling of the spatial oscillation.

The amplitude of the temporal oscillation is plotted as a function of Wi_{Up} in Fig. 5.10. Steady flow is indicated by the solid symbols, time-dependent flow by the hollow symbols. Noise in the data made it difficult to characterize the amplitude of oscillation near the onset point. For the data points with representing oscillation of finite amplitude, the error was of order ±10%, as shown in the graph. Scaling of the form in eq. (5.2) (square root of amplitude with Wi_{Up}) was consistent with the data, although the fit underpredicted the critical Weissenberg number ($Wi_{Up\ T2}$) for onset of the instability. The fitted scaling parameters for the temporal instability in the 2:1 contraction were $C_{T2} = 0.183$ [mm s^{-1}] and the critical value $Wi_{Up\ T2} = 1.29$. Square-root scaling of the amplitude near onset of temporal oscillation is observed for a supercritical Hopf bifurcation (Strogatz, 1995).

Global Flow Transitions in the 32:1 Contraction

LDV measurements were restricted by the size of the side window of the geometry to the region $-8 \leq \upsilon \leq 8$. Velocity measurements near the wall of the upstream channel in the 32:1 contraction (at $\upsilon = \pm 32$) could not be obtained; hence, in order to measure a large amplitude of oscillation associated with a flow transition, the v_y-component of the flow was measured. Spatial scans in the x-direction as well as time series information at a given point were acquired with the LDV system operated in frequency tracker mode. Flow phenomena which span the entire x-dimension are considered here; phenomena localized near the wall at $\chi = \pm 32$ are considered in §5.2.3. The spatial structure of the instability in the 32:1 contraction is considered first; then, the temporal structure is addressed.

Spatial Structure of Flow after Onset of the Instability

In contrast with flow in the 8:1 and 2:1 contractions, a transition from the two-dimensional base flow to a three-dimensional, but steady, spatial structure that encompassed the entire span of the x-dimension was not observed. Rather, an immediate transition from the base flow to a three-dimensional, time-dependent flow spanning the x-dimension was observed.

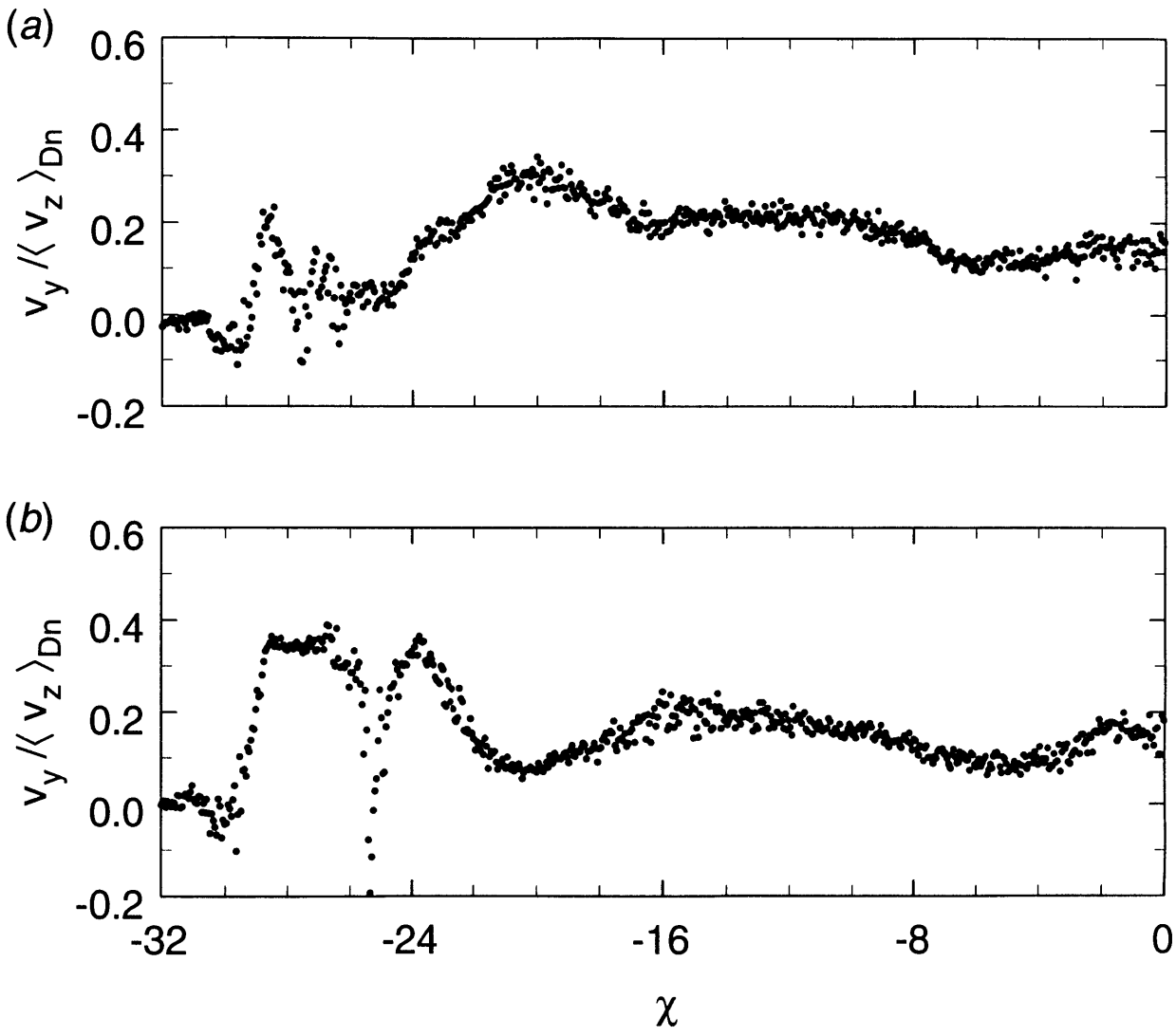

Figure 5.11 Dimensionless v_y vs. χ scan for flow through the 32:1 contraction with $Wi_{Up} = 0.039$. Spatial scans were performed over the range $-32 \leq \chi \leq 0$, $\upsilon = -1.50$, and $\zeta = -1.50$. (a) Velocity profile at time t = 0 [s]. (b) Velocity profile at a later time, $t \geq 120$ [s].

A spatial scan, performed at a time t = 0 [s] over the region $-32 \leq \chi \leq 0$, $\upsilon = -1.50$, and $\zeta = -1.50$ for a flow with $Wi_{Up} = 0.039$, is shown in Fig. 5.11a; Fig. 5.11b is a spatial scan over the same region but performed at a later time, $t \geq 120$ [s]. A specific wave speed was not calculated, but Figs. 5.11a and 5.11b are consistent with a wave originating at the bounding wall at $\chi = -32$ and sweeping in the positive x-direction toward the center of the flow. The scans were performed by moving the measuring volume in the negative x-direction at a constant rate of $v_{x\,scan} = 1.43$ [mm s^{-1}]. The scanning procedure did not substantially shorten the apparent wavelength since the voltage output of the tracker during the spatial scans shown in Figs. 5.11a and 5.11b had a lowest characteristic frequency on the order of 0.05 [s^{-1}] whereas the characteristic frequency of the temporal oscillation (discussed below) was much lower, 0.003 [s^{-1}].

One may also note from Figs. 5.11a and 5.11b that the variation in the $v_y/\langle v_z \rangle_{Dn}$ versus χ profile between two scans separated in time is greatest at the χ-positions closest to the bounding wall; i.e. in the range $-32 \leq \chi \leq -16$. The variation is much less near the center of the flow $-16 \leq \chi \leq 0$; moreover, a trough in the velocity profile is noticeable at $\chi \approx -5$ and a crest at $\chi \approx -2$ in both Figs. 5.11a and 5.11b. The fact that the profile near the center of the flow is only slightly affected by the wave associated with the temporal oscillation indicates that the temporal oscillation is superimposed upon a steady, spatial oscillation. The amplitude of the temporal oscillation is greatest near the wall ($\chi = -32$) where it dominates the $v_y/\langle v_z \rangle_{Dn}$ versus χ profile and prevents accurate characterization of the wavelength, amplitude, or onset Wi_{Up} of an underlying steady, spatial oscillation. The amplitude of the temporal oscillation weakens as the center of the flow ($\chi = 0$) is approached and the pattern of the underlying spatial oscillation becomes distinct. The issue of localization of the temporal oscillation near the bounding wall at $\chi = -32$ is discussed in greater detail in §5.2.3 below.

Characterization of Onset and Temporal Structure of Flow Transition

In order to characterize the temporal structure of the instability in the 32:1 contraction, the measurement volume was placed at the point $\chi = -1.50$, $\upsilon = -21.0$, and $\zeta = -1.50$. The flow rate was then set to a value corresponding to a specific Wi_{Up}, and the velocity recorded as a function of time. In this Section, the evolution of the temporal structure of

the flow for successively greater Wi_{Up} is described. Characterization of the dependence of the magnitude of the oscillation on Wi_{Up} was used to identify the critical Wi_{Up} for onset of the instability.

For $Wi_{Up} \leq 0.0352$ no time dependence of v_y was detected at the point in space where the LDV measuring volume was located. When the volumetric rate was increased to a value corresponding to $Wi_{Up} \geq 0.0356$, oscillations were apparent in the time-series data. The PS was calculated from the time-series data; the mean frequency of the oscillation peak was 0.0029 ± 0.0003 [s^{-1}]. The amplitude of oscillation is plotted as a function of Wi_{Up} in Fig. 5.12. Filled symbols indicate steady flow, hollow symbols represent time-dependent flow. For $Wi_{Up} > 0.0356$, the amplitude was observed to increase monotonically until $Wi_{Up} = 0.0424$; beyond this point the onset of additional harmonics resulted in a decrease in the amplitude of the primary peak. No hysteresis was noted in Wi_{Up} when it was dropped from $Wi_{Up} = 0.0386$ to $Wi_{Up} = 0.0345$, which was just below the critical point.

As shown in Fig. 5.12, the data for the amplitude as a function of Wi_{Up} near the critical value of Wi_{Up} fits the functional form

$$|v_z|_{osc} = C_{T32}(Wi_{Up} - Wi_{UpT32})^{1/2} \tag{5.3}$$

with fitted parameters $C_{T32} = 68.2$ [mm s^{-1}] and $Wi_{Up\ T32} = 0.0350$. $Wi_{Up\ T32}$ is the extrapolation of the fit to zero amplitude and is the predicted critical value for the onset of time-periodic flow. The error in the amplitude was of order 10% and is indicated by representative error bars in Fig. 5.12. Note from Fig. 5.12 that for $Wi_{Up} = 0.0352$ the flow is steady, hence eq. (5.3) slightly underpredicted the critical Wi_{Up} for instability onset. This discrepancy may be a consequence of error in the measurement. The temporal oscillations, the lack of hysteretic behavior, and the scaling of amplitude near instability onset as defined by eq. (5.3) are characteristic of a supercritical Hopf bifurcation (Strogatz, 1995).

For high volumetric rates corresponding to $Wi_{Up} \geq 0.0424$, pronounced secondary harmonic peaks are visible in the PS. The characteristic frequencies of the secondary peaks adjacent to the primary peak were consistent with doubled and halved harmonics of the

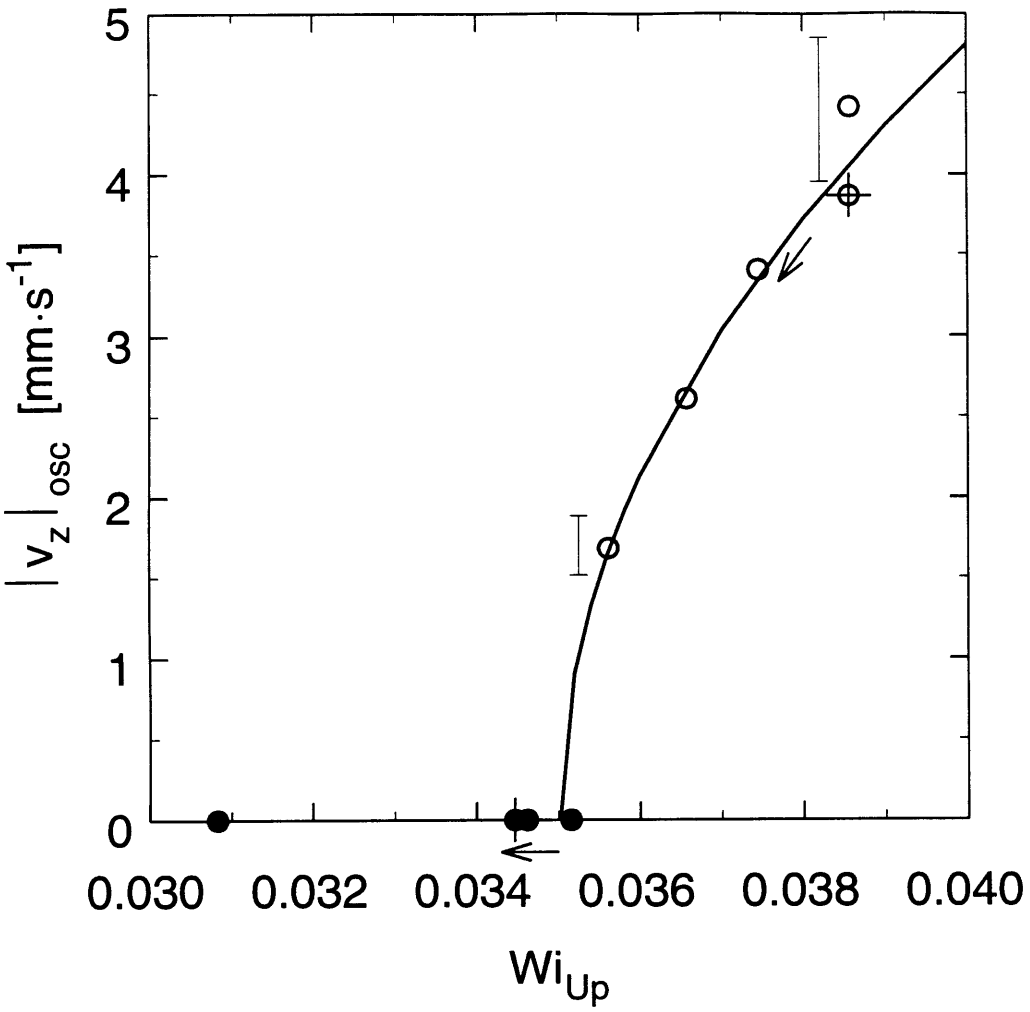

Figure 5.12 Amplitude of oscillation, $|v_z|_{osc}$, for time-dependent flow at the point χ =-21.0, υ =-1.50, ζ =-1.50 as a function of Wi_{Up} in the 32:1 contraction. Solid symbols indicate steady flow; hollow symbols denote time-dependent flow; (—), square-root-scaling fit to data near onset. Note that the fit slightly underpredicts the value of Wi_{Up} at onset of instability. (+) symbols and associated arrows indicate that in one of the runs the volumetric flow rate was decreased from Wi_{Up} = 0.0386 to Wi_{Up} = 0.0345; hysteresis was not observed. The order ±10% error associated with determination of the amplitude of oscillation is indicated by the two representative error bars.

fundamental frequency. However, the signal-to-noise ratio of the velocity data was too low to allow more detailed classification of the time-periodic flow in the nonlinear regime.

5.2.3 Local Evolution of Flow Near the Bounding Wall at $\chi = \pm 32$ in the 32:1 Contraction

A viscoelastic flow transition localized near the wall bounding the x-dimension was observed for flow through the 32:1 contraction. The spatial structure of this flow transition was characterized by operating the LDV system in the frequency-tracker mode. The measuring volume was scanned in the x-direction at a constant rate of $v_{x\ scan} = 1.43$ [mm s^{-1}] through the region of space corresponding to $-32 \leq \chi \leq 0$, $\zeta = -1.50$ for $\upsilon = -1.50$ and +1.50. The acquired set of velocity versus time data was then converted to velocity versus spatial position data. Confidence in the profile was improved by reproducing the measurements; a set of eight scans was used to develop a given profile.

The profile for $Wi_{Up} = 0.006$ is shown in Figs. 5.13a and 5.13b. In the middle section, $-24 \leq \chi \leq 0$, the flow appears uniform to within the accuracy of the measurement. For the scan with $\upsilon = -1.50$ (cf. Fig. 5.13a) the velocity is positive, fluid flows up toward the centerplane; for $\upsilon = +1.50$ (cf. Fig. 5.13b) the velocity is negative. The signal-to-noise ratio is low for these measurements because of the slow flow rate.

Near the wall, $-32 \leq \chi \leq -24$, the flow is nonuniform in the x-direction. In particular, the flows in Fig. 5.13a and Fig. 5.13b in the middle section ($-24 \leq \chi \leq 0$) are in opposite directions; however, the peak of the "spike", located at $\chi = -29$, is positive for both $\upsilon = -1.50$ and $\upsilon = +1.50$. The spike is not a measurement artifact. Four of the scans were performed with the measurement volume moving in the positive and four in the negative x-direction: the spike is not a transient resulting from finite response time of the tracker electronics. The length of the measurement volume in the x-direction was at most $L_m/h = 0.7$. Regions of high velocity gradient are prone to erroneous measurement; specifically, when the velocity changes substantially over the measuring volume, the tracker may be unable to lock onto a single frequency. However, the peak of the spike is located at $\chi = -29$, not immediately adjacent to the wall; examination of the output voltage data showed that tracker dropout was not the cause of the spike; and the reproducibility of the data indicated that the flow was accurately measured. Close examination of Fig. 5.13a also reveals a

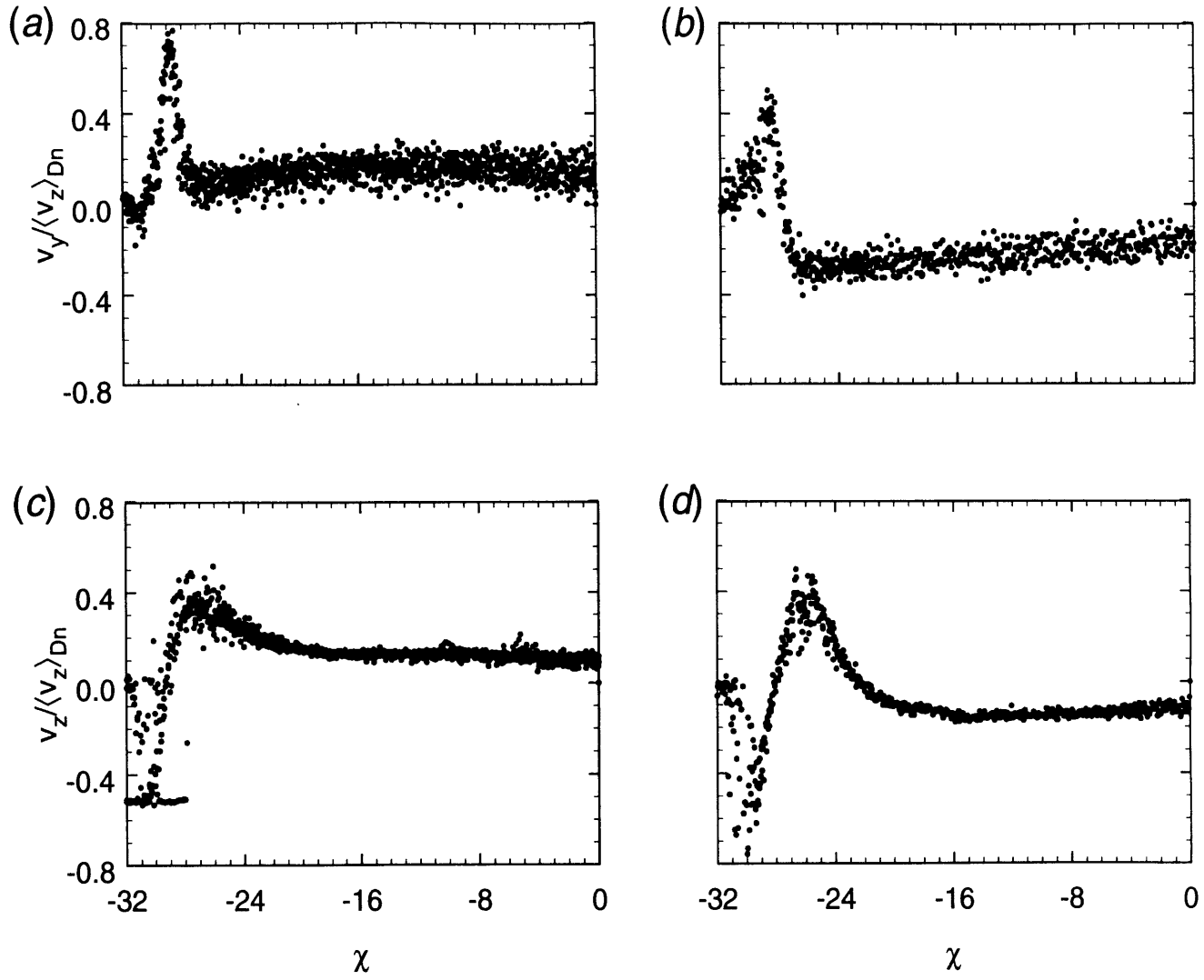

Figure 5.13 Dimensionless v_y vs. χ scan (ζ = -1.50) for flow through the 32:1 contraction: (a) Wi_{Up} = 0.006, υ = -1.50; (b) Wi_{Up} = 0.006, υ = +1.50; (c) Wi_{Up} = 0.031, υ = -1.50; (d) Wi_{Up} = 0.031, υ = +1.50.

small negative velocity in the region between the bounding wall and the positive spike, $-32 \leq \chi \leq -30.5$.

The velocity profile is illustrated in Figs. 5.13c and 5.13d along the x-direction for a higher flow rate corresponding to $Wi_{Up} = 0.031$. The flow is still steady, onset of time-dependent behavior occurred at $Wi_{Up\ T32} = 0.036$. As for the lower flow rate case shown in Figs. 5.13a and 5.13b, the velocity profile near the center of the flow ($-20 \leq \chi \leq 0$) is uniform and in opposite directions for $\upsilon = -1.50$ and $\upsilon = +1.50$. The nonuniform region of the profile has expanded to fill the range $-32 \leq \chi \leq -20$; both positive and negative values of v_y are apparent. Specifically, for the range $-32 \leq \chi \sim -28$ the velocity is negative on both sides of the centerplane, while for $-28 \sim \chi \leq -24$ the velocity is positive on both sides.

The velocity profiles given in Fig. 5.13a - 5.13d are consistent with the flow near the $\chi = -32$ wall having a vortex structure in the xy-plane. At the lower flow rate, $Wi_{Up} = 0.006$, the elliptic point of the vortex is located close to the wall, in the range $-32 \leq \chi \leq -30.5$ (Figs. 5.13a and 5.13b). At the higher flow rate the vortex has increased in size, with the elliptic point located within the region $-29.5 \leq \chi \leq -28$ (Figs. 5.13c and 5.13d). This vortex is a non-Newtonian phenomenon; a possible interpretation of its origin follows. At the low flow rate, $Wi_{Up} = 0.006$, the phenomenon is probably purely local, in extent as well as origin; note that the extent of the vortex is on the order of the downstream length scale, h, not the upstream length scale, H = 32h.

In the vicinity of the downstream slit the fluid near the wall at $\chi = \pm 32$ experiences a higher shear rate than fluid at other locations in the x-direction with the same υ- and ζ-values because of the additional no-slip boundary. This higher shear rate results in onset of an instability which is localized near the wall. At the elevated flow rate (Figs. 5.13c and 5.13d), there may be an interaction of global flow conditions with this local instability. As is discussed in detail in §5.3, when wall effects are negligible and two-dimensional flow is closely approximated throughout the geometry, the length scale of the spatial instability is set by the upstream half-height, H. However, for the 32:1 contraction ratio, the width of the geometry, i.e., the x-dimension, is only W = 2H. Therefore, the increased extent of the vortex at the elevated flow rate, $Wi_{Up} = 0.031$, may result from expansion of the local vortex near the wall, or could be a manifestation of the global spatial instability observed for

the 2:1 and 8:1 contractions but which is modified in structure by the presence of the bounding walls located at $x = \pm 32h = \pm H$.

The objective of this Chapter is to elucidate the global phenomena in the planar contraction flow; the local, side-wall-induced flow transition is a peripheral topic. In the case of the 2:1 and 8:1 contraction ratios, the upstream aspect ratio is sufficiently high ($W/2H = 16$ and 4 respectively), that the presence of a bounding wall at the extremes of the x-direction can be treated as a local imperfection to the two-dimensional base flow and to flow transitions at elevated Wi_{Up}. However, for the 32:1 contraction the upstream aspect ratio is unity; consequently, the walls bounding the x-direction affect the flow structure and the transition sequence throughout the upstream channel. The local instability near the bounding walls at $\chi = \pm 32$ noted in the 32:1 contraction may occur in the 2:1 and 8:1 contractions. Although effects of a local flow transition near the wall on the global flow field are not directly apparent, upon onset of global time-dependent flow, the local flow transition may act as a perturbation which sets the direction of movement of the vortices, from the bounding walls, $\chi = \pm 32$, toward the center of the flow, $\chi = 0$. Note that the effect of a wall bounding a "neutral" third dimension in an otherwise two-dimensional geometry has been studied by other researchers in the context of Newtonian flow. For example, Aidun *et al.* (1991) considered flow in a lid-driven cavity bounded in the "neutral" direction, and Tavener and Cliffe (1991) investigated the Taylor instability in a Couette cell with finite axial length to gap width ratio.

5.2.4 Quantitative Characterization of Centerline Velocity Profile Evolution

The LDV system was operated using burst analysis to measure the centerline velocity profile at several flow rates for the 2:1, 8:1, and 32:1 contractions. The global transitions to three-dimensional, steady flow described above appear to be associated with changes in the centerline profile. Upstream of the contraction plane, a decrease in the centerline velocity below that of fully developed upstream channel flow was noted at elevated Wi_{Up}. Closer to the contraction plane, in the entry flow region, an increase in the local elongational strain rate was found.

Centerline Velocity Profile Evolution in the 2:1 Contraction

The magnitude of the v_z velocity component along the centerline in the middle of the flow was measured for the 2:1 contraction; specifically, scans were performed over the range $\chi = 0$, $\upsilon = 0$, and $-40 \leq \zeta \leq 12$. The velocity data as a function of position, $v_z(z)$, was fit with a cubic spline; the fit was differentiated to obtain the strain-rate profile as a function of position, $\dot{\varepsilon}(z) = \partial v_z/\partial z$. The maximum dimensionless strain rate, $\dot{\varepsilon}_{max}(h/\langle v_z \rangle_{Dn})$, was used to quantify the sharpness of the peak in the centerline strain-rate profile. The base profile associated with low Wi_{Up} is presented first; salient features of the profile at elevated Wi_{Up}, after flow rearrangement, are then described.

The magnitude of v_z along the centerline at $Wi_{Up} = 0.37$ is shown in Fig. 5.14a. Far upstream of the contraction plane ($\zeta \lesssim -8$) the profile in the y-direction is parabolic because the fluid has nearly constant viscosity. Hence, the velocity along the centerline made dimensionless with the downstream mean velocity is approximately $v_z/\langle v_z \rangle_{Dn} \simeq (3/2)(h/H)$. When a fluid element approaches to within two downstream half-heights of the contraction plane ($\zeta > -2$) it suddenly accelerates to the downstream fully developed centerline velocity, $v_z \simeq (3/2)\langle v_z \rangle_{Dn}$. The dimensionless strain rate, $\frac{\partial v_z}{\partial z}\left(\frac{h}{\langle v_z \rangle_{Dn}}\right)$, is shown in Fig. 5.14b as a function of axial position. The acceleration of the fluid occurs over the range $-2 \leq \zeta \leq 1.5$. The maximum dimensionless strain rate of 0.57 is observed at a position $\zeta = -0.31$, immediately upstream of the contraction plane. Note that the oscillations in Fig. 5.14b for $\zeta < -3$ and $\zeta > 2$ are an artifact of the differentiation procedure, which acts to aggravate the noise in the velocity measurement; the oscillations have no physical significance.

At an elevated flow rate corresponding to $Wi_{Up} = 1.20$ the centerline velocity profile shows evidence of the diverging flow noted in the visualization study described in §5.2.1. Fig. 5.14c shows that the fluid initially *decelerates* from the fully developed upstream velocity and then *accelerates* in the vicinity of the contraction plane. Another contrast with the centerline velocity profile for low Wi_{Up} is that a pronounced velocity overshoot is observed immediately downstream of the contraction plane. The centerline strain-rate profile for the $Wi_{Up} = 1.20$ flow is shown in Fig. 5.14d. Diverging flow is evident as a region of negative strain rate over the range $-6 \leq \zeta \leq -2$; the minimum centerline velocity occurs

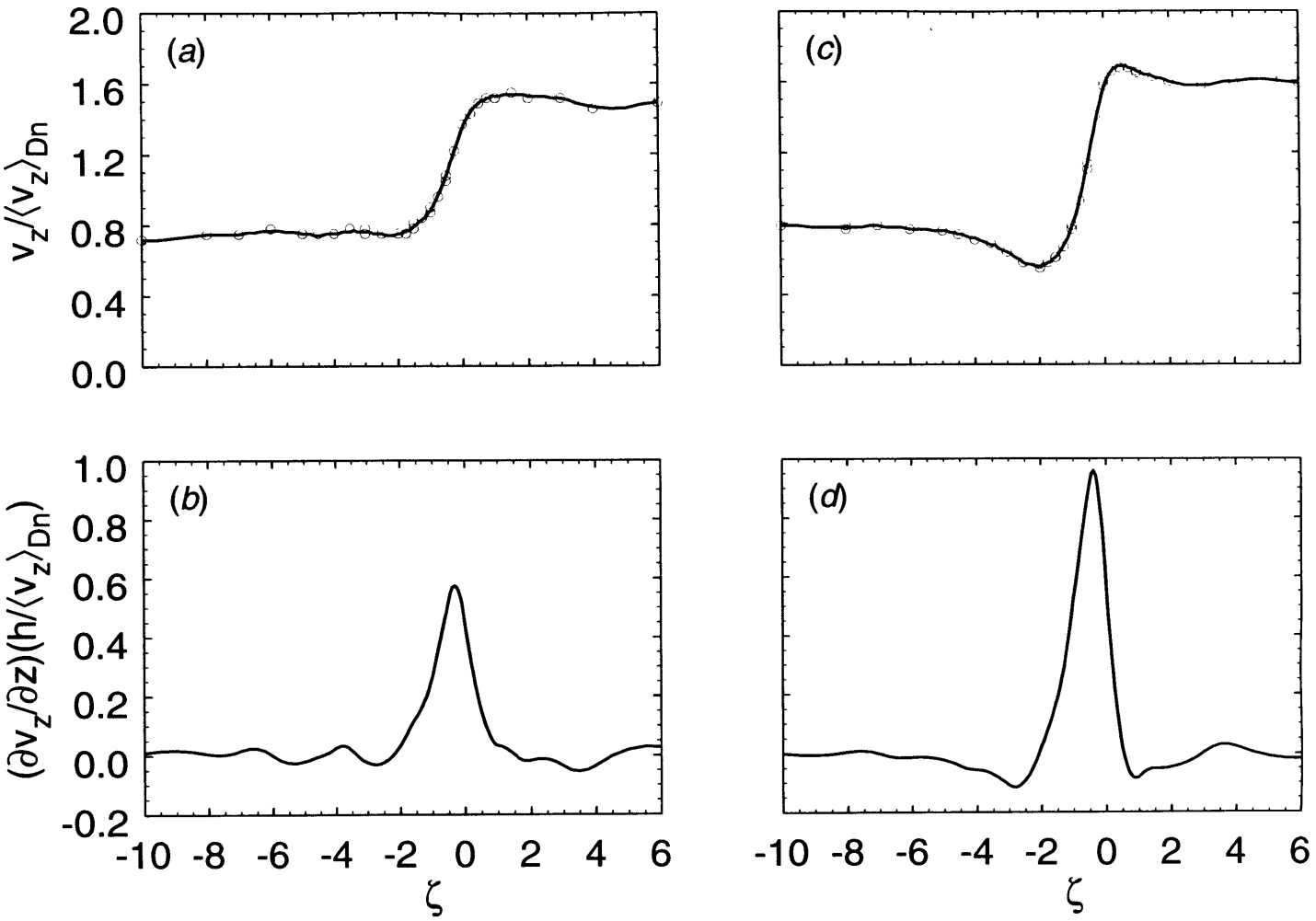

Figure 5.14 Centerline ($\upsilon = 0$) velocity and elongational strain-rate profiles for 2:1 contraction flow: (a) Dimensionless v_z vs. ζ, $Wi_{Up} = 0.37$; (b) Dimensionless $\dot{\varepsilon}$ vs. ζ, $Wi_{Up} = 0.37$; (c) Dimensionless v_z vs. ζ, $Wi_{Up} = 1.20$; (d) Dimensionless $\dot{\varepsilon}$ vs. ζ, $Wi_{Up} = 1.20$. (○) velocity data; (——) cubic spline fit.

at the position $\zeta = -2.1$. The acceleration of the fluid into the downstream region is apparent as the peak occupying the range $-2 < \zeta \leq 0.5$; the maximum dimensionless strain rate of 0.96 occurs at an axial position of $\zeta = -0.4$. The velocity overshoot appears as a region of negative strain rate located downstream of the contraction plane and extends over the range $0.5 < \zeta \leq 3$.

The maximum dimensionless strain rate achieved for the high Wi_{Up} flow is substantially greater than for the flow with low Wi_{Up}; this is attributable to two factors. Firstly, the difference between the minimum upstream and maximum downstream dimensionless velocity is greater for the high Wi_{Up} flow because of the phenomena of diverging flow and velocity overshoot. Secondly, the region over which the fluid accelerates from the upstream into the downstream slit decreases slightly in extent, from $-2 \leq \zeta \leq 1.5$ for the case with $Wi_{Up} = 0.37$ to $-2 \leq \zeta \leq 0.5$ for $Wi_{Up} = 1.20$. Recall that this flow rearrangement is related to the "elastic" nature of the flow since the Reynolds number is low, $Re_{Dn} < 7 \times 10^{-4}$.

Centerline Velocity Profile Evolution in 8:1 and 32:1 Contractions

The centerline velocity profile for flow through the 8:1 contraction at $Wi_{Up} = 0.070$ is shown in Fig. 5.15a; the corresponding centerline strain-rate profile is shown in Fig. 5.15b. The strain-rate profile appears qualitatively similar to the plot for the 2:1 contraction in Fig. 5.14b; however, in the 8:1 contraction the region over which the flow accelerates from the upstream into the downstream slit is greater in spatial extent, $-10 \lesssim \zeta \lesssim 1$. In contrast with the 2:1 contraction flow, the strain-rate profile is composed of two distinct regions: high strain rate, for which $\partial v_z/\partial z \geq 0.1$, is noted in the region $-3 < \zeta \lesssim 1$; a low strain-rate upstream "tail", for which $\partial v_z/\partial z < 0.1$, is found in the region $-10 \lesssim \zeta \lesssim -3$.

The velocity profile for flow with an elevated $Wi_{Up} = 0.169$ is shown in Fig. 5.15c; the characteristics of diverging flow and velocity overshoot described for the higher Wi_{Up} case in the 2:1 contraction are apparent. The corresponding centerline strain-rate profile for $Wi_{Up} = 0.169$ in the 8:1 contraction is shown in Fig. 5.15d. The diverging flow region is in the range $-20 < \zeta < -5.5$; the minimum velocity is observed at $\zeta = -5.5$. Acceleration of the fluid extends over the range $-5.5 < \zeta \lesssim 0.5$; there is a region of high strain rate restricted to the range $-2 \leq \zeta < 0$; the maximum strain rate of 0.98 is located at $\zeta = -0.42$.

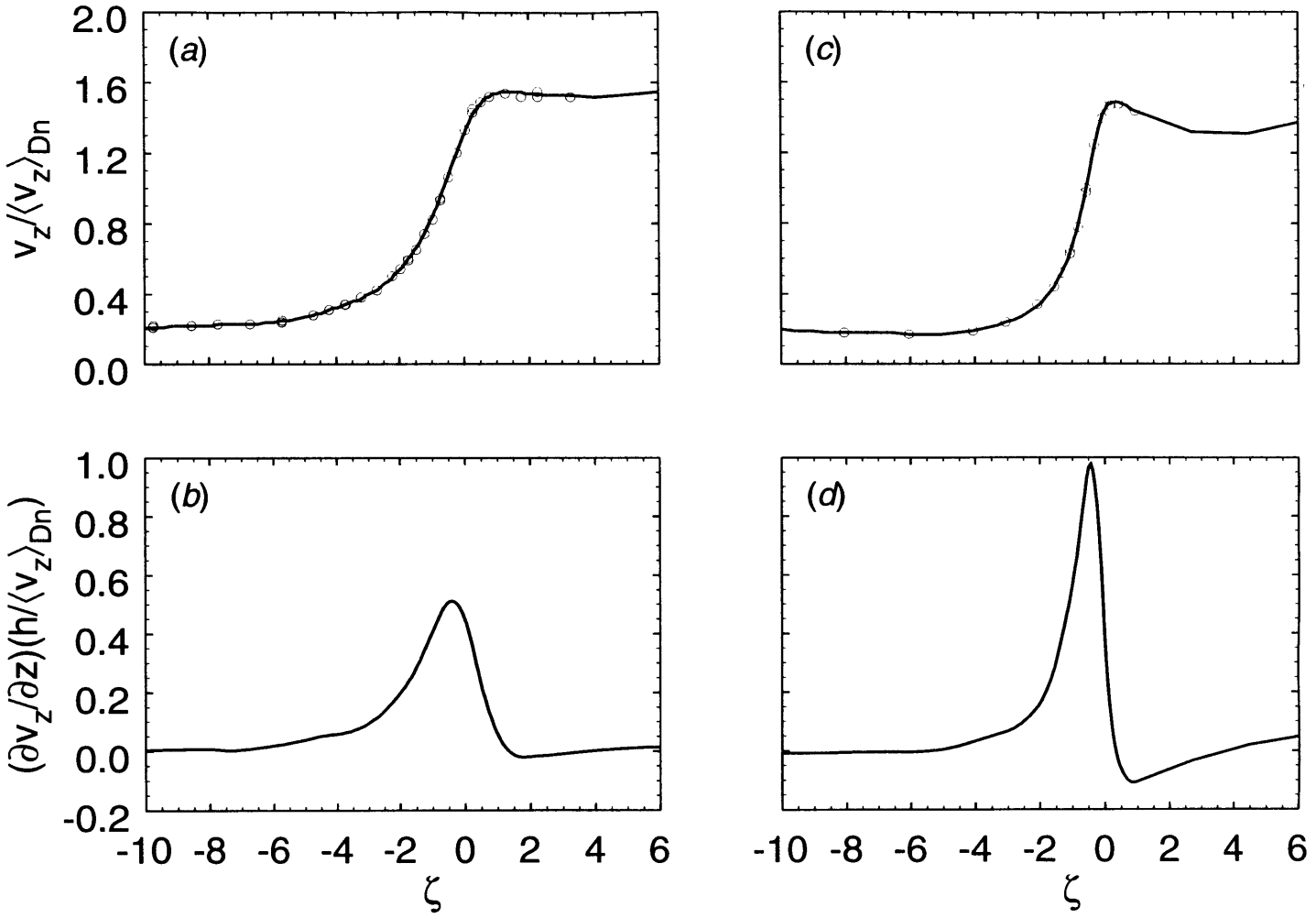

Figure 5.15 Centerline ($\upsilon = 0$) velocity and elongational strain-rate profiles for 8:1 contraction flow: (a) Dimensionless v_z vs. ζ, $Wi_{Up} = 0.070$; (b) Dimensionless $\dot{\varepsilon}$ vs. ζ, $Wi_{Up} = 0.070$; (c) Dimensionless v_z vs. ζ, $Wi_{Up} = 0.169$; (d) Dimensionless $\dot{\varepsilon}$ vs. ζ, $Wi_{Up} = 0.169$. (○) velocity data; (——) cubic spline fit.

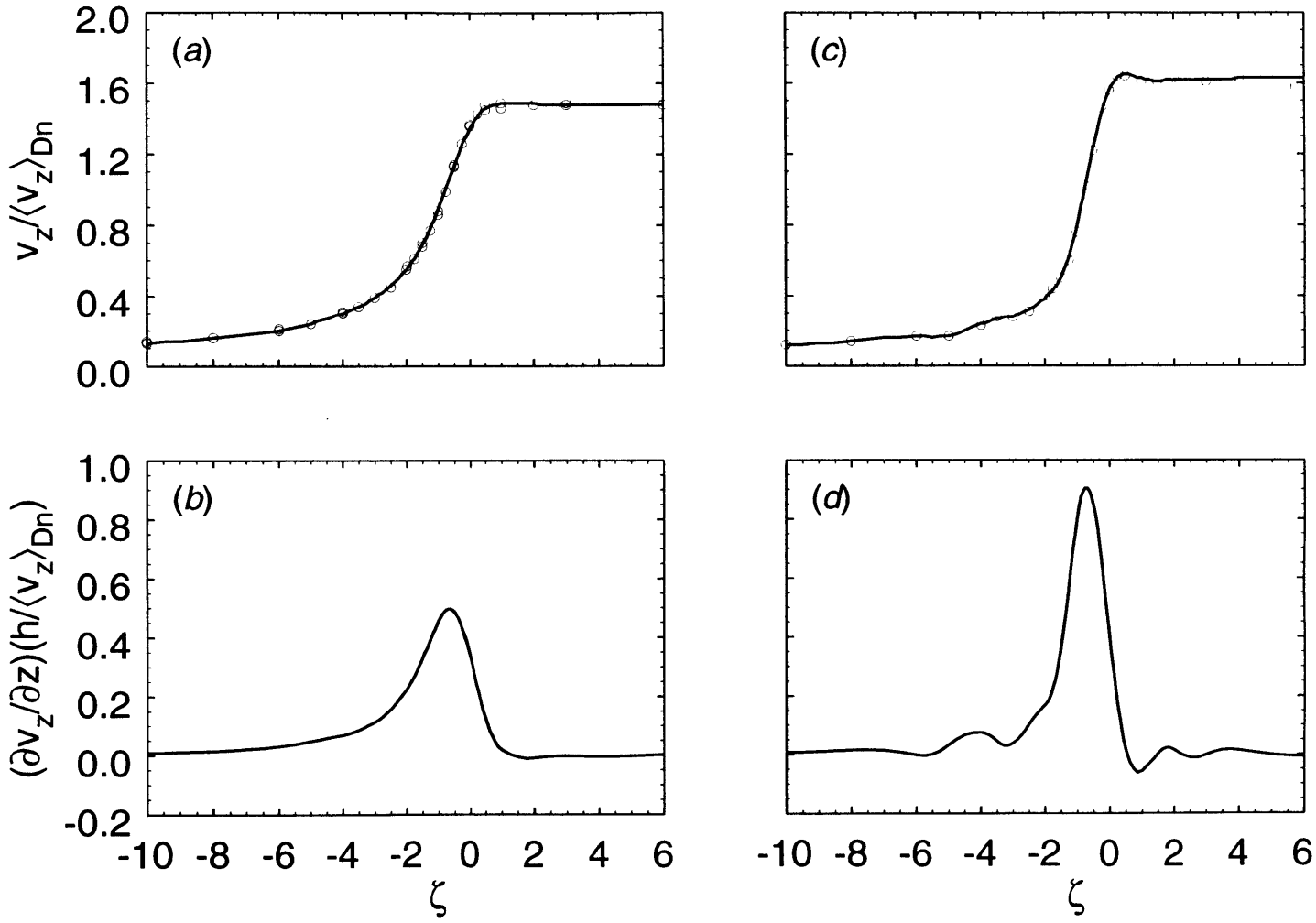

Figure 5.16 Centerline ($\upsilon = 0$) velocity and elongational strain-rate profiles for 32:1 contraction flow: (a) Dimensionless v_z vs. ζ, $Wi_{Up} = 0.0108$; (b) Dimensionless $\dot{\varepsilon}$ vs. ζ, $Wi_{Up} = 0.0108$; (c) Dimensionless v_z vs. ζ, $Wi_{Up} = 0.038$; (d) Dimensionless $\dot{\varepsilon}$ vs. ζ, $Wi_{Up} = 0.038$. (○) velocity data; (——) cubic spline fit.

There are not sufficient data points in the downstream region to define precisely the spatial extent of the velocity overshoot; however, it extends at least over the range $0.5 < \zeta \lesssim 1$.

The velocity profile is shown in Fig. 5.16a for flow through the 32:1 contraction at $Wi_{Up} = 0.0108$; the strain-rate profile is shown in Fig. 5.16b. In a similar manner as for the 8:1 contraction flow, a sharp peak corresponding to a region of high strain rate is evident over the range $-3 < \zeta \leq 1$, while a long, low strain-rate upstream "tail" extends over the range $-40 \lesssim \zeta \lesssim -3$. The precise distance which this tail extended upstream could not be determined since the region probed by LDV was restricted to $\zeta \geq -40$.

The velocity profile for flow through the 32:1 contraction at an elevated volumetric rate corresponding to $Wi_{Up} = 0.038$ is shown in Fig. 5.16c. An upstream region of diverging flow is not evident, this is addressed below. A region of velocity overshoot immediately downstream of the contraction plane may be present although noise in the data obscures its magnitude and extent. The corresponding centerline strain-rate profile is shown in Fig. 5.16d. The fluid accelerates over a range extending from far upstream to immediately downstream of the contraction plane, $-40 \lesssim \zeta \lesssim 0.5$. The region of greatest strain rate is restricted to the range $-2 \lesssim \zeta \leq 0.25$; the maximum dimensionless strain rate of 0.90 occurs at an axial position of $\zeta = -0.75$. The distinction between the high strain-rate region and low strain-rate "tail" is clearer in the case of the high Wi_{Up}. Furthermore in Fig. 5.16a the velocity profile appears smooth throughout the upstream region; in contrast, "kinks" in the velocity profile are evident in Fig. 5.16c in the region $-5 \lesssim \zeta \lesssim -2.5$, which lies between the low strain-rate "tail" and the high strain-rate region.

Summary of Evolution of Centerline Velocity Profile

In summary, the centerline profiles for the flows through the different contraction ratios appear to exhibit a common set of qualitative features. At low Wi_{Up}, there are two distinct regions of positive strain rate through which a fluid element on the centerline passes when accelerating from the slit upstream of the contraction plane to the slit downstream of the contraction plane. A low strain-rate upstream "tail" is evident in the profiles for the 32:1 and 8:1 contractions (Figs. 5.16b and 5.15b). The upstream extent of the tail appears to be set by the upstream half-height, $\zeta \sim H/h$ (although the restriction on LDV measurement to $\zeta \geq -40$ did not allow identification of the precise extent in the 32:1 con-

traction). At the location $\zeta \approx -3$, upstream of the contraction plane, the tail region adjoins a high strain-rate "peak". The location of the transition between the low strain-rate tail and high strain-rate peak appears to be set by the downstream half-height, h. The downstream limit of this high strain-rate peak is located at $\zeta \simeq 0.5$ and also seems to be set by the downstream half-height, h.

The existence of two distinct regions, one a long, low strain-rate upstream tail, the other a high strain-rate peak can be explained as follows. On the centerline and near the contraction plane, the flow field is governed primarily by the downstream slit; the region of high strain rate, the extent of which is set by the downstream half-height, is characteristic of this entry flow field. Stated another way, the flow near the slit does not "see" the upstream boundary conditions. Following this reasoning, a limiting profile is expected near the contraction plane for the case of an infinite contraction ratio (sink flow). However, for a flow with a finite contraction ratio, the upstream half-height, H, must play *some* role in determining the strain-rate profile. Specifically, the net Hencky strain experienced by a fluid element traveling along the centerline from the upstream to the downstream regions is set by the ratio of centerline velocities of the fully developed flows.

$$\varepsilon_{Hencky} = \ln\left(\frac{v_z(\upsilon = 0)_{Dn}}{v_z(\upsilon = 0)_{Up}}\right) \tag{5.4}$$

At a sufficient distance upstream of the contraction plane, the flow will "see" the upstream boundary conditions. Hence the upstream boundary conditions set the profile for the low strain-rate upstream tail, the spatial extent of which scales with the upstream half-height, H. A distinct transition between the upstream "tail" and downstream "peak" is not noted for the case of the 2:1 contraction, probably because the upstream and downstream half-heights are sufficiently similar that the two regions overlap.

A common set of flow phenomena also is noted for the flows through the different contractions at elevated Wi_{Up}. Specifically, in contrast with the flows for low Wi_{Up}, there is an increase in the maximum strain rate attained and a velocity overshoot is observed immediately downstream of the contraction plane. The spatial extent of the velocity overshoot in the downstream region is governed by the downstream half-height, h. This scal-

ing is probably a result of the strain rate in the vicinity of the downstream slit being much higher than that in the low strain-rate upstream tail; the fluid only "remembers" flow conditions near the downstream slit.

At elevated flow rates, diverging flow was noted upstream of the contraction plane for the 2:1 and 8:1 contractions. The point of minimum centerline velocity occurred for the 2:1 and 8:1 contractions at the boundary between the diverging flow ($\partial v_z/\partial z < 0$) and accelerating flow ($\partial v_z/\partial z > 0$) regimes. The location of this minimum velocity point appeared to scale with the upstream half-height, H. Specifically, for the 2:1 contraction, the minimum was at ζ = -2.1; for the 8:1 contraction, at ζ = -5.5. No diverging flow was noted for the 32:1 contraction; however, since the farthest point upstream which could be probed was located at ζ = -40, this observation is consistent with a scaling with the upstream half-height, H = 32h. For the case of the 8:1 contraction, after onset of diverging flow, the long upstream tail of low, positive strain rate did not extend as far upstream, reaching only to ζ = -5.5 instead of $\zeta \sim -10$; a limited number of data points prevents precise delineation of this change in extent.

The transition from a "moderately peaked" to a "sharply peaked" strain-rate profile occurs in a continuous manner over an intermediate range of Wi_{Up}. The maximum dimensionless strain rate, $\dot{\varepsilon}_{max}\left(\frac{h}{\langle v_z\rangle_{Dn}}\right)$, is shown as a function of Wi_{Up} in Fig. 5.17a for each of the contraction ratios investigated. A square-root function of the form

$$\dot{\varepsilon}_{max}(Wi_{Up})\left(\frac{h}{\langle v_z\rangle_{Dn}}\right) - \dot{\varepsilon}_{max0}\left(\frac{h}{\langle v_z\rangle_{Dn}}\right) = C\sqrt{Wi_{Up} - Wi_{Up,\,crit}} \qquad (5.5)$$

was fit to each data set associated with a given contraction ratio. Wi_{Up} is the independent variable, and $\dot{\varepsilon}_{max0}\left(\frac{h}{\langle v_z\rangle_{Dn}}\right)$ is the maximum dimensionless centerline strain rate in the limit of $Wi \to 0$, as inferred from the data. C and $Wi_{Up,crit}$ are the fitted parameters. These square-root fits are intended to act primarily as a guide to the eye. The data are consistent with a supercritical bifurcation at Wi_{Crit}; however, there are not sufficient data points for the bifurcation to be definitively classified. Two regions are apparent for the data associated with a given contraction ratio in Fig. 5.17a. At low Wi_{Up}, corresponding to the profiles shown in Plots a and b of Figs. 5.14 through 5.16, the maximum dimension-

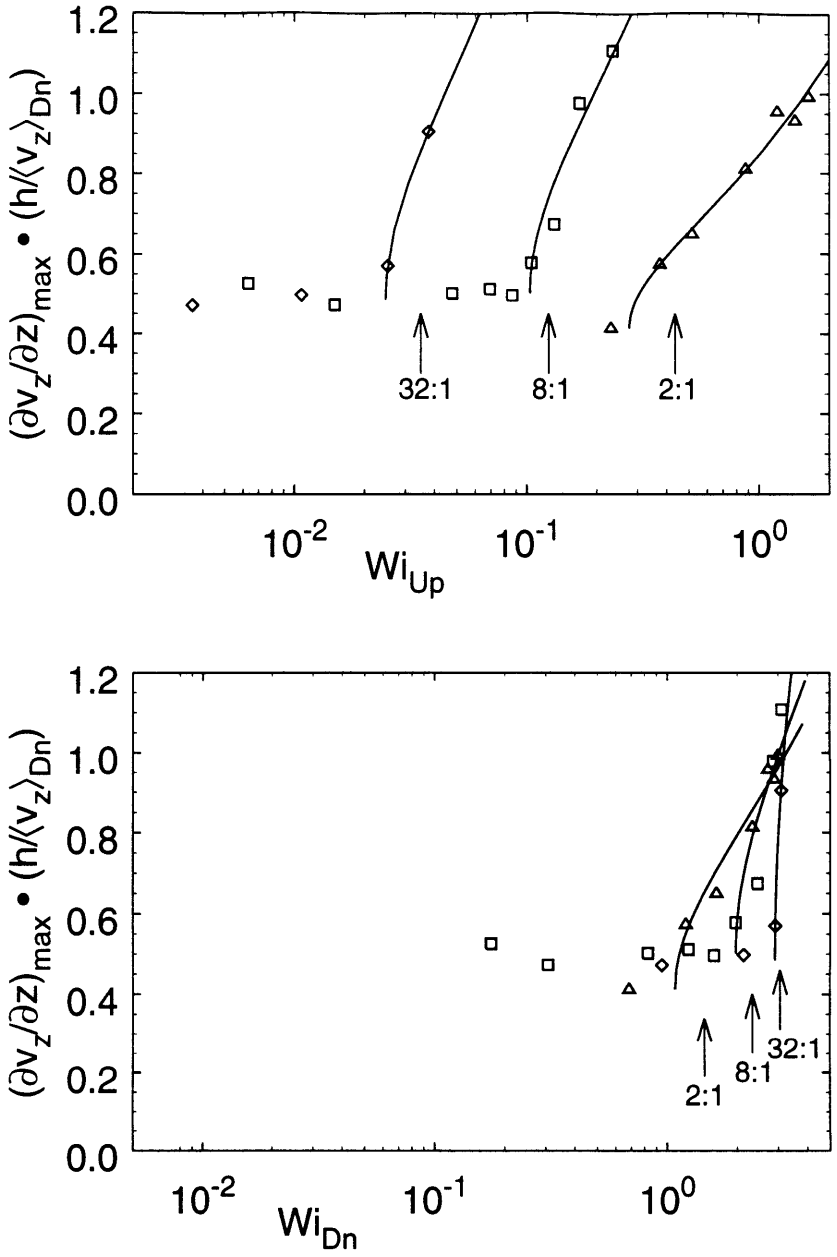

Figure 5.17 Maximum centerline dimensionless strain rate vs. Weissenberg number: (△) 2:1 contraction; (□) 8:1 contraction; (◇) 32:1 contraction. The lines are square-root fits to the data, the lower terminus of the line is the predicted onset point for the increase in dimensionless strain rate with Wi; the arrows indicate the Wi for which transition from global, two-dimensional base flow to three-dimensional flow occurs. (a) domain is Weissenberg number defined in terms of upstream flow parameters, Wi_{Up}; (b) domain is Weissenberg number defined in terms of down-stream flow parameters, Wi_{Dn}.

less strain rate is nearly independent of Wi_{Up}; this independence is evident in Fig. 5.17a for $Wi_{Up} < 0.1$, for the case of the 8:1 contraction flow, and for $Wi_{Up} < 0.02$, for the case of the 32:1 contraction flow. More generally, at low Wi_{Up} the dimensionless velocity profile is independent of the flow rate. At elevated Wi_{Up}, corresponding to the profiles shown in Plots c and d of Figs. 5.14 through 5.16, the maximum dimensionless strain rate is observed to increase with Wi_{Up}; this dependence is apparent in Fig. 5.17a for $0.4 < Wi_{Up}$ for the case of the 2:1 contraction, $0.1 < Wi_{Up}$ for the 8:1 contraction, and $Wi_{Up} < 0.02$ for the 32:1 contraction. Upstream diverging flow and downstream velocity overshoot are noted in the velocity profile for elevated volumetric flow rates; these phenomena result in the increase in maximum dimensionless strain rate. As discussed in the beginning of this Chapter, when the Weissenberg number is defined in terms of the upstream flow parameters, the critical value for transitions can be substantially less than one. This reflects the dependence of the flow rearrangement on contraction ratio as well as on Wi_{Up}.

Figure 5.17b shows the maximum dimensionless shear rate as a function of the Weissenberg number defined in terms of the mean *downstream* shear rate; i.e. $Wi_{Dn} = Wi(\langle v_z \rangle_{Dn}/h)$.[4] Note that when Wi_{Dn} is used, the critical parameters for onset of diverging flow differ by only a factor of 3 between H/h = 2 and H/h = 32, as opposed to the corresponding $Wi_{Up,crit}$, used in Fig. 5.17a, which differ by a factor of 20. However, distinct superposition of the curves in Fig. 5.17b is not observed. This is attributed to the role which the contraction ratio plays in governing the flow rearrangement; neither Wi_{Dn} nor Wi_{Up} alone fully describe the conditions for transition to diverging flow.

To decide whether Wi_{Up} or Wi_{Dn} is the more appropriate parameter to use, it is helpful to consider the critical Weissenberg number for flow rearrangement expected in the limits of $H/h \to 1$ (channel flow) and $H/h \to \infty$ (sink flow). For the sink-flow limit, it is expected that $Wi_{Dn,crit}$ is a non-zero, finite value. Specifically as $H/h \to \infty$, the upstream walls have less and less effect on what occurs in the vicinity of the downstream slit. In contrast, $Wi_{Up,crit}$ will continuously decrease and approach zero. In the channel-flow limit, it necessarily follows that $\lim_{H/h \to 1} Wi_{Up,\,crit} = Wi_{Dn,\,crit}$. In a channel, rearrangement to diverging flow is never observed; two scenarios may be envisioned as occurring as the

4. Note that the Weissenberg number defined in terms of downstream shear rate is used throughout Chapter 6 and is defined in eq. 6.2.

lower limit is approached. 1) The critical Weissenberg number may continuously approach infinity as the contraction ratio approaches one. In this case $Wi_{Up,crit}$ will monotonically increase with H/h, whereas $Wi_{Dn,crit}$ will first decrease (as shown in Fig. 5.17b) and then increase. 2) The critical Weissenberg number will approach a finite limit as $H/h \rightarrow 1$. $Wi_{Up,crit}$ will continuously increase, and Wi_{Dn} continuously decrease to the limit as channel flow is approached. By consideration of the critical values shown in Figs. 5.17a and 5.17b, this limiting value (should Scenario 2 apply) can be bounded as $\lim_{H/h \rightarrow 1} 0.3 < Wi_{Up,\,crit} = Wi_{Dn,\,crit} < 1.1$. Note, however, that when the limit H/h = 1 is reached, the solution will vanish since diverging flow does not occur in channel flow. Hence, as the contraction ratio increase from the channel- to the sink-flow limit, $Wi_{Up,crit}$ will monotonically decrease, regardless of whether Scenario 1 or Scenario 2 applies. This decrease reflects the importance of both nonlinear elastic effects (as parameterized by Wi_{Up}) and the imposed boundary conditions (as parameterized by H/h) in determining rearrangement to diverging flow; i.e. diverging flow is not noted in a channel of H/h = 1. In contrast, $Wi_{Dn,crit}$ *increases* with contraction ratio, at least over a certain range of H/h. Furthermore, $Wi_{Dn,crit}$ will not necessarily exhibit a monotonic dependence on H/h. These considerations supported the use of the Weissenberg number defined in terms of upstream flow conditions, Wi_{Up}, throughout this Chapter. A more detailed interpretation of the origin of the diverging flow phenomenon is given in §5.3.4.

5.3 Interpretation of Results

In §5.2, qualitative flow visualization studies and quantitative LDV measurements, used to characterize the evolution of the flow field with increasing Wi_{Up} for a set of planar contraction geometries, were described. These results are used in §5.3.1 to develop a unified picture of velocity field transitions in viscoelastic planar contraction flow which is presented in the form of a transition map. Characteristic length and time scales of flow structures after the transitions are identified and related to dimensions of the geometry in §5.3.2. The "viscoelastic Görtler" scaling described in Chapter 2 is used in §5.3.3 to understand the onset of instability in planar contraction flow in terms of the interaction of elastic stresses oriented in the streamwise direction with streamline curvature. Finally, a

correlation between the onset of diverging flow and global, spatial flow transition is noted in §5.3.4.

5.3.1 Flow Transition Map

The series of ordered flow transitions noted as Wi_{Up} was increased for a given contraction ratio are summarized in the transition map shown in Fig. 5.18a. The contraction ratio for a given set of measurements is plotted as the abscissa; the critical upstream Weissenberg number for a given transition, $Wi_{Up\ crit}$, is plotted as the ordinate.[5] The 2:1 and 8:1 contractions exhibit a common transition sequence: two-dimensional rearrangement to diverging flow, transition from two-dimensional to three-dimensional and steady flow, and onset of time-dependent flow.

Transitions in the 2:1 and 8:1 Contractions

For contraction ratios of H/h = 2 and 8 the flow is two-dimensional and steady at low Wi_{Up}. As Wi_{Up} is increased above a critical value, there is a change in the centerline velocity profile; diverging flow upstream of the contraction plane and velocity overshoot downstream of the contraction plane occur with an associated increase in the maximum dimensionless centerline strain rate. As the flow rate is increased yet further, a supercritical bifurcation to three-dimensional and steady flow throughout the upstream region is observed for the 2:1 and 8:1 contractions. For the case of the 2:1 contraction, wavenumber-doubling behavior was detected at yet higher values of Wi_{Up}.

The next transition observed with increasing volumetric rate was a bifurcation to time-dependent flow. As discussed in §5.2.2 the amplitude of the temporal oscillation of v_z grew continuously and monotonically with Wi_{Up}, consistent with the scaling of a supercritical Hopf bifurcation. Transition via supercritical Hopf bifurcation implies that the

5. Error bars are indicated for the experimentally determined critical Weissenberg numbers (Wi) for the transition to three-dimensional flow and for the transition to time-dependent flow in Figs. 5.18a and 5.18b (and in the subsequent Figs. 5.19a and 5.19b). The lower bound on the error bars indicates the Wi at which the base state (two-dimensional or steady flow) was definitively observed; the upper bound indicates the Wi at which the state to which transition is made (three-dimensional or time-dependent flow) was definitively observed. The critical Wi predicted by the square-root fit (cf. §5.2) is used for the symbol denoting onset of the instability when the value lies between the bounds of the error bars. In cases where the square-root fit underpredicts the critical Wi, the average of the bounds of the error bars is used for the symbol.

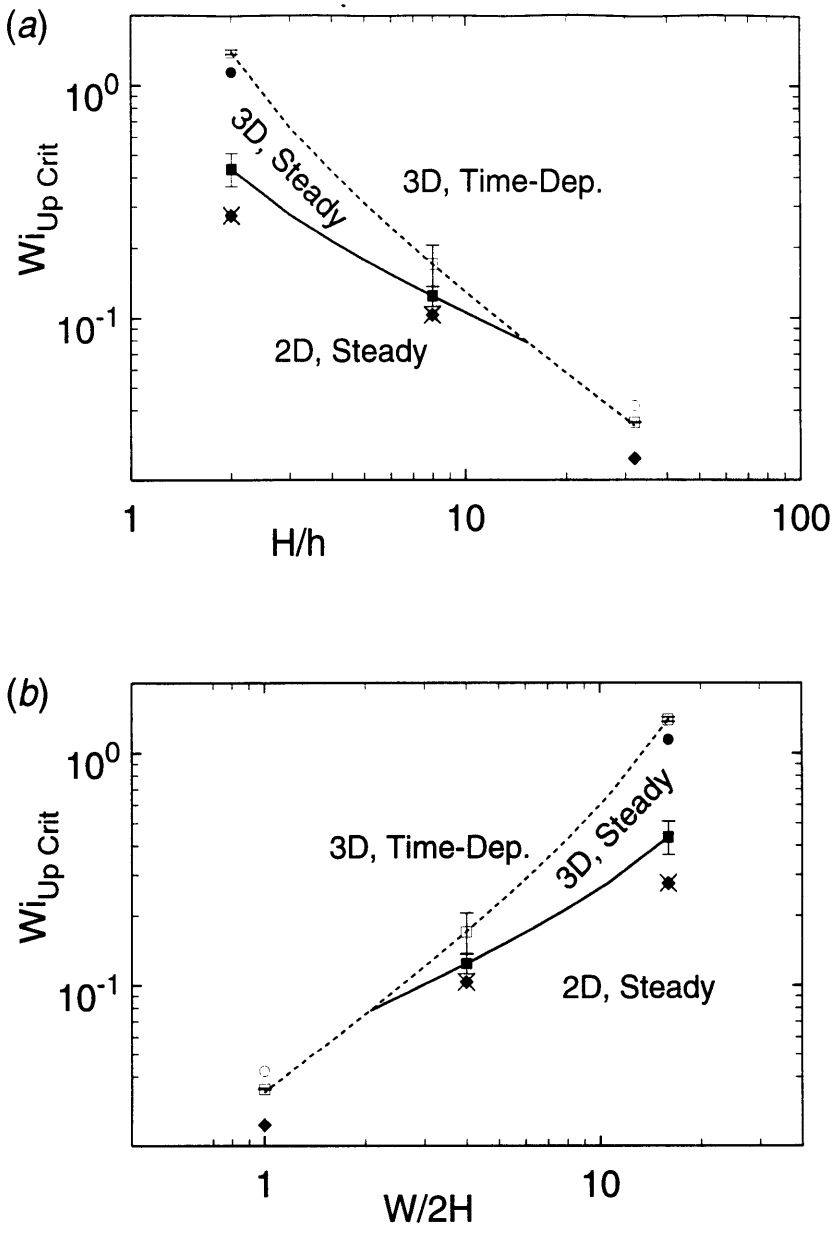

Figure 5.18 Maps of transitions observed in viscoelastic planar contraction flow: (a) critical Wi_{Up} vs. contraction ratio, H/h; (b) critical Wi_{Up} vs. upstream aspect ratio, W/2H. Experimentally observed transitions are denoted: (◆), onset of increase in maximum dimensionless centerline strain rate with Wi_{Up}; (×) diverging flow; (■), transition from two-dimensional, steady base flow to three-dimensional, steady flow; (□), transition from steady to time-dependent flow; (●), secondary spatial harmonics; (○) secondary spatio-temporal harmonics. Fits are denoted: (——), transition from two-dimensional, steady base flow to three-dimensional, steady flow; (- — -), transition from steady to time-dependent flow.

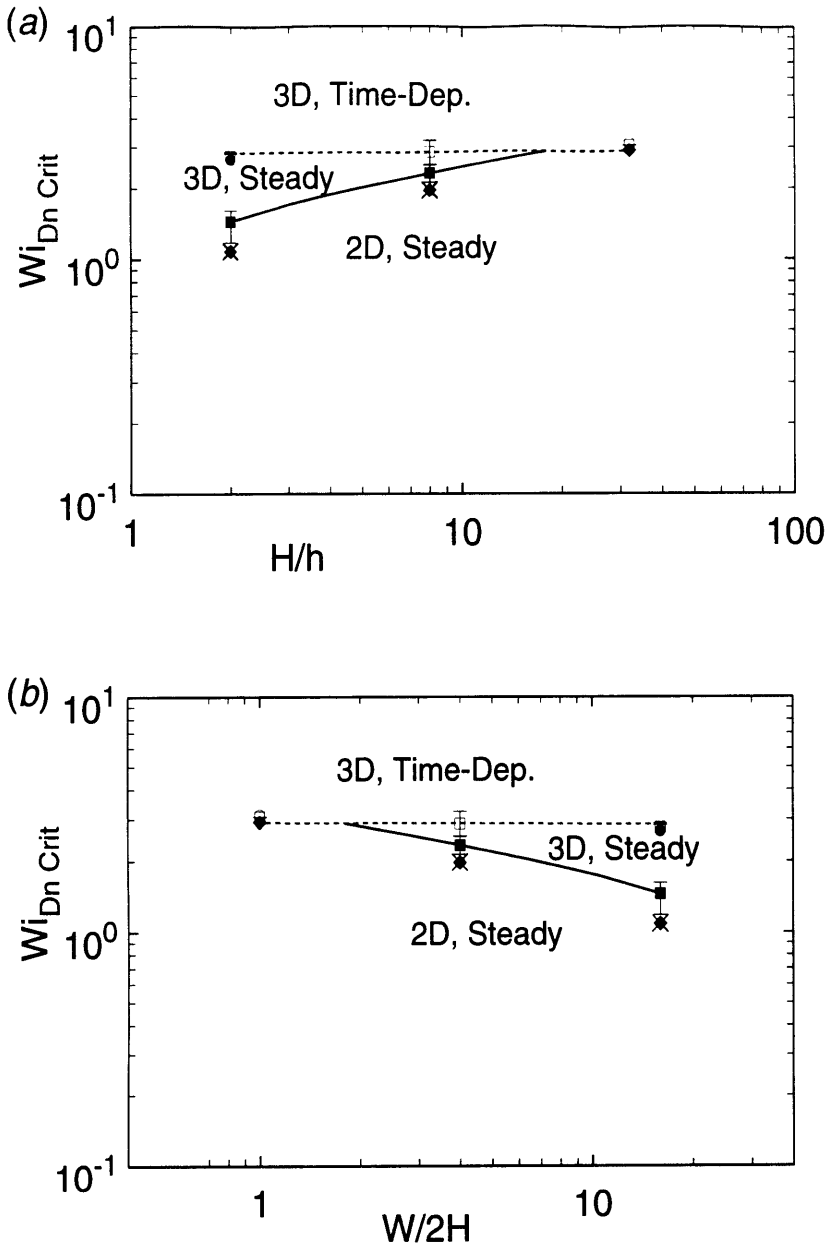

Figure 5.19 Maps of transitions observed in viscoelastic planar contraction flow: (a) critical Wi_{Dn} vs. contraction ratio, H/h; (b) critical Wi_{Dn} vs. upstream aspect ratio, W/2H. Experimentally observed transitions are denoted: (◆), onset of increase in maximum dimensionless centerline strain rate with Wi_{Up}; (×) diverging flow; (■), transition from two-dimensional, steady base flow to three-dimensional, steady flow; (□), transition from steady to time-dependent flow; (●), secondary spatial harmonics; (○) secondary spatio-temporal harmonics. Fits are denoted: (——), transition from two-dimensional, steady base flow to three-dimensional, steady flow; (- — -), transition from steady to time-dependent flow.

temporal oscillation (travelling waves) was superposed on the spatial oscillation (stationary waves). To understand this, consider the appearance of the time series if there were no superposition and the waves associated with the spatial oscillation suddenly started to move as a unit from the bounding wall at $\chi = \pm 32$ toward the center of the flow; a sudden jump, not a gradual increase, in the amplitude of temporal oscillation would be observed at a given point in space. Videotaped streakline images in the xz-plane of the 2:1 contraction were studied; there were indications that the spatio-temporal structure after onset of the temporal instability was more complex than that of a single set of waves travelling at a uniform velocity in the x-direction. However, the precise spatio-temporal structure could not be determined from these streakline images.

The flow visualization observations of the temporal instability described in §5.2.1 for the 8:1 contraction indicated that the "vortex bundles" travelled from the walls of the geometry toward the center of the flow; no underlying stationary wave pattern was observed. However, streakline visualization may not detect low amplitude oscillations near onset. Only images of the central region of the flow, $-23 \leq \chi \leq 23$, could be acquired. Since the amplitude of the temporal oscillation was greatest near the bounding walls ($\chi = \pm 32$), the flow visualization technique may not have been capable of resolving superposed temporal and spatial waves near onset of the temporal instability. The observation via light sheet visualization in the 8:1 contraction of moving streamline bundles (cf. Fig. 5.5), without an underlying stationary pattern, is probably a result of the Wi_{Up} being substantially greater than the critical value for onset of temporal instability, so that large amplitude travelling waves dominated over low amplitude stationary waves.

Flow Transitions in the 32:1 Contraction

At low Wi_{Up} the flow was steady and two-dimensional in the 32:1 contraction. As the Wi_{Up} was increased above a critical value an increase in the maximum dimensionless centerline strain-rate was observed. However, diverging flow was not noted; the strain rate was positive at all points on the centerline upstream of the contraction plane. The absence of diverging flow is discussed in §5.3.4.

At yet higher Wi_{Up} a direct transition from globally steady, two-dimensional flow to three-dimensional, time-dependent flow was found. This essential difference in the transi-

tion sequence from that observed for the 2:1 and 8:1 contractions is attributed to the low upstream aspect ratio, W/2H = 1. Specifically, the width of the geometry may have been too narrow for the steady, three-dimensional flow, characterized by oscillation of v_z in the x-direction, to "fit into"; this is addressed in §5.3.2 below. Alternately, as discussed in §5.2.3, it is possible that onset of the temporal flow transition is the result of an interaction between the local flow transition noticed at the bounding wall, $\chi = \pm 32$, and the global flow field. For high upstream aspect ratios, the local vortex at the wall would have to grow substantially, requiring high Wi_{Up}, before being able to interact with the entire flow field. In contrast, for low upstream aspect ratio, only a small amount of growth of this bounding wall vortex would be required, resulting in low Wi_{Up} for onset of the temporal instability. Hence, for the 32:1 contraction the extreme case of unit aspect ratio induces onset of the temporal oscillations before onset of steady, spatial oscillations. This view is supported by LDV measurements which indicated that the amplitude of the temporal oscillation was greatest near the bounding wall at $\chi = -32$ and weakest near the center of the flow ($\chi = 0$). At elevated flow rates, onset of harmonics in the frequency spectrum was noted. As discussed above, the harmonics were believed to occur via spatial wavenumber doubling of the wave structure and not doubling of the rate of wave propagation in the x-direction.

Summary of Transition Map

The map in Fig. 5.18a illustrates that there are commonalities in the sequence of transitions which occur for increasing Wi_{Up} for different contraction ratios; however, the critical values of Wi_{Up} for these transitions decrease with increasing contraction ratio. Note in Fig. 5.18a that the ratio of critical onset values, $Wi_{Up\ T}/Wi_{Up\ S}$, decreases between the contraction ratios 2:1 and 8:1 and apparently decreases to a value less than unity (no three-dimensional, steady-state flow was observed) for the 32:1 contraction.

The critical value for onset of the spatial instability, $Wi_{Up\ S}$, appeared to be directly related to the ratio of upstream to downstream half-height, H/h. This is addressed in greater detail in §5.3.3 where the scaling relation is applied which considers how streamline curvature and streamwise elastic stress interact to induce flow transitions. On the other hand, onset of the temporal flow transition was thought to be more closely related to the upstream aspect ratio, W/2H. The $Wi_{Up\ Crit}$ for the transitions is plotted as a function

of aspect ratio in Fig. 5.18b; the dependence of the $Wi_{Up\ Crit}$ on aspect ratio is considered in §5.3.3.

Transition Map in Terms of Wi_{Dn}

The transition map was also plotted as the critical Weissenberg number defined in terms of downstream flow parameters, $Wi_{Dn\ Crit}$, as a function of contraction ratio or aspect ratio in Figs. 5.19a and 5.19b. The transition from two- to three-dimensional flow is considered first, the transition from steady to time-dependent flow is then discussed. Note from Fig. 5.19a that the critical Weissenberg number defined in terms of the mean downstream shear rate for the spatial transition, $Wi_{Dn\ S}$, increases by a factor or order two as the contraction ratio increases from H/h = 2 to H/h = 8. This behavior may be contrasted with the decrease by a factor of four of $Wi_{Up\ S}$ for the same increase in contraction ratio (cf. Fig. 5.18a). Thus, when the range is defined in terms of $Wi_{Dn\ S}$, the curve associated with the spatial transition appears "flatter" than when the upstream Weissenberg number is used. Note, however, that whereas $Wi_{Up\ S}$ decreases with contraction ratio in Fig. 5.18a, $Wi_{Dn\ S}$ increases with contraction ratio in 5.19a. In §5.3.3 the relation of the critical Weissenberg number for the spatial transition to the streamline curvature around the outer corner which is induced by the greater-than-unity contraction ratio, H/h > 1, is discussed. Consideration of the streamline-curvature interaction leads to the expectation that for increased curvature the critical Weissenberg number will decrease. The observation that the Weissenberg number decreases when defined in terms of upstream parameters (cf. Fig. 5.18a) but not when defined in terms of downstream parameters (cf. Fig. 5.19a) supports the use of the upstream Weissenberg number, Wi_{Up}, throughout this Chapter.

The critical value for transition from steady to time-dependent flow, $Wi_{Dn\ T}$, shown in Fig. 5.19a, appears insensitive to contraction ratio, i.e. "flat". In contrast, $Wi_{Up\ T}$ for the temporal transition exhibits a strong dependence on contraction ratio, between H/h = 2 and H/h = 8 the onset parameter decreases by a factor of nearly eight. Superficially, this observation appears to indicate that the transition to time-dependent behavior is controlled by the parameter Wi_{Dn}. However, as discussed in §5.2.3, the temporal transition appears to be related to flow conditions induced by the presence of a wall bounding the x-dimension of the upstream channel. In this case, the appropriate Weissenberg number could be defined

in terms of the characteristic shear rate in the region near the centerplane, immediately adjacent to the wall bounding the x-dimension, and close to the contraction plane; $\dot{\gamma}_{xz,\,W} \equiv \dot{\gamma}_{xz}(\chi \approx \pm 32,\, \upsilon = 0,\, \zeta \approx -1)$. Since the width of the channel, W, and the half-height of the downstream channel, h, were fixed for all the experiments, the shear rate $\dot{\gamma}_{xz,\,W}$ is approximately proportional to the mean downstream shear rate, $\langle v_z \rangle / h$. Therefore, the flatness of the curve describing the temporal transition in Fig. 5.19a does not necessarily imply that downstream flow conditions control the spatial transition. Rather, this flatness may be related to a critical value of the wall shear rate, $\dot{\gamma}_{xz,\,W}$, and the particular geometry used for these experiments, in which the ratio of width to downstream half-height was constant, W/2h = 32.

5.3.2 Characteristic Length and Time Scales of Flow Structures

Characteristic length scales were associated with rearrangement to diverging flow and spatial transition to three-dimensional flow. These length scales were in turn related to geometric parameters of the planar contraction, as discussed below. A characteristic time scale was noted for the temporal oscillation; however, this time scale could not be related to specific parameters of the flow or fluid rheology (e.g. the λ_k's of the relaxation spectrum).

A length scale was associated with the diverging flow described in §5.2.4 by determining the distance of the point of minimum velocity on the centerline from the contraction plane at $\zeta = 0$. In Fig. 5.20, the dimensionless distance is plotted as a function of Wi_{Up} for flows through the 2:1 and 8:1 contractions. The point of minimum velocity in the diverging flow is found to be located a distance of the order of the upstream half-height, H, in front of the contraction plane. Data for the 32:1 contraction could not be plotted in Fig. 5.20 because no minimum was seen; the velocity continuously decreased with distance upstream from the contraction plane, out to the farthest point which could be probed, $\zeta = -40$. Note that location of the minimum at $\zeta < -40$ is consistent with the distance scaling with upstream half-height, H.

In Fig. 5.21, the wavenumber of the spatial oscillation after flow transition, made dimensionless with the upstream half-height, is plotted as a function of Wi_{Up} for the 2:1

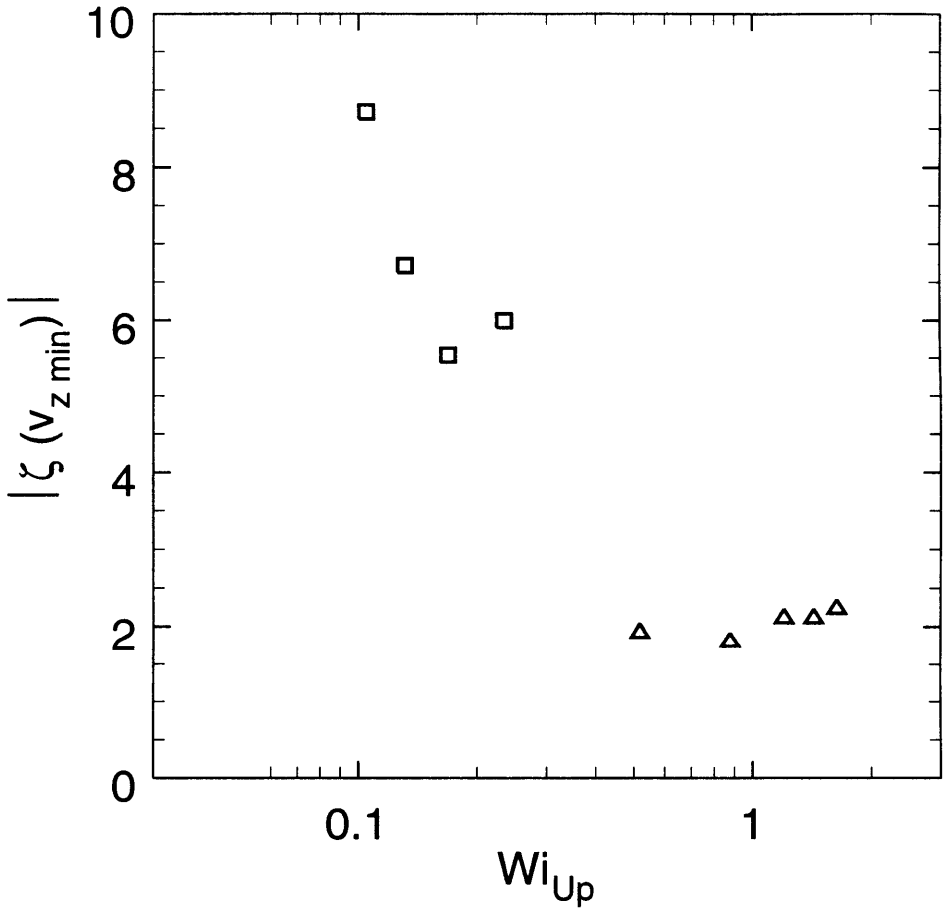

Figure 5.20 Distance of the point of minimum centerline velocity, $|\zeta(v_{z\,min})|$, upstream of the contraction plane vs. Wi_{Up} after onset of diverging flow: (△) 2:1 contraction; (□) 8:1 contraction.

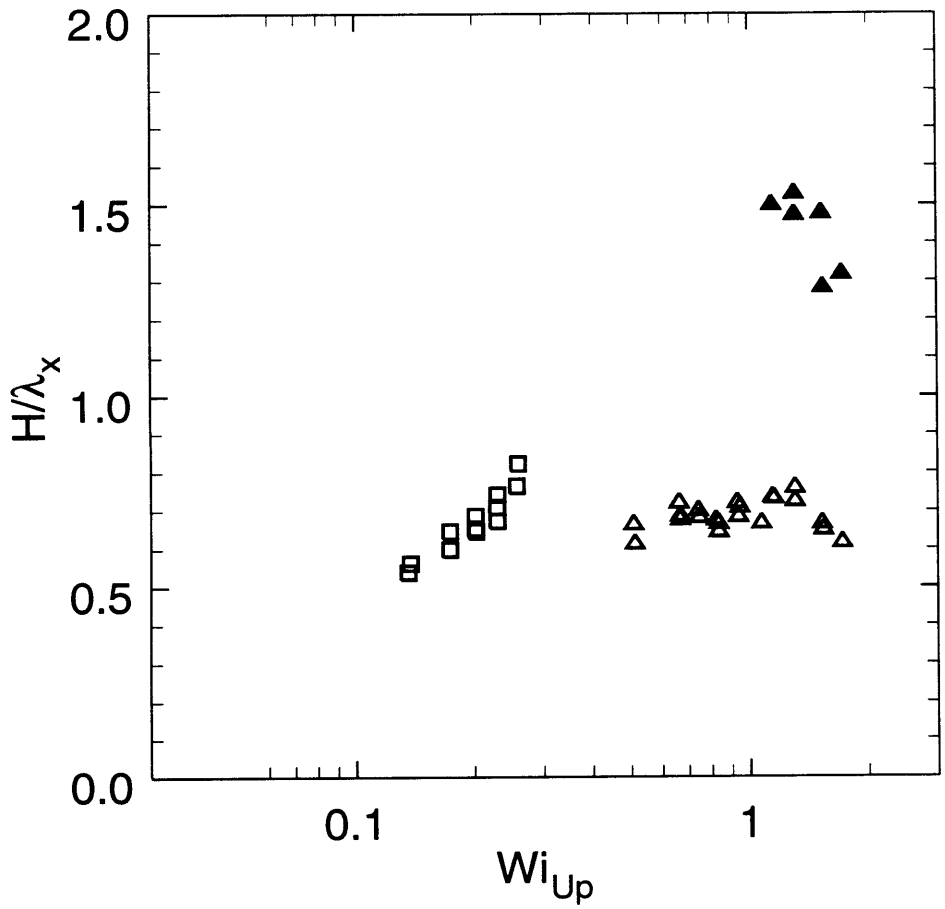

Figure 5.21 Dimensionless wavenumber, H/λ_x, vs. Wi_{Up} after onset of three-dimensional flow: (□) primary peak for the 8:1 contraction, streakline visualization data used; primary (△) and secondary (▲) peaks for the 2:1 contraction, LDV data used, scans performed over range $-26 \leq \chi \leq -1.5$ $\upsilon = -1.75$, $\zeta = -1.80$.

and 8:1 contraction ratios. For the 8:1 contraction, the dimensionless wavenumber increased with Wi_{Up}; for the case of the 2:1 contraction, no significant dependence of wavenumber on Wi_{Up} was noted. Above a critical Wi_{Up}, before onset of time-dependent flow, doubling of the spatial wavenumber in the 2:1 contraction was observed. Period doubling in the 8:1 contraction was not observed, probably because the wavenumber was estimated through analysis of videotaped streakline images, not LDV. The dimensionless wavenumber of the primary peak is of the same order for both the 2:1 and 8:1 contraction ratios, $H/\lambda_x \simeq 0.7$. As mentioned in §5.2.2, and discussed in §5.3.3 a three-dimensional and steady flow state was not noted for the 32:1 contraction.

The characteristic frequency of the temporal oscillation is shown as a function of Wi_{Up} for the 2:1 and 32:1 contraction ratios in Fig. 5.22. The time-series data used to determine the frequency associated with each data point was acquired with the LDV measuring volume placed approximately half-way between the center of the flow and the bounding wall of the channel: at $\chi = -20$ for the 2:1 contraction, and at $\chi = -21$ for the 32:1 contraction. The data in Fig. 5.22 indicate only a weak dependence of frequency on contraction ratio: the frequency of oscillation in the 2:1 contraction is higher than the frequency in the 32:1 contraction, but the frequency in both contractions was of the same order. Note that the period associated with the oscillation was $T_p = 180$ [s] for the 2:1 contraction and $T_p = 340$ [s] for the 32:1 contraction - in both cases much greater than the estimated zero-shear-rate relaxation time of the test fluid, $\lambda_{10} = \Psi_{10}/2\eta_0 \sim 1$ [s] (cf. Chapter 4). No trend of the frequency increasing or decreasing with Wi_{Up}, for a given contraction ratio, was observed. Data for the 8:1 contraction is not shown since LDV measurements were not taken; data was obtained via analysis of videotaped streakline images. As discussed above, flow visualization is limited in its ability to obtain quantitative information near instability onset.

5.3.3 Mechanism Driving Transition in Viscoelastic Planar Contraction Flow: Interaction of Streamwise Elastic Stress with Streamline Curvature

Consideration of structural features of the flow transitions and the scaling of onset Wi_{Up} with contraction ratio has elucidated the mechanism of viscoelastic instability in the planar contraction. In particular, these features were consistent with the interaction of streamwise elastic stress with streamline curvature around the outer corners of the planar

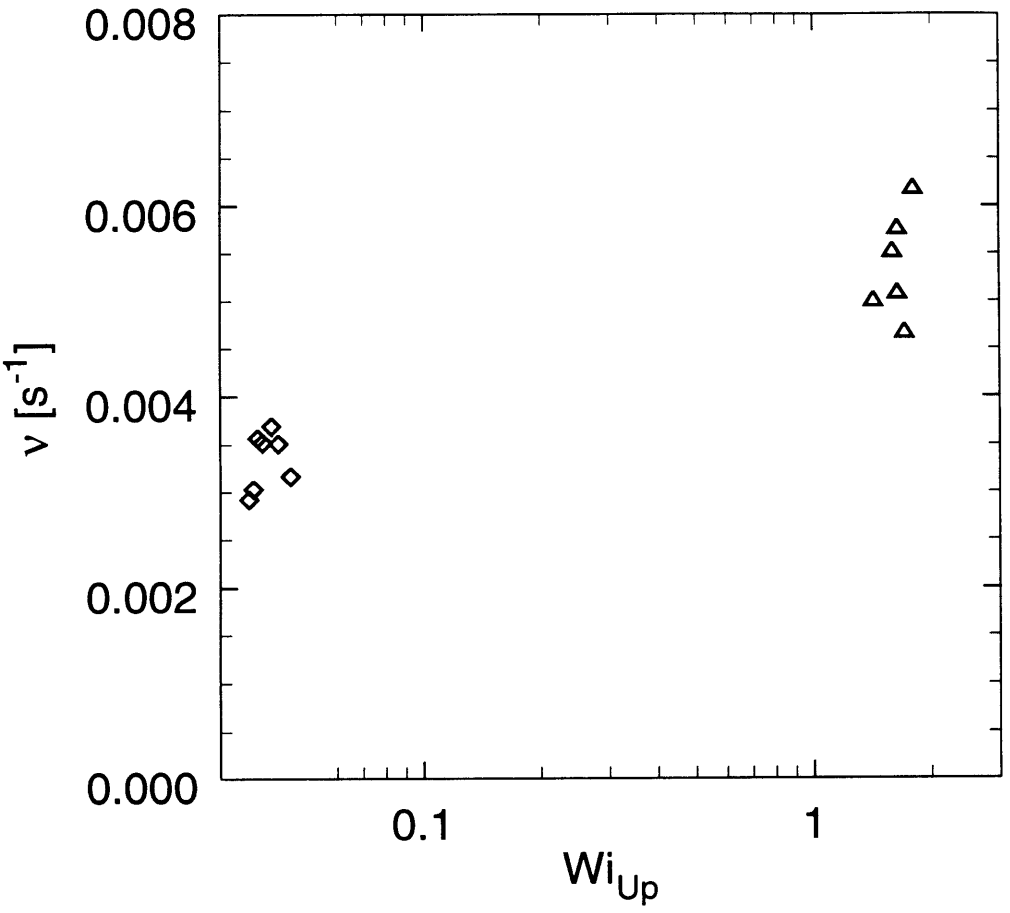

Figure 5.22 Frequency (ν) vs. Wi_{Up} after onset of time-dependent flow: (△), 2:1 contraction, v_z vs. t series acquired at χ = -20.0, υ = -1.75, ζ = -1.80; (◇), 32:1 contraction, v_y vs. t series acquired at χ = -21.0, υ = -1.51, ζ = -1.51.

contraction acting to induce flow transitions. The first part of this Section considers structural features of the flows, the second, application of the "viscoelastic Görtler" scaling to the flow transitions.

Shear flow rheological characterization of the Boger test fluid indicated that the fluid had a high zero-shear-rate relaxation time of $\lambda_{10} \gtrsim 1$ [s]. Inertia was negligible, $Re_{Dn} \leq 7 \times 10^{-4}$, for all the flows investigated, whereas elastic memory or nonlinear effects could influence the flows, since Wi_{Up} as great as 1.8 were attained. Therefore, although some structural features of the flow after onset of instability resemble those of Görtler vortices (Saric, 1994), the transitions were induced by the "elastic", not inertial, character of the flows.

The characteristic length scales of flow structures indicate that the transitions were driven by interaction of elastic stresses in the streamwise direction with streamline curvature in the *upstream* region of the flow. Specifically, the extent of the oscillations associated with the flow transitions upstream of the contraction plane, as indicated by the reattachment length of the outer corner vortex adjacent to the fast flow region, was of the order of the upstream half-height, H. The wavelength of the spatial oscillation was quantitatively characterized via LDV scans in the neutral x-direction and found to scale with upstream half-height. The characteristic dimensions of the oscillation in the x- and in the z-directions indicate the relation of the flow transition to streamline curvature in the flow around the outer corner, rather than around the reentrant corner.

The spatial structure of the flow after onset of the instability bore resemblance to viscometric flows for which it has been concluded that interaction of streamwise normal stresses with curved streamlines drives the instability (Joo and Shaqfeh, 1994; McKinley *et al.*, 1996). More detailed comparison of the instability noted in the viscoelastic flow through the planar contraction with instabilities found in other complex and viscometric flows follows in §5.4 below.

In Chapter 2, a number of successful applications of the "viscoelastic Görtler" scaling (McKinley *et al.*, 1996) to transitions observed in viscometric and non-viscometric flows were described. These examples serve to motivate the application of the scaling to the

"elastically-driven" instabilities in the planar contraction, in particular, the experimental data which were presented in the form of a transition map (cf. Figs. 5.18a and 5.18b).

Equation (2.3) is the starting point for the analysis; each term on the left side of the equation must be considered. As discussed above, the upstream half-height, H, is the characteristic length scale for the extent of the spatial oscillation upstream of the contraction plane and the wavelength of the oscillation; therefore, the flow transition seems to be related to streamline curvature around the outer corner of the contraction. Hence, it is natural to use the upstream flow conditions to define the terms in eq. (2.3).

In the first term, the curvature, $1/R_c$, must asymptotically approach zero as the contraction ratio approaches unity, $H/h \rightarrow 1$; this limit is equivalent to fully developed Poiseuille flow in a channel, where "elastically-driven" instabilities do not occur. As H/h increases, the dimensionless curvature, H/R_c, of the streamlines around the outer corner of the contraction is expected to increase. A simple expression which captures this behavior is

$$\frac{H}{R_c} = \frac{1}{A}\left(\frac{H}{h} - 1\right)^B \tag{5.6}$$

where A and B are constants which are greater than zero. The velocity, U, and shear rate, $\dot{\gamma}$, terms are related to upstream flow conditions as

$$\dot{\gamma} = \langle\dot{\gamma}\rangle_{Up} = \frac{U}{H} = \frac{Q}{2H^2W} \tag{5.7}$$

where W is the x-dimension of the geometry and Q, the volumetric flow rate. This shear rate is used in the evaluation of the polymeric relaxation time, λ_{1p}, and the streamwise polymeric stress, τ_{11p}. The expression for the critical condition for onset of instability in the planar contraction can then be rewritten in terms of a critical upstream shear-rate-dependent Weissenberg number, Wi_{Up} (defined in §5.1) as

$$Wi_{Up,\,crit} = M_{VG}\left(\frac{A(1-\eta_s/\eta)}{2}\right)^{1/2}\left(\frac{H}{h}-1\right)^{-B/2} \tag{5.8}$$

Since A and M_{VG} are both unknown, they can be combined into a single term, $S = M_{VG}\left(\frac{A(1-\eta_s/\eta)}{2}\right)^{1/2}$. Equation (5.8) can then be rewritten as

$$Wi_{Up,\,crit} = S\left(\frac{H}{h}-1\right)^{-B/2} \tag{5.9}$$

Experimental data for the critical upstream Weissenberg number, $Wi_{Up\,S}$, associated with the spatial flow transition in the 2:1 and 8:1 contractions have been presented in Sections 5.2.2 and 5.3.1 and are used to fit the unknown parameters in eq. 5.9. Specifically, a good match between eq. 5.9 and the data was obtained with $S_S = 0.44$ and $B_S/2 = 0.64$, as shown in Figs. 5.18a and 5.18b. Thus, eq. 5.9 has the correct functional form to describe the relation between the contraction ratio and $Wi_{Up\,S}$.

The conditions governing transition to time-dependent flow may be more complex than those controlling onset of three-dimensional, steady flow. As discussed above, a local flow transition near the wall bounding the x-dimension seems to play a role in the onset of the temporal transition; the vortex structure associated with this local transition scales with the downstream half-height, h, rather than the upstream half-height, H. The upstream aspect ratio, W/2H, in addition to the contraction ratio, H/h, may determine the $Wi_{Up\,T}$ for transition to time-dependent flow. Nevertheless, eq. (5.9) provides a good fit to the data for the critical Wi_{Up} for transition to time-dependent flow in the geometries with contraction ratio H/h = 2, 8, and 32, as shown in Figs. 5.18a and 5.18b. The fitted parameters had values of $S_T = 1.4$ and $B_T/2 = 1.1$; the root mean square of the fractional error of the fit was ±3%.

One can note from Fig. 5.18a that if the fit to the spatial transition data is extrapolated to higher contraction ratios the neutral stability curves for the predicted spatial (two-dimensional to three-dimensional flow) and temporal (steady to time-dependent flow) transitions intersect at a contraction ratio of $(H/h)_{ST} = 15$. In the experiments, the contraction ratio was adjusted by varying the upstream channel half-height for a fixed downstream half-height. Hence, an increase in the contraction ratio results in a decrease in the

upstream aspect ratio. In Fig. 5.18b it is shown that the point of intersection of the neutral stability curves corresponds to an upstream aspect ratio of $(W/2H)_{ST} = 2.1$. In §5.3.2, the dimensionless wavenumber for the 2:1 and 8:1 contractions was determined to be approximately $H/\lambda_x \approx 0.7$. Using this wavenumber, one can determine the number of wavecycles which would fit into the half-width of a geometry with an upstream aspect ratio of two; $W/(2\lambda_x) = 1.5 \sim 1$ is obtained. It is interesting that approximately one wave cycle of the spatial oscillation would fit into the half-width of the geometry with a contraction ratio such that Wi_{Up} is identical for onset of the spatial and temporal instabilities, $Wi_{Up\ S} = Wi_{Up\ T}$. This supports the concept that transition to time-dependent flow is related to a three-dimensional imperfection introduced by the wall bounding the x-dimension. In particular, the base flow may make a direct transition to time-dependent flow in the 32:1 contraction since a full cycle of the spatial oscillation cannot fit into the half-width of the upstream channel.

It is interesting to speculate on the nature of the nonlinear dynamics at onset of instability for flow through a geometry in which the critical Wi_{Up} for the transition to spatial and the transition to temporal oscillation are nearly identical. Specifically, a bifurcation of codimension-2 exists at the point where the neutral stability curves for the spatial and the temporal transitions intersect on the transition map (cf. Figs. 18a and 18b); i.e. at $H/h = 15$ (or $W/2H = 2.1$) and $Wi_{Up} = 0.08$. To achieve a bifurcation of codimension-2, two control parameters, in this case H/h (or W/2H) and Wi_{Up}, must be tuned to specific values. A dynamical system in the vicinity of a codimension-2 bifurcation can exhibit behavior which is essentially different from that observed near the individual neutral stability curves which intersect at the codimension-2 point. For example, a system may behave quasiperiodically or even chaotically when control parameters are nearly equal to values associated with the codimension-2 bifurcation, even if such behavior does not occur for either of the individual neutral stability curves (Guckenheimer and Holmes, 1983). A wider ranging discussion of the nature of flow transitions in viscoelastic flow through the planar contraction is deferred to §5.5.

5.3.4 Correlation between Onset of Diverging Flow and Flow Transitions

As shown in Figs. 5.18a and 5.18b for the 2:1 and 8:1 contractions, onset of three-dimensional, steady flow occurs for a Wi_{Up} immediately greater than the Wi_{Up} for which an increase in the maximum dimensionless centerline strain rate with Wi_{Up} is noted. As discussed in §5.2.2, a global transition to three-dimensional flow, distinct from the transition to time-dependent flow, was not noted for the case of the 32:1 contraction. However, the critical Wi_{Up} for direct transition from two-dimensional, steady to three-dimensional, time-dependent flow in the 32:1 contraction is greater than the critical Wi_{Up} for onset of increasing centerline maximum dimensionless strain rate with Wi_{Up}. Hence, the relation between flow transition and the dependence of peak strain rate on Wi_{Up} for the case of the 32:1 contraction is consistent with the relation observed for the 2:1 and 8:1 contractions.

It is possible that the two-dimensional flow rearrangement associated with the diverging flow promotes onset of the three-dimensional and steady instability. In particular, visualization of flow in the yz-plane indicates that after onset of diverging flow, the streamlines near the outer corner become more tightly curved. A smaller characteristic radius of curvature of the streamlines in conjunction with an increase in the local strain rate, associated with shift of the streamlines toward the contraction plane, may allow the critical "viscoelastic Görtler number", M_{VG}, (cf. eq. (2.3)) for onset of the instability, to be exceeded for a lower volumetric flow rate than if this two-dimensional streamline rearrangement did not first occur. This could explain why the critical Weissenberg number for transition to three-dimensional flow is immediately greater than the critical Wi_{Up} for onset of diverging flow.

5.4 Comparison of Viscoelastic Instabilities in the Planar Contraction with Instabilities in Other Flow Geometries

In §5.3, a map of the ordered series of flow transitions in the planar contraction was presented; the spatio-temporal flow structure associated with these transitions was characterized. Common spatial and temporal features of the instabilities in flows through geometries of different contraction ratios were noted and used to identify the interaction of streamwise stress with streamline curvature as the ("viscoelastic Görtler") mechanism

which drove the transitions. The role of the contraction ratio in setting the critical Wi_{Up} for transition from the two-dimensional, base to the three-dimensional flow was elucidated; the scaling of characteristic lengths in the velocity field with the upstream half-height was presented.

In this Section, the characteristics of flow transitions in the planar contraction noted in this study are contrasted with the results of previous investigations. Only aspects of prior studies essential for the comparison are presented; note that a detailed and comprehensive review of the literature is given in Chapter 2. Comparison of the findings of this study with published observations for viscoelastic planar contraction flow are discussed first. Common features of flow transitions in the planar contraction with velocity field evolution and structure in the axisymmetric contraction are then described. Other complex flows are considered; these differ substantially in geometry from the planar contraction, but the flow transitions are also thought to be driven by the interaction of streamwise elastic stresses with streamline curvature. Comparison between flow transitions noted in the planar contraction with those found in viscometric flows is then made; one may note that viscometric flows, which have a simple base flow structure, are amenable to analytical mathematical treatment. The nature of flow transitions observed in different systems of viscoelastic flow with curved streamlines is summarized at the end of this Section.

Planar Contraction Flows

Diverging flow has been observed in several investigations of viscoelastic flow through the planar contraction (Binding and Walters, 1988; Evans and Walters, 1989; Chiba *et al.*, 1990; Chiba *et al.*, 1992). This two-dimensional flow rearrangement was observed to precede the onset of spatial instability, which is consistent with the findings presented in Sections 5.2 and 5.3.

Chiba et al. (1990, 1992) observed a three-dimensional "Görtler-like" flow pattern with the same form as that described in §5.2. However, the dimensionless wavelength of the velocity field, λ_x/H, was found to depend on contraction ratio, H/h; in contrast, the study presented in this Chapter found the dimensionless wavelength to be independent of contraction ratio. Chiba et al. (1990, 1992) also noted transition to time-dependent flow at volumetric rates above those associated with inception of three-dimensional, steady flow.

However, Chiba et al. found that the vortex pairs oscillated in the neutral direction about a fixed point rather than continuously moving from the walls bounding the x-dimension toward the center. A possible cause for the discrepancies between the observations of this study and those of Chiba et al. was the fact that inertia was a significant factor in the flows used in the investigation of Chiba et al. For example, $Re_{Dn}(\dot{\gamma}) \sim O(100)$ at onset of time-dependent flow in the 10:1 contraction. In general, at volumetric rates for which "elasticity" had a substantial effect on the flow field, $Wi \gtrsim 1$, shear-thinning of the fluid viscosity resulted in $Re > 1$. The interaction of inertial with "elastic" phenomena can give rise to essentially different behavior from that observed under inertialess conditions (Joseph, 1990).

Axisymmetric Contraction Flows

The transition sequence and spatio-temporal structure of flow transitions observed in the planar contraction can be compared with observations in an analogous two-dimensional abrupt geometry, the axisymmetric contraction. Diverging flow, and an associated increase in the peak value of the dimensionless centerline strain rate, has been noted in the axisymmetric contraction (McKinley *et al.*, 1991). The scaling of the extent of the diverging flow region was different, specifically, the distance of the point of minimum centerline velocity upstream from the contraction plane increased monotonically, although not linearly proportionally, with upstream tube radius, R_{Up}. In contrast, for the planar contraction flow, the location of the point of minimum centerline velocity upstream of the contraction plane was linearly proportional to the upstream half-height, H (cf. §5.2). Diverging flow was observed only for lower axisymmetric contraction ratios $R_{Up}/R_{Dn} \leq 5$ by McKinley et al. (McKinley *et al.*, 1991) but was observed for contraction ratios at least as great as H/h = 8 in the planar contraction flow study presented in this thesis. A rationale addressing why diverging flow is observed at higher contraction ratios for the planar than for the axisymmetric geometry was given in Chapter 2. As found in the planar contraction, in the axisymmetric contraction two-dimensional rearrangement to diverging flow was observed to precede transition to three-dimensional flow.

The quantitative characterization of flow transitions in the axisymmetric contraction, conducted by McKinley et al. (1991) was discussed in Chapter 2. Essential aspects of this

study, required for the following contrast with the flow transitions observed in the planar contraction, are reiterated here. McKinley et al. constructed a transition map of flow states in the axisymmetric contraction for a range of Weissenberg number and contraction ratios. At elevated flow rates, a transition from steady to time-dependent flow was observed. For lower contraction ratios, $R_{Up}/R_{Dn} \leq 4$, the vortex remained axisymmetric but grew and decayed with a characteristic frequency (pulsating mode). In contrast, for $R_{Up}/R_{Dn} \geq 5$ the unstable vortex was nonaxisymmetric; as also noted by Binding and Walters (1988), in the rz-plane the outer corner vortex in one half of the plane was larger than in the other half. The nonaxisymmetric structure precessed around the perimeter of the cylinder with a characteristic frequency (rotating mode).

A parallel between the rotating-mode flow in the axisymmetric contraction and the time-dependent flow in the planar contraction, which consisted of vortices travelling in the "neutral" x-direction, can be made. Specifically, imagine splitting the upstream tube of the axisymmetric geometry into two halves, $0 < \theta < \pi$ [rad] and $0 < \theta < -\pi$ [rad], "unwrapping" these halves, and opposing the halves. A precessing vortex structure would equate to a large vortex travelling along one (call this the "top") of the halves of the mapping, opposed by a small vortex on the other ("bottom") half. In the middle of the temporal cycle, the large vortex will leave the "top" half and travel along the "bottom" half, opposed by a region with a small vortex on the "top" half. This picture resembles the time-dependent flow observed over a region spanning one wavelength in the "neutral" x-direction in the planar contraction: a region of fast flow, associated with a large vortex on one side of the centerplane, travels in the x-direction and is opposed by a region of slow flow with a small corner vortex. Halfway through the temporal cycle, the pattern is repeated, but this time on opposite sides of the centerplane.

An essential difference in the flow-transition sequence observed in the axisymmetric contraction from that found for the planar contraction is that in the axisymmetric case a three-dimensional, steady flow state is not observed. Full understanding of the structure of the transition map of the axisymmetric contraction and why it differs from the map for the planar contraction will probably require detailed three-dimensional and time-dependent numerical simulations. However, it is interesting to consider how a conflict in the axisymmetric contraction between required flow symmetry and the wavelength set by a

characteristic length scale may induce a direct transition from the two-dimensional, base state to the time-dependent, rotating-mode flow pattern.

Following the analogy between the θ-coordinate in the axisymmetric case and the x-coordinate in the planar contraction, the circumference (C_{Up}) of the upstream tube in the axisymmetric contraction is analogous to the width in the planar contraction. Thus, for the axisymmetric contraction the upstream "aspect ratio" is fixed at $C_{Up}/2R_{Up} = \pi$. For the three-dimensional flow state to be steady it must have an integer number of spatial cycles, N_{cyc}, around the circumference of the tube; the dimensionless wavelength at the perimeter of the upstream tube is then $\lambda_\theta/R_{Up} = 2\pi/N_{cyc}$. In §5.3.2, it was noted that the wavelength of the three-dimensional flow in the planar contraction was $\lambda_x/H \approx 3/2$. If the same wavelength, made dimensionless with the upstream tube radius, R_{Up}, were present in the axisymmetric contraction one would obtain a symmetry number of $N_{cyc} = 4\pi/3 \sim 4$. However, note that in the planar contraction, a "fast" region of flow with an associated large outer vortex is opposed by a "slow" region of flow with a small or absent outer vortex on the other side of the centerplane. For the three-dimensional flow in the axisymmetric contraction to have similar form (as is indicated by streakline images (Binding and Walters, 1988; Nguyên and Boger, 1979)), a "fast" region of flow would be opposed by a "slow" region located π [rad] away in the θ-direction. The instability is then required to have an odd symmetry number. The discrepancy between the wavenumber which would be set by the upstream radius ($N_{cyc} \sim 4$) and the required symmetry number (N_{cyc} = odd) may result in a steady, three-dimensional flow being inherently unstable and consequently a direct transition from two-dimensional, steady to three-dimensional, time-dependent, rotating-mode flow. In support of this reasoning is a similar conflict between a characteristic wavelength and a constraint on the number of wavecycles, which may exist in the planar contraction. Specifically, as described in §5.3.2, for contraction ratios of low upstream aspect ratio, $W/2H < 3/2$, a three-dimensional flow pattern of characteristic wavelength $\lambda_x/H \simeq 3/2$ will not be able to fit into the half-width, W/2. Consequently, a direct transition from two-dimensional and steady to three-dimensional and time-dependent flow is observed.

For particular values of Wi, contraction ratio, and upstream aspect ratio, the three-dimensional, time-dependent flow fields in the planar and in the axisymmetric contraction

are analogous; however, there are distinct differences between the boundary conditions of and the flow transitions seen in the axisymmetric and planar contraction geometries. As discussed in §5.2.3, the walls bounding the x-direction in the planar contraction act as an imperfection to the fully developed two-dimensional base flow. This imperfection was thought to play a key role in inducing onset of the time-dependent flow. Hence, time-dependent flow may not be an integral feature of a "perfect" two-dimensional planar contraction flow. Note that in the planar contraction, the upstream aspect ratio, W/2H, and the contraction ratio, H/h, can, in principle, be independently varied. In contrast, the upstream "aspect ratio" in the axisymmetric contraction, $C_{Up}/2R_{Up} = \pi$, is a fixed quantity; constraints imposed on the number of wavecycles and the symmetry are inherent to the geometry. This characteristic may preclude observation of a three-dimensional, steady state. Furthermore, because of the axisymmetric symmetry, there are no "preferred" locations (e.g., at bounding walls) in the "neutral" θ-direction where time-dependent oscillations are particularly large.

In the planar contraction, differences in the flow transition sequence among the various planar contraction geometries investigated were ascribed to variations in upstream aspect ratio, W/2H. The contraction ratio, H/h, was thought to influence the $Wi_{Up\ Crit}$ for a given flow transition, but not the order or the essential spatio-temporal structure of the transition flow states. In contrast, for the axisymmetric contraction, variation of the contraction ratio, H/h, caused essential differences in transition sequence and spatio-temporal structure; i.e., pulsating mode at low R_{Up}/R_{Dn} versus rotating mode at high R_{Up}/R_{Dn}. The upstream "aspect ratio" of the axisymmetric contraction cannot be a governing parameter since it is a fixed quantity, $C_{Up}/2R_{Up} = \pi$. One could speculate that the dependence of spatio-temporal structure on contraction ratio observed in the axisymmetric geometry is a consequence of the difference in circumference of the upstream and downstream tubes, specifically $C_{Up}/C_{Dn} = R_{Up}/R_{Dn}$; in contrast, in the planar contraction the width of the upstream and downstream ducts is equal and independent of contraction ratio.

In McKinley et al. (1991), the bifurcation to axisymmetric and time-dependent flow was not quantitatively characterized, precluding definitive classification. However, qualitative observation indicated that the bifurcation in the axisymmetric contraction flow was probably supercritical (McKinley, 1997). This further supports the analogy between the

fluid dynamics of viscoelastic flow through the axisymmetric contraction and through the planar contraction. In the planar contraction flow both the spatial transition from two-dimensional to three-dimensional flow and the temporal transition from steady to time-dependent flow were associated with supercritical bifurcations.

Driven Cavity Flow

Pakdel and McKinley (1996) have observed a transition to three-dimensional and time-dependent viscoelastic flow in the driven cavity. This transition was preceded by a two-dimensional flow rearrangement: a shift of the elliptic point of the recirculation associated with the base flow. Qualitative visual observation indicated that the spatio-temporal structure of the instability was of the form of "Görtler-type" vortices. The "viscoelastic Görtler" scaling presented in Chapter 2 was found to be valid, indicating that the interaction of streamwise stress and streamline curvature was the driving mechanism.

A noteworthy parallel is that the dimensionless temporal period of the driven cavity instability was of order $T_p/\lambda_1(\dot{\gamma}_{Up}) \sim 100$, similar to the period of the temporal instabilities observed in the planar contraction and discussed in §5.3.2. Pakdel and McKinley have indicated that additional quantitative detail on the spatio-temporal structure of the driven cavity instability is forthcoming, allowing for more detailed comparison.

Cylinder in Channel Flow

The transition sequence noted for the cylinder-in-channel flow (Byars, 1996; Özetkin *et al.*, 1997; McKinley, 1991) resembled that observed for the planar contraction; i.e. two-dimensional flow rearrangement followed by a supercritical bifurcation from two-dimensional, steady flow to three-dimensional, steady flow and ultimately transition to three-dimensional, time-dependent flow. Both the spatial and temporal structures of the instabilities were similar to those observed in the planar contraction. The temporal instability in the cylinder in channel flow differed from the instability in the planar contraction in that the vortex pairs moved toward, rather than away from the walls bounding the "neutral" x-dimension.

Viscometric Flows

A "Görtler-type" instability has been observed in viscoelastic Couette cell flow (Larson *et al.*, 1990). The flow underwent a subcritical bifurcation from the base flow to a three-dimensional state (Baumert and Muller, 1995); in contrast, a supercritical bifurcation was observed in the planar contraction.

The behavior of the temporal instability observed in the Couette cell was substantially different from that in the planar contraction. The temporal instability in the Couette cell was a transient phenomenon; the flow eventually adopted a three-dimensional and steady configuration (Baumert and Muller, 1995). In the planar contraction, after onset of the time-dependent instability, the movement of the vortices was at a constant speed, in one direction (from the bounding walls toward the center of the "neutral" x-direction); annihilation of the vortices only occurred at the point where they met, in the center of the flow. In contrast, in the Couette cell, the axial direction was divided into many "cells" in which pairs of vortices were "born", collided, and were destroyed. Furthermore, Baumert and Muller did not mention that for the unstable Couette cell flow the behavior near the walls bounding the axial direction differed from that in the remainder of the gap. In contrast, the bounding walls appeared to play a critical role in the planar contraction, setting the direction of movement of the vortices in, and probably influencing the critical onset value, $Wi_{Up\,T}$, of time-dependent flow.

No evidence of transient nature of the temporal instability in the planar contraction was noted. In the planar contraction the evolution of the flow at a given Wi was either directly from the base flow to the steady and three-dimensional state or to the time-dependent and three-dimensional state. None of the observations indicated that the three-dimensional and steady state was preceded by a transient, time-dependent state. In the 8:1 contraction at $Wi_{Up} = 0.23$, well above the critical value of $Wi_{Up\,T} = 0.17 \pm 0.03$, vortex movement in the x-direction was observed for a total of 3.2×10^3 [s]; the flow did not "settle down" to a steady state. Hence, while time-dependent behavior is a transient response in the case of the Couette cell viscoelastic instability, it is a persistent state distinct from the spatial instability in the case of the planar contraction flow.

"Görtler-like" vortices were also noted in viscoelastic cone-and-plate flow (McKinley *et al.*, 1995). The base flow underwent a subcritical Hopf bifurcation to a time-dependent, three-dimensional state. Unlike for the case of the Couette cell, the time-dependent flow persisted and was not transient. The subcritical Hopf bifurcation noted in cone-and-plate flow may be contrasted with the supercritical bifurcation observed in the planar contraction.

Summary of Viscoelastic Instabilities Observed in Flows with Curved Streamlines

In this Section, the transition sequences for viscoelastic flow through several different geometries have been contrasted with the sequence observed in the planar contraction. A common feature of the complex flows was that two-dimensional flow rearrangement preceded the transition to three-dimensional and/or time-dependent flow. As discussed here and in Chapter 2, the velocity fields after transition had similar spatio-temporal structure; i.e., the form of Görtler vortices. A series of these counter-rotating vortex pairs was spaced along a coordinate axis with no velocity gradient, the "neutral" direction. In all cases, the transitions appeared to be driven by the interaction of streamwise stress with streamline curvature. The "viscoelastic Görtler" scaling (cf. eq. (2.3)) has proven useful in identifying this common mechanism. Of particular interest was the applicability of the "viscoelastic Görtler" scaling to complex flows, such as in the driven cavity and in the planar contraction, which are not amenable to analytical mathematical treatment (e.g., linear stability analysis). For the planar contraction, an empirical power-law relation between the characteristic dimensionless streamline curvature (H/R_c) and a geometric parameter (contraction ratio, H/h) was used.

However, variation in boundary conditions among the flows considered above resulted in distinct differences in the sequence of flow transitions with increasing Wi, the class of bifurcation associated with the transitions, and the temporal structure of the flows after transition. For example, in the planar contraction, the first transition was from two-dimensional, steady to three-dimensional, steady flow, the second from steady to time-dependent flow (for geometries with upstream aspect ratios substantially greater than unity). In contrast, in the axisymmetric contraction and in the cone-and-plate flows, the first transition was from steady to time-dependent flow. Viscoelastic flow in the Couette cell showed an

intermediate time-dependent state, which had long duration but was transient, before ultimate transition to steady-state flow. The viscometric flows in the Couette cell and cone-and-plate geometries exhibited subcritical bifurcations from the base state whereas the complex flows in the abrupt contraction and cylinder-in-channel geometries underwent supercritical bifurcations.

The characterization of instabilities observed in planar contraction flow, along with results of previous investigations, has indicated a common driving mechanism and common spatio-temporal features of transitions in viscoelastic flow. However, substantial work is still required before a unified framework for understanding the nature of transitions induced by the interaction of streamwise elastic stress and streamline curvature can be constructed.

5.5 Future Research Directions

The quantitative experimental results presented and discussed in Sections 5.2 and 5.3 support the concept that the interaction of streamwise stress with streamline curvature induces transition to three-dimensional flow in complex flows, such as in the planar contraction. In this Section, future research is suggested to build on the work presented in this Chapter and address the following issues: (1) more detailed information on the stress-curvature mechanism which drives the transition to three-dimensional flow is required and (2) the influence of three-dimensionality in the base flow, introduced by the wall bounding the "neutral" x-dimension, on the flow transition sequence should be studied further. Both of these avenues of research would use numerical simulation in conjunction with experiments to extend the range of observed variables and accelerate the acquisition of data.

In viscometric flows, application of techniques such as linear stability analysis and energy analysis have improved understanding of the mechanism through which the coupling of the conformation of polymer molecules (modeled as dumbbells) to the macroscopic flow field can induce flow transition. Since flows through abrupt contractions are not amenable to such analytical techniques, a more detailed understanding of the mechanism which drives flow transition will require a numerical approach. The computational simulation of flow transitions from two-dimensional and steady to three-dimensional and/

or time-dependent states in complex flows remains a challenge. However, the increasing availability of computational resources and the development of more efficient and accurate algorithms should make such simulations possible in the near future.

By selectively varying parameters of the constitutive equation in such a simulation, e.g. the modal relaxation times, insight will be gained into the relation between macromolecular structure and instability onset. Specific information not attainable through experiment can be acquired via these simulations. For example, detailed information on the stress field may be obtained for a simulated three-dimensional flow; note that the flow induced birefringence technique (cf. Chapters 2 and 6) is limited to two-dimensional, planar flows. Determination of the class of bifurcation associated with a given flow transition via experimental means is often complicated by the difficulty of obtaining a sufficient number of accurate data points near onset of instability; characterization of the bifurcation is more readily achieved via numerical means. The experimental planar contraction flow system is only *approximately* two-dimensional. The finite upstream aspect ratio affects the flow transition sequence, as discussed in §5.3. In contrast, ideal two-dimensional boundary conditions can be achieved in numerical simulations. Data for a range of boundary conditions, e.g. different contraction ratios, can be acquired much more rapidly by computational than by experimental means. Note that three-dimensional, time-dependent numerical simulations acts as a complement to, not a substitute for, experimental investigation of viscoelastic flow through complex geometries. Specifically, the experimental data presented in this Chapter will play a crucial role in validating the accuracy of numerical simulations.

The experimental results presented in §5.2, and discussed in §5.3 have indicated that the walls bounding the "neutral" x-dimension of the planar contraction geometry can act as an imperfection to the nominally two-dimensional base flow and alter the essential nature of the flow transition sequence. On the one hand, as mentioned in the preceding paragraph, this additional complication can be an impediment to achieving detailed understanding of the mechanism driving the transition from the two-dimensional, steady base flow to the three-dimensional, steady flow. On the other hand, such an imperfection can give rise to a rich array of complex dynamics which present stimulating research opportunities. Consideration of the influence of three-dimensionality in the base flow on the flow

transition sequence is of practical, as well as theoretical, interest. An "expert system", useful for the design and optimization of industrial polymer processes (cf. Chapter 1), must be able to model three-dimensional, time-dependent flows.

The transition from the two-dimensional, steady base flow in the planar contraction is thought to be driven by the interaction of streamwise stress with streamline curvature. This implies that such a transition would be observed in an ideal, two-dimensional planar contraction flow. An imperfection in the form of finite, but large, upstream aspect ratio might modify this transition but would not be expected to change its essential nature. In contrast, the experimental results presented in this Chapter indicate that the upstream aspect ratio, W/2H, plays an essential role in defining the critical conditions for transition from steady to time-dependent flow. Supporting this idea is the observation that the amplitude of the time-dependent oscillation was strongest in the vicinity of the wall bounding the "neutral" x-dimension and weakest near the midpoint of the x-dimension.

The idea that the upstream aspect ratio is an important control parameter for the temporal, but not for the spatial transition indicates that the transition map for viscoelastic flow through a planar contraction of finite upstream aspect ratio is most appropriately represented in a three-parameter space. The upstream Weissenberg number (Wi_{Up}), the upstream aspect ratio (W/2H), and the contraction ratio (H/h) are the independent parameters which determine the flow state of the system and are each associated with a coordinate axis of the space. Figure 5.23 shows a hypothetical transition map in this three-parameter space for flow through the planar contraction which is consistent with the results presented in Sections 5.2 and 5.3. The neutral-stability boundary for the spatial transition from two-dimensional, steady base flow to three-dimensional, steady flow is represented as a two-dimensional surface within this space; for Fig. 5.23 this "spatial transition surface" was assumed to be independent of aspect ratio. The neutral-stability boundary identified with the steady to time-dependent temporal transition is represented as a second surface; for Fig. 5.23 this "temporal transition surface" was assumed to be independent of contraction ratio. The intersection of the two neutral-stability surfaces defines a one-dimensional curve on which a codimension-2 bifurcation occurs.

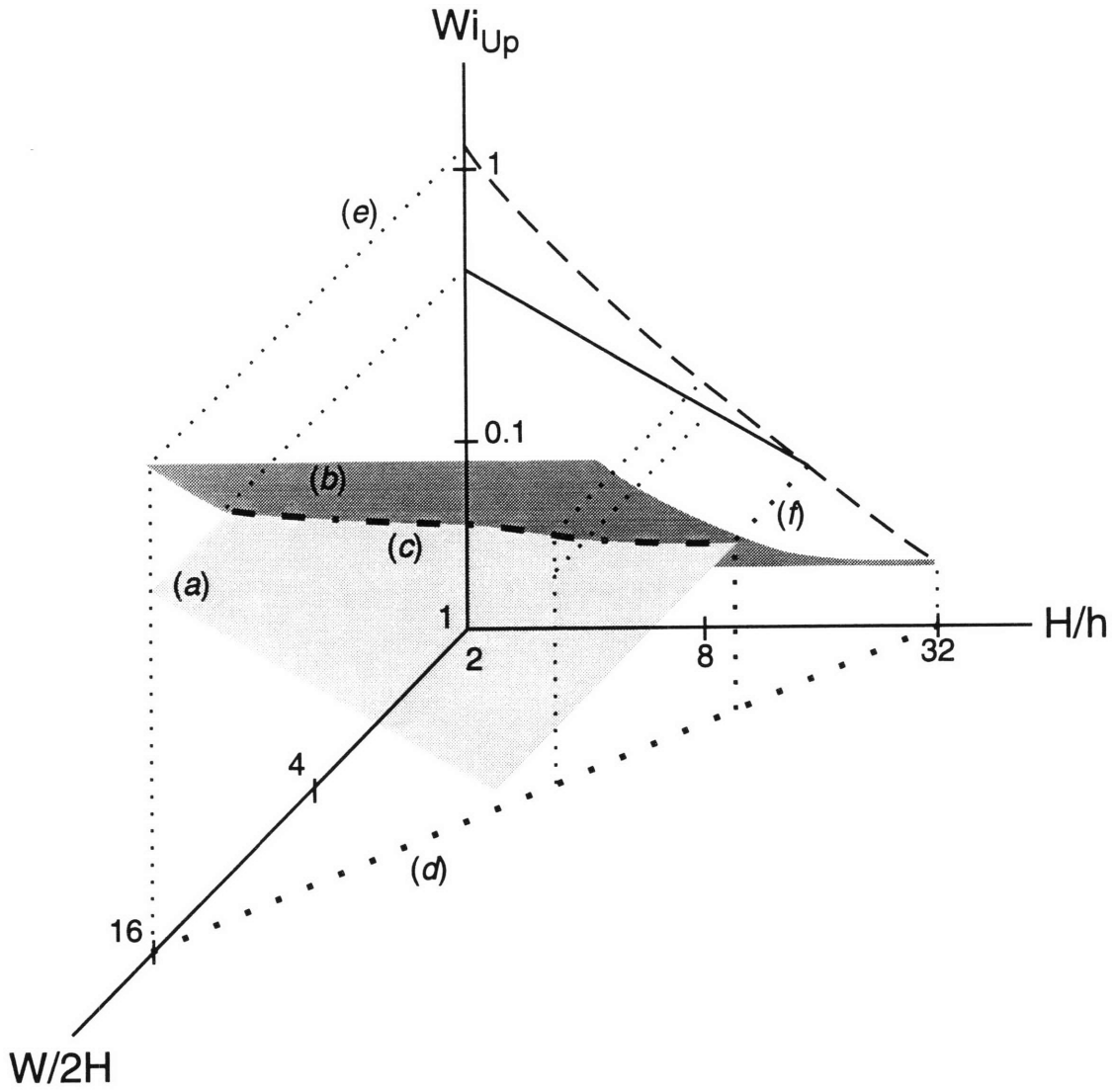

Figure 5.23 Hypothetical representation of flow transition map for the planar contraction in three-parameter space: ((a), light gray plane) neutral-stability surface for spatial transition from two- to three-dimensional steady flow; ((b), dark gray plane) neutral-stability surface for temporal transition from steady to time-dependent flow; ((c), ▬ ▪ ▬) curve for codimension-2 bifurcation at the intersection of the neutral stability surfaces; ((d), ▪▪▪▪▪▪) projection of the experimental subspace onto the W/2H × H/h plane; construction lines indicating the projection onto the Wi_{Up} × H/h plane of the intersection of the experimental subspace with neutral stability surfaces ((e), · · · · · ·) and with the curve representing the codimension-2 bifurcation ((f), ▪ ▪ ▪ ▪ ▪).

In the experiments presented in §5.2 and discussed in §5.3, the upstream aspect ratio, W/2H, and the contraction ratio, H/h, were simultaneously varied. The relation between the two parameters was

$$(W/2H) = \frac{(W/2h)}{(H/h)} \tag{5.10}$$

The *downstream* aspect ratio was constant throughout the experiments and is given as $(W/2h) = 32$. Equation (5.10) defines a two-dimensional "experimental subspace", which can be represented as a surface (invariant along the Wi_{Up} axis) in the three-dimensional transition map. The intersection of the experimental subspace with a given neutral-stability boundary described above is the one-dimensional subset of the boundary which was probed in the experiments presented in §5.2. The projection of the one-dimensional neutral-stability subsets onto the $Wi_{Up} \times H/h$ plane yields the two-dimensional transition map shown in Fig. 5.18a; similarly, projection onto the $Wi_{Up} \times W/2H$ plane yields Fig. 5.18b.

The concept of a three-parameter transition map discussed above is consistent with the experimental results presented in this Chapter but admittedly speculative. Moreover, the form of the full three-parameter transition map outside of the "experimental subspace" defined by eq. (5.10) can only be supposed. Nevertheless, the concept of a three-parameter transition map provides guidance for the design of future experiments to conclusively define the form of said map. Development of a complete three-parameter transition map exclusively by experimental means would be extremely time consuming; the number of possible combinations of the independent Wi_{Up}, H/h, and W/2H parameters which would have to be probed is daunting. Three-dimensional, time-dependent numerical simulation could facilitate the development of the map. Specifically, the flow state would be rapidly determined via numerical means at a number of points in the (Wi_{Up}, H/h, W/2H) parameter space; the neutral stability surfaces would be located. Experiments, performed for a much smaller number of points in parameter space, would be used to check the accuracy of the simulations. Certain regions in the three-dimensional parameter space of particular interest for experimental study may be identified; two sets of experiments which would answer specific questions are described here.

1) A set of experiments could be conducted to verify that the neutral-stability surface for the spatial transition (from the two-dimensional base state to three-dimensional, steady flow) is only weakly dependent on the upstream aspect ratio. Specifically, the $Wi_{Up\ S}$ would be identified for a set of upstream aspect ratios while holding the contraction ratio constant. This would be achieved by simultaneously varying the upstream and downstream channel half-heights.

2) In §5.3, it is noted that a codimension-2 bifurcation is likely to exist in the vicinity of the point in parameter space with coordinates $Wi_{Up} = 0.08$, $H/h = 15$, and $W/2H = 2.1$. The value of the upstream aspect ratio, W/2H, is interesting in that approximately one cycle of the spatial oscillation could "fit into" the half-width of the geometry, W/2. It would be interesting to determine whether the one-dimensional curve defining the location of the codimension-2 bifurcation lies entirely within (or near to) the plane in parameter space defined by $W/2H = 2$.[6] For the set of experiments, the critical Wi_{Up} for the spatial and temporal transitions would be determined for different contraction ratios, H/h, while holding the upstream aspect ratio constant at $W/2H = 2$. This would be achieved by varying the downstream half-height, h, for a fixed upstream half-height, H.

In addition to these sets of experiments, designed to map the transitions in parameter space, detailed characterization of the flow dynamics should be conducted for parameters in the vicinity of the codimension-2 bifurcation. Of particular interest is whether the dynamics are essentially different from behavior observed on the neutral stability surfaces where the bifurcation has codimension-1. For example, the flow could exhibit complex dynamics such as quasiperiodicity or chaos for control parameters in the vicinity of the codimension-2 bifurcation (Guckenheimer and Holmes, 1983).

---

6. Note that because of the choice of the form of the two hypothetical neutral-stability surfaces, shown in Fig. 5.23, their intersection, i.e. the curve associated with the codimension-2 bifurcation, does not have W/2H constant. It must be emphasized that Fig. 5.23, although consistent with the observations presented in §5.2, is a hypothetical representation intended only to facilitate visualization of the concepts discussed in this Section.

Chapter 6

Measurement of Centerline Stress and Velocity Fields and Comparison with Predictions of Viscoelastic Constitutive Models

This Chapter presents the measurements of the stress and velocity fields of fluid flowing along the centerline of the planar contraction geometry. The experimental data are used to develop a quantitative understanding of the elongational response of a viscoelastic fluid in a transient shearfree flow. Limitations on the use of the test flow to evaluate the accuracy of constitutive models are elucidated. In particular, it is shown that the centerline flow in the planar contraction only probes the linear viscoelastic response of a fluid. Limitations of the flow-induced birefringence (FIB) technique for acquisition of stress-field information in the planar contraction flow also are discussed.

A brief review of the theoretical understanding of polymer molecular extension and associated nonlinear behavior in elongational flows is given in §6.1. Constitutive models used in this Chapter are briefly described and some aspects of the application of the flow-induced birefringence measurement technique discussed. In §6.2 the experimental methods used in this Chapter are presented. In particular, experimental conditions were selected to extend the range of the parameters of total Hencky strain and Weissenberg number which have been attained in previously published investigations. In §6.3, the kinematic structure of the centerline flow is discussed in context of the effect on FIB measurements. In particular, nonidealities and transitions in the flow are indicated and used to set limits on where the FIB measurement may be directly interpreted in terms of stress. Results of the investigation are presented in §6.4. The experimentally determined values of the centerline velocity and stress fields are given and compared with predictions of linear and nonlinear constitutive models. In §6.5, it is shown that the form of the strain-rate profile of flow on the centerline of the planar contraction is only capable of exciting a weakly nonlinear viscoelastic response. The influence of the elongational response of the fluid on the streamwise stress away from the centerline, and consequently on the critical condition for transition from the base to three-dimensional flow is considered in §6.6.

Conclusions of the investigation presented in this Chapter and broader implications for the study of elongational material properties of viscoelastic fluids are discussed in §6.7.

6.1 Theoretical Background: Configurational State of Polymer Molecules in Elongational Flows

In this Section, theoretical background is provided which is useful in understanding the results presented and discussed in Sections 6.4 and 6.5. In §6.1.1 a physical description of polymer molecular extension in elongational flow is given; specific phenomena represented by the models used in Sections 6.4 and 6.5 are described. In §6.1.2 a brief description and contrast of the behavior of linear and nonlinear constitutive models in the context of planar elongational flow is given. In §6.1.3 the relation of the flow-induced birefringence of polymer solutions to configurational states of the polymer molecules attained in elongational flows is discussed.

6.1.1 Polymer Extension in Elongational Flow

Previous theoretical and experimental work provides a basis for understanding the response of a polymer molecule to an elongational flow field. The nature of the response is dependent on the state of entanglement of the polymer molecules. The better understood case of dilute solutions is discussed first in this Section; the case of concentrated solutions and melts is then addressed. The response of semidilute solutions, such as the 0.30 wt% PIB in PB test fluid used in this study, is less well understood than the limiting cases of dilute and concentrated solutions. Nevertheless, semidilute solutions are expected to exhibit behavior intermediate between the dilute and concentrated solution responses.

For a dilute solution, the configuration of a polymer molecule is determined solely by its interaction with the flow field of a surrounding Newtonian solvent (Larson, 1988). At equilibrium, the mean configurational state of the molecule resembles a ball. At low elongational strain rates, the molecule is slightly perturbed, specifically it deforms into a prolate ellipsoid with the long axis oriented along the principal axis of the rate-of-strain tensor. When the molecule becomes progressively more distorted with increasing elongational strain rate but retains an essentially ellipsoidal form, the molecule is described as

being in the "coiled" state. At a critical strain rate there is a change in response of the molecule. As the molecule becomes more extended, the entropic restoring force which acts to the return the molecule to its equilibrium "ball" state increases. However, the velocity difference between the ends of the long axis of the ellipsoid also increases as $\Delta v_z = \dot{\varepsilon} L_z$, where L_z denotes the length of the long axis of the ellipsoid which represents the polymer, $\dot{\varepsilon}$ is the strain rate, and Δv_z indicates the velocity difference. The increase in the velocity difference results in a corresponding increase in the hydrodynamic force which acts to stretch the ellipsoid. Once the critical strain rate is exceeded, the hydrodynamic forces dominate over the entropic forces and the molecule elongates to a "stretched" state in which the long axis of the ellipsoid approaches the contour length of the polymer molecule (de Gennes, 1974; Larson, 1988). The value of the critical strain rate and the precise configuration of a molecule in the "stretched" state is dependent on details of the constitutive model. The simple Oldroyd-B model represents the polymer molecule as two beads connected by a linear (Hookean) spring; this representation is often termed a Hookean "dumbbell". Each of the "dumbbells" are surrounded by Newtonian solvent; this "dumbbell solution" is dilute, i.e., the "dumbbells" do not interact with each other. Because of the linearity of the entropic restoring ("spring") force, once the critical strain rate is exceeded, the molecule will stretch indefinitely.[1] More realistic models recognize that the restoring force is nonlinear. The nonlinear restoring force in the FENE-P model ensures that the extension of the "dumbbell" is less than the finite contour length of the polymer chain. Specifically, as the polymer molecule approaches a fully extended configuration, the nonlinearity in the restoring force becomes more pronounced; attainment of a fully stretched configuration would require imposition of an infinite force (Bird *et al.*, 1987b).

More sophisticated dilute solution models represent the polymer molecule more realistically than as a "dumbbell". An example is consideration of the effect of intramolecular shielding of the polymer chain in the interior of the molecule from the flow field. De Gennes (1974, 1979) theoretically investigated the transition of a polymer molecule from

1. For the upper convected Maxwell model, the constitutive equation has the same for m as that of Oldroyd-B, but the contribution of the solvent to the total stress tensor is excluded. Note that a constitutive model with more that upper convected Maxwell mode, plus a solvent mode, is referred to as a "multimode upper convected Maxwell plus solvent" or simply a "multimode upper convected Maxwell" model.

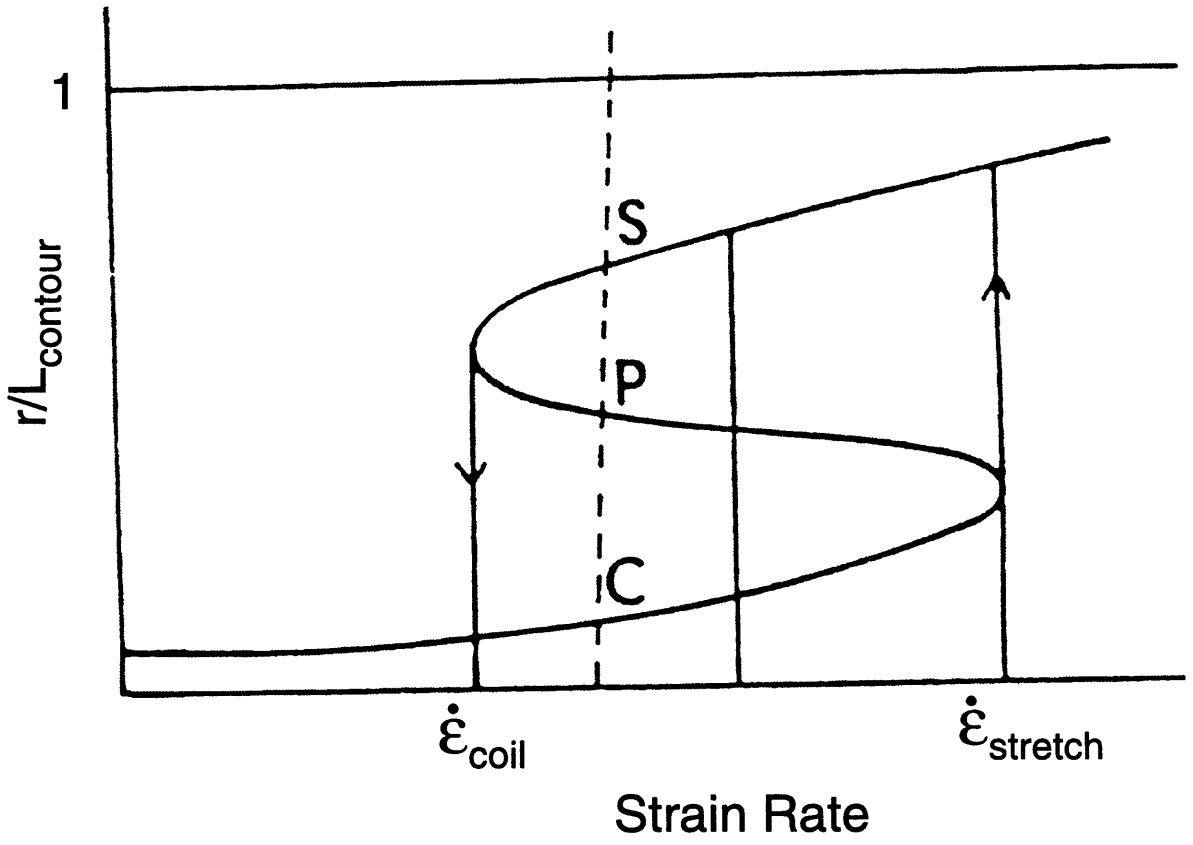

Figure 6.1 Coil-stretch transition in an elongational flow. The reduced extension, $r/L_{contour}$, is shown as a function of the strain rate. C indicates the coiled state of the molecule, S, the stretched state, and P, an unstable state. $\dot{\varepsilon}_{stretch}$ indicates the critical strain rate at which the molecule abruptly unravels to the stretched state. $\dot{\varepsilon}_{coil}$ indicates the critical strain rate at which the molecule suddenly collapses to the coiled configuration (*Reproduced from* (de Gennes, 1974)).

the "coiled" to the "stretched" state with such a model. Specifically, in the coiled state, only the relatively small fraction of monomers lying within the hydrodynamic penetration depth of the surface are affected by the flow field. Therefore, the coil only gradually becomes elongated with increasing strain rate (cf. Fig. 6.1). However, as the molecule is extended, a greater fraction of the polymer molecule is exposed to the flow field. Eventually, at a critical strain rate, $\dot{\varepsilon}_{stretch}$, the molecule abruptly unravels and the "stretched" state is attained. The model predicts hysteretic behavior: when the strain rate is subsequently decreased the molecule remains in the "stretched" state, since essentially all of the monomer units comprising the chain are exposed to the flow field. Only when the strain rate drops below a second critical value, $\dot{\varepsilon}_{stretch} < \dot{\varepsilon}_{coil}$, do entropic effects overwhelm hydrodynamic effects so that the molecule abruptly collapses to the coiled configuration. However, as discussed in Sections 6.4 and 6.5, for the fluid/flow system investigated here, the high molecular weight polymer molecule does not become highly extended. Consequently, such hydrodynamic shielding and hysteretic phenomena are not considered further.

One must recognize that the above descriptions are for homogeneous flow fields for which the duration of the experiment is sufficiently long that the molecule can attain its steady-state configuration. If the strain rate exceeds the critical value, but the duration for which the molecule is exposed to the flow is short, the molecule will not have time to extend very far. In the limiting case, for very high strain rate, the entropic restoring force will be negligible when compared with the hydrodynamic force on the molecule (e.g., on the "beads" of the "dumbbell"). Hence the ends of the molecule are convected away from each other by the fluid, with essentially no "slip" between the polymer (bead) and the fluid. For a finite time, the extension of the molecule will then be

$$L_z(t)/\sqrt{\langle r^2\rangle_0} = \exp(\dot{\varepsilon}\Delta t), \tag{6.1}$$

where Δt denotes the elapsed time, $\sqrt{\langle r^2\rangle_0}$ is the equilibrium root-mean-square (r.m.s.) end-to-end length of the dumbbell, and $L_z(t)$ represents the length after being convected with the fluid. This idealized picture allows an estimate to be made of the minimum Hencky strain which a polymer in solution must undergo to become fully elongated from

an initial coiled state; specifically $\varepsilon_{est} = \ln(L_c/\sqrt{\langle r^2 \rangle_0})$, where L_c is the contour length of the fully extended molecule and $\sqrt{\langle r^2 \rangle_0}$ is the length for the equilibrium configuration as described in §4.1.2. From the ratio of these limiting lengths, for the PIB in PB fluid used in this study (cf. eq. (4.5)), one obtains $\varepsilon_{est} = \ln(80) = 4.4$. This provides only a simple estimate. For cases where the magnitude of the restoring force is substantial compared with the hydrodynamic force, there will be "slip" between the "beads" and the surrounding solvent, so that the extension of the molecule for a given duration of time, Δt, will be less than prescribed by eq. (6.1) (Bird *et al.*, 1987b). Other factors which may affect the Hencky strain required to elongate the molecule include the effects of hydrodynamic shielding discussed above or the formation of local "kinks" and entanglements during the stretching process. Such "kinks" could retard the rate at which the polymer unravels, lowering the required Hencky strain below ε_{est}. Alternately, "knots" could prevent the polymer molecule from ever extending fully; the smaller maximum extensible distance could result in the required Hencky strain being below ε_{est} (Hinch, 1994; Shaqfeh, 1996). A polymer molecule exposed to a flow field for a short time will be only slightly perturbed from the equilibrium configuration, even if the strain rate is much greater than the critical value. Realization of the importance of the duration for which the molecule is exposed to the flow field, in conjunction with the strain rate, in determining extension of the molecule (Ferguson and Hudson, 1993; Malkin and Petrie, 1997) is essential to interpretation of the results of the experiment discussed in Sections 6.4 and 6.5.

Constitutive equations which accurately model concentrated (including melts) and semidilute solutions must consider interactions between the polymer molecules. The reptation concept of de Gennes has found widespread acceptance (de Gennes, 1971; Doi and Edwards, 1978; Doi and Edwards, 1979; Larson, 1988); the theory maintains that the polymer molecules surrounding a given molecule in a melt form an enclosing "tube". The molecule in the tube has anisotropic mobility; it can more easily move back and forth along the contour of the tube than side to side. Incorporation of anisotropic mobility in a constitutive model leads to prediction of the experimentally observed shear thinning of the material functions (cf. Chapter 4).

The Giesekus model has proved useful in realistically describing the behavior of semidilute and concentrated solutions (Giesekus, 1982b; Giesekus, 1982a; Bird *et al.*, 1987a).

The model incorporates the concept of anisotropic drag and Brownian motion, which is at the core of de Gennes's (1971) reptation theory. As presented in §4.3.4, the Giesekus model has the advantage of being relatively simple in form; in addition to the zero-shear rate relaxation time and viscosity, there is only one adjustable parameter, α, which describes the anisotropic mobility. In addition to predicting thinning of the shear-flow material functions, the Giesekus model predicts an upper bound to the steady-state elongational viscosity for all strain rates. This bound is a consequence of the anisotropic drag, rather than finite extensibility of the chain. Specifically, the drag along the contour of the polymer chain is less than the drag perpendicular to the contour. Consequently, there is enhanced "slip" between the polymer molecule and the surrounding medium as the segments comprising the polymer chain become aligned in the flow direction. This results in an upper bound on the elongational viscosity associated with the molecule (Bird *et al.*, 1987a; Bird *et al.*, 1987b), without inclusion of a nonlinear spring force.

The Bird-DeAguiar model, which does simultaneously incorporate the phenomena of finite chain extensibility and anisotropic mobility, is often referred to as an "encapsulated dumbbell" model (Bird and DeAguiar, 1983; DeAguiar, 1983). Since the polymer molecules were found not to become highly extended in the transient elongational flow on the centerline of the planar contraction, consideration of the finite extensibility of the chain via use of the Bird-DeAguiar model was not necessary for the investigation presented in this Chapter.

6.1.2 Contrast of Linear, Quasilinear, and Nonlinear Constitutive Models

Linear, quasilinear, and nonlinear constitutive models have been described in §4.3. Essential differences in the types of flow to which these models may be appropriately applied are reiterated here. The differing responses of linear, quasilinear, and nonlinear models to steady-state and start-up of planar elongational flow are contrasted.

Linear models can accurately describe flows in which a given fluid element has "memory" of only an infinitesimal amount of strain experienced. Such restricted "memory" can arise in two limiting types of flow. The amount of total strain achieved in the flow may be low; this is the case in the oscillating, small-amplitude shear flow in the cone-and-plate

geometry discussed in §4.2.1. Alternately, if the flow is by some measure "slow" in contrast with the relaxation time or "memory" of the fluid, even if the total strain is high, the strain "remembered" by the fluid at any given instant will be small. Linear constitutive models have several essential features in common. In a transient flow, the profile of a rheological quantity (e.g. elongational viscosity) plotted as a function of the dimensionless time, t/λ_1, is independent of the characteristic strain rate of the flow. At long times, the Newtonian limit of the rheological quantity is approached. With regard to steady shearfree flows, "elongational thickening" is not observed; the elongational viscosity conforms to the Newtonian limit (cf. § 4.2.2) for all strain rates.

Quasilinear models, such as Oldroyd-B, may be applied to flows in which a fluid element does have "memory" of a finite amount of strain. To incorporate accurately this feature in a frame-invariant manner, convected derivatives are used in the differential formulation of a quasilinear model instead of the material derivatives used for the linear models.[2] In contrast with a linear model, the profile of a rheological quantity as a function of dimensionless time in a transient flow *can* depend on strain rate. As mentioned in §6.1.1, quasilinear models can predict features of the stress response exhibited by real viscoelastic fluids in flows in which a fluid element "remembers" a finite amount of strain. These features include induction of normal stresses by shear flows and, in steady shearfree flows, "thickening" of the elongational viscosity above the Newtonian limit. However, the accuracy with which quasilinear models can model viscoelastic fluid flows is limited; e.g., above a critical strain rate, a transient elongational viscosity which is unbounded and continuously increases with time is predicted.

Nonlinear models can more accurately represent the response of viscoelastic materials to flows than quasilinear models. There are various aspects of the response of a polymer molecule to a flow in which the nonlinearity can be incorporated; e.g., a nonlinear entropic ("spring") force can relate extension of the molecule to the imposed force (as in the case of the FENE-P model), or a nonconstant, anisotropic "drag coefficient" can relate the imposed hydrodynamic force to the flow field (as in the case of the Giesekus model). The inclusion of nonlinear terms allows the models to make more realistic predictions of the

2. Note that when the material derivative term in the linear Jeffries model is replaced by a convected derivative term, the Oldroyd-B (also called "convected Jeffreys") model is obtained.

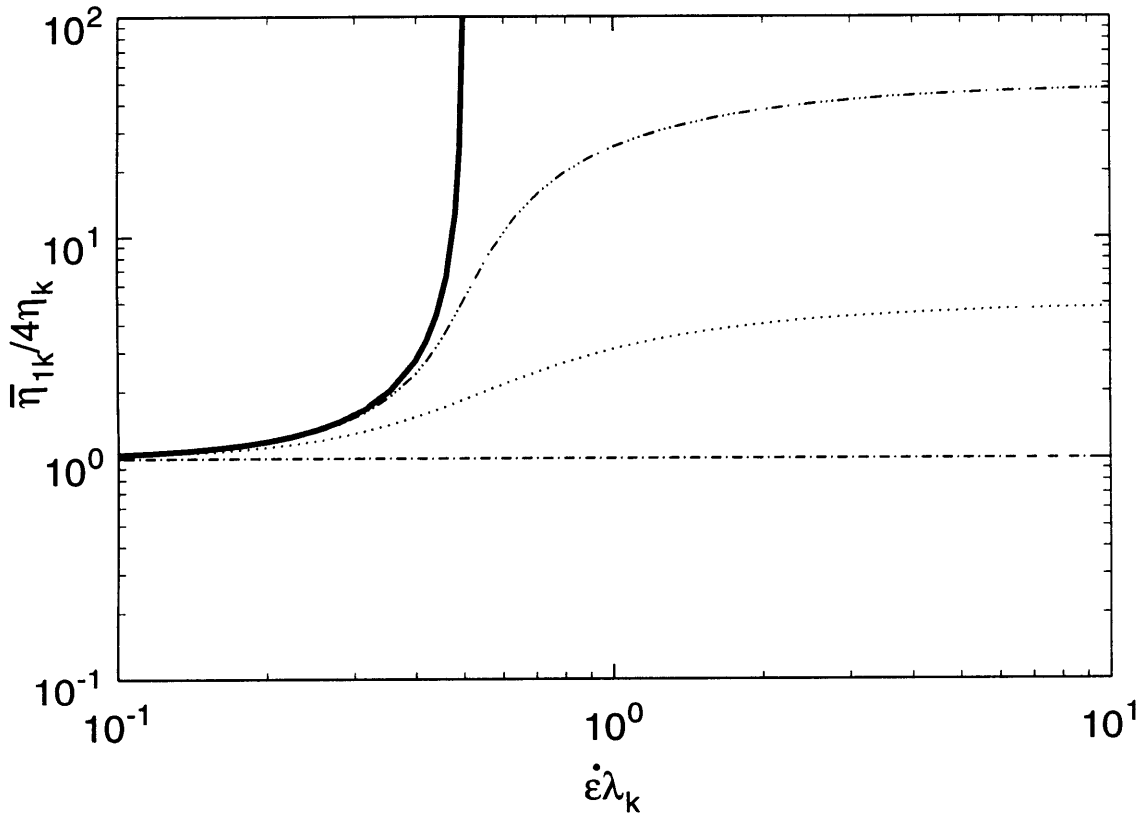

Figure 6.2 Plots of the first planar elongational viscosity made dimensionless with four times the viscosity for a given mode of a constitutive model, $\bar{\eta}_{1k}/4\eta_k$, as a function of the strain rate made dimensionless with the relaxation time of the mode, $\dot{\varepsilon}\lambda_k$. (▬▬) upper convected Maxwell model. Plots are shown of the Giesekus modes with different values of the anisotropy parameter:(– --- –) $\alpha_k = 0.01$; (·····) $\alpha_k = 0.1$; (– - –) $\alpha_k = 0.5$. The prediction of the linear Maxwell model superposes on that of the Giesekus mode with $\alpha_k = 0.5$.

stress response of a viscoelastic fluid to a flow. As mentioned in §6.1.1, both the Giesekus and the FENE-P models predict a bounded transient elongational viscosity for all strain rates.

The differing responses of representative linear, quasilinear, and nonlinear constitutive models to a shearfree steady planar elongational flow is shown in Fig. 6.2. Specifically, the steady-state elongational viscosity of the k^{th} mode of a given model, made dimensionless with four times the viscosity, $\bar{\eta}_{1k}/4\eta_k$, is plotted as a function of the strain rate made dimensionless with the relaxation time associated with the k^{th} mode, $\dot{\varepsilon}\lambda_k$. On Fig. 6.2 is indicated the response of a mode of a linear Maxwell model, a mode of an upper convected Maxwell model, and three different modes associated with a Giesekus model. Each of the Giesekus modes has a different value of the anisotropy parameter α_k. Recall that the upper convected Maxwell model can be viewed as a limiting case of the Giesekus model with $\alpha_k \to 0$.

As mentioned above, the linear Maxwell model predicts $\bar{\eta}_1/4\eta = 1$, the Newtonian limit, for all strain rates. In contrast, the upper convected Maxwell model predicts $\bar{\eta}_1/4\eta = 1$ only in the limit $\dot{\varepsilon}\lambda_1 \to 0$. In physical terms, for these low strain rates, the rate at which a fluid element accumulates strain is sufficiently slow that the polymer molecules "forget" all but the most recently experienced infinitesimal strain; the flow is said to be in the linear viscoelastic limit. As the strain rate increases from zero, the elongational viscosity rises above the prediction of the linear Maxwell model; this deviation is associated with the convected derivative in the quasilinear upper convected Maxwell model which has replaced the material derivative in linear Maxwell. In physical terms, a fluid element accumulates strain sufficiently fast enough that stress continually accumulates with strain, despite the fact that the polymer molecules "forget" strain experienced far in the past. The elongational viscosity predicted by the upper convected Maxwell model increases monotonically until a critical strain rate $\lambda_1\dot{\varepsilon}_{crit} = 1/2$ is reached. At this critical strain rate the predicted elongational viscosity is undefined; from a time-dependent perspective, as long as a fluid element is strained, the stress will increase exponentially with the accumulated strain. In the context of the Oldroyd-B "dumbbell" model (which is identical to the upper convected Maxwell model with an additional Newtonian solvent term), this is a consequence of the linear, Hookean "spring" which connects the "beads"

and the isotropic, fixed value of the "drag coefficient" of the "beads". For strain rates greater than the critical value, $\lambda_1\dot{\varepsilon} > 1/2$, aphysical, negative elongational viscosities are predicted.

For low to intermediate strain rates, the various modes of the Giesekus model display a similar response as the upper convected Maxwell model. As the critical strain rate is approached, there is a sudden increase in the steady-state elongational viscosity of the Giesekus mode with strain rate. This increase indicates the domination of hydrodynamic drag forces over entropic forces, which results in unraveling of the polymer molecules. Note that the increase in transient elongational viscosity with strain rate exhibited by the Giesekus mode is less than that of the upper convected Maxwell model; the Giesekus modes diverge from the upper convected Maxwell model at high strain rates. From a physical perspective, viewing the polymer molecule as a "dumbbell", at the point where the models diverge, the "dumbbell" has been sufficiently extended that the nonconstant, anisotropic "drag coefficient" of the beads comes into play, which restricts the extension of the "dumbbell" to a finite value.

The steady-state value of the elongational viscosity predicted by the Giesekus model is bounded for all shear rates; in particular, the limiting value of the Trouton ratio at high strain rates is set by the anisotropy parameter[3] as $\lim_{\dot{\varepsilon}\lambda_k \to \infty} \bar{\eta}_{1k}/4\eta_k = 1/2\alpha_k$. One may note that the concept of a critical strain rate may also be applied to the multimode form of the Giesekus model. One simply considers whether the strain rate is above the critical value, $\dot{\varepsilon}_{crit,\,k}$, for each mode having a characteristic relaxation time, λ_k, to determine whether the nonlinear response is excited for that particular mode.

The stress-growth response of the linear Maxwell, the quasilinear upper convected Maxwell, and the nonlinear Giesekus models to start-up of planar elongational flow is illustrated in Fig. 6.3 for several different dimensionless strain rates, $\dot{\varepsilon}\lambda_k$; note that for each of the Giesekus modes $\alpha_k = 0.01$. The dimensionless response time of the linear Maxwell model is independent of $\dot{\varepsilon}\lambda_k$; 63% of the ultimate value of the elongational vis-

3. Note that for the Giesekus constitutive equation to be physically meaningful one must have $0 \le \alpha \le 1/2$. In the limit $\alpha = 0$, the Giesekus model reduces to the upper convected Maxwell model. The upper limit is set by the fact that in steady shear flow, for $\alpha > 1/2$, the steady-state shear stress, τ_{zy}, plotted as a function of the shear rate $\dot{\gamma}_{zy}$, will exhibit an aphysical maximum for finite $\dot{\gamma}_{zy}$ (Giesekus, 1982a).

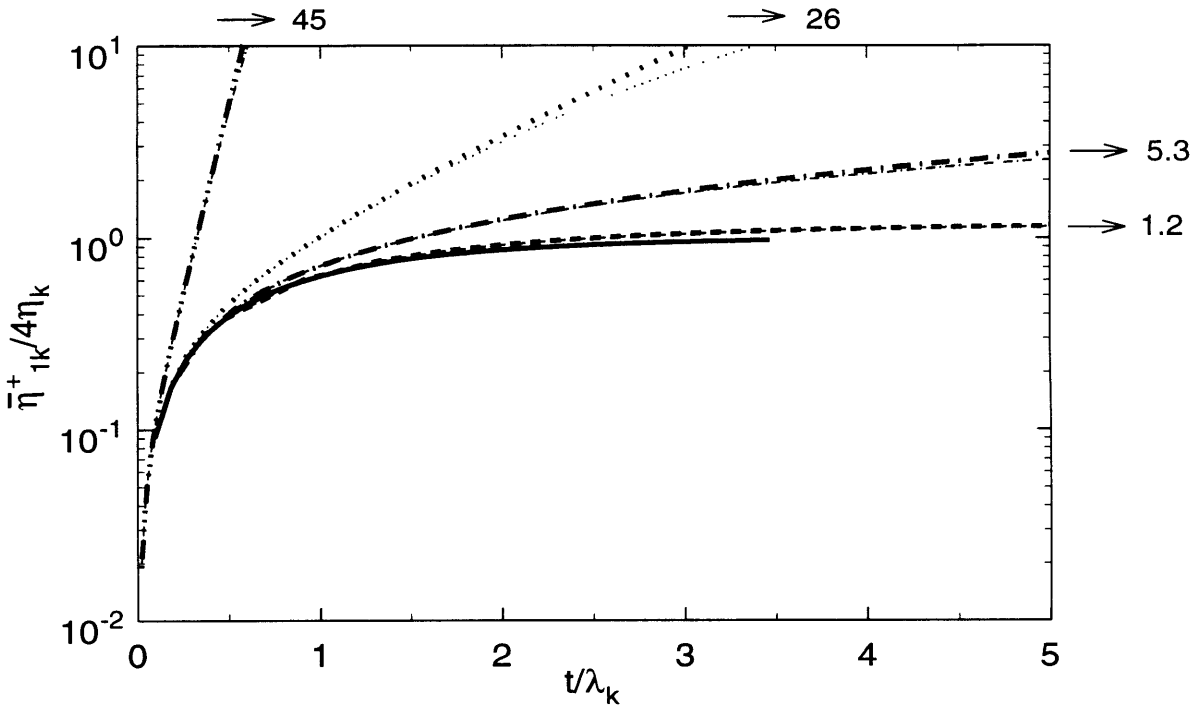

Figure 6.3 Plots of the stress-growth response of the linear Maxwell (thick solid line, ——), upper convected Maxwell (thick dashed lines), and Giesekus (thin dashed lines) models to start-up of planar elongational flow. The dimensionless transient first planar elongational viscosity, $\bar{\eta}^{+}_{1k}/4\eta_k$, is given as a function of the dimensionless time, t/λ_k. For the upper convected Maxwell and Giesekus models plots are shown for different values of dimensionless strain rate: (- – – -) $\dot{\varepsilon}\lambda_k = 0.2$; (– - –) $\dot{\varepsilon}\lambda_k = 0.5$; (· · · · · ·) $\dot{\varepsilon}\lambda_k = 1$; (– --- –) $\dot{\varepsilon}\lambda_k = 5$. For each of the Giesekus modes $\alpha_k = 0.01$; limiting values of $\bar{\eta}^{+}_{1k}/4\eta_k$ as $t/\lambda_k \to \infty$ are indicated.

cosity is achieved at $t/\lambda_k = 1$. For short times or low strain rates (cf. the upper convected Maxwell prediction for $\dot{\varepsilon}\lambda_k = 0.2$) the prediction of the upper convected Maxwell model is close to the prediction of the linear Maxwell model. In the first limit, the polymer molecule does not have sufficient time to extend far from its equilibrium conformation, even if the strain rate is high. In the second limit, the low strain rate results in even the ultimate conformation at $t/\lambda_k \to \infty$ being only a mild perturbation from the equilibrium state, as discussed in the context of steady planar elongational flow above. When the conditions of sufficiently long time and sufficiently high strain rate are met, the polymer molecule "recalls" a finite amount of strain so that the linear viscoelastic limit does not apply and the predictions of the upper convected Maxwell and linear Maxwell models diverge; the polymer molecule is stretched from the equilibrium configuration.

At strain rates substantially lower than the critical value the prediction of the Giesekus model is close to that for the upper convected Maxwell model for all times (for $\dot{\varepsilon}\lambda_k = 0.2$ the predictions of the two models nearly superpose in Fig. 6.3); this is expected from comparison of steady-state values (cf. Fig. 6.2) which indicate that the "molecules" which each model represents only become mildly stretched. As the strain rate is increased to approach, but remain less than the critical value, $\dot{\varepsilon}\lambda_k \to 1/2$, the difference in the ultimate values predicted by the Giesekus and upper convected Maxwell models increases and the dimensionless time interval required to observe divergence of the model predictions decreases. The polymer molecule represented by the Giesekus model is stretched faster so that nonlinear effects manifest themselves sooner. As the strain rate is increased beyond the critical value, this trend of divergence of the models at ever earlier dimensionless times continues (cf. the predictions for $\dot{\varepsilon}\lambda_k = 0.5$, 1, and 5 in Fig. 6.3). As discussed above, the steady-state solution for the upper convected Maxwell model becomes aphysical when the critical strain rate is exceeded. However, the transient solution can be calculated even for $\dot{\varepsilon}\lambda_k > 1/2$, since when the "dumbbell" is stretched for a finite time, its extent is finite.

Figure 6.4 also compares the response to start-up of elongational flow exhibited by the linear Maxwell, the quasilinear upper convected Maxwell, and the nonlinear Giesekus models; the first planar transient elongational viscosity is plotted as a function of dimensionless time. For each of the models, the dimensionless strain rate is held fixed,

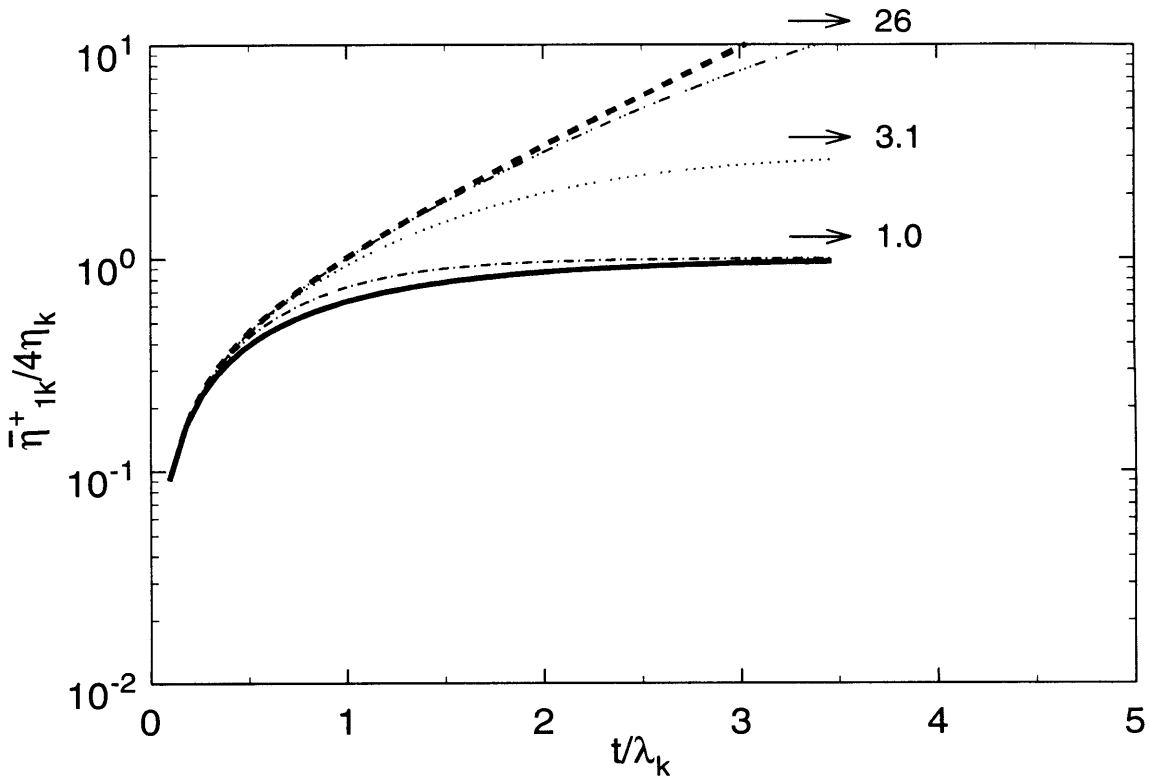

Figure 6.4 Plots of the stress-growth response of the linear Maxwell (thick solid line, ▬▬), upper convected Maxwell (thick dashed line, ▬ ▬ ▬), and Giesekus (thin dashed lines) models to start-up of planar elongational flow. The dimensionless transient first planar elongational viscosity, $\bar{\eta}^+_{1k}/4\eta_k$, is given as a function of the dimensionless time, t/λ_k. For each of the models $\dot{\varepsilon}\lambda_k = 1$. Each Giesekus mode has a different value of the "anisotropy parameter": (– --- –) $\alpha_k = 0.01$; (· · · · · ·) $\alpha_k = 0.1$; (– – –) $\alpha_k = 0.5$. Limiting values of $\bar{\eta}^+_{1k}/4\eta_k$ as $t/\lambda_k \to \infty$ are given for the predictions of the Giesekus model.

$\varepsilon\lambda_{1k} = 1$. As considered above, for short times, the prediction of the upper convected Maxwell model is similar to that for linear Maxwell; at longer times, the models diverge. The predictions of the Giesekus model superpose on the upper convected Maxwell prediction for a certain interval of time, and then diverge. For low values of the anisotropy parameter, the prediction of the Giesekus model conforms to that of the upper convected Maxwell model for a long time interval. In physical terms, the molecule must become greatly extended before nonlinear effects become significant. Also recall that in the limit $\alpha_k \to 0$, the Giesekus model reduces to the upper convected Maxwell model. As the anisotropy parameter is increased, nonlinear effects manifest themselves earlier and the upper convected Maxwell and Giesekus models diverge at shorter time intervals. In the limit $\alpha_k = 0.5$ the prediction of the Giesekus model remains close to (but does not exactly superpose on) the linear Maxwell model for all time. This is expected since the steady-state value of the Giesekus model in this limit is the same as that of the linear Maxwell model, $\bar{\eta}_{1k}/4\eta_k = 1$.

Figures 6.5a-d shows the response of the linear Maxwell, quasilinear upper convected Maxwell, and nonlinear Giesekus models to start-up of planar elongational flow in terms of the dimensionless transient first planar elongational viscosity, $\bar{\eta}^{+}_{1k}/4\eta_k$, plotted as a function of the Hencky strain experienced by a fluid element, ε. Graphs for different values of $\dot{\varepsilon}\lambda_k$ are shown. Figure 6.5 indicates that at low strains, $\varepsilon < 1$, regardless of the value of $\dot{\varepsilon}\lambda_k$, the prediction of the upper convected Maxwell model is close to that of the linear Maxwell model. For strain rates at or above the critical value, $\dot{\varepsilon}\lambda_k \geq 1/2$ (cf. Figs. 6.5b-d), a fluid element must experience a Hencky strain $\varepsilon \gtrsim 1$ before prediction of the nonlinear model diverges substantially from that of the linear model; e.g., $\eta_{Giesekus}/\eta_{LinMax} \sim 2$ for $\varepsilon = 1$. Referring back to Fig. 6.4, note that the criterion of an Hencky strain of order unity for the prediction of the upper convected Maxwell model to exceed that of the linear Maxwell model is insensitive to the value of the anisotropy parameter, α_k, when $\dot{\varepsilon} \geq \dot{\varepsilon}_{crit}$ and $\alpha_k < 0.5$. Conversely, if the steady-state elongational viscosity predicted by the Giesekus model is approximately the same as that predicted by the linear Maxwell model, the transient elongational viscosity profiles will be similar for all times or Hencky strains. This is evident in Fig. 6.5a where $\dot{\varepsilon}\lambda_k = 0.2$ and in Fig. 6.4 for $\alpha_k = 0.5$. The above findings are consistent with the concept that a flow may be con-

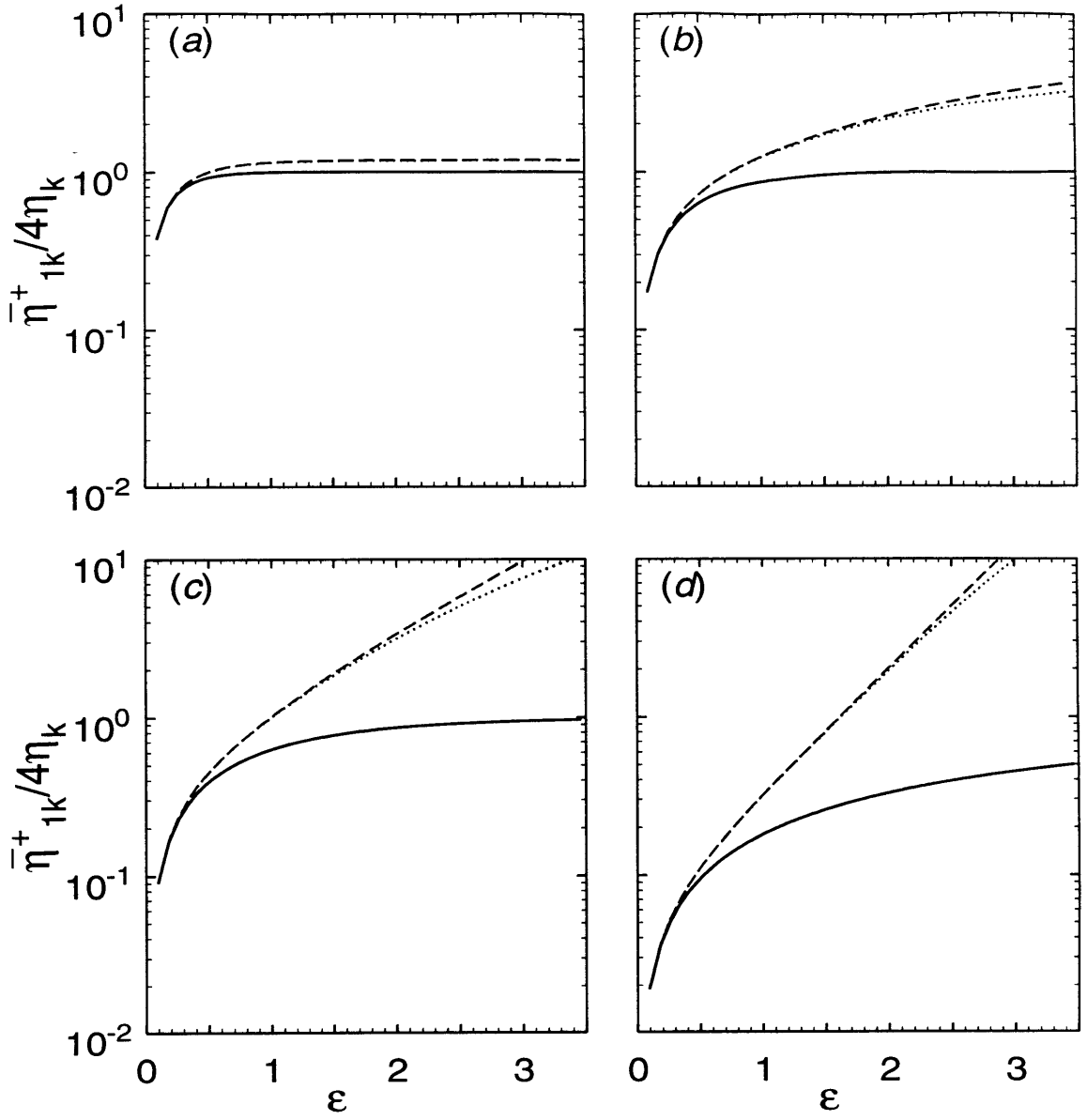

Figure 6.5 Plots of the stress-growth response of the linear Maxwell (———), upper convected Maxwell (- – – -), and Giesekus (· · · · · ·) models to start-up of planar elongational flow. The dimensionless transient first planar elongational viscosity, $\bar{\eta}^+_{1k}/4\eta_k$, is given as a function of the Hencky strain, ε. Plots are shown for different values of dimensionless strain rate: (a) $\dot{\varepsilon}\lambda_{1k} = 0.2$; (b) $\dot{\varepsilon}\lambda_{1k} = 0.5$; (c) $\dot{\varepsilon}\lambda_{1k} = 1$; (d) $\dot{\varepsilon}\lambda_{1k} = 5$. For each of the Giesekus modes $\alpha_k = 0.01$.

sidered to be in the linear viscoelastic regime when only small strains are experienced, i.e., $\varepsilon < 1$, or the flow is "slow", i.e. $\dot{\varepsilon}\lambda_k < 1/2$. In Figs. 6.5b-d, divergence of the nonlinear Giesekus model from the quasilinear upper convected Maxwell model is noted at a Hencky strain substantially greater than unity. The particular Hencky strain at which the quasilinear and nonlinear models diverge is dependent on the dimensionless strain rate, $\dot{\varepsilon}\lambda_k$. In general, as the strain rate is increased the strain at which the models decreases (cf. Figs. 6.5b-c). Note that in Fig. 6.5a, the quasilinear and nonlinear models superpose for all Hencky strains; the strain rate of $\dot{\varepsilon}\lambda_k = 0.2$ is too low to extend the polymer molecule to the point where nonlinear behavior is manifested.

The experimental results on the response of the test fluid to the transient, nonhomogeneous flow on the centerline of the planar contraction are presented and interpreted in Sections 6.4 and 6.5 of this Chapter. To facilitate understanding of the response to this nonhomogeneous flow, it is useful to first estimate the transient response of the 0.30 wt% PIB in PB test fluid to the simpler, homogeneous start-up of planar elongation flow (cf. Fig. 6.6). The multimode linear Maxwell, quasilinear upper convected Maxwell, and nonlinear Giesekus models are used with the parameters given in Table 4.5. The strain rate for this mock start-up of planar elongation flow was selected to be equal to the maximum value, $\dot{\varepsilon} = 3.21\ [s^{-1}]$, on the centerline of the 32:1 planar contraction for a test flow with $Wi_{Dn} = 2.14$, described in §6.4 of this Chapter.[4] The profiles were computed up to a Hencky strain of $\varepsilon = 3.5$, which corresponds to the total strain experienced by a fluid element traveling along the centerline of the 32:1 planar contraction. The Newtonian limit of the planar elongational viscosity, $4\eta_0$, is indicated on the diagram, note that the prediction of the linear Maxwell model monotonically increases to this value. In contrast, the profile of the quasilinear upper convected Maxwell model is observed to exceed the Newtonian limit; at $\varepsilon = 3.5$ the nonlinear model predicts a transient elongational viscosity a factor of five greater than the prediction of the linear Maxwell model. At high strain rates the nonlinear Giesekus model diverges from the upper convected Maxwell model; however, at $\varepsilon = 3.5$ the difference between these models is only 8%. Table 6.1 gives the critical strain rate, $\dot{\varepsilon}_{crit,\,k}$, for each k^{th} relaxation mode of the 0.30 wt% PIB in PB test fluid, and gives

4. Wi_{Dn} is the shear-rate-dependent Weissenberg number defined in terms of the mean shear rate in the downstream slit (cf. §6.2).

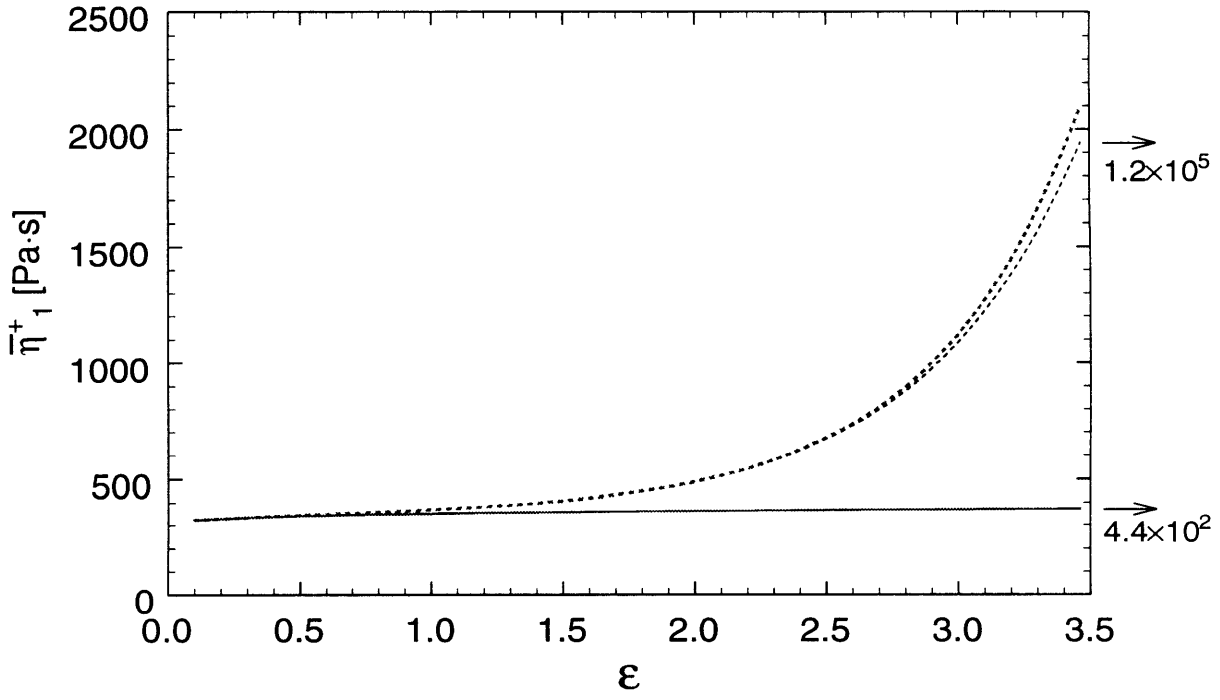

Figure 6.6 Plots of the stress-growth response predicted by the multimode linear Maxwell (———), quasilinear upper convected Maxwell (- — — -), and Giesekus (- – – -) models for start-up of planar elongational flow. The transient first planar elongational viscosity, $\bar{\eta}^{+}_{1k}$, is shown as a function of the Hencky strain, ε. A strain rate of $\dot{\varepsilon} = 3.21\ [s^{-1}]$ is used. Model parameters are fitted to the 0.30 wt% PIB in PB test fluid and are given in Table 4.5. Ultimate values of $\bar{\eta}^{+}_{1k}$ for the multimode Giesekus model as $\varepsilon \rightarrow \infty$ are indicated at the right of the graph.

the viscosity ratio, $\eta_{1k}/4\eta_k$, predicted by the Giesekus model, which is associated with steady planar elongational flow at a strain rate of $\dot{\varepsilon}_{crit,\,k}$.

Mode No.	$\dot{\varepsilon}_{crit,\,k} = \frac{1}{2\lambda_k}$ [s^{-1}]	η_k [Pa s]	$\frac{\bar{\eta}_{1k}(\dot{\varepsilon}_{crit,\,k})}{4\eta_k}$
1	0.025	8.0	1.84
2	0.104	7.4	44
3	0.46	9.5	14
4	4.2	6.5	9.4
Solvent	—	79	1

Table 6.1 Critical parameters and values of the four-mode Giesekus representation of the 0.30 wt% PIB in PB test fluid for planar elongational flow.

6.1.3 Flow-Induced Birefringence in Elongational Flows

The physical underpinnings of the stress-optical rule which postulates a linear relationship between the refractive index and stress tensors has been discussed in §3.4. In particular, the derivation of the stress-optical rule from polymer molecular theory by relation of both the stress and refractive index tensors to the configurational state of the polymer molecules was described (Doi and Edwards, 1986; Dupuis *et al.*, 1986). It was further indicated that this linear stress-optical relationship breaks down when the polymer molecule approaches a fully extended state, either by "saturation" of the birefringence or the development of pathological "kinked" configurational states (Wales, 1976; Janeschitz-Kriegl, 1969; Kobe and Wiest, ; Shaqfeh, 1996). When considering the response of a polymer molecule to an imposed velocity field it is useful to distinguish "strong" flows, in which the velocity gradient tensor has at least one eigenvalue with positive real part, from "weak" flows, for which no eigenvalue satisfies this condition (Tanner and Huilgol, 1975). Steady shearfree flows are "strong": certain material lines grow exponentially in time. In contrast, steady simple shear flow is "weak": material lines grow approximately linearly in time. "Strong" flows are more "efficient" than "weak" flows in the sense that lower rates

of strain are required to extend polymer molecules; the planar elongational flow on the centerline of the planar contraction is such a "strong" flow (Larson, 1988; Hinch, 1977). Nevertheless, in Sections 6.4 and 6.5 of this Chapter it is shown that polymer molecules in the transient planar elongational flow on the centerline do not approach the fully extended state. Consequently, the stress-optical rule was valid for all the flows investigated.

6.2 Experimental Methods

The construction and function of the planar contraction geometry used to produce the shearfree centerline flow was presented in Chapter 3, along with the LDV and FIB measurement techniques used to obtain velocity- and stress-field information, respectively. Detailed information on the rheology of the test fluid was given in Chapter 4. This Section focuses on aspects of the fluid flow and measurement techniques specific to the determination of the transient elongational viscosity profile. The nature of the flow generated in the geometry is reviewed, and the "downstream shear-rate-dependent Weissenberg number" used throughout this Chapter, defined. The selection of specific experimental parameters for the investigation presented in this Chapter is then discussed; specifically, this selection was guided by the results of previously published experiments. At the end of this Section, limitations on the use of FIB to obtain stress-field information are briefly addressed.

The planar contraction flow considered as a whole is complex; i.e. the rate-of-strain tensor in most regions of the flow contains contributions from both the elongational and the shear components of the velocity gradient tensor. However, on the centerline of the flow, because of symmetry about the centerplane, the flow is shearfree: specifically, it is a spatially nonhomogeneous planar elongational flow. The planarity of the flow field allows for direct interpretation of birefringence measurements in terms of stress, as described in §3.4. Therefore, the stress response of the viscoelastic fluid to a shearfree flow field may be compared with the predictions of constitutive equations. One must recognize that although the centerline flow is shearfree, it is not homogeneous; i.e., the strain rate and the normal stress vary along the centerline. However, since the LDV and FIB techniques obtain pointwise, quantitative information, comparison of measured values with the pre-

dictions of constitutive equations can be made despite the non-homogeneous nature of the centerline flow.

As discussed in Chapter 5, the downstream half-height, h, is the length scale which controls the form of the region of high strain rate on the centerline. In particular, the maximum strain rate along the centerline, $\dot{\varepsilon}_{max}$, is of the same order as the average shear rate in the downstream slit, $\langle\dot{\gamma}\rangle_{Dn} \equiv \langle v_z\rangle_{Dn}/h$. Therefore, throughout this Chapter, the shear-rate-dependent Weissenberg number defined in terms of the downstream channel flow conditions is used

$$Wi_{Dn} \equiv \lambda(\langle\dot{\gamma}\rangle_{Dn})\langle\dot{\gamma}\rangle_{Dn} \tag{6.2}$$

In contrast, in Chapter 5, the shear-rate-dependent Weissenberg number defined in terms of the upstream flow conditions was used.

In the investigations of Galante and Frattini (Galante and Frattini, 1993; Galante, 1991) and of Quinzani (Quinzani *et al.*, 1994; Quinzani *et al.*, 1995) viscoelastic flow through a planar contraction geometry with an upstream to downstream half-height contraction ratio of H/h = 4 was used. Different viscoelastic fluids were used in the studies; Galante and Frattini used a polymer melt whereas Quinzani used a concentrated polymer solution. Nevertheless, in both investigations only low to moderate downstream, shear-rate-dependent Weissenberg numbers were attained, $Wi_{Dn} < 1$. In both of the investigations, the viscoelastic fluid was observed to exhibit an essentially linear response. This finding was not surprising in view of the low total Hencky strains, $\varepsilon \leq 1.4$, and low Weissenberg numbers which were attained.

The limitations imposed by the geometry and test fluids used in these previous investigations guided the selection of experimental conditions for the study presented in this Chapter. As discussed in §3.1 the contraction ratio of the test geometry could be varied by changing the upstream inserts. This allowed the influence of the total Hencky strain on the viscoelastic fluid response to be investigated. Contraction ratios as great as H/h = 32 could be studied, corresponding to a total Hencky strain of $\varepsilon = 3.5$. It was shown in §6.1 that, for a homogeneous flow in which such a Hencky strain is attained, the test fluid is expected to exhibit a substantial nonlinear viscoelastic response.

A polymer solution consisting of 0.30 wt% polyisobutylene (PIB) in polybutene (PB) was used as the test fluid. The nearly constant viscosity nature of the fluid allowed high Weissenberg numbers to be attained without introducing effects of fluid inertia. Specific details of the composition and shear rheology of the test fluid are given in Chapter 4; the parameter fits of the linear Maxwell and Giesekus models used in this Chapter are also described. Use of a two-component Boger test fluid was found to alleviate the problems of beam divergence which had previously been observed when a ternary Boger fluid was sheared in a Couette cell (Quinzani *et al.*, 1992; Byars, 1992).

General information on the configuration, resolution, and accuracy of the two-color flow birefringence (TCFIB) and laser Doppler velocimetry (LDV) systems used to obtain the stress and velocity field information presented in this Chapter has been presented in Sections 3.3 and 3.4. However, in the case of the TCFIB measurement one must also consider limits on quantitative interpretation in terms of the stress field which are imposed by the structure of the velocity field in the planar contraction flow; such limits are discussed in §6.3.

6.3 Kinematic Structure of Centerline Flow: Effect on FIB Measurements

In this Section, features of the velocity field and their effect on the direct interpretation of a birefringence measurement in terms of stress are described. In §6.3.1 characteristics of the velocity field present at all flow rates and consistent with an ideal two-dimensional flow field are discussed. §6.3.2 describes how the presence of a boundary in the "neutral" x-direction of the upstream duct may impart a non-ideal, three-dimensional character to the flow. The effect of this three-dimensional aspect of the flow on interpretation of the FIB measurement is examined. In §6.3.3 the importance of inhomogeneities in the stress field over the area probed by the laser beam in the interpretation of FIB measurements is discussed. In §6.3.4 nonidealities in the flow field associated with elastically-driven flow transitions at elevated flow rates are considered. §6.3.5 addresses limits on FIB measurement imposed by beam divergence induced by refractive index gradients associated with thermal gradients generated by viscous heating. §6.3.6 contains a summary of these phe-

nomena which impose restrictions on the interpretation of FIB measurements in terms of the stress field for the experiments discussed in Sections 6.4 and 6.5.

6.3.1 Characteristics of Ideal, Two-Dimensional, Centerline Velocity Field

At sufficiently low flow rates and correspondingly low Weissenberg number the elastic nature of the fluid plays an insignificant role in determining the structure of the velocity field. The shearfree, nonhomogeneous planar elongational flow is on the centerline. The total Hencky strain, ε, experienced by a fluid element starting far upstream of the contraction plane and travelling into the downstream slit to a region of fully developed channel flow can be determined by considering the flow velocities at these limiting points. Specifically, one may write

$$\varepsilon = \ln\left(\frac{V_{zDn}}{V_{zUp}}\right) \tag{6.3}$$

In the case of the constant viscosity test fluid used in this study, the velocity profile in fully developed channel flow is parabolic and the maximum velocity in the channel for a given volumetric flow rate is inversely proportional to the channel height so that

$$\varepsilon = \ln\left(\frac{H}{h}\right) \tag{6.4}$$

One should note that consideration of the centerline velocity in fully developed upstream and downstream channel flow does not allow for calculation of the strain experienced by a fluid element located between these limiting points. In particular, when there is a transition to a diverging flow field, as discussed in §6.3.4, a fluid element at an intermediate point has a velocity *less than* the upstream channel flow and consequently experiences a negative Hencky strain.

As discussed in Chapter 5, the centerline base flow consists of two distinct regions. The first regions includes a high strain-rate "spike", located immediately upstream of the contraction plane. The downstream slit half-height, h, was the length scale which determined the upstream extent of and the maximum strain rate in the spike. Variation of the

upstream half-height, H, had little effect on the strain-rate profile of the spike. The second distinct region of flow was a long "tail" of low strain rate relative to that of the spike. The tail extended from a position of order h upstream of the contraction plane to a position of order H upstream. The upstream half-height H was the length scale which set the extent of the "tail". As a result of the strain-rate profile consisting of the "spike" and "tail" being controlled by different geometrical parameters, an increase in the contraction ratio, H/h, resulted in an increase in the strain experienced by a fluid element travelling through the "tail" region but did not induce a substantial increase in the strain experienced within the "spike" region. This scaling behavior plays an essential influence on the ability of the planar contraction flow to excite a nonlinear viscoelastic response in flows of high Hencky strain.

6.3.2 Nonidealities in the Base Flow: Effects of Three-Dimensional Flow Field on FIB Measurement

A two-dimensional planar contraction flow is *approximated* by the flow geometry. However, the presence of a bounding wall, specifically the side window shown in Fig. 3.2, in the nominally "neutral" x-dimension introduces a locally three-dimensional character into the flow. The downstream channel aspect ratio is high for all flows investigated: $\Lambda_{Dn} = W/2h = 32$, where W indicates the width of the channel. In consequence, a two-dimensional flow is closely approximated, except in the immediate vicinity of the walls bounding the x-dimension. The aspect ratio in the upstream channel is lower and is inversely proportional to the contraction ratio

$$\Lambda_{Up} = \frac{W}{2H} = \frac{32}{(H/h)} \tag{6.5}$$

For the case of the 8:1 contraction, $\Lambda_{Up} = 4$; consequently, the fully developed flow in the upstream channel has pronounced three-dimensional character. As discussed in Chapter 3, variation of the stress field along the direction of propagation of the probe beam can preclude direct, quantitative interpretation of an FIB measurement in terms of the stress field. However, the region of high elongational strain rate, $\partial v_z/\partial z$, located immediately upstream of the contraction plane, and of interest for the measurements presented and dis-

cussed in Sections 6.4 and 6.5, approximates two-dimensional flow over a region greater in extent than for flow in the duct far upstream of the contraction plane. In this Section, the region where the flow is nearly two-dimensional is identified via LDV measurements. The case of the 8:1 contraction is used as an example, since several v_z-versus-χ profiles were obtained for this flow. An order of magnitude analysis is used to show that the region adjacent to the walls has a small effect on the FIB measurement. The findings are extended to other contraction ratios. At the end of this Section, the characteristic of "fluid memory" is taken into account.

Profiles of the velocity, v_z, as a function of position in the neutral x-direction, obtained on the centerplane ($\upsilon = 0$) for several different axial positions, ζ, are shown in Fig. 6.7. The flow was through the 8:1 contraction at a volumetric rate corresponding to $Wi_{Dn} = 1.98$; i.e., before the onset of diverging or unstable flow. Far upstream of the contraction plane, e.g. at $\zeta = -19.7$, the velocity is highest in the middle of the channel ($\chi = 0$) and remains nearly constant with increasing absolute position, $|\chi|$, until the walls are closely approached for positions $|\chi| \gtrsim 24$. Because of the nearly constant viscosity of the fluid, the flow on the centerplane, in the upstream duct, is similar to that for fully developed Newtonian channel flow. A Newtonian profile was computed via a Fourier transformation technique; the solution is

$$\frac{v_z(\hat{x}, \hat{y})}{\langle v_z \rangle_{Up}} = \frac{\displaystyle\sum_{p=1,\,odd}^{\infty} p^{-3} \sin\left[\frac{p\pi}{2}(\hat{y}+1)\right]\left\{\frac{\sinh[p\pi\hat{x}] + \sinh[p\pi(\Lambda_{Up}-\hat{x})]}{\sinh[p\pi\Lambda_{Up}]} - 1\right\}}{\dfrac{4}{\pi}\displaystyle\sum_{p=1,\,odd}^{\infty} p^{-4}\left\{\frac{\cosh[p\pi\Lambda_{Up}]-1}{p\pi\Lambda_{Up}\sinh[p\pi\Lambda_{Up}]} - \frac{1}{2}\right\}} \tag{6.6}$$

where the position variables are defined as $\hat{x} = (h/H)\chi$ and $\hat{y} = (h/H)\upsilon$. The average velocity in the channel is represented by $\langle v_z \rangle_{Up} = Q/(2HW)$, where Q indicates the volumetric flow rate. Twenty terms were used in computing the solution to eq. (6.6), the profile $v_z(\chi, \upsilon = 0)$ is shown in Fig. 6.7. Note that the velocity exceeds 80% of the maximum value in the profile for the span $-23.5 \le \chi \le 23.5$; the decrease in velocity near the bounding wall occurs over a dimensionless distance of $\Delta\chi_B \approx W/(2\Lambda h)$. Equation (6.6)

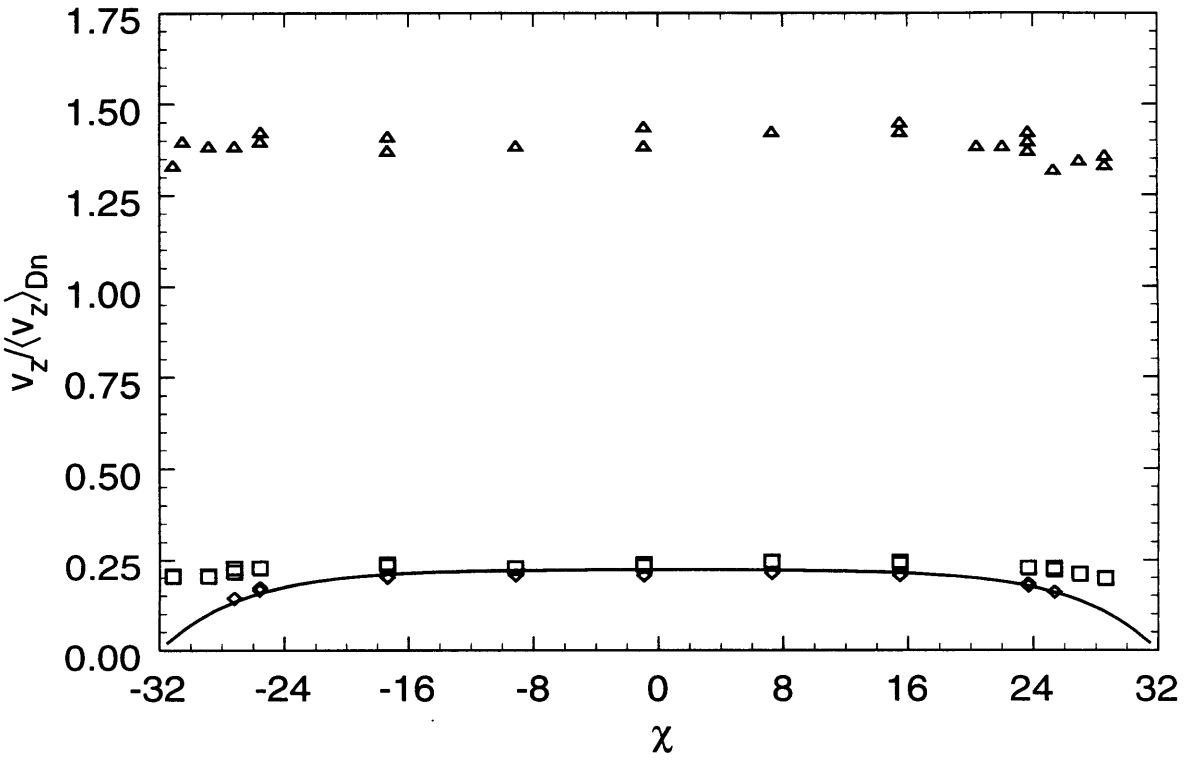

Figure 6.7 Profiles of the dimensionless velocity, $v_z/\langle v_z\rangle_{Dn}$, versus position in the "neutral" direction, χ. All profiles are located within the centerplane, $\upsilon = 0$, at different axial positions: (△), $\zeta = 0.28$; (□), $\zeta = -5.72$; (◇), $\zeta = -19.72$. The measurements were conducted with flow through the 8:1 contraction, at a flow rate corresponding to $Wi_{Dn} = 1.98$. The Newtonian solution for flow through the upstream W/2H = 4 duct is shown, (———).

predicts that in the high-aspect-ratio downstream slit and on the centerplane, the velocity is at 80% of the maximum value across the span $-31 \le \chi \le +31$. The flow field is not fully developed at $\zeta = 0.28$, however, the measured profile for v_z, shown in Fig. 6.7, is consistent with the prediction for the fully developed Newtonian profile. It is not clear why the data points for $\chi > 24$, associated with the $\zeta = 0.28$ profile, are lower than in the remainder of the profile. This discrepancy may be attributable to experimental error resulting from the attenuation of the backscattered light resulting from passage through the fluid and across the width (W = 70 [mm]) of the geometry.

To adapt from the velocity field in the upstream to that in the downstream channel, the flow assumed a nearly two-dimensional pattern in an intermediate region which extended several half-heights, h, from either side of the centerplane ($\upsilon = 0$) and upstream of the contraction plane ($\zeta = 0$). This two-dimensionality is illustrated in Fig. 6.7 by the profile for $\zeta = -5.7$, which shows that the velocity remains at over 80% of the maximum value over a span encompassing $-28 \le \chi \le 28$, considerably broader than the span for the far upstream region of the channel given above. This uniformity over the x-direction was also maintained for off-centerplane positions. Figure 6.8 shows the velocity profile as a function of υ-position near the contraction plane ($\zeta = +0.27$). Scans were performed near the center of the width ($\chi = -0.9$) and approximately three-quarters of the way toward the wall ($\chi = -25.6$). Within the error of the measurement, no significant difference was noted between the y-scans taken at the different χ-positions. In a similar manner, scans in the y-direction were taken near the center of the flow and approximately three-quarters of the way toward the wall at an axial position several half-heights upstream, $\zeta = -5.7$. At a given υ-position, the value of the velocity for the scan closer to the wall was over 90% of that of a corresponding point taken near the center of the flow; $v_z(\chi = -25.6)/v_z(\chi = -0.9) \ge 0.9$. Thus, the information presented in Figs. 6.7 and 6.8, indicates that in the region defined by $\zeta \ge -5.7$, $-1 \le \upsilon \le +1$, and $-28 \le \chi \le +28$, two-dimensional flow in the yz-plane was approximated. This region of approximate two-dimensional flow encompassed the high strain-rate part of the centerline profile, shown in Fig. 6.9; the strain rate at $\zeta \ge -5.7$, $(\partial v_z/\partial z)(h/\langle v_z \rangle_{Dn}) = 0.02$, is less than 5% of the maximum value.

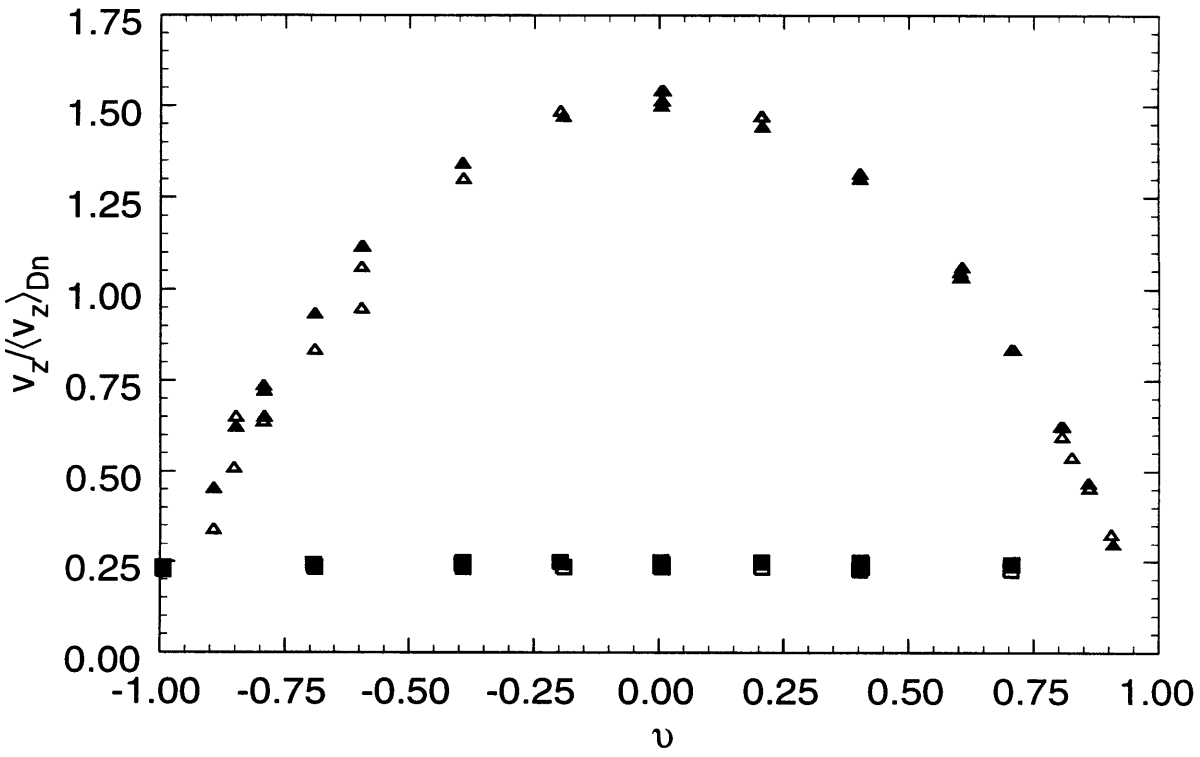

Figure 6.8 Profiles of the dimensionless velocity, $v_z/\langle v_z\rangle_{Dn}$, versus υ. Four different scans are shown; these were conducted at the positions χ = -0.9 (filled symbols) and -25.6 (open symbols), and at the axial positions ζ = +0.27 (△) and -5.72 (□). The measurements were conducted with flow through the 8:1 contraction, at a flow rate corresponding to Wi_{Dn} = 1.98.

Given the approximate two-dimensionality of the flow over the region of high strain rate, the effect of the walls bounding the x-dimension on the FIB measurement were expected to be minimal; an order of magnitude analysis is now described to support this intuition. In Sections 6.4 and 6.5 results of the FIB measurement are presented for the 8:1 contraction ratio for flow rates corresponding to $Wi_{Dn} \leq 2.86$; the maximum flow rate for this range is used throughout the analysis. Chapter 5 indicated that at $Wi_{Dn} = 2.86$ the flow had a diverging and three-dimensional structure distinct from the form of the base flow. However, at this flow rate the phenomena did not yet have a deleterious effect on the FIB measurement. In the case of diverging flow, the region of high strain rate is shifted closer to the contraction plane, consequently the bounding walls are expected to have even less of an effect on the FIB measurement than for the base flow. At $Wi_{Dn} = 2.86$, the three-dimensional oscillation of the velocity in the x-direction within the contraction plane was small, this point is addressed below. The profile in the x-direction on the centerplane at an axial position $\zeta = -5.7$ is considered first. This scan lies at the boundary of the region which is "nearly two-dimensional". In consequence, the influence of the "end effects" relative to that of the ideal two-dimensional flow on the FIB measurement is expected to be greater than in other regions of the "nearly two-dimensional" flow. This conservative estimate is extended to other axial positions near to the end of this Section.

The effects of a three-dimensional flow field on an FIB measurement can be quantitatively assessed via integration of eq. (3.5) over a known stress field by invoking the stress-optical rule, cf. eq. (3.3). Obtaining the required stress field information is problematic: only a limited set of velocity field information is available, e.g., Figs. 6.7, 6.8, and 6.9, and the accuracy of the constitutive model used for a streamwise integration procedure must be assumed. However, such detailed quantitative analysis is not necessary; the objective of this Section is simply to obtain an estimate of the error introduced by three-dimensional "end effects" over the flow region where FIB measurements were performed. To facilitate this estimation, two primary assumptions are made: 1) the x-dimension can be divided into three regions within which the rate-of-strain field is essentially homogeneous and 2) non-linear and memory viscoelastic effects may be neglected and the fluid response approximated via a Newtonian constitutive equation. These assumptions are justified below.

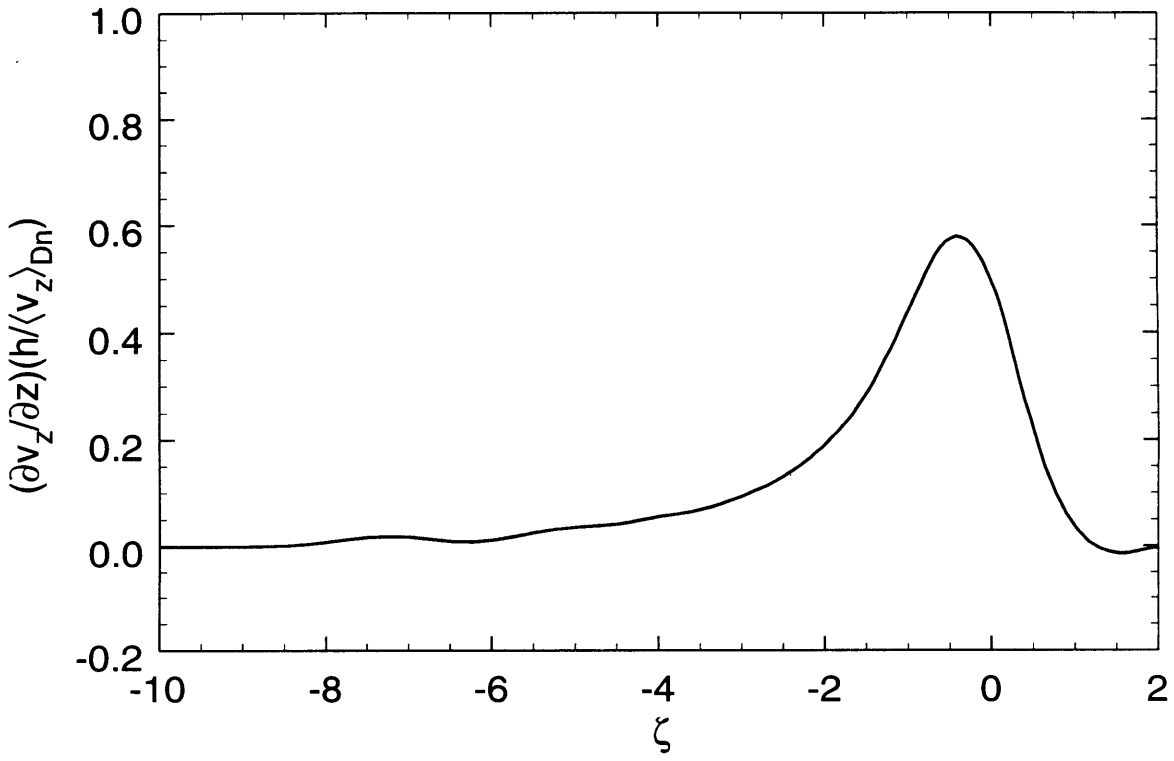

Figure 6.9 Profile of the dimensionless strain rate, $(\partial v_z/\partial z)(h/\langle v_z\rangle_{Dn})$, in the axial direction, ζ, with $\chi = 0$ and $\upsilon = 0$. The measurements were conducted with flow through the 8:1 contraction, at a flow rate corresponding to $Wi_{Dn} = 1.98$.

The profiles presented in Fig. 6.7 indicate that on the centerplane of the flow, upstream of the contraction plane, a scan in the x-direction passes through three domains: a "core region" of uniform v_z such that $\dot{\gamma}_{xz} \sim 0$, which is flanked on either side by "boundary regions" characterized by an elevated shear component of the rate-of-strain tensor, $|\dot{\gamma}_{xz}| > 0$. For the specific case of the profile of v_z-versus-χ obtained at $\upsilon = 0$ and $\zeta = -5.7$, the core region spans ($-28 \leq \chi \leq +28$) and the boundary regions span $-32 < \chi < -28$ and $28 < \chi < 32$. Identification of these distinct regions suggests use of a "sandwich model"; specifically, each of the regions is considered to have a uniform rate-of-shear field and the effect on the FIB measurement, obtained via a light beam travelling in the x-direction, analyzed accordingly (Galante, 1991).

Before proceeding to the actual order-of-magnitude analysis, it is necessary to give consideration to the effect of the flow field on the configurational state of a polymer molecule in each region of the "sandwich", and the consequent influence on the probe beam used to perform the FIB interrogation. Note that the following discussion applies strictly only to flow within the centerplane ($\upsilon = 0$). An orientation vector used to describe the configuration of the polymer molecule is defined as an integral over the contour of the polymer molecule

$$\mathbf{R} = \int_0^L \left(\frac{d}{dl}\mathbf{r}\right) dl \tag{6.7}$$

where L represents the contour length of the molecule, and $\mathbf{r}$ is the vector representing the orientation of a segment at position l along the chain backbone (Doi and Edwards, 1986). One can note that this orientation vector is related to the deviatoric part of the refractive index tensor as

$$\mathbf{n}' = J\left\langle \mathbf{RR} - \frac{\boldsymbol{\delta}}{3}(\mathbf{R}\cdot\mathbf{R})\right\rangle \tag{6.8}$$

where J is a scalar related to the anisotropic polarizability, $\Delta\alpha$, of the chain backbone (Doi and Edwards, 1986). In the core region, the planar elongational flow will cause the orientation vector to lie in the xz-plane. The component of the orientation vector in the

direction of flow (z) is non-zero. However, the magnitude of the x-component is not set by the flow since planar extensional flow is strong, but only neutrally aligning (Larson, 1988). However, since the polymer molecules are randomly oriented before entering the region of planar elongational flow, by symmetry the orientation vector must be parallel to the z-axis.

In the boundary region, the smaller, but still non-zero, elongational components of the rate-of-strain tensor, $\dot{\gamma}_{xx} = \dot{\gamma}_{zz} \neq 0$, cause the orientation vector to lie in the xz-plane. However, in contrast to the core region, the non-zero $\dot{\gamma}_{xz}$ component sets the time-averaged direction of the orientation vector within this plane. In particular, when the shear components of the stress tensor dominates over the elongational components, the orientation vector lies in the xz-plane with an extinction angle $\chi_{xz} = \pi/4$ [rad] with respect to the mean flow direction, z.

As discussed in Chapter 3, the birefringence and extinction angle of a flowing polymer solution are related to the mean orientation of the segments comprising the polymer chain. In particular, an FIB measurement is sensitive to the *projection* of the orientation vector onto the plane perpendicular to the direction of beam propagation. The probe beam used to perform the FIB interrogation travels in the x-direction and is sensitive to the configuration of the polymer molecule as projected onto the yz-plane. The orientation vector projected onto the yz-plane is parallel to the z-axis both for polymer molecules in the core region and in the boundary regions. In other words, the extinction angle detected by the probe beam is $\chi_{yz} = 0$ with respect to the z-axis. The constant nature of the extinction angle along the x-direction (the direction of beam propagation) greatly simplifies the analysis. For a constant extinction angle, the tensorial differential eq. (3.5) reduces to a scalar integral equation, termed Wertheim's law (Theocaris and Gdoutos, 1979; Galante and Frattini, 1993), which may be written as

$$(\chi_1 - \chi_0)\Delta n_m = \int_{\chi_0}^{\chi_1} \Delta n(\chi')d\chi' \tag{6.9}$$

where Δn_m indicates the birefringence "observed" by a probe beam travelling through the flowing fluid from χ_0 to χ_1, and $\Delta n(\chi')$ represents the birefringence locally associated with a position χ' in the flow; a prime denotes a "dummy" integration variable.

For a polymer molecule in the core region of the flow, since the orientation vector is parallel to the z-direction, the stress-optical rule can be applied in its familiar form, $\Delta n_{zy} = C(\tau_{zz} - \tau_{yy})$. By contrast, in the boundary region, the orientation vector has no component in the y-direction, but has non-zero components in both the x- and z-directions. Since the vector does not lie in the yz-plane, but rather at an oblique angle to it, χ_{xz}, the projection of the refractive index tensor onto the yz-plane is used to determine the birefringence. One can then write

$$\Delta n_{yz} = \cos\chi_{xz} C \Delta\tau_{xz} \tag{6.10}$$

where the first term on the right side is the projection operator.

The contribution of the core region to the birefringence is considered first. The strain rate at position ζ = -5.7 is shown in Fig. 6.9 as $(\partial v_z/\partial z)(h/\langle v_z\rangle_{Dn}) = 0.02$. The fluid in this region displays a linear viscoelastic response. In consequence, by using the constitutive equation for a Newtonian fluid, the normal stress, $N_1 = \tau_{zz} - \tau_{yy} = -4\eta(\partial v_z/\partial z)$, is overestimated; however, this is inconsequential for the purpose of this order-of-magnitude analysis. The PIB and PB components of the fluid have different values of the stress-optical coefficient, but since the ratio of their stress-optical coefficients is order one, specifically $C_{PIB}/C_{PB} = 1.51$, a single variable, C, will be used to describe the stress-optical coefficient of the fluid below. By invoking the stress-optical rule (cf. eq. (3.3)), the integral on the right-side of eq. (6.9) is evaluated over the core region as

$$\int_{\chi=-28}^{\chi=28} \Delta n(\chi')d\chi' = 4C\eta\left(\frac{\partial v_z}{\partial z}\right)56 = 4.5C\eta\left(\frac{\langle v_z\rangle_{Dn}}{h}\right) \tag{6.11}$$

To facilitate consideration of the boundary regions adjoining the core region, it is useful to assume that the elongational components of the rate-of-strain tensor may be neglected in light of the greater magnitude of the shear components. The xz-component of the rate-of-strain tensor is approximated by assuming a linear velocity gradient profile

between the wall, at $\chi = -32$, and the boundary with the core region, at $\chi = -28$. The velocity at the boundary is approximated as the maximum value in the v_z-versus-χ profile for ($\nu = 0, \zeta = -5.7$), i.e., $0.25\langle v_z\rangle_{Dn}$ as shown in Fig. 6.7. The approximate shear rate is then $\dot{\gamma}_{xz} \sim \frac{0.25\langle v_z\rangle_{Dn}}{4h} = 0.063(\langle v_z\rangle_{Dn}/h)$. This is greater than (although of the same order as) the elongational strain rate given above, $\dot{\gamma}_{zz} = 0.02(\langle v_z\rangle_{Dn}/h)$; therefore, the effect of elongational rate-of strain components will be neglected. The downstream shear rate associated with the flow in question corresponds to $\langle v_z\rangle_{Dn}/h = 14\ [s^{-1}]$. In consequence, the shear-rate-dependent Weissenberg number associated with the flow near the wall is $Wi(\dot{\gamma}_{xz,B}) = 0.4$. In consequence, nonlinear viscoelastic effects are neglected in this analysis. Also neglecting the effect of fluid memory allows use of the Newtonian constitutive equation for flow in the boundary region, so that the stress field is linearly proportional to the rate-of-strain field.

Since a Newtonian constitutive equation is used and elongational components of the rate-of-strain tensor are considered negligible, the stress tensor in the boundary region consists exclusively of the shear component, $\tau_{xz} = \eta\dot{\gamma}_{xz}$; the extinction angle describing the direction of the orientation vector is $\chi_{xz} = \pi/4$ [rad]. As described above, the refractive index tensor must be projected onto the yz-plane to determine the birefringence measured by the probe beam; using the known extinction angle one obtains, via evaluation of eq. (6.10), the expression $\Delta n_{yz} = (C/\sqrt{2})\Delta\tau_{xz}$. Then, using the Newtonian constitutive equation and the estimated shear rate one has

$$\Delta n_{zy} = \frac{C}{\sqrt{2}} \cdot \frac{\eta(\langle v_z\rangle_{Dn}/h)}{16} \tag{6.12}$$

as the birefringence associated with flow in the boundary region. Using eq. (6.12) to evaluate the right side of eq. (6.9)

$$2\int_{\chi=-32}^{\chi=-28} \Delta n(\chi')d\chi' = \frac{2C}{\sqrt{2}} \cdot \frac{\eta(\langle v_z\rangle_{Dn}/h)}{16} 4 = 0.35C\eta\left(\frac{\langle v_z\rangle_{Dn}}{h}\right) \tag{6.13}$$

is obtained; the prefactor of 2 indicates that a boundary region is on either side of the core region. Comparison of eq. (6.13) with eq. (6.11) indicates that the contribution of the

boundary region relative to the contribution of the core region to the measured birefringence is small

$$\frac{2\int_{\chi=-32}^{\chi=-28}\Delta n(\chi')d\chi'}{\int_{\chi=-28}^{\chi=28}\Delta n(\chi')d\chi'} = 0.078 \tag{6.14}$$

The error introduced by the boundary regions is only of order 10%, this may be partially cancelled by the lower elongational contribution to the rate-of-strain tensor in the boundary regions.

The conclusions on the influence of "end effects" on the FIB measurement are now extended to axial positions of $\zeta > -5.7$. The characteristic shear rate associated with the flow in the boundary region on the centerplane is $\dot{\gamma}_{xz,B} \approx \left.\frac{v_{z,max}}{\Delta x_B}\right|_{\zeta}$; where the bar on the right indicates that the expression is evaluated at axial position ζ, and the subscript "max" indicates the velocity in the center of the flow; i.e. at position $(\chi = 0, \upsilon = 0)$. The contribution of the two boundary regions to the birefringence is then written as

$$2\int_{\Delta\chi_B(\zeta)}\Delta n(\chi',\zeta)d\chi' \approx C\sqrt{2}\eta v_{z,max}\big|_{\zeta}. \tag{6.15}$$

where $\Delta\chi_B(\zeta) = \Delta x_B(\zeta)/h$. At ζ = -5.7, the core region extends over a distance Δx_C such that $\Delta x_C/W \approx 0.9$; i.e., most of the width. This fraction of the width can only increase to a slightly greater value as the contraction plane is approached (since it is already nearly equal to unity). In consequence, when assessing the contribution of the core region to the birefringence, the change in extent of the core region with axial position can be neglected. Taking the ratio of eqs. (6.15) and (6.11), evaluated at arbitrary axial position ζ, one obtains

$$\frac{2\int_{\Delta\chi_B(\zeta)}^{\Delta\chi_C(\zeta)} \Delta n(\chi',\zeta)d\chi'}{\int_{\Delta\chi_C(\zeta)} \Delta n(\chi',\zeta)d\chi'} \approx \frac{v_z/\langle v_z\rangle_{Dn}}{(\partial v_z/\partial z)(h/\langle v_z\rangle_{Dn})}\frac{\sqrt{2}}{4\cdot 56}\Bigg|_\zeta \approx 6\times10^{-3}\frac{v_z/\langle v_z\rangle_{Dn}}{(\partial v_z/\partial z)(h/\langle v_z\rangle_{Dn})}\Bigg|_\zeta \tag{6.16}$$

Thus, the ratio of the dimensionless velocity to the dimensionless strain rate is the relevant quantity for assessing the influence of end effects on the birefringence measurement. In order for the contribution of the boundary regions to the birefringence to be less than 10%, the ratio of the dimensionless velocity to the dimensionless strain rate must be less than 16. Note from Fig. 6.10 that this condition is met for axial positions in the range $-5.7 \le \zeta \le 0.8$.

Scans in the x-direction were not obtained for the 32:1 contraction flow; this precluded direct assessment of the three-dimensionality of the flow. In the far upstream region, the $\Lambda = \frac{W}{2H} = 1$ aspect ratio, corresponding to a square duct, results in v_z varying substantially over the entire x-dimension; in the downstream slit, the 32:1 aspect ratio results in a good approximation to two-dimensional flow over nearly the entire width of the channel. As for the case of the 8:1 contraction, in the region of intermediate axial position the flow must adapt from the form of the upstream to that of the downstream slit. In consequence, a nearly two-dimensional region of flow is expected to extend several half-heights upstream of the contraction plane. As described at the beginning of this Section, in fully developed Newtonian channel flow the extent of the boundary region scales as $\Delta x_B \approx W/\Lambda$. For a fixed volumetric flow rate and channel width, the maximum velocity on the centerplane of the duct scales as $v_{z,\,max} \approx \frac{3Q\Lambda}{2W^2}$. These scalings lead to the relation

$$\Delta\chi_B(\zeta) \approx \frac{3Q}{2Whv_{z,\,max}(\zeta)} \tag{6.17}$$

Equation (6.17) is used to relate the extent of the boundary region at a given axial position, ζ, to the velocity in the center of the flow at that axial position. In Fig. 6.11, the velocity

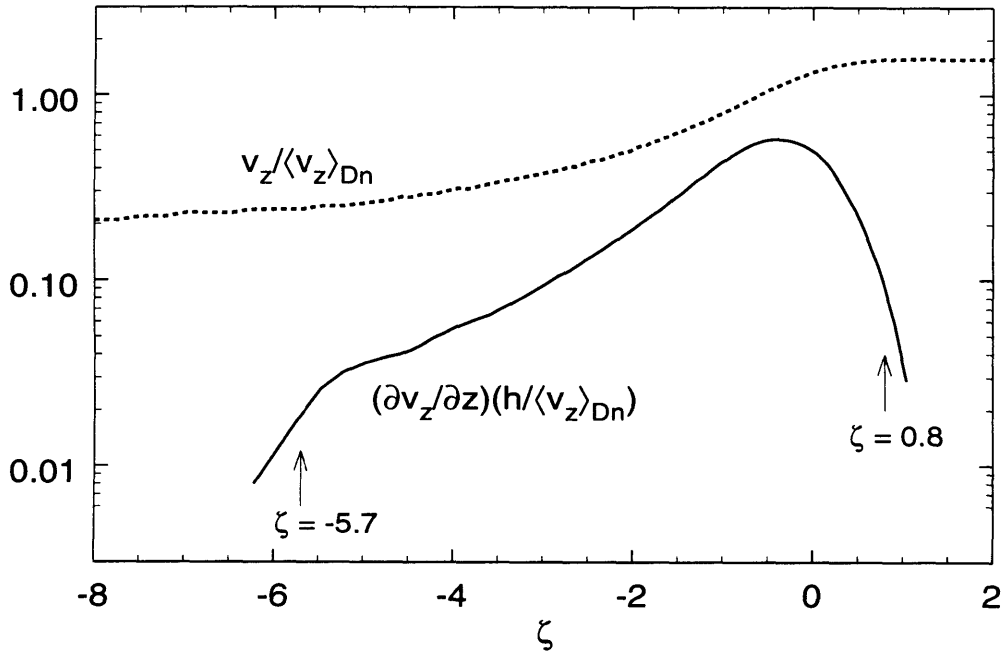

Figure 6.10 Centerline profiles of the dimensionless velocity, $v_z/\langle v_z\rangle_{Dn}$ (- - - -), and strain rate, $(\partial v_z/\partial z)(h/\langle v_z\rangle_{Dn})$ (———), as a function of axial position, ζ. Indicated on the plot are the points were the dimensionless velocity exceeds the strain rate by a factor no greater than 16. For intermediate axial positions, $-5.7 \le \zeta \le 0.8$, the influence of the "boundary regions" on the FIB measurement may be neglected. The profiles are derived from measurements conducted with flow through the 8:1 contraction, at a flow rate corresponding to $Wi_{Dn} = 1.98$.

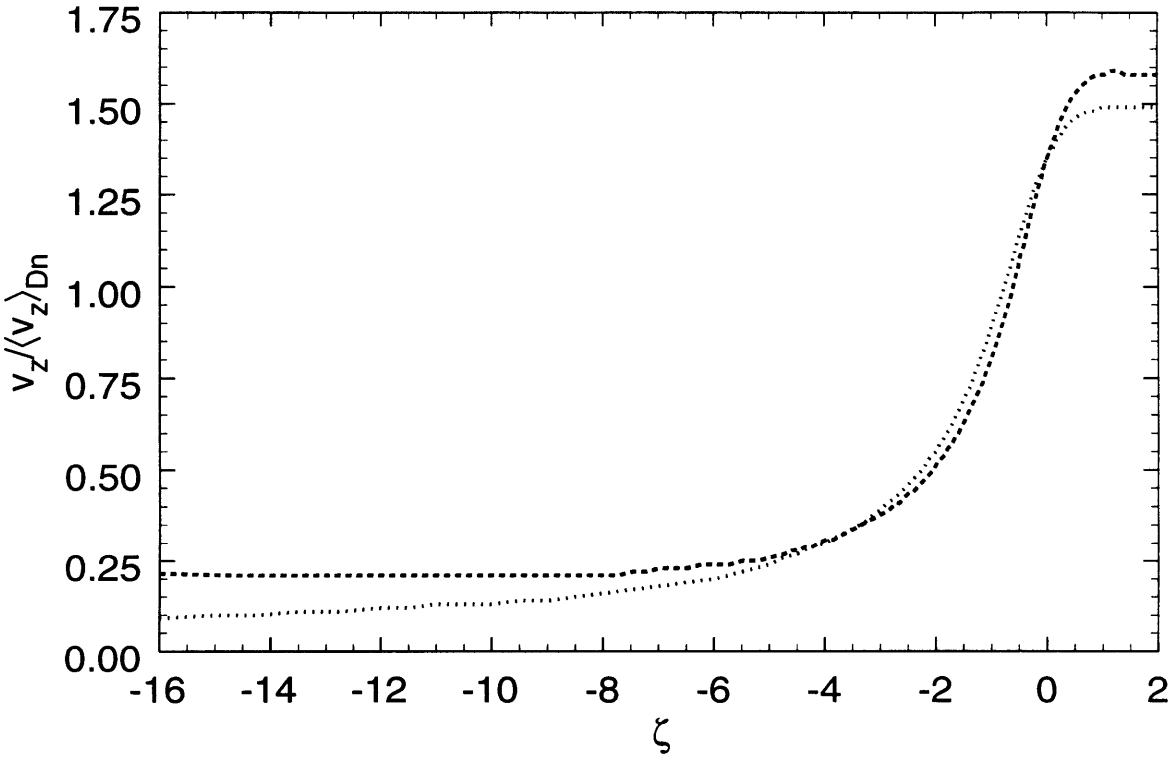

Figure 6.11 Centerline profiles of the dimensionless velocity, $v_z/\langle v_z\rangle_{Dn}$, as a function of axial position, ζ, for flows through the 8:1 (- – – -) and 32:1 (· · · · · · ·) contractions. Flow rates were similar for the two flows, $Wi_{Dn} = 1.98$ and $Wi_{Dn} = 2.14$, respectively. Note the coincidence of the curves, to within a fractional discrepancy of ±10% for $\zeta \geq -5$.

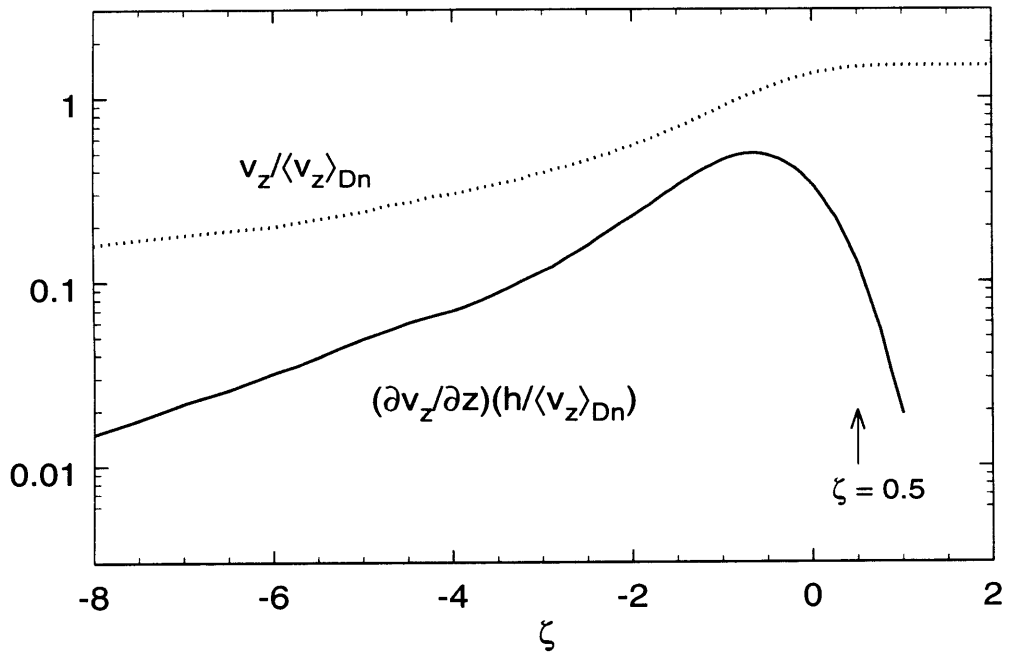

Figure 6.12 Centerline profiles of the dimensionless velocity, $v_z/\langle v_z\rangle_{Dn}$ (· · · · · ·), and strain rate, $(\partial v_z/\partial z)(h/\langle v_z\rangle_{Dn})$ (———), as a function of axial position, ζ. Indicated on the plot is the rightmost point where the dimensionless velocity exceeds the strain rate by a factor no greater than 16. The profiles are derived from measurements conducted with flow through the 32:1 contraction, at a flow rate corresponding to $Wi_{Dn} = 2.14$.

profiles for the base flow through the 8:1 and 32:1 contractions at flow rates corresponding to Wi_{Dn} = 1.98 and 2.14, respectively, are compared. The profiles are identical to within ±10% for axial positions of $\zeta \geq -5$. Since the "nearly two-dimensional" region in the 8:1 contraction was located at axial positions $\zeta \geq -5.7$, the 32:1 contraction flow is expected to be "nearly two-dimensional" for at least the range $\zeta \geq -5$. The influence of the "end effects" on the birefringence measurement may then be assessed via eq. (6.16). A plot of the centerline dimensionless velocity and strain rate is shown for flow through the 32:1 contraction at a volumetric rate corresponding to Wi_{Dn} = 2.14. Equation (6.16) is less than 0.1 for an axial range extending over $-12 \leq \zeta \leq 0.5$. Hence, Figs. 6.11 and 6.12 indicate that the flow in the 32:1 planar contraction may be treated as two-dimensional for the purpose of evaluation of the FIB measurement for a range $-5 \leq \zeta \leq 0.5$.

The assumption which was mentioned at the beginning of this Section, that memory effects resulting from the elastic nature of the fluid are negligible, is now examined. The specific question is: does the effect of the three-dimensional flow field on the stress of a given fluid element in the far upstream region of the flow persist into the region of nearly two-dimensional flow? To answer this question, a characteristic "relaxation length", l_λ, is calculated from the product of a characteristic relaxation time of the fluid and a characteristic velocity in the flow, and compared with the size of the two-dimensional region. The "relaxation length", written in dimensionless terms, is

$$\frac{l_\lambda}{h} \sim \lambda_0 \left(\frac{v_z(\zeta)}{\langle v_z \rangle_{Dn}} \right) \left(\frac{\langle v_z \rangle_{Dn}}{h} \right) \tag{6.18}$$

The zero-shear-rate plateau for the viscometric material functions could not be experimentally determined (cf. Chapter 4); therefore, the extrapolated value from the Giesekus fit described in Chapter 4, $\lambda_0 = 1.9\,[s^{-1}]$, is used in eq. (6.18). The downstream shear rate for a flow through the 8:1 contraction corresponding to Wi_{Dn} = 2.9 is $\langle v_z \rangle_{Dn}/h = 14\,[s^{-1}]$. When this shear rate is used, and eq. (6.18) is evaluated at $\zeta = -5.0$, using the dimensionless velocity profile shown in Fig. 6.11, a "relaxation length" of $l_\lambda/h = 7$ is obtained. This length is of the same order as the distance which the two-dimensional region extends upstream of the contraction plane. Equation (6.18) provides a conservative

estimate; specifically, use of the zero-shear-rate relaxation time should overestimate the "relaxation length". Fluid memory of the strain experienced in the three-dimensional region of the flow may have an influence on the degree to which the flow in the boundary regions affects the FIB measurement. However, for the purpose of this order-of-magnitude analysis, the general conclusions presented above, for which memory effects were neglected, is expected to remain valid.

6.3.3 Nonidealities in the Base Flow: Effect of Finite Beam Area on the FIB Measurement

The flow field along the centerline is shearfree. As one moves away from the centerline, the contribution of shear velocity gradient components to the rate-of-strain tensor must be considered. In consequence, the stress field will not be perfectly homogeneous over the area of the FIB probe beam even when the beam is centered on the centerline of the flow. The magnitude of stress-field variation associated with this inhomogeneity depends on the velocity gradient tensor associated with the flow and the diameter of the probe beam. As discussed in §3.4, the radius of the FIB beam is $r_b/h = 0.2$. In the upstream region, e.g. $\zeta = -5.7$, shown in Fig. 6.8, the variation in velocity over this distance is very small. However, near the contraction plane ($\zeta = +0.27$) and within the downstream slit the variation of the velocity gradient tensor over this area cannot be neglected and will affect the FIB measurement. A set of assumptions is invoked to show that in the upstream region defined by $\zeta \leq -0.5$ the stress field is effectively homogeneous over the beam area, but for $\zeta > -0.5$ inhomogeneity in the stress field prevents direct interpretation of the FIB measurement in terms of the stress field.

The effect of stress field inhomogeneities over the area of the probe beam on an FIB measurement was described for a general flow. A beam-averaged Muller matrix, $\langle M \rangle$, is calculated by integrating over local values of the Muller matrix, M(y, z), weighted by the local beam intensity, I(y, z), according to eq. (3.7). The problem is reconsidered here for the specific case of flow on the centerline of the planar contraction. For this purpose, only one beam of the TCFIB system need be considered; essential components of the optical train are schematically represented in Fig. 3.5a. A beam of the TCFIB system is represented by means of the Muller calculus

$$I_D = \begin{bmatrix} 1 & 0 & 0 & 0 \end{bmatrix} \bullet \frac{1}{2} \begin{bmatrix} & & 0 \\ & \hat{M}_{PA} & 0 \\ & & 0 \\ 0 & 0 & 1 \end{bmatrix} \bullet \langle M_S \rangle \bullet \frac{1}{2} \begin{bmatrix} & & 0 \\ & \hat{M}_{PG} & 0 \\ & & 0 \\ 0 & 0 & 1 \end{bmatrix} \bullet \begin{bmatrix} I_i \\ S_{i2} \\ S_{i3} \\ S_{i4} \end{bmatrix} \tag{6.19}$$

The terms (representing optical elements) on the right-hand side of eq. (6.19) are now defined from right-to-left order, as parallels the propagation of light through the system. The Stokes vector on the extreme right of eq. (6.19) represents a laser beam of arbitrary polarization and intensity, I_i; the actual polarization of the initial laser beam can be corrected for by a normalization procedure as described in §3.4.3. The light is then linearly polarized at a specific angle α by the polarization state generator (PSG), represented by the second matrix element from the right of the equation. One may note that the components in the fourth row and fourth column of the Muller matrix representing the PSG (M_{PG}) are all zero except for $M_{PG\ 44}$, which is unity. The remaining components in the upper-left section are represented by the 3×3 submatrix $\hat{M}_{PG}$. The beam averaged Muller matrix of the sample (third term from the right) is represented by $\langle M_S \rangle$. The polarization state analyzer (PSA) is the fourth term in the product. The PSA is oriented $\pi/2$ [rad] with respect to the PSG and can be completely described by means of the 3×3 submatrix $\hat{M}_{PA}$. The photodetector measures the intensity of the light, I_D, transmitted through the entire optical train. The unit vector simply selects the intensity component from the Stokes vector which is the product of multiplication of the right-most four terms. The zero components of the matrix and vector elements of eq. (6.19) allow reduction of the system to a 3×3 matrix equation

$$\frac{I_D}{I_i} = \frac{1}{4} \begin{bmatrix} 1 & -\cos 2\alpha & -\sin 2\alpha \end{bmatrix} \bullet \begin{bmatrix} 1 & 0 & 0 \\ 0 & \langle M_{S22} \rangle & \langle M_{S32} \rangle \\ 0 & \langle M_{S23} \rangle & \langle M_{S33} \rangle \end{bmatrix} \bullet \begin{bmatrix} 1 \\ \cos 2\alpha \\ \sin 2\alpha \end{bmatrix} \tag{6.20}$$

Where the Muller matrix for the sample, $\langle M_S \rangle$, has been expanded into component form. The off-diagonal components in the first row and column of the Muller matrix for the sample, which exhibits birefringence but not dichroism, are zero. The local values of the com-

ponents $M_{S23}(y, z)$ and $M_{S32}(y, z)$ of the sample exhibit even functional dependence on the extinction angle, χ. Since the flow is symmetric about the centerline, and the probe beam over which the integration is performed is centered on the centerline, the beam averaged value of components which exhibit such even functional dependence is zero

$$\langle M_{S32} \rangle = \langle M_{S23} \rangle = 0 \tag{6.21}$$

Consideration of the specific dependence of the diagonal components of a Muller matrix representing a birefringent sample on the extinction angle and retardation allows for calculation of an apparent retardation, δ'_m, which will be observed by the probe beam of finite diameter

$$\delta'_m = \cos^{-1}(\langle M_{S22} \rangle + \langle M_{S33} \rangle - 1) \tag{6.22}$$

Using the fact that the averaging operator, $\langle\ \rangle$, is linear, the apparent retardation can then be related to the local, actual retardation, $\delta'(y, z)$, throughout the probe beam area

$$\delta'_m = \cos^{-1}\langle \delta'(y, z) \rangle \tag{6.23}$$

Because of symmetry about the centerline, the apparent extinction angle is zero, $\chi_m = 0$.

The apparent retardation, δ'_m, is dependent, via eq. (6.23), upon the local retardation, but not the extinction angle, throughout the probe beam. This is a consequence of the symmetry of the stress field about the centerline and the center of the beam. Consequently, when estimating the influence of inhomogeneity in the stress field on the apparent retardation, only the magnitude of the local retardation, $\delta'(y, z)$, throughout the area probed by the beam must be considered.

Relation of the apparent retardation observed by each of the probe beams in the TCFIB system to the birefringence determined by the system is not straightforward; this is a consequence of the fact that the probe beams have different wavelength. However, such detailed consideration is not necessary here. Specifically, if the inhomogeneities in the stress field affect *either* the blue or green beams, a simple (directly proportional) interpretation of the measured birefringence in terms of the normal stress difference,

$N_1 = \tau_{zz} - \tau_{yy}$, on the centerline is not possible. The goal of this presentation is simply determination of the degree of stress-field inhomogeneity within the beam area which is tolerable, and consequently the identification of the region of flow where the FIB measurement may be directly interpreted in terms of stress. Equation (6.23) simplifies this task by rigorously showing that it suffices to consider only the retardation over the area of the probe beam; consideration of the local extinction angle is not necessary. For the following discussion, one should note that the retardation is linearly proportional to the birefringence

$$\delta' = \frac{2\pi d\Delta n}{\Lambda} \tag{6.24}$$

The region of the flow where the treatment of the stress field as approximately homogeneous over the beam area is valid is identified by making a number of simplifying assumptions; these are described in the remainder of this Section.

A complicating factor in the determination of the stress field from the FIB measurement arises from the fact that the test fluid used for the investigations comprising this thesis is a polymer blend. Specifically, the birefringence is linearly related to the first principal stresses (defined as $\Delta\tau = \sqrt{4\tau_{zy} + (\tau_{11} - \tau_{22})^2}$) of the components of the blend weighted by the respective stress-optical coefficients, as given in eq. (3.4). The stress of the Newtonian polybutene component, τ_{PB}, is directly related to the velocity gradient tensor of the flow at a point in space which is interrogated by the beam. However, because the polyisobutylene component is viscoelastic, in principle, the entire strain history of a fluid element must be considered in order to determine the stress, τ_{PIB}, at a given point.

Consequently, a rigorous assessment of heterogeneity in the stress field across the streamlines would require a two-dimensional flow simulation or streamline integration of a constitutive model along the paths of individual streamlines, in conjunction with a known velocity field. In either case, an accurate constitutive equation must be selected for the integration along the streamlines. Such a constitutive equation could be fit to the shear rheological data for the test fluid described in Chapter 4. However, a complete set of unambiguous elongational rheological data is not available. Furthermore, even if a constitutive equation could be fit to both accurate shear and rheological data, one could not be certain that the model would accurately predict the response of a viscoelastic fluid in a

complex flow. The need for only an order-of-magnitude estimate of the importance of inhomogeneities in the stress field, in conjunction with the necessity of assuming the accuracy of a constitutive model does not justify the effort required to conduct streamwise integration of the stress along the streamlines or a two-dimensional flow simulation.

An evaluation which is less "rigorous" but much simpler to conduct considers the components of the rate-of-strain tensor along the path of the streamlines. Specifically, the rate-of-strain tensor for the streamline on the centerline of the flow has a contribution only from the elongational, not from the shear components. As one moves off the centerline in the y-direction, the rate-of-strain tensor has progressively greater contributions from the shear components, while the elongational component remains essentially the same. This is illustrated via the profile of v_z-versus-υ of Fig. 6.8 which indicates that the velocity is nearly constant across the streamlines at a given position ζ, even in the vicinity of the contraction plane, $\zeta = +0.27$. As a consequence, the elongational component of the rate-of-strain tensor, $\partial v_z/\partial z$, will be nearly constant across the streamlines which pass through the probe beam at the contraction plane, $\zeta = 0$. However, as discussed above, the magnitude of the derivative of the profile, $|\partial v_z/\partial y|$, is not constant. Therefore, any inhomogeneity in the stress field within the probe beam can be considered to arise from differences in the shear component of the rate-of-strain tensor for the different streamlines. It seems reasonable to assume that if the contribution from the elongational component to the rate-of-strain tensor is much greater than the contribution from the shear component at all points along a given streamline, the stress profile along that streamline should be similar to the profile along the centerline. Alternately, if the contribution from the shear component is greater than or equal to the contribution from the elongational component, the stress profile may differ substantially from that of the centerline. The elongational ($\partial v_z/\partial z$) and shear ($\partial v_z/\partial y$) components of the rate-of-strain tensor at different points in the flow are plotted in Fig. 6.13. The elongational component on the shearfree centerline is plotted for different positions, ζ; this profile is expected to be nearly the same for all of the streamlines which pass through the probe beam at $\zeta = 0$. The shear component is plotted for a profile with constant $y = r_b$, i.e., the outer limit of the probe beam area from the centerline. A more conservative estimate of the importance of the shear component considers not only the value at a given point, but accounts for the memory of the fluid by considering the

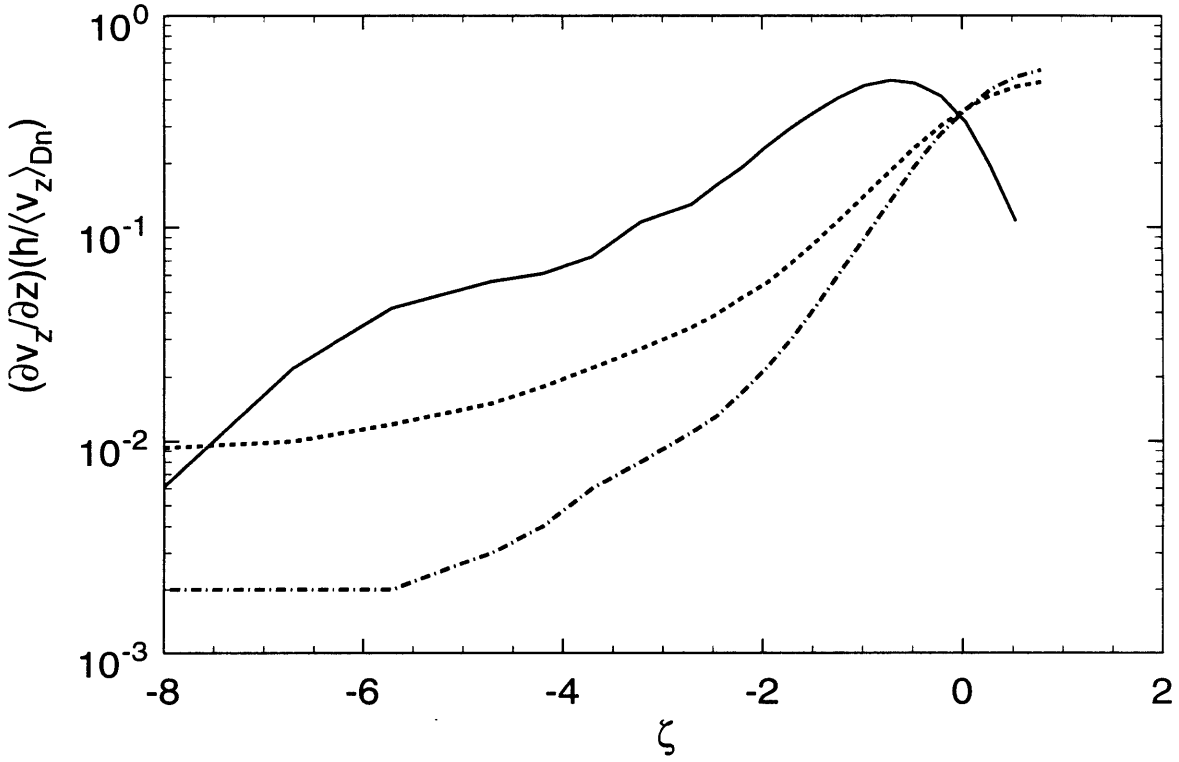

Figure 6.13 Dimensionless components of the velocity gradient tensor as a function of axial position, ζ: (———) elongational component, $(\partial v_z/\partial z)(h/\langle v_z\rangle_{Dn})$, on the centerline, $\upsilon = 0$; (– - –) shear component, $(\partial v_z/\partial y)(h/\langle v_z\rangle_{Dn})$, for $\upsilon = r_b/h$; (— —) shear component, $(\partial v_z/\partial y)(h/\langle v_z\rangle_{Dn})$, for streamline passing through the point $(\nu, \zeta) = (r_b/h, 0)$ described by $\upsilon = (r_b/h)(v_z(0)/v_z(\zeta))$. The profiles shown are for flow through the 8:1 contraction with $Wi_{Dn} = 1.59$.

contribution of the shear component to the rate-of-strain tensor at previous points occupied by the fluid element on the streamline in question. Therefore, the shear contribution is also plotted for points on the streamline which passes through the outer limit of the probe beam, at the contraction plane; i.e., the point ($\nu = r_b/h$, $\zeta = 0$). This represents an upper bound on the importance of the shear contribution to the rate-of-strain tensor for an FIB measurement taken with a probe beam centered on the centerline and upstream of the contraction plane, $\zeta \leq 0$. Using this conservative estimate, it is noted from Fig. 6.13 that the elongational contribution to the centerline rate-of-strain tensor is at least a factor of 3.3 greater than the shear contribution over the range $-5.7 \leq \zeta \leq -1.0$. The contribution of the elongational component to the rate-of-strain tensor then levels out while the shear contribution continues to increase: the ratio of the components narrows to a factor $\frac{\partial v_z/\partial z}{\partial v_z/\partial y} = 2.0$ at the point $\zeta = -0.5$. The shear contribution slightly exceeds the elongational contribution at the contraction plane, $\zeta = 0$. In consequence, the assumption of a homogeneous stress field should be valid up to at least $\zeta = -1$, and possibly $\zeta = -0.5$, but is almost certainly invalid for $\zeta \geq 0$. For the results presented in §6.4, direct interpretation of the birefringence measurement in terms of the stress field will be taken to be valid for axial positions of $-5.7 \leq \zeta \leq -0.5$.[5]

6.3.4 Nonidealities Resulting from Transitions at Elevated Flow Rates

As discussed in Chapter 5, at an elevated volumetric rate a flow transition occurs, as detected in the dimensionless strain rate versus ζ profile. Specifically, a region of diverging flow, having negative strain rate, is found in the upstream region. Also associated with this transition is a high strain rate "spike" having greater maximum dimensionless strain rate than for the base flow. The change in the dimensionless strain-rate profile prevents direct comparison of transient elongational viscosity profiles with those for the base flow in §6.4. However, since flow rearrangement is two-dimensional in nature, the ability to directly interpret birefringence measurements in terms of the stress field is not compromised, and the data can be used to test constitutive models as originally intended.

---

5. On the Figures of §6.4, some data points outside of this range are also shown.

At a flow rate greater than, but of the same order as that associated with the two-dimensional flow rearrangement, a transition to three-dimensional, steady flow (discussed in Chapter 5) occurs. The magnitude of the spatial oscillation was greatest near the bounding walls at y = ±H and weakest near the centerplane. Consequently, near the centerplane ($\upsilon = 0$), the three-dimensional and steady instability is not expected to have a deleterious effect on the use of FIB to obtain stress-field information.

At yet a higher flow rate, a transition to three-dimensional, time-dependent flow was observed; this instability is described in Chapter 5. As in the case of the preceding three-dimensional and steady instability, the amplitude of oscillation is greatest near the bounding walls at y = ±H and weakest near the centerplane. At a flow rate corresponding to $Wi_{Dn} = 2.90$ in the 8:1 contraction, greater than but close to the estimated critical value for onset of the instability, a scan over the x-direction on the centerplane (cf. Fig. 6.14) indicates that although there is variation in the velocity, the variation is sufficiently small that it may be neglected for the purpose of obtaining stress-field information from the birefringence measurement. However, when the flow rate is increased such that $Wi_{Dn} = 3.10$, the spatial variation in the x-direction associated with the instability, even near the centerplane, becomes sufficiently great that birefringence measurements cannot be directly interpreted in terms of stress, as shown in Fig. 6.15. One should note that the velocity data in Figs. 6.14 and 6.15 were obtained via LDV operating in the burst-analysis mode. Acquisition of each data point takes on the order of 60 [s]. Since the flow is time-dependent, the data shown in Figs. 6.14 and 6.15 do not represent instantaneous profiles. Consequently, the variation of the data points for the scan over x at a fixed ζ-position provides a lower bound on the magnitude of the oscillation; the "time averaging" acts to smooth variations.

6.3.5 Beam Divergence Induced by Thermal Gradients

As mentioned in §4.2.1, when a viscous fluid is sheared, mechanical energy is converted to heat. Consequently, a fluid of finite thermal conductivity driven through a planar contraction exhibits thermal gradients. Materials exhibit a correlation between temperature and the magnitude of the refractive index; specifically, an increase in temperature

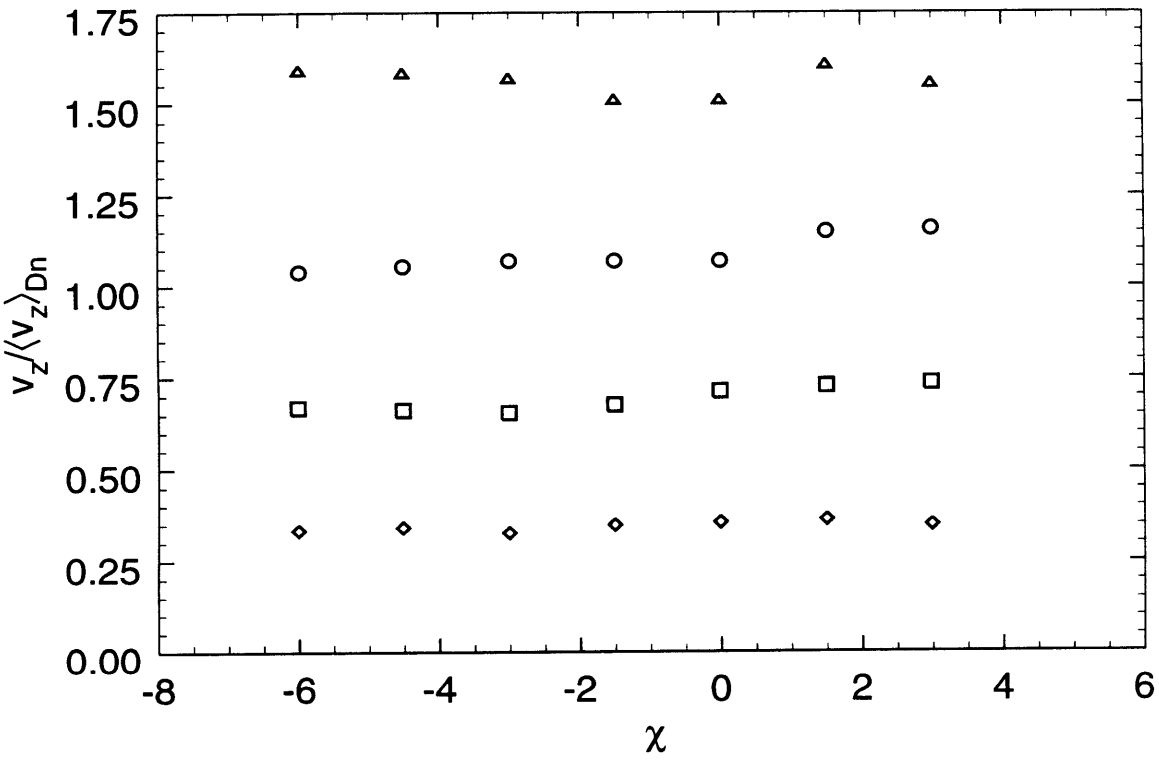

Figure 6.14 Profiles of dimensionless velocity, $v_z/\langle v_z\rangle_{Dn}$, as a function of position in the "neutral" direction, χ. Scans are taken on the centerplane, $\upsilon = 0$, at different axial positions: (△) ζ = -0.00; (○) ζ = -0.51; (□) ζ = -1.01; (◇) ζ = -2.01. Flow is through the 8:1 contraction with Wi_{Dn} = 2.90.

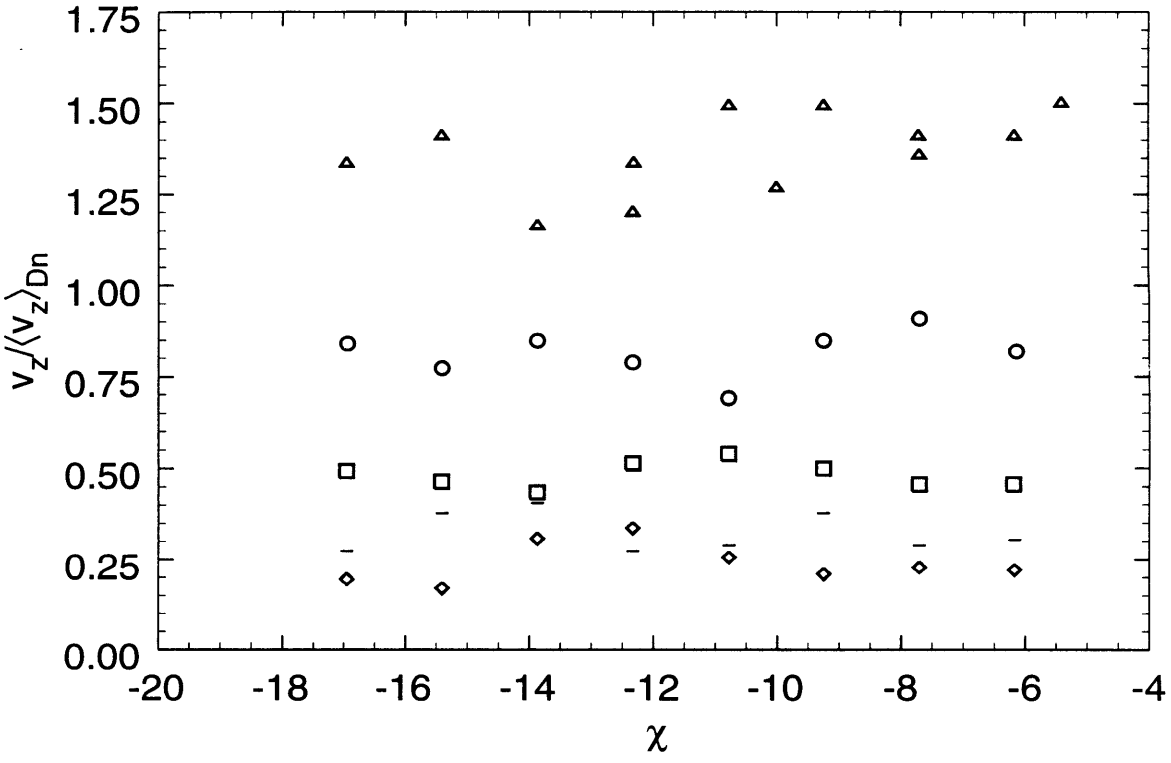

Figure 6.15 Profiles of dimensionless velocity, $v_z/\langle v_z\rangle_{Dn}$, as a function of position in the "neutral" direction χ. Scans are taken on the centerplane, $\upsilon = 0$, at different axial positions: (△) ζ = -0.05; (○) ζ = -0.56; (□) ζ = -1.05; (—) ζ = -1.55; (◇) ζ = -2.05. Flow is through the 8:1 contraction with Wi_{Dn} = 3.10.

results in a decrease in the refractive index. As a result, the 0.30 wt% PIB in PB test fluid exhibits refractive index gradients in the planar contraction flow. A sufficiently high variation in refractive index in the plane normal to the direction of propagation of the FIB probe beam causes the fluid flowing through the channel to act as a gradient refractive index lens. This lensing characteristic can induce deflection and/or divergence of the probe beam as it travels in the "neutral" direction through the channel and prevent an FIB measurement from being taken.

Galante (1991) discussed the effect of thermal gradients on beam deflection in detail; he presented a quantitative analysis for the case of fully developed flow and experimental data for flow of a polymer melt through the planar contraction. Beam deflection was detected but was sufficiently small so as not to have a deleterious effect on experimental measurements. Stress gradients can also induce beam deflection and broadening (Pindera and Hecker, 1987); Galante reviewed this phenomenon in the context of viscoelastic fluid flow. Galante found that in his experiments the effect of stress gradients on beam deflection was a factor of order ten less than the effect of thermal gradients (Galante, 1991). For the case of the fluid, flow rates, and geometry used in this investigation, beam divergence induced via thermal and/or stress gradients was noted in the vicinity of the entry of and within the downstream slit. The phenomenon was only observed for high flow rates corresponding to $Wi_{Dn} > 3.1$.

6.3.6 Summary of Factors which Limit Use of FIB Measurement to Determine Stress

A summary of factors which limit the flow rate for which FIB information may be directly interpreted in terms of the stress field, for flow of the viscoelastic test fluid through the planar contraction, is provided in Table 6.2.

H/h	8		32	
	Upstream ($\zeta \leq -0.5$)	Downstream & Contr. Plane ($\zeta > -0.5$)	Upstream ($\zeta \leq -0.5$)	Downstream & Contr. Plane ($\zeta > -0.5$)
Base Flow: Inhomogeneous Stress along Beam Path	$Wi_{Dn} > 0$ for $\zeta < -5.7, 0.8 < \zeta$		$Wi_{Dn} > 0$ for $\zeta < -5, 0.5 < \zeta$	
Three-Dimensional Flow	> 2.9	—	> 2.9	—
Inhomogeneous Stress over Beam Area	—	> 0	—	> 0
Thermal- and/or Stress-Gradient Induced Beam Div.	—	> 3.1	—	> 3.1

Table 6.2 Wi_{Dn} associated with flow phenomena which limit FIB measurement in the 8:1 and 32:1 planar contractions.

For the case of the base flow, the boundary regions within which the stress field is different than in the core region are expected to preclude the direct interpretation of FIB measurements in terms of the stress field in the regions far upstream of the contraction plane and in the downstream slit; i.e, axial positions of $\zeta < -5.7, 0.8 < \zeta$ for the 8:1 contraction and positions of $\zeta < -5, 0.5 < \zeta$ for the 32:1 contraction. In the upstream region over which the stress field is determined, i.e. $-5.7 \leq \zeta \leq 0.8$ for the 8:1 contraction and $-5 \leq \zeta \leq 0.5$ for the 32:1 contraction, the limiting factor is variation of the velocity field along the "neutral" x-direction following onset of the three-dimensional, time-dependent instability. The critical Weissenberg number defined in terms of the downstream parameters, Wi_{Dn}, increases with contraction ratio. If the Weissenberg number is defined in terms of the upstream parameters, as in Chapter 5, the critical Wi_{Up} *decreases* with the contraction ratio. As discussed in §6.3.4, FIB measurements can be made for Wi_{Dn} somewhat greater than the value associated with transition to three-dimensional, time-dependent flow.

In the region in the vicinity of the contraction plane and in the downstream slit, $\zeta > -0.5$, inhomogeneities in the stress field within the yz-plane normal to the direction of beam propagation, rather than variation in the direction of beam propagation (x-direction) pre-

vent direct interpretation of the FIB measurement in terms of the stress field. Since both the elongational and shear components of the velocity gradient tensor scale proportionally with the volumetric flow rate (when viscoelastic effects are neglected and before onset of flow instabilities) inhomogeneities in the stress field limit FIB measurements in the vicinity of the contraction plane and in the downstream region at all flow rates. The factors of three-dimensional unstable flow and stress inhomogeneities over the beam area preclude the direct interpretation of the birefringence measurement in terms of the stress field in the upstream and downstream regions of the flow before thermal- and/or stress-induced beam divergence must be considered. Thus, the onset of thermal- and/or stress-induced beam divergence is not a limiting factor.

6.4 Results: Comparison of Experimentally Determined Centerline Stress-Field Information with Model Predictions

In this Section, the results of the FIB measurements in terms of the centerline stress field for a set of flows are presented. In §6.4.1 the determination of the stress-optical coefficients, required to calculate the stress tensor from birefringence information, is discussed. The transient elongational viscosity which is used throughout this Section to present the stress field on the centerline is defined in §6.4.2. The effect on the transient elongational viscosity profile of varying the flow rate is presented in §6.4.3. The transient elongational viscosity profiles for flows through the 8:1 contraction geometry and through the 32:1 contraction geometry are compared in §6.4.4.

6.4.1 Determination of Stress-Optical Coefficients

The stress-optical coefficients were determined using the Couette cell apparatus described in §3.4. The inner spindle of the filled cell was rotated at a fixed angular velocity; the associated shear rate in the annular gap was calculated using the dimensions of the Couette cell. The stress tensor in the fluid was determined from the known shear rate and the steady shear rheology described in §4.4. The birefringence and extinction angle of the shearing fluid were measured using the TCFIB system. A set of data comprised of measurements taken at several rotation rates with the spindle rotated in both clockwise and

counter-clockwise directions was obtained. A plot of either the diagonal or the off-diagonal components of the refractive index tensor versus the stress tensor are used to calculate the stress-optical coefficient.

The birefringence in the flow of a polymer blend is related by eq. (3.4) to the contributions to the stress field caused by the component polymers. The determination of stress in the flow of the 0.30 wt% PIB in PB test fluid through the planar contraction requires the stress-optical coefficients of both the high MW polyisobutylene solute component and the medium MW polybutene solvent component. The measurement of the stress-optical coefficient for the polybutene solvent, C_{PB}, is first discussed; the calculation of the coefficient for the polyisobutylene solute is then presented. The stress-optical coefficients determined in this investigation are then compared with results previously presented in the literature.

As described in Chapter 4, for the flows considered in the planar contraction and for the range of shear rates accessible with the rheometer, the polybutene solvent is inelastic and non-shear-thinning; it acts as a Newtonian fluid. Consequently, in the Couette cell flow, the polybutene will exhibit zero normal stress; the only nonzero component of the stress tensor is $\tau_{r\theta}$. A plot of the off-diagonal component of the refractive index tensor, n_{21}, as a function of the shear stress, $\tau_{r\theta}$, is shown in Fig. 6.16. The linear relation of the quantities is evident; the stress-optical rule is consistent with the experimentally observed behavior. The stress-optical coefficient of the polybutene is equivalent to the slope of the line, $C_{PB} = 0.98 \times 10^{-9} \pm 0.07 \times 10^{-9}$ [Pa^{-1}]. The range of shear stress for making measurements is limited by two factors. The DC gear motor (Electro-Craft Motomatic, E652-MGHD) which drives the spindle is specified to have a speed range of $0.004 \leq \Omega_{motor} \leq 3.0$ [rad s^{-1}]. For the experiments, it was found that the slowest speed for which the motor rotation was steady, as required to obtain accurate birefringence data, was equivalent to a shear rate in the Couette cell of approximately 1 [s^{-1}]. The maximum shear rate which can be generated in the Couette cell is limited by the torque output of the motor, 33 [N m], and slip of the drive belt. Within the bounds set by the minimum speed and maximum torque output of the motor, measurements were conducted over a full decade of shear stress, $1\times10^2 \leq \tau \leq 1\times10^3$ [Pa], allowing accurate determination of C_{PB}.

In contrast with the pure polybutene solvent, the 0.30 wt% PIB in PB solution is elastic. Consequently, a non-zero normal, or "hoop", stress, $N_1 = \tau_{\theta\theta} - \tau_{rr}$, is observed in the

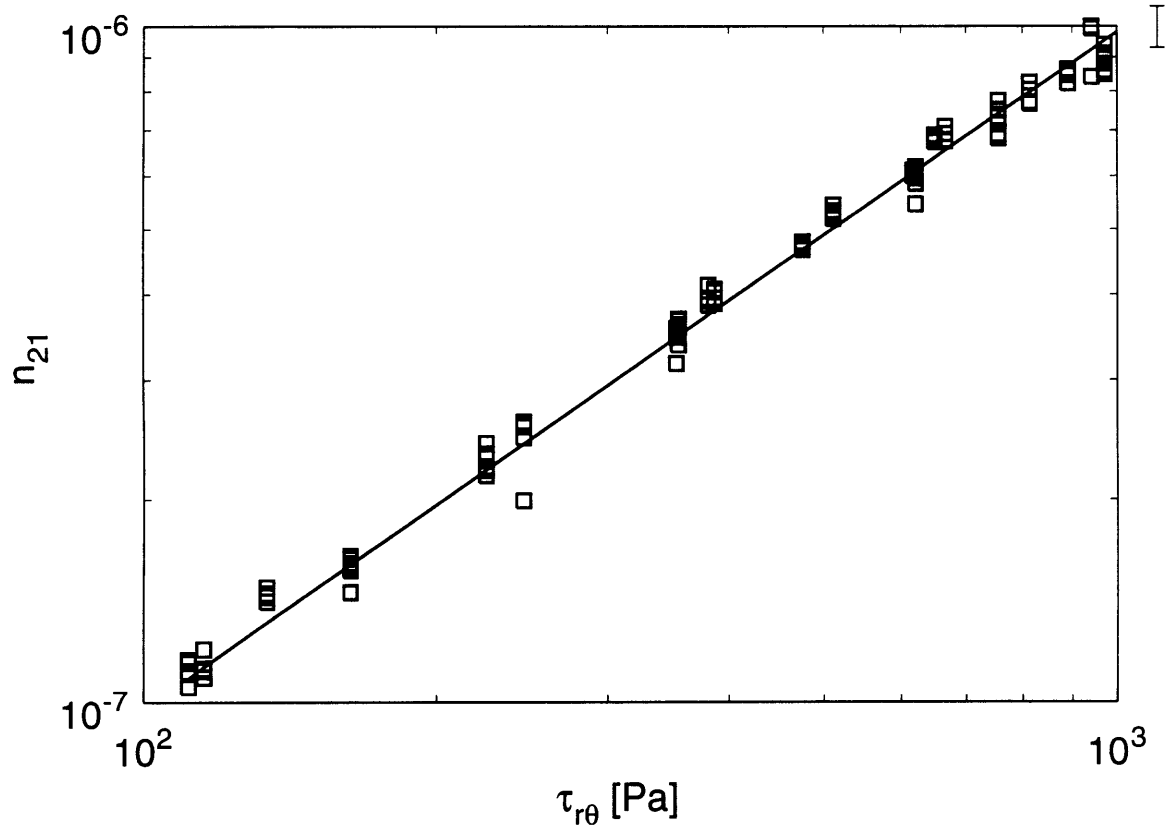

Figure 6.16 Determination of the stress-optical coefficient of polybutene, C_{PB}, in the Couette cell. The experimentally measured shear component of the refractive index tensor, n_{21}, is plotted as a function of the shear stress, $\tau_{r\theta}$, via the □ symbols. The slope of the fitted line (———) corresponds to $C_{PB} = 0.98 \times 10^{-9}$ [Pa^{-1}]. The error bar shown at the right of the graph indicates the ±7% standard deviation of the fit to the data.

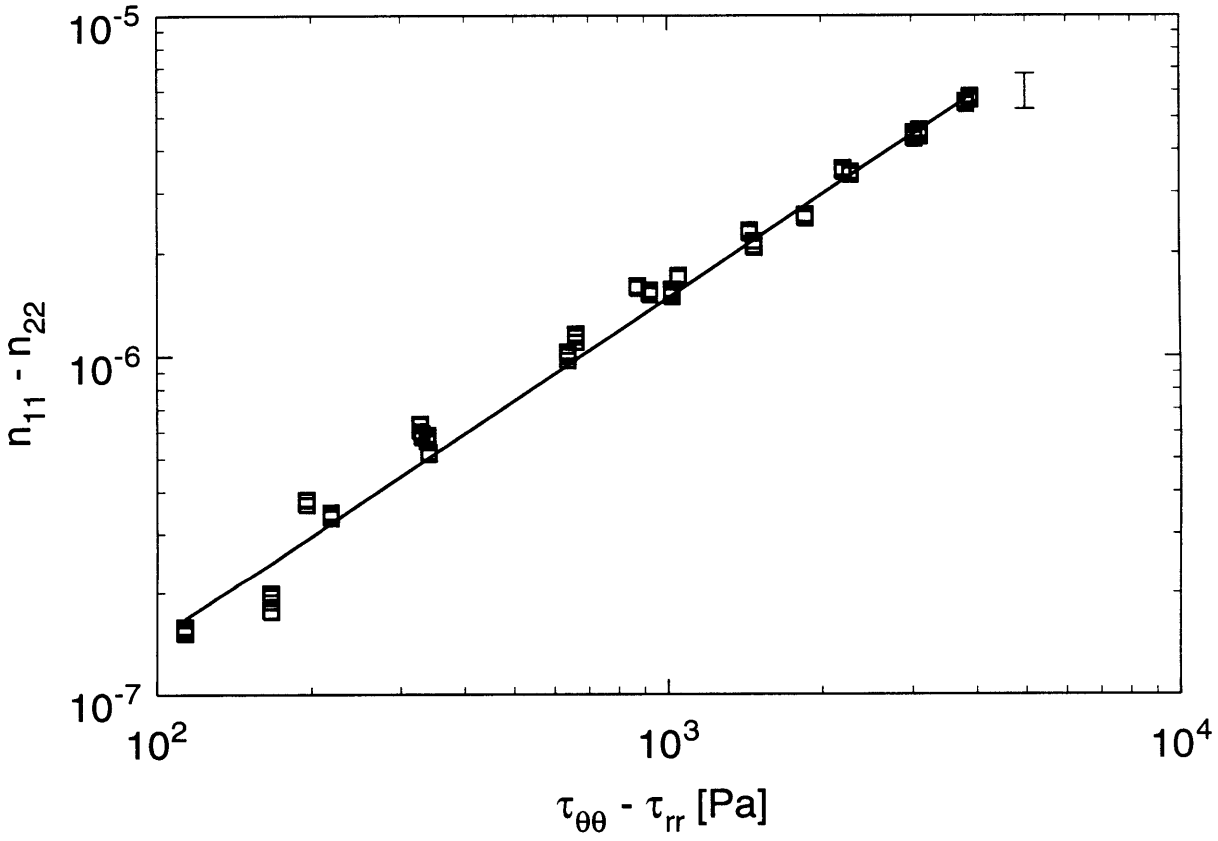

Figure 6.17 Determination of the stress-optical coefficient of polyisobutylene, C_{PIB} in the Couette cell. The experimentally measured difference of the normal components of the refractive index tensor, $n_{11} - n_{22}$, is plotted as a function of the first normal stress difference, $\tau_{\theta\theta} - \tau_{rr}$, via the □ symbols. The slope of the fitted line (———) corresponds to $C_{PIB} = 1.48 \times 10^{-9}$ [Pa^{-1}]. The error bar shown at the right of the graph indicates the ±12% standard deviation of the fit to the data.

Couette cell flow. Since, as described in the preceding paragraph the polybutene solvent does not contribute to the normal stress in the flow, the normal stress in the solution must arise exclusively from the contribution of the polyisobutylene solute component, $N_1 = N_{1PIB} = -\Psi_{1PIB}\dot{\gamma}^2$. Consequently, the stress-optical rule for polymer blends, eq. (3.4), reduces to

$$n_{11} - n_{22} = C_{PIB}N_{1PIB} \tag{6.25}$$

for the difference of the diagonal components of the refractive index and stress tensors.

The refractive index tensor was measured via TCFIB and the stress tensor determined for a set of rotation rates in the Couette cell for the 0.30 wt% PIB in PB test fluid; a plot of the results is given in Fig. 6.17. A straight line provides a good fit to the data, indicating consistency of the experimental results with the stress-optical rule. From the slope of the line, the stress-optical coefficient of the polyisobutylene solute component was determined to be $C_{PIB} = 1.48 \times 10^{-9} \pm 0.18 \times 10^{-9}$ [Pa^{-1}]. The lower bound on the normal stress difference, N_1, for which data could be obtained was set by the lowest speed of the DC motor which could be maintained without fluctuation in the rate of revolution. The upper bound on N_1 was set by onset of a three-dimensional instability which precluded quantitative FIB measurements from being made (the effect of variation of the stress tensor in the direction of beam propagation on FIB measurement has been discussed in Sections 3.4 and 6.3). The instability is induced by the interaction of streamwise elastic "hoop" stresses with the streamline curvature. The nature of this class of instability and theoretical and experimental studies of the elastically driven Couette cell instability in particular has been discussed in Chapter 5. Within the bounds set by the specifications of the DC motor and onset of flow instability, data are obtained over one-and-one-half decades of normal stress, $1\times10^2 \le N_1 \le 4\times10^3$ [Pa], enabling accurate calculation of C_{PIB}.

There are previously published values of the stress-optical coefficient for polyisobutylene. A summary of values of C_{PIB} obtained in bulk and in solution with different solvents is given in Table 6.3. These literature results are interpreted below and then compared with the stress-optical coefficient of polyisobutylene obtained for the PIB in PB solution used in this study.

Solvent (n)	C [10^{-9} Pa^{-1}]	c [g/100 cm^3]	Reference
Bulk (n_{PIB} = 1.50)[a]	1.4	—	Stein et al. (1954)
	1.50	—	Brodnyan et al. (1957)
Decalin (1.47)[b]	1.50	0.2 - 9.0	
	1.65	3.0	Philippoff (1962)
PIB Oligomer (1.50)[a]	1.80	0.2 - 2.0	den Otter (1967)
Tetradecane (1.43)[b]	1.87	3.8	Quinzani (1991)
Benzene (1.50)[b]	1.7	not reported	Tsvetkov (1957)
	2.18	3.0	Philippoff (1962)
Tetralin (1.54)[b]	2.49	3.0	
n-Octane (1.40)[b]	3.07	3.0	

Table 6.3 Published literature values for the stress-optical coefficient of polyisobutylene, C_{PIB}, in bulk and in various solvents. The invariant refractive index, n, of the solvent is given in the leftmost column; the concentration, c, of PIB solute in solvent is given.

a. PIB invariant refractive index from Philippoff (1962).
b. Solvent invariant refractive indices from Weast (1987).

The stress-optical rule was found to be independent of concentration of high molecular weight (MW) polymer solute in solvent (Brodnyan *et al.*, 1957) and independent of the MW of the solute (Fuller, 1995). However, as one may note from Table 6.3, the stress-optical coefficient *is* dependent on the chemical nature of the solvent (Philippoff, 1962); the origins of this dependency are considered below.

Form birefringence caused the PIB stress-optical coefficient reported for the PIB/solvent systems listed in Table 6.3 to differ from the value found for bulk PIB. The form birefringence phenomenon can be understood by considering a suspension of bodies in a medium. Both within the suspended particles and the suspending fluid the refractive index tensor is homogeneous and isotropic; however, the isotropic component of the refractive index tensor, n = trace(**n**), here termed the "invariant refractive index", is different for the

fluid and the particles. Despite the internal isotropy of the suspended particles, if the particles have a mean characteristic anisotropic shape, the net, macroscopically observed refractive index tensor will be anisotropic. This anisotropy is represented as the form birefringence, Δn_f (Doi and Edwards, 1986; Fuller, 1995; Quinzani, 1991).

To consider the form birefringence of a polymer/solvent system, the individual polymer molecules may be approximated as spheroids having homogeneous invariant refractive index. When subjected to a flow field of a characteristic velocity gradient, the spheroid will deform. If the polymer molecule is surrounded by a solvent with the same invariant refractive index, i.e. a "matching solvent", there will be no form contribution to the birefringence, despite the mean anisotropy of the particles. The macroscopically observed birefringence is then equal to the *intrinsic birefringence*, which is associated with the orientation of segments within the polymer chains and the anisotropic polarizability of the polymer backbone (cf. Chapter 3). However, if the invariant refractive indices of the polymer and the solvent differ, there is a form, in addition to an intrinsic, contribution to the observed birefringence, $\Delta n_{obs} = \Delta n_f + \Delta n_i$. If the polymer molecule is deformed into a prolate ellipsoid, as is the case for the shearing flows used to obtain the results presented in Table 6.3, the form birefringence causes a positive increase in the value of the ratio of the birefringence to the principle stress difference, $\Delta n/\Delta\tau$, above the value which would be observed if only intrinsic birefringence were present. The contribution of the form birefringence to the stress-birefringence ratio is always positive for particles of a prolate form, irrespective of whether the polymer or the solvent has the greater invariant refractive index. Note that unlike the intrinsic birefringence, the form birefringence does not exhibit a linear dependence on the imposed principle stress difference; this can result in a deviation from the linear stress-optical rule which is generally undesirable from an experimental viewpoint (Doi and Edwards, 1986; Fuller, 1995; Quinzani, 1991).

When a matching solvent is used, the birefringence-stress ratio for the polymer solute will be minimized and the stress-optical rule strictly apply: $C = \Delta n/\Delta\tau$ for all imposed stresses, for which the polymer chains have an approximately Gaussian configurational distribution (cf. Chapter 3). Note that the invariant refractive indices of the decalin, tetralin, tetradecane, and n-octane solvents differ from the value for the polyisobutylene polymer, $n_{PIB} = 1.50$, as shown in Table 6.3. With the possible exception of the decalin solvent

system (for which reported values differ by 10%), the stress-optical coefficients reported for the investigations using these solvents were all greater than that observed for PIB in bulk, $1.4 \leq C_{PIB} \leq 1.50$. However, this reasoning does not explain the elevated values of the stress-optical coefficient reported for solvents of benzene or PIB oligomer, both of which matched the refractive index of PIB to within 1%. The elevated value is especially surprising for the latter case, wherein the chemical structure of the solvent was identical to the PIB solute, differing only in molecular weight.

The solvent "quality" is not expected to directly affect the stress-optical coefficient. Specifically, when only intrinsic birefringence is considered, the relation between the stress-optical coefficient and the anisotropic polarizability, $(\alpha_{\parallel} - \alpha_{\perp})_{PIB}$, is

$$C_{PIB} = \frac{2\pi}{45k_BT}\frac{(n_{PIB}^2 + 2)^2}{n_{PIB}}(\alpha_{\parallel} - \alpha_{\perp})_{PIB} \tag{6.26}$$

where k_B is Boltzmann's constant and T is the absolute temperature. Microstructural terms such as the segment length or the number of segments in the polymer do not enter into eq. (6.26). In consequence, it does not matter if the polymer coil is relatively more expanded or compacted with respect to its configuration in a theta solvent (Doi and Edwards, 1986; Philippoff, 1956; Lodge, 1956; Kuhn and Kuhn, 1943).

It has been hypothesized that the high MW polymer chains may act locally to orient surrounding solvent molecules (Fukuda *et al.*, 1971). This mechanism may explain how the stress-optical coefficient for a high MW PIB solute in an oligomeric PIB solvent could differ from the value obtained in bulk. However, the concept of "local solvent orientation" is difficult to verify experimentally and is not considered further in this thesis. The potential role of experimental error must be considered when interpreting the data presented in Table 6.3; specifically, compare the results of different investigations which used the same polymer/solvent system (bulk PIB, PIB in decalin, or PIB in benzene). The values of the PIB stress-optical coefficient reported for a given polymer/solvent system differed from 10% to 30%.

The PIB in PB solution is well suited for use in birefringence investigations in that the PB solvent has an invariant refractive index of $n_{PB} = 1.50$ (Amoco Chemical Company,

1992) and is a matching solvent for PIB. The value of the stress-optical coefficient, C_{PIB} = 1.48×10^{-9} [Pa^{-1}], obtained in the experiments presented here is within the range of values reported for investigations with bulk PIB, $1.4 \leq C_{PIB} \leq 1.50$, as shown in Table 6.3. This consistency in the results supports the conclusion that form birefringence is negligible and the intrinsic birefringence associated with polymer segment orientation is the only contributing factor to the macroscopically observed birefringence for the 0.30 wt% PIB in PB test fluid.

Previously published stress-optical coefficient data for the polybutene solvent used in the composition of the test fluid were not available. The polybutene backbone is comprised of isobutylene and 1- and 2-butene monomer units (Amoco Chemical Company, 1992). The stress-optical coefficient for polyisobutylene has been discussed above. Stress-optical data for polypropylene are available in the literature; polypropylene has a backbone structure similar to poly(1-butene); i.e., alternate backbone carbons have a single attached side chain. A value stated in the literature for bulk isotactic polypropylene was $C_{PP} = 0.94 \times 10^{-9}$ [Pa^{-1}] (Adamse *et al.*, 1968). Note that the stress-optical coefficient for the polybutene solvent obtained in this investigation, $C_{PB} = 0.98 \times 10^{-9}$ [Pa^{-1}], has a value between those found for bulk polyisobutylene and bulk polypropylene.

6.4.2 Transient First Planar Elongational Viscosity

The stress response of the viscoelastic fluid to the transient planar elongational flow along the centerline may be conveniently represented by the "transient first planar elongational viscosity", $\bar{\eta}_c(\zeta)$ (Quinzani *et al.*, 1995).[6] Specifically, the profile of the normal stress difference, $N_1(\zeta) = \tau_{zz} - \tau_{yy}$, is normalized with the maximum strain rate experienced by fluid travelling along the centerline of the flow, $\dot{\varepsilon}_{max}$, to obtain

$$\bar{\eta}_c(\zeta) = \frac{N_1(\zeta)}{\dot{\varepsilon}_{max}} \tag{6.27}$$

6. Throughout the remainder of the text, for conciseness, $\bar{\eta}_c(\zeta)$ will be referred to simply as the "transient elongational viscosity profile".

One may note that for a Newtonian fluid in a planar elongational flow the transient elongational viscosity profile would have the same shape as the strain-rate profile, $\partial v_z(\zeta)/\partial z$, but be scaled with the factor 4μ, where μ is the viscosity of the Newtonian fluid. The "memory" characteristic of viscoelastic fluids will generally result in a more complex relation between the strain-rate and the transient elongational viscosity profiles. To understand the nature of a viscoelastic fluid from the transient elongational viscosity profile one must concurrently use the strain-rate profile. Specifically, the experimentally determined $\bar{\eta}_c(\zeta)$ is compared with the profile predicted by a linear or nonlinear constitutive model with the strain-rate profile. If the experimental and predicted profiles match, the constitutive model accurately represents the behavior of the viscoelastic fluid in the given transient planar elongational flow.

Representative stress and strain-rate profiles obtained in the 8:1 contraction at a flow rate corresponding to $Wi_{Dn} = 1.59$ are shown in Fig. 6.18. As discussed in Chapter 5, the strain-rate profile is characterized by a long "tail" of low strain rate extending far upstream, and a "spike" of high strain rate which reaches a maximum approximately 0.5h in front of the contraction plane. The profile of $\bar{\eta}_c$ exhibits similar features; specific aspects of the response of the fluid are discussed in the remainder of §6.4 and in §6.5. One may note that an abscissa other than axial position, ζ, can be useful for interpreting the transient elongational viscosity data; time (defined as $t = 0$ for a given fluid element at $\zeta = 0$) and strain (defined as $\varepsilon = 0$ at $\zeta = 0$) are used in §6.5.

6.4.3 Effect of Flow Rate on Transient Elongational Viscosity Profile

In this Section, centerline transient elongational viscosity profiles are shown for different volumetric flow rates through the 8:1 contraction. Comparison is made with two constitutive models: linear Maxwell and the nonlinear Giesekus model. The lowest flow rate for which a complete set of data was obtained corresponded to $Wi_{Dn} = 1.24$. The results for this flow rate are discussed first and in detail; the results serve as a reference to which data obtained for other flow rates are compared. Specifically, later in this Section the results for flows with $Wi_{Dn} = 0.83$, 1.59, 1.98, and 2.86 are discussed.

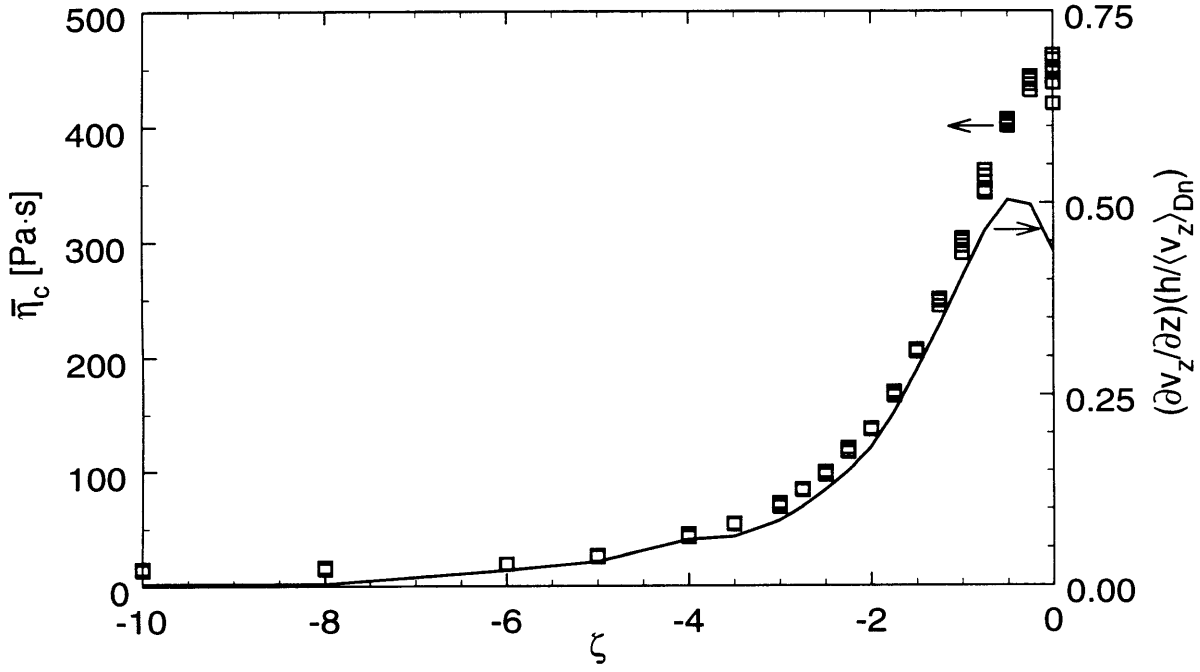

Figure 6.18 Representative experimentally determined centerline profiles of the transient first planar elongational viscosity, $\bar{\eta}_c$, (□ , plotted against the left axis) and the dimensionless elongational strain rate, $(\partial v_z/\partial z)(h/\langle v_z\rangle_{Dn})$, (——, plotted against the right axis). Both quantities are shown as functions of dimensionless axial position, ζ. Flow was through the 8:1 contraction with $Wi_{Dn} = 1.59$, which corresponds to a mean downstream shear rate of $h/\langle v_z\rangle_{Dn} = 4.0\ [s^{-1}]$.

A semilog plot of the experimentally measured transient elongational viscosity as a function of axial position is shown in Fig. 6.19a for flow through the 8:1 contraction with an associated $Wi_{Dn} = 1.24$. The shape of the profile is similar to that of the strain-rate profile for the flow shown in Fig. 6.19b. Specifically, far upstream of the contraction plane the strain rate and the transient elongational viscosity are low. As the contraction plane is approached, both quantities increase. The predictions of the linear Maxwell and nonlinear Giesekus constitutive equations also are shown in Fig. 6.19a; detail on the specific steps used to obtain these predictions is provided below. Far upstream, where the strain rate is low, the predictions of the linear and nonlinear models superimpose. This is expected because at a low "local elongational Weissenberg number", $Wi_{LE} = \lambda_{1char}\dot{\varepsilon}(\zeta)$ (λ_{1char} represents a characteristic relaxation time), any viscoelastic fluid responds linearly. Closer to the contraction plane, the strain rate rises to a sufficiently high level that the predictions of the linear and nonlinear constitutive models diverge. The semilog plot of Figure 6.19a highlights the increase in the percentage difference between the predictions of the linear and nonlinear models as the contraction plane ($\zeta = 0$) is approached. This divergence is a result of the increase in local strain rate and of accumulated strain; detailed discussion of the response of linear and nonlinear constitutive models to the centerline strain-rate profile characteristic of planar contraction flow is deferred to §6.5.

As discussed in §6.3, stress-field inhomogeneities restrict quantitative interpretation of the birefringence measurement in terms of the stress field to axial positions $\zeta < -0.5$. However, the predictions of the constitutive models imply that $\bar{\eta}_c$ continues to increase for ζ slightly greater than the point where the maximum strain rate is attained, $\zeta = -0.4$; such behavior can be attributed to the "memory" characteristic of the viscoelastic fluid. For the remainder of the flow on the centerline, over which the local strain rate was observed to decrease with increasing axial position, $\zeta > -0.25$, the most dramatic difference is noted between the predictions of the linear and nonlinear models. Again, the downstream region of the flow is not experimentally accessible to quantitative FIB measurements.

From Figure 6.19a, the distance between the experimental data and the model predictions of $\bar{\eta}_c$ is seen to be nearly constant over all the upstream axial positions shown on the semilog plot: the experimental data is greater than the prediction of the models by a constant percentage. This constant factor indicates a systematic error on the order of 20%.

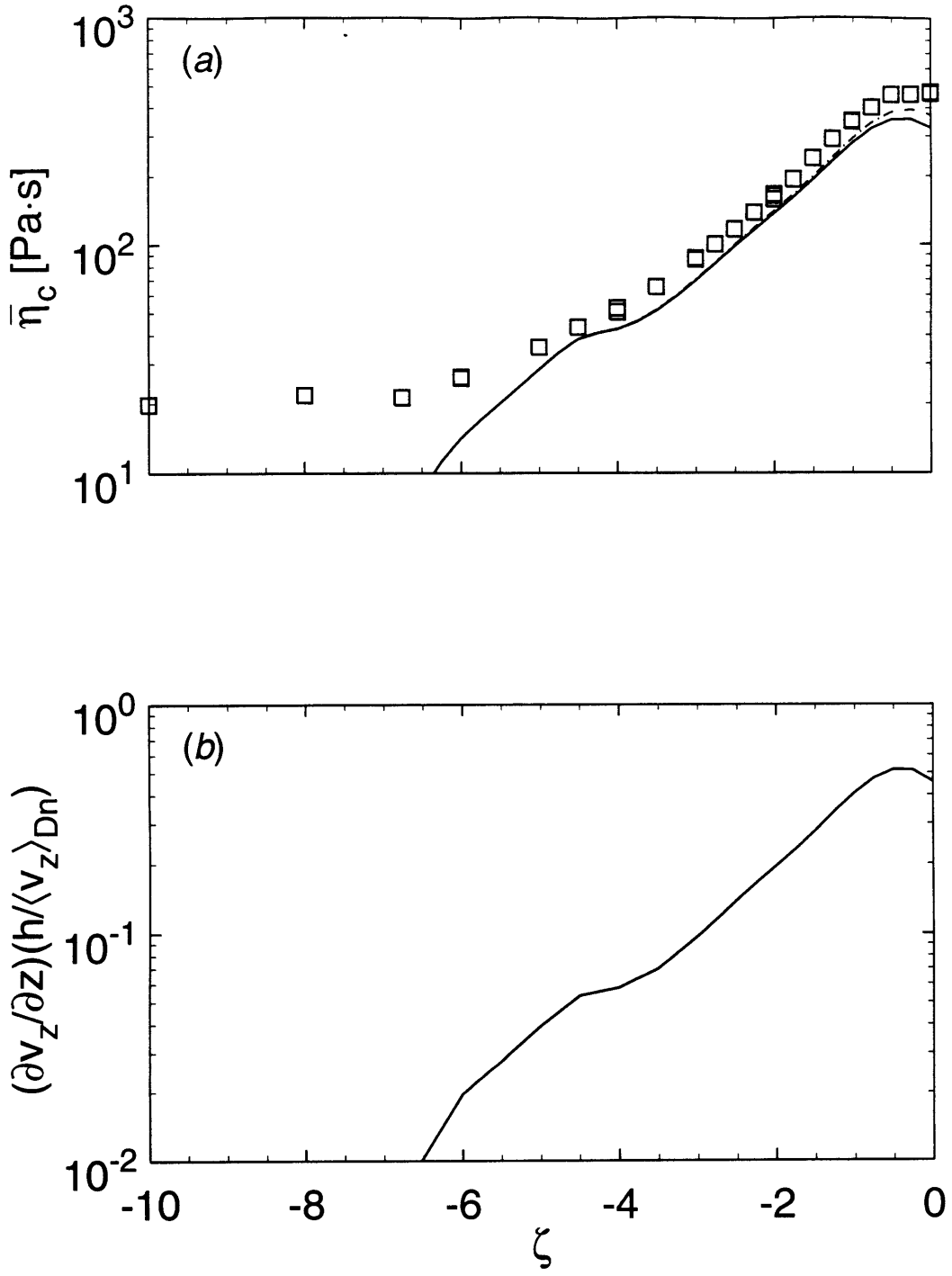

Figure 6.19 Centerline profiles as a function of axial position, ζ. Flow was through the 8:1 contraction with Wi_{Dn} = 1.24. (a) Transient elongational viscosity profile, $\bar{\eta}_c$: □ , experimental data points; (——) prediction of linear Maxwell; (– · –) prediction of Giesekus. (b) Dimensionless elongational strain rate, $(\partial v_z/\partial z)(h/\langle v_z\rangle_{Dn})$.

The basis for this interpretation and possible sources of error is discussed here. Far upstream of the contraction plane, the predictions shown in Fig. 6.19a of the linear and nonlinear models coincide. Consequently, if there were no error in the measurements, the fact that the flow in the upstream region only excited a linear response should result in the measured data superposing on the model predictions. This was not observed, the percentage offset of the data from the models was essentially the same in the upstream region as near the contraction plane, where the models indicated that a mildly nonlinear response could be excited. Consequently, the discrepancy of the experimental data with the prediction of the nonlinear model cannot be ascribed to inaccuracy in the fitted nonlinear parameters or to the inappropriateness of the Giesekus model.

A discrepancy of 20% is not surprising when one considers the steps in the data reduction required to obtain the transient elongational viscosity profile from the experimental data, shown in Figs. 6.19a and 6.19b. The propagation of error is now considered and is used to estimate the error associated with the experimentally determined transient elongational viscosity profile. Consider a multivariate function, $y = f(\mathbf{x})$, where $\mathbf{x} = \{x_1 \ldots x_n\}$ are uncorrelated independent variables. Take $\mathbf{x}_0$ to be the mean value of the dependent variables and $\boldsymbol{\sigma}_x = \{\sigma_{x_1} \ldots \sigma_{x_n}\}$ to be the standard deviation of the dependent variables about this mean. If the function is linear, the standard deviation of the dependent variable, σ_y, is related to the standard deviation of the independent variables as

$$\sigma_y^2 = \sum_{i=1}^{n} \sigma_i^2 \frac{\partial}{\partial x_i} f(\mathbf{x}_0) \tag{6.28}$$

Alternately, consider a function which is nonlinear, but differentiable about the point $\mathbf{x}_0$, so that for sufficiently small variation, $\mathbf{x} = \mathbf{x}_0 + \boldsymbol{\epsilon}$, the value of the function varies linearly with $\boldsymbol{\epsilon}$; i.e., $y = f(\mathbf{y}_0) + (\partial f / \partial \mathbf{x}) \cdot \boldsymbol{\epsilon}$, where $\mathbf{y}_0 = f(\mathbf{x}_0)$. Equation (6.28) can be applied to the function within this linear region (Box *et al.*, 1978). If $f(\mathbf{x})$ is a nonlinear function which is a product of the independent variables each raised to a power

$$f(\mathbf{x}) = \prod_{i=1}^{n} x_i^{p_i} \tag{6.29}$$

then the fractional standard deviation of the dependent variable, $\delta_y = \sigma_y / y_0$, is related to those of the independent variables, $\boldsymbol{\delta}_{\mathbf{x}} = \{(\sigma_{x_1}/x_{0,1}) \ldots (\sigma_{x_1}/x_{0,n})\}$, as

$$\delta_y = \sqrt{\sum_{i=1}^{n} \delta_{x_i}^2 p_i^2} \tag{6.30}$$

The transient elongational viscosity profile, defined in eq. (6.27), was calculated from the experimentally determined stress-optical coefficient, the birefringence profile, and the maximum value of the strain rate profile. Tests conducted with a quarter-wave plate indicated error in the retardation measured by the TCFIB apparatus (described in §3.4) of order $\delta_{\Delta n} = 2\,\%$; the fractional error for the lower retardations which are typically measured in the Couette cell and along the centerline of the planar contraction flow are expected to be greater. Furthermore, stress-field inhomogeneities along the beam path (x-direction), and within the plane for which the components of the refractive index tensor are determined (yz-plane) can affect the birefringence measurement, as discussed in Sections 6.3.2 and 6.3.3. Stress-field variation along the beam path could have induced error as great as $\delta_{\Delta n,\,x} = 10\,\%$ within the range $-5.7 \le \zeta \le 0.8$; variation within the beam area as great as $\delta_{\Delta n,\,yz} = 30\,\%$ over the range $-5.7 \le \zeta \le -1$. Both of these estimates are conservative, the actual error introduced was probably less. Taking the root mean square of the three factors, one obtains an estimate of the fractional deviation of the measured birefringence from the value associated with the stress field on the centerline for ideal two-dimensional flow; $\delta_{\Delta n,\,\text{Pl Contr}} = \sqrt{\delta_{\Delta n} + \delta_{\Delta n,\,x} + \delta_{\Delta n,\,yz}} = 32\%$.

Determination of the stress-optical coefficients has been discussed in §6.4.1; the fractional standard deviations associated with the fits to the data were $\delta_{C_{PIB},\text{fit}} = \pm 12\%$ and $\delta_{C_{PB},\text{fit}} = \pm 7\%$. The relation of the stress-optical coefficient to the birefringence and the stress is of the form in eq. (6.30). Given the $\delta_{\Delta n} = 2\%$ error associated with the measurement of birefringence (end effects in the Couette cell are negligible), the $\delta_\eta = 5\%$ error

associated with the measurement of the viscosity, and the $\delta_{\Psi_1} = 10\%$ error associated with measurement of the first normal stress coefficient, the expected fractional standard deviations for the stress-optical coefficients are $\delta_{C_{PIB}} = \sqrt{\delta_{\Delta n}^2 + \delta_{\Psi_1}^2} = 10\%$ and $\delta_{C_{PB}} = \sqrt{\delta_{\Delta n}^2 + \delta_{\eta}^2} = 5\%$. This is similar to the fractional standard deviations found when the data presented in Figs. 6.16 and 6.17 were fitted.

Velocity data on flow through the planar contraction was acquired via LDV, with an accuracy of order ±2%; the differential pressure which drove the fluid flow was measured to within ±5%. The centerline velocity profile was fit with a cubic spline, and the fit differentiated to determine the centerline strain-rate profile; note that the differentiation operation has the effect of increasing measurement noise. The volumetric flow rate through the system was measured via LDV for several pressure drops; the relation between volumetric flow rate and pressure differential was linear for all the experiments conducted for this thesis. The centerline birefringence and velocity data were obtained in separate runs; consequently, the imposed pressure drop, ΔP, could differ slightly. This discrepancy in the pressure differential was corrected for by using the linear relation between volumetric rate and pressure differential. Knowledge of the volumetric flow rate also allowed estimation of the Weissenberg numbers defined in terms of the upstream and downstream flow parameters, Wi_{Up} and Wi_{Dn}. When the different stress-optical coefficients of the PIB solute and the PB solvent are taken into account, the equation for reduction of the data to obtain the transient elongational viscosity profile is

$$\bar{\eta}_c(\zeta) = \frac{1}{4\dot{\varepsilon}_{max}}\left(\frac{\Delta n}{C_{PIB}}\right)\left(\frac{\Delta P_{LDV}}{\Delta P_{FIB}}\right) + \frac{\eta_{PB}\dot{\varepsilon}(\zeta)}{\dot{\varepsilon}_{max}}\left(1 - \frac{C_{PB}}{C_{PIB}}\right) \tag{6.31}$$

A rigorous analysis of the propagation of the error would require application of eq. (6.28) to eq. (6.31); the error associated with each data point would have to be evaluated separately. This rigorous analysis is not justified since correlation between the standard deviations of the $\dot{\varepsilon}(\zeta)$ and $\dot{\varepsilon}_{max}$ terms exists in eq. (6.31); correlation may exist between the C_{PB} and C_{PIB} terms and between the ΔP_{LDV} and ΔP_{FIB} terms but cannot be quantified. Since only a general estimate of the error is sought, only the first term on the right side of eq. (6.31) is considered. This allows application of eq. (6.30) to obtain

$$\delta_{\bar{\eta}_c} = \sqrt{\delta^2_{\Delta n,\,\text{Pl Contr}} + \delta^2_{C_{PIB}} + \delta^2_{\dot{\varepsilon}} + 2\delta^2_{\Delta P}} \tag{6.32}$$

The fractional standard deviations of the terms on the right side of eq. (6.32) were $\delta_{\Delta n,\,\text{Pl Contr}} = 32\%$, $\delta_{C_{PIB}} = 10\%$, $\delta_{\dot{\varepsilon}} = 2\%$, and $\delta_{\Delta P} = 5\%$, which yields a fractional standard deviation of the calculated transient elongational viscosity of $\delta_{\bar{\eta}_c} = 34\%$. This conservative estimate of the error is similar to the 20% discrepancy between the experimental and the predicted transient elongational viscosity profiles. Note that the error defined by eq. (6.32) is dominated by the $\delta_{\Delta n,\,\text{Pl Contr}}$ term. It is described above that the magnitude of this term is set primarily by the error associated with stress-field inhomogeneity along the beam path, $\delta_{\Delta n,\,x} = 10\,\%$, and within the beam area, $\delta_{\Delta n,\,yz} = 25\,\%$. Note that the error terms associated with stress-field inhomogeneity along the beam path and within the beam area both act to increase the experimentally determined stress above the value for flow along the centerline of an ideal, two-dimensional planar contraction. This is consistent with the results shown in Fig. 6.19a and for most of the results presented throughout Sections 6.4.3 and 6.4.4, for which the experimentally determined stress was approximately 20% greater than the predicted value.

Note that the shape of the experimental and predicted profiles in Figure 6.19a over the upstream region (specifically $\zeta \geq -0.5$) was clearly similar. A downward shift of 20% of the experimental data would result in good superposition of the experimental and the predicted profiles. One can note that the difference between the profiles predicted by the linear and nonlinear models is small, even near the peak of the profile at $\zeta = -0.25$. This indicates that only a mildly nonlinear response of the fluid is expected. Consequently, comparison of the shape of the experimental profile with the Giesekus prediction cannot unambiguously verify the accuracy of this or any other nonlinear constitutive model.

Transient elongational viscosity profiles for flow through the 8:1 contraction corresponding to $Wi_{Dn} = 0.83$ are shown in Fig. 6.20a and the associated strain-rate profile is given in Fig. 6.20b. Essential features of the experimentally determined, and of the linear and nonlinear model predicted profiles are the same as for the $Wi_{Dn} = 1.24$ flow discussed above. Only a few experimental data points near the contraction plane were obtained for the flow corresponding to $Wi_{Dn} = 0.83$. The anomalous, sudden decrease in the predicted

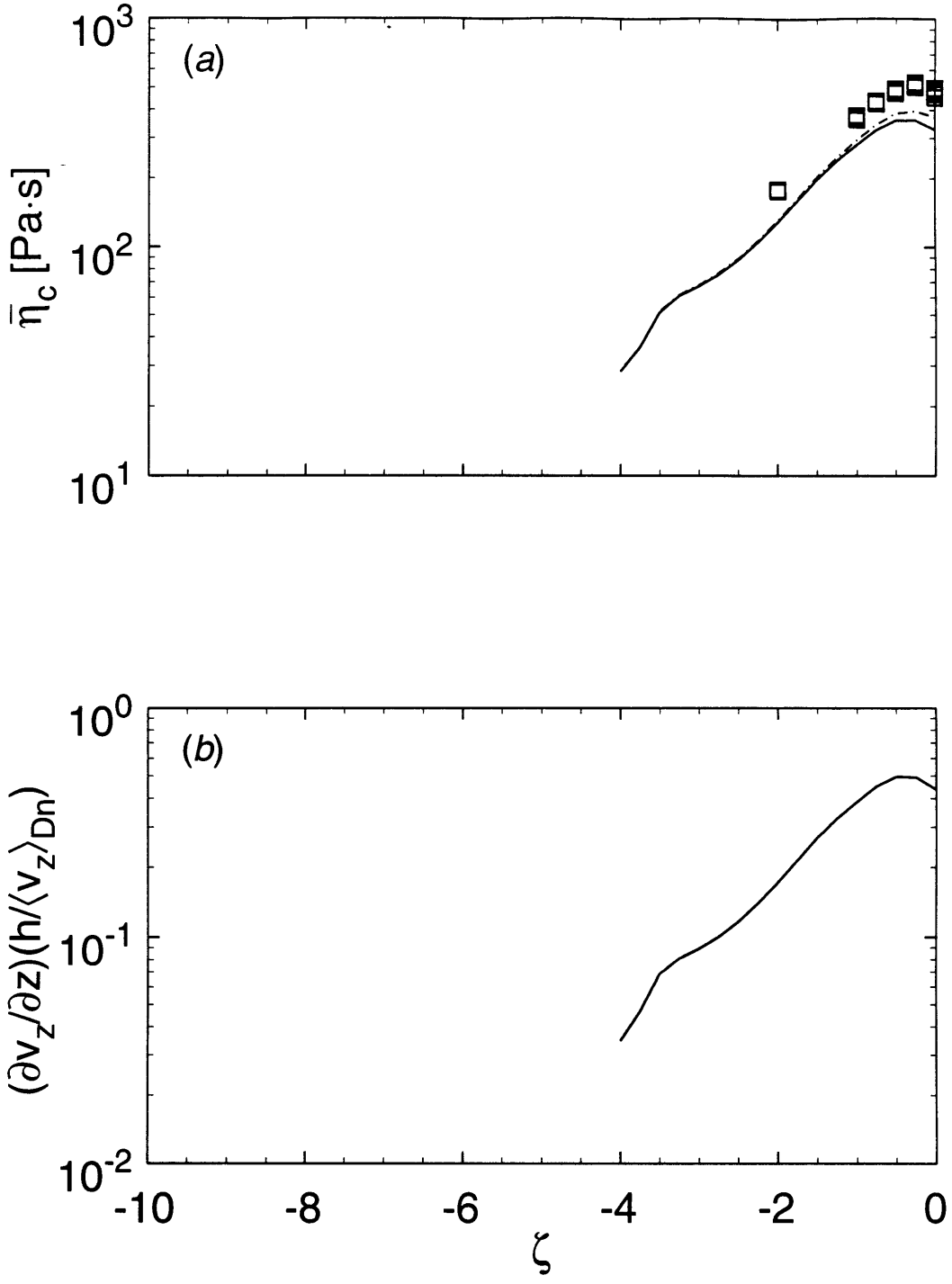

Figure 6.20 Centerline profiles as a function of axial position, ζ. Flow was through the 8:1 contraction with $Wi_{Dn} = 0.83$. (a) Transient elongational viscosity profile, $\bar{\eta}_c$: □, experimental data points; (——) prediction of linear Maxwell; (– · –) prediction of Giesekus. (b) Dimensionless elongational strain rate, $(\partial v_z/\partial z)(h/\langle v_z\rangle_{Dn})$.

transient elongational viscosity profiles at $\zeta = -4$, (cf. Fig. 6.20a) is not significant. This artifact results from a spurious "dip" in the strain-rate profile (cf. Fig. 6.20b), which is a consequence of limited accuracy of the velocity measurement in the upstream region of low velocity and strain rate.

Good superposition of the experimentally measured and the predicted elongational viscosity profiles may be noted in Fig. 6.21a, which corresponds to a flow with $Wi_{Dn} = 1.59$. One must realize that this agreement does not necessarily indicate more accurate data than that obtained for the $Wi_{Dn} = 1.24$ flow described above. Again, of primary importance is the match in the shapes of the experimental and the predicted profiles.

Profiles for a flow corresponding to $Wi_{Dn} = 1.98$ are shown in Fig. 6.22a. Both the shape and the relative displacement of the experimentally determined and the predicted transient elongation profiles resemble those shown for the $Wi_{Dn} = 1.24$ flow described above. The experimental data is shifted upward from the predicted profile by a constant factor of order 20%. The increased discrepancy for axial positions $\zeta \geq -0.5$ is attributed to the effect of stress-field inhomogeneities over the beam area.

At $Wi_{Dn} = 2.86$ the magnitude of the centerline strain-rate profile, shown in Fig. 6.23b, is greater for axial positions near the contraction plane than the profile for $Wi_{Dn} = 1.98$ (cf. Fig. 6.22b); in particular, the peak value of the dimensionless strain rate is higher. This rearrangement of the velocity (and consequently the rate-of-strain) fields has been discussed in Chapter 5. The flow has undergone a transition to a three-dimensional flow pattern at this flow rate. However, as discussed in §6.3, the effect of the instability on the variation of centerline strain-rate profile in the "neutral" or x-direction is minimal, allowing for quantitative interpretation of the birefringence data in terms of the stress field. The experimentally determined profile shown in Fig. 6.23a is order 20% greater than the predicted transient elongational viscosity profile. The curves in the stress-growth region ($\zeta < -0.5$) are similar to each other, although the match in the shape of the experimental and predicted profiles is not as close for the lower volumetric flow rate described above. Even at this elevated flow rate, with concomitant high values of the dimensional strain rate, there is little difference between the profiles predicted by the linear and the nonlinear constitutive models for axial positions $\zeta \leq 0$. The nature of a strain-rate profile capable of exciting a nonlinear viscoelastic response is discussed in greater detail in §6.5.

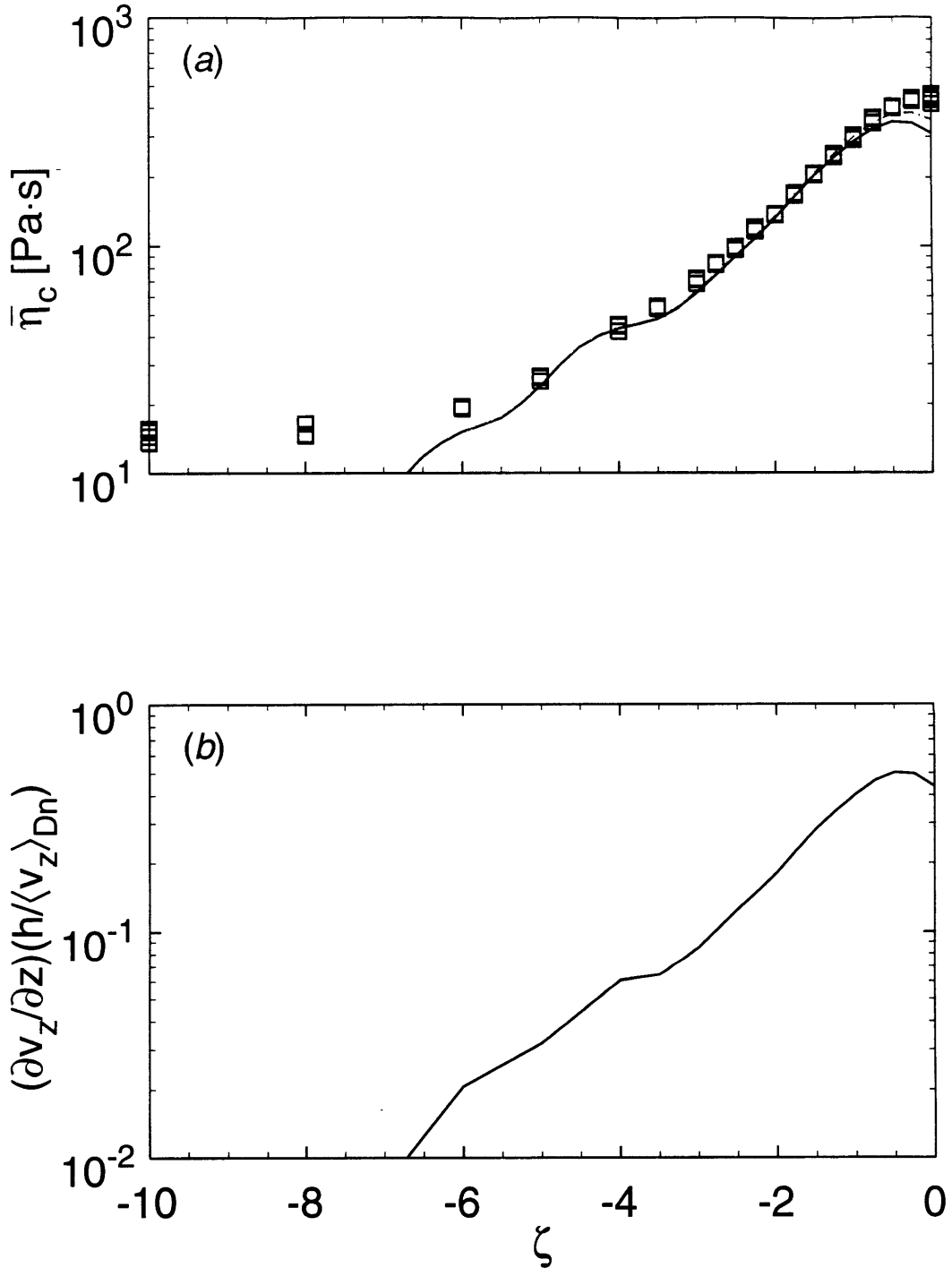

Figure 6.21 Centerline profiles as a function of axial position, ζ. Flow was through the 8:1 contraction with $Wi_{Dn} = 1.59$. (a) Transient elongational viscosity profile, $\bar{\eta}_c$: □, experimental data points; (——) prediction of linear Maxwell; (– · –) prediction of Giesekus. (b) Dimensionless elongational strain rate, $(\partial v_z/\partial z)(h/\langle v_z\rangle_{Dn})$.

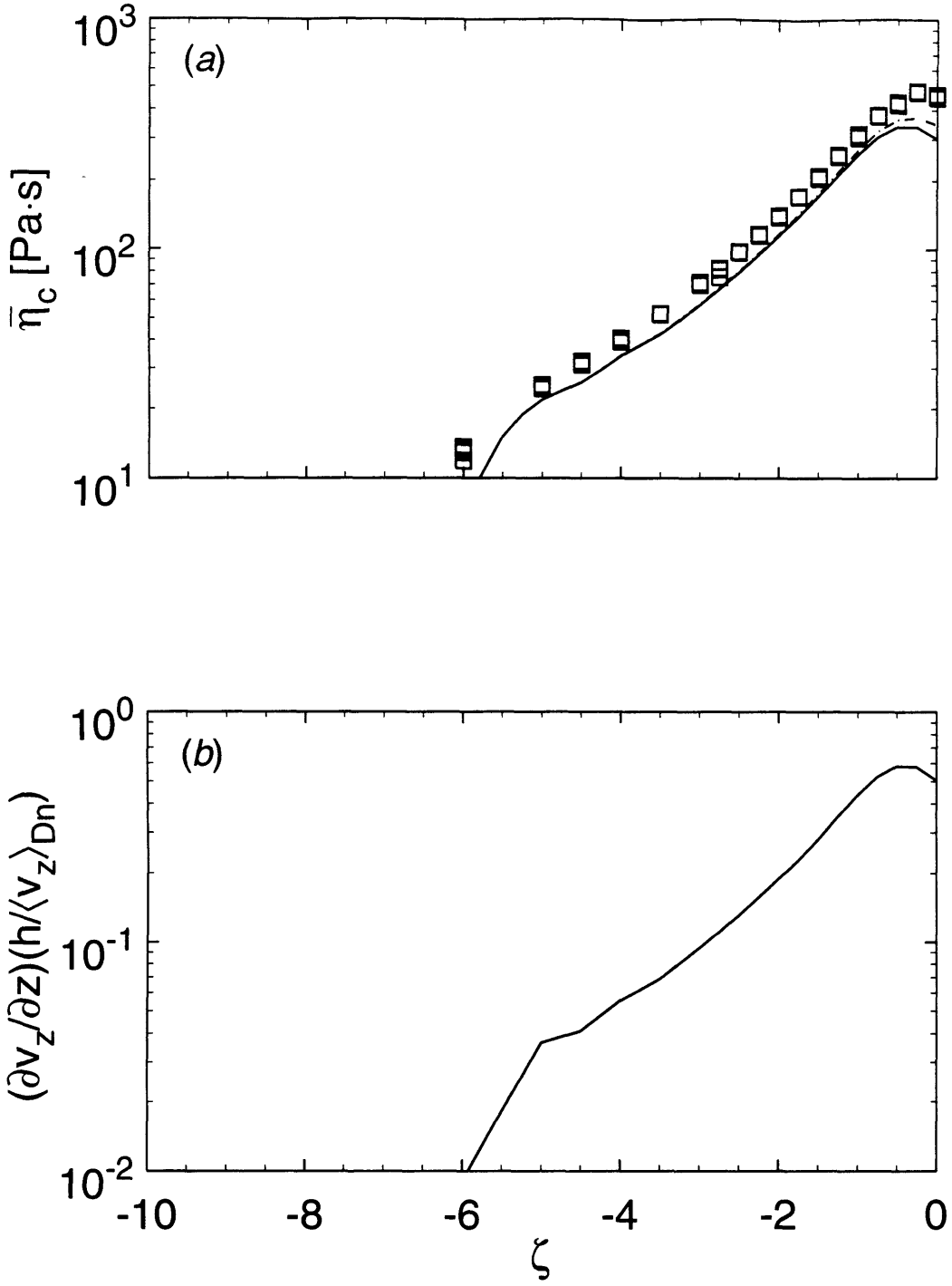

Figure 6.22 Centerline profiles as a function of axial position, ζ. Flow was through the 8:1 contraction with $Wi_{Dn} = 1.98$. (a) Transient elongational viscosity profile, $\bar{\eta}_c$: □, experimental data points; (——) prediction of linear Maxwell; (– · –) prediction of Giesekus. (b) Dimensionless elongational strain rate, $(\partial v_z/\partial z)(h/\langle v_z\rangle_{Dn})$.

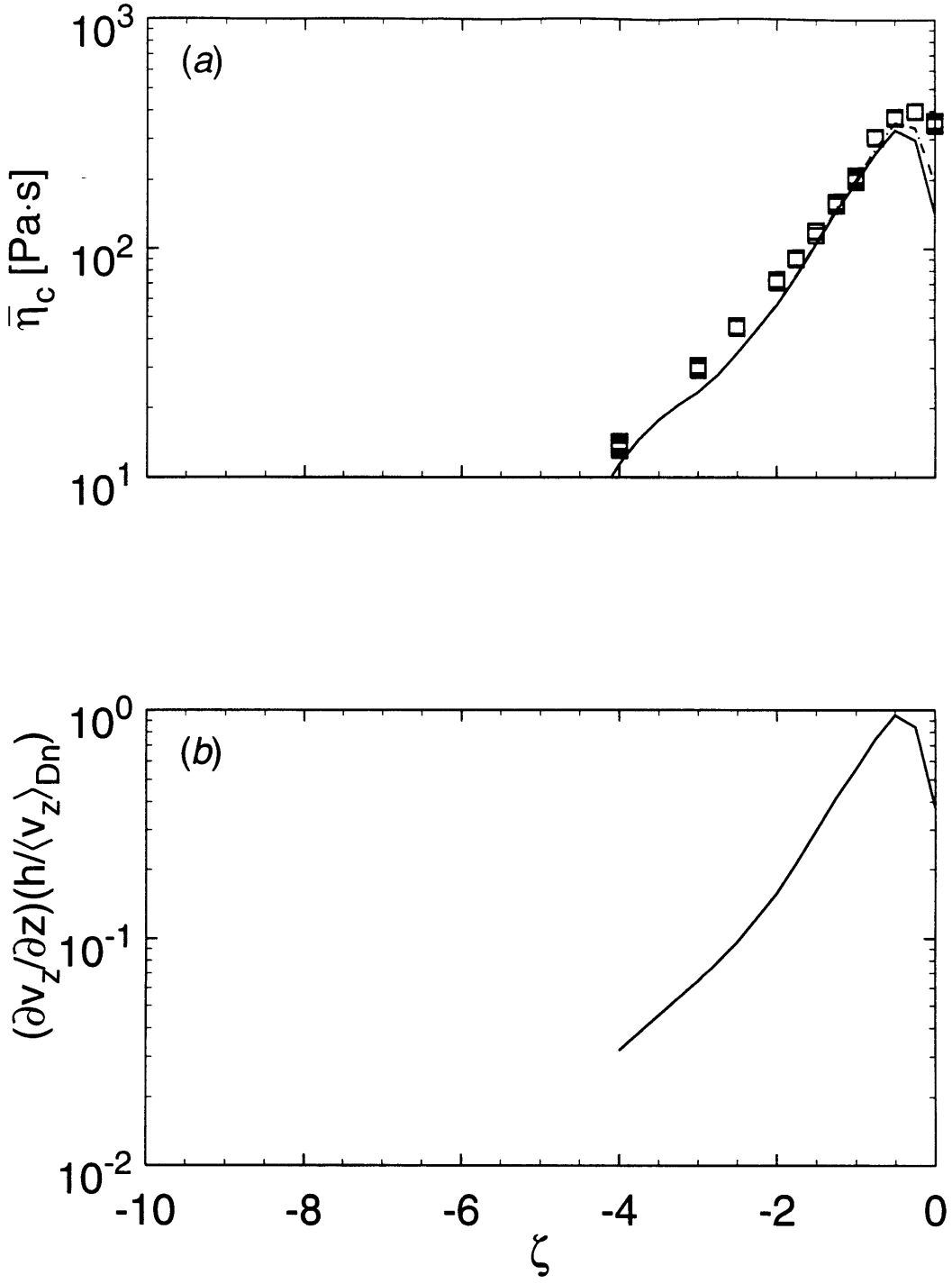

Figure 6.23 Centerline profiles as a function of axial position, ζ. Flow was through the 8:1 contraction with $Wi_{Dn} = 2.86$. (a) Transient elongational viscosity profile, $\bar{\eta}_c$: □ , experimental data points; (——) prediction of linear Maxwell; (– · –) prediction of Giesekus. (b) Dimensionless elongational strain rate, $(\partial v_z/\partial z)(h/\langle v_z\rangle_{Dn})$.

6.4.4 Effect of Contraction Ratio on Transient Elongational Viscosity Profile

Transient elongational viscosity profiles for flow along the centerline of the 32:1 contraction with an associated Wi_{Dn} = 0.95 are shown in Fig. 6.24a. One may compare the dimensionless centerline strain-rate profiles for the 32:1 and the 8:1 contractions, taken at similar Wi_{Dn}, in Figs. 6.24b and 6.20b. The effect of varying the contraction ratio on the centerline dimensionless strain-rate profile was discussed in detail in Chapter 5. The shape of the profile near the contraction plane is not affected by increasing the contraction ratio. However, the strain rate at a given axial position within the upstream "tail" ($\zeta < -3$) is greater for the 32:1 contraction flow than for the 8:1 contraction. As discussed in Chapter 5, a fluid element traveling along the centerline of the flow through the geometry of larger contraction ratio experiences greater total Hencky strain; this additional Hencky strain occurs in the upstream "tail".

The general shape of the experimental and of the predicted transient elongational viscosity profiles in the 8:1 and 32:1 contraction flows with $Wi_{Dn} \sim 1.0$ are shown in Figs. 6.20a and 6.24a and are similar in the vicinity of the contraction plane, $-3 \leq \zeta \leq 0$. Despite the greater Hencky strain along the centerline of the 32:1 contraction, the difference between the linear and nonlinear profiles near their peak is not much greater than in the 8:1 contraction: a substantial nonlinear response is not excited in the 32:1 contraction flow. The experimental profile has a shape similar to the predicted profiles, and, as in the case of the 8:1 contraction flows, is offset from the predicted profiles by approximately 20%.

The transient elongational viscosity profile measured for the 32:1 contraction at a flow rate corresponding to Wi_{Dn} = 2.14 is shown in Fig. 6.25a. The experimental and predicted profiles are similar to corresponding profiles shown in Figure 6.24a for the lower flow rate of Wi_{Dn} = 0.95. One can note that despite the increase in the dimensional strain rate at a given position along the profile a substantial nonlinear response is neither observed experimentally nor predicted by the models.

The profiles for a flow corresponding to Wi_{Dn} = 2.92 through the 32:1 contraction are shown in Figs. 6.26a and 6.26b. The dimensionless strain-rate profile shown in Fig. 6.26b is slightly more sharply peaked and the magnitude of the maximum strain rate is greater

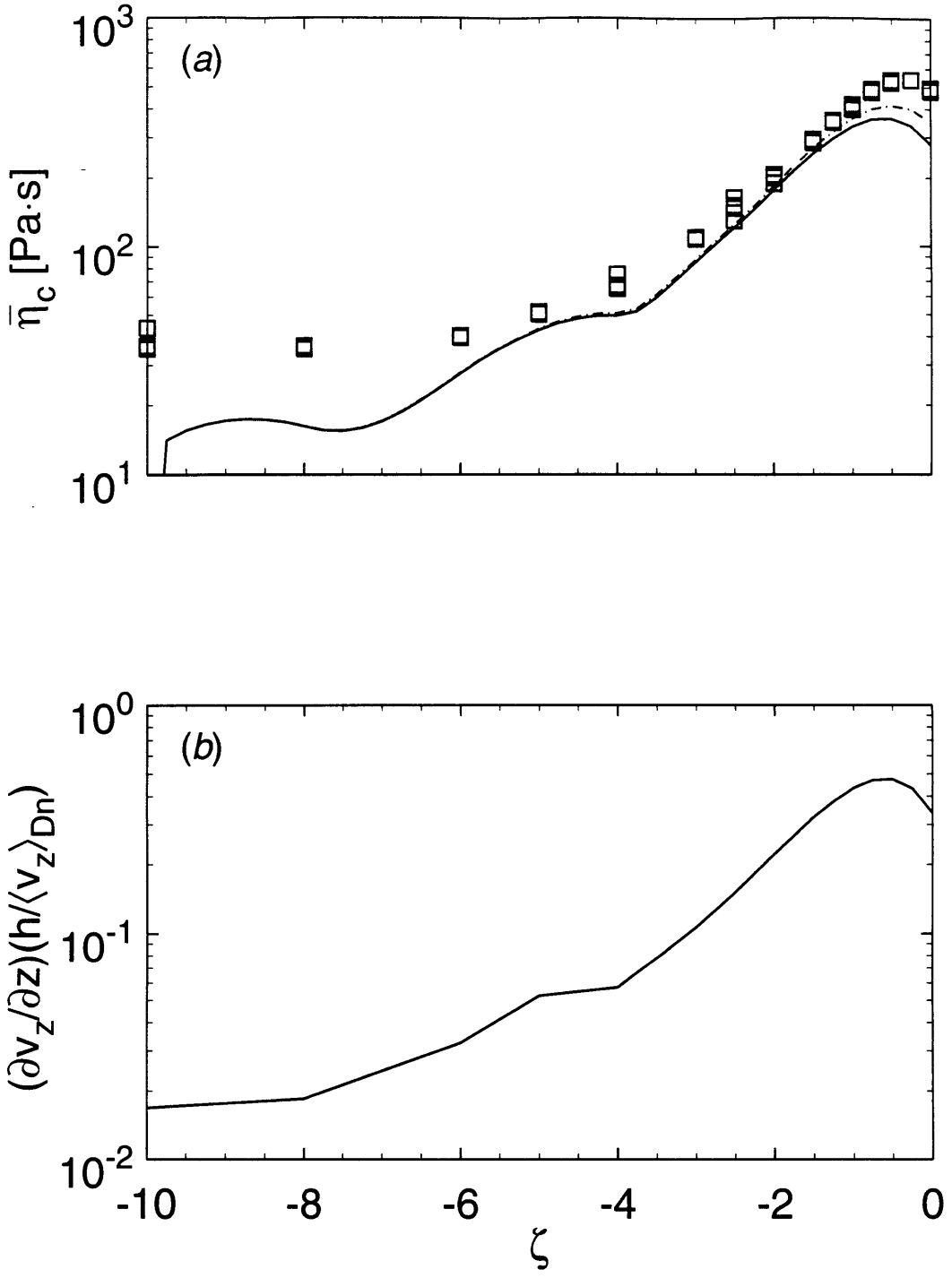

Figure 6.24 Centerline profiles as a function of axial position, ζ. Flow was through the 32:1 contraction with $Wi_{Dn} = 0.95$. (a) Transient elongational viscosity profile, $\bar{\eta}_c$: □, experimental data points; (——) prediction of linear Maxwell; (– · –) prediction of Giesekus. (b) Dimensionless elongational strain rate, $(\partial v_z/\partial z)(h/\langle v_z\rangle_{Dn})$.

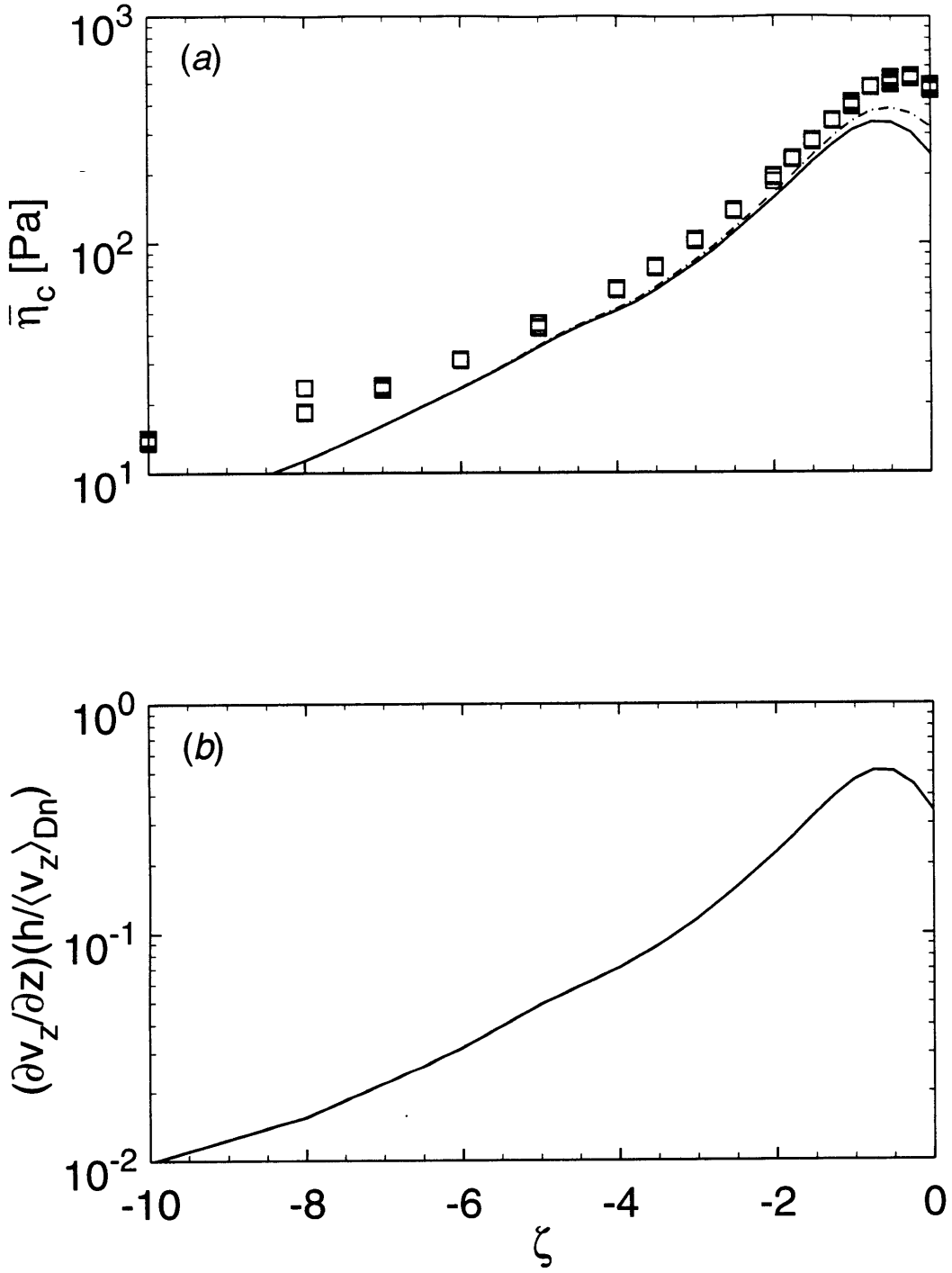

Figure 6.25 Centerline profiles as a function of axial position, ζ. Flow was through the 32:1 contraction with $Wi_{Dn} = 2.14$. (a) Transient elongational viscosity profile, $\bar{\eta}_c$: □, experimental data points; (——) prediction of linear Maxwell; (– · –) prediction of Giesekus. (b) Dimensionless elongational strain rate, $(\partial v_z/\partial z)(h/\langle v_z\rangle_{Dn})$.

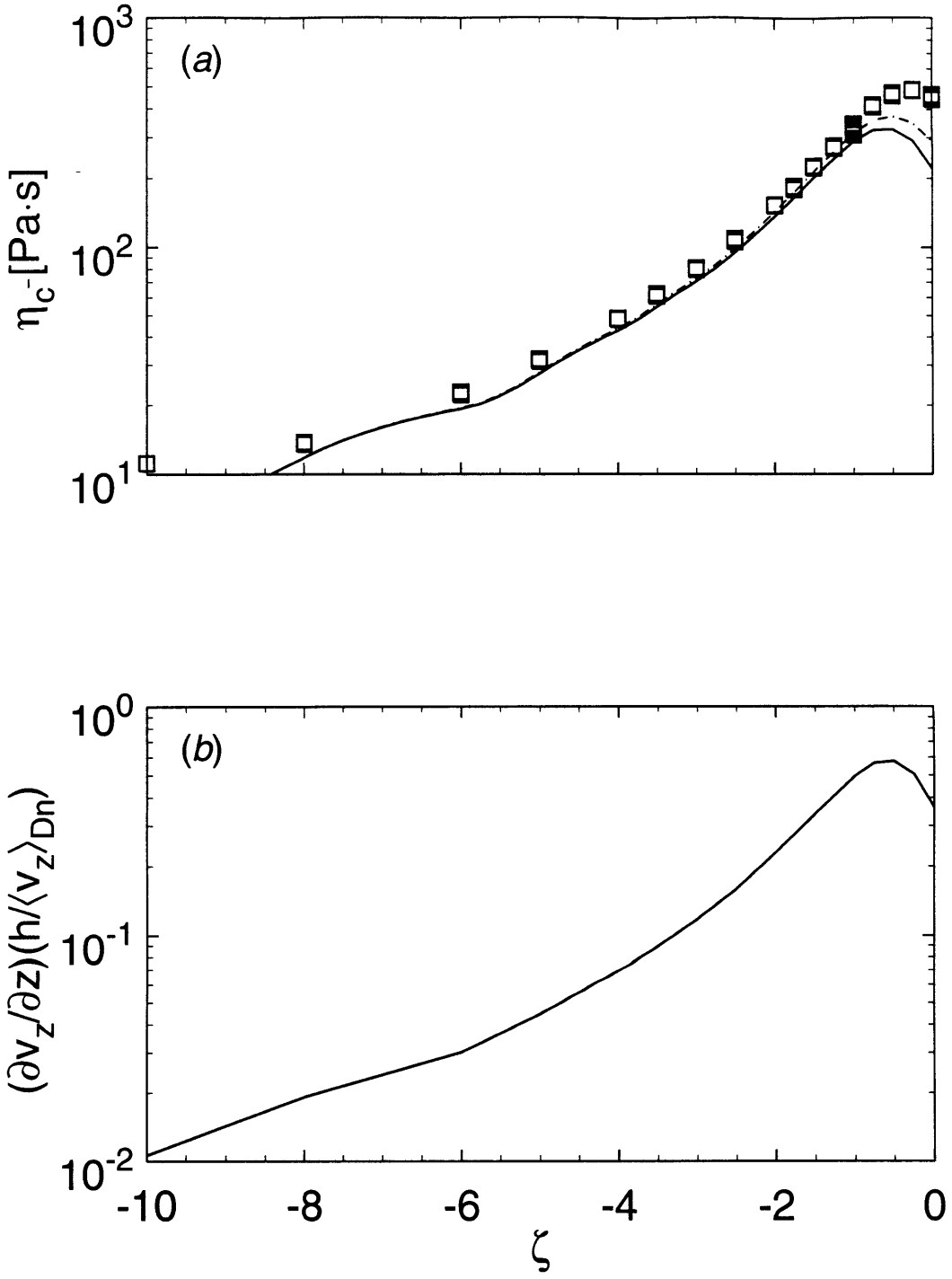

Figure 6.26 Centerline profiles as a function of axial position, ζ. Flow was through the 32:1 contraction with Wi_{Dn} = 2.92. (a) Transient elongational viscosity profile, $\bar{\eta}_c$: □, experimental data points; (——) prediction of linear Maxwell; (– · –) prediction of Giesekus. (b) Dimensionless elongational strain rate, $(\partial v_z/\partial z)(h/\langle v_z\rangle_{Dn})$.

than for the lower flow rates shown in Figs. 6.24b and 6.25b. This transition in the dimensionless elongational viscosity profile was described in detail in Chapter 5. The difference in the strain-rate profile is manifested as slightly more sharply peaked transient elongational viscosity profiles in Fig. 6.26a than observed for the lower flow rates. Neither the experimental data nor the predictions indicate a substantial nonlinear elongational response in the region of increasing strain rate ($\zeta < -0.5$), even at this elevated flow rate. The predictions of the models indicate substantial difference in the stress decay for $\zeta > -0.25$; the nonlinear Giesekus model predicts a much slower decay than the linear Maxwell model. However, as discussed in §6.3, inhomogeneities in the stress field within the probe beam prevent quantitative interpretation of birefringence measurements in terms of stress for $\zeta > -0.5$.

6.5 Interpretation of Results

The results presented in §6.4 indicate that for the flow conditions and geometries used in this investigation, a strong nonlinear viscoelastic response was not excited; the transient elongational viscosity profile predicted by the nonlinear Giesekus model was only slightly higher than the response predicted by the linear Maxwell model. This difference was less than the experimental error of the FIB measurement. Consequently, the measurement could not be used to assess the accuracy of the Giesekus model, of which only a weakly nonlinear response was excited. The inefficaciousness of the 32:1 contraction flow in exciting a nonlinear planar elongational flow response is surprising when one considers the predicted nonlinear response of the test fluid to a homogeneous planar contraction flow as discussed in §6.1.2. The factor of five difference between the prediction of the linear and the nonlinear models at a Hencky strain of $\varepsilon = \ln(32) = 3.47$ would have been readily detected by the FIB measurement technique. Consequently, a homogeneous planar elongational flow is much more "efficient" at stretching a polymer molecule than the strain-rate profile associated with centerline flow through the planar contraction, despite the fact that the flows have comparable total strains and strain rates. The importance of the shape of the strain-rate profile is a result of the finite response time and the finite strain required to observe a substantial nonlinear response.

The question is: why was a strong nonlinear response not stimulated by the centerline planar contraction flow? This question is answered in this Section. In §6.5.1 the response of the individual modes comprising the Giesekus model are compared with corresponding modes of the linear Maxwell of the upper convected Maxwell models. Understanding is gained by recalling the characteristic response of linear and nonlinear models to planar elongational flow, discussed in §6.1. An increase of the flow rate and variation of geometrical parameters are considered in Sections 6.5.2 and 6.5.3 as means to elicit a nonlinear response in the planar contraction flow.

6.5.1 Response of Individual Modes of Linear, Quasilinear, and Nonlinear Constitutive Equations

The response of individual modes of the linear and nonlinear constitutive equations to the planar contraction flow are compared here; the centerline velocity profile associated with the $Wi_{Dn} = 2.14$ flow through the 32:1 planar contraction is used as an example.

Experimental velocity data could only be obtained along the centerline of the planar contraction flow for axial positions $\zeta \gtrsim -10$. At locations farther upstream from the contraction plane, the velocity could not be measured with sufficient accuracy to allow for determination of the strain rate: calculation of the strain rate from the velocity, a differentiation operation, acts to aggravate measurement noise. However, one cannot necessarily neglect the effect of the far upstream region, $\zeta < -10$, on a fluid element; as discussed in Chapter 5, a substantial part of the Hencky strain which a particle along the centerline undergoes is experienced in the low strain-rate "tail" which extends far upstream from the contraction plane.

The strain-rate profile determined from experimental velocity measurements at $Wi_{Dn} = 2.14$ is shown in Fig. 6.27 together with the profile obtained via a two-dimensional finite-element simulation of Newtonian flow[7]; the calculated and experimental strain-rate profiles are in close agreement. At this flow rate, which corresponds to $Wi_{Up} = 0.011$, below the critical value for onset of the flow transitions described in Chapter 5, the velocity field is primarily determined by the viscous nature of the fluid. Since the test fluid has

7. The finite element simulations of Newtonian flow through the planar contraction used throughout §6.5 were performed by M.D. Smith (1997).

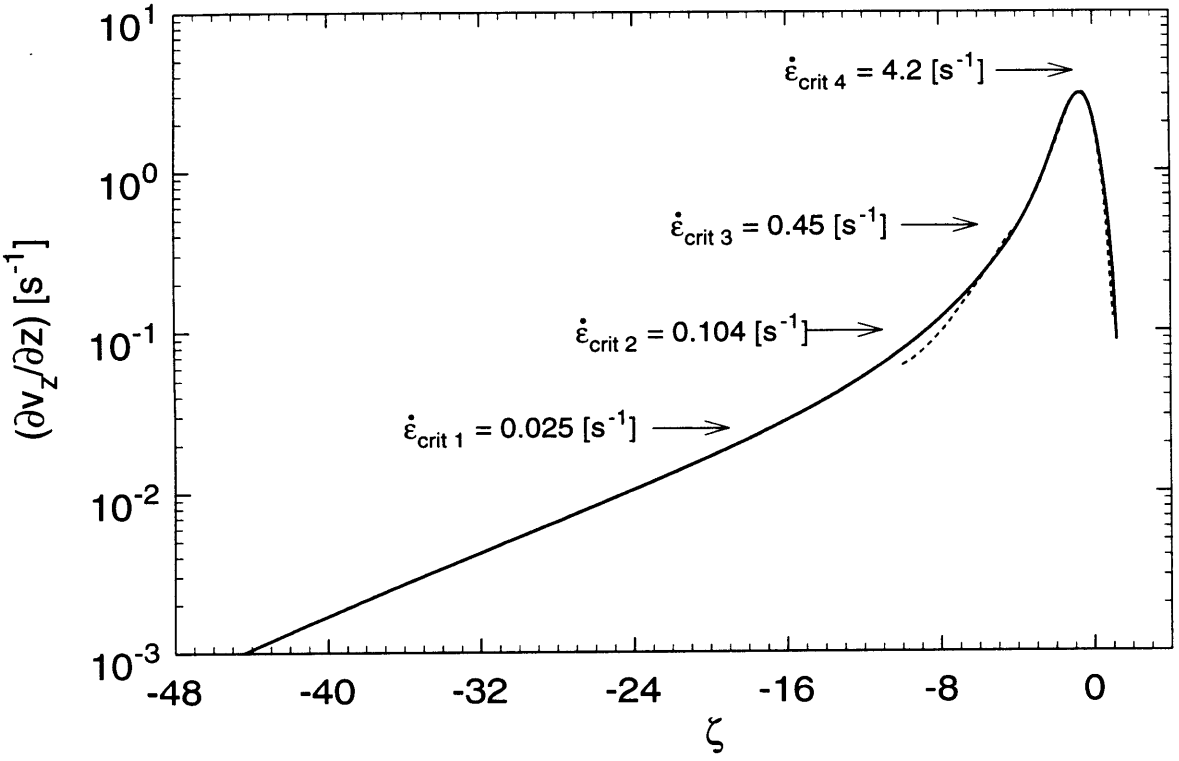

Figure 6.27 Centerline elongational strain-rate profile, $(\partial v_z/\partial z)$, as a function of axial position, ζ. Plot corresponds to flow through the 32:1 contraction with Wi_{Dn} = 2.14. (- - -) profile determined from spline fit to measured velocity data; (——) prediction of Newtonian flow simulation. The critical strain rate, $\dot{\varepsilon}_{crit,k}$, is shown for each relaxation mode.

nearly constant viscosity, the velocity field is similar to that for a Newtonian fluid. The advantage of using a numerically computed, rather than an experimentally measured centerline profile in the remainder of this Section is that accurate values of the strain rate for axial positions far upstream of the contraction plane are obtained. The critical strain rates associated with individual modes of the upper convected Maxwell and Giesekus models, described in §6.1 and listed in Table 6.1, are shown in Fig. 6.27. A similar plot of the numerically calculated centerline strain rate with the Hencky strain as the domain is given in Fig. 6.28. The Hencky strain is specifically defined as $\varepsilon(\zeta) = \ln((v_z(\zeta))/v_z(\zeta = 0))$; i.e., negative in the upstream region and zero at the contraction plane. One may note from Fig. 6.28 that the critical strain rate for Mode 1 is exceeded at $\varepsilon = -2.83$. The critical strain rate for Mode 2 is reached at $\varepsilon = -2.21$, for Mode 3 at $\varepsilon = -1.48$ and is not attained for Mode 4. The centerline strain-rate profile is plotted as a function of time in Fig. 6.29.

The response of individual modes of the linear Maxwell and the nonlinear Giesekus equations to the simulated centerline flow are shown in Fig. 6.30a for the volumetric rate corresponding to $Wi_{Dn} = 2.14$ through the 32:1 abrupt planar contraction. The transient elongational viscosity, $\bar{\eta}_c$, for a given mode is plotted on a log scale as a function of axial position, ζ. A similar plot in which the modes of the Giesekus model are compared to those of the upper convected Maxwell model is given in Fig. 6.30b. Note the superposition of the predictions of the models for a given mode, with the exception of the curves for Mode 1, associated with the longest relaxation time. As discussed in §6.1, it has been empirically observed and is predicted by constitutive models that in start-up of elongational flow (transient, but homogeneous), for a nonlinear response to be excited (i.e divergence of the predictions of linear and nonlinear models) the critical strain rate must be exceeded, and the total strain experienced by a fluid element must be greater than order unity, $\varepsilon \gtrsim 1$. Although the strain rate is not constant in the flow on the centerline of the planar contraction, one would expect a similar dependence of the response of a fluid element on the experienced Hencky strain to hold. Divergence of the linear and nonlinear models is defined here as having occurred at the point where the nonlinear constitutive model predicts a value of $\bar{\eta}_c$ approximately twice that predicted by the linear model for a given relaxation mode. In Fig. 6.31a, the response of the linear Maxwell and the Giesekus modes to the simulated flow through the 32:1 contraction with volumetric rate correspond-

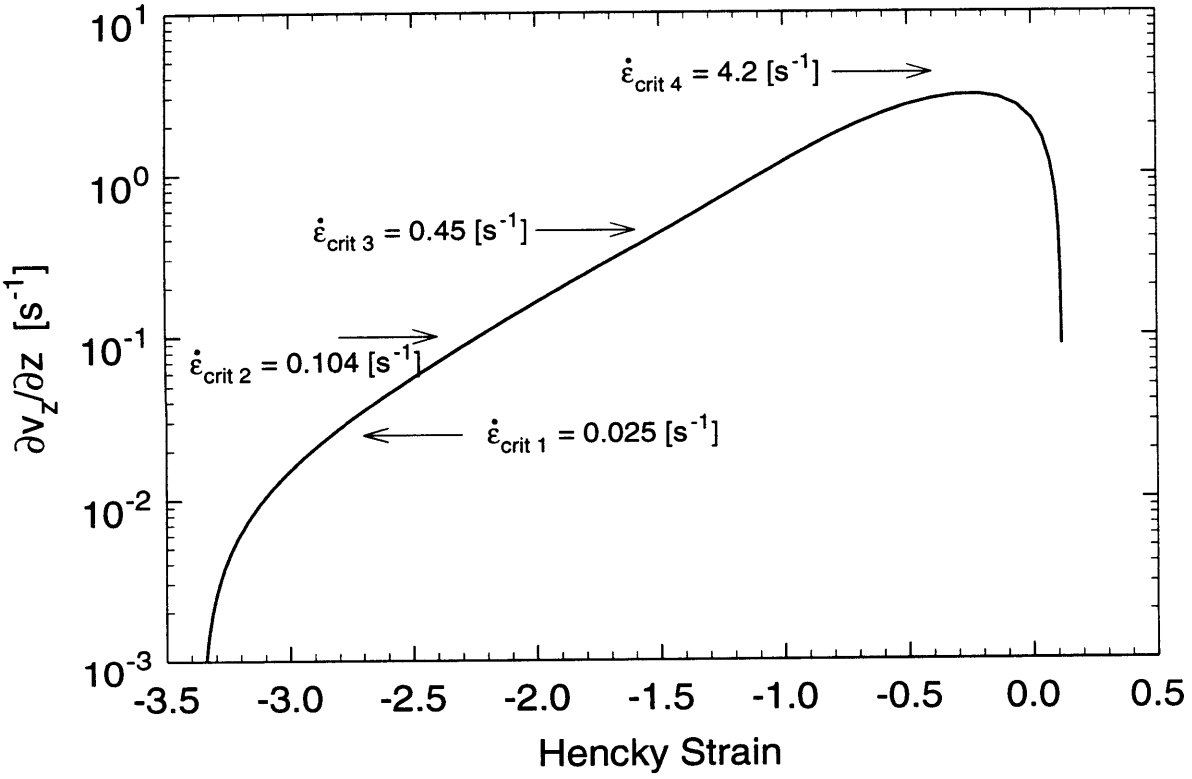

Figure 6.28 Centerline elongational strain-rate profile, $(\partial v_z/\partial z)$, as a function of Hencky strain, ε. Prediction by Newtonian flow simulation for flow through the 32:1 contraction at a volumetric rate corresponding to $Wi_{Dn} = 2.14$. The critical strain rate, $\dot{\varepsilon}_{crit,k}$, is shown for each relaxation mode.

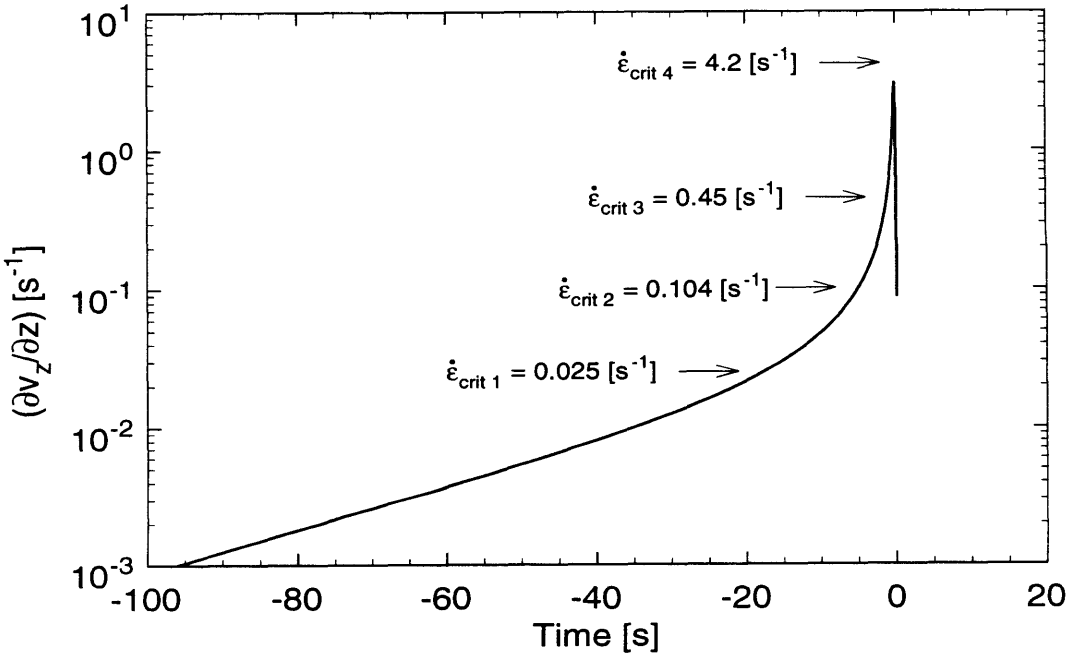

Figure 6.29 Centerline elongational strain-rate profile, $(\partial v_z/\partial z)$, as a function of time, t. Prediction by Newtonian flow simulation for flow through the 32:1 contraction at a volumetric rate corresponding to $Wi_{Dn} = 2.14$. The critical strain rate, $\dot{\varepsilon}_{crit,k}$, is shown for each relaxation mode.

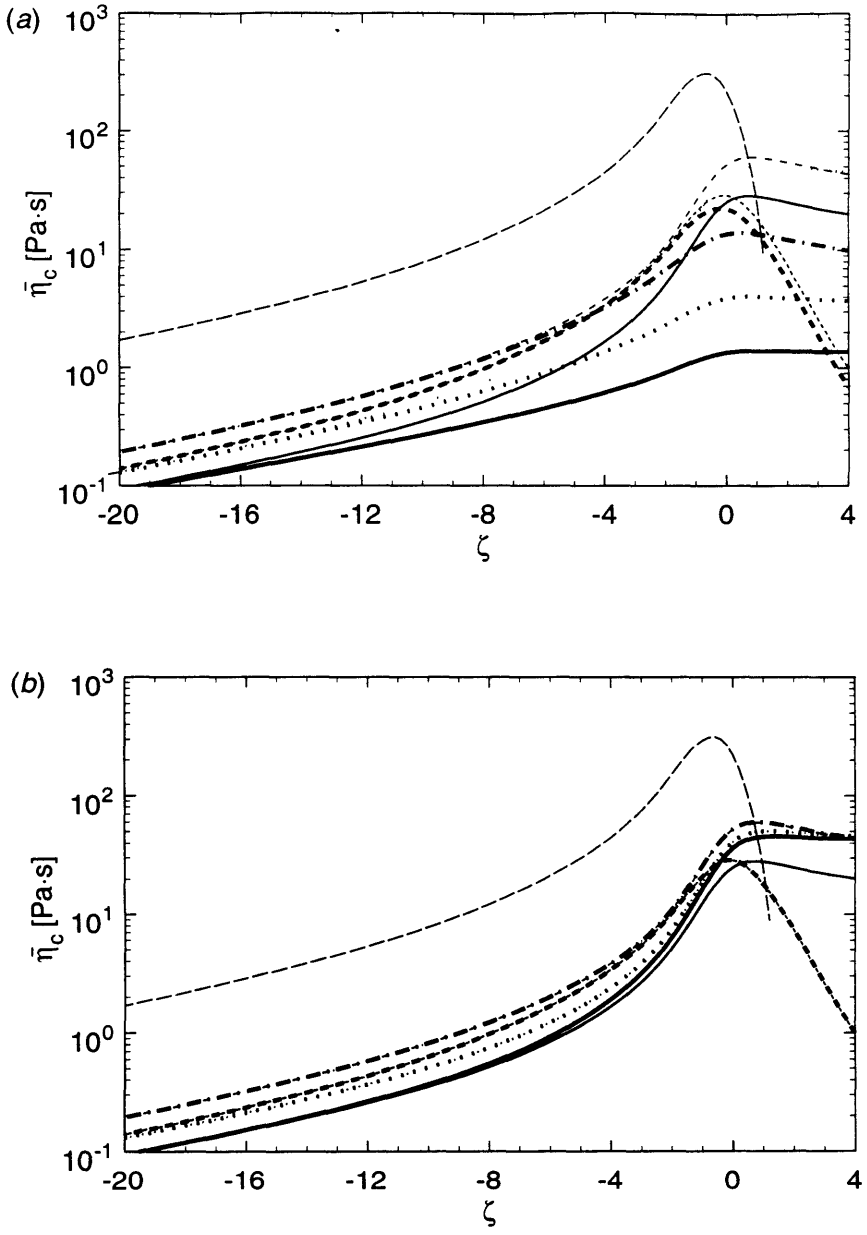

Figure 6.30 Profiles of the transient elongational viscosity, η_c, as a function of axial position, ζ. Flow is through the 32:1 contraction for a volumetric rate corresponding to $Wi_{Dn} = 2.14$. Each line indicates a prediction of a constitutive model for a given mode of the relaxation spectrum: (——) $\lambda_1 = 20$ [s]; (· · · · ·) $\lambda_2 = 4.8$ [s]; (– – –) $\lambda_3 = 1.1$ [s]; (– · – ·) $\lambda_4 = 0.12$ [s]. The uppermost dashed line indicates the profile for the Newtonian solvent (— —). (a) Profiles predicted by the linear Maxwell model are shown as thick lines; profiles predicted by the Giesekus model are shown as thin lines. (b) Profiles predicted by the upper convected Maxwell model are shown as thick lines; profiles predicted by the Giesekus model are shown as thin lines.

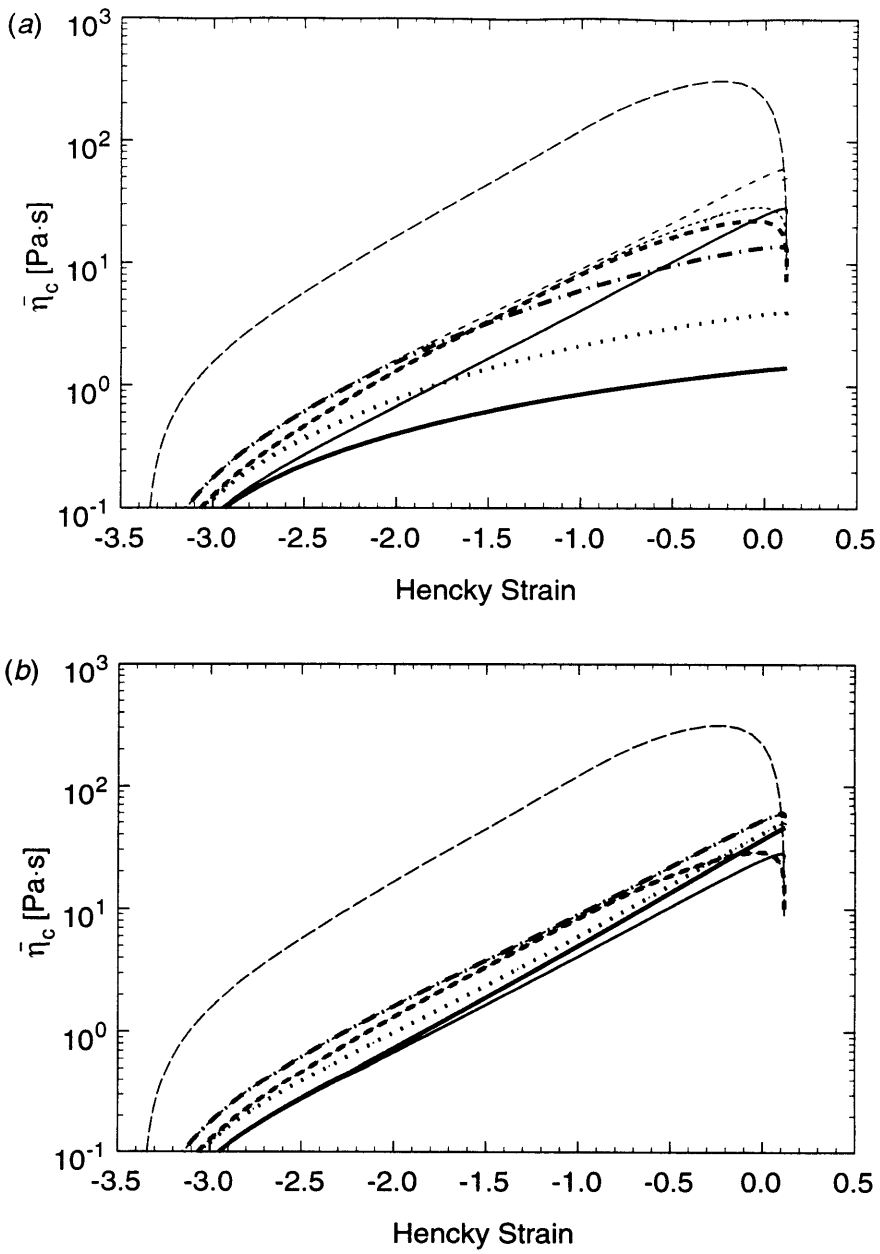

Figure 6.31 Profiles of the transient elongational viscosity, η_c, as a function of Hencky strain, ε. Flow is through the 32:1 contraction for a volumetric rate corresponding to $Wi_{Dn} = 2.14$. Each line indicates a prediction of a constitutive model for a given mode of the relaxation spectrum: (——) $\lambda_1 = 20$ [s]; (· · · · ·) $\lambda_2 = 4.8$ [s]; (— · —) $\lambda_3 = 1.1$ [s]; (- - - -) $\lambda_4 = 0.12$ [s]. The uppermost dashed line indicates the profile for the Newtonian solvent (— —). (a) Profiles predicted by the linear Maxwell model are shown as thick lines; profiles predicted by the Giesekus model are shown as thin lines. (b) Profiles predicted by the upper convected Maxwell model are shown as thick lines; profiles predicted by the Giesekus model are shown as thin lines.

ing to $Wi_{Dn} = 2.14$ is plotted as a function of Hencky strain. Mode 1 exhibits divergence at $\varepsilon = -1.79$ on the graph, approximately one unit of strain beyond the point where the centerline strain rate exceeded the critical value. The linear and nonlinear predictions for the second mode diverge at $\varepsilon = -1.34$, and for the third mode at $\varepsilon = -0.62$, in both cases approximately one unit of strain after the critical strain rate for the given mode was exceeded. Figure 6.31b compares the predictions of the Giesekus and upper convected Maxwell models for the individual modes. As shown in Fig. 6.30b the predictions for a given mode superpose, with the exception of the Mode 1, associated with the longest relaxation time. These results are consistent with the observations made for the responses of the linear Maxwell, quasilinear upper-convected Maxwell, and nonlinear Giesekus models to start-up of planar elongational flow in §6.1.2, and specifically illustrated via Fig. 6.5. The quasilinear and nonlinear models first diverge from the linear model at a strain of order unity. Only at strains substantially greater than unity does the nonlinearity of the Giesekus model manifest itself, in that the predictions of the Giesekus and upper convected Maxwell models diverge. Modes 2, 3, and 4 (cf. Fig. 6.31b) do not experience a sufficient interval of strain, in which the strain rate exceeds the critical value for the given mode, for the nonlinearity to manifest itself. Mode 1 is the only mode which exhibits substantial divergence between the predictions of the upper convected Maxwell and Giesekus models; this mode is associated with the longest relaxation time and consequently experiences the greatest interval of strain for which the strain rate exceeds the critical value. The profiles predicted by the linear Maxwell, upper convected Maxwell, and Giesekus constitutive models (sum of all relaxation modes, including solvent) are shown in Fig. 6.32. The profiles for the sum of the non-solvent modes predicted by linear Maxwell, upper convected Maxwell, and Giesekus models are given in Fig. 6.33; these plots are used for comparison in §6.5.2.

6.5.2 Effect of Strain-Rate Magnitude on Response of Linear, Quasilinear, and Nonlinear Constitutive Equations

Increasing the volumetric rate was considered as a route to excitation of a more pronounced nonlinear response of a viscoelastic fluid to the shearfree flow on the centerline of the planar contraction. As discussed in Chapter 5, increasing the flow rate eventually

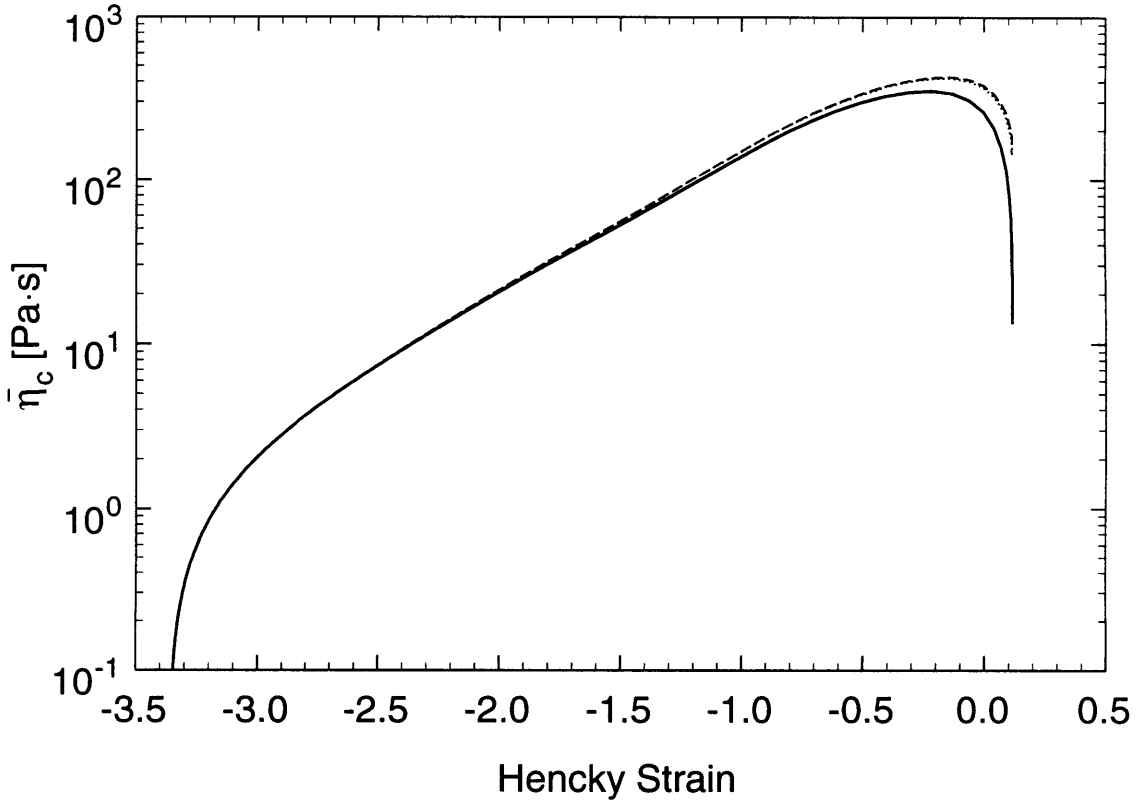

Figure 6.32 Profiles of the summed contributions of all the modes (including solvent) to the transient elongational viscosity, $\bar{\eta}_c$, as a function of Hencky strain, ε. Flow is through the 32:1 contraction for a volumetric rate corresponding to $Wi_{Dn} = 2.14$. The profiles predicted by the linear Maxwell (——), upper convected Maxwell (— —), and Giesekus (· · · · ·) models are shown.

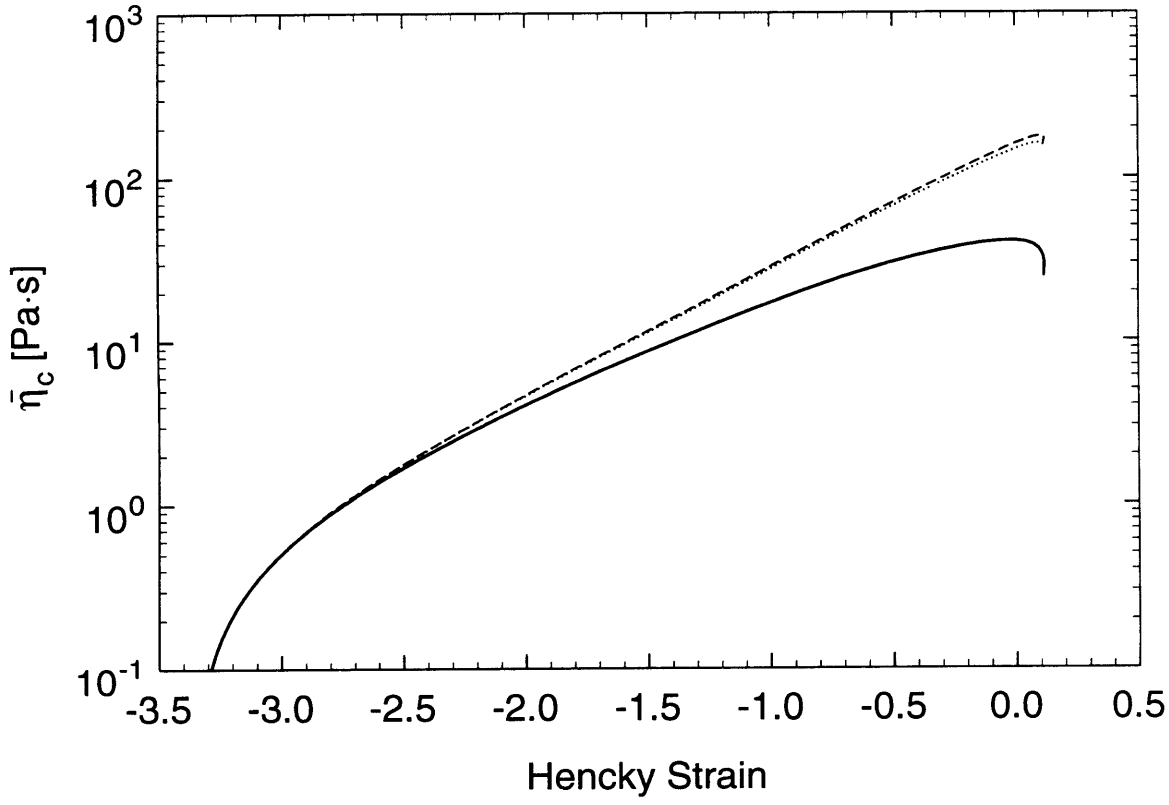

Figure 6.33 Profiles of the summed contributions of all the non-solvent modes to the transient elongational viscosity, $\bar{\eta}_c$, as a function of Hencky strain, ε. Flow is through the 32:1 contraction for a volumetric rate corresponding to $Wi_{Dn} = 2.14$. The profiles predicted by the linear Maxwell (——), upper convected Maxwell (— —), and Giesekus (· · · · ·) models are shown.

induces flow transitions which alter the dimensionless strain-rate profile. Nevertheless, to explore the effect of increased strain rate on the viscoelastic response, a hypothetical case is considered in this Section for which the *dimensionless* strain-rate profile is the same as for the base flow (i.e. identical to that considered in §6.5.1), but the *dimensional* strain-rate profile has a magnitude ten times as great. For this case, the criterion of $\dot{\varepsilon} > \dot{\varepsilon}_{crit}$ for a given viscoelastic mode is met at axial positions farther upstream; consequently, there is a greater interval of accumulated strain over which the response of a given mode of a non-linear model diverges from that of the linear model.

Figure 6.34 shows the dimensional strain-rate profile along the centerline for this hypothetical flow of high volumetric rate; the $\dot{\varepsilon}_{crit}$ for the individual modes, listed in Table 6.1, are indicated. Note in Fig. 6.35 that the critical strain rate for a given mode is attained at a lower strain (corresponding to a position farther upstream) than in the case of the lower volumetric rate flow considered in §6.5.1. The response of the individual modes of the linear Maxwell and nonlinear Giesekus models to the strain-rate profile associated with the higher volumetric rate flow is shown by plotting $\bar{\eta}_c$ as a function of Hencky strain in Fig. 6.36a. As discussed in §6.5.1, a strain interval of approximately unity beyond the point where the strain rate exceeded $\dot{\varepsilon}_{crit}$ was required to observe divergence of the nonlinear prediction from that of the linear prediction for a given mode. Since the critical strain rate is achieved earlier for a given mode, the ratio of the values of $\bar{\eta}_c$ predicted by the Giesekus model at, say, the contraction plane ($\varepsilon = 0$) are greater than for the case of the lower flow rate.

However, it is interesting to note in Fig. 6.36b, that divergence between the quasilinear upper convected Maxwell and the nonlinear Giesekus models was noted only for the mode of longest relaxation time, despite the elevated flow rate. In fact, divergence occurs later and the ratio of predicted transient elongational viscosities at the contraction plane ($\varepsilon = 0$) is lower than for the lower flow rate (cf. Fig. 6.31b). Although counterintuitive, this result is consistent with observations for the case of start-up of planar elongational flow. Specifically, in Fig. 6.5b, at a strain interval of 2.5, the transient elongational viscosity predicted by the upper convected Maxwell model exceeds that of the Giesekus model by 7%. When the strain rate is increased, for a fixed relaxation time, (cf. Fig. 6.5c) the fractional difference between the models at $\varepsilon = 0$ increases to 15%. However, when the

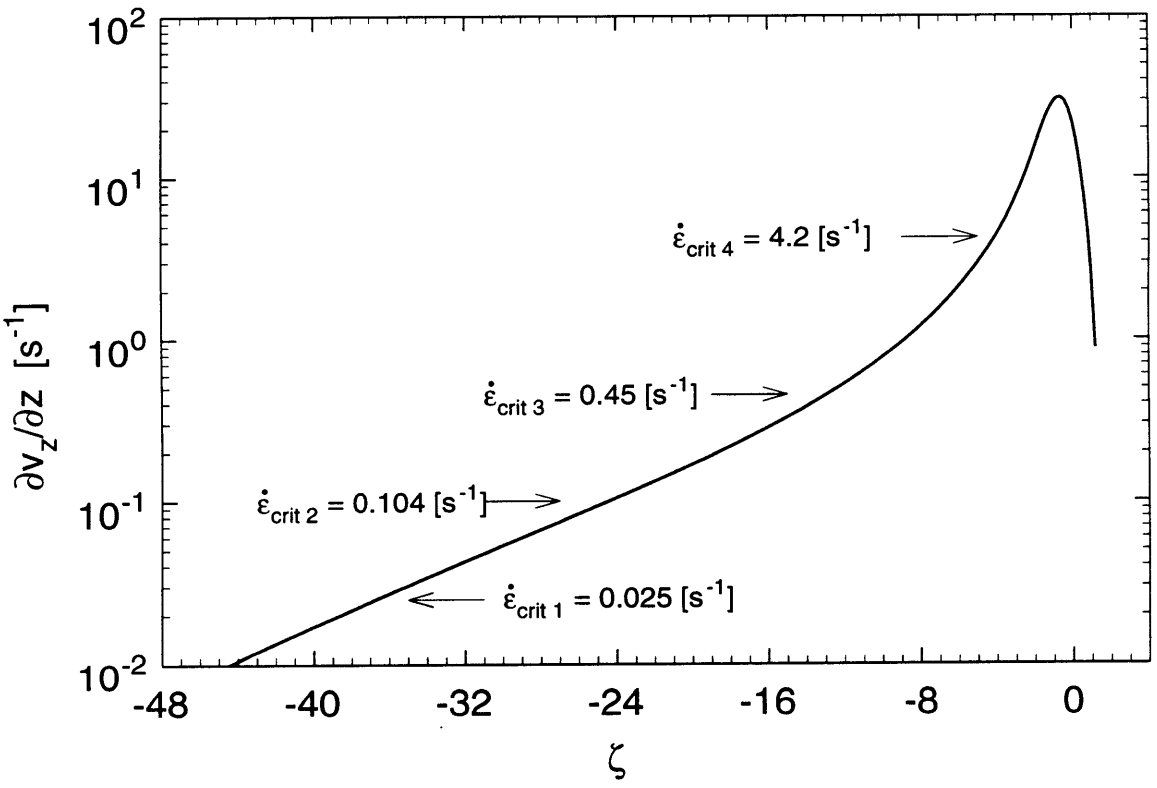

Figure 6.34 Centerline elongational strain-rate profile, $(\partial v_z/\partial z)$, as a function of axial position, ζ. Newtonian flow simulation is used to predict the profile corresponding to flow through the 32:1 contraction for a volumetric rate ten times greater than that associated with $Wi_{Dn} = 2.14$. The critical strain rate, $\dot{\varepsilon}_{crit,k}$, is shown for each relaxation mode.

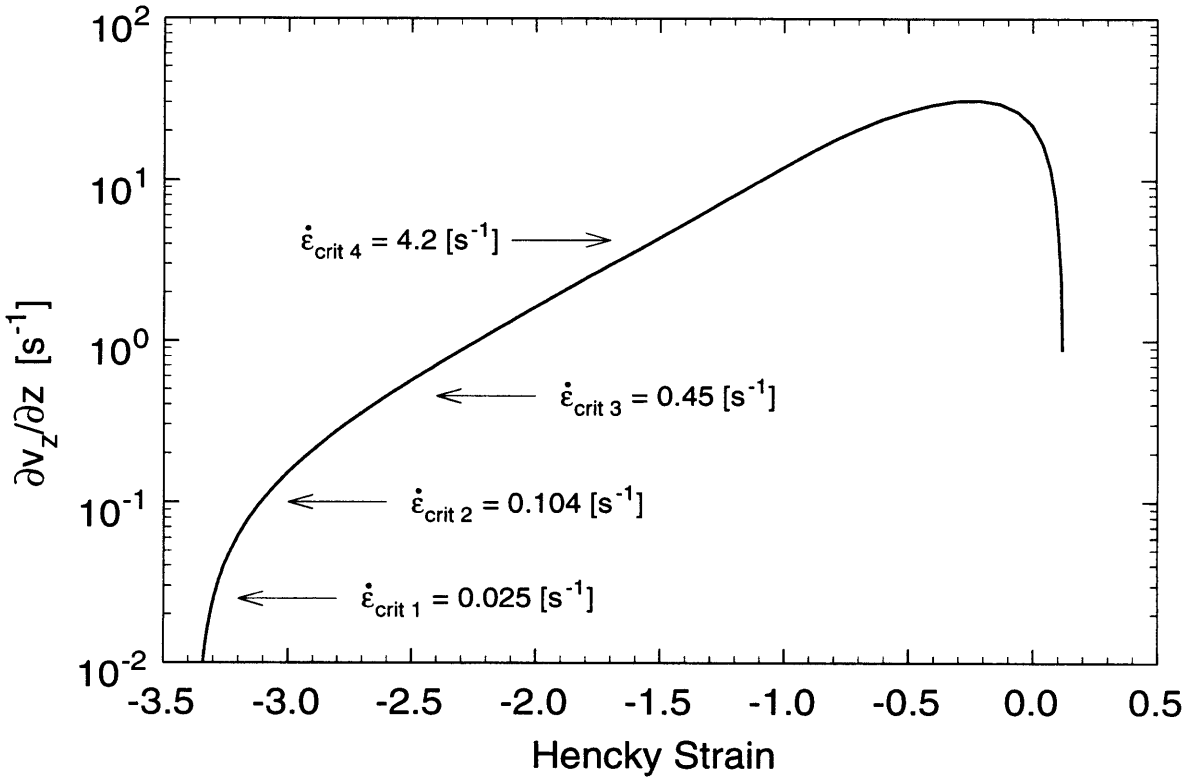

Figure 6.35 Centerline elongational strain-rate profile, $(\partial v_z/\partial z)$, as a function of Hencky strain, ε. Newtonian flow simulation is used to predict the profile corresponding to flow through the 32:1 contraction for a volumetric rate ten times greater than that associated with $Wi_{Dn} = 2.14$. The critical strain rate, $\dot{\varepsilon}_{crit,k}$, is shown for each relaxation mode.

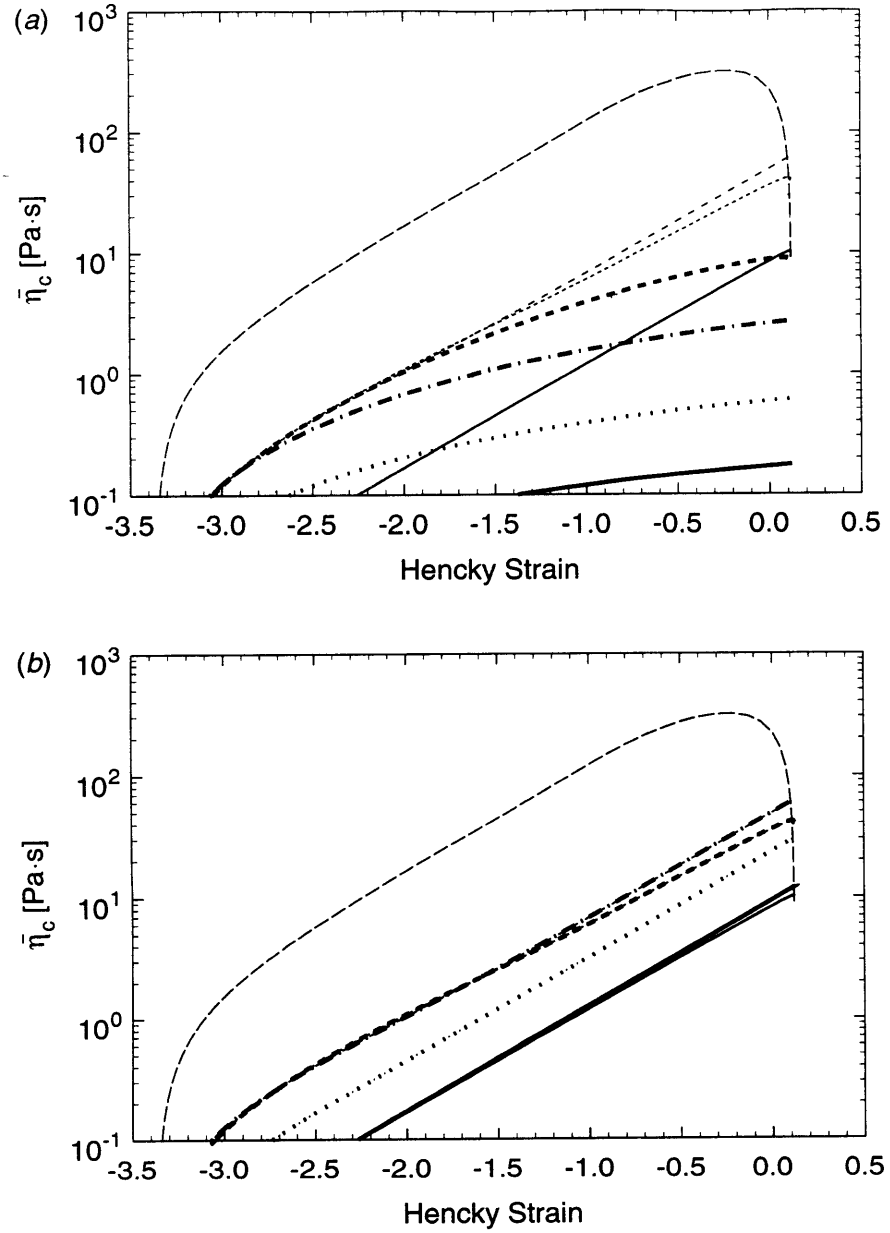

Figure 6.36 Profiles of the transient elongational viscosity, $\bar{\eta}_c$, as a function of Hencky strain, ε. Flow is through the 32:1 contraction for a volumetric rate ten times greater than that associated with $Wi_{Dn} = 2.14$. Each line indicates a prediction of a constitutive model for a given mode of the relaxation spectrum: (——) $\lambda_1 = 20$ [s]; (· · · · ·) $\lambda_2 = 4.8$ [s]; (— · —) $\lambda_3 = 1.1$ [s]; (— · · —) $\lambda_4 = 0.12$ [s]. The uppermost dashed line indicates the profile for the Newtonian solvent (— —). (a) Profiles predicted by the linear Maxwell model are shown as thick lines; profiles predicted by the Giesekus model are shown as thin lines. (b) Profiles predicted by the upper convected Maxwell model are shown as thick lines; profiles predicted by the Giesekus model are shown as thin lines.

strain rate is increased yet further (cf. 6.5d), the fractional difference between the upper convected Maxwell and Giesekus models *decreases* to 10%.

The sum of the transient elongational viscosities predicted for the non-solvent modes with the linear Maxwell and Giesekus models is shown in Fig. 6.37 for the higher volumetric rate flow. These profiles are compared with those obtained for the lower flow rate discussed in §6.5.1 and shown in Fig. 6.33. The magnitude of the sum-of-nonsolvent-modes profile calculated by linear Maxwell decreases with increased flow rate. This result is expected; a given fluid element has less time to respond to the imposed strain in the case of the higher volumetric rate flow. For the case of the Giesekus model, as discussed in the preceding paragraph, divergence from the prediction of the linear model occurs at a lower Hencky strain than for the case of the lower volumetric rate. In consequence, the difference in magnitude of the transient elongational viscosity profiles predicted by the linear and nonlinear models is greater for the higher volumetric rate flow. The dependence of the magnitude of the Giesekus and upper convected Maxwell predictions for the sum of nonsolvent modes on the volumetric rate is the result of two competing influences; the shorter time interval available for response, and the divergence of the linear and nonlinear model predictions at lower Hencky strain. Comparison of Figs. 6.37 and 6.33 reveals that the magnitude of the transient elongational viscosity predicted by the upper convected Maxwell and Giesekus models at $\varepsilon = 0$ for the higher flow rate decreases slightly from the values predicted for the lower flow rate. Hence, increasing the volumetric rate does not increase the magnitude of the quasilinear or nonlinear responses. In addition, as discussed above, the fractional difference between the prediction for a mode by the nonlinear Giesekus and by the quasilinear upper convected Maxwell models at a given Hencky strain is less for the higher than for the lower flow rate. In Fig. 6.33, the curves for the upper convected Maxwell and for the Giesekus models are distinguishable; in contrast, the superpose in Fig. 6.37. In consequence, increasing the volumetric flow rate does not offer a route for facilitating evaluation of the accuracy of a given nonlinear model via comparison of model predictions with an experimentally determined transient elongational viscosity profile. Moreover, it is evident from comparison of Figs. 6.36 and 6.37 and from comparison of Figs. 6.31 and 6.33 that the contribution of the solvent mode is of the same order as the sum of the nonsolvent modes for the linear, quasilinear, or nonlinear model predic-

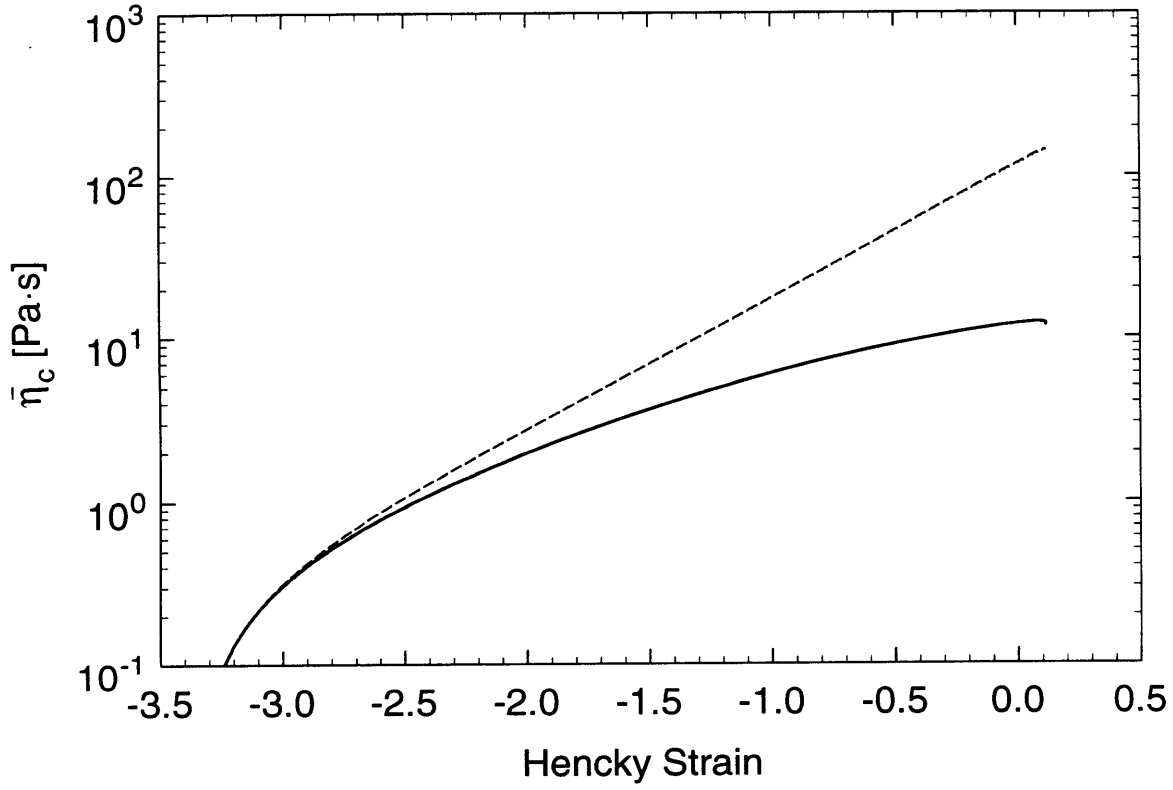

Figure 6.37 Profiles of the summed contributions of all the non-solvent modes to the transient elongational viscosity, $\bar{\eta}_c$, as a function of Hencky strain, ε. Flow is through the 32:1 contraction for a volumetric rate ten times greater than that associated with $Wi_{Dn} = 2.14$. Profiles predicted by the linear Maxwell (——), upper convected Maxwell (— —), and Giesekus (· · · · ·) models are shown.

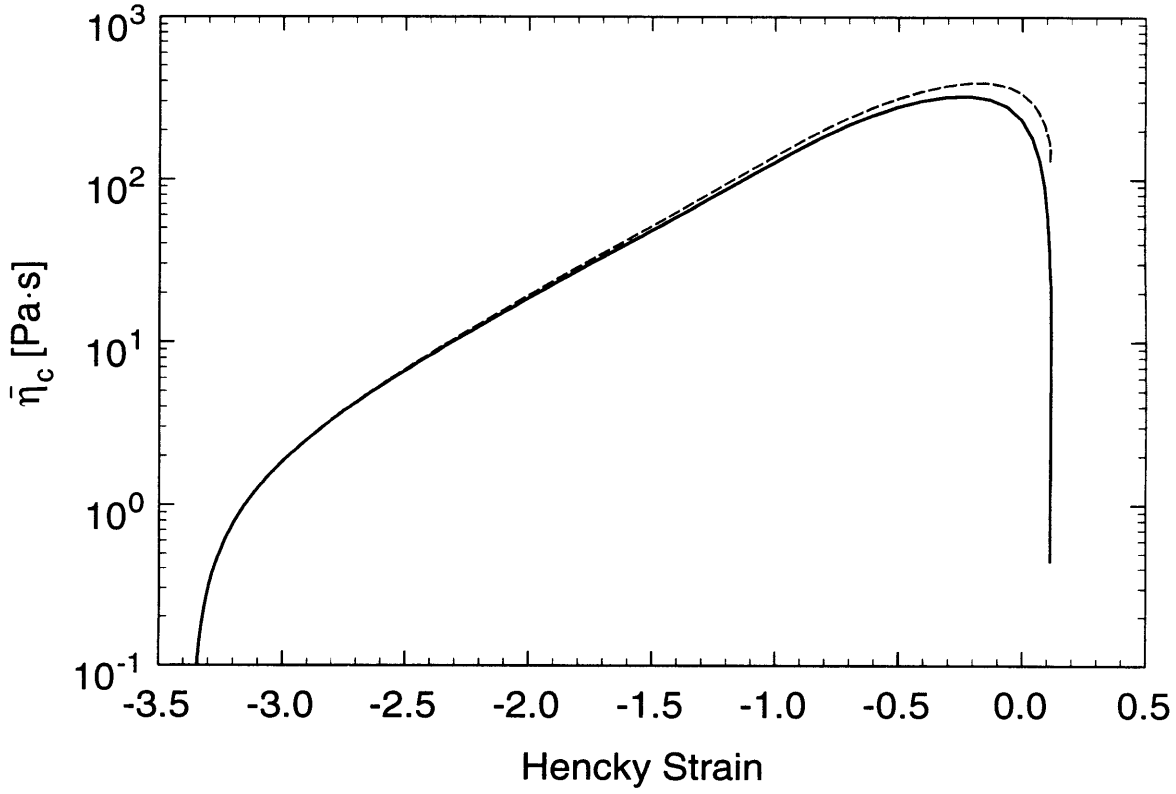

Figure 6.38 Profiles of the summed contributions of all the modes (including solvent) to the transient elongational viscosity, $\bar{\eta}_c$, as a function of Hencky strain, ε. Flow is through the 32:1 contraction for a volumetric rate ten times greater than that associated with $Wi_{Dn} = 2.14$. Profiles predicted by the linear Maxwell (——), upper convected Maxwell (— —), and Giesekus (· · · · ·) models are shown.

tions. In consequence, the solvent contribution dominates over the difference between the predictions of the Giesekus and linear Maxwell models of the sum of the nonsolvent modes. The total elongational viscosity (sum of viscoelastic modes plus the solvent contribution) is shown in Figs. 6.38 and 6.32; these Figures indicate that the prediction of the quasilinear model is only slightly greater than the prediction of the linear Maxwell model and the predictions of the quasilinear and nonlinear models are essentially indistinguishable, irrespective of the volumetric rate.

6.5.3 Effect of Variation of Geometrical Parameters on Response of Linear, Quasilinear, and Nonlinear Constitutive Models

In §6.4.2, it was indicated that the relative magnitude of the linear and nonlinear responses at comparable maximum strain rates exhibited little dependence on the contraction ratio. An explanation was given in §6.5.2 as to why only a weakly nonlinear response was excited, even for the case of flow through the 32:1 contraction which induced a substantial total Hencky strain of 3.5. Because the downstream half-height, h, is the relevant length scale controlling the form of the high strain-rate region, increasing the contraction ratio does not, in and of itself, provide a route to enhance the nonlinear viscoelastic response in the planar contraction.

As discussed in §6.5, the homogeneous strain rate in start-up of planar elongational flow is more "efficient" at elongating the polymer molecule and exciting a nonlinear response than the transient elongational flow which is evoked in the planar contraction. This dependence of the response of a viscoelastic fluid element on the shape of the strain-rate versus strain profile implied that alteration of the shape of the profile associated with centerline flow through the planar contraction to more closely resemble a homogeneous profile could favor excitation of a nonlinear response. In particular, tapering of the entry region of the planar contraction flow was explored as a means to this end. As discussed above in §6.5.1 a centerline strain-rate profile which was computed via a numerical simulation of flow through the abrupt planar contraction was in good agreement with the experimentally determined strain-rate profile for flow of the test fluid. Consequently, numerical simulation of Newtonian flow through a tapered-entry planar contraction should provide a reasonable estimate of the actual flow of the viscoelastic test fluid (at flow rates lower than

those for which the elastically driven transitions discussed in Chapter 5 occur). The result of the Newtonian simulation for flow through a tapered contraction with an included half-angle of $\kappa = \pi/16$ (cf. Fig. 6.39) at a volumetric rate corresponding to $Wi_{Dn} = 2.14$ is shown as a plot of the strain rate as a function of axial position in Fig. 6.40. The strain rate on the centerline is plotted as a function of Hencky strain in Fig. 6.41; the shape of the profile closely resembles that for the abrupt contraction (cf. Fig. 6.28). The only substantial difference is that the maximum strain rate in the tapered geometry is a factor of five less than that observed for flow through the abrupt contraction. A plot of the strain rate as a function of time is shown in Fig. 6.42. Again, the profile resembles that observed for the abrupt contraction (cf. Fig. 6.29) with the exception that the maximum strain rate is lower and the profile is stretched by a factor of approximately five along the time axis. A factor of five increase in the flow rate through the tapered contraction over the flow rate through the abrupt contraction would result in the strain-rate versus strain and strain-rate versus time profiles for the flows through the different geometries being identical. Consequently, tapering the entry region of the contraction does not provide a route to making the strain-rate profile along the centerline of the planar contraction "more homogeneous". One should note that the "no-slip" boundary condition in the tapered-entry planar contraction distinguishes this flow from the "lubricated die" configuration described in §4.2.2.

As discussed in Chapter 5, at elevated flow rates a rearrangement of the velocity field occurs, with the peak in the strain-rate versus axial position profile shifting closer to the contraction plane and increasing in magnitude. However, the essential nonhomogeneous form of the strain-rate profile was not altered from that observed for lower flow rates. Consequently, the profile is not expected to favor excitation of a nonlinear response. This is consistent with the results for $Wi_{Dn} \approx 2.9$ for the 8:1 and 32:1 contractions shown in Figs. 6.23a and 6.26a.

6.6 Consideration of the Influence of the Fluid Elongational Response on Flow Transitions

The findings described in Sections 6.4 and 6.5 are now used to gain insight into the effect of the elongational response of the test fluid on the off-centerline stress field. In par-

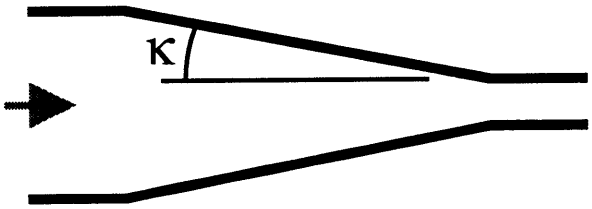

Figure 6.39 Diagram of a tapered-entry planar contraction geometry with included half-angle .

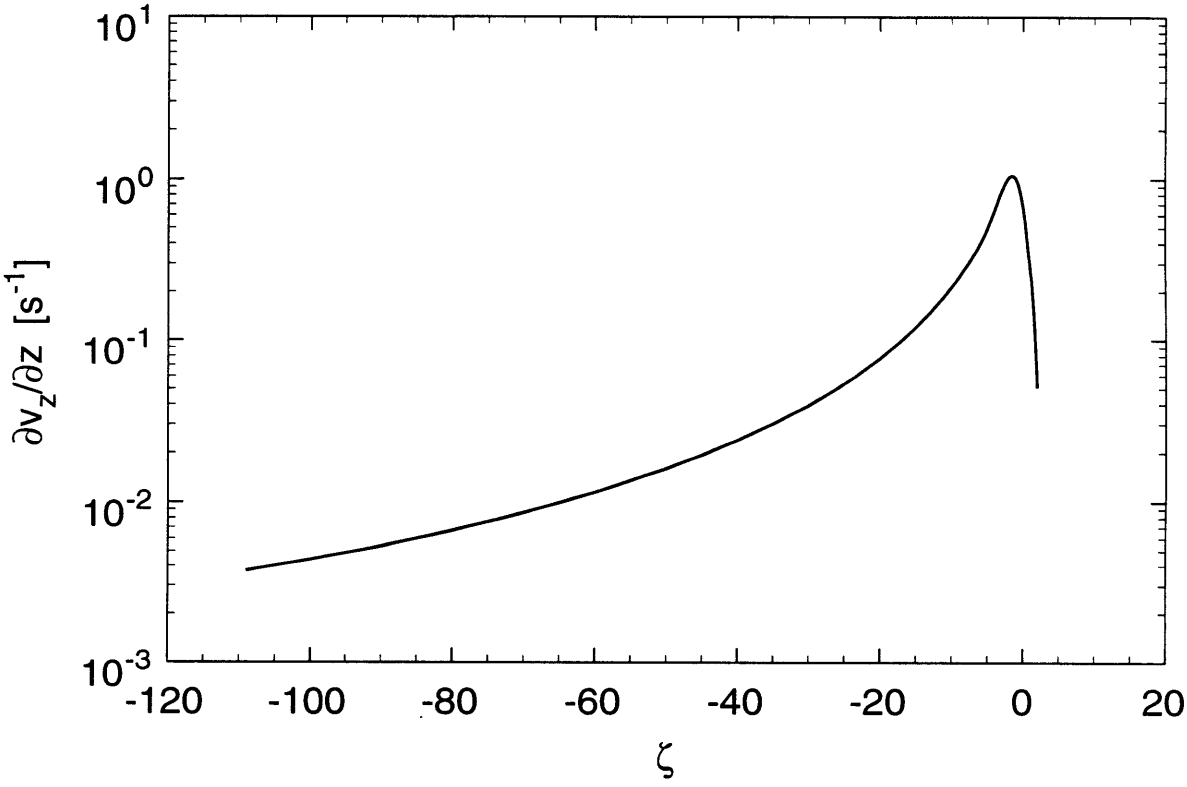

Figure 6.40 Centerline strain rate, $(\partial v_z/\partial z)$, as a function of axial position, ζ, for flow through a tapered contraction with an included half-angle of $\kappa = \pi/16$ [rad]. Profile was calculated via a Newtonian flow simulation with a volumetric flow rate corresponding to $Wi_{Dn} = 2.14$.

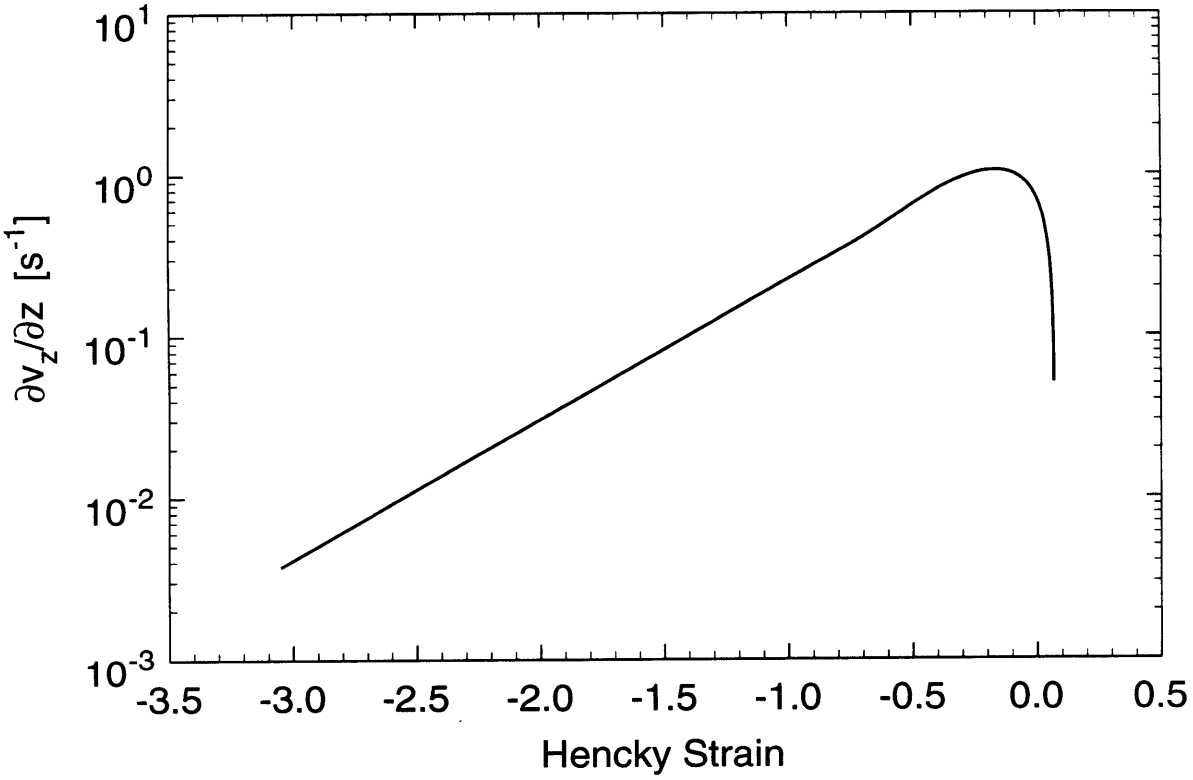

Figure 6.41 Centerline strain rate, $(\partial v_z/\partial z)$, as a function of Hencky strain, ε, for flow through a tapered contraction with an included half-angle of $\kappa = \pi/16$ [rad]. Profile was calculated via a Newtonian flow simulation with a volumetric flow rate corresponding to $Wi_{Dn} = 2.14$.

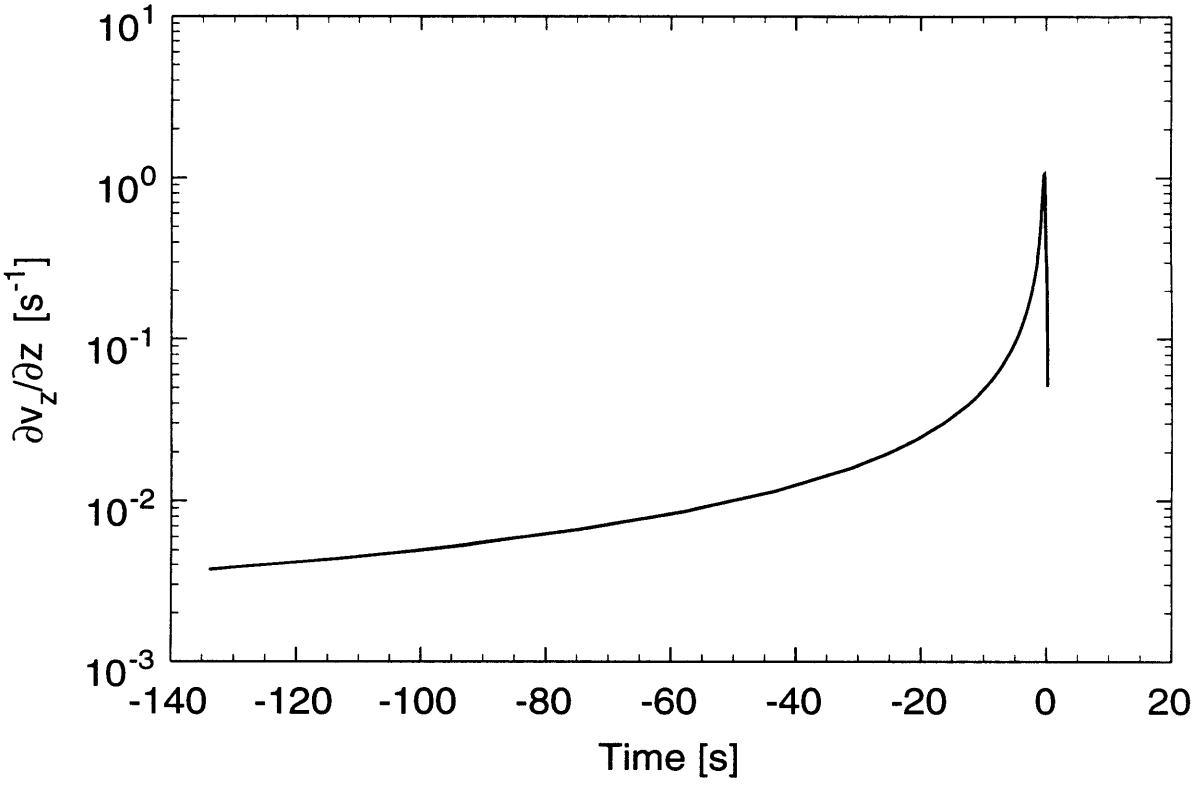

Figure 6.42 Centerline strain rate, $(\partial v_z/\partial z)$, as a function of time, t, for flow through a tapered contraction with an included half-angle of $\kappa = \pi/16$ [rad]. Profile was calculated via a Newtonian flow simulation with a volumetric flow rate corresponding to $Wi_{Dn} = 2.14$.

ticular, the influence of the elongational response on the flow transitions described in Chapter 5 is considered. Near the centerline of the planar contraction, the flow is exclusively elongational. However, as one moves toward the bounding wall in the upstream channel, $\upsilon = H/h$, the flow becomes complex; the rate-of-strain tensor has both shear and elongational components. In Chapter 5 it was shown that onset of the instability is driven by an interaction of streamwise stress with streamline curvature. The question then arises: what are the relative contributions of the elongational and shear components of the rate-of-strain tensor to the streamwise stress? The highest curvature in the flow occurs in the vicinity of the outer corner; however, quantitative, experimental velocity field data for this region is not available. Progress can be made if the velocity field is assumed to resemble the Moffatt solution for Stokes flow around a corner; this assumption is consistent with the flow visualization results reported in Chapter 5. A cylindrical coordinate system is used to present the Moffat solution, as shown in Fig. 6.43. The origin, $r = 0$, is located at the outer corner. The angle included by the corner is represented as 2α; the bisector of the angle defines $\theta = 0$. Along the upstream channel wall $\theta = -\alpha$, and along the wall defining the contraction plane $\theta = \alpha$. The antisymmetric solution is then given in the form of the stream function as

$$\psi = Kr^{\lambda_1}\{\cos(\lambda_1\theta)\cos((\lambda_1 - 2)\alpha) - \cos((\lambda_1 - 2)\theta)\cos(\lambda_1\alpha)\} \tag{6.33}$$

where λ_1 is the eigenvalue which dominates the solution near the corner and K is a constant which depends on boundary conditions far from the corner. For an included angle of $2\alpha = \pi/2$, the eigenvalue is complex, $\lambda_1 = 3.74 + 1.13i$ (Moffat, 1964). The form of a streamline associated with the antisymmetric solution is depicted in Fig. 6.43. Note that the complex value of λ_1 implies the existence of a series of vortices whose elliptic points are located on the $\theta = 0$ bisector; in the experiment presented in Chapter 5 only one vortex (not a sequence of vortices) was observed near the corner since the intensity of the successive vortices rapidly decreases with decreasing radial distance, r (Moffat, 1964).

The maximum curvature along a given streamline occurs on the bisector, $\theta = 0$. Since the instability arises via an interaction between the curvature and the stress, in this Section

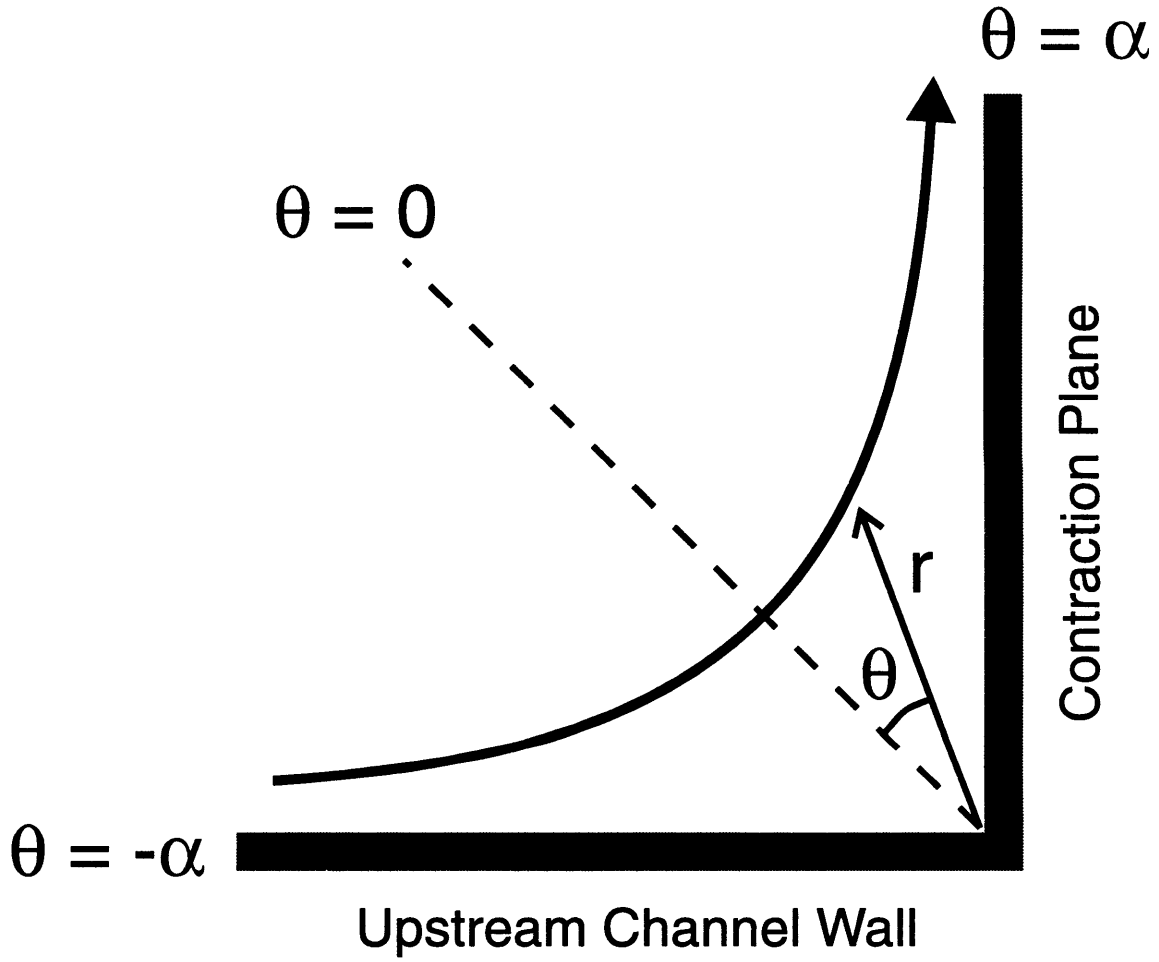

Figure 6.43 Illustration of a streamline of flow around a corner as predicted by the antisymmetric solution of the analysis of Moffatt (1964). A cylindrical coordinate system is used. In the context of flow around the outer corner of the planar contraction, $\theta = -\alpha = -\pi/4$ [rad] corresponds to the upstream channel wall, $\theta = \alpha = \pi/4$ [rad] corresponds to the wall defining the contraction plane, and $\theta = 0$ is the bisector of the angle included by the corner.

attention is focused on the flow in the vicinity of the bisector. Within this region the streamline is nearly tangent to the θ-direction; specifically, the velocity components are

$$\begin{aligned} v_r &\approx Kr^{\lambda_1 - 1}\{-\theta\lambda_1^2\cos((\lambda_1 - 2)\alpha) + \theta(\lambda_1 - 2)^2\cos(\lambda_1\alpha)\} \\ v_\theta &\approx K\lambda_1 r^{\lambda_1 - 1}\{-\cos(((\lambda_1 - 2)\alpha) + \cos(\lambda_1\alpha))\} \end{aligned} \tag{6.34}$$

Note that approximations have been made using the fact that θ is small in the vicinity of the bisector; specifically, for $\theta \lesssim 0.1$[rad], trigonometric expressions are approximated as $\cos(\theta\lambda_1) \approx 1$, $\sin(\theta\lambda_1) \approx \theta\lambda_1$, $\cos(\theta(\lambda_1 - 2)) \approx \theta(\lambda_1 - 2)$, and $\sin(\theta(\lambda_1 - 2)) \approx \theta(\lambda_1 - 2)$. The components of the velocity gradient tensor are

$$\begin{aligned} \{\nabla\mathbf{v}\}_{rr} &\approx \theta Kr^{\lambda_1 - 2}(\lambda_1 - 1)\{-\lambda_1^2\cos((\lambda_1 - 2)\alpha) + (\lambda_1 - 2)^2\cos(\lambda_1\alpha)\} \\ &\approx -\theta(14 + 170i)Kr^{\lambda_1 - 2} \\ \{\nabla\mathbf{v}\}_{r\theta} &\approx Kr^{\lambda_1 - 2}\lambda_1(\lambda_1 - 1)\{-\cos((\lambda_1 - 2)\alpha) + \cos(\lambda_1\alpha)\} \\ &\approx (33 + 61i)Kr^{\lambda_1 - 2} \\ \{\nabla\mathbf{v}\}_{\theta r} &\approx Kr^{\lambda_1 - 2}\{(1 - \lambda_1^2)\cos((\lambda_1 - 2)\alpha) + ((\lambda_1 - 2)^2 - 1)\cos(\lambda_1\alpha)\} \\ &\approx (21 + 49i)Kr^{\lambda_1 - 2} \\ \{\nabla\mathbf{v}\}_{\theta\theta} &\approx \theta Kr^{\lambda_1 - 2}(\lambda_1 + 1)\{-\lambda_1^2\cos((\lambda_1 - 2)\alpha) + (\lambda_1 - 2)^2\cos(\lambda_1\alpha)\} \\ &\approx -\theta(67 + 270i)Kr^{\lambda_1 - 2} \end{aligned} \tag{6.35}$$

For the purpose of this approximate analysis, only the order of magnitude of the real part of the terms shown in eq. (6.35) are of interest. Note that on the bisector, θ = 0, the shear components of the velocity gradient tensor have approximately equal magnitude and the elongational components are zero; in the vicinity of the bisector (θ is small), the shear components dominate over the elongational components.

Note that the Moffat solution can only be valid for a restricted region in the planar contraction flow. Equation (6.35) indicates that for $\theta < 0$, $\{\nabla v\}_{\theta\theta} > 0$, i.e. the fluid is accelerating as the bisector, θ = 0, is approached. Conversely, for $\theta > 0$, $\{\nabla v\}_{\theta\theta} < 0$, i.e. the fluid decelerates. More specifically, the θθ-component of the velocity gradient tensor is anti-

symmetric about the bisector: $\{\nabla v(r, \theta)\}_{\theta\theta} = -\{\nabla v(r, -\theta)\}_{\theta\theta}$. This antisymmetry holds true for the rr-component of the velocity gradient tensor as well. In consequence, when a fluid element travels from the point (r, -θ) to the point (r, θ) the net Hencky strain experienced by the element is zero. However, in the planar contraction, after the fluid element passes the bisector and approaches the entry to the downstream slit, it must eventually accelerate. Furthermore, the net Hencky strain, ε, experienced by a fluid element travelling from the fully-developed flow in the upstream region to the fully-developed flow in the downstream region along any streamline is nonzero. Specifically, consider a fluid element moving along a streamline ψ which passes near the outer upstream wall; the net Hencky strain experienced is

$$\varepsilon(\psi) = \ln\left(\frac{v_z(\nu(\psi, \zeta), \zeta \to \infty)}{v_z(\nu(\psi, \zeta), \zeta \to -\infty)}\right) \tag{6.36}$$

Since the fully developed flow in both the upstream and downstream ducts is parabolic, the net Hencky strain is $\varepsilon(\psi) = \ln(H/h)$, the same as for a fluid element travelling on the centerline. However, if the Moffat analysis is valid in the vicinity of the bisector, a fluid element at $\theta = 0$ will be at a local maximum in accumulated Hencky strain. However, the Moffat analysis cannot determine whether the Hencky strain which has been experienced by the fluid element up to this point is less than or greater than the total strain (as defined by eq. (6.36)) which it will ultimately experience.

Keeping the restricted validity of the Moffatt analysis in mind, the contribution of the elongational components of the velocity gradient tensor to the streamwise stress, in the vicinity of the bisector, is now considered from two perspectives. First, assume that the fluid has a short relaxation time. In this case, a fluid element on the bisector will only recall strain history experienced for $|\theta| \ll 1$ [rad]. As shown in eq. (6.35) the elongational components of the velocity gradient tensor are then very small. In consequence, the fluid response will be dominated by the shear components of the velocity gradient tensor; the elongational response of the fluid is not important.

In the second case, assume that the fluid has a long relaxation time. In this case the stress of a fluid element on the bisector will be a function of the strain history which it has

experienced, extending far upstream. As mentioned above, the Hencky strain experienced by a fluid element is at a local maximum on the bisector. In consequence, the strain history of the fluid element is substantially different from that of an element travelling on the centerline, where no such local maximum of Hencky strain exists upstream of the contraction plane. Since the fluid element recalls its strain history, it is possible that the streamwise stress of the fluid element on the bisector will be substantially greater than if the elongational components of the velocity gradient tensor had been neglected. In this case, the elongational response of the fluid may be important.

Use of the Moffat solution alone cannot answer whether elongational components of the velocity gradient tensor induce stresses on streamlines of high curvature substantially greater than if only the shear components were present. A definitive answer to this question can be obtained via two-dimensional, steady numerical simulation of viscoelastic flow. The limiting cases of a fluid with short, and a fluid with long relaxation time discussed above should help guide interpretation of the results from such a simulation.

6.7 Summary

The shearfree centerline flow in the planar contraction geometry was considered for use in evaluating the accuracy of constitutive equations in predicting the nonlinear elongational response of a viscoelastic fluid. However, both the experimental results and calculations presented in Sections 6.4 and 6.5 indicated that the centerline of the planar contraction flow only stimulates a weak deviation from the linear viscoelastic response. Furthermore, the predictions of the quasilinear upper convected Maxwell and nonlinear Giesekus models were essentially indistinguishable. The inefficacy of the flow in stimulating a nonlinear response was attributed to the particular form of the nonhomogeneous strain-rate versus strain profile on the centerline. One should note that flows with Hencky strains as high as 3.5 and maximum strain rates well above the expected critical value for the coil-stretch transition could not excite a substantial nonlinear response. This observation underscores the necessity of considering the entire strain history of a viscoelastic fluid element, which has "memory", in a flow (Ferguson and Hudson, 1993; Malkin and Petrie, 1997). Modification of the strain-rate profile via use of a tapered contraction was explored

computationally; however, this strategy proved ineffective in altering the essential structure of the strain-rate versus strain profile.

The planar contraction flow may find application in the evaluation of the accuracy of the nonlinear elongational response predicted by constitutive equations for test fluids and in experimental configurations different from those used in this study. Specifically, greater deviation from the linear response may possibly be observed for test fluids with a low solvent contribution to the viscosity (e.g. concentrated solutions or melts). The solvent contribution would not dominate the data in the stress-growth region. However, even if the deviation from the linear viscoelastic response were substantial, it is not certain that the flow would prove useful in distinguishing between constitutive models with different form of a nonlinearity (e.g. upper convected Maxwell versus Giesekus).

The flow on the centerline excites only a weakly nonlinear response, but regions of complex flow (with the rate-of-strain tensor having both shear and elongational components), such as in the vicinity of the reentrant corner, may excite a nonlinear response. Note, however, that the high velocity and stress gradients in the flow near the reentrant corner and the limited resolution of the FIB probe beam may preclude such studies from providing accurate quantitative information which is useful for the evaluation of constitutive models. The influence of the elongational response of the viscoelastic fluid on the streamwise stress away from the centerline was considered in §6.6. Of particular interest was the stress in the region of high streamline curvature in the vicinity of the outer corner where the critical condition for transition from the two-dimensional, base flow to three-dimensional flow, as specified by eq. (2.3), is expected to first be met. Two limiting cases were identified when the flow near the outer corner was assumed to conform to the Moffat solution (Moffat, 1964). For a fluid with short relaxation time, the small magnitude of the elongational components of the velocity gradient tensor in the region of high curvature imply that their contribution to the streamwise stress is negligible. Alternately, if the fluid has a long relaxation time, a fluid element "recalls" the finite Hencky strain accumulated during its passage from the upstream region to the region of high curvature. This may result in a substantial elevation of the streamwise stress, in the high curvature region, above the level which would be determined if only the shear components of the velocity gradient tensor along the streamline were considered.

The study presented in this Chapter underscores the necessity of using multiple, well-characterized experimental techniques to understand the elongational response of a viscoelastic fluid. In a practical context, understanding of the role of the elongational response in an industrial polymer process can be best gained via study of a test flow with similar boundary conditions. For example, a fiber-spinning operation typically incorporates high draw ratios (and consequently, high Hencky strains); the response of the spun material to such high strains could not be probed with the planar contraction geometry. To study such a response, it would be necessary to use a device such as the fiber-spinning or filament-pulling apparatus described in §3.2.2. However, these devices have their own associated limitations and sources of ambiguity in measurement. The planar contraction flow resembles industrial polymer flows upstream of a die land or in injection-molding operations. Of particular interest for developing understanding of flow field evolution in such industrial systems are the stress and velocity fields in the region of high streamline curvature where the transition from the base flow to three-dimensional flow is expected to first be manifested. Full-field flow simulations should prove valuable in quantifying the stress and velocity fields in regions of complex flow near the outer corner, in which experimental data may be difficult to obtain. The considerations of §6.6 provide guidance for the interpretation of computational results.

Chapter 7

Conclusions

This thesis contains investigations of two aspects of the flow of a viscoelastic polymer solution through the planar contraction. In Chapter 5, the spatiotemporal structure of a sequence of flow transitions was quantitatively defined; the mechanism driving the first, spatial transition to three-dimensional flow was attributed to interaction between streamline curvature and streamwise stress. In Chapter 6, the response of the viscoelastic test fluid to the shearfree planar elongational flow along the centerline was measured. Interpretation of the results in terms of integration of linear and nonlinear constitutive models indicated that the form of the strain-rate profile on the centerline could only stimulate an essentially linear response. In this Chapter, essential findings of these two investigations are reviewed, conclusions are summarized in terms of the physical nature of the phenomena, and broader implications of the studies are described which may motivate future work.

Quantitative LDV measurement in conjunction with qualitative velocity-field visualization was used to characterize the spatial structure of a transition to three-dimensional, steady viscoelastic flow observed in the planar contraction. After transition, the velocity field had the form of pairs of counter-rotating vortices, arrayed in the "neutral" x-direction and interlaced across the centerplane (cf. Fig. 5.7); this representation was consistent with the findings of previously published studies which have been reviewed in Chapter 2 (Chiba *et al.*, 1990; Chiba *et al.*, 1992). However, in these prior studies, the onset of the transition was not unambiguously attributed to the elastic nature of the fluid, because inertia was a factor in the flows. One significant contribution of this thesis was the development and use of a Boger test fluid, so that the influence of inertia was negligible and deviations of the velocity field from that of Stokes flow could be unambiguously attributed to the elastic nature of the fluid.

The wavelength of the three-dimensional, steady flow in the "neutral" x-direction scaled with the upstream half-height, H, and extended on the order of H upstream of the contraction plane. These scalings indicated that the global instability described in Chapter

5 was associated with flow around the *outer* corner of the contraction, instead of the *reentrant* corner. The spatial structure of the flow in the planar contraction resembled the "Görtler-like" vortices observed in simple, viscoelastic shear flows with curved streamlines. This resemblance, in conjunction with the noted importance of curved streamlines around the outer corner, led to the hypothesis that the transition to three-dimensional, steady flow in the planar contraction was driven by the interaction between streamline curvature and stress along the streamlines (McKinley *et al.*, 1996; Larson *et al.*, 1990; Joo and Shaqfeh, 1994). To quantitatively explore the role of the stress-curvature interaction, the concept of a "viscoelastic Görtler" scaling proposed by McKinley et al. (1996) was applied. The functional form of the relation between the critical upstream Weissenberg number for onset of the spatial instability ($Wi_{Up\ S}$) and the contraction ratio of the geometry derived from the scaling was able to fit the data. However, the relation contained an additional parameter, not present in the relation used by McKinley et al. (1996), which probably played the role of relating the characteristic curvature of the streamlines to the contraction ratio of the flow.

A second, temporal transition to time-dependent flow was identified which generally occurred at a critical upstream Weissenberg number ($Wi_{Up\ T}$) greater than that associated with transition from two- to three-dimensional flow, i.e. $Wi_{Up\ T} > Wi_{Up\ S}$. Observation of a decrease in amplitude of the temporal oscillation with increasing distance from the wall bounding the "neutral" x-dimension supported the hypothesis that the time-dependent flow was induced not only by the interaction of streamwise stress with streamline curvature in the yz-plane of the flow but also by a three-dimensional perturbation to the flow introduced by the wall bounding the x-dimension. The temporal instability appeared to be a fundamentally local phenomenon, most pronounced near the bounding wall. Similarities in the temporal structure of time-dependent flows through planar geometries of different contraction ratios were identified. Specifically, the period of temporal oscillation was of the same order for all the geometries, approximately 100 [s]. However, relation of this value of the period to specific parameters characteristic of the test fluid and/or the flow was not obvious; the characteristic relaxation time of the test fluid was much shorter, on the order of 1 [s]. Despite the greater complexity of the conditions which induce transition to time-dependent flow, the same functional form of the relation between the critical Weis-

senberg number and the contraction ratio, used for fitting the transition to three-dimensional, steady flow, was applied to the temporal transition. A good fit to the data was obtained. The curves obtained from the fits to the onset conditions ($Wi_{Up\ S} = Wi_{Up\ S}(H/h)$) for the spatial transition and for the temporal transition ($Wi_{Up\ T} = Wi_{Up\ T}(H/h)$) were observed to intersect at a value of H/h such that for the corresponding upstream aspect ratio, W/2H, only order one wavelength would fit across half the width of the "neutral" x-dimension of the test geometry. This observation further supported the idea that the transition to time-dependent flow was related to the presence of walls bounding the x-dimension.

Parallels between the spatiotemporal structure of flow transitions observed in the planar contraction and transitions in viscoelastic flow through other geometries were identified. For example, the form of counter-rotating vortices was common to the planar contraction, cylinder-in-channel, and driven-cavity flows [Byars, 1996 #14; McKinley, 1991 #15; Özetkin, 1995 #38; McKinley, 1996 #10]. The findings presented in Chapter 5 serve to develop understanding of conditions which control flow transition in the planar contraction and the spatiotemporal structure of the resultant flow. This information is useful for future investigations. Specifically, the determination of critical parameters for onset of three-dimensional flow and identification of regions in which three-dimensional flow occurs indicates where and under what conditions birefringence measurements may be directly interpreted in terms of stress. Identification of onset conditions for transition to three-dimensional and time-dependent flow also provides bounds on the validity of two-dimensional, steady numerical simulations of viscoelastic flow.

Three-dimensional and time-dependent simulations of viscoelastic flows are expected to become tractable in the near future. The quantitative data presented in Chapter 5 provide a benchmark with which the accuracy of these computations may be assessed. Such simulations may be necessary to obtain a deeper, more quantitative understanding of the role played by interaction between streamline curvature and streamwise stress in the transition from the base flow to three-dimensional, steady flow. Specifically, transition in flows for which the velocity-gradient field of the base flow is complex (has both shear and elongational components) are not amenable to study via analytical methods, such as have

been applied to transitions associated with simple base flows (Larson *et al.*, 1990; Joo and Shaqfeh, 1994; Özetkin and Brown, 1994; McKinley *et al.*, 1995).

Numerical simulations may play a crucial role in elucidating the mechanism which induces transition from steady to time-dependent flow. Stress- and velocity-field information can be rapidly acquired for geometries in which boundary conditions can be ideal (e.g. truly two-dimensional) and chosen at will. This quality could facilitate the development of a map of viscoelastic flow transitions in planar contraction geometries with finite upstream aspect ratio. In particular, the neutral stability boundary for onset of time-dependent flow would lie in a three-dimensional parameter space with Wi_{Up}, upstream aspect ratio (W/2H), and contraction ratio (H/h) as independent variables. Computational fluid dynamics, in conjunction with selected experiments, could elucidate the form of the curve which demarcates the codimension-2 bifurcation at the intersection of the neutral stability boundary associated with transition from two-dimensional to three-dimensional flow with the boundary associated with transition from steady to time-dependent flow. Location of the curve in parameter space could be coupled with experiments directed at determination of spatiotemporal dynamics in the vicinity of the codimension-2 bifurcation and identification of any essential differences with the dynamics associated with other regions in parameter space. For example, quasiperiodic or chaotic behavior may occur near the codimension-2 bifurcation.

The stress response of a viscoelastic fluid to the transient shearfree elongational flow on the centerline of the planar contraction was investigated and described in Chapter 6. Two sets of conclusions were drawn from the study. First, the efficacy of transient strain-rate profiles of the type on the centerline of the planar contraction in exciting a nonlinear viscoelastic response was assessed. Second, information on the application of the FIB technique to acquisition of stress-field data in complex viscoelastic flows was obtained.

Experimental results in conjunction with the predictions of linear and nonlinear constitutive models indicated that the centerline flow could only excite a weakly nonlinear viscoelastic response. This result was surprising; the total Hencky strain of $\varepsilon = 3.5$ (for the 32:1 contraction) and high maximum strain rates attained on the centerline of the planar contraction would have resulted in excitation of a nonlinear response if the flow were homogeneous. The stimulation of an essentially linear response on the centerline of the

planar contraction was attributed to the particular form of the transient and nonhomogeneous elongational strain-rate profile, in conjunction with the large contribution of the Newtonian solvent which masked any deviation from a linear response. This finding underscored the need to consider the entire strain history of a viscoelastic fluid element when estimating its stress response (Ferguson and Hudson, 1993; Malkin and Petrie, 1997); the representation of the strain history by a small subset of characteristic values (e.g. total Hencky strain and maximum strain rate) can lead to erroneous conclusions.

Different approaches to modify the flow field in order to enhance a nonlinear response were explored. Increasing the volumetric flow rate to increase the magnitude of the strain-rate profile or increasing the contraction ratio to increase the total Hencky strain did not result in stimulation of a strong nonlinear response. Modification of the form of the centerline strain-rate profile to more closely approximate a homogeneous flow, which can induce a strong nonlinear response, was then considered. In particular, tapering of the entry region of the planar contraction was explored computationally. However, tapering of the entry region did not modify the essential form of the centerline strain-rate profile.

In §6.6, the streamwise stress along the off-centerline curved streamlines was considered in light of the results presented and discussed in Sections 6.4 and 6.5. Since the stress and strain history along streamlines away from the centerline were not measured, the corner-flow solution of Moffat (1964) was used. Consideration of the Moffat solution alone could not determine whether the elongational strain experienced by a fluid element moving along a curved streamline would result in streamwise stresses substantially greater than if only the shear components of the velocity-gradient tensor were present. However, two limiting scenarios were identified. In the first scenario, the fluid has a short relaxation time, so that at the point of maximum curvature on the streamline nearly all prior strain history will have been "forgotten". Since the elongational components of the velocity-gradient tensor are vanishingly small near the point of maximum curvature, the streamwise stress is not be affected by the response of the fluid to the elongational components. In the second scenario, the fluid has a long relaxation time, such that a fluid element recalls the elongational strain experienced during its passage from the upstream region to the point of maximum curvature. In consequence, the streamwise stress may be substantially elevated above the level associated with the shear components of the velocity-gradient tensor. Since

the Moffat solution is restricted to the corner region (and strictly only applies to Newtonian flows) full-field numerical simulation is required to determine which of these scenarios is appropriate for a given flow and to calculate the magnitude of the streamwise stresses in the regions of high curvature.

Information pertaining to application of the FIB technique for determination of the stress field in complex viscoelastic flows was obtained in this thesis. Shear-induced turbidity, which has been observed for polymer solutions, can induce beam divergence and prevent FIB measurements from being taken (Byars, 1992; Quinzani *et al.*, 1992; Helfand and Frederickson, 1989; Krämer-Lucas *et al.*, 1988a; Krämer-Lucas *et al.*, 1988b; Osaki *et al.*, 1979; Rangel-Nafaile *et al.*, 1984; Yanase *et al.*, 1991). To avoid this problem, a two-component Boger test fluid was developed for the experiments of this thesis. Exclusion of a ternary cosolvent eliminated the problem of shear-induced turbidity. Additional research must be performed to elucidate the mechanism of shear-induced turbidity; this active area of investigation lies outside of the scope of this thesis. However, the development of a Boger fluid for which shear-induced turbidity is not observed provides a useful tool for experimental viscoelastic fluid mechanics research.

This thesis delineated the effect of inhomogeneities in the stress field on interpretation of FIB measurements in terms of the stress field. Stress-field inhomogeneities over the area of the probe beam prevented direct interpretation of the birefringence measurement in terms of the stress field in the region of the flow downstream of the contraction plane. The effect of variation of the stress field along the beam path was also considered. The order of magnitude of the error introduced by stress-field inhomogeneities along the path and within the cross-sectional area of the probe beam for measurements conducted in the upstream region of the planar contraction flow was estimated.

The investigation presented in Chapter 6 has advanced understanding of the response of viscoelastic fluids to transient nonhomogeneous elongational flows. Knowledge of the potential and limitations of the FIB technique in determining the stress field in viscoelastic flows has also been developed. These findings may motivate new research. For example, one of the primary contributions of the thesis has been the identification of the inefficacy of the stress-growth region on the centerline of planar contraction flow in characterizing the nonlinear elongational response of fluids in which a large contribution to the viscosity

arises from the Newtonian solvent. However, in other viscoelastic materials, which do not have a large solvent contribution to the viscosity (e.g. polymer melts), the accuracy of a given nonlinear constitutive model could possibly be assessed.

Another potential area for future investigation is determination of the stress field in regions of complex flow in the planar contraction and elucidation of the role the stress field plays in transition from the two-dimensional base flow. As alluded to above, numerical simulation could be used to assess the influence of elongational components of the velocity gradient tensor on the streamwise stress along streamlines of high curvature. Verification of the accuracy of the constitutive equation for this complex flow could possibly be attained via FIB measurement along the streamlines. However, high velocity gradients may be present in the vicinity of streamlines of high curvature. As discussed in Chapter 5, stress-field inhomogeneities within the area probed by the FIB beam complicate interpretation of the birefringence measurement in terms of the stress field. Hence, FIB measurements in this region of the flow may not be practical.

Another motivation for study of the stress response in complex flow is to achieve better understanding of the mechanism which drives the two-dimensional rearrangement of streamlines to the diverging flow configuration. Note that two-dimensional, steady numerical simulations of flow through the planar contraction have not predicted the diverging flow which was experimentally observed (Coates, 1992). This may indicate that the constitutive model did not accurately capture the stress response of the fluid to the complex flow away from the centerline, for which elongational and shear components of the velocity-gradient tensor were of similar magnitude. In particular, as discussed in Chapter 2, the shear components may have resulted in "elasticity thinning" and a consequent redistribution of fluid from the centerline to the region closer to the wall bounding the y-dimension (McKinley, 1991). Should FIB measurement along the streamlines which have high curvature prove feasible, the information could prove useful in elucidating the factors which induce streamline rearrangement to the diverging flow configuration. From a rheological point of view, comparison of numerical predictions of stress with experimental measurements along streamlines away from the centerline will allow evaluation of constitutive models in regions of complex flow. In particular, the question can be addressed: does accuracy of a constitutive equation in the context of exclusively shear or shearfree rate-of-

strain fields necessarily imply that the equation will be accurate for a complex rate-of-strain field having both shear and elongational character?

A considerable challenge is the acquisition of stress-field information for three-dimensional and/or nonplanar flows via the FIB technique. As discussed above, three-dimensional and time-dependent flow simulation may provide insight into the mechanism driving flow transition in the planar contraction. In general, the stress field of a flow is a more sensitive function of the rheological properties of a viscoelastic fluid (or the parameters of the constitutive equation for the case of numerical simulation) than the velocity field. In consequence, experimental determination of the stress field in complex flows would be a useful tool for evaluating the accuracy of three-dimensional, time-dependent numerical simulations. As discussed in Chapter 3, deconvolution of birefringence data in three-dimensional or nonplanar flows via a tomographic technique is probably only possible for flows with a high degree of symmetry, such as axisymmetric flows (Funatsu and Kajiwara, 1988; Funatsu *et al.*, 1988; Andrienko *et al.*, 1992b; Andrienko *et al.*, 1992a). However, an alternative to deconvolution is the direct comparison of measured birefringence with birefringence predicted from numerical simulation. Specifically, birefringence data, in conjunction with full-field velocity information, can be experimentally acquired for a three-dimensional flow. The velocity-field information can then be used, together with a constitutive model, to predict the stress field. The computed three-dimensional stress field are then be used to *predict* the apparent birefringence (and extinction angle) for a set of FIB probe beams (Li and Burghardt, 1995). The predicted birefringence can then be compared with the measured quantities; a match confirms the accuracy of the constitutive equation for the particular flow. One problem in this approach is the potential for non-uniqueness; i.e., different stress fields can yield the same apparent birefringence for a given probe beam. However, knowledge of the full velocity field - possibly obtained via DPIV - in conjunction with multiple FIB measurements, especially if these are taken along different directions, should allow identification of a unique solution. A second challenge is analysis of deviation of the predicted from the measured birefringence. Specifically, it is unlikely that a given constitutive equation provides an *exact* match to the data. Criteria must be developed to quantitatively characterize how accurate a constitutive model is, based on the closeness of the predicted and measured birefringence data.

The study of Chapter 6 highlighted the importance of using multiple approaches to understand the response of a viscoelastic fluid to an elongational flow. In particular, to assess the influence of the elongational response in a particular industrial flow, it is generally necessary to use a test system with a similar flow configuration. For example, in fiber-spinning operations, high Hencky strains are achieved. Such high Hencky strains cannot be attained on the centerline of the planar contraction, but can be attained in devices such as the filament-spinning apparatus or the filament-stretching apparatus (Tirtaatmadja and Sridhar, 1995; Sridhar *et al.*, 1991; Spiegelberg *et al.*, 1996; Sridhar *et al.*, 1986; Gupta *et al.*, 1986). However, as discussed in Chapters 2 and 4, such experimental configurations also have associated limitations. In addition to the insight which a particular experimental configuration may provide into a given industrial process, data from a number of such configurations should allow development of an accurate constitutive equation of general applicability to elongational flows.

Chapter 8

References

Adamse, J.W., Janeschitz-Kriegl, H., den Otter, J.L. and Wales, J.L.S. 1968 *J. Polym. Sci. A2* **6**, 871.

Amoco Chemical Company 1992 Amoco Polybutene Physical Properties; Bulletin 12-23,

Andrienko, Y.A., Dubovikov, M.S. and Gladun, A.D. 1992a Optical Tensor Field Tomography: the Kerr Effect and Axisymmetric Integrated Photoelasticity. *J. Optical Society of America* **9**(10), 1765-1768.

Andrienko, Y.A., Dubovikov, M.S. and Gladun, A.D. 1992b Optical Tomography of a Birefringent Medium. *J. Optical Society of America* **9**(10), 1761-1764.

Azzam, R.M.A. 1978 Propagation of Partially Polarized Light through Anisotropic Media with or without Depolarization: A Differential 4 x 4 Matrix Calculus. *J. Optical Society of America* **68**(12), 1756-1767.

Azzam, R.M.A. and Bashara, N.M. 1987 *Ellipsometry and Polarized Light.* North-Holland, Amsterdam.

Baird, D.G. and Collias, D.I. 1995 *Polymer Processing: Principles and Design.* Butterworth-Heinemann, Boston.

Batchelor, G.K. 1967 *An Introduction to Fluid Dynamics.* Cambridge University Press, Cambridge.

Baumert, B.M. and Muller, S.J. 1995 Flow Visualization of the Elastic Taylor-Couette Instability in Boger Fluids. *Rheol. Acta* **34**, 147-159.

Binding, D.M. and Walters, K. 1988 On the Use of Flow Through a Contraction in Estimating the Extensional Viscosity of Mobile Polymer Solutions. *J. Non-Newtonian Fluid Mech.* **30**, 233-250.

Bird, R.B., Armstrong, R.C. and Hassager, O. 1987a *Dynamics of Polymeric Liquids. Volume 1: Fluid Mechanics.* 2nd Edition, Wiley, New York.

Bird, R.B., Curtiss, C.F., Armstrong, R.C. and Hassager, O. 1987b *Dynamics of Polymeric Liquids. Volume 2: Kinetic Theory.* 2nd Edition, Wiley, New York.

Bird, R.B. and DeAguiar, J.R. 1983 *J. Non-Newtonian Fluid Mech* **13**, 149-160.

Bird, R.B., Stewart, W.E. and Lightfoot, E.N. 1960 *Transport Phenomena.* Wiley, New York.

Boger, D.V. 1977/1978 A Highly Elastic, Constant-Viscosity Fluid. *J. Non-Newtonian Fluid Mech.* **3**, 87-91.

Boger, D.V., Hur, D.U. and Binnington, R.J. 1986 Further Observations of Elastic Effects in Tubular Entry Flows. *J Non-Newtonian Fluid Mech.* **20**, 31-49.

Box, G.E.P., Hunter, W.G. and Hunter, J.S. 1978 *Statistics for Experimenters: An Introduction to Design, Data Analysis, and Model Building.* Wiley, New York.

Brandup, J. and Immergut, E.H. (Eds.) 1975 *Polymer Handbook*, Wiley, New York.

Brodnyan, J.G., Gaskins, F.H. and Philippoff, W. 1957 On Normal Stresses, Flow Curves, Flow Birefringence, and Normal Stresses of PIB Solutions. Part II: Experimental. *Trans. Soc. Rheol.* **1**, 109-118.

Byars, J.A. 1992 *personal communication.*

Byars, J.A. 1996 Experimental Characterization of Viscoelastic Flow Instabilities. Ph.D. thesis, Massachusetts Institute of Technology, Cambridge, MA.

Chiba, K., Sakatani, T. and Nakamura, K. 1990 Anomalous Flow Patterns in Viscoelastic Entry Flow through a Planar Contraction. *J. Non-Newtonian Fluid Mech.* **36**, 193-203.

Chiba, K., Tanaka, S. and Nakamura, K. 1992 The Structure of Anomalous Entry Flow Patterns through a Planar Contraction. *J. Non-Newtonian Fluid Mech.* **42**, 315-322.

Chow, A.W. and Fuller, G.G. 1984 Response of Moderately Concentrated Xanthan Gum Solutions to Time-Dependent Flows using Two-Color Flow Birefringence. *J. Rheol.* **28**, 23-43.

Chow, A.W. and Fuller, G.G. 1985 Some Experimental Results on the Development of Couette Flow for Non-Newtonian Fluids. *J. Non-Newtonian Fluid Mech.* **17**, 233-243.

Coates, P.J. 1992 Simulation of the Flow of Viscoelastic Fluids in Contraction Geometries. Ph.D. thesis, Massachusetts Institute of Technology, Cambridge, MA.

Cogswell, F.N. 1968 *Plast. Polym.* **36**, 109-111.

de Gennes, P.G. 1971 *J. Chem. Phys.* **55**, 572-579.

de Gennes, P.G. 1974 Coil-Stretch Transition of Dilute Flexible Polymers under Ultrahigh Velocity Gradients. *J. Chem. Phys.* **60**(12), 5030-5042.

de Gennes, P.G. 1979 *Scaling Concepts in Polymer Physics.* Cornell University Press, Ithaca, NY.

DeAguiar, J.R. 1983 *J. Non-Newtonian Fluid Mech.* **13**, 161-179.

Doi, M. and Edwards, S.F. 1978 *J. Chem. Soc., Faraday Trans. II* **74**, 1789-1832.

Doi, M. and Edwards, S.F. 1979 *J. Chem. Soc., Faraday Trans. II* **75**, 38-154.

Doi, M. and Edwards, S.F. 1986 *The Theory of Polymer Dynamics.* Oxford University Press, New York.

Drain, L.E. 1980 *The Laser Doppler Velocimetry Technique.* John Wiley & Sons, Chichester.

Dupuis, D., Layec, Y. and Wolff, C. 1986 In *Optical Properties of Polymers.* Meeten, G. (Ed.) Elsevier, London.

Durnin, J., Miceli, J.J. and Eberly, J.H. 1987 Reply to 'Comment on "Diffraction-Free" Beams'. *Phys. Rev. Lett.* **59**(22), 2612.

Durst, F., Melling, A. and Whitelaw, J.H. 1981 *Principles and Practice of Laser-Doppler Anemometry.* Second Edition, Academic Press, London.

Evans, R.E. and Walters, K. 1989 Further Remarks on the Lip-Vortex Mechanism of Vortex Enhancement in Planar-Contraction Flows. *J. Non-Newtonian Fluid Mech.* **32**, 95-105.

Ferguson, J. and Hudson, N.E. 1993 Transient Elongational Rheology of Polymeric Fluids. *Eur. Polym. J.* **29**(2/3), 141-147.

Ferry, J.D. 1980 *Viscoelastic Properties of Polymers.* John Wiley & Sons, New York.

Flory, P.J. 1953 *Principles of Polymer Chemistry.* Cornell University Press, Ithaca.

Franck, A. and Meissner, J. 1984 *Rheol. Acta* **23**, 117-123.

Frattini, P.L. and Fuller, G.G. 1984 A Note on Phase-Modulated Flow Birefringence: A Promising Rheo-Optical Method. *J. Rheol.* **28**, 61-70.

Fukuda, M., Wilkes, G.L. and Stein, R.S. 1971 Stress-Optical Coefficient of Poly-1,4-butadienes. *J. Polym. Sci. A2* **9**, 1417-1447.

Fuller, G.G. 1990 Optical Rheometry. *Annu. Rev. Fluid Mech.* **22**, 387-417.

Fuller, G.G. 1995 *Optical Rheometry of Complex Fluids.* Oxford University Press, New York.

Fuller, G.G., Cathey, C.A., Hubbard, B. and Zebrowski, B.E. 1987 Extensional Viscosity Measurements for Low-Viscosity Fluids. *J. Rheol.* **31**(3), 235-249.

Funatsu, K. and Kajiwara, T. 1988 Approximate Analysis of an Axisymmetric Field of Stress by a Transmitted-Light, Flow-Birefringence Technique. *International Chemical Engineering* **28**(3), 504-511.

Funatsu, K., Kajiwara, T. and Shiraishi, Y. 1988 Stress Distribution and Drag Force in Creeping Flow around a Falling Sphere. Measurement by a Flow-Birefringence Technique. *International Chemical Engineering* **28**(4), 634-641.

Galante, S.R. 1991 An Investigation of Planar Entry Flow Using a High-Resolution Flow Birefringence Method. Ph.D. thesis, Carnegie Mellon University, Pittsburgh, PA.

Galante, S.R. and Frattini, P.L. 1993 Spatially Resolved Birefringence Studies of Planar Entry Flow. *J. Non-Newtonian Fluid Mech.* **47**, 289-337.

Giesekus, H. 1982a A Simple Constitutive Equation for Polymer Fluids Based on the Concept of Deformation-Dependent Tensorial Mobility. *J. Non-Newtonian Fluid Mech.* **11**, 69-109.

Giesekus, H. 1982b A Unified Approach to a Variety of Constitutive Models for Polymer Fluids Based on the Concept of Configuration-Dependent Molecular Mobility. *Rheol. Acta.* **21**, 366-375.

Giesekus, H. 1983 *J. Non-Newtonian Fluid Mech.* **12**, 367-374.

Gortemaker, F.H., Hansen, M.B., deCindo, B., Laun, H.M. and Janeschitz-Kriegl, H. 1976 Redesigned Cone-and-Plate Apparatus for Measurement of Flow Birefringence of Polymer Melts. *Rheol. Acta* **15**, 242-256.

Guckenheimer, J. and Holmes, P. 1983 *Nonlinear Oscillations, Dynamical Systems, and Bifurcations of Vector Fields.* Springer-Verlag, New York.

Gupta, R.K., Puszynski, J. and Sridhar, T. 1986 Steady Spinning of the Oldroyd Fluid B. I: Theory. *J. Non-Newtonian Fluid Mech.* **21**, 99-113.

Helfand, E. and Frederickson, G.H. 1989 Large Fluctuations in Polymer Solutions under Shear. *Phys. Rev. Lett.* **62**(21), 2468-2471.

Hinch, E.J. 1977 Mechanical Models of Dilute Polymer Solutions in Strong Flows. *Physics of Fluids, Pt. II* **20**(10), S22-S30.

Hinch, E.J. 1994 Uncoiling a Polymer Molecule in a Strong Extensional Flow. *J. Non-Newtonian Fluid Mech.* **54**, 209-230.

Janeschitz-Kriegl, H. 1969 Flow Birefringence of Elastico-Viscous Polymer Systems. *Adv. Polym. Sci.* **6**, 170-318.

Jones, D.M., Walters, K. and Williams, P.R. 1987 On the Extensional Viscosity of Mobile Polymer Solutions. *Rheol. Acta.* **26**, 20-30.

Joo, Y.L. and Shaqfeh, E.S.G. 1992 A Purely Elastic Instability in Dean and Taylor-Dean Flow. *Phys. Fluids A* **4**(3), 524-543.

Joo, Y.L. and Shaqfeh, E.S.G. 1994 Observations of Purely Elastic Instabilities in the Taylor-Dean Flow of a Boger Fluid. *J. Fluid Mech.* **262**, 27-73.

Joseph, D.D. 1990 *Fluid Dynamics of Viscoelastic Liquids.* Springer-Verlag, New York.

Kobe, J.M. and Wiest, J.M. Finitely Extensible Beas-Spring Chain Macromolecules in Steady Elongational Flows. *J. Rheol.*

Krämer-Lucas, H., Schenck, H. and Wolf, B.A. 1988a Influence of Shear on the Demixing of Polymer Solutions, 1: Apparatus and Experimental Results. *Makromol. Chem.* **189**, 1613-1625.

Krämer-Lucas, H., Schenck, H. and Wolf, B.A. 1988b Influence of Shear on the Demixing of Polymer Solutions, 2: Stored Energy and Theoretical Calculations. *Makromol. Chem.* **189**, 1627-1634.

Kuhn, W. and Kuhn, H. 1943 Die Frage nach der Aufrollung von Fadenmolekeln in strömenden Lösungen. *Helv. Chim. Acta* **26**, 1394-1465.

Lamb, H. 1945 *Hydrodynamics.* Dover, New York.

Larson, R.G. 1988 *Constitutive Equations for Polymer Melts and Solutions.* Butterworths, Boston.

Larson, R.G., Shaqfeh, E.S.G. and Muller, S.J. 1990 A Purely Elastic Instability in Taylor-Couette Flow. *J. Fluid Mech.* **218**, 573-600.

Laun, H.M. and Münstedt, H. 1976 *Rheol. Acta* **15**, 517-524.

Laun, H.M. and Schuch, J. 1989 Transient Elongational Viscosities and the Drawability of Polymer Melts. *J. Rheol.* **33**, 110-175.

Leal, L.G. 1992 *Laminar Flow and Convective Transport Processes: Scaling Principles and Asymptotic Processes.* Butterworth-Heinemann, Boston.

Li, J.-M. and Burghardt, W.R. 1995 Flow Birefringence in Axisymmetric Geometries. *J. Rheol.* **39**(4), 743-766.

Lodge, A.S. 1955 Variation of Flow Birefringence with Stress. *Nature* **176**, 838-839.

Lodge, A.S. 1956 A Network Theory of Flow Birefringence and Stress in Concentrated Polymer Solutions. *Trans. Faraday Soc.* **52**, 120-130.

Malkin, A.Y. and Petrie, C.J.S. 1997 Some Conditions for Rupture of Polymer Liquids in Extension. *J. Rheol.* **41**(1), 1-25.

Matthys, E.F. and Khatami, M. 1988 Local Measurements of Velocity and Deformation Rates in Extensional Flows of Polymer Solutions: The Aspirated Jet. In *Proc. X^{th} Intl. Cong. Rheol.*, **2**, *Sydney.*

McKinley, G.H. 1991 Nonlinear Dynamics of Viscoelastic Flows in Complex Geometries. Ph.D. thesis, Massachusetts Institute of Technology, Cambridge, MA.

McKinley, G.H. 1997 *personal communication.*

McKinley, G.H., Özetkin, A., Byars, J.A. and Brown, R.A. 1995 Self-Similar Spiral Instabilities in Elastic Flows Between a Cone and a Plate. *J. Fluid Mech.* **285**, 123-164.

McKinley, G.H., Pakdel, P. and Özetkin, A. 1996 Geometric and Rheological Scaling of Purely Elastic Flow Instabilities. *J. Non-Newtonian Fluid Mech.* **67**, 19-48.

McKinley, G.H., Raiford, W.P., Brown, R.A. and Armstrong, R.C. 1991 Nonlinear Dynamics of Viscoelastic Flow in Axisymmetric Abrupt Contractions. *J. Fluid Mech.* **223**, 411-456.

Meissner, J. 1971 *Rheol. Acta* **10**, 230-242.

Meissner, J. 1985 *Chem. Eng. Commun.* **33**, 159-180.

Moan, M. and Mageur, A. 1988 Transient Extensional Viscosity of Dilute Flexible Polymer Solutions. *J. Non-Newtonian Fluid Mech.* **30**, 343-354.

Moffat, H.K. 1964 Viscous and Resistive Eddies Near Sharp Corners. *J. Fluid Mech.* **18**, 1-18.

Müller, A.J. 1988 Elongational Flow and Rheology of Monodisperse Polymers in Solution. *J. Non-Newtonian Fluid Mech.* **30**, 99-118.

Muller, S.J. 1986 Experimental Analysis of Flow through an Axisymmetric Sudden Contraction: Rheological Characterization and LDV Measurements. Ph.D. thesis, Massachusetts Institute of Technology, Cambridge, MA.

Muller, S.J. 1992 *personal communication.*

Münstedt, H. 1975 *Rheol. Acta.* **14**, 1077-1088.

Münstedt, H. 1979 *J. Rheol.* **23**, 421-436.

Ng, R.C.-Y. and Leal, L.G. 1993 Concentration Effects on Birefringence and Flow Modification of Semidilute Polymer Solutions in Extensional Flows. *J. Rheol.* **37**(3), 443-468.

Nguyêñ, H. and Boger, D.V. 1979 The Kinematics and Stability of Die Entry Flows. *J. Non-Newtonian Fluid Mech.* **5**, 353-368.

Oldroyd, J.G. 1984 *J. Non-Newtonian Fluid Mech.* **14**, 9-46.

Oliver, D.R. 1994 Stretching Flow Tests on Liquid S! and Similar Liquids. *J. Non-Newtonian Fluid Mech.* **52**, 183-195.

Onuki, A. 1989 Elastic Effects in the Phase Transition of Polymer Solutions under Shear Flow. *Phys. Rev. Lett.* **62**(21), 2472-2475.

Osaki, J., Bessho, N., Kojimoto, T. and Kurata, M. 1979 Flow Birefringence of Polymer Solutions in Time-Dependent Field. *J. Rheol.* **23**, 457-475.

Öttinger, H.C. 1996 Cracking Polymer Kinetic Theory. In *XIIth Int. Congr. on Rheology, Quebec City, Canada.*

Özetkin, A. and Brown, R.A. 1994 Quantitative Prediction of the Viscoelastic Instability in Cone-and-Plate Flow of a Boger Fluid Using a Multi-Mode Giesekus Model. *J. Non-Newtonian Fluid Mech.*

Özetkin, A., Byars, J.A., Liu, A.W., Armstrong, R.C. and Brown, R.A. 1997 Three-Dimensional Wake Instability in Viscoelastic Flow past a Cylinder: Theory and Experiment. in preparation.

Pakdel, P. and McKinley, G.H. 1996 Elastic Instability and Curved Streamlines. *Phys. Rev. Lett.* **77**(12), 2459-2462.

Pakdel, P. and McKinley, G.H. 1997 Digital Particle Imaging Velocimetry of Viscoelastic Fluids. *AICHE J.* in press.

Pakdel, P., Spiegelberg, S.H. and McKinley, G.H. 1997 Cavity Flows of Elastic Liquids: Two-Dimensional Flows. *Physics of Fluids* submitted.

Philippoff, W. 1956 Flow Birefringence and Stress. *J. Appl. Phys.* **27**(9), 984-989.

Philippoff, W. 1962 The Rheology of Polymer Solutions in Oil. *J. Polym. Sci.* **57**, 141-159.

Piau, J.-M., El Kissi, N. and Tremblay, B. 1990 Influence of Upstream Instabilities and Wall Slip on Melt Fracture and Sharkskin Phenomena during Silicones Extrusion through Orifice Dies. *J. Non-Newtonian Fluid Mech.* **34**, 145-180.

Pindera, J.T. and Hecker, F.W. 1987 Basic Theory and Experimental Techniques of the Strain-Gradient Method. *Expt. Meth.* **27**(3), 314-327.

Press, W.H., Flannery, B.P., Teukolsky, S.A. and Vetterling, W.T. 1988 *Numerical Recipes in C: The Art of Scientific Computing.* Cambridge University Press, Cambridge.

Proc. of Int'l Conf. on Extensional Flow 1990 Project M1. *J. Non-Newtonian Fluid Mech.* **35**, 85-470.

Quinzani, L.M. 1991 Birefringence Studies of Entry Flows of Concentrated Polymer Solutions. Ph.D. thesis, Massachusetts Institute of Technology, Cambridge, MA.

Quinzani, L.M., Armstrong, R.C. and Brown, R.A. 1994 Birefringence and Laser-Doppler Velocimetry (LDV) Studies of Viscoelastic Flow through a Planar Contraction. *J. Non-Newtonian Fluid Mech.* **52**, 1-36.

Quinzani, L.M., Armstrong, R.C. and Brown, R.A. 1995 Use of Coupled Birefringence and LDV Studies of Flow through a Planar Contraction to Test Constitutive Equations for Concentrated Polymer Solutions. *J. Rheol.* **39**(6), 1201-1228.

Quinzani, L.M., Byars, J.A. and Banks, A. 1992 *personal communication.*

Quinzani, L.M., McKinley, G.H., Brown, R.A. and Armstrong, R.C. 1990 Modeling the Rheology of Polyisobutylene Solutions. *J. Rheol.* **34**(5), 705-748.

Raiford, W.P. 1989 Laser Doppler Velocimetry Measurements of Nonlinear Viscoelastic Flow Transitions in the Axisymmetric Sudden Contraction. Ph.D. thesis, Massachusetts Institute of Technology, Cambridge, MA.

Rangel-Nafaile, C., Metzner, A.B. and Wissbrun, K. 1984 Analysis of Stress-Induced Phase Separations in Polymer Solutions. *Macromolecules* **17**, 1187-1195.

Reiner, M. 1964 The Deborah Number. *Physics Today* **17**(Jan.), 62.

Rodriguez, F. 1989 *Principles of Polymer Systems.* Hemisphere, New York.

Rosen, S.L. 1982 *Fundamental Principles of Polymeric Materials.* Wiley, New York.

Saric, W.S. 1994 Görtler Vortices. *Annu. Rev. Fluid Mech.* **26**, 379-409.

Schmidt, J.R. and Wolf, B.A. 1979 *Colloid. Polym. Sci.* **257**, 1188.

Schunk, P.R., de Santos, J.M. and Scriven, L.E. 1990 Flow of Newtonian Liquids in Opposed-Nozzles Configuration. *J. Rheol.* **34**(3), 387-414.

Shaqfeh, E.S.G. 1996 Brownian Dynamics Simulation of Polymer Rheology: Local and NonLocal Problems, Massachusetts Institute of Technology, Cambridge, MA.

Soskey, P.R. and Winter, H.H. 1985 Equibiaxial Extension of Two Polymer Melts: Polystyrene and Low-Density Polyethylene. *J. Rheol.* **29**, 493-517.

Spiegelberg, S.H., Ables, D.C. and McKinley, G.H. 1996 The Role of End-Effects on Measurements of Extensional Viscosity in Filament Stretching Rheometers. *J. Non-Newtonian Fluid Mech.* **64**, 229-267.

Sridhar, T., Gupta, R.K., Boger, D.V. and Binnington, R. 1986 Steady Spinning of the Oldroyd Fluid B. II: Experimental Results". *J. Non-Newtonian Fluid Mech.* **21**, 115-126.

Sridhar, T., Tirtaatmadja, V., Nguyen, D.A. and Gupta, R.K. 1991 Measurement of Extensional Viscosity of Polymer Solutions. *J. Non-Newtonian Fluid Mech.* **40**, 271-280.

Strogatz, S.H. 1995 *Nonlinear Dynamics and Chaos.* Addison-Wesley, Reading, MA.

Sureshkumar, R., Beris, A.N. and Avgousti, M. 1994 Non-Axisymmetric Subcritical Bifurcations in Viscoelastic Taylor-Couette Flow. *Proc. R. Soc. Lond. A* **447**, 135-153.

Tanner, R.I. and Huilgol, R.R. 1975 *Rheol. Acta.* **14**, 959-962.

Theocaris, P.S. and Gdoutos, E.E. 1979 *Matrix Theory of Photoelasticity.* Springer-Verlag, Berlin.

Tirtaatmadja, V. and Sridhar, T. 1995 Comparison of Constitutive Equations for Polymer Solutions in Uniaxial Extension. *J. Rheol.* **39**(6), 1133-1160.

TSI Seminar on Laser Doppler Velocimetry (LDV) and Particle Image Velocimetry (PIV),

van Egmond, J.W. and Fuller, G.G. 1993 Concentration Fluctuation Enhancement in Polymer Solutions by Extensional Flow. *Macromolecules* **26**, 7182-7188.

Vinogradov, G.V., Fikhman, V.D. and Radushkevich, B.V. 1972 *Rheol. Acta* **11**, 286-291.

Vinogradov, G.V., Radushkevich, B.V. and Fikhman, V.D. 1970 *J. Polym. Sci., A2* **8**, 1-17.

Wales, J.L.S. 1976 The Application of Flow Birefringence to Rheological Studies of Polymer Melts. Delft University, Delft, The Netherlands.

Walters, K. 1992 Recent Developments in Rheometry. In *Theoretical and Applied Rheology,* **1**, *Brussels,*Elsevier.

Weast, R.C., Astle, M.J. and Beyer, W.H. (Eds.) 1987 *CRC Handbook of Chemistry and Physics*, CRC Press, Boca Raton, Florida.

Wiest, J.M. Birefringence in Strong Flows of Dilute Polymer Solutions. *J. Non-Newtonian Fluid Mech.*

Yanase, H., Moldenaers, P., Mewis, J., Abetz, V., van Egmond, J. and Fuller, G.G. 1991 Structure and Dynamics of a Polymer Solution Subject to Flow-Induced Phase Transition. *Rheol. Acta* **30**, 89-97.